

Author name(s)

Book title

– Monograph –

January 4, 2022

Springer Nature

*Use the template dedic.tex together with the
Springer document class SVMono for
monograph-type books or SVMult for
contributed volumes to style a quotation or a
dedication at the very beginning of your book*

Foreword

Use the template *foreword.tex* together with the document class SVMono (monograph-type books) or SVMult (edited books) to style your foreword.

The foreword covers introductory remarks preceding the text of a book that are written by a *person other than the author or editor* of the book. If applicable, the foreword precedes the preface which is written by the author or editor of the book.

Place, month year

Firstname Surname

Preface

This book explores the development of PDE (partial differential equation) backstepping controllers for the suppression of stop-and-go instabilities and oscillations in congested traffic flows. As such, the book should be considered at least as much as an addition to the literature on boundary control of coupled systems of first-order hyperbolic PDEs as an addition to the traffic control literature.

The motivation for the work comes from traffic dynamics in the congested regime. It is only in the congested regime, when the vehicles are relatively close by, that stop-and-go oscillations develop. Stop-and-go is simply the consequence of sensory and cognitive limitations of the humans participating in traffic. Every driver has a reaction delay that is on the order of a second. Moreover, an average human driver is not even able to predict the dynamic response of his own vehicle to the accelerator and brake pedal inputs that he applies, let alone predicting the motion of the vehicle in front of him, and even much less the motion of the whole chain of vehicles further ahead. In conclusion, as long as operating their own vehicles is an option that humans are free to exercise, stop-and-go oscillations will be a part of traffic flows.

Stop-and-go does not only carry a high cost in comfort and frustration. Societal cost in traffic safety, the additional fuel consumption, and the total driving time are enormous. These are the reasons that make even partial suppression of stop-and-go oscillations an important pursuit.

For us personally, the importance of this pursuit is not less worthy due to the complex control design task of developing feedback laws for the extremely high-dimensional traffic flow systems, whose neatest modeling is in the form of PDEs, and which, in spite of their high dimensionality, have to be controlled using one or very few inputs, such as ramp metering or variable speed limits. That one input, or those few inputs, are located at boundaries of freeway segments and the entire traffic between the locations of such inputs, which involves hundreds, and sometimes thousands of vehicles, needs to be controlled from the boundary. It is this type of a control design challenge that attracts PDE control designers to traffic flows.

While variable speed limit signs are not uncommon in certain metropolitan areas, ramp metering, applied with traffic lights that let on only one or two cars onto the freeway, at certain time intervals (on the order of seconds, or tens of seconds), are

very common. By not keeping the length of those time intervals constant, but by varying them instead, it is possible to vary the flow of traffic at the location of the on-ramp.

An increased flow at the on-ramp influences the drivers approaching the on-ramp on the freeway mainline to respond to the increased flow from the on-ramp by slowing down. In particularly concrete terms, the following process takes place: the vehicles entering from the on-ramp are trying to merge into the freeway traffic flow; the drivers on the freeway observe the vehicles entering the freeway on their right; the drivers on the mainline freeway respond to the fact that vehicles are merging from the on-ramp by adjusting their speeds, in order to avoid a collision with the merging vehicles.

So, the modulation of the duration of the red and green lights on the on-ramp influences the speed, and the density, of the vehicles immediately upstream of the on-ramp. How can this control capability of the on-ramp traffic lights be exploited to impact the traffic flow a great distance away from the on-ramp?

Four possibilities exist in this regard. Ramp metering can be employed to control traffic both downstream and upstream. And the traffic on either freeway segment (downstream or upstream of the on-ramp) can be in either the free or the congested regime. So, there exists a set of 2×2 , namely, four combinations of traffic flow possibilities.

Among those four combinations, one is not controllable (traffic upstream of the on-ramp in the free regime), two are trivial, requiring either no control (traffic downstream of the on-ramp in free regime) or a simple collocated proportional feedback (traffic downstream of the ramp in the congested regime), and only one of these four cases is challenging and truly interesting: control of traffic flow upstream of the on-ramp in the congested regime.

How can one possibly control the dynamics of traffic *upstream* of an on-ramp by varying the duration of the on-ramp's traffic lights? In the congested regime, this is possible. In the congested regime, the vehicles are relatively close by and the drivers respond to the changes in the distances relative to the cars immediately in front of them. These responses are "chain reactions," which propagate upstream. In intuitive terms, in congested traffic, the reactions of drivers to the variations in distance progress in the upstream direction faster than the cars move in the downstream direction. It is due to this effect, of a "human behavioral wave" (of braking or accelerating) that modulations of a traffic light at an on-ramp can affect the traffic dynamics a long distance upstream of the ramp.

The colloquial depiction of the possibility of controlling congested traffic upstream of an on-ramp also has its formal, rigorous representation in PDE models of traffic. The suitable model for stop-and-go oscillations is the Aw-Rascle-Zhang (ARZ) model. This model incorporates two coupled nonlinear first-order hyperbolic PDEs, one for the density and one for velocity. In such a model with two hyperbolic PDEs, two waves arise, which propagate in certain directions and at certain speeds. It happens so that in the free traffic the two waves both propagate in the downstream direction, whereas in the congested traffic one wave propagates in the downstream direction whereas the other wave propagates in the upstream direction.

It is this wave in the system of two hyperbolic PDEs, which propagates in the upstream direction in the congested regime, that is related to the drivers' responses to the distance fluctuations and that runs "backward," being passed to the driver behind the reacting driver.

In summary, in the congested regime, the ARZ PDE model of traffic is controllable by ramp metering in the upstream direction. It is this property that we build on, advancing from the mere controllability to a feedback design methodology for stabilizing the stop-and-go oscillations.

Our feedback design is based on the method of *PDE backstepping*. While PDE control can be approached also with linear quadratic (LQR, LQG) methods, as well as methods based on pole placement for reduced models of PDEs, backstepping has the advantages of neither requiring model reduction of the PDE plant nor the approximation of solutions of nonlinear infinite-dimensional equations such as operator Riccati equations.

Backstepping, introduced by the second author, with early contributions by his student Andrey Smyshlyaev and postdocs Weijiu Liu and Andras Balogh, initially for parabolic PDEs, employs a spatial Volterra transformation to convert the plant PDE, which may be unstable, into a "target system." The target system is chosen by the designer, as a PDE of a relatively simple and familiar form, within the same class as the plant PDE. By its very selection, the target system's stability is relatively easy to establish.

The Volterra kernel of the backstepping transformation is a linear PDE of the Goursat form which can be transformed from a PDE into an integral equation. In its integral equation form, this transformation kernel can be computed fairly easily, using successive approximations. The existence and uniqueness of solutions to this kernel PDE can be established much more easily than for operator Riccati equations or other standard PDEs that are not in the Goursat form.

It is for these reasons that PDE backstepping has seen a wide adoption, both among theorists and in PDE control applications. The applications are numerous and we leave out the common strings and beams but emphasize turbulent flows, water canals, phase change in materials, including thermal dynamics with liquid-solid transitions, as in 3D printing, and industrial applications in state estimation for Lithium-ion batteries and in oil drilling.

The interest in developing backstepping controllers for traffic began in 2007, with the one-semester stay of the second author at University of California, Berkeley, where he taught a course on PDE backstepping control. At that time, backstepping was not yet developed for hyperbolic PDEs. The breakthrough in this development took place in the 2013 paper on PDE backstepping for 2×2 hyperbolic systems by Coron, Vazquez, Krstic, and Bastin.

Our work on applying PDE backstepping for hyperbolic PDEs to traffic flows began in 2016 with the development of an adaptive control design for the ARZ model of traffic with unknown parameters. Backstepping makes parameter-adaptivity viable in PDE control due to the nearly-explicit form of the gain functions. This and other results in this book have been developed in the course of the first author's doctoral

and postdoctoral research at UC San Diego with the second author, from 2016 until 2021.

What Does the Book Cover?

Whom Is the Book For?

This book deals with control theory, dynamical systems, partial differential equations, and traffic flows. In integrating these subjects, it may offer material of interest to readers who conduct research in these areas and have training in areas as diverse as electrical engineering, mechanical engineering, civil engineering and transportation, applied mathematics, applied physics, and even machine learning and computer science.

In dealing with suppression of traffic instability, the primary audience of this research monograph are control theorists working on control of systems modeled by PDEs and traffic engineers and applied scientists working unsteady traffic flows.

For PDE control theorists, especially those focusing on feedback design and stability analysis, this book provides an entry point into one of the most exciting application areas for PDE control, especially for application of PDE control of hyperbolic PDEs. While coupled hyperbolic PDEs arise in many relevant sub-areas of flow control, including control of compressible fluids, such as those that are encountered in oil drilling, control of traffic flows offers as much technical challenge as any applications in one-dimensional fluid dynamics, while carrying the potential for orders of magnitude more in societal impact. In fact, stabilization of unsteady congested traffic is arguably the application of PDE control that is the most relatable of for a lay audience. We know no PDE control application for which a non-expert has a comparable level of intuition and unequivocal belief in its importance. For this reason, we are hopeful that this book will serve to advance the interest in PDE control, and especially boundary control of PDEs, beyond the specific content of this book and our own work.

For a PDE control theorist interested in the range of capabilities of the PDE backstepping method we particularly recommend Chapter 9 in which, in the context of a two-class traffic (such as a mix of large/inert and small/agile vehicles, or a mix of defensive and aggressive drivers) a coupled hyperbolic heterodirectional structure of the form $(3 + 1) \times (3 + 1)$ arises, in which a boundary control input (by ramp metering) is available only in one PDE channel, which convects in the upstream direction, whereas the three unactuated PDE channels convect in the downstream direction. This is a good example of the capability of PDE backstepping to stabilize a system of four PDEs using a single boundary input.

For traffic engineers and scientists, this book provides tools that have been previously unavailable for suppressing stop-and-go oscillations in congested traffic using actuation that is very sparsely located along the freeway, such as ramp metering or variable speed limits. During the next one or several decades, until automation of vehicles and their connectivity (such as in CAVs—connected and automated vehicles) achieves sufficient levels of penetration (the pace of which appears a lot slower than the predictions of about a decade ago), and until such vehicle-level automation

makes the suppression of traffic flow instabilities easier to achieve, the advanced and fairly complex methods introduced by this book will be an important option for the designer of traffic flow management systems.

PDE backstepping, the method upon which the designs presented in this book rely, are not simple to learn even for advanced control theorists. So we do not expect these methods' effortless adoption by traffic engineers, whose core training in control may be around methods like LQR or basic nonlinear control for finite-dimensional systems. Cognizant of this challenge, we have made our exposition as accessible as possible, as self-contained as possible, and as stripped of mystifying conventions that are common in the exposition of material within mathematical fields like analysis of PDEs and PDE control. This deliberate commitment to accessibility deprives the more mathematical specialist in PDE control nearly nothing that they will not infer themselves from the context.

Parts of the book will be of interest to control engineers who do not intend to specialize in PDE control but specialize in other areas. For example, a specialist in extremum seeking will be inspired by the role this model-free optimization methodology has to play in traffic control by reading Chapter 14. Likewise, a specialist in delay systems will find it revealing that predictor-based feedback designs, for compensation of input delays, are the key ingredient for regulating the position of a moving shock in traffic density on a congested freeway by reading Chapter 13. A specialist in adaptive control will see how far the boundaries of this classical field can be taken by reading about adaptive control design for the ARZ PDE model of traffic in Chapter 5. A specialist in sampled-data control, used to studies in emulating continuous-time control designs for linear and nonlinear PDEs, will see how those techniques extend to PDE control, with the aid of ISS and small-gain theorems for PDEs, by reading Chapter 6.

Finally, for a specialist outside of the classical field of control theory—a reader interested in reinforcement learning and, more generally, machine learning and AI methods—the book offers, in Chapter 7 a thought-provoking comparison between model-based PDE control and learning-based acquisition of a similar capability through simulation-based training.

Huan Yu
Miroslav Krstic

Acknowledgements

We thank Alexandre Bayen and Qijian Gan for sharing with us their knowledge with us on state estimation of freeway traffic in Chapter 4, as well as Alexandre Bayen, Scott Moura, and Saehong Park for lending us their expertise on Reinforcement Learning Control in Chapter 7. We are grateful to Nicolas Espitia for his contribution to sampled-data design of traffic PDE model in Chapter 6, as well as to Jean Auriol for his contribution to control of the underactuated cascaded freeway systems in Chapter 10. For his contribution in Chapter 9 to control of two-class traffic, we thank Mark Burkhardt, whereas for the contribution in Chapter 12 to control design for traffic flow under routing-induced feedforward instability we thank Stephen Chen. Finally, we appreciate Mamadou Diagne and Liguozhang providing us with the motivation for the traffic shockwave problem in Chapter 13 and thank Tiago Roux Oliveira for his guidance on extremum seeking control of delay system for the downstream bottleneck problem in Chapter 14.

If we have been successful in advancing the subject of stabilization of traffic flows, this has been greatly due to the foundations laid on control of coupled hyperbolic PDEs in collaborations with Rafael Vazquez, Jean-Michel Coron, Georges Bastin, Florent Di Meglio, Long Hu, Federico Bribiesca Argomedo, Andrey Smyshlyaev, and Iasson Karafyllis, as well as the applications of this work with Ole Morten Aamo, Henrik Anfinssen, Agus Hassan, Mamadou Diagne, Shuxia Tang, Pauline Bernard, Ji Wang, Junmin Wang, and Lingling Su.

Much of the inspiration for our attempt to contribute to the field of transportation systems comes from the achievements, spanning decades, by Petros Ioannou, Pravin Varaiya, Masayoshi Tomizuka, Roberto Horowitz, the late Karl Hedrick, Carlos Canudas de Wit, Markos Papageorgiou, Alexandre Bayen, Paola Goatin, Swaroop Darbha, and more recently by Iasson Karafyllis, Nikolaos Bekiaris-Liberis, Christophe Prieur, Liguozhang, Saurabh Amin, Karl Johansson, Antonella Ferrara, Dan Work, and Christian Claudel. On the topics of modeling, we have benefited significantly from interactions with Benjamin Seibold and Michael Zhang, as well as from studying the work of Michael Herty. In bridging control theory with implementations in automotive industry, the impact of Mrdjan Jankovic is unequalled and inspirational.

This work was supported in part by the National Science Foundation grant 1711373.

Contents

Part I Part Title

1	Introduction	3
1.1	The Basics of Traffic Flow Modeling	3
1.2	Macroscopic Traffic PDE Models	5
1.3	Linearized Models and Free/Congested Regimes	6
1.4	Traffic Actuation	9
1.5	A Brief Review of Literature on Traffic Control	11
1.6	Boundary Control by RM or VSL	13
1.7	Open-loop Stability	14
1.8	Numerical Simulation	19
1.9	Notes and References	22
2	Backstepping for Coupled Hyperbolic PDEs	23
2.1	A Brief History of PDE Backstepping	23
2.2	Coupled Hyperbolic PDEs	24
2.3	Backstepping Control for Coupled Hyperbolic PDEs	25
2.4	Observer and Output-Feedback Design for General Hyperbolic PDEs	30
2.5	Backstepping Control for second-order Hyperbolic PDEs	33
2.6	Observer and Collocated Output-Feedback Design for Second-order Hyperbolic PDEs	38
2.7	Notes and References	41

Part II Basic Backstepping Control of Freeway Traffic

3	Stabilization of ARZ Model with Known Parameters and Fundamental Diagram	45
3.1	What Can Be Controlled and Is Worth Controlling with Ramp Metering?	45
3.2	Stop-and-Go Instabilities	46
3.3	Boundary Control Model	47

3.4	DORM Control Design	51
3.5	UORM Control Designs	54
3.6	Numerical Simulation	60
3.7	Notes and References	60
4	Observer Validation on Freeway Data	63
4.1	Introduction to Traffic State Estimation	64
4.2	Boundary Observer Design	65
4.3	Nonlinear observer	68
4.4	Numerical Simulation	70
4.5	Model calibration with NGSIM data	73
4.6	Data validation of Observer with Calibrated Parameters	79
4.7	Notes and References	81
5	Adaptive Control of ARZ Traffic Model	85
5.1	Parametric Uncertainties in the ARZ Model	85
5.2	Adaptive Control for PDEs Enabled by Backstepping	86
5.3	Adaptive Output Feedback: Simultaneous Identification, Observer, adn Control Design	86
5.4	Validation of Adaptive Design: Stability Proof and Simulations	89
5.5	The ARZ PDE Model with Parameter Uncertainty	89
5.6	Parametric Model and Parameter Estimation	92
5.7	Filter-based Observer Design	96
5.8	Adaptive output-feedback control Design	98
5.9	Lyapunov Stability Analysis	102
5.10	Numerical Simulation	106
5.11	Notes and References	106
6	Event-Triggered Control of ARZ Model	109
6.1	VSL Full-state Feedback Control Design	110
6.2	Event-triggered Strategies for boundary control	112
6.3	Absence of the Zeno Phenomenon	114
6.4	Stability Results	116
6.5	Numerical simulations	117
6.6	Notes and References	119
7	Comparison of Backstepping with Reinforcement Learning	121
7.1	From (Model-Based) Adaptive Control to (Less Model-Based) Reinforcement Learning	121
7.2	RL Control Approach	125
7.3	Boundary Control Problem Reformulation	126
7.4	Control of ARZ Model by Reinforcement Learning	130
7.5	Comparative Simulation Study	136
7.6	Notes and References	144

Part III Advanced Backstepping for Traffic Flows

8	Two-Lane Traffic Control	169
8.1	Modeling and Controlling Two Lanes—by Four PDEs and Two VSL Inputs	169
8.2	Two-lane Traffic ARZ Model	170
8.3	Full-state Feedback Control Design	177
8.4	Collocated Observer and output-feedback control	180
8.5	Numerical Simulation	186
8.6	Notes and References	190
9	Two-Class Traffic Control	191
9.1	Diverse Driver and Vehicle Classes: Additional PDEs Controlled by a Single Input	191
9.2	Two-class ARZ Traffic Model	193
9.3	Boundary control design model	200
9.4	Full-state Feedback Control	205
9.5	Anti-collocated Boundary Observer Design	209
9.6	Output feedback control design	214
9.7	Numerical Simulation	215
9.8	Notes and References	218
10	Control of Two Cascaded Freeway Segments	219
10.1	Taking the ARZ Control Design Beyond a Single Freeway Segment	219
10.2	Possible Control Configurations for a Cascade of Freeway Segments	222
10.3	ARZ PDE Model of a Cascade of Freeway Segments	224
10.4	State feedback Control Designs	232
10.5	Boundary Observer Designs	236
10.5.1	Observer with measurement at outlet	239
10.6	Output Feedback Laws	242
10.7	Robustness to Input Delays	244
10.8	Simulation results	246
10.9	Notes and References	251
11	Estimation of Freeway Diverge Flows	253
11.1	PDE model of one incoming and two outgoing roads	254
11.2	Linearized model in the Riemann coordinates	256
11.3	Boundary observer design	258
11.4	Robustness to disturbance and noise	261
11.5	Notes and References	268
12	Control under Routing-Induced Instability	269
12.1	ARZ Model with Routing Feedback	270
12.2	Feedback design for the linearized system	271
12.3	Closed-loop stability	276
12.4	Existence of solutions to kernel equations	278
12.5	Notes and References	280

13	Bilateral Regulation of Moving Shock Position	281
13.1	Delay-Compensating Predictors for PDE-ODE Models of Traffic Shock Movement	281
13.2	Moving Shockwave Model	283
13.3	State-dependent PDE-ODE Model	287
13.4	Predictor-based Control Design	288
13.5	Lyapunov Analysis	294
13.6	Numerical Simulation	299
13.7	Notes and References	300
14	Extremum Seeking of Downstream Bottleneck	303
14.1	Bottleneck: Unknown Fundamental Diagram and Maximizing the Flow	303
14.2	Lane-Drop Bottleneck Control Problem	306
14.3	Online Optimization by Extremum Seeking Control	310
14.4	Stability Analysis (Averaging, Backstepping, and Lyapunov)	313
14.5	Numerical Simulation	320
14.6	Notes and References	322
	Glossary	325
	Solutions	327

Acronyms

Use the template *acronym.tex* together with the document class SVMono (monograph-type books) or SVMult (edited books) to style your list(s) of abbreviations or symbols.

Lists of abbreviations, symbols and the like are easily formatted with the help of the Springer-enhanced `description` environment.

ABC	Spelled-out abbreviation and definition
BABI	Spelled-out abbreviation and definition
CABR	Spelled-out abbreviation and definition

Part I
Part Title

Use the template *part.tex* together with the document class SVMono (monograph-type books) or SVMult (edited books) to style your part title page and, if desired, a short introductory text (maximum one page) on its verso page.

Chapter 1

Introduction

The preface of this book has much to say about the book's scope. The reader is encouraged not to skip the Preface as we don't reiterate here what is already expressed there.

This whole book—except the present chapter—is devoted to feedback design for traffic flows, predominantly in the congestion-induced unstable (or very lightly damped) regime.

The control and observer designs for traffic flows begin in Chapter 3, after a general introduction to backstepping for hyperbolic PDEs in Chapter 2.

This introductory chapter reviews material other than control: the macroscopic (PDE) models of traffic flows, the notions of free and congested regimes of traffic, the linearized versions of the PDE models of traffic and their structural distinctions in the free and congested regimes, a study of eigenvalues and linear stability of the PDE models of traffic, the options of actuation (applying inputs) on freeways and in PDE models of freeway traffic, and numerical methods for simulating PDE models of traffic.

1.1 The Basics of Traffic Flow Modeling

Macroscopic and microscopic models

Traffic flow theory and modeling have their origins in the 1930s when Bruce D. Greenshields carried out an experiment on a highway, using photographic measurements to characterize the relations between traffic flow, traffic density, and speed. Since then, researchers have developed a wide variety of models that describe traffic flow dynamics at different aggregation levels and present them as different mathematical structures. The traffic models are mostly classified into macroscopic, mesoscopic and microscopic models [?, ?].

Macroscopic models describe collective behaviors of traffic flows, analogously to the flows of fluids such as gases flowing through ducts. The traffic flow state variables are aggregated quantities: traffic density, speed, and flow. Since the models focus on the spatial and temporal evolution of the traffic states, they are particularly suited to describe the accumulated traffic phenomena such as freeway traffic congestion and propagation of traffic waves. The macroscopic models are governed by Partial Differential Equations (PDE) in which traffic states are functions of continuous time and space.

In contrast to the macroscopic models, *microscopic models* focus on single vehicle-driver units or road units. They may model the traffic dynamics of a road unit or the velocity and position of single vehicle. The car-following models describe how each vehicle reacts to the surrounding traffic while the cellular automation models depict the evolution of traffic dynamics on divided sections of a road. Microscopic models are given by Ordinary Differential Equations (ODE) because such models consider discretized space, as in cellular automata models, or individual driver-vehicle unit, as in car-following models. In comparison with the macroscopic models, the microscopic models are able to describe *individual* human driving behavior and assess interactions between different traffic components.

Mesoscopic traffic models are hybrids of the microscopic and macroscopic models.

LWR and ARZ macroscopic models

This book mainly focuses on the freeway traffic congestion problems, which are collective traffic phenomena and benefit from being described by macroscopic PDE models. Two macroscopic models that are used throughout the book are introduced in this chapter.

In the development of macroscopic traffic models, the first and widely-used one is proposed by Lighthill, Whitham, and Richards (LWR) [?, ?] in 1950s, which is a first-order, scalar conservation law of density. The LWR model predicts the formation and propagation of traffic shockwaves on the freeway but fails to describe the stop-and-go oscillatory phenomenon, which does not obey the static density-velocity relation as depicted by the LWR model. In particular, the velocity oscillations in the stop-and-go traffic need more sophisticated models. Several second-order models have been developed over the decades to allow the deviation from the density-velocity equilibrium by adding a velocity equation to the LWR model.

The state-of-the-art Aw-Rascle [?] and Zhang [?] (ARZ) models have been proposed to describe the stop-and-go traffic instabilities. On the basis of the LWR model, a family of flow-density relation is parameterized in the ARZ model by characterizing each vehicle's property as opposed to the averaged static dynamics of the flow-density relation depicted by the LWR model. The macroscopic model predicts the evolution of continuous traffic states in the temporal and spatial domain by employing hyperbolic PDEs to govern the dynamics of traffic density and velocity. The ARZ model is a quasilinear second-order hyperbolic PDE system. In the later

chapters, we mainly use the LWR model and ARZ model to describe various traffic phenomena on the freeway.

1.2 Macroscopic Traffic PDE Models

Lighthill-Whitham-Richards model

Consider the dynamics of traffic density on a freeway segment of length L . Traffic density $\rho(x, t)$ is governed by the following first-order nonlinear hyperbolic PDE,

$$\partial_t \rho + \partial_x (Q(\rho)) = 0, \quad (1.1)$$

where $x \in [0, L]$, $t \in [0, \infty)$, and $Q(\rho)$ is a fundamental diagram which describes the equilibrium relation between the density and traffic flow rate. The fundamental diagram $Q(\rho)$ is defined as

$$Q(\rho) = \rho V(\rho), \quad (1.2)$$

and shown in the example in Fig. 1.1. The equilibrium velocity $V(\rho)$ is a decreasing function of density. For example, we choose the following Greenshield's model,

$$V(\rho) = v_m - v_m \left(\frac{\rho}{\rho_m} \right)^\gamma, \quad (1.3)$$

where v_m is the maximum speed, ρ_m is the maximum density, q_m is the maximum flow rate, $\gamma > 0$. The Greenshield's model $V(\rho)$ of density and velocity relation yields a strictly concave fundamental diagram $Q(\rho)$ of density and flow relation, as in Fig. 1.1. The concavity of the fundamental diagram guarantees the hyperbolicity of the LWR model. The free and congested traffic regimes are also captured by the fundamental diagram which will be discussed in more detail later in this chapter.

Aw-Rascle-Zhang model

The evolution of the dynamics of the traffic density $\rho(x, t)$ and velocity $v(x, t)$, defined for $x \in [0, L]$, $t \in [0, \infty)$, on a road segment of length L , is modeled by the ARZ model,

$$\partial_t \rho + \partial_x (\rho v) = 0, \quad (1.4)$$

$$\partial_t (\rho(v + p(\rho))) + \partial_x (\rho v(v + p(\rho))) = - \frac{\rho(v - V(\rho))}{\tau}, \quad (1.5)$$

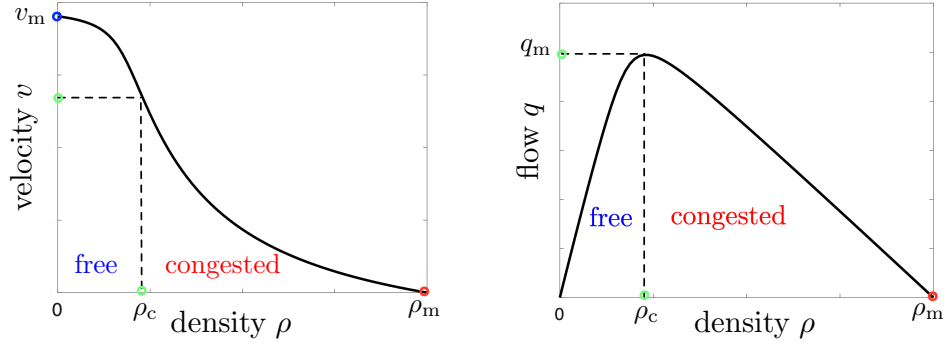


Fig. 1.1 Equilibrium relations of velocity and flow relative to density; $v = V(\rho)$, $q = Q(\rho)$, and $Q(\rho) = \rho V(\rho)$.

where the function $p(\rho)$ is defined as the traffic pressure, an increasing function of density,

$$p(\rho) = C_0 \rho^\gamma, \quad (1.6)$$

where $C_0, \gamma \in \mathbb{R}_+$, $p'(\rho) > 0$, and $p(0) = 0$ are assumed. The coefficient $\gamma > 0$ represents the aggressiveness of an individual driver, reflecting the driver's change of speed in response to the increase or decrease of local density. The pressure function $p(\rho)$ is chosen to relate the equilibrium velocity-density function $V(\rho)$ in the following fashion:

$$p(\rho) = V(0) - V(\rho) = v_m - V(\rho). \quad (1.7)$$

Given $V(\rho)$ in (1.3), from (1.6) the traffic pressure (1.7) becomes

$$p(\rho) = v_m \left(\frac{\rho}{\rho_m} \right)^\gamma. \quad (1.8)$$

The inhomogeneous ARZ model includes a relaxation term on the right hand side of the velocity PDE (1.5). The constant parameter τ is the relaxation time which describes the drivers' behavior of adapting to the equilibrium density-velocity relation $V(\rho)$ over time.

There are no explicit solutions for the LWR and ARZ PDE models. The approximations to the solutions of these PDEs can be computed numerically. Our primary interest is in neither analytical nor numerical solutions but in pursuing stabilization of these PDE systems by feedback control.

1.3 Linearized Models and Free/Congested Regimes

Linearized LWR model

To linearize the LWR PDE model around the steady-state $\rho^* > 0$, let us introduce the density variation

$$\tilde{\rho}(x, t) = \rho(x, t) - \rho^*. \quad (1.9)$$

The linearized LWR model is then given by

$$\partial_t \tilde{\rho}(x, t) + \lambda \partial_x \tilde{\rho}(x, t) = 0. \quad (1.10)$$

where λ represents the characteristic speed of density variations propagation and satisfies

$$\lambda = Q'(\rho)|_{\rho=\rho^*} = V(\rho^*) + \rho^* V'(\rho)|_{\rho=\rho^*}. \quad (1.11)$$

In the LWR PDE (1.10), density variations propagate with the characteristic speed λ . The characteristic speed characterizes the free and congested regimes of traffic, which is also illustrated by the fundamental diagram in Fig. 1.1. There is a critical density $\rho_c > 0$ such that $Q'(\rho)|_{\rho=\rho_c} = 0$ is satisfied, that is, $V(\rho_c) + \rho_c V'(\rho)|_{\rho=\rho_c} = 0$. This critical density,

$$\rho_c = \frac{\rho_m}{(1 + \gamma)^{1/\gamma}}, \quad (1.12)$$

segregates the free and congested traffic density of the LWR PDE model.

- Free-flow regime : $\lambda > 0$, namely, $\rho^* < \rho_c$.
In the free-flow regime with light traffic, the traffic density variations are transported in the downstream direction with the characteristic speed $Q'(\rho)|_{\rho=\rho^*} > 0$.
- Congested regime : $\lambda < 0$, namely, $\rho^* > \rho_c$.
The congested regime with denser traffic has its density variations transported in the upstream direction with the characteristic speed $Q'(\rho)|_{\rho=\rho^*} < 0$.

The traffic becomes bumper-to-bumper jammed when the traffic density reaches its maximum and the traffic speed equals zero. The steady-state density then satisfies $\rho^* = \rho_m$ and its corresponding static velocity is $V(\rho_m) = 0$.

For illustration, let us consider the LWR model with Greenshield's map (1.3) with $\gamma = 1$. The critical density in that case is $\rho_c = \frac{1}{2}\rho_m$. When the steady-state density $\rho^* < \frac{1}{2}\rho_m$, the traffic is in the free regime. When the steady-state density is $\rho^* > \frac{1}{2}\rho_m$, the traffic is in the congested regime.

Linearized ARZ model

The traffic density is the number of vehicles per unit length. The traffic flow rate is defined as the number of vehicles per unit time which cross a given point on the road. The traffic flow rate q is alternatively defined as the product of density and velocity, namely,

$$q(x, t) = \rho(x, t)v(x, t). \quad (1.13)$$

Traffic flow q and velocity v are the most accessible physical variables to measure in freeway traffic. Flow q is commonly measured by loop detectors and v can be obtained by GPS or high-speed cameras. Therefore, we rewrite the ARZ model in the state variables of traffic flow q and traffic velocity v for $x \in [0, L]$, $t \in [0, \infty)$,

$$\partial_t q + v \partial_x q = \frac{q(\gamma p - v)}{v} \partial_x v + \frac{q(v_m - p - v)}{\tau v}, \quad (1.14)$$

$$\partial_t v - (\gamma p - v) \partial_x v = \frac{v_m - p - v}{\tau}. \quad (1.15)$$

There is no explicit solution to the above quasilinear hyperbolic (q, v) -system in (1.14), (1.15). To gain easier understanding of the dynamics of the ARZ traffic model, we linearize the model around the steady-state (q^*, v^*) . The small variations from the steady-states are defined as

$$\tilde{q}(x, t) = q(x, t) - q^*, \quad (1.16)$$

$$\tilde{v}(x, t) = v(x, t) - v^*. \quad (1.17)$$

The linearized ARZ model is described with the following (\tilde{q}, \tilde{v}) -system,

$$\partial_t \tilde{q}(x, t) + v^* \partial_x \tilde{q}(x, t) - \frac{q^*(\gamma p^* - v^*)}{v^*} \partial_x \tilde{v}(x, t) = -\frac{q^*}{\tau} \left(\frac{1}{v^*} - \frac{1}{\gamma p^*} \right) \tilde{v}(x, t) - \frac{\gamma p^*}{\tau v^*} \tilde{q}(x, t), \quad (1.18)$$

$$\partial_t \tilde{v}(x, t) - (\gamma p^* - v^*) \partial_x \tilde{v}(x, t) = \frac{\gamma p^* - v^*}{\tau v^*} \tilde{v}(x, t) - \frac{\gamma p^*}{\tau q^*} \tilde{q}(x, t), \quad (1.19)$$

where the two characteristic speeds of the above linearized PDE model are

$$\lambda_1 = v^*, \quad (1.20)$$

$$\lambda_2 = -(\gamma p^* - v^*). \quad (1.21)$$

We define the free and congested regimes of the ARZ model by studying the two characteristic speeds λ_1 and λ_2 of flow and velocity variations \tilde{q} and \tilde{v} . In particular, we are interested in the sign of the characteristic speed λ_2 because $\lambda_1 = v^* > 0$ is always satisfied.

When $\lambda_2 > 0$, it is straightforward to obtain the following inequalities:

$$\rho^* < \frac{\rho_m}{(1+\gamma)^{1/\gamma}} \Leftrightarrow v^* > \frac{\gamma}{\gamma+1} v_m. \quad (1.22)$$

When $\lambda_2 < 0$, the following inequalities hold:

$$\rho^* > \frac{\rho_m}{(1+\gamma)^{1/\gamma}} \Leftrightarrow v^* < \frac{\gamma}{\gamma+1} v_m. \quad (1.23)$$

- Free-flow regime : $\lambda_1 > 0$, $\lambda_2 > 0$
In the free-flow regime, both the variations of traffic flow and the variations of velocity travel downstream, at the respective characteristic speeds λ_1 and λ_2 . The linearized ARZ model in the free-flow regime is a homo-directional hyperbolic system.
- Congested regime: $\lambda_1 > 0$, $\lambda_2 < 0$
In the congested regime, the traffic density is greater than the critical value ρ_c , which satisfies $Q(\rho)'|_{\rho_c} = 0$, and the second characteristic speed λ_2 becomes negative. Therefore, the variations of the traffic speed travel upstream with the speed λ_2 while the variations of the traffic flow are carried downstream with the characteristic speed λ_1 . The hetero-directional propagations of variations force the vehicles into the stop-and-go driving. This kind of instability in traffic causes unsafe driving conditions, extra fuel consumption and may ultimately evolves into a bumper-to-bumper jam.

The traffic becomes bumper-to-bumper jammed when the traffic density reaches its maximum and traffic speed equals zero. The steady-state density and velocity satisfy $\rho^* = \rho_m$ and $v^* = 0$.

1.4 Traffic Actuation

The freeway traffic management systems regulate traffic flow on freeways by controlling the vehicles in a collective manner. In order to improve the performance of traffic networks, static and dynamic traffic control are implemented.

Dynamic traffic control refers to automatic methods that are designed to regulate traffic in response to real-time scenarios. By mitigating freeway traffic congestion, the control objective is to improve stability, efficiency, safety of traffic flow and other performance such as total travel time, fuel consumption, drivers' comfort, and pollutant emissions [?]. There are also traffic management operations that are non-automated, performed by human operators at some traffic control centers, and provided for emergency services, e.g., road signs for work-zones.

In contrast to dynamic traffic control, static control usually refers to time-invariant control strategies in a period of time. The fixed-time control strategies, namely, open-loop control signals, use historical traffic data to determine control schedules for traffic regulation such as metering rates of on-ramp traffic lights [?, ?]. The variations in the traffic demand and spatio-temporal evolution of the actual real-time traffic are not taken into account, which may lead to worsening of traffic congestion.

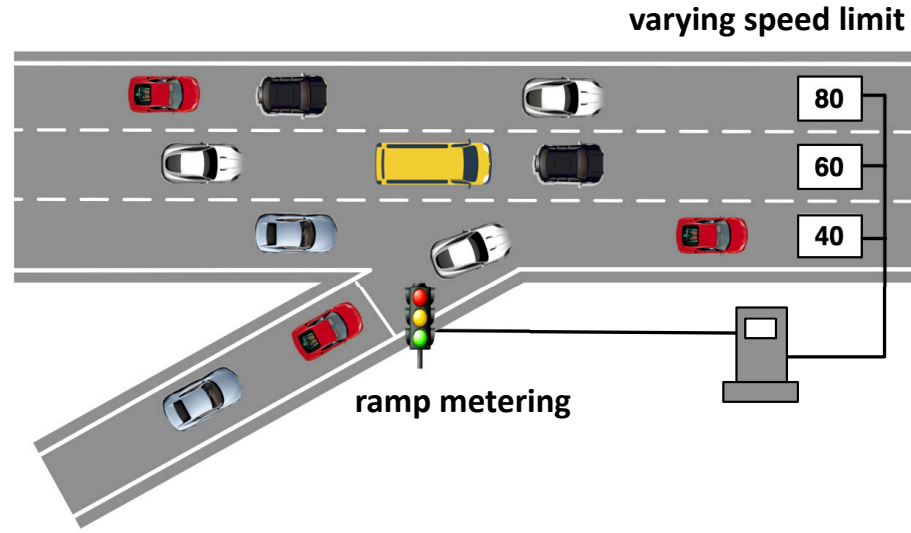


Fig. 1.2 Freeway boundary actuation in which control is implemented by ramp metering and/or varying speed limits.

For this reason, static control of certain operations is mainly studied in the field of transportation planning, managing traffic demand over longer timescales, through traffic policy development, new road constructions, and software traffic assignment.

Control Measures: Ramp Metering (RM) and Variable Speed Limits (VSL)

The dynamic control measures are implemented mainly through two types of road infrastructures: ramp metering (RM) and varying speed limits (VSL). Road-based control strategies have been applied through RM and VSL in many countries worldwide, including the United States [?], the European countries [?] and Canada [?].

As sketched in Fig. 1.2, RM is located at on-ramp entries to facilitate the merging of on-ramp flows into the mainstream traffic. The RM control strategies are designed to reduce traffic congestion and to optimize traffic conditions on the mainline [?], [?]. VSL employ variable message signs to display driving velocity in response to the real-time traffic conditions. VSL are employed to homogenize the velocities of individual vehicles and are also used to slow down the traffic and create controlled mainstream flow such that the traffic safety is improved and the formation of congestion is prevented [?], [?]. The RM and VSL control strategies can be combined with other

control measures that redirect drivers to different lanes or routes due to work zones or accidents, for example, lane control [?] or route guidance control [?].

We use the acronym VSL as both singular and plural, namely, to refer to either one or multiple signs. We follow this acronym convention because we consider repeatedly writing VSL to be cumbersome.

Distributed and in-domain actuation: CAVs

In addition to the road-based traffic control systems, vehicle-based traffic control measures are being explored. The emerging development of Connected and Automated Vehicles (CAV) provides new opportunities for control of transportation systems through information sharing and vehicle coordination operations [?, ?, ?, ?]. The overall traffic efficiency could be greatly improved in mixed traffic by avoiding the dependence on static infrastructures and drivers' compliance. The previously mentioned infrastructure-based control strategies can be combined with vehicle-based traffic control measures through vehicle-to-infrastructure communication [?].

Vehicle-based traffic control is out of the scope of this book. We have a strong reason for restricting our attention to RM and VSL control at the traffic segment boundaries. The CAV capability, which introduces the possibility of *distributed in-domain actuation* of traffic, does not necessarily completely trivialize the stabilization of stop-and-go traffic, the task of suppression of stop-and-go is vastly more complex by boundary control, having to rely on the behavioral interactions among the drivers, rather than on a wireless connectivity among the vehicles. Therefore, as long as RM and VSL are the primary actuation options, and the CAV penetration is low, the boundary control designs, and particularly those developed based on PDE backstepping in this book, will be an important tool for suppression of stop-and-go instabilities.

1.5 A Brief Review of Literature on Traffic Control

This section provides an overview of dynamic traffic control strategies for freeway traffic systems in the currently existing literature. Macroscopic models represent the traffic dynamics at an aggregate level, and therefore are particularly useful for freeway traffic sensing and actuation. They may be used for control design in their original PDE forms, through ODEs that are derived from discretization of PDEs in space, and as difference equations that are derived from discretization of PDEs both in space and time.

The macroscopic models, namely, the LWR and ARZ PDE models, have been extensively discussed in Section 1.1. The discrete traffic models are obtained by discretization of macroscopic models in time and space. The most commonly used first-order discrete traffic model is the Cell Transmission Model (CTM). This ODE

model is derived from the first-order LWR PDE model for a road segment [?] and then is extended to traffic networks [?]. Variations of CTM include [?, ?, ?]. Discrete versions of second-order traffic models have also been developed, such as in [?], based on Payne-Whitham (PW) PDE model [?, ?], and have been extended to a freeway network named METANET [?].

Dynamic traffic control techniques that are applied to freeway traffic systems can be categorized into the following three major control methodologies.

Control employing PI and backstepping feedback

In feedback (closed-loop) control a measured state or output of the controlled system is introduced back into the traffic flow through a control input so that a desired stability, transient behavior, or disturbance attenuation properties of the traffic system are ensured.

For macroscopic traffic models that are described by PDEs and are continuous in space and time, the feedback control laws are usually constructed by application of a particular control design method to the model of the traffic system dynamics. Closed-loop stability is obtained by using a Lyapunov proof, either subsequently to the control design or simultaneously with the control design.

In-domain speed control laws of freeway traffic are developed in [?, ?] and ensure local exponential stability.

Boundary feedback control laws are proposed in [?, ?, ?, ?, ?, ?], on the basis of the ARZ model, for stop-and-go traffic mitigation. In particular, in [?], a nonlinear boundary feedback law is designed which actuates the inlet flow and achieves global stabilization for a modified second-order ARZ model. In [?, ?, ?], we introduce backstepping boundary control designs, based on the linearized inhomogeneous ARZ models of multi-lane and multi-class traffic, to achieve stop-and-go suppression by guaranteeing exponential stability and finite-time convergence in the spatial L^2 sense. The applicability of PI controllers is studied in [?, ?] for inlet traffic flow rate control through ramp metering and outlet velocity control through VSL. The control gains are chosen such that exponential stability is achieved for the linearized homogenous ARZ model.

For discrete macroscopic traffic models given by difference equations, local feedback control strategies have been proposed for ramp metering including a proportional controller based on occupancy measurement upstream of the ramp [?], a widely-used integral regulator ALINEA based on occupancy measurement downstream of the ramp [?], and an extended version of a proportional–integral controller called PI-ALINEA [?]. The more sophisticated variations based on ALINEA and PI-ALINEA were developed in [?, ?, ?, ?, ?]. Based on ALINEA, local feedback strategies were developed for VSL in [?, ?, ?, ?, ?, ?, ?]. The coordinated RM and VSL strategies were developed by integrating on-ramp control and mainstream VSL [?, ?, ?, ?].

Optimal control

Optimal control has been widely applied in freeway traffic systems, from macroscopic to microscopic models. The control problem is formulated in terms of an objective function which describes the system's performance over a given period of time and the controller is computed to obtain optimal solutions to the objective function.

For macroscopic traffic models, [?, ?, ?, ?, ?, ?] formulated PDE model-based traffic network control problems whose objectives are to minimize total travel time or maximize the system outflow. The PDE models are usually discretized in space using the Godunov method and then the resulting nonlinear or linear optimal control problems are solved numerically.

For discrete macroscopic traffic models, optimal control problems are numerically solved for the first-order CTM models in [?, ?, ?, ?] and for the second-order METANET models in [?, ?].

Model predictive control

The freeway traffic control has been extensively studied using model predictive control (MPC). MPC employs dynamic models to predict the future system output over a finite horizon and iteratively solves optimal control problems at each time step in a receding-horizon framework, to minimize an objective function with updated measurements. The results in [?, ?, ?, ?] consider the discrete CTM model for traffic prediction and solve a finite-horizon optimal control problem. In contrast, second-order dynamics are considered in [?, ?, ?, ?], which solve MPC problems based on the METANET models in which control is realized with RM, VSL or coordination of the both. The MPC approaches generally demand relatively high computational power as the associated finite-time optimal control problems are solved with large numbers of variables at each time step.

Other control problems and strategies

Traffic state estimation plays an important role in traffic control. The state information is predicted with partially observed traffic data and some prior knowledge of traffic. Traffic state estimation approaches fall into three categories [?]: model driven, data driven, and streaming data driven. Among them, the model-driven approach is the most popular one and has been widely used to solve various traffic estimation problems [?, ?, ?, ?, ?, ?, ?, ?, ?] and can be integrated with traffic control strategies directly.

The application of control approaches for freeway traffic networks has been explored with hierarchical control in which multi-layer control architectures were established with supervisory controllers. The upper level of a hierarchical architec-

For more detailed and comprehensive surveys of the literature on freeway traffic control, the reader is referred to [?, ?, ?, ?]. For control of urban traffic network, readers are referred to [?, ?, ?, ?, ?, ?, ?]

$$\partial_t v - (\gamma p - v) \partial_x v = \frac{v_m - p - v}{\tau}. \quad (1.25)$$

Traffic flow boundary control by Ramp Metering

When we consider on-ramp metering control as shown in Fig. 1.2, the actuated boundary condition, located at $x = 0$, is defined as

$$q(0, t) = q^* + U_0(t), \quad (1.26)$$

where q^* represents a nominal flow rate, which is the sum of the equilibrium mainline flow and the equilibrium on-ramp inflow, whereas $U_0(t)$ is the control input applied by flow rate variations.

Depending on the traffic scenario we consider, and on the direction of the characteristic speeds of the traffic waves, the flow rate and the velocity could be controlled at either boundary. More details will be discussed in the later chapters.

Traffic velocity boundary control by Varying Speed Limits

When we consider VSL control as shown in Fig. 1.2, the actuated boundary condition, located at $x = L$, is defined as

$$v(L, t) = v^* + U_L(t), \quad (1.27)$$

where v^* represents a nominal velocity of the vehicles leaving the segment and $U_L(t)$ is the control input applied by velocity variations and is to be designed (assuming that the drivers obey signs just as in RM).

1.7 Open-loop Stability

In this section we discuss the linear stability of the LWR and ARZ models in the free and congested regimes, respectively, when constant, equilibrium-inducing control is applied at the boundaries.

Linear stability of LWR model

Consider the LWR model,

$$\partial_t \rho(x, t) + \partial_x (Q(\rho(x, t))) = 0, \quad (1.28)$$

where $x \in [0, L]$, $t \in [0, \infty)$, with a flow rate control applied at the inlet boundary if the traffic is in the free-flow regime, with flow given by

$$\rho(0, t)V(\rho(0, t)) = q^* + U_q(t), \quad (1.29)$$

or with a velocity control applied at the outlet boundary if the traffic is in the congested regime, with flow given by

$$V(\rho(L, t)) = v^* + U_v(t). \quad (1.30)$$

We take $\gamma = 1$ for the Greenshield's model in (1.3),

$$V(\rho) = v_m - \frac{v_m}{\rho_m} \rho, \quad (1.31)$$

$$Q(\rho) = v_m \rho - \frac{v_m}{\rho_m} \rho^2, \quad (1.32)$$

Then the linearized LWR model around the steady-state density ρ^* is

$$\partial_t \tilde{\rho}(x, t) + \lambda \partial_x \tilde{\rho}(x, t) = 0. \quad (1.33)$$

where $\tilde{\rho}(x, t) = \rho(x, t) - \rho^*$ represents the density variations around the steady-state and $\lambda = Q'(\rho)|_{\rho=\rho^*}$ is the characteristic speed of density variations propagation. The initial condition is $\tilde{\rho}(0, t) = \rho_0 \in L^2([0, L])$. If the traffic is in the free-flow regime, i.e., when $\lambda > 0$, it is only feasible to have a boundary condition at $x = 0$ which, by linearizing (1.29), becomes

$$Q'(\rho^*)\tilde{\rho}(0, t) = U_q(t), \quad (1.34)$$

whereas if the traffic is in the congested regime, we have a boundary condition at $x = L$ which, by linearizing (1.30), becomes

$$V'(\rho^*)\tilde{\rho}(L, t) = U_v(t). \quad (1.35)$$

The PDE (1.33) is referred to as the transport PDE. It carries a signal from the inlet boundary of the PDE to the outlet boundary. An explicit solution can be obtained for the initial-boundary value problem of the transport PDE. The explicit solution to the linearized LWR PDE (1.33) with the initial condition ρ_0 and the boundary condition (1.34) is given for the free regime as

$$\tilde{\rho}(x, t) = \begin{cases} \tilde{\rho}_0(x - \lambda t), & t < \frac{x}{\lambda}, \\ \tilde{\rho}(0, t - \frac{x}{\lambda}), & t \geq \frac{x}{\lambda}, \end{cases} \quad (1.36)$$

With the boundary condition (1.35), for the congested regime, the solution is

$$\tilde{\rho}(x, t) = \begin{cases} \tilde{\rho}_0(x + \lambda t), & t < \frac{L-x}{\lambda}, \\ \tilde{\rho}(L, t - \frac{L-x}{\lambda}), & t \geq \frac{L-x}{\lambda}. \end{cases} \quad (1.37)$$

Substituting the boundary control inputs, one has (1.36) for the free regime after $t \geq \frac{x}{\lambda}$,

$$\tilde{\rho}(x, t) = \frac{1}{Q'(\rho^*)} U_q \left(t - \frac{x}{\lambda} \right), \quad (1.38)$$

or (1.37) for the congested regime after $t \geq \frac{L-x}{\lambda}$

$$\tilde{\rho}(x, t) = \frac{1}{V'(\rho^*)} U_v \left(t - \frac{L-x}{\lambda} \right). \quad (1.39)$$

For the open-loop system, zero boundary control inputs (equilibrium values and no variations) are considered, namely, $U_q(t) = 0$ and $U_v(t) = 0$. In that case, we have after $t \geq \frac{L}{\lambda}$, the solution

$$\tilde{\rho}(x, t) \equiv 0. \quad (1.40)$$

for both the free-flow and congested regimes. When we use the LWR model to describe the traffic dynamics, only transport behavior of traffic flow is exhibited. The linearized PDE of the LWR model in both free and congested regimes has no spectrum (except at negative infinity, therefore, no stability issue arises).

Linear stability of ARZ model

Consider the ARZ model,

$$\partial_t q + v \partial_x q = \frac{q(\gamma p - v)}{v} \partial_x v + \frac{q(v_m - p - v)}{\tau v}, \quad (1.41)$$

$$\partial_t v - (\gamma p - v) \partial_x v = \frac{v_m - p - v}{\tau}. \quad (1.42)$$

We apply an open-loop flow rate control at the inlet boundary and a constant density at the outlet boundary,

$$q(0, t) = q^* + U_q(t), \quad (1.43)$$

$$v(L, t) = \frac{1}{\rho^*} q(L, t). \quad (1.44)$$

The linearized ARZ model with state variations $\tilde{q}(x, t)$ and $\tilde{v}(x, t)$ around steady-states (q^*, v^*) is then given for $x \in [0, L]$, $t \in [0, \infty)$, by

$$\tilde{q}_t + v^* \tilde{q}_x - \frac{q^*(\gamma p^* - v^*)}{v^*} \tilde{v}_x = -\frac{q^*}{\tau} \left(\frac{1}{v^*} - \frac{1}{\gamma p^*} \right) \tilde{v} - \frac{\gamma p^*}{\tau v^*} \tilde{q}, \quad (1.45)$$

$$\tilde{v}_t - (\gamma p^* - v^*) \tilde{v}_x = \frac{\gamma p^* - v^*}{\tau v^*} \tilde{v} - \frac{\gamma p^*}{\tau q^*} \tilde{q}, \quad (1.46)$$

$$\tilde{q}(0, t) = 0, \quad (1.47)$$

$$\tilde{v}(L, t) = \frac{1}{\rho^*} \tilde{q}(L, t), \quad (1.48)$$

where the flow rate and velocity variations are defined as

$$\tilde{q}(x, t) = q(x, t) - q^*, \quad (1.49)$$

$$\tilde{v}(x, t) = v(x, t) - v^*, \quad (1.50)$$

and the input $U_q(t) = 0$ is considered for the open-loop system.

In order to analyze stability of the above open-loop PDE system with zero input in (1.45)–(1.48), we seek the spectrum of the linearized PDE by representing the infinite-dimensional PDE state as the sum of a set of linearly independent basis functions. The solution of the PDE is then written as a sum of orthogonal basis functions. We then analyze stability of the PDE by studying the corresponding eigenvalue problems. In particular, we find under what conditions the flow and velocity variations grow in the traffic flow and ultimately cause the traffic congestion.

We analyze stability of the linearized ARZ model (1.45)–(1.48). Applying the Fourier transform with respect to the spatial variable x and the Laplace transform with respect to temporal variable t , we have

$$\tilde{q}(x, t) = q(k) \exp \left(\frac{ikx}{L} + \lambda(k)t \right), \quad (1.51)$$

$$\tilde{v}(x, t) = v(k) \exp \left(\frac{ikx}{L} + \lambda(k)t \right), \quad (1.52)$$

where the solution ansatz assumes that the flow rate and velocity variations are represented by periodic functions as $\exp \left(\frac{ikx}{L} \right) = \cos \left(\frac{kx}{L} \right) + i \sin \left(\frac{kx}{L} \right)$. Substituting (1.51), (1.52) into (1.45)–(1.46), we obtain

$$\begin{pmatrix} \lambda + \frac{ikv^*}{\tau q^*} & \frac{q^*(\gamma p^* - v^*)}{v^*} \frac{ik}{L} \\ \frac{\gamma p^*}{\tau q^*} & \lambda + \frac{ik(v^* - \gamma p^*)}{L} - \frac{\gamma p^* - v^*}{\tau v^*} \end{pmatrix} \begin{pmatrix} q(k) \\ v(k) \end{pmatrix} = \begin{pmatrix} 0 \\ 0 \end{pmatrix},$$

where the eigenvalue λ represents the growth rate of the flow rate and velocity perturbations over time. To obtain the k th pair of eigenvalues, we solve the quadratic equation

$$\lambda^2 + \left(\frac{2v^* - \gamma p^*}{L} ik + \frac{1}{\tau} \right) \lambda - \frac{v^*(v^* - \gamma p^*)}{L^2} k^2 + \frac{v^* - \gamma p^*}{\tau L} ik = 0. \quad (1.53)$$

The discriminant is given by

$$\Delta = \left(\frac{\gamma p^*}{L} ik \right)^2 + \frac{2\gamma p^*}{\tau L} ik + \left(\frac{1}{\tau} \right)^2, \quad (1.54)$$

which is a complete square

$$\Delta = \left(\frac{\gamma p^*}{L} ik + \frac{1}{\tau} \right)^2. \quad (1.55)$$

In conclusion, there is one set of eigenvalues in the left half plane, and one set on the imaginary axis, given, respectively by

$$\lambda_1 = \frac{\gamma p^* - v^*}{L} ik, \quad (1.56)$$

$$\lambda_2 = -\frac{1}{\tau} - \frac{v^*}{L} ik. \quad (1.57)$$

Let us examine these eigenvalues. The eigenvalues λ_1 only contain imaginary parts. As for λ_2 , the longer the relaxation time τ , the smaller the negative real part of λ_2 . We are interested in the congested regime of the ARZ model such that

$$\gamma p^* - v^* > 0. \quad (1.58)$$

As $\tau \rightarrow \infty$ and $k \rightarrow \infty$,

$$\lambda_1 \rightarrow \text{Im}(+\infty), \quad (1.59)$$

$$\lambda_2 \rightarrow \text{Im}(-\infty). \quad (1.60)$$

In summary, according to the above spectral analysis, two sets of eigenvalues have their loci along the imaginary axis. The linearized ARZ model is marginally stable and there are persistent oscillations in the domain when the input to the system is zero in (3.46)–(3.49), which results from the positive and negative imaginary parts in (1.56)–(1.57).

The linearized model around (q^*, v^*) can be unstable when the traffic pressure function $p(\rho)$ happens to be such that the following inequality is satisfied:

$$p'(\rho^*) < -V'(\rho^*). \quad (1.61)$$

In that case there is a positive real part appearing in λ_1 , for which we refer the interested reader to [?].

We conclude that small variations of the flow rate and velocity in the congested traffic exhibit oscillatory (or at least lightly damped) behaviors and, under certain conditions, grow into stop-and-go instabilities in the traffic flow. Therefore, it is meaningful to study control design for the congested ARZ PDE system.

1.8 Numerical Simulation

This section presents the basic options for the numerical simulation of the LWR and ARZ nonlinear PDE models.

Numerical simulation of the LWR PDE model

The LWR model is a scalar conservation law,

$$\partial_t \rho + \partial_x (Q(\rho)) = 0. \quad (1.62)$$

We apply the Godunov scheme [?] to numerically approximate the LWR model. The scheme is first-order accurate in space and time. The finite volume Godunov method is designed based on the integral form of the conservation law. The numerical flow is defined as $Q = Q(\rho)$. Using the Godunov scheme on a grid of cell size Δx and time step Δt , the Courant-Friedrichs-Lewy (CFL) condition, a necessary condition for numerical convergence, is defined as:

$$\max |\lambda| \leq \frac{\Delta x}{\Delta t}. \quad (1.63)$$

The cell average is updated at each time step by the following equation

$$\rho_j^{n+1} = \rho_j^n - \frac{\Delta t}{\Delta x} (Q_{j+\frac{1}{2}}^n - Q_{j-\frac{1}{2}}^n), \quad (1.64)$$

where

$$Q_{j+\frac{1}{2}}^n = Q(\rho_j^n, \rho_{j+1}^n), \quad (1.65)$$

$$Q_{j-\frac{1}{2}}^n = Q(\rho_j^{n-1}, \rho_j^n). \quad (1.66)$$

The numerical flow is defined as

$$(1.69)$$

$$Q(\rho_L, \rho_R) = \min_{\rho_L \leq \rho \leq \rho_R} Q(\rho), \text{ if } \rho_L < \rho_R, \quad \max_{\rho_R \leq \rho \leq \rho_L} Q(\rho),$$

where ρ_L and ρ_R represent the state values evaluated at the left cell interface and right cell interface. The entropy condition is satisfied with the above definition of numerical flow which guarantees a unique weak solution when there are shock waves.

We illustrate the propagation and formation of a traffic shock wave modeled by the LWR model with the following simulation example. We simulate a traffic

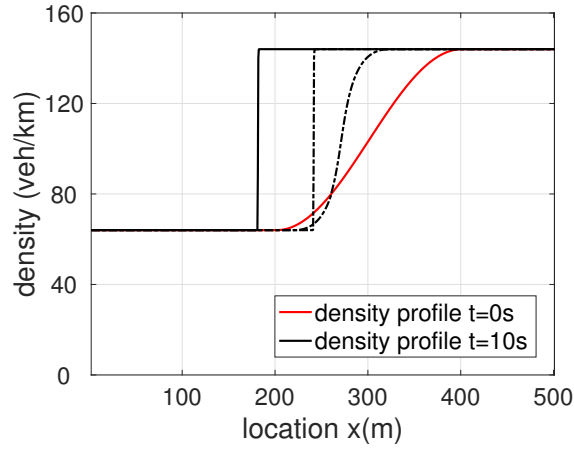


Fig. 1.3 Density spatial profile evolution over time.

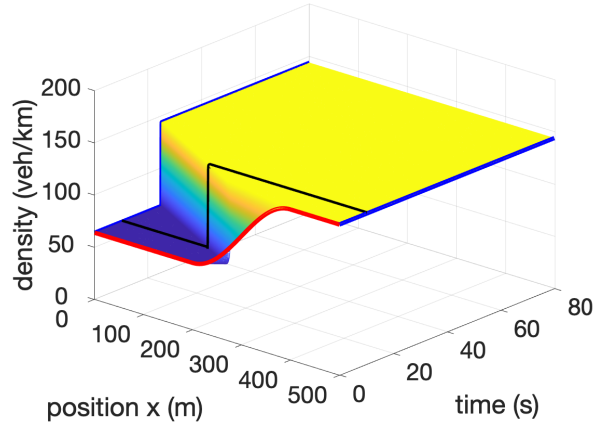


Fig. 1.4 Density evolution of the open-loop LWR PDE model.

condition in a 500-meter freeway segment where the upstream traffic is free and the downstream traffic is congested. The maximum velocity is $v_m = 144$ km/hr and maximum density is $\rho_m = 160$ veh/km. The initial condition of the traffic profile consists of free traffic of $\rho_f^* = 32$ veh/km before around 300 m and congested traffic of $\rho_c^* = 128$ veh/km after around 300 m, as shown in Fig. 1.3. The red line shows the initial density profile at $t = 0$. The downstream congested traffic propagates upstream and gradually forms the traffic shockwave, namely the density discontinuity at $t = 10$ s. Fig. 1.4 shows how the density evolves in the temporal and spatial domain, where the congested downstream traffic propagates upstream. The boundary conditions are marked with blue and the initial condition is marked with red. The corresponding

density spatial profile at $t = 10$ s is also illustrated in the Fig. 1.4. We discuss how to halt such congestion propagation in Chapter 13 with closed-loop bilateral boundary control.

Numerical simulation of the ARZ PDE model

We apply a two-stage Lax-Wendroff scheme to both nonlinear ARZ model and linearized model. The scheme is second-order accurate in space and time. The grid resolution is chosen to be small so that the numerical errors are smaller than the model errors and therefore the simulation is valid for this continuum model. The inhomogeneous nonlinear ARZ model written in the conservative form is given by

$$\rho_t + (\rho v)_x = 0, \quad (1.70)$$

$$y_t + (yv)_x = -\frac{y}{\tau}, \quad (1.71)$$

where ρ and y are conservative variables, and y is defined as $y = \rho(v - V(\rho))$. The numerical flows are defined as

$$F_\rho = y + \rho V(\rho), \quad (1.72)$$

$$F_y = \frac{y^2}{\rho} + yV(\rho), \quad (1.73)$$

We use the Lax-Wendroff scheme on a grid of cell size Δx and time step Δt . The CFL condition, a necessary condition for numerical convergence, is defined as

$$\max |\lambda_{1,2}| \leq \frac{\Delta x}{\Delta t}. \quad (1.74)$$

At the first stage, the update law of (ρ_j^n, y_j^n) to $(\rho_{j+\frac{1}{2}}^{n+\frac{1}{2}}, y_{j+\frac{1}{2}}^{n+\frac{1}{2}})$ is given by

$$\rho_{j+\frac{1}{2}}^{n+\frac{1}{2}} = \frac{1}{2} (\rho_j^n + \rho_{j+1}^n) - \frac{\Delta t}{2\Delta x} ((F_\rho)_{j+1}^n - (F_\rho)_j^n), \quad (1.75)$$

$$y_{j+\frac{1}{2}}^{n+\frac{1}{2}} = \frac{1}{2} (y_j^n + y_{j+1}^n) - \frac{\Delta t}{2\Delta x} ((F_y)_{j+1}^n - (F_y)_j^n) - \frac{\Delta t}{4\tau} (y_j^n + y_{j+1}^n). \quad (1.76)$$

Then we calculate the numerical flow at the intermediate points of the state variables and then obtain the final stage as

$$\rho_j^{n+1} = \rho_j^n - \frac{\Delta t}{\Delta x} ((F_\rho)_{j+\frac{1}{2}}^{n+\frac{1}{2}} - (F_\rho)_{j-\frac{1}{2}}^{n+\frac{1}{2}}), \quad (1.77)$$

$$y_j^{n+1} = y_j^n - \frac{\Delta t}{\Delta x} ((F_y)_{j+\frac{1}{2}}^{n+\frac{1}{2}} - (F_y)_{j-\frac{1}{2}}^{n+\frac{1}{2}}) - \frac{\Delta t}{2\tau} (y_{j+\frac{1}{2}}^{n+\frac{1}{2}} + y_{j-\frac{1}{2}}^{n+\frac{1}{2}}). \quad (1.78)$$

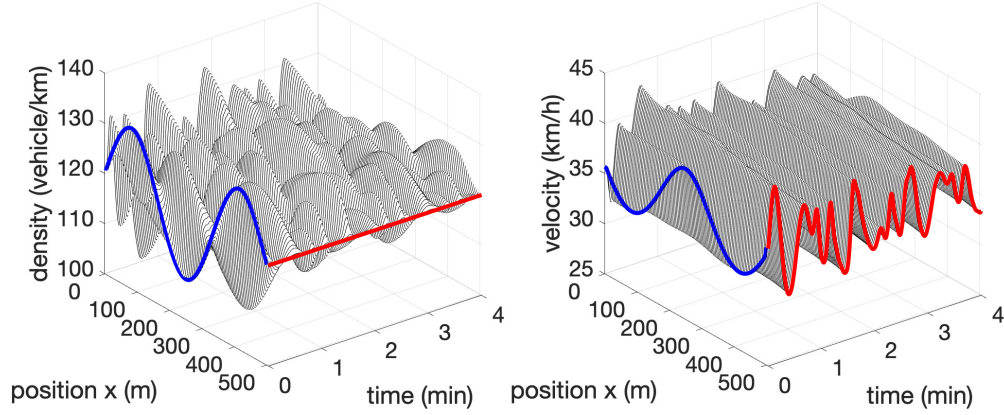


Fig. 1.5 Density and velocity evolution of the open-loop ARZ PDE model.

We specify the state values at both $x = 0$ and $x = L$ boundaries by implementing the boundary conditions. The numerical scheme picks up some combination of ρ and v at each of the two boundaries, depending on the direction of characteristics. The same numerical method is also applied to the linearized ARZ model with the same order of numerical simulation errors.

We are interested in the stop-and-go traffic described by the nonlinear ARZ PDE model, so we assume that the initial conditions are spatial sinusoids around the steady-states (ρ^*, v^*) , with values $\rho^* = 120$ veh/km and $v^* = 36$ km/hr. The steady-state traffic is in the congested regime. The initial conditions are chosen as

$$\rho(x, 0) = 0.1 \sin\left(\frac{3\pi x}{L}\right) \rho^* + \rho^*, \quad (1.79)$$

$$v(x, 0) = -0.1 \sin\left(\frac{3\pi x}{L}\right) v^* + v^*. \quad (1.80)$$

We consider a 500-meter freeway segment and evolution of traffic states density and velocity are shown for 4 min. The maximum velocity is $v_m = 144$ km/hr and maximum density is $\rho_m = 160$ veh/km. We consider a constant incoming flow and constant outgoing density for boundary conditions (1.43), (1.44).

In Fig. 1.5, traffic density and velocity are lightly damped and keep oscillating in the domain. It takes the vehicles that are initially in the domain only 50 seconds to leave it, however, the density-velocity oscillations sustain for more than 4 min, which means the following incoming vehicles enter the acceleration-deceleration cycles under the influence of the stop-and-go waves that are left in the wake of their predecessor vehicles in the domain. The traffic equilibrium is chosen to be in the congested regime and the stop-and-go phenomenon is demonstrated in the simulation in Fig. 1.5. In Chapters 3-7, we discuss how to design boundary controllers to suppress stop-and-go traffic oscillations.

1.9 Notes and References

In order to represent more sophisticated traffic dynamics on the freeway, multi-lane traffic with lane-changing and multi-class traffic with heterogeneous drivers and creeping effect have been studied. A first-order multi-lane model is introduced in [?] and second-order multi-lane models are developed in [?, ?, ?]. A multi-class traffic flow model as an extension of LWR model with heterogeneous drivers is formulated in [?]. The macroscopic second-order multi-class models are introduced in [?] and in particular the ones based on the ARZ PDE model are developed in [?, ?]. The ARZ model with phase transitions is developed in [?].

For large-scale freeway traffic modeling, the macroscopic models have been extended to different road networks. The macroscopic traffic network model based on the LWR model is developed in [?, ?]. A two-dimensional conservation law for a dense urban area is studied in [?]. More recently, the macroscopic road networks based on the ARZ family of models have been developed in [?, ?].

Freeway traffic control based on the macroscopic traffic PDE models can be categorized into feedback control and optimal control. In-domain feedback control approach in [?] is based on an extended LWR model and the VSL control is applied continuously in time and space to regulate freeway traffic. Boundary feedback control have been widely developed for RM and VSL control in [?, ?, ?, ?]. In [?], a nonlinear boundary feedback law was designed that controls the inlet flow and achieves global stabilization for a modified ARZ model. Using the integration of ramp metering and VSL, [?] considers PI boundary control for homogeneous ARZ model. The backstepping control approach is first proposed for the ARZ model in [?], which provides an effective and systematic way to design boundary feedback control for traffic stabilization. In this book, we mainly discuss the application of backstepping control in traffic control problems.

Chapter 2

Backstepping for Coupled Hyperbolic PDEs

2.1 A Brief History of PDE Backstepping

The backstepping method was initially developed, around 1990 and through the rest of that decade, for nonlinear and adaptive ODE systems [?]. In finite dimension (for ODEs), this method is referred to as integrator backstepping. The notion of backstepping through integrators does not extend to infinite dimension—it fails to converge, just as the Brunowsky form does not have a meaningful infinite limit. The backstepping method has had to be developed for PDEs using a different formulation, employing spatial Volterra operators.

PDE backstepping, as a feedback stabilization method, was conceived in the late 1990s by the second author of this book and pursued in the work with and by his postdocs and students at the time (Balogh, Boskovic, and Liu). The breakthrough in the development of PDE backstepping came with the paper [?, ?] by Smyshlyaev and Krstic. At that time the focus in developing this design approach was on unstable parabolic PDEs.

A glance at the graduate textbook [?] gives insight into the status of this subject around 2008: hyperbolic PDE systems had still barely received any consideration by PDE backstepping, except for wave equations and single first-order hyperbolic partial integro-differential equations. No backstepping design applicable to traffic control was yet available. The field was still about three years away from the breakthrough in extending backstepping from parabolic to coupled hyperbolic PDEs, first reported in the conference paper [?]. It is that result that opened the pathway to applying backstepping to the ARZ model and unstable traffic flows.

A series of further advances and generalizations [?, ?, ?, ?] laid the foundations for backstepping design for general coupled hyperbolic PDEs. This chapter presents a self-contained account of those results for the benefit, primarily, of a reader from the field of traffic engineering. A control theorist, particular one specializing in boundary control, is encouraged to study the details contained in the original sources.

The general class of coupled hyperbolic systems is divided into two categories: homodirectional systems of m transport PDEs and heterodirectional systems of $n+m$ transport PDEs.

The homodirectional coupled hyperbolic PDE systems comprise m PDEs which all convect in the same direction, i.e., with the same signs of transport velocities. The homodirectional coupled hyperbolic systems are inherently stable due to the finite length of their spatial transport domain. Coupling among homodirectional PDEs may result in the growth of a signal applied at the inlet boundary as it reaches the outlet boundary in finite time. But such coupling cannot drive the state to infinity.

For a hyperbolic PDE system to be called heterodirectional, there must be at least two PDEs that convect in the opposite directions. It is the coupling among such counterconvecting PDEs that can cause instability in the overall system, just as in the ARZ model, in which stop-and-go instability may arise.

This chapter focuses on the heterodirectional coupled hyperbolic PDE systems where m PDEs convect in one direction and n PDEs convect in the opposite direction. The convention is that the control input enters the boundary of the former set of m PDEs.

The PDE backstepping method achieves Lyapunov stabilization by a change of variables which incorporates a spatial Volterra operator, the conversion of the PDE into a “target system” in which the destabilizing terms are eliminated or dominated, and boundary feedback to make the boundary condition of the target systems homogeneous and, hence, make the target system stable.

In this chapter, we introduce the basic ideas of the PDE backstepping approach for stabilization of systems of coupled hyperbolic PDEs. We introduce designs for general $(n+m) \times (n+m)$ heterodirectional systems and specialize them to the 2×2 case of which the ARZ system is an exemplar. We present backstepping designs for three classes of problems: full-state feedback, observers, and observer-based output-feedback control.

2.2 Coupled Hyperbolic PDEs

This section introduces the general linear hyperbolic systems and their properties. Following [?], the general first-order hyperbolic linear PDE is defined for $u(x, t) = (u_1, u_2 \dots u_n)^T \in \mathbb{R}^n$, $v(x, t) = (v_1, v_2 \dots v_m)^T \in \mathbb{R}^m$ where $x \in [0, 1]$, $t \in [0, +\infty)$,

$$\partial_t u(x, t) + \Lambda^+ \partial_x u(x, t) = \Sigma^{++}(x)u(x, t) + \Sigma^{+-}(x)v(x, t), \quad (2.1)$$

$$\partial_t v(x, t) - \Lambda^- \partial_x v(x, t) = \Sigma^{-+}(x)u(x, t) + \Sigma^{--}(x)v(x, t), \quad (2.2)$$

where the constant characteristic speeds are

$$\Lambda^+ = \text{diag}(\lambda_1, \lambda_2, \dots, \lambda_n), \quad (2.3)$$

$$\Lambda^- = \text{diag}(\mu_1, \mu_2, \dots, \mu_m), \quad (2.4)$$

satisfying

$$-\mu_1 < \dots < -\mu_m < 0 < \lambda_1 < \dots < \lambda_n \quad (2.5)$$

In the coupled hyperbolic PDE system (2.1)–(2.2), all the m PDEs convect in the same direction with positive signs of transport velocities Λ^+ and the n PDEs convect in the opposite direction with negative signs of transport velocities Λ^- . The m PDEs and the heterodirectional n PDEs are coupled inside the domain. The in-domain coupling matrices comprise spatially varying coefficients,

$$\Sigma^{++}(x) = \{\sigma_{ij}^{++}(x)\}_{1 \leq i \leq n, 1 \leq j \leq n}, \quad \Sigma^{+-}(x) = \{\sigma_{ij}^{+-}(x)\}_{1 \leq i \leq n, 1 \leq j \leq m}, \quad (2.6)$$

$$\Sigma^{-+}(x) = \{\sigma_{ij}^{-+}(x)\}_{1 \leq i \leq n, 1 \leq j \leq m}, \quad \Sigma^{--}(x) = \{\sigma_{ij}^{--}(x)\}_{1 \leq i \leq m, 1 \leq j \leq m}, \quad (2.7)$$

where $\sigma_{jj}^{--}(x) = 0, j = 1, \dots, m$ is assumed without loss of generality. Such couplings are removed for application of backstepping design, using a change of coordinates [?].

The following boundary conditions are considered:

$$u(0, t) = Q_0 v(0, t), \quad (2.8)$$

$$v(1, t) = R_1 u(1, t) + U(t), \quad (2.9)$$

where the boundary coefficients are matrices with elements given by

$$Q_0 = \{q_{ij}\}_{1 \leq i \leq n, 1 \leq j \leq m}, \quad (2.10)$$

$$R_1 = \{r_{ij}\}_{1 \leq i \leq m, 1 \leq j \leq n}. \quad (2.11)$$

The control input vector $U(t) = (U_1(t), U_2(t) \dots U_m(t))^T$ is considered to be applied at boundary $x = 1$ without loss of generality.

The diagram of the coupled hyperbolic PDE system is shown in Fig. 2.1. The coupled hyperbolic PDE system contains two parts: m actuated transport PDEs convecting in the upstream direction and n unactuated transport PDEs convecting in the downstream direction. The coupling within each of the two homedirectional subsystems could cause undesirable transient behaviors but these homodirectional subsystems, taken on their own, are inherently stable. The heterodirectional coupling between the u and v PDE subsystems, which convect in mutually opposite directions, may cause instability.

2.3 Backstepping Control for Coupled Hyperbolic PDEs

The main idea of backstepping design consists of three steps.

First, we identify the undesirable terms in a PDE model, for example, by computing the open-loop eigenvalues as in Chapter 1.7. Second, we decide on a target system in which the undesirable terms are canceled by a change of variables and

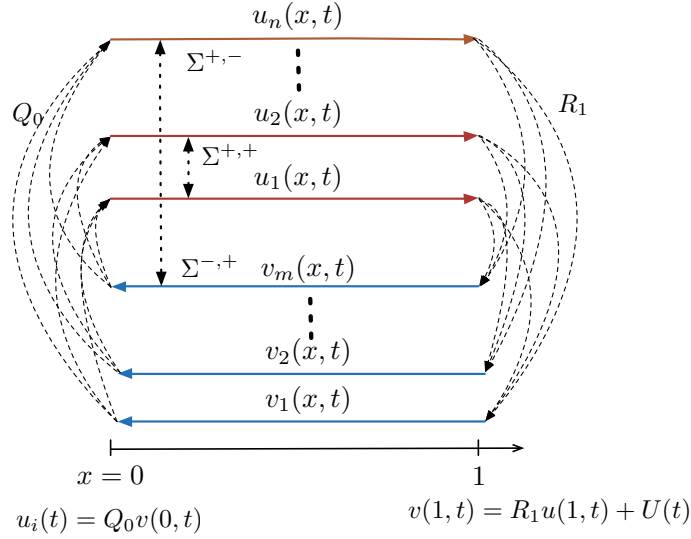


Fig. 2.1 Control diagram of the general coupled hyperbolic PDEs.

design of boundary feedback. The change of variable shifts the system state by a Volterra spatial transformation and brings the undesirable terms to the boundary. Third, through the design of a boundary state feedback controller, we stabilize the PDE system.

We also propose an observer with boundary sensing for state estimation, and construct an output-feedback controller combining the state feedback controller and the observer. In this section, we show how to design a backstepping output-feedback control law for general $n + m$ coupled hyperbolic PDE system, which ensures finite-time convergence of all the states to zero [?].

Target system

We first identify the undesirable coupling terms in (2.1)–(2.2), which introduce spatially in-domain and boundary couplings, and then propose a target system. Applying the backstepping method, we seek to map the system in (2.1)–(2.2) with boundary conditions (2.8)–(2.9) to the following system

$$\begin{aligned} \partial_t \alpha(x, t) + \Lambda^+ \partial_x \alpha(x, t) = & \Sigma^{++}(x) \alpha(x, t) + \Sigma^{+-}(x) \beta(x, t) \\ & + \int_0^x C^+(x, \xi) \alpha(\xi, t) d\xi + \int_0^x C^-(x, \xi) \beta(\xi, t) d\xi \end{aligned} \quad (2.12)$$

$$\partial_t \beta(x, t) - \Lambda^- \partial_x \beta(x, t) = G(x) \beta, \quad (2.13)$$

$$\alpha(0, t) = Q_0 \beta(0, t), \quad (2.14)$$

$$\beta(1, t) = 0, \quad (2.15)$$

where C^+ and C^- are L^∞ matrix functions in the triangular domain $\mathcal{T} = \{(x, \xi) : 0 \leq \xi \leq x \leq 1\}$, and $G \in L^\infty L^2([0, 1])$ is a lower triangular matrix defined as

$$G(x) = \begin{bmatrix} 0 & \dots & \dots & 0 \\ g_{2,1}(x) & \ddots & \ddots & \vdots \\ \vdots & \ddots & \ddots & \vdots \\ g_{m,1}(x) & \dots & g_{m,m-1}(x) & 0 \end{bmatrix}. \quad (2.16)$$

The coefficients of C^+ , C^- and G will be defined later after the introduction of the backstepping transformation.

The explicit solution to (2.12)–(2.15) can be derived by solving the β -system recursively. Exploiting the autonomous nature of the β -subsystem, and the cascade structure among the components of the β -vector, which is reflected in the structure of the matrix $G(x)$ in (2.16), we first have the explicit solution of β_1 as

$$\beta_1(x, t) = \begin{cases} \beta_1(x + \mu t, 0), & t < \frac{1-x}{\mu_1}, \\ 0, & t \geq \frac{1-x}{\mu_1}. \end{cases} \quad (2.17)$$

Thus after $t \geq \frac{1}{\mu_1}$, one has

$$\beta_1(x, t) \equiv 0, \quad (2.18)$$

and then $\beta_2(x, t)$ satisfies the following equation

$$\partial_t \beta_2(x, t) - \mu_2 \partial_x \beta_2(x, t) = 0. \quad (2.19)$$

In the same fashion, one obtains that after $t \geq \frac{1}{\mu_1} + \frac{1}{\mu_2}$,

$$\beta_2(x, t) \equiv 0. \quad (2.20)$$

Therefore, one can get that after $t = \sum_{j=1}^m \frac{1}{\mu_j}$,

$$\beta_j(x, t) \equiv 0, \quad (2.21)$$

where $j = 1, 2, \dots, m$. From the time $t = \sum_{j=1}^m \frac{1}{\mu_j}$ on, as β_j vanish, the α -system in (2.12) becomes autonomous,

$$\partial_t \alpha(x, t) + \Lambda^+ \partial_x \alpha(x, t) = \Sigma^{++}(x) \alpha(x, t) + \int_0^x C^+(x, \xi) \alpha(\xi, t) d\xi, \quad (2.22)$$

with the boundary conditions

$$\alpha(0, t) = 0. \quad (2.23)$$

Since the integral with the kernel C^+ constitutes only a spatially feedforward (and not feedback) operation, namely, an operation in the direction of convection, it is straightforward to solve (2.22) with (2.23) and to show that

$$\alpha(x, t) \equiv 0 \quad (2.24)$$

holds for $t \geq t_F$, where

$$t_F = \sum_{j=1}^m \frac{1}{\mu_j} + \frac{1}{\lambda_1}. \quad (2.25)$$

The following lemma states the finite-time convergence of the target system.

Lemma 2.1 *Consider target system (2.12)–(2.15). The equilibrium $\alpha = \beta = 0$ is stable and reached in finite time $t = t_F$, where*

$$t_F = \sum_{j=1}^m \frac{1}{\mu_j} + \frac{1}{\lambda_1}. \quad (2.26)$$

Backstepping transformation

In order to map the coupled hyperbolic PDE system (2.1), (2.2) with boundary conditions (2.8), (2.9) into the target system (2.12)–(2.15), we apply the following backstepping transformation

$$\alpha(x, t) = u(x, t), \quad (2.27)$$

$$\beta(x, t) = v(x, t) - \int_0^x K(x, \xi) u(\xi, t) d\xi - \int_0^x L(x, \xi) v(\xi, t) d\xi, \quad (2.28)$$

where the kernels K and L are defined in the triangular domain \mathcal{T} . Differentiating (2.28) with respect to space and time and substituting the results into the target system yields the following kernel equations

$$0 = \Lambda^- \partial_x K(x, \xi) - \partial_\xi K(x, \xi) \Lambda^+ - K(x, \xi) \Sigma^{++} - L(x, \xi) \Sigma^{-+}, \quad (2.29)$$

$$0 = \Lambda^- \partial_x L(x, \xi) - \partial_\xi L(x, \xi) \Lambda^- - L(x, \xi) \Sigma^{--} - K(x, \xi) \Sigma^{+-}, \quad (2.30)$$

$$0 = K(x, x) \Lambda^+ + \Lambda^- K(x, x) + \Sigma^{-+}, \quad (2.31)$$

$$0 = \Lambda^- L(x, x) - L(x, x) \Lambda^- + \Sigma^{--}, \quad (2.32)$$

$$0 = K(x, 0) \Lambda^+ Q_0 + G(x) - L(x, 0) \Lambda^-, \quad (2.33)$$

and yields the following equations for $C^-(x, \xi)$ and $C^+(x, \xi)$

$$C^-(x, \xi) = \Sigma^{+-} L(x, \xi) + \int_\xi^x C^-(x, s) L(s, \xi) d\xi, \quad (2.34)$$

$$C^+(x, \xi) = \Sigma^{+-} K(x, \xi) + \int_\xi^x C^-(x, s) K(s, \xi) d\xi. \quad (2.35)$$

Expanding the kernel equations and boundary conditions, we have the following PDE system for $1 \leq i \leq m$ and $1 \leq j \leq n$,

$$\mu_i \partial_x K_{ij}(x, \xi) - \lambda_j \partial_\xi K_{ij}(x, \xi) = \sum_{k=1}^n \sigma_{kj}^{++} K_{ik}(x, \xi) + \sum_{l=1}^m \sigma_{lj}^{-+} L_{ls}(x, \xi), \quad (2.36)$$

$$K_{ij}(x, x) = -\frac{\sigma_{ij}^{-+}}{\mu_i + \lambda_j}. \quad (2.37)$$

For $1 \leq i \leq m$ and $1 \leq j \leq m$, we have the PDE system

$$\mu_i \partial_x L_{ij}(x, \xi) - \mu_j \partial_\xi L_{ij}(x, \xi) = \sum_{l=1}^m \sigma_{lj}^{--} L_{lp}(x, \xi) + \sum_{k=1}^n \sigma_{kj}^{+-} K_{ik}(x, \xi), \quad (2.38)$$

$$L_{ij}(x, x) = -\frac{\sigma_{ij}^{--}}{\mu_i - \mu_j}, \quad (2.39)$$

with the artificial boundary condition for $L_{ij}(i > j)$ added for the well-posedness of the kernel equations

$$L_{ij}(1, \xi) = -\frac{\sigma_{ij}^{--}}{\mu_i - \mu_j}. \quad (2.40)$$

The well-posedness of the kernel equations can be proved using the method of characteristics and successive approximations, which is completed in [?]. There exists a unique solution K and L in $L^\infty(\mathcal{T})$. One can obtain that there exists a unique matrix-valued function $\mathcal{R} \in L^\infty[(0, 1)]^{(n+m) \times (n+m)}$ such that the inverse transformation of (2.27) and (2.28) holds

$$\begin{bmatrix} u(x, t) \\ v(x, t) \end{bmatrix} = \begin{bmatrix} \alpha(x, t) \\ \beta(x, t) \end{bmatrix} - \int_0^x \mathcal{R}(x, \xi) \begin{bmatrix} \alpha(\xi, t) \\ \beta(\xi, t) \end{bmatrix} d\xi. \quad (2.41)$$

We can then study the stability of the target system (2.12)–(2.15) due to its equivalence to the original system (2.1)–(2.9).

Full-state feedback design

Evaluating transformation (2.28) at $x = 1$ yields the full-state feedback controller,

$$U(t) = -R_1 u(1, t) + \int_0^1 K(1, \xi) u(\xi) + L(1, \xi) v(\xi) d\xi. \quad (2.42)$$

According to Lemma 2.1 and the equivalence between the target system (2.12)–(2.15) and the original system, we state the main stabilization result.

Theorem 2.1 *Consider system (2.1), (2.1) with boundary conditions (2.8), (2.9), and the full-state feedback law (2.42). For any initial condition $(u_0, v_0) \in L^\infty[(0, 1)]^{(n+m) \times (n+m)}$, the equilibrium $u = v = 0$ is stable and reached in finite time $t = t_F$, where t_F is given in (2.26).*

2.4 Observer and Output-Feedback Design for General Hyperbolic PDEs

In this section, we present an observer that relies on the boundary sensing of the state vector v at $x = 0$,

$$y(t) = v(0, t), \quad (2.43)$$

which is anti-collocated with the control law (2.42) located at $x = 1$. Employing the state estimates, from the observer, in the control law, we derive an output-feedback controller.

Boundary sensing for state estimation

We design an observer to estimate $u(x, t)$ and $v(x, t)$ in the form of a copy of the original system (2.1)–(2.9) with output estimation error injection terms, driven by $\hat{v}(0, t) - v(0, t)$. The observer is given as

$$\begin{aligned}\partial_t \hat{u}(x, t) + \Lambda^+ \partial_x \hat{u}(x, t) &= \Sigma^{++}(x) \hat{u}(x, t) + \Sigma^{+-}(x) \hat{v}(x, t) \\ &\quad - P^+(x)(\hat{v}(0, t) - v(0, t)),\end{aligned}\quad (2.44)$$

$$\begin{aligned}\partial_t \hat{v}(x, t) - \Lambda^- \partial_x \hat{v}(x, t) &= \Sigma^{-+}(x) \hat{u}(x, t) + \Sigma^{--}(x) \hat{v}(x, t) \\ &\quad - P^-(x)(\hat{v}(0, t) - v(0, t)),\end{aligned}\quad (2.45)$$

$$\hat{u}(0, t) = Q_0 v(0, t), \quad (2.46)$$

$$\hat{v}(1, t) = R_1 \hat{u}(1, t) + U(t), \quad (2.47)$$

where $\hat{u}(x, t)$ and $\hat{v}(x, t)$ are the estimates of the state variables $u(x, t)$ and $v(x, t)$. The term P^+ and P^- are output injection gains to be designed. The estimation error system is obtained by subtracting the observer (2.44)–(2.47) from the original system (2.1)–(2.9),

$$\begin{aligned}\partial_t \tilde{u}(x, t) + \Lambda^+ \partial_x \tilde{u}(x, t) &= \Sigma^{++}(x) \tilde{u}(x, t) + \Sigma^{+-}(x) \tilde{v}(x, t) \\ &\quad - P^+(x) \tilde{v}(0, t),\end{aligned}\quad (2.48)$$

$$\begin{aligned}\partial_t \tilde{v}(x, t) - \Lambda^- \partial_x \tilde{v}(x, t) &= \Sigma^{-+}(x) \tilde{u}(x, t) + \Sigma^{--}(x) \tilde{v}(x, t) \\ &\quad - P^-(x) \tilde{v}(0, t),\end{aligned}\quad (2.49)$$

$$\tilde{u}(0, t) = 0, \quad (2.50)$$

$$\tilde{v}(1, t) = R_1 \tilde{u}(1, t), \quad (2.51)$$

where the estimation error states are defined as

$$\tilde{u}(x, t) = u(x, t) - \hat{u}(x, t), \quad (2.52)$$

$$\tilde{v}(x, t) = v(x, t) - \hat{v}(x, t). \quad (2.53)$$

We then derive a target system, and using the backstepping transformation, design observer gains P^+ and P^- which yield finite-time stability of the error system (2.48)–(2.51).

We map the error system into the following target system

$$\partial_t \tilde{\alpha}(x, t) + \Lambda^+ \partial_x \tilde{\alpha}(x, t) = \Sigma^{++}(x) \tilde{\alpha}(x, t) + \int_0^x D^+(x, \xi) \tilde{\alpha}(\xi) d\xi, \quad (2.54)$$

$$\partial_t \tilde{\beta}(x, t) - \Lambda^- \partial_x \tilde{\beta}(x, t) = \Sigma^{-+}(x) \tilde{\alpha}(x, t) + \int_0^x D^-(x, \xi) \tilde{\alpha}(\xi) d\xi, \quad (2.55)$$

$$\tilde{\alpha}(0, t) = 0, \quad (2.56)$$

$$\tilde{\beta}(1, t) = R_1 \tilde{\alpha}(1, t) - \int_0^1 H(\xi) \tilde{\beta}(\xi) d\xi, \quad (2.57)$$

where D^+ and D^- are L^∞ matrix functions on the domain \mathcal{T} and $H \in L^\infty([0, 1])$ is an upper triangular matrix,

$$H(x) = \begin{bmatrix} 0 & h_{1,2}(x) & \cdots & h_{1,m}(x) \\ \vdots & \ddots & \ddots & \vdots \\ \vdots & \ddots & \ddots & h_{m-1,m}(x) \\ 0 & \cdots & \cdots & 0 \end{bmatrix}, \quad (2.58)$$

which will be defined later with the introduction of a backstepping transformation and kernel equations that govern the backstepping kernels.

The target system consists of the autonomous $\tilde{\alpha}$ -system (with a zero input at its inlet at $x = 0$) cascaded into the $\tilde{\beta}$ -system. The $\tilde{\beta}$ -system is an internally cascaded vector PDE system itself with slower components of the $\tilde{\beta}$ vector state cascading into the faster component states through boundary condition (2.57). The cascade structure of the boundary condition is the consequence of the upper triangularity of the matrix $H(x)$.

Following the same steps as in solving (2.12)–(2.15), we obtain the following lemma.

Lemma 2.2 *Consider the target system (2.54)–(2.57). The equilibrium $\tilde{\alpha} = \tilde{\beta} = 0$ is stable and reached in finite time $t = t_F$, where*

$$t_F = \sum_{j=1}^m \frac{1}{\mu_j} + \frac{1}{\lambda_1}. \quad (2.59)$$

To map the error system (2.48)–(2.51) to the target system (2.54)–(2.57), we apply the following backstepping transformation

$$\tilde{u}(x, t) = \tilde{\alpha}(x, t) + \int_0^x M(x, \xi) \tilde{\beta}(\xi) d\xi, \quad (2.60)$$

$$\tilde{v}(x, t) = \tilde{\beta}(x, t) + \int_0^x N(x, \xi) \tilde{\beta}(\xi) d\xi, \quad (2.61)$$

where the kernels M and N are defined on \mathcal{T} . The kernel M is governed by the following kernel PDE equation system with boundary conditions, for $1 \leq i \leq n$ and $1 \leq j \leq m$,

$$\lambda_i \partial_x M_{ij}(x, \xi) - \mu_j \partial_\xi M_{ij}(x, \xi) = \sum_{k=1}^n \sigma_{ik}^{++} M_{kj}(x, \xi) + \sum_{p=1}^m \sigma_{ip}^{+-} N_{pj}(x, \xi), \quad (2.62)$$

$$M_{ij}(x, x) = \frac{\sigma_{ij}^{+-}}{\mu_i + \lambda_j}. \quad (2.63)$$

The kernel PDE for N is governed, for $1 \leq i \leq m$ and $1 \leq j \leq m$, by the PDE system

$$\mu_j \partial_x N_{ij}(x, \xi) - \mu_j \partial_\xi N_{ij}(x, \xi) = \sum_{k=1}^n \sigma_{ik}^{-+} M_{kj}(x, \xi) + \sum_{p=1}^m \sigma_{ip}^{--} N_{pj}(x, \xi), \quad (2.64)$$

$$N_{ij}(x, x) = \frac{\sigma_{ij}^{--}}{\mu_i - \mu_j}, \quad i \neq j. \quad (2.65)$$

The following boundary condition is obtained by evaluating (2.60)–(2.61) at $x = 1$ for $1 \leq j \leq i \leq m$,

$$N_{ij}(1, x) = \sum_{k=1}^n \rho_{ik} M_{kj}(1, x). \quad (2.66)$$

We add the artificial boundary conditions for N_{ij} , ($1 \leq i < j \leq m$) for the well-posedness of the kernel equations,

$$N_{ij}(x, 0) = 0. \quad (2.67)$$

The kernels of the “disturbing terms” in the target system, namely, the kernels D^+ , D^- , and H , are given by

$$d_{ij}^+(x, \xi) = - \sum_{k=1}^m M_{ik}(x, \xi) \sigma_{kj}^{-+} + \int_\xi^x \sum_{k=1}^m M_{ik}(x, s) d_{kj}^- d\xi, \quad (2.68)$$

$$d_{ij}^-(x, \xi) = - \sum_{k=1}^m N_{ik}(x, \xi) \sigma_{kj}^{-+} + \int_\xi^x \sum_{k=1}^m N_{ik}(x, s) d_{kj}^- d\xi, \quad (2.69)$$

$$h_{ij}(x) = N_{ij}(1, x) - \sum_{k=1}^n \rho_{ik} M_{kj}(1, x). \quad (2.70)$$

Finally, and most importantly, the observer gains P^+ and P^- are defined as

$$p_{ij}^+(x) = \mu_j m_{ij}(x, 0), \quad (2.71)$$

$$p_{ij}^-(x) = \mu_j n_{ij}(x, 0). \quad (2.72)$$

The well-posedness of the system of kernel equations (2.62)–(2.67) of the observer is equivalent to that of the controller kernels (2.36)–(2.40) and the proof follows the same steps in [?]. We then reach our theorem for the observer design.

Theorem 2.2 *Consider the system (2.48)–(2.51) with initial conditions $\tilde{u}_0, \tilde{u}_0 \in L^2[0, L]$. It holds that*

$$\|u(\cdot, t) - \hat{u}(\cdot, t)\| \rightarrow 0, \quad (2.73)$$

$$\|v(\cdot, t) - \hat{v}(\cdot, t)\| \rightarrow 0. \quad (2.74)$$

The equilibrium $u - \hat{u} = v - \hat{v} = 0$ is stable and reached in finite time $t = t_F$, given in (2.26).

Output feedback design

Combining the full state feedback control law (2.42) and the observer estimates, we propose the output-feedback control law

$$U(t) = -R_1 \hat{u}(1, t) + \int_0^1 K(1, \xi) \hat{u}(\xi, t) d\xi + \int_0^1 L(1, \xi) \hat{v}(\xi, t) d\xi, \quad (2.75)$$

where state estimates $\hat{u}(x, t)$ and $\hat{v}(x, t)$ are obtained from the observer (2.44)–(2.47). The control gain kernels K and L are obtained from solving the kernel equations (2.36)–(2.40). The output injection gains of the observer (2.71)–(2.72) are obtained from solving the kernel equations (2.62)–(2.67). Then we reach the following main theorem combining Theorem 2.1 and Theorem 2.2.

Theorem 2.3 *Consider system (2.76)–(2.79) with initial conditions $u_0, v_0 \in L^2[0, L]$ and the output-feedback control law (2.150), where the kernels K and L are obtained from solving the kernel equations (2.98)–(2.105) and the output injection gains of the observer (2.138)–(2.139) are obtained from solving the kernel equations (2.130)–(2.137). The equilibrium $u = \hat{u} = v = \hat{v} = 0$ is stable and reached in finite time $t = 2t_F$ given in (2.26).*

2.5 Backstepping Control for second-order Hyperbolic PDEs

In this section, we present in some additional detail the special case of the backstepping control design for the coupled second-order hyperbolic PDE system. We incorporate the details of this special case from the chapter [?].

The second-order coupled hyperbolic PDE case, or, as it is also referred to as the 2×2 case is relevant for the material in our book because the basic ARZ traffic flow model falls into the 2×2 category.

So, let us consider the following 2×2 hyperbolic PDE system with boundary conditions,

$$\partial_t u(x, t) + \lambda \partial_x u(x, t) = c_1(x) v(x, t), \quad (2.76)$$

$$\partial_t v(x, t) - \mu \partial_x v(x, t) = c_2(x) u(x, t), \quad (2.77)$$

$$u(0, t) = q_0 v(0, t), \quad (2.78)$$

$$v(1, t) = r_1 u(1, t) + U(t), \quad (2.79)$$

where $\lambda, \mu_1 > 0$, $q_0, r_1 \in \mathbb{R}$ and initial conditions $u(0, t), v(0, t) \in L^2([0, 1])$. The objective is to design a feedback law, implemented using the input signal $U(t)$, such that the closed-loop system is exponentially stable.

Target system

We first identify the undesirable coupling terms in (2.76)–(2.79). Such coupling terms appear both throughout the spatial domain and in the boundary conditions. We propose a target system free of such detrimental terms. Applying backstepping method, we seek to map the system in (2.76)–(2.79) to the following chosen target system

$$\partial_t \alpha(x, t) + \lambda \partial_x \alpha(x, t) = 0, \quad (2.80)$$

$$\partial_t \beta(x, t) - \mu \partial_x \beta(x, t) = 0, \quad (2.81)$$

$$\alpha(0, t) = q_0 \beta(0, t), \quad (2.82)$$

$$\beta(1, t) = 0, \quad (2.83)$$

where the control signal $U(t)$ is chosen in accordance with the backstepping transformation and such that the homogeneous Dirichlet boundary condition (2.83) is enforced.

The initial conditions are defined as $\alpha_0(x) = \alpha(x, 0)$ and $\beta_0(x) = \beta(x, 0)$ and $\alpha_0(x), \beta_0(x) \in L^2([0, 1])$. The explicit solution to (2.80)–(2.83) is given by

$$\alpha(x, t) = \begin{cases} \alpha_0(x - \lambda t), & t < \frac{x}{\lambda}, \\ q_0 \beta_0(0, t - \frac{x}{\lambda}), & t \geq \frac{x}{\lambda}, \end{cases} \quad (2.84)$$

$$\beta(x, t) = \begin{cases} \beta_0(x + \mu t), & t < \frac{1-x}{\mu}, \\ 0, & t \geq \frac{1-x}{\mu}. \end{cases} \quad (2.85)$$

Thus after $t \geq \frac{1}{\mu}$, one has

$$\alpha(x, t) \equiv 0, \quad (2.86)$$

and after $t \geq \frac{1}{\mu} + \frac{1}{\lambda}$, it holds that

$$\beta(x, t) \equiv 0. \quad (2.87)$$

Therefore, it holds that for $t \geq t_f$,

$$\alpha(x, t) \equiv \beta(x, t) \equiv 0, \quad (2.88)$$

where

$$t_f = \frac{1}{\mu} + \frac{1}{\lambda}. \quad (2.89)$$

Lyapunov Stability Analysis

To show the exponential stability of the target system in the L^2 sense, we construct the following Lyapunov functions $V(t) = V_1(t) + V_2(t)$,

$$V_1(t) = \frac{1}{2} \int_0^1 \frac{2-x}{\lambda} \alpha^2(x, t) dx, \quad (2.90)$$

$$V_2(t) = \frac{1}{2} \int_0^1 \frac{2q_0^2(1+x)}{\mu} \beta^2(x, t) dx, \quad (2.91)$$

and differentiate the Lyapunov functions in time. We obtain the following inequalities, integrating by parts,

$$\dot{V}_1 \leq -\alpha^2(1, t) + 2\alpha^2(0, t) - \|\alpha\|^2, \quad (2.92)$$

$$\dot{V}_2 \leq 4q_0^2\beta^2(1, t) - 2q_0^2\beta^2(0, t) - 2q_0^2\|\beta\|^2. \quad (2.93)$$

Applying boundary conditions (2.82)–(2.83), it holds that

$$\begin{aligned} \dot{V} &= -\alpha^2(1, t) - \|\alpha\|^2 - 2q_0^2\|\beta\|^2 \\ &\leq -c_0 V, \end{aligned} \quad (2.94)$$

where

$$c_0 = \min(\lambda, \mu). \quad (2.95)$$

The exponential stability of the target system (2.80)–(2.81) is summarized in the following theorem.

Theorem 2.4 *Consider the target system (2.80)–(2.81) with initial conditions $\alpha_0(x), \beta_0(x) \in L^2([0, 1])$. The equilibrium $\alpha(x, \cdot) \equiv \beta(x, \cdot) \equiv 0$ is exponentially stable in the L^2 sense and it is reached in finite time $t = t_f$ given in (2.89).*

Full-State Feedback Design

To map the original system (2.76)–(2.79) into the target system (2.80)–(2.83), we apply the following Volterra spatial transformation,

$$\alpha(x, t) = u(x, t) - \int_0^x K_{11}(x, \xi) u(\xi, t) d\xi - \int_0^x K_{12}(x, \xi) v(\xi, t) d\xi, \quad (2.96)$$

$$\beta(x, t) = v(x, t) - \int_0^x K_{21}(x, \xi) u(\xi, t) d\xi - \int_0^x K_{22}(x, \xi) v(\xi, t) d\xi, \quad (2.97)$$

where the kernels $K_{ij}(x, \xi), i, j = 1, 2$ evolve in the triangular domain $\mathcal{T} = \{(x, \xi) : 0 \leq \xi \leq x \leq 1\}$.

By introducing the transformation (2.96), (2.97) into the target system, we obtain a set of kernel equations that govern the kernels variables in the transformation,

$$\lambda \partial_x K_{11}(x, \xi) + \lambda \partial_\xi K_{11}(x, \xi) = -c_2(\xi) K_{12}(x, \xi), \quad (2.98)$$

$$\lambda \partial_x K_{12}(x, \xi) - \mu \partial_\xi K_{12}(x, \xi) = -c_1(\xi) K_{11}(x, \xi), \quad (2.99)$$

$$\mu \partial_x K_{21}(x, \xi) - \lambda \partial_\xi K_{21}(x, \xi) = c_2(\xi) K_{22}(x, \xi), \quad (2.100)$$

$$\mu \partial_x K_{22}(x, \xi) + \mu \partial_\xi K_{22}(x, \xi) = c_1(\xi) K_{21}(x, \xi), \quad (2.101)$$

with boundary conditions

$$K_{11}(x, 0) = \frac{\mu}{q_0 \lambda} K_{12}(x, 0), \quad (2.102)$$

$$K_{12}(x, x) = \frac{c_1(x)}{\lambda + \mu}, \quad (2.103)$$

$$K_{21}(x, x) = -\frac{c_2(x)}{\lambda + \mu}, \quad (2.104)$$

$$K_{22}(x, 0) = \frac{q_0 \lambda}{\mu} K_{21}(x, 0), \quad (2.105)$$

The well-posedness of the kernel equations and the boundedness of the kernel variables can be proved by following the same steps of proof in [?], using method of characteristics and successive approximations.

To study the invertibility of the backstepping transformation in (2.96)–(2.97), we consider the following transformation that maps the target system (2.80)–(2.83) back into the original system,

$$u(x, t) = \alpha(x, t) - \int_0^x L_{11}(x, \xi) \alpha(\xi, t) d\xi - \int_0^x L_{12}(x, \xi) \beta(\xi, t) d\xi, \quad (2.106)$$

$$v(x, t) = \beta(x, t) - \int_0^x L_{21}(x, \xi) \alpha(\xi, t) d\xi - \int_0^x L_{22}(x, \xi) \beta(\xi, t) d\xi, \quad (2.107)$$

where the kernels $L_{ij}(x, \xi)$, $i, j = 1, 2$ evolve in the triangular domain $\mathcal{T} = \{(x, \xi) : 0 \leq \xi \leq x \leq 1\}$. By introducing the transformation (2.106), (2.107) into the original system (2.76)–(2.79), we obtain a set of kernel equations that govern the kernels variables in the inverse transformation,

$$\lambda \partial_x L_{11}(x, \xi) + \lambda \partial_\xi L_{11}(x, \xi) = c_1(x) L_{21}(x, \xi), \quad (2.108)$$

$$\lambda \partial_x L_{12}(x, \xi) - \mu \partial_\xi L_{12}(x, \xi) = c_1(\xi) L_{22}(x, \xi), \quad (2.109)$$

$$\mu \partial_x L_{21}(x, \xi) - \lambda \partial_\xi L_{21}(x, \xi) = -c_2(\xi) L_{11}(x, \xi), \quad (2.110)$$

$$\mu \partial_x L_{22}(x, \xi) + \mu \partial_\xi L_{22}(x, \xi) = -c_2(\xi) L_{12}(x, \xi), \quad (2.111)$$

with boundary conditions

$$L_{11}(x, 0) = \frac{\mu}{q_0\lambda} L_{12}(x, 0), \quad (2.112)$$

$$L_{12}(x, x) = \frac{c_1(x)}{\lambda + \mu}, \quad (2.113)$$

$$L_{21}(x, x) = -\frac{c_2(x)}{\lambda + \mu}, \quad (2.114)$$

$$L_{22}(x, 0) = \frac{q_0\lambda}{\mu} L_{21}(x, 0). \quad (2.115)$$

The well-posedness of the kernel equations of the inverse backstepping transformation can be proven in the same fashion as proving the well posedness of the kernel equations of the direct backstepping transformation. Therefore, the invertibility of the backstepping transformation in (2.96)–(2.97) is guaranteed. We study the stability of the plant by studying the stability of the target system due to their L^2 -equivalence.

Evaluating the transformation (2.97) at $x = 1$ and substituting it into the boundary condition (2.83), we have

$$U(t) = -r_1 u(1, t) + \int_0^1 K_{21}(1, \xi) u(\xi, t) d\xi + \int_0^1 K_{22}(1, \xi) v(\xi, t) d\xi. \quad (2.116)$$

This state feedback control law stabilizes the closed-loop system. According to Theorem 2.4 and the equivalence between the target and original system, we summarize the main state feedback stabilization result in the following theorem.

Theorem 2.5 *Consider system (2.76)–(2.79) with initial conditions $u_0, v_0 \in L^2[0, L]$ and the control law (2.116). The equilibrium $u \equiv v \equiv 0$ is exponentially stable in the L^2 sense and it is reached in finite time $t = t_f$ given in (2.89).*

2.6 Observer and Collocated Output-Feedback Design for Second-order Hyperbolic PDEs

Boundary sensing for state estimation

We consider a ‘proximal’—or ‘collocated’—boundary measurement, defined as

$$Y(t) = u(1, t). \quad (2.117)$$

We design an observer to estimate the states $u(x, t)$ and $v(x, t)$ by constructing the observer system as a copy of the original system (2.76)–(2.79) with the injection of output estimation error $u(L, t) - \hat{u}(L, t)$. The observer is given as

$$\partial_t \hat{u}(x, t) + \lambda \partial_x \hat{u}(x, t) = c_1(x) \hat{v}(x, t) + r(x)(u(L, t) - \hat{u}(L, t)), \quad (2.118)$$

$$\partial_t \hat{v}(x, t) - \mu \partial_x \hat{v}(x, t) = c_2(x) \hat{u}(x, t) + s(x)(u(L, t) - \hat{u}(L, t)), \quad (2.119)$$

$$\hat{u}(0, t) = q_0 \hat{v}(0, t), \quad (2.120)$$

$$\hat{v}(1, t) = -r_1 Y(t) + U(t), \quad (2.121)$$

where $\hat{u}(x, t)$ and $\hat{v}(x, t)$ are the estimates of the state variables $u(x, t)$ and $v(x, t)$. The functions $r(x)$ and $s(x)$ are output injection gains to be designed. The estimation error system is obtained by subtracting the observer (2.118)–(2.121) from the original system (2.76)–(2.79),

$$\partial_t \tilde{u}(x, t) + \lambda \partial_x \tilde{u}(x, t) = c_1(x) \tilde{v}(x, t) - r(x) \tilde{u}(L, t), \quad (2.122)$$

$$\partial_t \tilde{v}(x, t) - \mu \partial_x \tilde{v}(x, t) = c_2(x) \tilde{u}(x, t) - s(x) \tilde{u}(L, t), \quad (2.123)$$

$$\tilde{u}(0, t) = q_0 \tilde{v}(0, t), \quad (2.124)$$

$$\tilde{v}(1, t) = 0, \quad (2.125)$$

where the estimation error states are defined as

$$\tilde{u}(x, t) = u(x, t) - \hat{u}(x, t), \quad (2.126)$$

$$\tilde{v}(x, t) = v(x, t) - \hat{v}(x, t). \quad (2.127)$$

We need to find the output injection gains $r(x)$ and $s(x)$ that guarantee the error system decays to zero. Using a backstepping transformation, we transform the error system (2.122)–(2.125) into the target system (2.80)–(2.83).

The backstepping transformation is

$$\tilde{\alpha}(x, t) = \tilde{u}(x, t) - \int_0^x \tilde{K}_{11}(x, \xi) \tilde{u}(\xi, t) d\xi - \int_0^x \tilde{K}_{12}(x, \xi) \tilde{v}(\xi, t) d\xi, \quad (2.128)$$

$$\tilde{\beta}(x, t) = \tilde{v}(x, t) - \int_0^x \tilde{K}_{21}(x, \xi) \tilde{u}(\xi, t) d\xi - \int_0^x \tilde{K}_{22}(x, \xi) \tilde{v}(\xi, t) d\xi, \quad (2.129)$$

where the kernels $\tilde{K}_{ij}(x, \xi)$, $i, j = 1, 2$ evolve in the triangular domain $\mathcal{T} = \{(x, \xi) : 0 \leq \xi \leq x \leq 1\}$. By introducing the transformation (2.128), (2.129) into the target system, we obtain a set of kernel equations that govern the kernels variables in the transformation,

$$\lambda \partial_x \tilde{K}_{11}(x, \xi) + \lambda \partial_\xi \tilde{K}_{11}(x, \xi) = -c_2(\xi) \tilde{K}_{12}(x, \xi), \quad (2.130)$$

$$\lambda \partial_x \tilde{K}_{12}(x, \xi) - \mu \partial_\xi \tilde{K}_{12}(x, \xi) = -c_1(\xi) \tilde{K}_{11}(x, \xi), \quad (2.131)$$

$$\mu \partial_x \tilde{K}_{21}(x, \xi) - \lambda \partial_\xi \tilde{K}_{21}(x, \xi) = c_2(\xi) \tilde{K}_{22}(x, \xi), \quad (2.132)$$

$$\mu \partial_x \tilde{K}_{22}(x, \xi) + \mu \partial_\xi \tilde{K}_{22}(x, \xi) = c_1(\xi) \tilde{K}_{21}(x, \xi), \quad (2.133)$$

with boundary conditions

$$\tilde{K}_{11}(x, 0) = q_0 \tilde{K}_{21}(x, 0), \quad (2.134)$$

$$\tilde{K}_{12}(x, x) = \frac{c_1(x)}{\lambda + \mu}, \quad (2.135)$$

$$\tilde{K}_{21}(x, x) = -\frac{c_2(x)}{\lambda + \mu}, \quad (2.136)$$

$$\tilde{K}_{22}(x, 0) = \frac{1}{q_0} K_{12}(x, 0). \quad (2.137)$$

The well-posedness of the kernel equations and the boundedness of the kernel variables can be proved in the same fashion as for the kernel PDEs for the backstepping transformation in the full-state feedback design, namely, using method of characteristics and successive approximations. The output injection gain $r(x)$ and $s(x)$ are

$$r(x) = -\lambda \tilde{K}_{11}(x, 1), \quad (2.138)$$

$$s(x) = -\lambda \tilde{K}_{21}(x, 1). \quad (2.139)$$

To study the invertibility of the backstepping transformation in (2.128)–(2.129), we consider the following transformation that maps the target system (2.80)–(2.83) back into the estimation error system (2.122)–(2.125),

$$\tilde{u}(x, t) = \tilde{\alpha}(x, t) - \int_0^x \tilde{L}_{11}(x, \xi) \tilde{\alpha}(\xi, t) d\xi - \int_0^x \tilde{L}_{12}(x, \xi) \tilde{\beta}(\xi, t) d\xi, \quad (2.140)$$

$$\tilde{v}(x, t) = \tilde{\beta}(x, t) - \int_0^x \tilde{L}_{21}(x, \xi) \tilde{\alpha}(\xi, t) d\xi - \int_0^x \tilde{L}_{22}(x, \xi) \tilde{\beta}(\xi, t) d\xi, \quad (2.141)$$

where the kernels $\tilde{L}_{ij}(x, \xi)$, $i, j = 1, 2$ evolve in the triangular domain $\mathcal{T} = \{(x, \xi) : 0 \leq \xi \leq x \leq 1\}$. The set of kernel equations that govern the kernels variables in the inverse transformation are given by

$$\lambda \partial_x \tilde{L}_{11}(x, \xi) + \lambda \partial_\xi \tilde{L}_{11}(x, \xi) = c_1(x) \tilde{L}_{21}(x, \xi), \quad (2.142)$$

$$\lambda \partial_x \tilde{L}_{12}(x, \xi) - \mu \partial_\xi \tilde{L}_{12}(x, \xi) = c_1(\xi) \tilde{L}_{22}(x, \xi), \quad (2.143)$$

$$\mu \partial_x \tilde{L}_{21}(x, \xi) - \lambda \partial_\xi \tilde{L}_{21}(x, \xi) = -c_2(\xi) \tilde{L}_{11}(x, \xi), \quad (2.144)$$

$$\mu \partial_x \tilde{L}_{22}(x, \xi) + \mu \partial_\xi \tilde{L}_{22}(x, \xi) = -c_2(\xi) \tilde{L}_{12}(x, \xi), \quad (2.145)$$

with boundary conditions

$$\tilde{L}_{11}(x, 0) = q_0 \tilde{L}_{12}(x, 0), \quad (2.146)$$

$$\tilde{L}_{12}(x, x) = \frac{c_1(x)}{\lambda + \mu}, \quad (2.147)$$

$$\tilde{L}_{21}(x, x) = -\frac{c_2(x)}{\lambda + \mu}, \quad (2.148)$$

$$\tilde{L}_{22}(x, 0) = \frac{q_0 \lambda}{\mu} \tilde{L}_{21}(x, 0). \quad (2.149)$$

The well-posedness of the kernel equations can be proved in the same fashion as in the previously mention cases of the kernel PDE systems, i.e., using the approach from [?]. Therefore, the invertibility of the backstepping transformation in (2.128)–(2.129) is guaranteed.

We can study the stability of target system and, due to its equivalence to the estimation error system in the original variables (\hat{u}, \hat{v}) , infer convergence in those variables to the unmeasured (u, v) . Therefore, by studying the stability of the target system we establish the exponential stability of estimation error system in the L^2 sense and its finite-time convergence to zero.

Theorem 2.6 *Consider system (2.122)–(2.125) with initial conditions $\tilde{u}_0, \tilde{v}_0 \in L^2[0, L]$. The equilibrium $\tilde{u} \equiv \tilde{v} \equiv 0$ is exponentially stable in the L^2 sense. Furthermore, $\|u(\cdot, t) - \hat{u}(\cdot, t)\| \rightarrow 0$ and $\|v(\cdot, t) - \hat{v}(\cdot, t)\| \rightarrow 0$ as time approaches the finite value $t = t_f$.*

Output feedback design

Combining the full state feedback control law (2.116) and the observer estimates, we propose the output-feedback control law

$$U(t) = -r_1 \hat{u}(1, t) + \int_0^1 K_{21}(1, \xi) \hat{u}(\xi, t) d\xi + \int_0^1 K_{22}(1, \xi) \hat{v}(\xi, t) d\xi, \quad (2.150)$$

where state estimates $\hat{u}(x, t)$ and $\hat{v}(x, t)$ are obtained from the observer (2.118)–(2.121). The control gain kernels K_{21} and K_{22} are obtained from solving the kernel equations (2.98)–(2.105). The output injection gains of the observer (2.138)–(2.139) are obtained from solving the kernel equations (2.130)–(2.137). Then we reach the following main theorem combining Theorems 2.5 and 2.6.

Theorem 2.7 *Consider system (2.76)–(2.79) with initial conditions $u_0, v_0 \in L^2[0, L]$ and the output-feedback control law (2.150), where the kernels K_{21} and K_{22} are obtained from solving the kernel equations (2.98)–(2.105) and the output injection gains of the observer (2.138)–(2.139) are obtained from solving the kernel equations (2.130)–(2.137). The equilibrium $u = v = \hat{u} = \hat{v} = 0$ is exponentially stable in the L^2 sense and the equilibrium is reached in finite time $t = 2t_f$ given in (2.89).*

2.7 Notes and References

The landmark references on stabilization of coupled systems of first-order hyperbolic PDEs by the backstepping method are [?], where a system of two counter-convecting PDEs is stabilized with a single boundary input, [?], where an extension is presented which allows for a single input to stabilize a system in which n PDEs convect in the direction opposite to the direction of propagation of the input, and [?, ?], where a general $(n + m) \times (n + m)$ structure is considered, with m boundary inputs to m upstream-convecting PDEs and n unactuated downstream-convecting PDEs.

Hyperbolic PDE systems appear in many physical processes where the system dynamics involve transport behaviors. Boundary feedback control is applied when such processes can be controlled through boundary values of a spatial domain. Besides traffic flow system, backstepping control of the hyperbolic PDE systems is used in a wide range of applications including oil drilling [?, ?, ?]. Robustness properties of backstepping designs applied to hyperbolic systems are investigated in [?].

Backstepping control of related parabolic PDE systems arises in turbulent flows [?], battery management [?], and 3D printing [?].

Part II
Basic Backstepping Control of Freeway
Traffic

Chapter 3

Stabilization of ARZ Model

3.1 What Can Be Controlled and Is Worth Controlling with Ramp Metering?

In this chapter, we develop our first and most basic controllers for the suppression of stop-and-go oscillations in traffic flows. If a reader had the time to read only one chapter in this book, this is the chapter to read.

Before presenting our key designs, which happen to occupy Section 3.5, we answer some basic questions such as:

- What are the worthwhile control objectives for a freeway segment?
- What kind of inputs are available for control?
- Should an input like ramp metering be used to control traffic downstream or upstream of it; in free flow or in congested flow?
- As it is impossible to measure the fully spatially distributed density and velocity profiles, what kind of quantities, at a point on the freeway, are meaningful to adopt as measured outputs with which to build state estimators/observers?

In this chapter only, we consider both challenging and trivial control problems. In order to set trivial problems aside we do show their simple solutions in this chapter and then proceed through the rest of the book with challenging problems only.

It happens so that the problem of suppressing traffic oscillations downstream of ramp metering (DORM) is simple and we discuss it first, using simple proportional collocated feedback (only the P component of the elementary PID control).

Then, in Section 3.5, we take on the far more challenging problem of suppressing stop-and-go oscillations upstream of the ramp metering input (UORM). To solve this problem, a sophisticated feedback law is needed, which either employs feedback of the full traffic state, along the entire freeway segment, or employs a state estimate of the full traffic state. We design a feedback law for the UORM problem using the PDE backstepping design, introduced for general/abstract coupled hyperbolic PDE systems in Chapter 2.

To go beyond the limitation of full-state feedback, we design state observers, both using collocated measurements with the ramp and anti-collocated/distal mea-

surements relative to the actuated ramp. Our state observer design is also based on PDE backstepping, particularly for the case of a collocated observer design. We combine the observers and controllers into output feedback laws. For example, we present UORM control designs that necessitate traffic flow measurement only near the location of the actuated ramp, for the suppression of the stop-and-go oscillations upstream of the ramp.

The exponential stability in the L^2 sense, as well as finite-time convergence to the equilibrium, are proved for our controllers, observers, and output-feedback laws, using PDE backstepping transformations into easy-to-analyze target systems.

We also illustrate the designs with simulations.

The ARZ model parameters are assumed to be known in this chapter. An adaptive control design, under parametric uncertainty in the model, is presented in Chapter 5.

3.2 Stop-and-Go Instabilities

It bears repeating that stop-and-go traffic is a common and detrimental phenomenon in congested freeways, causing increased consumption of fuel and unsafe driving conditions. The oscillations appear with no apparent road change and can be simply initiated by a delay in the response of some of the drivers—often a single driver overreacting by braking to hard in response to the driver in front of him slowing down. Traffic instabilities, including those referred to as “jamitons” [?], are well represented by the ARZ PDE model. This capability of the ARZ model results from the model being a second-order (rather than a mere first-order) nonlinear hyperbolic PDE whose state is not just the traffic density but also the traffic velocity.

Recalling the stability analysis of the ARZ model in Chapter 1, we find that the traffic instabilities appear under certain densities in the congested regime of the ARZ model. The oscillations of the density travel with the vehicles in the downstream direction, whereas the oscillations of the velocity travel in the upstream direction of traffic. The stop-and-go traffic is captured by the ARZ PDE model. We focus on the congested linearized model and study how to design boundary controllers to suppress the stop-and-go oscillations.

We consider the stop-and-go traffic on a freeway segment. The ARZ model on $x \in [0, L]$, $t \in [0, \infty)$, linearized around the steady-states (q^*, v^*) with boundary conditions, is given by

$$\tilde{q}_t + v^* \tilde{q}_x - \frac{q^*(\gamma p^* - v^*)}{v^*} \tilde{v}_x = -\frac{q^*}{\tau} \left(\frac{1}{v^*} - \frac{1}{\gamma p^*} \right) \tilde{v} - \frac{\gamma p^*}{\tau v^*} \tilde{q}, \quad (3.1)$$

$$\tilde{v}_t - (\gamma p^* - v^*) \tilde{v}_x = \frac{\gamma p^* - v^*}{\tau v^*} \tilde{v} - \frac{\gamma p^*}{\tau q^*} \tilde{q}, \quad (3.2)$$

$$\tilde{q}(0, t) = 0, \quad (3.3)$$

$$\tilde{v}(L, t) = \frac{1}{\rho^*} \tilde{q}(L, t). \quad (3.4)$$

where the flow rate and velocity variations $\tilde{q}(x, t)$ and $\tilde{v}(x, t)$ are defined

$$\tilde{q}(x, t) = q(x, t) - q^*, \quad (3.5)$$

$$\tilde{v}(x, t) = v(x, t) - v^*. \quad (3.6)$$

Since we consider the congested regime, the flow rate variations are transported in the downstream direction with steady-state velocity v^* and the velocity variations are transported in the upstream direction with characteristic speed $\gamma p^* - v^*$. For the congested regime, the steady-state flow rate is lower than the maximum flow rate, and the density and velocity satisfy the following inequalities, recalling (1.23)

$$\rho^* > \frac{\rho_m}{(1 + \gamma)^{1/\gamma}} \Leftrightarrow v^* < \frac{\gamma}{\gamma + 1} v_m \quad (3.7)$$

The control objective is to suppress the stop-and-go oscillations modeled by the ARZ model using stabilizing feedback implemented with boundary actuation.

3.3 Boundary Control Model

Before we apply boundary control to the linearized ARZ model in (\tilde{q}, \tilde{v}) , we represent the system in the Riemann variables and then map it to a decoupled first-order 2×2 hyperbolic system whose static variables are denoted by (\bar{w}, \bar{v}) . We propose two different control strategies for the hyperbolic (\bar{w}, \bar{v}) -system through ramp metering boundary control.

We first introduce the Riemann variables (w, \bar{v})

$$w = \tilde{q} - q^* \left(\frac{1}{v^*} - \frac{1}{\gamma p^*} \right) \tilde{v}, \quad (3.8)$$

$$\bar{v} = \frac{q^*}{\gamma p^*} \tilde{v}, \quad (3.9)$$

They are governed by the PDEs

$$\partial_t w(x, t) + v^* \partial_x w(x, t) = -\frac{1}{\tau} w(x, t), \quad (3.10)$$

$$\partial_t \bar{v}(x, t) - (\gamma p^* - v^*) \partial_x \bar{v}(x, t) = -\frac{1}{\tau} w(x, t), \quad (3.11)$$

$$w(0, t) = -\frac{\gamma p^* - v^*}{v^*} \bar{v}(0, t), \quad (3.12)$$

$$\bar{v}(L, t) = w(L, t). \quad (3.13)$$

In order to decouple (3.10) and (3.13), we introduce an exponentially scaled state as follows:

$$\bar{w}(x, t) = \exp\left(\frac{x}{\tau v^*}\right) w(x, t). \quad (3.14)$$

This scaling transforms the (w, \bar{v}) Riemann system into the first-order 2×2 hyperbolic system

$$\partial_t \bar{w}(x, t) + v^* \partial_x \bar{w}(x, t) = 0, \quad (3.15)$$

$$\partial_t \bar{v}(x, t) - (\gamma p^* - v^*) \partial_x \bar{v}(x, t) = c(x) \bar{w}(x, t), \quad (3.16)$$

$$\bar{w}(0, t) = -k_0 \bar{v}(0, t), \quad (3.17)$$

$$\bar{v}(L, t) = \kappa \bar{w}(L, t), \quad (3.18)$$

where

$$c(x) = -\frac{1}{\tau} \exp\left(-\frac{x}{\tau v^*}\right), \quad (3.19)$$

$$k_0 = \frac{\gamma p^* - v^*}{v^*}, \quad (3.20)$$

$$\kappa = \exp\left(\frac{-L}{\tau v^*}\right). \quad (3.21)$$

The spatially varying coefficient $c(x)$ is a strictly increasing function and is bounded by

$$-\frac{1}{\tau} \leq c(x) \leq -\frac{\kappa}{\tau}. \quad (3.22)$$

The following relations for boundary values are obtained from (3.8)–(3.9),

$$\tilde{q}(0, t) = \bar{w}(0, t) + k_0 \bar{v}(0, t), \quad (3.23)$$

$$\tilde{q}(L, t) = \kappa \bar{w}(L, t) + k_0 \bar{v}(L, t), \quad (3.24)$$

The boundary input applied to the system can be traffic flow at either the inlet or at the outlet of a freeway section.

We summarize the transformation from the linearized ARZ model represented by the (\tilde{q}, \tilde{v}) -system to the (\bar{w}, \bar{v}) -system as

$$\bar{w}(x, t) = \exp\left(\frac{x}{\tau v^*}\right) (\tilde{q}(x, t) - \rho_1 \tilde{v}(x, t)), \quad (3.25)$$

$$\bar{v}(x, t) = \rho_2 \tilde{v}(\xi, t). \quad (3.26)$$

The inverse of this transformation is given by

$$\tilde{q}(x, t) = \exp\left(-\frac{x}{\tau v^*}\right) \bar{w}(x, t) + k_0 \bar{v}(x, t), \quad (3.27)$$

$$\tilde{v}(x, t) = \frac{1}{\rho_2} \bar{v}(\xi, t), \quad (3.28)$$

where the constant positive coefficients are defined as follows:

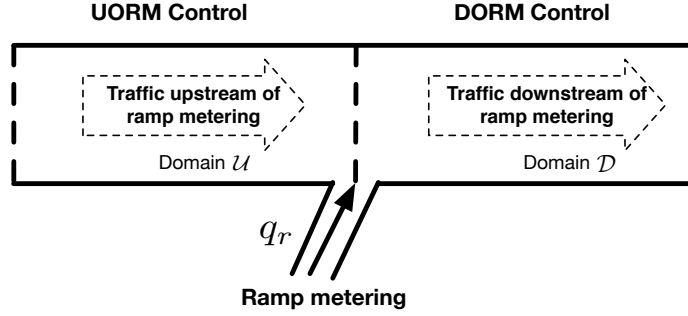


Fig. 3.1 A freeway segment controlled by ramp-metering.

$$\rho_1 = q^* \left(\frac{1}{v^*} - \frac{1}{\gamma p^*} \right), \quad (3.29)$$

$$\rho_2 = \frac{q^*}{\gamma p^*}. \quad (3.30)$$

Therefore, we can study the stability of the (\tilde{q}, \tilde{v}) -system through the (\bar{w}, \bar{v}) -system due to their equivalence. The control laws we obtain later for the (\bar{w}, \bar{v}) -system guarantee the equivalent stability properties of the (\tilde{q}, \tilde{v}) -system.

We suppose that ramp metering is installed at a freeway on-ramp with the purpose of reducing the oscillations in congested traffic. We propose two different control designs. Which of the two control designs would be employed depends on whether the user (the organization managing the freeway) is interested in suppressing the stop-and-go oscillations downstream or upstream of the metered ramp.

If we consider controlling the traffic downstream of the ramp metering (DORM), namely in the domain \mathcal{D} in Fig. 3.1, the ramp metering is located at the inlet of the domain \mathcal{D} and $U_{\text{in}}(t)$ is the control law to be designed. The DORM controller $U_{\text{in}}(t)$ is applied with $\tilde{q}(0, t)$.

In the case where we want to control the traffic upstream of the ramp metering (UORM), namely in the domain \mathcal{U} , the controller $U_{\text{out}}(t)$ is located at the outlet of domain \mathcal{U} . The UORM controller $U_{\text{out}}(t)$ is applied with $\tilde{q}(L, t)$.

DORM control

We define a ramp metering boundary control input $U_{\text{in}}(t)$ at the inlet of \mathcal{D} , while keeping the downstream boundary unactuated,

$$q_r(t) = \tilde{q}(0, t) = U_{\text{in}}(t), \quad (3.31)$$

$$\tilde{q}(L, t) = \rho^* \tilde{v}(L, t). \quad (3.32)$$

The DORM control input $U_{\text{in}}(t)$ is applied by means of physical variation of the traffic flow at the inlet of domain \mathcal{D} . We need to implement a density metering at mainline outlet so that a constant density is enforced.

Substituting (3.31) into (3.23), we obtain the controlled boundary. The DORM control model is given by the (\bar{w}, \bar{v}) -system in (3.15), (3.16) with controlled boundary at the inlet in (3.35),

$$\bar{\partial}_t w(x, t) + v^* \partial_x \bar{w}(x, t) = 0, \quad (3.33)$$

$$\bar{\partial}_t v(x, t) - (\gamma p^* - v^*) \partial_x \bar{v}(x, t) = c(x) \bar{w}(x, t), \quad (3.34)$$

$$\bar{w}(0, t) = -k_0 \bar{v}(0, t) + U_{\text{in}}(t), \quad (3.35)$$

$$\bar{v}(L, t) = \kappa \bar{w}(L, t). \quad (3.36)$$

UORM control

We consider a constant traffic flow entering the domain \mathcal{U} and the control input $U_{\text{out}}(t)$ is implemented with ramp metering at the outlet of the domain. For the inlet, we need to implement flow metering at the mainline so that constant flow is enforced, namely,

$$\tilde{q}(0, t) = 0. \quad (3.37)$$

The total traffic flow variation at the outlet of domain \mathcal{U} includes the traffic flow variation from the mainline and from the ramp,

$$\tilde{q}(L^+, t) = \tilde{q}(L^-, t) + U_{\text{out}}(t). \quad (3.38)$$

The mainline flow variation $\tilde{q}(L^-, t)$ in the domain is given by (3.24). The flow variation $\tilde{q}(L^+, t)$ immediately downstream of the domain \mathcal{U} is governed by the boundary condition (3.4). Substituting (3.4) and (3.24) into (3.38), we obtain the UORM control model with controlled boundary at the outlet in (3.42),

$$\partial_t \bar{w}(x, t) + v^* \partial_x \bar{w}(x, t) = 0, \quad (3.39)$$

$$\partial_t \bar{v}(x, t) - (\gamma p^* - v^*) \partial_x \bar{v}(x, t) = c(x) \bar{w}(x, t), \quad (3.40)$$

$$\bar{w}(0, t) = -k_0 \bar{v}(0, t), \quad (3.41)$$

$$\bar{v}(L, t) = \kappa \bar{w}(L, t) + U_{\text{out}}(t). \quad (3.42)$$

Spectrum analysis of control models with zero input

In order to explore the traffic dynamics in the open loop-system, we consider the zero input for the DORM or UORM control configurations,

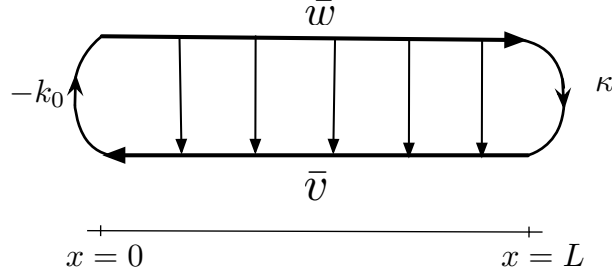


Fig. 3.2 Diagram of the control model with zero input.

$$q_r(t) = 0, \quad (3.43)$$

$$U_{\text{in}}(t) = 0, \quad (3.44)$$

$$U_{\text{out}}(t) = 0. \quad (3.45)$$

According to boundary conditions in (3.35), (3.36) or (3.41), (3.42), we have the following zero input system that holds for both control models

$$\partial_t \bar{w}(x, t) + v^* \partial_x \bar{w}(x, t) = 0, \quad (3.46)$$

$$\partial_t \bar{v}(x, t) - (\gamma p^* - v^*) \partial_x \bar{v}(x, t) = c(x) \bar{w}(x, t), \quad (3.47)$$

$$\bar{w}(0, t) = -k_0 \bar{v}(0, t), \quad (3.48)$$

$$\bar{v}(L, t) = \kappa \bar{w}(L, t), \quad (3.49)$$

where $x \in [0, L]$ and $t > 0$. The diagram is shown in Fig. 3.2. The above zero-input system is equivalent to the open-loop (\bar{q}, \bar{v}) -system in (1.45)–(1.48). Thus there are two sets of eigenvalues in the left half plane,

$$\lambda_1 = \frac{\gamma p^* - v^*}{L} n i, \quad (3.50)$$

$$\lambda_2 = -\frac{1}{\tau} - \frac{v^*}{L} n i. \quad (3.51)$$

For $n \in \mathbb{Z}$, the eigenvalue λ_1 is imaginary. As for the eigenvalue λ_2 , the longer the relaxation time τ , the smaller the negative real part in the eigenvalue λ_2 . As $\tau \rightarrow \infty$ and $n \rightarrow \infty$,

$$\lambda_1 \rightarrow \text{Im}(+\infty), \quad (3.52)$$

$$\lambda_2 \rightarrow \text{Im}(-\infty). \quad (3.53)$$

According to the above spectral analysis, two sets of eigenvalues are lined along the imaginary axis. The system is marginally stable and there are persistent oscillations in the domain of the zero-input system shown in (3.46)–(3.49). Therefore, it is necessary to pursue a feedback control design to exponentially (or finite-time) stabilize the PDE system.

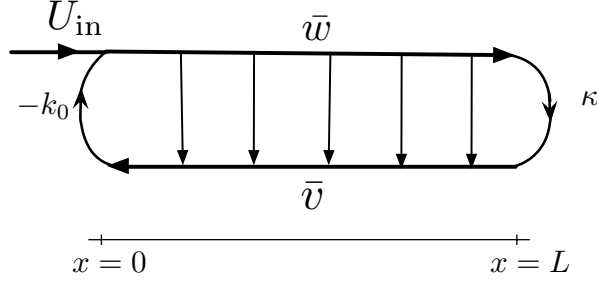


Fig. 3.3 Diagram of DORM control model.

3.4 DORM Control Design

DORM is the easier of the two control problems we consider (DORM and UORM) and we present it first. The harder control problem, UORM, is presented in Section 3.5. The DORM control model is given by

$$\partial_t \bar{w}(x, t) + v^* \partial_x \bar{w}(x, t) = 0, \quad (3.54)$$

$$\partial_t \bar{v}(x, t) - (\gamma p^* - v^*) \partial_x \bar{v}(x, t) = c(x) \bar{w}(x, t), \quad (3.55)$$

$$\bar{w}(0, t) = -k_0 \bar{v}(0, t) + U_{\text{in}}(t), \quad (3.56)$$

$$\bar{v}(L, t) = \kappa \bar{w}(L, t), \quad (3.57)$$

where $x \in \mathcal{D} \triangleq [0, L]$ and $t > 0$. The diagram of the DORM control model is shown in Fig. 3.3.

If we choose the DORM controller as simple static collocated output feedback,

$$U_{\text{in}}(t) = k_0 \bar{v}(0, t), \quad (3.58)$$

we get $\bar{w}(0, t) = 0$, which renders the \bar{w} transport PDE homogeneous, i.e., autonomous. The explicit solution to the resulting autonomous \bar{w} -system (3.54) with the DORM control law (3.58) substituted into (3.56) is

$$\bar{w}(x, t) = \begin{cases} \bar{w}(x - v^* t, 0), & t < \frac{x}{v^*}, \\ \bar{w}(0, t - \frac{x}{v^*}), & t \geq \frac{x}{v^*}, \end{cases} \quad (3.59)$$

and for $t \geq \frac{x}{v^*}$,

$$\bar{w}(x, t) \equiv 0. \quad (3.60)$$

Solving (3.55), (3.57) for $\bar{v}(x, t)$, we have

$$\bar{v}(x, t) = \begin{cases} \bar{v}(x + (\gamma p^* - v^*)t, 0) + \int_0^t c(x + (\gamma p^* - v^*)(t-s)) \bar{w}(0, s) ds, & t < \frac{L-x}{\gamma p^* - v^*}, \\ \kappa \bar{w}\left(L, t - \frac{L-x}{\gamma p^* - v^*}\right) + \frac{1}{\gamma p^* - v^*} \int_x^L c(s) \bar{w}\left(0, t + \frac{x-s}{\gamma p^* - v^*}\right) ds, & t \geq \frac{L-x}{\gamma p^* - v^*}. \end{cases} \quad (3.61)$$

Thus for $t \geq t_f$, it holds that

$$\bar{v}(x, t) \equiv 0. \quad (3.62)$$

where

$$t_f = \frac{L}{v^\star} + \frac{L}{\gamma p^\star - v^\star}. \quad (3.63)$$

Substituting k_0 into (3.20) and \bar{v} into (3.26), we get

$$U_{\text{in}}(t) = \rho_1 \bar{v}(0, t). \quad (3.64)$$

The DORM boundary control input $U_{\text{in}}(t)$, thus, employs a control law that requires only the measurement of the collocated quantity $\bar{v}(0, t)$.

To show the exponential stability of the system in the L^2 sense, we construct the following Lyapunov functions

$$V_1(t) = \frac{1}{2v^\star} \int_0^L e^{-x} \bar{w}^2(x, t) dx, \quad (3.65)$$

$$V_2(t) = \frac{1}{2(\gamma p^\star - v^\star)} \int_0^L e^x \bar{v}^2(x, t) dx, \quad (3.66)$$

and differentiate the Lyapunov functions in time. We obtain the following inequalities using the Cauchy-Schwarz inequality and Young's inequality,

$$\dot{V}_1 \leq -e^{-L} (\bar{w}^2(L) + \|\bar{w}\|^2), \quad (3.67)$$

$$\dot{V}_2 \leq e^L \bar{v}^2(L) - \bar{v}^2(0) - \|\bar{v}\|^2 + \frac{1}{\gamma p^\star - v^\star} \int_0^L e^x \bar{v}(x) c(x) \bar{w}(x) dx.$$

According to the boundedness of $c(x)$ in (3.22), we have

$$|c(x)| \leq C_0 = \frac{1}{\tau} \quad (3.68)$$

Then it holds that

$$\dot{V}_2 \leq e^L \kappa^2 \bar{w}^2(L) + \frac{1}{2d_1(\gamma p^\star - v^\star)} \|\bar{w}\|^2 - \left(1 - \frac{d_1 C_0^2 e^{2L}}{2(\gamma p^\star - v^\star)}\right) \|\bar{v}\|^2, \quad (3.69)$$

where d_1 is an arbitrary positive constant which we choose as

$$d_1 < \frac{2\tau^2(\gamma p^\star - v^\star)}{e^{2L}}. \quad (3.70)$$

Consider the following Lyapunov function

$$V = d_2 V_1 + V_2, \quad (3.71)$$

where

$$d_2 = \max \left(e^{2L} \kappa^2, \frac{e^{2L}}{2d_1(\gamma p^* - v^*)} \right). \quad (3.72)$$

It holds that

$$\dot{V} \leq -d_0 V, \quad (3.73)$$

where

$$d_0 = \min \left(\frac{d_2}{e^L} - \frac{1}{2d_1(\gamma p^* - v^*)}, 1 - \frac{d_1 C_0^2 e^{2L}}{2(\gamma p^* - v^*)} \right). \quad (3.74)$$

The exponential stability of the system (3.54)–(3.57) with the DORM boundary controller (3.58) is thus established. From the explicit solution of the system, it holds for $t \geq t_f$,

$$\bar{w}(x, t) \equiv \bar{v}(x, t) \equiv 0, \quad (3.75)$$

We summarize the above result in the following theorem.

Theorem 3.1 *Consider system (3.54)–(3.57) with initial conditions $\bar{w}_0, \bar{v}_0 \in L^2[0, L]$ and the control law (3.58). The equilibrium $\bar{w} \equiv \bar{v} \equiv 0$ is exponentially stable in the L^2 sense and is reached in finite time $t = t_f$ given in (3.63).*

3.5 UORM Control Designs

The DORM control design (3.58) was a simple collocated proportional feedback since the coupling $-k_0$ in Fig. 3.3 is collocated with the control input. The UORM problem is much more difficult as the feedback coupling of the two PDEs extends all the way to the distal boundary relative to the input. Because of this domain-wide coupling, a much more complex feedback is needed and we design it using the PDE backstepping method.

The UORM control model is

$$\partial_t \bar{w}(x, t) + v^* \partial_x \bar{w}(x, t) = 0 \quad (3.76)$$

$$\partial_t \bar{v}(x, t) - (\gamma p^* - v^*) \partial_x \bar{v}(x, t) = c(x) \bar{w}(x, t), \quad (3.77)$$

$$\bar{w}(0, t) = -k_0 \bar{v}(0, t), \quad (3.78)$$

$$\bar{v}(L, t) = \kappa \bar{w}(L, t) + U_{\text{out}}(t), \quad (3.79)$$

where $x \in \mathcal{U} \triangleq [0, L]$ and $t > 0$, and its diagram is shown in Fig. 3.4.

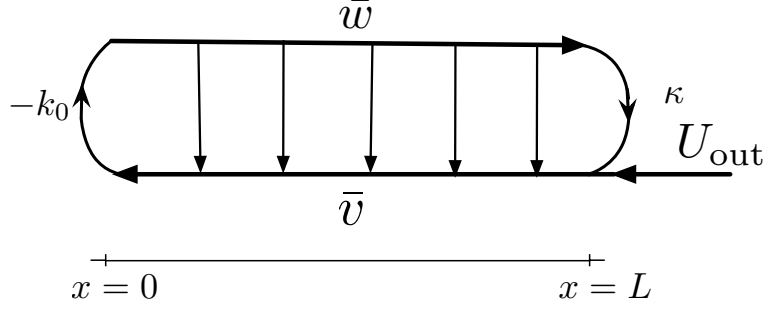


Fig. 3.4 Diagram of the UORM control model.

UORM full-state feedback control design

Using the following backstepping transformation,

$$\alpha(x, t) = \bar{w}(x, t), \quad (3.80)$$

$$\beta(x, t) = \bar{v}(x, t) - \int_0^x M(x - \xi) \bar{v}(\xi, t) d\xi - \int_0^x K(x, \xi) \bar{w}(\xi, t) d\xi, \quad (3.81)$$

we transform the UORM control model (3.76)–(3.79) into the target system where, in particular, $\bar{w}(0, t) = \alpha(0, t)$ and $\bar{v}(0, t) = \beta(0, t)$,

$$\partial_t \alpha(x, t) + v^* \partial_x \alpha(x, t) = 0, \quad (3.82)$$

$$\partial_t \beta(x, t) - (\gamma p^* - v^*) \partial_x \beta(x, t) = 0, \quad (3.83)$$

$$\alpha(0, t) = -k_0 \beta(0, t), \quad (3.84)$$

$$\beta(L, t) = 0. \quad (3.85)$$

To find the backstepping transformation kernels M and K in (3.81) so that (3.77) is transformed into (3.85), we take the time derivative and the spatial derivative of (3.81).

After lengthy calculations as shown in Chapter 2, we obtain that the following kernel PDE and associated boundary condition need to be satisfied,

$$(\gamma p^* - v^*) \partial_x K(x, \xi) - v^* \partial_\xi K(x, \xi) = c(\xi) K(x - \xi, 0), \quad (3.86)$$

$$K(x, x) = -\frac{c(x)}{\gamma p^*}, \quad (3.87)$$

where $K(x, \xi)$ evolves in the triangular domain $\mathcal{Z} = \{(x, \xi) : 0 \leq \xi \leq x \leq L\}$, and where $M(x)$ is defined as

$$M(x) = -K(x, 0). \quad (3.88)$$

The well-posedness of the kernel equations (3.86)–(3.88) and the boundedness of kernel variables are obtained following the same steps of the proof in the Appendix of [?]. Therefore, invertibility of the backstepping transformation in (3.80), (3.81) is established and we can study the target system for stability of the plant.

The UORM full-state feedback controller is chosen as

$$U_{\text{out}}(t) = -\kappa \bar{w}(L, t) + \int_0^L M(L - \xi) \bar{v}(\xi, t) d\xi + \int_0^L K(L, \xi) \bar{w}(\xi, t) d\xi, \quad (3.89)$$

so that $\beta(L, t) = 0$ is satisfied. One can easily find the explicit solution to the target system (3.82)–(3.85) and obtain that

$$\alpha(x, t) \equiv \beta(x, t) \equiv 0, \quad (3.90)$$

after $t_f = t_\alpha + t_\beta = \frac{L}{v^\star} + \frac{L}{\gamma p^\star - v^\star}$. Thus α and β go to zero in finite time $t = t_f$. It is straightforward to prove with a Lyapunov functional similar to (3.65), (3.66), and (3.71) that the α, β system is L^2 exponentially stable. Due to the invertibility of the transformation, the (\bar{w}, \bar{v}) -system is also L^2 exponentially stable.

Theorem 3.2 *Consider system (3.76)–(3.79) with initial conditions $\bar{w}_0, \bar{v}_0 \in L^2[0, L]$ and the control law (3.89) where the kernels $K(x, \xi)$ and $M(x)$ are obtained by solving (3.86)–(3.88). The equilibrium $\bar{w} \equiv \bar{v} \equiv 0$ is exponentially stable in the L^2 sense and is reached in finite time $t = t_f$ given in (3.63).*

Transforming \bar{w} and \bar{v} in (3.89) to \tilde{q} and \tilde{v} using the inverse transformation in (3.27)–(3.28), we get the control law in (\tilde{q}, \tilde{v}) as

$$\begin{aligned} U_{\text{out}}(t) = & -\tilde{q}(L, t) + \rho_1 \tilde{v}(L, t) + \rho_1 \int_0^L M(L - \xi) \tilde{v}(\xi, t) d\xi \\ & - \kappa \int_0^L K(L, \xi) \exp\left(\frac{\xi}{\tau v^\star}\right) \tilde{v}(\xi, t) d\xi \\ & + k_0 \int_0^L K(L, \xi) \exp\left(\frac{\xi}{\tau v^\star}\right) \tilde{q}(\xi, t) d\xi. \end{aligned} \quad (3.91)$$

Due to the invertibility of the transformation (3.25)–(3.28) between (\bar{w}, \bar{v}) and (\tilde{q}, \tilde{v}) , the (\tilde{q}, \tilde{v}) -system is exponentially stable and converges to zero in the finite time. Therefore, the (q, v) system is exponentially stable and converges to (q^\star, v^\star) in the finite time t_f .

To implement $U_{\text{out}}(t)$, we need the measurements of \tilde{v} and \tilde{q} along the entire domain \mathcal{U} , which might be realized by traffic cameras and fleet GPS data. Instead, we propose next a boundary observer design, to alleviate the difficulties and costs to install sensors along the entire freeway. We introduce two boundary observers: one is located at the same boundary with the full-state feedback controller and the other one is anti-collocated with the controller.

UORM anti-collocated boundary observer design

We employ the following anti-collocated boundary measurement of velocity fluctuation:

$$Y_a(t) = \bar{v}(0, t). \quad (3.92)$$

According to (3.26), we obtain $\bar{v}(0, t) = \rho_2 \tilde{v}(0, t)$, by the measurement of $\tilde{v}(0, t)$. Then we design an observer by constructing the following system,

$$\partial_t \hat{w}(x, t) + v^* \partial_x \hat{w}(x, t) = 0, \quad (3.93)$$

$$\partial_t \hat{v}(x, t) - (\gamma p^* - v^*) \partial_x \hat{v}(x, t) = c(x) \hat{w}(x, t), \quad (3.94)$$

$$\hat{w}(0, t) = -k_0 Y_a(t), \quad (3.95)$$

$$\hat{v}(L, t) = \kappa \hat{w}(L, t) + U_{\text{out}}(t), \quad (3.96)$$

where \hat{w} and \hat{v} are the estimates of state variables \bar{w} and \bar{v} . This is a trivial observer, with output injection appearing only in the boundary condition (3.95). The error system is obtained by subtracting the above estimates from (3.76)–(3.79),

$$\partial_t \check{w}(x, t) + v^* \partial_x \check{w}(x, t) = 0, \quad (3.97)$$

$$\partial_t \check{v}(x, t) - (\gamma p^* - v^*) \partial_x \check{v}(x, t) = c(x) \check{w}(x, t), \quad (3.98)$$

$$\check{w}(0, t) = 0, \quad (3.99)$$

$$\check{v}(L, t) = \kappa \check{w}(L, t), \quad (3.100)$$

where

$$\check{w} = \bar{w} - \hat{w}, \quad (3.101)$$

$$\check{v} = \bar{v} - \hat{v}. \quad (3.102)$$

The error system is the same as (3.54)–(3.57) with (3.64). According to Theorem 1, the error system is exponentially stable in the L^2 sense and converges to zero in finite time t_f .

Theorem 3.3 Consider system (3.97)–(3.100) with initial conditions $\check{w}_0, \check{v}_0 \in L^2[0, L]$. The equilibrium $\check{w} \equiv \check{v} \equiv 0$ is exponentially stable in the L^2 sense, which implies that $\|\bar{w}(\cdot, t) - \hat{w}(\cdot, t)\| \rightarrow 0$ and $\|\bar{v}(\cdot, t) - \hat{v}(\cdot, t)\| \rightarrow 0$. The convergence to 0 is achieved in finite time $t = t_f$.

UORM collocated boundary observer design

The collocated observer is more complex than the trivial anti-collocated observer (3.93)–(3.96). We employ a collocated boundary measurement

$$Y_c(t) = \bar{w}(L, t). \quad (3.103)$$

Since

$$\bar{w}(L, t) = \frac{1}{\kappa} (\tilde{q}(L, t) - \rho_1 \tilde{v}(L, t)), \quad (3.104)$$

the output (3.103) is obtained by the measurement of $\tilde{q}(L, t)$ and $\tilde{v}(L, t)$. Then we design a collocated boundary observer to estimate $\bar{w}(x, t)$ and $\bar{v}(x, t)$ by constructing the system

$$\partial_t \hat{w}(x, t) + v^* \partial_x \hat{w}(x, t) = r(x)(\bar{w}(L, t) - \hat{w}(L, t)), \quad (3.105)$$

$$\partial_t \hat{v}(x, t) - (\gamma p^* - v^*) \partial_x \hat{v}(x, t) = c(x) \hat{w}(x, t) + s(x)(\bar{w}(L, t) - \hat{w}(L, t)), \quad (3.106)$$

$$\hat{w}(0, t) = -k_0 \hat{v}(0, t), \quad (3.107)$$

$$\hat{v}(L, t) = \kappa Y_c(t) + U_{\text{out}}(t), \quad (3.108)$$

where \hat{w} and \hat{v} are the estimates of the state variables \bar{w} and \bar{v} . The terms $r(x)$ and $s(x)$ are output injection gains to be designed. The error system is obtained by subtracting the estimates from (3.76)–(3.79),

$$\partial_t \check{w}(x, t) + v^* \partial_x \check{w}(x, t) = -r(x) \check{w}(L, t), \quad (3.109)$$

$$\partial_t \check{v}(x, t) - (\gamma p^* - v^*) \partial_x \check{v}(x, t) = c(x) \check{w}(x, t) - s(x) \check{w}(L, t), \quad (3.110)$$

$$\check{w}(0, t) = -k_0 \check{v}(0, t), \quad (3.111)$$

$$\check{v}(L, t) = 0, \quad (3.112)$$

where

$$\check{w} = \bar{w} - \hat{w}, \quad (3.113)$$

$$\check{v} = \bar{v} - \hat{v}. \quad (3.114)$$

We need to find the output injection gains $r(x)$ and $s(x)$ which guarantee the error system's state decays to zero. Using a backstepping transformation, we transform the error system (3.109)–(3.112) into the following system

$$\partial_t \check{\lambda}_t(x, t) + v^* \partial_x \check{\lambda}(x, t) = 0, \quad (3.115)$$

$$\partial_t \check{v}(x, t) - (\gamma p^* - v^*) \partial_x \check{v}(x, t) = 0, \quad (3.116)$$

$$\check{\lambda}(0, t) = -k_0 \check{v}(0, t), \quad (3.117)$$

$$\check{v}(L, t) = 0. \quad (3.118)$$

The backstepping transformation is postulated as

$$\check{\lambda}(x, t) = \check{w}(x, t) - \int_x^L \check{K}(L + x - \xi) \check{w}(\xi, t) d\xi, \quad (3.119)$$

$$\check{v}(x, t) = \check{v}(x, t) - \int_x^L \check{M}(v^*x + (\gamma p^* - v^*)\xi) \check{w}(\xi, t) d\xi, \quad (3.120)$$

where the kernel \check{L} is given by

$$\check{M}(x) = -\frac{1}{\gamma p^*} c\left(\frac{x}{\gamma p^*}\right). \quad (3.121)$$

For boundary condition (3.117) to hold, the kernels \check{K} and \check{M} must satisfy the relation

$$\check{K}(L - \xi) = \check{M}((\gamma p^* - v^*)\xi). \quad (3.122)$$

The kernel \check{K} is then obtained as

$$\check{K}(x) = -\frac{1}{\gamma p^*} c\left(\frac{\gamma p^* - v^*}{\gamma p^*}(L - x)\right), \quad (3.123)$$

and satisfies

$$|\check{K}(x)| \leq \frac{1}{\gamma p^* \tau}, \quad (3.124)$$

due to the boundedness of $c(x)$ in (3.68). The output injection gains $r(x)$ and $s(x)$ are

$$r(x) = v^* \check{K}(x) = -\frac{v^*}{\gamma p^*} c\left(\frac{\gamma p^* - v^*}{\gamma p^*}(L - x)\right), \quad (3.125)$$

$$\begin{aligned} s(x) &= -v^* \check{M}(v^*x + (\gamma p^* - v^*)L) \\ &= \frac{v^*}{\gamma p^*} c\left(\frac{v^*}{\gamma p^*}x - \frac{\gamma p^* - v^*}{\gamma p^*}L\right). \end{aligned} \quad (3.126)$$

The backstepping transformation is invertible. Therefore, we study the stability of the error system through the target system (3.115)–(3.118). It is straightforward to prove the exponential stability of the error system in the L^2 sense and its finite-time convergence.

Theorem 3.4 *Consider system (3.109)–(3.112) with initial conditions $\check{w}_0, \check{v}_0 \in L^2[0, L]$. The equilibrium $\check{w} \equiv \check{v} \equiv 0$ is exponentially stable in the L^2 sense, which means that $\|\check{w}(\cdot, t) - \hat{w}(\cdot, t)\| \rightarrow 0$ and $\|\check{v}(\cdot, t) - \hat{v}(\cdot, t)\| \rightarrow 0$. In addition the convergence of the observer error state to equilibrium is achieved in finite time $t = t_f$.*

We have completed the designs of an anti-collocated boundary observer and a collocated boundary observer. Both of them achieve exponential stability of estimation errors in the L^2 sense and finite-time convergence to 0. A comparison of the two

designs reveals that the collocated boundary observer needs two spatially-varying output injection gains but could be easier to realize in practice since the sensor is located at the same boundary with the UORM control input $U_{\text{out}}(t)$.

UORM output-feedback control design

Combining the state feedback controller and the boundary observers, we have the output-feedback controller

$$U_{\text{out}}(t) = -\kappa \hat{w}(L, t) + \int_0^L M(L - \xi) \hat{v}(\xi, t) d\xi + \int_0^L K(L, \xi) \hat{w}(\xi, t) d\xi, \quad (3.127)$$

where \hat{w} and \hat{v} can be obtained either from the anti-collocated boundary observer in (3.93)–(3.96) with measurement $Y_a(t) = \bar{v}(0, t)$ or from the collocated boundary observer in (3.109)–(3.112) with measurement $Y_c(t) = \bar{w}(L, t)$ and with observer gains given in (3.125), (3.126). The following theorem summarizes the results from Theorem 3.1 to Theorem 3.4.

Theorem 3.5 *Consider system (3.76)–(3.79) with initial conditions $\hat{w}_0, \hat{v}_0 \in L^2[0, L]$ and with the output-feedback control law (3.127), where the kernels $K(x, \xi)$, $M(x)$ are obtained by solving (3.86)–(3.88). The equilibrium $\bar{w} \equiv \bar{v} \equiv \hat{w} \equiv \hat{v} \equiv 0$ is exponentially stable in the L^2 sense.*

By employing the inverse change of variables (3.27), (3.28), the result of this theorem holds also for the original physical variations state (\tilde{q}, \tilde{v}) .

3.6 Numerical Simulation

The length of the freeway section is chosen to be $L = 1$ km. The free speed is $v_m = 40$ m/s and the maximum density is $\rho_m = 150$ vehicles/km. The steady-states (ρ^*, v^*) are chosen as (120 vehicles/km, 10 m/s) which is in the congested regime. We take $\gamma = 1$ and relaxation time $\tau = 60$ s. We assume constant incoming flow and constant outgoing density for boundary conditions and use sinusoidal initial conditions.

Fig. 2.5 shows that in the open-loop system the density and velocity are lightly damped and keep oscillating, with a slow decay, taking tens of minutes to fully settle. In Fig. 2.6, the closed-loop system with DORM control is stabilized and converges to the steady-states in the finite time of about 2.5 min.

The closed-loop system with UORM full-state feedback control in Fig. 2.7 is stabilized and converges to the reference and the finite convergence time is $t_f = L/v^* + L/(\gamma p^* - v^*) = 150$ s = 2.5 min. The evolution of ramp metering control input is plotted with red color at outlet $x = 1000$ m. We see that the control input oscillates around every half minute, which is reasonable for on-ramp traffic lights.

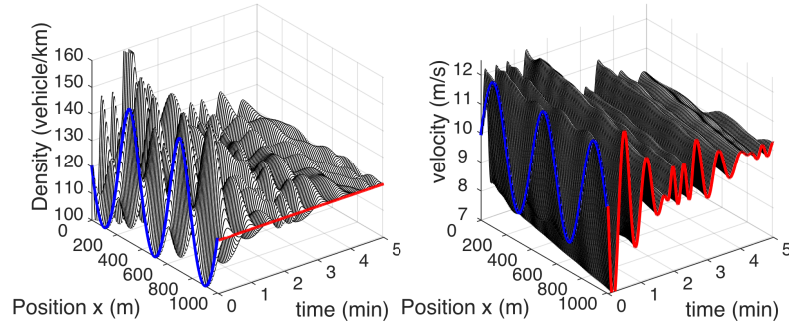


Fig. 3.5 Open-loop response of the ARZ model.

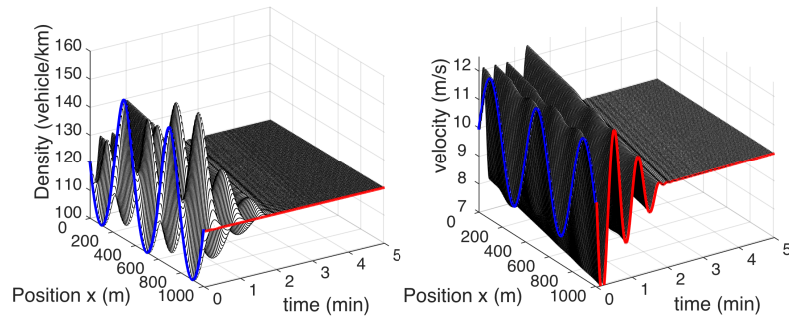


Fig. 3.6 Closed-loop response with DORM control.

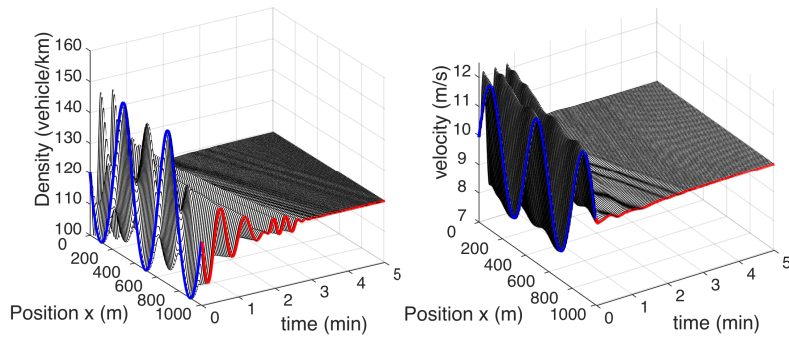


Fig. 3.7 Closed-loop response with UORM full-state feedback.

Fig. 2.8 shows that the closed-loop system with UORM output-feedback control (collocated observer) is stabilized and converges to the steady-states in about 5 min

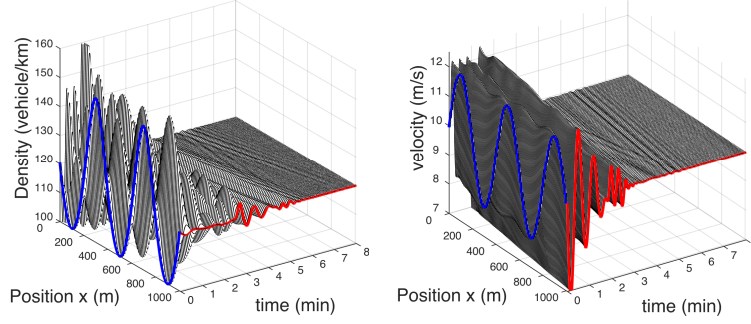


Fig. 3.8 Closed-loop response with UORM output feedback.

since it takes the collocated observer 2.5 min to estimate state variables and another 2.5 min for state feedback control to converge to the steady-states.

3.7 Notes and References

This chapter addresses the boundary feedback control problem of ARZ traffic model with relaxation term. To stabilize the oscillations of congested traffic regime, two control designs are introduced for the second-order coupled hyperbolic system. The key idea in the DORM control design is to cancel the forward coupling in the system. In the more challenging case, UORM control design uses the backstepping method to cancel the coupling throughout the domain. In this fashion, the UORM design achieves exponential stability and finite-time convergence to the steady-state.

The results of this chapter, in their concise form, were introduced in [?].

In Chapter 5, we propose an adaptive boundary control design for the linearized ARZ model in the absence of the knowledge of certain model parameters. In the next immediate chapter, Chapter 4, we use traffic field data to validate our observer design.

Chapter 4

Observer Validation on Freeway Data

Traffic state observers perform the estimation of the state, such as the distribution of velocity or density along the freeway, from partially observed traffic data in real time. Due to financial and technical limitations, it is usually difficult to measure such distributed traffic states everywhere, and at all times, on mainline freeways. Therefore, at places where direct measurement and detection is missing, it is important to estimate the traffic states. This is important both for control purposes and, in the absence of real-time control of the freeway, for the sake of model calibration or policy development.

This chapter validates and generalizes the boundary observer introduced in Chapter 4. In that chapter the observer was introduced for the purpose of stabilization of stop-and-go oscillations using output-feedback control. In this chapter we build on this observer for the sake of state estimation, in the absence of a control task.

The objective of the boundary observer in this chapter is the accurate estimation of freeway traffic states, based on the ARZ PDE model, in the congested regime where, in the absence of a stabilizing control that suppresses oscillations, the stop-and-go behavior makes the state of the traffic flow unsteady. To accurately capture such an unsteady motion of traffic, which requires the fully nonlinear ARZ model to capture the traffic state motions away from the underlying equilibria, we need an ARZ-based observer which is likewise nonlinear. In this chapter we provide a nonlinear generalization of the observer that we presented in Chapter 3.

This chapter presents results based on experimental traffic data. Vehicle trajectory data are used to first calibrate the ARZ model and to then validate the boundary observer design, constructed based on the macroscopic ARZ model, on actual microscopic traffic data.

4.1 Introduction to Traffic State Estimation

The traffic state needs to be estimated by typically using partially observed traffic data and some prior knowledge of traffic. This topic has been extensively studied, attracting particular attention in recent decades.

The approaches to traffic estimation fall into the following three categories: model-driven, data-driven, and streaming data-driven. Among them, the model-driven approach is the most popular one and has been widely used to solve various traffic estimation problems.

Compared with the data-driven approach, the model-based approach provides an accurate estimation with less input data. The model-based estimation can be integrated with traffic control operations directly. The disadvantage of this approach is that it requires careful selection and calibration of the model. As a first step in the model-driven approach, traffic flow models are often used to describe traffic dynamics and are calibrated with historical data. Then state estimates are obtained based on the calibrated model and real-time data inputs. Therefore, it is crucial for traffic estimation to have an advanced physical model which is capable of capturing the freeway traffic dynamics accurately. This motivates us to employ a state-of-the-art second-order traffic PDE model, namely, the ARZ model, for traffic state estimation.

Freeway traffic dynamics in spatial and temporal domains are usually described using macroscopic models with aggregated variables of traffic density, velocity and flow. These aggregated variables average out small-scale noise of freeway traffic and can be directly measured by stationary/point-based sensors like loop detectors. Among the macroscopic models, the LWR model is one of the most commonly applied models. This model is a first-order scalar hyperbolic PDE of density, and can predict the propagation and dissipation of traffic shockwaves and represent fundamental phenomena of free and congested regime of traffic. Many studies have used such a model for traffic states estimation due to its simplicity and efficiency in model calibration and numerical simulation. However, the LWR model fails to describe stop-and-go traffic, which is the oscillatory behavior that accompanies congested traffic. The reason for LWR's failure to capture stop-and-go is because it models the relationship between the density and velocity in a static manner and is thus unable to reproduce the non-equilibrium density-velocity relation occurring in the stop-and-go traffic. In order to address this limitation, second-order models are proposed to employ a nonlinear hyperbolic PDE for traffic velocity, in addition to the density conservation equation. The deviations from the equilibrium traffic relation are allowed in the second-order model since dynamics of the velocity are captured by their own PDE. Therefore, in order to accurately estimate the non-equilibrium traffic states for congested traffic, this chapter employs the state-of-the-art second-order ARZ PDE model.

An observer employing only measurements on one boundary of a freeway segment is designed for the ARZ model using the backstepping method and is validated with traffic field data. For the sake of brevity, we refer to such an observer as a "boundary observer," or a "backstepping observer."

Compared with the data assimilation approach, the observer proposed in this chapter requires less measurement information, easier model calibration and works directly with the original second-order PDE model instead of a discretized one.

In Chapter 3, an observer design was proposed for the linearized ARZ model in an effort to construct an output-feedback controller. In this chapter, we generalize that previous observer design in order to address the freeway traffic estimation problem from a more practical perspective. Specifically, the generalized observer design is developed for the full nonlinear version of the ARZ model, with certain assumptions regarding the boundary conditions removed. The observer itself is nonlinear and enables accurate estimation of the traffic state even under large fluctuations of the density and velocity states.

We do not claim that the initial estimates of the density and velocity profiles are allowed to be taken very far from the actual initial profiles but, if the initial estimates are, in fact, not too far from the actual profiles, the nonlinear observer can track large fluctuations in the nonlinear ARZ model, using only measurements from a boundary of the freeway segment.

The observer design presented in this chapter accepts a general functional form of the equilibrium density-velocity relation rather than only the basic choice of Greenshield's model. This allows the PDE model to have better data fitting in calibration. Vehicle trajectory data [?] are used to construct and to test the performance of the observer design.

4.2 Boundary Observer Design

Boundary sensing is employed in our observer design. We pursue the state estimation of the nonlinear ARZ model using the PDE backstepping method. The output injection gains are designed for the linearized ARZ model and then are added to a copy of the nonlinear plant. Recall the ARZ PDE model linearized around steady-states (q^*, v^*) ,

$$\partial_t \tilde{q}(x, t) + v^* \partial_x \tilde{q}(x, t) - \frac{q^*(\gamma p^* - v^*)}{v^*} \partial_x \tilde{v}(x, t) = -\frac{q^*}{\tau} \left(\frac{1}{v^*} - \frac{1}{\gamma p^*} \right) \tilde{v}(x, t) - \frac{\gamma p^*}{\tau v^*} \tilde{q}(x, t), \quad (4.1)$$

$$\partial_t \tilde{v}(x, t) - (\gamma p^* - v^*) \partial_x \tilde{v}(x, t) = \frac{\gamma p^* - v^*}{\tau v^*} \tilde{v}(x, t) - \frac{\gamma p^*}{\tau q^*} \tilde{q}(x, t) \quad (4.2)$$

$$\tilde{q}(0, t) = 0, \quad (4.3)$$

$$\tilde{v}(L, t) = \frac{1}{\rho^*} \tilde{q}(L, t), \quad (4.4)$$

where the flow rate and velocity variations are defined as

$$\tilde{q}(x, t) = q(x, t) - q^*, \quad (4.5)$$

$$\tilde{v}(x, t) = v(x, t) - v^*, \quad (4.6)$$

and $x \in [0, L]$, $t \in [0, \infty)$.

The boundary values of state variations from the steady-states are defined as

$$Y_{q,\text{in}}(t) = \tilde{q}(0, t), \quad (4.7)$$

$$Y_{q,\text{out}}(t) = \tilde{q}(L, t), \quad (4.8)$$

$$Y_v(t) = \tilde{v}(L, t), \quad (4.9)$$

where the values of $\tilde{q}(0, t)$, $\tilde{q}(L, t)$ and $\tilde{v}(L, t)$ are obtained by subtracting the setpoint values (q^* , v^*) from the sensing of incoming traffic flow $q(0, t)$, outgoing flow $q(L, t)$, and outgoing velocity $v(L, t)$. In practice, sensing of the aggregated values of the traffic flow and velocity

$$y_q(t) = q(0, t), \quad (4.10)$$

$$y_{\text{out}}(t) = q(L, t), \quad (4.11)$$

$$y_v(t) = v(L, t), \quad (4.12)$$

is usually obtained by high-speed cameras or induction loop detectors. The induction loops are coils of wire embedded in the surface of the road to detect changes of inductance caused by the passage of vehicles. The high-speed cameras record the vehicle trajectories for a freeway segment.

Output injection for the linearized ARZ model

As introduced in Chapter 3, the linearized ARZ PDE model is first converted into the Riemann variables in order to diagonalize the equations. Second, a spatial scaling transformation is applied to eliminate any diagonal reaction terms. The transformation from the (\tilde{q}, \tilde{v}) -system to the (\bar{w}, \bar{v}) -system is

$$\bar{w}(x, t) = \exp\left(\frac{x}{\tau\lambda_1}\right) \left(\frac{\rho^*\lambda_2}{\lambda_1 - \lambda_2} \tilde{v}(x, t) + \tilde{q}(x, t) \right), \quad (4.13)$$

$$\bar{v}(x, t) = \frac{q^*}{\lambda_1 - \lambda_2} \tilde{v}(x, t), \quad (4.14)$$

and the inverse transformation is given by

$$\tilde{q}(x, t) = \exp\left(-\frac{x}{\tau\lambda_1}\right) \bar{w}(x, t) - \frac{\lambda_2}{\lambda_1} \bar{v}(x, t), \quad (4.15)$$

$$\tilde{v}(x, t) = \frac{\lambda_1 - \lambda_2}{q^*} \bar{v}(x, t). \quad (4.16)$$

This results in the system

$$\partial_t \bar{w}(x, t) + \lambda_1 \partial_x \bar{w}(x, t) = 0, \quad (4.17)$$

$$\partial_t \bar{v}(x, t) + \lambda_2 \partial_x \bar{v}(x, t) = c(x) \bar{w}(x, t), \quad (4.18)$$

$$\bar{w}(0, t) = \frac{\lambda_2}{\lambda_1} \bar{v}(0, t) + Y_{q, \text{in}}(t), \quad (4.19)$$

$$\bar{v}(L, t) = \frac{q^*}{\lambda_1 - \lambda_2} Y_v(t), \quad (4.20)$$

where $\lambda_1 = v^*$, $\lambda_2 = \gamma p^* - v^*$ and the spatially-varying parameter $c(x)$ is defined as

$$c(x) = -\frac{1}{\tau} \exp\left(-\frac{x}{\tau \lambda_1}\right). \quad (4.21)$$

Parameter $c(x)$ is a strictly increasing function and bounded by

$$-\frac{1}{\tau} \leq c(x) \leq -\frac{1}{\tau} \exp\left(-\frac{L}{\tau \lambda_1}\right). \quad (4.22)$$

Then we design a boundary observer for the linearized ARZ model to estimate $\bar{w}(x, t)$ and $\bar{v}(x, t)$ by constructing the following system

$$\partial_t \hat{w}(x, t) + \lambda_1 \partial_x \hat{w}(x, t) = r(x)(\bar{w}(L, t) - \hat{w}(L, t)), \quad (4.23)$$

$$\begin{aligned} \partial_t \hat{v}(x, t) + \lambda_2 \partial_x \hat{v}(x, t) = & c(x) \hat{w}(x, t) \\ & + s(x)(\bar{w}(L, t) - \hat{w}(L, t)), \end{aligned} \quad (4.24)$$

$$\hat{w}(0, t) = \frac{\lambda_2}{\lambda_1} \hat{v}(0, t) + Y_{q, \text{in}}(t), \quad (4.25)$$

$$\hat{v}(L, t) = \frac{q^*}{\lambda_1 - \lambda_2} Y_v(t), \quad (4.26)$$

where $\hat{w}(x, t)$ and $\hat{v}(x, t)$ are the estimates of the state variables $\bar{w}(x, t)$ and $\bar{v}(x, t)$. The value $\bar{w}(L, t)$ is obtained from (4.8) and (4.9): by substituting the measurements $Y_v(t) = \bar{v}(L, t)$ and $Y_{q, \text{out}}(t) = \bar{q}(L, t)$, we obtain

$$\bar{w}(L, t) = \exp\left(\frac{L}{\tau \lambda_1}\right) \left(\frac{\rho^* \lambda_2}{\lambda_1 - \lambda_2} Y_v(t) + Y_{q, \text{out}}(t) \right). \quad (4.27)$$

We denote estimation errors as

$$\check{w}(x, t) = \bar{w}(x, t) - \hat{w}(x, t), \quad (4.28)$$

$$\check{v}(x, t) = \bar{v}(x, t) - \hat{v}(x, t). \quad (4.29)$$

The error system is obtained by subtracting the estimates (4.23)–(4.26) from (4.17)–(4.20),

$$\partial_t \check{w}(x, t) + \lambda_1 \partial_x \check{w}(x, t) = r(x) \check{w}(L, t), \quad (4.30)$$

$$\partial_t \check{v}(x, t) + \lambda_2 \partial_x \check{v}(x, t) = c(x) \check{w}(x, t) + s(x) \check{w}(L, t), \quad (4.31)$$

$$\check{w}(0, t) = \frac{\lambda_2}{\lambda_1} \check{v}(0, t), \quad (4.32)$$

$$\check{v}(L, t) = 0. \quad (4.33)$$

The terms $r(x)$ and $s(x)$ are output injection gains that are designed using back-stepping method in the previous chapter and are explicitly given by

$$r(x) = -\frac{\lambda_1}{\lambda_1 - \lambda_2} c \left(-\frac{\lambda_2}{\lambda_1 - \lambda_2} (L - x) \right), \quad (4.34)$$

$$s(x) = \frac{\lambda_1}{\lambda_1 - \lambda_2} c \left(x - \frac{\lambda_2}{\lambda_1 - \lambda_2} (L - x) \right). \quad (4.35)$$

According to Theorem 3.3, the convergence of the state estimates to the state values is reached in the finite time $t = t_f$ given by

$$t_f = \frac{L}{|\lambda_1|} + \frac{L}{|\lambda_2|}. \quad (4.36)$$

4.3 Nonlinear observer

To design a nonlinear version of the observer, we take the output injection terms that we designed for the linearized ARZ model and then insert them into a copy of the original nonlinear ARZ model.

First we recall the transformation (4.13), (4.14) and its inverse (4.15), (4.16). The same transformation holds between the estimates (\hat{w}, \hat{v}) of the transformed states (\bar{w}, \bar{v}) and the state estimates (\check{q}, \check{v}) of (\tilde{q}, \tilde{v}) -system. Due to the equivalence between $(\bar{w}, \bar{v}, \hat{w}, \hat{v})$ and $(\tilde{q}, \tilde{v}, \check{q}, \check{v})$ -system, we arrive at the following theorem for the linearized ARZ model according to the stability property of the estimation error system in Theorem 3.3. The estimation errors of the linearized system (4.1)–(4.4) are denoted by $\dot{q} = \tilde{q} - \check{q}, \dot{v} = \tilde{v} - \check{v}$.

Theorem 4.1 *Consider the linearized ARZ model (4.1)–(4.4) with initial conditions $\tilde{q}_0, \tilde{v}_0 \in L^2([0, L])$, along with the observer (4.23)–(4.26) initialized using the initial estimated states $\check{q}_0, \check{v}_0 \in L^2([0, L])$. The equilibrium $\dot{q} \equiv \dot{v} \equiv 0$ of the observer error system, represented in the original physical density and velocity variation states, is exponentially stable in the L^2 sense. It also holds that*

$$\|\tilde{q}(\cdot, t) - \check{q}(\cdot, t)\| \rightarrow 0 \quad (4.37)$$

$$\|\tilde{v}(\cdot, t) - \check{v}(\cdot, t)\| \rightarrow 0 \quad (4.38)$$

as time approaches the finite time $t = t_f$.

We denote the error injections designed for the linearized ARZ model (4.23)–(4.26) as

$$E_w(x, t) = r(x)(\bar{w}(L, t) - \hat{w}(L, t)), \quad (4.39)$$

$$E_v(x, t) = s(x)(\bar{w}(L, t) - \hat{w}(L, t)). \quad (4.40)$$

The output injection gains $r(x)$, $s(x)$ are designed in (4.34) and (4.35). According to (4.27), $\bar{w}(L, t)$ is obtained from the real-time measurement of the traffic boundary data in (4.7)–(4.9). Therefore, the values of output injections $E_w(t)$ and $E_v(t)$ are known.

The nonlinear implementation of the observer for state estimation of density and velocity $(\hat{\rho}(x, t), \hat{v}(x, t))$ is obtained by combining the copy of the nonlinear ARZ model (ρ, v) given by (1.4), (1.5), and the above linear injection errors in the original physical density and velocity state variables,

$$\partial_t \hat{\rho} + \partial_x(\hat{\rho} \hat{v}) = \frac{1}{v^*} \left(\exp\left(-\frac{L}{\tau \lambda_1}\right) E_w - E_v \right), \quad (4.41)$$

$$\partial_t \hat{v} + (\hat{v} + \hat{\rho} V'(\hat{\rho})) \partial_x \hat{v} = \frac{V(\hat{\rho}) - \hat{v}}{\tau} + \frac{\lambda_1 - \lambda_2}{q^*} E_v, \quad (4.42)$$

where the linear injections on the right hand side are obtained from (4.15), (4.16), (4.39), (4.40). The boundary conditions are

$$\hat{\rho}(0, t) = \frac{y_q(t)}{\hat{v}(0, t)}, \quad (4.43)$$

$$\hat{v}(L, t) = y_v(t). \quad (4.44)$$

The boundary measurement of the incoming traffic flow $y_q(t)$ and the outgoing velocity $y_v(t)$ is used in the above boundary conditions of the proposed observer. The boundary measurement of the outgoing traffic flow $y_{\text{out}}(t)$ and the outgoing velocity $y_v(t)$ appears in the output error injection terms (4.39), (4.40), and thus in the observer equations (4.41), (4.42). The output injection terms drive the observer to converge to the original nonlinear ARZ model.

When the initial state of the system is close to the equilibrium, the linearized part dominates in the nonlinear estimation error system. Therefore the L^2 exponential stability and the finite-time convergence are achieved for the linearized ARZ model. In [?], the local exponential stability in H^2 sense is obtained for a quasilinear hyperbolic PDE system with a backstepping full-state feedback controller. The duality of the proposed observer design in (4.41)–(4.44) to the stabilization problem in [?] would yield a local H^2 stability result for the estimation problem, following the Lyapunov proof of Theorem 4.1 in [?]. Since we mainly focus on the practical implementation of the observer, we do not pursue a theoretical proof by local H^2 analysis of the error system.

Compared with the linearized observer design, the nonlinear observer yields a better estimation result due to the fact that it induces less error brought in by the

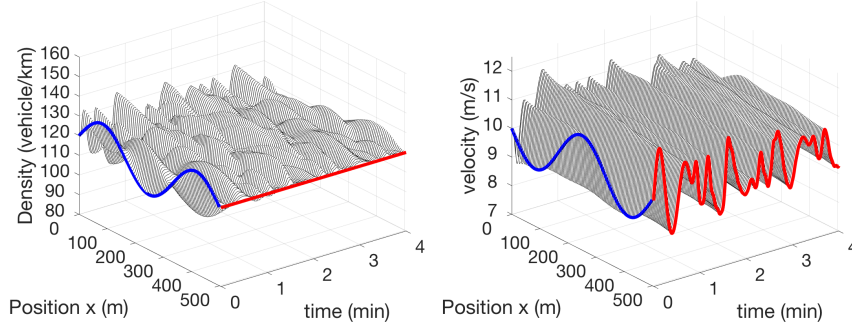


Fig. 4.1 Density $\rho(x, t)$ and velocity $v(x, t)$ of nonlinear ARZ model.

model linearization. In the following sections, the estimation result is first validated in numerical simulation with an ad-hoc choice of model parameters and initial conditions, and then validated with traffic field data.

4.4 Numerical Simulation

For simulation of the nonlinear ARZ PDE model on a freeway segment of 500 m, we assume that the initial conditions are spatial sinusoids around the steady-states (ρ^*, v^*) , with the steady state values in the congested regime. The initial conditions are specifically chosen as

$$\rho(x, 0) = 0.1 \sin\left(\frac{3\pi x}{L}\right) \rho^* + \rho^*, \quad (4.45)$$

$$v(x, 0) = -0.1 \sin\left(\frac{3\pi x}{L}\right) v^* + v^*. \quad (4.46)$$

Model parameters of a one-lane traffic in the congested regime is considered and chosen the same as the previous chapter. In the next section, we validate the observer design with the traffic field data. Instead of prescribing boundary values in this chapter, we use field data to estimate in-domain traffic states.

We use the finite volume method numerical approach in Section. 1.8, which divides the freeway segment into cells and then approximates the cell values considering the balance of flow through the boundaries of the adjacent cells. In order to obtain the numerical flow, we write the ARZ model in the conservative variables, then apply the two-stage Lax-Wendroff scheme to discretize the ARZ model in the spatio-temporal domain. The scheme is second-order accurate in space and first-order in time. The spatial grid resolution is chosen to be smaller than the average vehicle size so that the numerical errors are smaller than the model errors. Therefore the numerical simulation is valid for this continuum model.

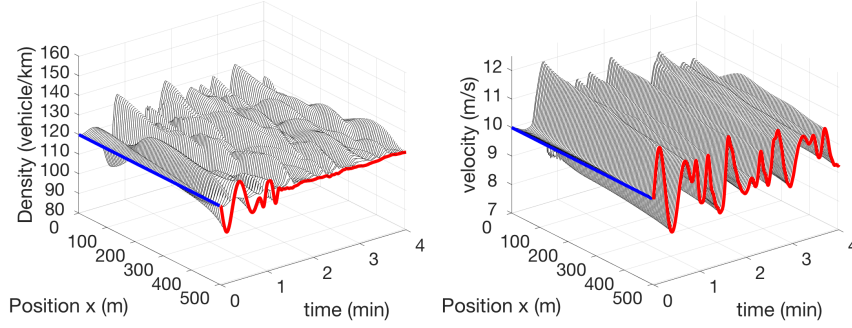


Fig. 4.2 States estimates $\hat{\rho}(x, t)$ and $\hat{v}(x, t)$ of nonlinear boundary observer.

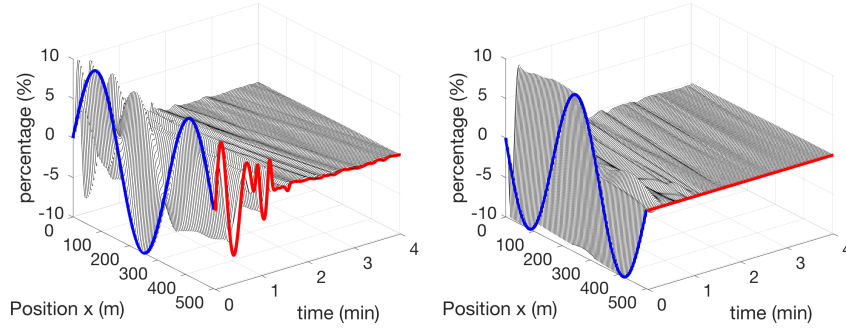


Fig. 4.3 Estimation errors $\check{\rho}(x, t)$ and $\check{v}(x, t)$.

For the numerical stability of the Lax-Wendroff scheme, the spatial grid size $\Delta x = 4$ m and time step $\Delta t = 0.15$ s is chosen so that CFL condition is satisfied:

$$\max |\lambda_{1,2}| \leq \frac{\Delta x}{\Delta t}, \quad (4.47)$$

The numerical simulation result of the nonlinear ARZ, the nonlinear boundary observer estimation and the estimation errors are plotted in Fig. 4.1– Fig. 4.3. Blue lines represent the initial conditions while the red lines represent the evolution of outlet state values in the temporal domain. The simulation is performed for a 500 m length of freeway segment and the evolution of traffic states density and velocity is plotted for 4 min.

In Fig. 4.1, traffic density and velocity oscillations are lightly damped. It takes the vehicles that are initially in the domain only 50 s to leave it, however, the oscillations sustain for more than 4 min, which means that the incoming vehicles enter the acceleration-deceleration cycles under the influence of stop-and-go waves. The traffic states are in the congested regime. The stop-and-go phenomenon is demonstrated in the simulation.

State estimation of traffic density and velocity by the nonlinear implementation of the observer is shown in Fig. 4.2. The measurement is taken for the outgoing velocity and outgoing flow. The incoming flow is assumed to be at the setpoint value of the traffic flow and thus measurement is not needed at the inlet. In the next section, validation with freeway data, this assumption of the incoming flow is removed. The measurement of the incoming flow is used as the boundary condition of the observer to reflect its influence on the traffic state estimation of the considered segment. We do not assume any prior knowledge of the initial conditions and set the initial conditions to be at the setpoint density and velocity. We can see that state estimates converge to the true values after 75 s.

In Fig. 4.3, the evolution of estimation errors are shown. After 75 s, the state estimation errors for density and velocity converge to a value that is below 1% of the setpoint value. There are still relatively small estimation errors remaining in the domain. They remain for two reasons. Our result only guarantees the convergence of estimates in the spatial L^2 norm. In addition, there could be nonlinearities of the error system not driven to zero by the linear output injections of the nonlinear boundary observer design.

4.5 Model calibration with NGSIM data

In this section, we validate our boundary observer design with Next Generation Simulation (NGSIM) traffic data [?], which provides vehicle trajectories with substantial details and accuracy. The NGSIM trajectory data set was collected on April 13, 2005 by a Federal Highway Administration project. The study area is a segment of Interstate 80 located at Emeryville, California. The dataset gathers trajectories of vehicles over a total of 45 minutes during rush hour: 4:00pm - 4:15pm, 5:00pm - 5:15pm, 5:15pm - 5:30pm.

Firstly, we calibrate the nonlinear ARZ model with a part of the NGSIM data to obtain calibrated model parameters including the steady-state values, the equilibrium velocity-density function $V(\rho)$ and the relaxation time τ . Then the rest of the datasets is used to test the observer design for the calibrated ARZ model. The results of estimation of traffic states are compared with the NGSIM data. The boundary data are extracted directly from the NGSIM data and traffic states are estimated for the considered domain. The reconstructed traffic data and boundary observer state estimates are compared.

Data Reconstruction

We aim to calibrate the ARZ model, which is a macroscopic model describing aggregated values, whereas, the NGSIM data set consists of microscopic measurements. The data were recorded with high-speed cameras for every 0.1 seconds. We need

to process NGSIM trajectory data into macroscopic scale before we can use it to calibrate the ARZ model.

The data were recorded on a 537-meter long freeway segment with six lanes for a time period of 15-minutes. Due to insufficient data collection at boundaries of the segment, onset and offset of recording, the viable domain we choose to use in calibration and validation is 400-meter during a time period around 10-minutes. When calibrating the parameters of the ARZ model and the fundamental diagram, we consider the freeway segment as a macroscopic general one-lane problem. That being said, all six-lane state values need and are to be taken into account.

We use Edie's formula [?] to calculate the aggregated traffic states $\rho(x, t)$, $v(x, t)$ and $q(x, t)$ from the trajectory data of vehicles $x(t)$ with a resolution 0.1 s. At each time instance, positions of the multiple vehicles are collected. Consider a time-space domain $[0, T] \times [0, L]$. We divide it into $N \times M$ grid cells,

$$[i\Delta t, (i+1)\Delta t] \times [j\Delta x, (j+1)\Delta x],$$

where $i \in 1, 2, \dots, N$ and $j \in 1, 2, \dots, M$. Within each cell, we consider $\rho_{i,j}, q_{i,j}, v_{i,j}$ to be constant. Edie's formula maps a set of vehicles' trajectories to speed, flow, and density over the space-time grid. For each cell, suppose there are N_{ij} vehicle traces passing through the cell $[i\Delta t, (i+1)\Delta t] \times [j\Delta x, (j+1)\Delta x]$,

$$\rho_{i,j} = \frac{\sum_{k=1}^{N_{ij}} t_k}{\Delta x \Delta t}, \quad (4.48)$$

$$q_{i,j} = \frac{\sum_{k=1}^{N_{ij}} x_k}{\Delta x \Delta t}, \quad (4.49)$$

$$v_{i,j} = \frac{q_{i,j}}{\rho_{i,j}}. \quad (4.50)$$

After obtaining the cell values $\rho_{i,j}, q_{i,j}, v_{i,j}$, they can be compared later with the observer estimates $\hat{\rho}_{i,j}, \hat{q}_{i,j}, \hat{v}_{i,j}$ with the same gridding. The number of cells is chosen such that in each cell there are enough trajectory data. Otherwise, there could be cells that no trajectory has crossed. On the other hand, noises appear if a very fine discretization of grids is chosen. The following simulation is performed in a 41×41 grid.

We reconstruct the aggregated traffic states from all the three datasets. In Fig. 4.4 and Fig. 4.5, we show the surface plot of the density and velocity states for the dataset of 4:00 pm-4:15 pm and the dataset of 5:00 pm-5:15 pm. The initial conditions are highlighted with red and the boundary conditions at outlet are highlighted with blue. The congestion forms as time goes by and propagates in the upstream direction. The most congested traffic appears at the inlet where the traffic density is relatively high and velocity is low.

We are mostly interested in the congested traffic, which is the traffic condition in which the estimation of the traffic states is more relevant than it is in free traffic. The linearized ARZ model around the uniform reference is analyzed and employed for the observer design. By taking the average of the traffic aggregated values, we obtain

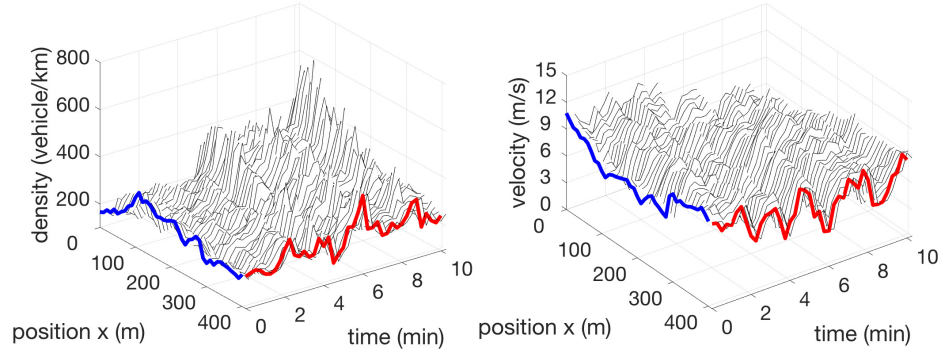


Fig. 4.4 Density and velocity reconstructed from data of 4:00 pm-4:15 pm.

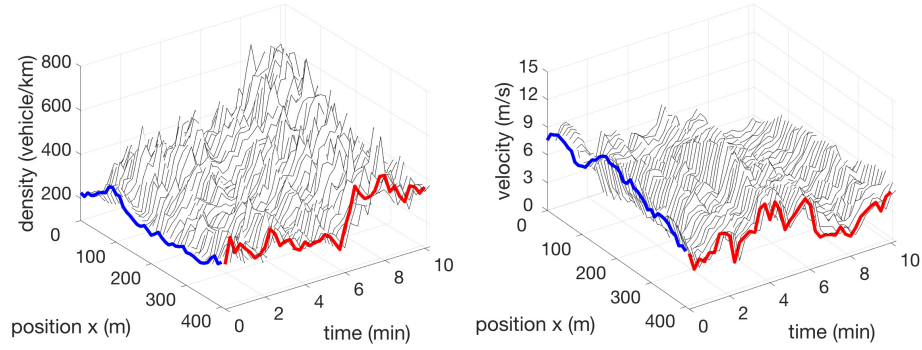


Fig. 4.5 Density and velocity reconstructed from data of 5:00 pm-5:15 pm.

Table 4.1 Averaged aggregate traffic data

Data Set	Density (veh/km)	Velocity (km/h)	Flow (veh/h)
4:00 pm-4:15 pm	267	28.27	7548
5:00 pm-5:15 pm	353	20.23	7141
5:15 pm-5:30 pm	375	19.35	7256

the reference values ρ^* , v^* and q^* of each dataset. The averaged values of density, velocity and flow in each time period are calculated and shown in the Table 4.1. We observe that among the three datasets, the traffic is the most congested during 5:15 pm-5:30 pm with the largest averaged density and smallest velocity value. Whether the traffic states are in the congested or free regime will be determined after we introduce a calibrated fundamental diagram.

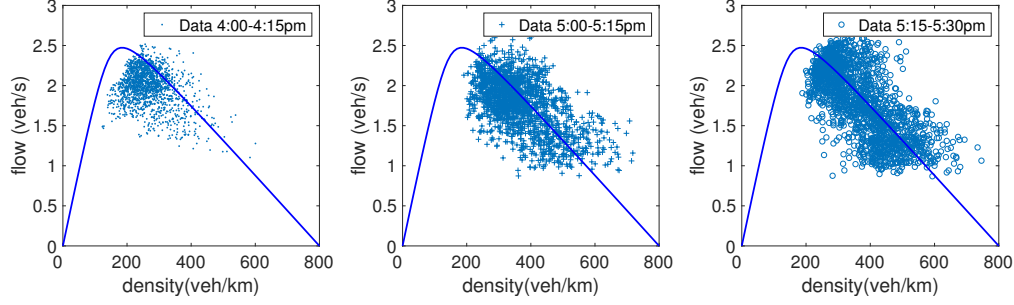


Fig. 4.6 Density and flow from data of 4:00 pm-4:15 pm, 5:00 pm-5:15 pm and 5:15 pm-5:30 pm.

Calibration of Model Parameters

For the ARZ model,

$$\partial_t \rho + \partial_x(\rho v) = 0, \quad (4.51)$$

$$\partial_t v + (v + \rho V'(\rho)) \partial_x v = \frac{V(\rho) - v}{\tau}, \quad (4.52)$$

the model parameters to be calibrated from the dataset are the parameters of the equilibrium density-velocity relation $V(\rho)$ and the relaxation time τ . The fundamental diagram describing the equilibrium relation between density and flow,

$$Q(\rho) = \rho V(\rho), \quad (4.53)$$

is usually obtained by long-term measurement via loop-detectors. The loop-detector data set provides macroscopic density and flow rate data. Its recording resolution is 30s. In the previous section, we use Greenshield's model for $V(\rho)$ as a simple choice for the boundary observer design. The Greenshield's fundamental diagram $Q(\rho)$ is given by

$$Q(\rho) = \rho v_f \left(1 - \left(\frac{\rho}{\rho_m} \right)^\gamma \right). \quad (4.54)$$

But Greenshield's model cannot accurately represent the data for the equilibrium density-flow relation. The critical density ρ_c satisfies $Q'(\rho)|_{\rho_c} = 0$ and segregates the free and congested regimes. The critical density ρ_c of the Greenshield's model ($\gamma = 1$) occurs at $\rho_c = \frac{1}{2}\rho_m$. However, the critical density obtained from empirical traffic data usually shows up at $\rho_c = \frac{1}{4}\rho_m$. Hence, we need to consider a more realistic functional form for $Q(\rho)$. Many approaches have been proposed for the calibration of the fundamental diagram [?, ?, ?, ?]. Here we employ a three-parameter fundamental diagram proposed in [?].

In [?], the following three-parameter (λ, p, α) fundamental diagram is calibrated with the NGSIM detector data set of the same freeway segment,

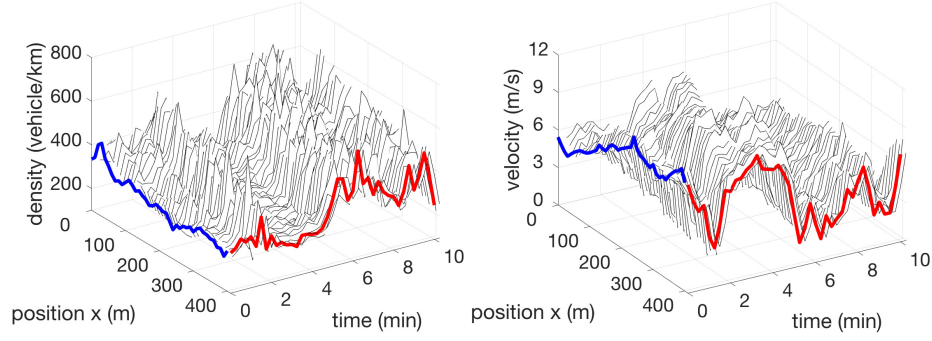


Fig. 4.7 Density and velocity reconstructed from the data of 5:15pm-5:30pm.

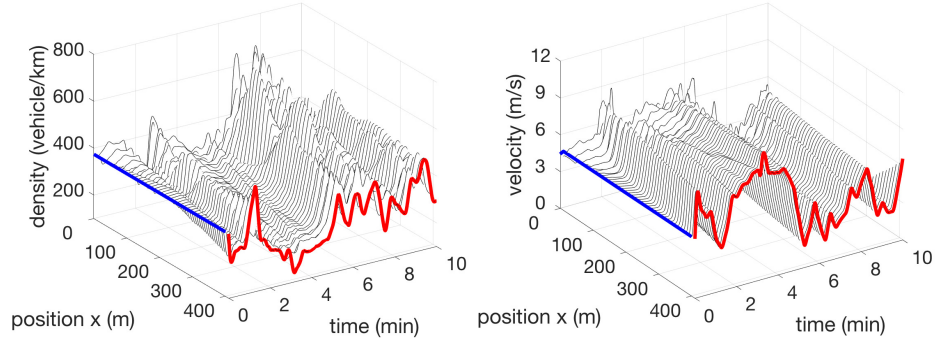


Fig. 4.8 Estimates of density and velocity from the data of 5:15pm-5:30pm.

$$Q(\rho) = \alpha \left(a + (b - a) \frac{\rho}{\rho_m} - \sqrt{1 + \lambda^2 \left(\frac{\rho}{\rho_m} - p \right)^2} \right), \quad (4.55)$$

where a and b are denoted by

$$a = \sqrt{1 + (\lambda p)^2}, \quad (4.56)$$

$$b = \sqrt{1 + (\lambda(1 - p))^2}. \quad (4.57)$$

The parameters (λ, p, α) do not have physical meaning but represent the shape of the functional form where λ represents the roundness, p tunes the critical density, α determines the maximum flow rate. The hyperbolicity $Q''(\rho) < 0, V'(\rho) < 0$ is guaranteed. The three parameters (λ, p, α) are determined using least-squares fitting with historical loop detector data.

Due to the lack of data near the maximum density, the value of ρ_m is prescribed according to the following equation

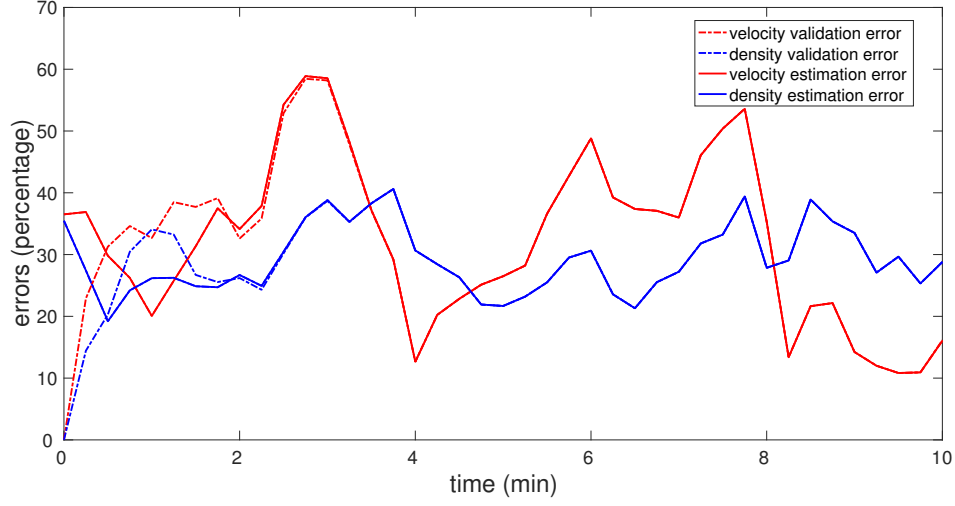


Fig. 4.9 Density and velocity estimation errors and validation errors for the field data of 5:15 pm-5:30 pm.

$$\rho_m = \frac{\text{number of lanes}}{\text{typical vehicle length} \times \text{safety distance factor}}. \quad (4.58)$$

The freeway segment in the NGSIM dataset consists of 6 lanes and we consider the typical vehicle length to be 5 meters and the safety distance factor is 50% of vehicle length. Therefore, for all lanes in our simulation we have

$$\rho_m = 800 \text{ veh/km}. \quad (4.59)$$

The calibrated fundamental diagram is plotted in Fig. 4.6. The traffic density and flow rates of the three datasets are plotted on the calibrated fundamental diagram. We see that during the time interval 4:00pm-4:15pm the traffic is in transition, where the data points are partially in the free regime and partially in the congested regime. The traffic data of the 5:00pm-5:15pm and 5:15pm-5:30pm intervals are scattered in the congested regime of the fundamental diagram.

With the calibrated fundamental diagram $V(\rho)$, we choose the relaxation time τ from a range between 10s and 100s and calibrate it with the dataset of 5:00pm-5:15pm. The optimal relaxation time is $\tau = 30s$ where the total error between the calibrated model and data is the lowest. In the next step, we use the calibrated fundamental diagram $V(\rho)$ and the relaxation time τ to construct the boundary observer.

4.6 Data validation of Observer with Calibrated Parameters

We use the data of the interval 5:15 pm-5:30 pm to test the boundary observer design. The reference set of values (ρ^*, v^*, q^*) is obtained from Table 4.1. Along with the calibrated parameters of $V(\rho)$ and the calibrated τ , the nonlinear implementation of the observer is constructed with a copy of the nonlinear ARZ model with the output injection gains that drive the estimation errors to zero. The numerical solution of the nonlinear PDE is approximated with the Lax-Wendroff method. The boundary data are implemented with the ghost cells. The ARZ model collects the boundary values based both on the flow in the computational domain and the boundary data of the ghost cells. Using the boundary measurements of the inlet and outlet of the freeway segment, the state estimation $(\hat{\rho}(x, t), \hat{v}(x, t))$ is generated without the knowledge of the initial condition. In Fig. 4.7, $(\rho(x, t), v(x, t))$ is obtained from the reconstruction of the data set of 5:15pm-5:30pm. Fig. 4.8 shows the evolution of the state estimates $(\hat{\rho}(x, t), \hat{v}(x, t))$. The initial condition, highlighted with color blue, is assumed to be the uniform reference (ρ^*, v^*, q^*) which represents the averaged values of the dataset. The boundary conditions at outlet are highlighted with red color which gives the output injections in the observer. We notice that, when density values are higher than 600 veh/km at inlet around 7 min, the estimation result is not satisfactory as large spikes appear in the estimation. This could be related to the ARZ model's inaccuracy in predicting traffic states near maximum density since non-unique maximum densities exist for the ARZ model, as pointed out by [?].

For the error analysis of the observer estimation, the estimation errors are evaluated in the L^2 -norm, defined as

$$S_\rho(t) = \left[\frac{1}{L} \int_0^L \left(\frac{\rho(x, t) - \hat{\rho}(x, t)}{\rho^*} \right)^2 dx \right]^{1/2}, \quad (4.60)$$

$$S_v(t) = \left[\frac{1}{L} \int_0^L \left(\frac{v(x, t) - \hat{v}(x, t)}{v^*} \right)^2 dx \right]^{1/2}, \quad (4.61)$$

where ρ^* and v^* are the averaged state values of the traffic data. We choose the averaged space L^2 -norm of the estimation errors. The local stability in the L^2 -sense for the estimation errors is guaranteed in Theorem 2. In addition, the spatial averaged errors can remove the influence of noise and outliers of the traffic data.

The temporal evolution of the space-averaged estimation errors and the validation errors of density and velocity in the L^2 -sense is shown in Fig. 4.9. In the model validation result, the initial condition is given by the traffic field data. As can be seen in the figure, the errors between the model-predicted state values and the NGSIM data, plotted with the dashed lines, are zeros at $t = 0$. The dashed lines show the evolution of the validation errors between the model-predicted values and the NGSIM data. The estimation result reveals that the errors of the density and velocity estimates start at $t = 0$ between 30% and 40%, which are also shown with the blue lines highlighting the discrepancy between the initial condition of the data in Fig. 4.7

and the initial condition of the estimation states in Fig. 4.8. The finite convergence time of the estimation values to the model-predicted values is around $t_f = 3$ min, where the dashed lines and the solid lines coincide after the convergence time.

We find that the proposed PDE backstepping observer accurately estimates the traffic flow states that are predicted by the ARZ PDE model. The estimation errors remaining after the convergence time are due to the model-predicted errors that come from the discrepancy between the NGSIM data and the calibrated ARZ model. The data noise, the reconstruction errors, and the numerical approximation errors could contribute to the remaining spatial averaged errors between the model-predicted values and the NGSIM traffic data.

4.7 Notes and References

In this chapter, which expands upon our initial work in [?], we developed a PDE backstepping observer for the second-order nonlinear ARZ model to estimate the traffic states of density and velocity. We then validated the design with the NGSIM traffic data. The analysis of the linearized ARZ model leads us to focus on the congested regime where the stop-and-go traffic appears. Using spatial transformations and the PDE backstepping method, we construct a boundary observer with a copy of the nonlinear plant and output injection employing measurement errors. The exponential stability of the estimation error dynamics in the L^2 norm and finite-time convergence to zero are guaranteed. Numerical simulations are performed for a freeway segment. The nonlinear implementation of the observer is tested with a calibrated ARZ model obtained from the NGSIM data. This test demonstrates that the PDE backstepping observer estimates the experimental (i.e., microscopically-generated) traffic states rapidly and accurately, using a macroscopic ARZ model.

Chapter 5

Adaptive Control of ARZ Traffic Model

5.1 Parametric Uncertainties in the ARZ Model

The ARZ model can capture the stop-and-go motions quite faithfully and, in that fashion, serve effectively for control design for suppressing those oscillations. However, the ARZ model is successful in capturing accurately the stop-and-go oscillations only when it is properly calibrated—when its parameters and nonlinearities are chosen to match a significant volume of past traffic data.

But how can a single selection of parameters and nonlinearities serve as proper calibration of the ARZ model in all the possible traffic conditions? How can behaviorally-motivated parameters be valid both in daylight conditions and at night or under fog? Visibility is not the only factor that influences the driver behavior—weather conditions, such as rain, snow, or icy road conditions influence the drivers' preferences for speed and inter-vehicle distance. Furthermore, if drivers of different types and ages (and not just different numbers of drivers) are on the freeway during the commute-to-work hours, versus during the work hours, versus during the evening hours, how can a single set of parameters be valid in all those situations? How can parameters selected to match the traffic dynamics of a normally operated freeway be also valid for a freeway where a part of a lane might be occupied by road work or due to an accident? Once all these possibilities are considered, the notion of having a well-calibrated ARZ model seems like an illusion.

Model parameters being inherently uncertain is not a peculiarity of traffic flow models. Uncertainty is present in virtually all control-oriented models. The need to deal with parametric uncertainties online has given rise to the field of adaptive control, which began in earnest as a research field in the late 1950s. Adaptive control incorporates online estimation of unknown parameters. The parameters being adjusted in a real-time operation may be the parameters of the model based on which the control is being designed (indirect adaptive control) or of the postulated controller structure (direct adaptive control).

In the context of control design of traffic flows, namely, the context in which the ARZ model is employed for the control design, real-time estimation of various

parameters of either the ARZ model or of a postulated controller structure can be pursued. This parameter estimation can adjust for changes in the driver behavior or road conditions. Such parameter estimation also obviates the need for a priori calibration of the ARZ model, although well-selected baseline values of parameters will improve the convergence time in real-time estimation.

5.2 Adaptive Control for PDEs Enabled by Backstepping

Since the ARZ model is a PDE system, adaptive control of traffic flows calls for the development of adaptive controllers for PDEs. For ODE systems, adaptive control has a history of over sixty years, dating back, as we indicated, to the late 1950s, and having gone through the peak of its development for linear plants in the 1970s–1980s, in the form of model-reference and pole-placement adaptive controllers, and for nonlinear plants in the 1990s, thanks to the adaptive backstepping methods.

The development of adaptive controllers for PDEs is much more recent. Its first notable successes took place in the late 2000s, with the advances in PDE backstepping and the emergence of feedback laws that have explicit dependence on the model parameters.

Those first breakthroughs in adaptive control for PDEs did not occur for classes of hyperbolic PDE systems, such as the ARZ model, but for parabolic PDEs. The 2010 book [?] gives a comprehensive account of methods of adaptive control for parabolic PDEs. Those methods can be categorized into Lyapunov-based and estimation-based, with the estimation-based category further divided into methods employing passive identifiers and methods employing swapping-based identifiers.

It took a decade for the advances in PDE backstepping to be transferred from parabolic PDEs to coupled hyperbolic PDEs. It, likewise, took nearly a decade for adaptive control to be advanced from the class of parabolic PDEs [?] to the class of coupled hyperbolic PDEs, for which a comprehensive development of adaptive control methodologies is introduced in the 2019 book [?].

While the developments presented in this chapter, for adaptive control of the ARZ model, did occur independently from the developments leading to the comprehensive designs for coupled hyperbolic PDEs in [?], the designs in [?] are applicable, in principle, to the ARZ system in its basic form and in many extended configurations for which even non-adaptive designs are yet to be developed.

5.3 Adaptive Output Feedback: Simultaneous Identification, Observer, and Control Design

Let us now turn our attention to the contents of this chapter and to the design of adaptive controllers for the ARZ model. Adaptive control represents a simultaneous application of parameter estimation (system identification) and control, using the

parameter estimates generated online. So, for the ARZ model we need to design both a system identification (parameter estimation) algorithm and a control algorithm.

We have already designed control algorithms for the ARZ model in Chapter 3. However, for an adaptive control use, we will need to design a quite different controller structure than in Chapter 3, which should be for a representation of the system from which parameter estimates and adaptive state estimates can be generated.

In addition to the need to estimate the unknown parameters in the ARZ model, the adaptive controller needs estimates of the unmeasured density and velocity states along the freeway segment. Measurement at a point, for example, collocated with the ramp, is feasible. Measurement along the entire freeway carries a prohibitive infrastructural cost. So, we will need both a parameter estimator and a state estimator, namely, an observer.

When plant parameters are unknown, it is not only the controller that needs to be made adaptive. The observer also needs to be made parameter-adaptive. In other words, we will need to design an adaptive observer for the ARZ model.

To summarize, the adaptive design process upon which we are about to embark, in the rest of this chapter, will need to produce three algorithms: a parameter estimator (identifier), an adaptive observer, and an adaptive controller.

The adaptive control module is designed independently from the identifier and observer modules. The identifier and the observer are designed in a somewhat joint fashion—as an adaptive observer. To be precise, the parameter estimator is designed independently, whereas the state estimator—the adaptive observer—is designed in a manner that depends on the design of the parameter estimator.

The approach to the adaptive observer design that we employ, from among the approaches introduced (for parabolic PDEs) in [?], is the swapping-based identifier design. This is the most suitable among the design options for our intended adaptive output-feedback application.

How is the said swapping-based identifier, or adaptive observer, to be designed? This is the central question in this chapter. The ARZ model, in its given form, is not suitable for parameter estimation with the measurement of only boundary velocity. The reason for the ARZ model in its native representation being unsuitable for parameter estimation is that, in the ARZ model, the unknown parameters appear as multiplied with unmeasured density and velocity along the freeway. When a quantity is a product of two unknowns, it is impossible to estimate the independent unknowns, even if one measures the product.

For this reason, an approach has to be taken that converts the model into a form in which the unknown parameters, which need to be estimated, are multiplied by a measured quantity, such as the boundary velocity. Such a model conversion is complex. The model format that is sought, for the purpose of parameter estimation, is a PDE counterpart of the observer canonical form for ODEs. The observer canonical form has the distinction of having the unknown parameters multiplied only by the measured output, and not by all the unmeasured state variables. It is that type of a canonical form into which we seek to convert the ARZ model.

We convert the ARZ model into a PDE equivalent of the observer canonical form in Section 5.5. A conversion of a model into the observer canonical form is

not trivial even for linear ODEs—it requires a particular similarity transformation, which for ODEs is a matrix. For the ARZ model, the model conversion is performed by a backstepping transformation. While we have previously used backstepping transformations in this book for the purpose of design—of controllers or observers—the backstepping transformation has a very different purpose here: the purpose is to produce a parameterization of the ARZ dynamics that lends itself to system identification. It appears entirely coincidental that our primary design tool also serves a role of model transformation.

Converting the ARZ model, whose parameters are impossible to estimate using only boundary measurements, into the observer canonical form where the parameters can be estimated using just the boundary measurements, comes with a price. The parameter representation changes and the unknown parameters become “overparametrized” in the observer canonical form. This overparametrization is quite drastic—even a few unknown scalar parameters lead to a functional parametrization (an unknown function, which needs to be estimated). This is the price paid for solvability of the problem of adaptive control of the ARZ model without having to instrument the entire freeway with density and velocity sensors. It is a rather modest numerical price to avoid a high infrastructural price.

Once the ARZ system is converted into the equivalent of the observer canonical form, an adaptive observer—a combination of a parameter estimator and a state estimator—can be designed. The parameter estimator is designed in Section 5.6. The state estimator is designed in Section 5.7.

The state estimator design in Section 5.7 takes a special approach. The design employs particular PDE filters. These filters allow to build an adaptive estimate of the unmeasured state by combining the estimates from the identifier in Section 5.6 with the filters in Section 5.7. Since this approach is inspired by Kreisselmeier’s use of filters in adaptive observers for linear ODEs, and by the subsequent use of such filters in output-feedback adaptive backstepping for nonlinear ODEs [?], we refer to these PDE filters as Kreisselmeier filters, or K-filters. The approach based on the K-filters generates adaptive estimates of the unmeasured states by using filter dynamics of a higher order than the ARZ PDE. This price in dynamic order, which is paid to achieve simultaneous estimation of the unknown parameters and state, is common to all adaptive observers, to varying degrees.

The adaptive controller is designed using a certainty-equivalence version of PDE backstepping. A backstepping controller, for the system in the PDE equivalent of the observer canonical form, is designed and then supplied with the adaptive estimates of the unknown parameters and of the unmeasured states. This adaptive controller design is performed in Section 5.8.

5.4 Validation of Adaptive Design: Stability Proof and Simulations

The Lyapunov stability and state regulation analysis, performed in Section 5.9, is the most “nonlinear” section of this book. Since the deployment of parameter estimates, substituted nonlinearly into the controller gains and the adaptive estimates of the states, results in a nonlinear closed-loop system even for the linearized version of the ARZ model, the resulting stability and convergence analyses involve nonlinear estimates of decays of various norms and signals. In spite of this nonlinearity, the stability properties obtained for linearized ARZ system are global.

The simulation results in Section 5.10 show three time intervals in the stabilization transient. Parameter estimation transients dominate the early period—neither good estimation of the states nor good control can take place with bad parameter estimates. State estimation dominates the second period—the state estimated need to be reasonably accurate to be useful in the controller. And, finally, the state is driven to the equilibrium, by the control law, in the third period.

It is also illustrated with the simulations in Section 5.10 that, as typical in adaptive control, the parameter estimates do not converge to the true unknown values but to “good enough” values for driving the state to the equilibrium.

The unusually long overture to this chapter is for two reasons. First, this is truly a central chapter of the book—it solves perhaps the hardest problem in stop-and-go suppression: a simultaneous stabilization and model identification. Second, the content of this chapter is methodologically the most involved and demands a road map for the reader.

5.5 The ARZ PDE Model with Parameter Uncertainty

The previous basic non-adaptive feedback control designs in Chapter 3 are based on the knowledge of the parameters of the ARZ model. Recall the linearized ARZ PDE model after spatial transformation, which is given by a first-order 2×2 hyperbolic system

$$\partial_t \bar{w}(x, t) + v^* \partial_x \bar{w}(x, t) = 0, \quad (5.1)$$

$$\partial_t \bar{v}_t(x, t) - (\gamma p^* - v^*) \partial_x \bar{v}(x, t) = c(x) \bar{w}(x, t), \quad (5.2)$$

$$\bar{w}(0, t) = -k_0 \bar{v}(0, t), \quad (5.3)$$

$$\bar{v}(L, t) = \kappa \bar{w}(L, t) + U(t), \quad (5.4)$$

where

$$c(x) = -\frac{1}{\tau} \exp\left(-\frac{x}{\tau v^*}\right), \quad (5.5)$$

$$k_0 = \frac{\gamma p^* - v^*}{v^*}, \quad (5.6)$$

$$\kappa = \exp\left(\frac{-L}{\tau v^*}\right). \quad (5.7)$$

In practice, the relaxation time τ , the property of a “typical” or “average” driver is hard to measure and is affected by many factors. In addition, coefficient γ in the pressure-density relation reflects the drivers’ aggressiveness and relates to the road situation. Due to the change of the road at the inlet or the outlet with an on-ramp, values of γ are different for the interior of the domain and the boundaries. We consider γ to be unknown at the boundaries but a known coefficient within the domain \mathcal{U} . According to (5.6), k_0 is considered as an unknown constant parameter at the boundary. The adaptive control law that is proposed in this chapter can also be used as an alternative to the non-adaptive output-feedback control design when parameters are known but expected to possibly change.

Consider the ARZ system with a control input $U(t)$ at the freeway outlet in (5.4) and with the measurement $Y(t)$ at the inlet,

$$Y(t) = \bar{v}(0, t). \quad (5.8)$$

The relation of this measured output with the boundary value of the state \bar{v} is given by

$$\bar{v}(0, t) = \rho_2 Y(t), \quad (5.9)$$

where

$$\rho_2 = \frac{q^*}{\gamma p^*}, \quad (5.10)$$

is unknown since γ is unknown.

In summary, the coefficients k_0 , ρ_2 and $\kappa = \exp\left(\frac{-L}{\tau v^*}\right)$ are unknown constant boundary parameters and $c(x) = -\frac{1}{\tau} \exp\left(-\frac{x}{\tau v^*}\right)$ is an unknown spatially-varying parameter, since τ is unknown. The steady-states p^* , q^* , and v^* are known. The control objective is to design an adaptive output feedback law applied with $U(t)$ and using only the measurement $Y(t)$.

Scaling the states

First we scale the state variable $\bar{w}(x, t)$ with the unknown constant κ and $\bar{v}(x, t)$ with unknown constant ρ_2 for the convenience of parameter estimation,

$$\omega(x, t) = \frac{\kappa}{\rho_2} \bar{w}(x, t), \quad (5.11)$$

$$\tilde{v}(x, t) = \frac{1}{\rho_2} \bar{v}(x, t). \quad (5.12)$$

The system becomes

$$\partial_t \omega(x, t) + v^* \partial_x \omega(x, t) = 0, \quad (5.13)$$

$$\partial_t \tilde{v}(x, t) - (\gamma p^* - v^*) \tilde{v}_x(x, t) = \bar{c}(x) \omega(x, t), \quad (5.14)$$

$$\omega(0, t) = -\kappa k_0 \tilde{v}(0, t), \quad (5.15)$$

$$\tilde{v}(L, t) = \omega(L, t) + \frac{1}{\rho_2} U(t), \quad (5.16)$$

where the unknown parameters are defined as

$$\bar{c}(x) = \frac{c(x)}{\kappa}, \quad (5.17)$$

$$r_0 = -\kappa k_0, \quad (5.18)$$

$$r_1 = \frac{1}{\rho_2}, \quad (5.19)$$

with measurement

$$\tilde{v}(0, t) = Y(t). \quad (5.20)$$

The scaling of \bar{w} and \bar{v} reduces the number of couplings between the unknown coefficients and the unmeasured state variables.

Observer canonical form

In order to decouple the (ω, \bar{v}) -system in the domain, we use the following back-stepping transformation:

$$\alpha(x, t) = \omega(x, t) - \int_0^x \bar{M}(x - \xi) \omega(\xi, t) d\xi, \quad (5.21)$$

$$\beta(x, t) = \tilde{v}(x, t) - \int_0^x \bar{K}(v^* x + (\gamma p^* - v^*) \xi) \omega(\xi, t) d\xi. \quad (5.22)$$

We transform the (ω, \bar{v}) -system into an observer canonical form,

$$\alpha_t(x, t) = -v^* \alpha_x(x, t) + \theta_1(x)Y(t), \quad (5.23)$$

$$\beta_t(x, t) = (\gamma p^* - v^*)\beta_x(x, t) + \theta_2(x)Y(t), \quad (5.24)$$

$$\alpha(0, t) = r_0 \beta(0, t), \quad (5.25)$$

$$\beta(L, t) = \alpha(L, t) + r_1 U(t), \quad (5.26)$$

where $\theta_1(x) = -v^* r_0 \bar{M}(x)$ and $\theta_2(x) = -v^* r_0 \bar{K}(v^* x)$. The measurement is

$$\alpha(0, t) = r_0 Y(t), \quad (5.27)$$

$$\beta(0, t) = Y(t). \quad (5.28)$$

To obtain the target system, we take the time and spatial derivatives on both sides of (5.21), (5.22). The kernels are

$$\bar{M}(x) = -\frac{1}{\gamma p^*} \bar{c} \left(L - \frac{\gamma p^* - v^*}{\gamma p^*} x \right), \quad (5.29)$$

$$\bar{K}(x) = -\frac{1}{\gamma p^*} \bar{c} \left(\frac{x}{\gamma p^*} \right), \quad (5.30)$$

and new spatial parameters are

$$\theta_1(x) = \frac{r_0 v^*}{\gamma p^*} \bar{c} \left(L - \frac{\gamma p^* - v^*}{\gamma p^*} x \right), \quad (5.31)$$

$$\theta_2(x) = \frac{r_0 v^*}{\gamma p^*} \bar{c} \left(\frac{v^*}{\gamma p^*} x \right). \quad (5.32)$$

For $\forall x \in [0, L]$, the following holds,

$$|\theta_1(x)| \leq \Theta, \quad (5.33)$$

$$|\theta_2(x)| \leq \Theta, \quad (5.34)$$

for

$$\Theta \triangleq \frac{\gamma p^* - v^*}{\gamma p^* \tau}. \quad (5.35)$$

5.6 Parametric Model and Parameter Estimation

We find the relation between the control input and the measured output of the observer canonical form by solving the system (5.23)–(5.26) directly,

$$\alpha(x, t) = \begin{cases} \alpha(x - v^* t, 0) + \int_0^t \theta_1(x - v^*(t-s))Y(s)ds, & t < \frac{x}{v^*}, \\ \alpha(0, t - \frac{x}{v^*}) + \frac{1}{v^*} \int_0^x \theta_1(s)Y(t - \frac{x-s}{v^*})ds, & t \geq \frac{x}{v^*}. \end{cases} \quad (5.36)$$

From (5.27), substituting $\alpha(0, t) = r_0 Y(t)$ into (5.36), we find, for $t \geq \frac{x}{v^\star}$:

$$\alpha(x, t) = r_0 Y\left(t - \frac{x}{v^\star}\right) + \frac{1}{v^\star} \int_0^x \theta_1(s) Y\left(t - \frac{x-s}{v^\star}\right) ds. \quad (5.37)$$

Thus we obtain $\alpha(L, t)$ in terms of the history of $Y(t)$ from $t - \frac{L}{v^\star}$ to t ,

$$\alpha(L, t) = r_0 Y\left(t - \frac{L}{v^\star}\right) + \frac{1}{v^\star} \int_0^L \theta_1(s) Y\left(t - \frac{L-s}{v^\star}\right) ds. \quad (5.38)$$

Given $\beta(L, t) = \alpha(L, t) + r_1 U(t)$, we solve for $\beta(x, t)$,

$$\beta(x, t) = \begin{cases} \beta(x + (\gamma p^\star - v^\star)t, 0) + \int_0^t \theta_2(x + (\gamma p^\star - v^\star)(t-s)) Y(s) ds, & t < \frac{L-x}{\gamma p^\star - v^\star}, \\ \beta\left(L, t - \frac{L-x}{\gamma p^\star - v^\star}\right) + \frac{1}{\gamma p^\star - v^\star} \int_x^L \theta_2(s) Y\left(t - \frac{s-x}{\gamma p^\star - v^\star}\right) ds, & t \geq \frac{L-x}{\gamma p^\star - v^\star}. \end{cases} \quad (5.39)$$

We now find, for $t \geq \frac{L-x}{\gamma p^\star - v^\star}$,

$$\beta(x, t) = \beta\left(L, t - \frac{L-x}{\gamma p^\star - v^\star}\right) + \frac{1}{\gamma p^\star - v^\star} \int_x^L \theta_2(s) Y\left(t - \frac{s-x}{\gamma p^\star - v^\star}\right) ds,$$

and thus, for $t \geq \frac{L}{\gamma p^\star - v^\star}$, we have

$$\begin{aligned} \beta(0, t) = & \alpha\left(L, t - \frac{L}{\gamma p^\star - v^\star}\right) + r_1 U\left(t - \frac{L}{\gamma p^\star - v^\star}\right) \\ & + \frac{1}{\gamma p^\star - v^\star} \int_0^L \theta_2(s) Y\left(t - \frac{s}{\gamma p^\star - v^\star}\right) ds. \end{aligned} \quad (5.40)$$

By substituting (5.28) and (5.37) into (5.40), we obtain the input/output parametric model,

$$\begin{aligned} Y(t) = & r_1 U\left(t - \frac{L}{\gamma p^\star - v^\star}\right) + r_0 Y\left(t - \frac{L}{v^\star} - \frac{L}{\gamma p^\star - v^\star}\right) \\ & + \int_{t - \frac{L}{v^\star} - \frac{L}{\gamma p^\star - v^\star}}^{t - \frac{L}{\gamma p^\star - v^\star}} \theta_1\left(v^\star(s-t) + \frac{\gamma p^\star}{\gamma p^\star - v^\star} L\right) Y(s) ds \\ & - \int_{t - \frac{L}{\gamma p^\star - v^\star}}^t \theta_2((\gamma p^\star - v^\star)(t-s)) Y(s) ds + \varepsilon(t), \end{aligned} \quad (5.41)$$

where $\varepsilon(t)$ is defined as the error of the parametric model. The value of $\varepsilon(t)$ is arbitrary for $t \in [0, \frac{L}{v^\star} + \frac{L}{\gamma p^\star - v^\star}]$ and depends on the initial values of $\alpha(x, 0)$, $\beta(x, 0)$. The value of $\varepsilon(t)$ is zero for $t \in [\frac{L}{v^\star} + \frac{L}{\gamma p^\star - v^\star}, \infty)$. We use this input/output parametric model to estimate the unknown spatially-varying parameters $\theta_1(x)$, $\theta_2(x)$ and unknown constant boundary parameter r_0 and r_1 .

The following update laws are based on the gradient algorithm with normalization and projection,

$$\partial_t \hat{\theta}_1(x) = (\tau_1(x, t), \hat{\theta}_1(x, t)), \quad (5.42)$$

$$\partial_t \hat{\theta}_2(x) = (\tau_2(x, t), \hat{\theta}_2(x, t)), \quad (5.43)$$

$$\partial_t \hat{r}_0 = \frac{\gamma_3}{\sigma(t)} Y \left(t - \frac{L}{v^*} - \frac{L}{\gamma p^* - v^*} \right) \tilde{\beta}(0, t), \quad (5.44)$$

$$\partial_t \hat{r}_1 = \frac{\gamma_4}{\sigma(t)} U \left(t - \frac{L}{\gamma p^* - v^*} \right) \tilde{\beta}(0, t), \quad (5.45)$$

where $\gamma_1(x)$, $\gamma_2(x)$, γ_3 and γ_4 are positive adaptation gains and

$$\tau_1(x, t) = \frac{\gamma_1(x) Y \left(t - \frac{L-x}{v^*} - \frac{L}{\gamma p^* - v^*} \right)}{\sigma(t) v^*} \tilde{\beta}(0, t), \quad (5.46)$$

$$\tau_2(x, t) = \frac{\gamma_2(x) Y \left(t - \frac{x}{\gamma p^* - v^*} \right)}{\sigma(t) (\gamma p^* - v^*)} \tilde{\beta}(0, t), \quad (5.47)$$

The projection operator is given by

$$(\tau_i, \hat{\theta}_i) = \begin{cases} \tau_i, & |\hat{\theta}_i| < \Theta \quad \text{or} \quad \hat{\theta}_i \tau_i \leq 0, \\ 0, & |\hat{\theta}_i| = \Theta \quad \text{and} \quad \hat{\theta}_i \tau_i > 0. \end{cases} \quad (5.48)$$

The normalization $\sigma(t)$ is given by

$$\begin{aligned} \sigma(t) = & 1 + Y^2 \left(t - \frac{L}{v^*} - \frac{L}{\gamma p^* - v^*} \right) + U^2 \left(t - \frac{L}{\gamma p^* - v^*} \right) \\ & + \int_{t - \frac{L}{v^*} - \frac{L}{\gamma p^* - v^*}}^t Y^2(s) ds. \end{aligned} \quad (5.49)$$

The adaptive estimation error $\tilde{\beta}(0, t)$ of parameter estimates $\hat{\theta}_1(x)$, $\hat{\theta}_2(x)$, \hat{r}_0 and \hat{r}_1 are obtained from the input/output parametric model as follows,

$$\begin{aligned} \tilde{\beta}(0, t) = & \beta(0, t) - \hat{\beta}(0, t) \\ = & Y(t) - \hat{r}_1 U \left(t - \frac{L}{\gamma p^* - v^*} \right) - \hat{r}_0 Y \left(t - \frac{L}{v^*} - \frac{L}{\gamma p^* - v^*} \right) \\ & + \int_{t - \frac{L}{v^*} - \frac{L}{\gamma p^* - v^*}}^{t - \frac{L}{\gamma p^* - v^*}} \hat{\theta}_1 \left(v^*(s - t) + \frac{\gamma p^*}{\gamma p^* - v^*} L \right) Y(s) ds \\ & - \int_{t - \frac{L}{\gamma p^* - v^*}}^t \hat{\theta}_2 ((\gamma p^* - v^*)(t - s)) Y(s) ds + \varepsilon(t). \end{aligned} \quad (5.50)$$

Inserting $Y(t)$ in (5.41) into (5.50), we obtain

$$\begin{aligned}
\tilde{\beta}(0, t) = & \tilde{r}_1 U \left(t - \frac{L}{\gamma p^\star - v^\star} \right) + \tilde{r}_0 Y \left(t - \frac{L}{v^\star} - \frac{L}{\gamma p^\star - v^\star} \right) \\
& - \int_{t - \frac{L}{v^\star} - \frac{L}{\gamma p^\star - v^\star}}^{t - \frac{L}{\gamma p^\star - v^\star}} \tilde{\theta}_1 \left(v^\star(s - t) + \frac{\gamma p^\star}{\gamma p^\star - v^\star} L \right) Y(s) ds \\
& + \int_{t - \frac{L}{\gamma p^\star - v^\star}}^t \tilde{\theta}_2 ((\gamma p^\star - v^\star)(t - s)) Y(s) ds,
\end{aligned} \tag{5.51}$$

where the parameter estimation errors are

$$\tilde{\theta}_i(x, t) = \theta_i(x) - \hat{\theta}_i(x, t), \quad i = 1, 2 \tag{5.52}$$

$$\tilde{r}_j(t) = r_j - \hat{r}_j(t), \quad j = 0, 1. \tag{5.53}$$

Lemma 5.1 *The update laws (5.42)–(5.45) guarantee that for all $x \in [0, L]$, $t \leq 0$,*

$$|\hat{\theta}_1(x)|, |\hat{\theta}_2(x)| \leq \Theta, \tag{5.54}$$

$$\|\tilde{\theta}_1\|, \|\tilde{\theta}_2\|, \tilde{r}_0, \tilde{r}_1 \in \mathcal{L}_\infty, \tag{5.55}$$

$$\|\partial_t \hat{\theta}_1\|, \|\partial_t \hat{\theta}_2\|, \partial_t \hat{r}_0, \partial_t \hat{r}_1, \frac{\tilde{\beta}(0, \cdot)}{\sqrt{\sigma(\cdot)}} \in \mathcal{L}_2 \cap \mathcal{L}_\infty. \tag{5.56}$$

where the norms $\mathcal{L}_\infty, \mathcal{L}_2$ are with respect to time.

Proof The property (5.54) follows from the projection (5.48). The projection has the following effect on (5.42) and (5.43):

$$\partial_t \hat{\theta}_1(x)^2 \leq \tau_1^2(x), \tag{5.57}$$

$$\partial_t \hat{\theta}_2(x)^2 \leq \tau_2^2(x). \tag{5.58}$$

Taking the following Lyapunov functional,

$$V = \frac{1}{2} \|\tilde{\beta}\|^2 + \int_0^L \frac{\tilde{\theta}_1(x)^2}{2\gamma_1(x)} dx + \int_0^L \frac{\tilde{\theta}_2(x)^2}{2\gamma_2(x)} dx + \frac{1}{2\gamma_3} \tilde{r}_0^2 + \frac{1}{2\gamma_4} \tilde{r}_1^2, \tag{5.59}$$

and differentiating it with respect to time, we have

$$\begin{aligned}
\dot{V} &= - \int_0^L \tilde{\beta} \tilde{\beta}_x dx - \int_0^L \frac{\tilde{\theta}_1(x) \partial_t \theta_1(x)}{\gamma_1(x)} dx - \int_0^L \frac{\tilde{\theta}_2(x) \partial_t \theta_2(x)}{\gamma_2(x)} dx - \frac{1}{\gamma_3} \tilde{r}_0 \partial_t \tilde{r}_0 - \frac{1}{\gamma_4} \tilde{r}_1 \partial_t \tilde{r}_1 \\
&= - \frac{1}{2} \beta^2(0) + \frac{(\beta(0) - \hat{\beta}(0)) \hat{\beta}(0)}{\sigma(t)} \\
&\leq - \frac{1}{2} \beta^2(0) + \frac{\beta^2(0) - \hat{\beta}^2(0)}{2\sigma(t)} \\
&\leq - \frac{1}{2} \left(1 - \frac{1}{\sigma(t)}\right) \beta^2(0) - \frac{1}{2} \frac{\hat{\beta}^2(0)}{\sigma(t)} \\
&\leq - \frac{1}{2} \frac{\hat{\beta}^2(0)}{\sigma(t)}.
\end{aligned} \tag{5.60}$$

Thus V is bounded and non-increasing, and, therefore, has a limit as $t \rightarrow \infty$. The properties (5.54) follow immediately from (5.59) and (5.60). Integrating (5.60) from zero to infinity gives

$$\frac{\tilde{\beta}(0, t)}{\sqrt{\sigma(t)}} \in \mathcal{L}_2 \tag{5.61}$$

The rest of the properties follow from (5.57)–(5.58) and the update laws (5.42)–(5.45). \square

5.7 Filter-based Observer Design

Our construction of an adaptive observer employs a PDE version of the Kreisselmeier filters, popularized in output-feedback adaptive backstepping [?]. First, we introduce an output filter with the output Y entering at the inlet, $x = 0$,

$$\partial_t \phi_1(x, t) = -v^* \partial_x \phi_1(x, t), \tag{5.62}$$

$$\phi_1(0, t) = Y(t), \tag{5.63}$$

$$\phi_1(x, 0) = \phi_{10}(x), \tag{5.64}$$

and an output filter with the output Y entering at the outlet, $x = L$,

$$\partial_t \phi_2(x, t) = (\gamma p^* - v^*) \partial_x \phi_2(x, t), \tag{5.65}$$

$$\phi_2(L, t) = Y(t), \tag{5.66}$$

$$\phi_2(x, 0) = \phi_{20}(x), \tag{5.67}$$

where $x \in [0, L]$, and ϕ_{10}, ϕ_{20} are arbitrary initial conditions. Then we introduce an input filter, with the input U entering at the outlet, $x = L$,

$$\partial_t \hat{\psi}(x, t) = (\gamma p^\star - v^\star) \partial_x \hat{\psi}(x, t), \quad (5.68)$$

$$\hat{\psi}(L, t) = \hat{\beta}(L, t), \quad (5.69)$$

$$\hat{\psi}(x, 0) = \hat{\psi}_0(x), \quad (5.70)$$

where $\hat{\beta}(L, t) = \hat{r}_1 U(t) + \hat{\alpha}(L, t)$ and $\hat{\alpha}(L, t)$ will be defined shortly. This allows us next to introduce the adaptive state estimates based on the input and output filters $\phi_1, \phi_2, \hat{\psi}$,

$$\hat{\alpha}(x, t) = \hat{r}_0 \phi_1(x, t) + \frac{1}{v^\star} \int_0^x \hat{\theta}_1(\xi) \phi_1(x - \xi, t) d\xi, \quad (5.71)$$

$$\hat{\beta}(x, t) = \hat{\psi}(x, t) + \frac{1}{\gamma p^\star - v^\star} \int_x^L \hat{\theta}_2(\xi) \phi_2(L + x - \xi, t) d\xi. \quad (5.72)$$

The signal $\hat{\alpha}(L, t)$ is obtained from (5.38) with updated parameters $\hat{\theta}_1(x, t)$ and $\hat{r}_1(t)$,

$$\hat{\alpha}(L, t) = \hat{r}_0 Y \left(t - \frac{L}{v^\star} \right) + \frac{1}{v^\star} \int_0^L \hat{\theta}_1(s) Y \left(t - \frac{L - s}{v^\star} \right) ds. \quad (5.73)$$

The explicit solutions to the PDE filters $\hat{\psi}, \phi_1, \phi_2$, for $t > \max \left(\frac{L}{v^\star}, \frac{L}{\gamma p^\star - v^\star} \right)$ are given by

$$\hat{\psi}(x, t) = \hat{r}_1 U \left(t - \frac{L - x}{\gamma p^\star - v^\star} \right) + \hat{\alpha} \left(L, t - \frac{L - x}{\gamma p^\star - v^\star} \right), \quad (5.74)$$

$$\phi_1(x, t) = Y \left(t - \frac{x}{v^\star} \right), \quad (5.75)$$

$$\phi_2(x, t) = Y \left(t - \frac{L - x}{\gamma p^\star - v^\star} \right). \quad (5.76)$$

The adaptive estimates $\hat{\alpha}(x, t)$ and $\hat{\beta}(x, t)$ are governed by the PDEs

$$\partial_t \hat{\alpha} = -v^\star \partial_x \hat{\alpha} + \hat{\theta}_1(x) Y(t) + \partial_t \hat{r}_0 \phi_1(x, t) + \frac{1}{v^\star} \int_0^x \partial_t \hat{\theta}_1(\xi) \phi_1(x - \xi, t) d\xi, \quad (5.77)$$

$$\partial_t \hat{\beta} = (\gamma p^\star - v^\star) \partial_x \hat{\beta} + \hat{\theta}_2(x) Y(t) + \frac{1}{\gamma p^\star - v^\star} \int_x^L \partial_t \hat{\theta}_2(\xi) \phi_2(L + x - \xi, t) d\xi, \quad (5.78)$$

with boundary conditions

$$\hat{\alpha}(0, t) = \hat{r}_0 \phi_1(0, t) = \hat{r}_0 Y(t), \quad (5.79)$$

$$\hat{\beta}(L, t) = \hat{\psi}(L, t) = \hat{r}_1 U(t) + \hat{\alpha}(L, t). \quad (5.80)$$

Let us now consider the adaptive observer errors

$$\tilde{\alpha}(x, t) = \alpha(x, t) - \hat{\alpha}(x, t), \quad (5.81)$$

$$\tilde{\beta}(x, t) = \beta(x, t) - \hat{\beta}(x, t). \quad (5.82)$$

They are governed by the PDEs

$$\begin{aligned} \tilde{\alpha}_t = & -v^* \tilde{\alpha}_x + \tilde{\theta}_1(x)Y(t) - \partial_t \hat{r}_0 \phi_1(x, t) \\ & - \frac{1}{v^*} \int_0^x \partial_t \hat{\theta}_1(\xi) \phi_1(x - \xi, t) d\xi, \end{aligned} \quad (5.83)$$

$$\begin{aligned} \tilde{\beta}_t = & (\gamma p^* - v^*) \tilde{\beta}_x + \tilde{\theta}_2(x)Y(t) \\ & - \frac{1}{\gamma p^* - v^*} \int_x^L \partial_t \hat{\theta}_2(\xi) \phi_2(L + x - \xi, t) d\xi, \end{aligned} \quad (5.84)$$

with boundary conditions

$$\tilde{\alpha}(0, t) = \tilde{r}_0 Y(t), \quad (5.85)$$

$$\tilde{\beta}(L, t) = \tilde{r}_1 U(t) + \tilde{\alpha}(L, t). \quad (5.86)$$

5.8 Adaptive output-feedback control Design

To obtain the adaptive control law for the input $U(t)$ appearing in (5.80), we apply the backstepping transformation to the adaptive state estimate $\hat{\beta}$ in (5.78). The transformed state is given by

$$\begin{aligned} \eta(x) &= \hat{\beta}(x) - \frac{1}{\gamma p^* - v^*} \int_0^x \hat{K}_2(x - \xi) \hat{\beta}(\xi) d\xi \\ &\triangleq (\mathcal{I} - \mathcal{F})[\hat{\beta}](x), \end{aligned} \quad (5.87)$$

where \hat{K}_2 is obtained by solving online the following Volterra equation,

$$\hat{K}_2(x) = -\hat{\theta}_2(x) + \frac{1}{\gamma p^* - v^*} \int_0^x \hat{K}_2(x - \xi) \hat{\theta}_2(\xi) d\xi. \quad (5.88)$$

The kernels $\hat{K}_2(x)$ and $\hat{\theta}_2(x)$ are functions of time, i.e., $\hat{K}_2(x, t)$ and $\hat{\theta}_2(x, t)$, though we suppress the dependence throughout for compactness. The inverse transformation is then given by

$$\begin{aligned} \hat{\beta}(x) &= \eta(x) - \frac{1}{\gamma p^* - v^*} \int_0^x \hat{\theta}_2(x - \xi) \hat{\eta}(\xi) d\xi \\ &\triangleq \hat{\eta} - \frac{1}{\gamma p^* - v^*} \hat{\theta}_2 * \hat{\eta}. \end{aligned} \quad (5.89)$$

With a lengthy but straightforward calculation, we obtain that

$$\eta_t = (\gamma p^\star - v^\star) \eta_x - \hat{K}_2(x) \tilde{\beta}(0) + \eta * \mathcal{F}[\partial_t \hat{\theta}_2](x) + \frac{1}{\gamma p^\star - v^\star} \left(\int_x^L \partial_t \hat{\theta}_2(\xi) \phi_2(L+x-\xi, t) d\xi \right), \quad (5.90)$$

$$\eta(L) = 0, \quad (5.91)$$

and the adaptive control law is derived from (5.91), and will be given shortly in (5.117).

We summarize the transformation and inverse transformation between the original system $(\bar{w}, \bar{v}, \hat{\psi}, \phi_1, \phi_2)$ and the final target system $(\tilde{\alpha}, \tilde{\beta}, \hat{\zeta}, \hat{\eta}, \phi_1, \phi_2)$ as:

$$\phi_1 = \phi_1, \quad (5.92)$$

$$\phi_2 = \phi_2, \quad (5.93)$$

$$\hat{\alpha} = \mathcal{T}_\alpha[\phi_1], \quad (5.94)$$

$$\eta = (\mathcal{I} - \mathcal{F})[\hat{\psi} + \mathcal{T}_\beta[\phi_2]], \quad (5.95)$$

$$\tilde{\beta} = (\mathcal{I} - \mathcal{G})[\bar{v}/k_2] - (\hat{\psi} + \mathcal{T}_\beta[\phi_2]), \quad (5.96)$$

$$\tilde{\alpha} = (\mathcal{I} - \mathcal{G})[-\kappa \bar{w}] - \mathcal{T}_\alpha[\phi_1], \quad (5.97)$$

and we can obtain the original states from the inverse transformation as:

$$\phi_1 = \phi_1, \quad (5.98)$$

$$\phi_2 = \phi_2, \quad (5.99)$$

$$\hat{\psi} = \eta - \frac{1}{v^\star} \hat{\theta}_2 * \eta - \mathcal{T}_\beta[\phi_2], \quad (5.100)$$

$$\bar{w} = -\frac{1}{\kappa} (\mathcal{I} - \mathcal{G})^{-1} [\tilde{\alpha} + \hat{\alpha}], \quad (5.101)$$

$$\bar{v} = k_2 (\mathcal{I} - \mathcal{G})^{-1} [\tilde{\beta} + \hat{\psi} + \mathcal{T}_\beta[\phi_2]]. \quad (5.102)$$

Due to the invertibility of the above transformation, we can obtain the stability of the original system $(\bar{w}, \bar{v}, \hat{\psi}, \phi_1, \phi_2)$ by studying the system in the equivalent variables $(\tilde{\alpha}, \tilde{\beta}, \hat{\alpha}, \eta, \phi_1, \phi_2)$. The target system $(\tilde{\alpha}, \tilde{\beta}, \hat{\alpha}, \eta, \phi_1, \phi_2)$ is governed by the following PDEs,

$$\begin{aligned}\tilde{\alpha}_t = & -v^\star \tilde{\alpha}_x + \tilde{\theta}_1(x)Y(t) - \partial_t \hat{r}_0 \phi_1(x, t) \\ & - \frac{1}{v^\star} \int_0^x \partial_t \hat{\theta}_1(\xi) \phi_1(x - \xi, t) d\xi,\end{aligned}\quad (5.103)$$

$$\tilde{\alpha}(0, t) = \tilde{r}_0 Y(t), \quad (5.104)$$

$$\begin{aligned}\tilde{\beta}_t = & (\gamma p^\star - v^\star) \tilde{\beta}_x + \tilde{\theta}_2(x)Y(t) \\ & - \frac{1}{\gamma p^\star - v^\star} \int_x^L \partial_t \hat{\theta}_2(\xi) \phi_2(L + x - \xi, t) d\xi,\end{aligned}\quad (5.105)$$

$$\tilde{\beta}(L, t) = \tilde{\alpha}(L, t) + \tilde{r}_1 U(t), \quad (5.106)$$

$$\begin{aligned}\hat{\alpha}_t = & -v^\star \hat{\alpha}_x + \hat{\theta}_1(x)Y(t) + \partial_t \hat{r}_0 \phi_1(x, t) \\ & + \frac{1}{v^\star} \int_0^x \partial_t \hat{\theta}_1(\xi) \phi_1(x - \xi, t) d\xi,\end{aligned}\quad (5.107)$$

$$\hat{\alpha}(0, t) = \hat{r}_0 Y(t), \quad (5.108)$$

$$\begin{aligned}\eta_t = & (\gamma p^\star - v^\star) \eta_x - \hat{K}_2(x) \tilde{\beta}(0) + \eta * \mathcal{F}[\partial_t \hat{\theta}_2](x) \\ & + \frac{1}{\gamma p^\star - v^\star} \mathcal{F} \left[\int_x^L \partial_t \hat{\theta}_2(\xi) \phi_2(L + x - \xi, t) d\xi \right],\end{aligned}\quad (5.109)$$

$$\eta(L, t) = 0, \quad (5.110)$$

$$\partial_t \phi_2(x, t) = (\gamma p^\star - v^\star) \partial_x \phi_2(x, t), \quad (5.111)$$

$$\phi_2(L, t) = Y(t), \quad (5.112)$$

$$\partial_t \phi_1(x, t) = -v^\star \partial_x \phi_1(x, t), \quad (5.113)$$

$$\phi_1(0, t) = Y(t). \quad (5.114)$$

The output $Y(t) = \eta(0) + \tilde{\beta}(0)$. According to the backstepping transformation (5.87), we can obtain from (5.110) that

$$\hat{\beta}(L, t) = \int_0^L \hat{K}_2(L - \xi) \hat{\beta}(\xi, t) d\xi. \quad (5.115)$$

Substituting $\hat{\beta}(L, t) = \hat{r}_1 U(t) + \hat{\alpha}(L, t)$, we have

$$U(t) = \frac{1}{\hat{r}_1} \int_0^L \hat{K}_2(L - \xi) \hat{\beta}(\xi, t) d\xi - \frac{1}{\hat{r}_1} \hat{\alpha}(L, t). \quad (5.116)$$

Using the adaptive estimates $\hat{\beta}(x, t)$ in (5.72) and $\hat{\alpha}(L, t)$ in (5.73), the adaptive controller is then obtained in an explicit integral form, consisting of delayed values of the input and the output,

$$\begin{aligned}
U(t) = & \frac{1}{\hat{r}_1} \int_{t-\frac{L}{\gamma p^* - v^*}}^t \hat{K}_2(v^*(t-\xi)) U(\xi) d\xi - \frac{\hat{r}_0}{\hat{r}_1} \hat{Y}\left(t - \frac{L}{v^*}\right) - \frac{1}{\hat{r}_1} \int_{t-\frac{L}{v^*}}^t m_1(t-\xi) Y(\xi) d\xi \\
& + \frac{\hat{r}_0}{\hat{r}_1} \int_{t-\frac{L}{v^*}-\frac{L}{\gamma p^* - v^*}}^{t-\frac{L}{v^*}} m_2(t-\xi) Y(\xi) d\xi + \frac{1}{\hat{r}_1} \int_{t-\frac{L}{\gamma p^* - v^*}}^t m_3(t-\xi) \int_{\xi-\frac{L}{v^*}}^{\xi} m_4(\mu) Y(\mu) d\mu d\xi \\
& + \frac{1}{\hat{r}_1} \int_{t-\frac{L}{\gamma p^* - v^*}}^t m_5(t-\xi) Y(\xi) d\xi, \tag{5.117}
\end{aligned}$$

where m_i are defined as

$$m_1(t) = \hat{\theta}_1(L - v^*(t)), \tag{5.118}$$

$$m_2(t) = \hat{K}_2\left((\gamma p^* - v^*)\left(t - \frac{L}{v^*}\right)\right), \tag{5.119}$$

$$m_3(t) = \hat{K}_2((\gamma p^* - v^*)t), \tag{5.120}$$

$$m_4(\xi) = \hat{\theta}_1(L - v^*\xi), \tag{5.121}$$

$$m_5(t) = \int_{(\gamma p^* - v^*)t}^L \hat{K}_2(\mu) \hat{\theta}_2((\gamma p^* - v^*)(t + L - \mu)) d\mu. \tag{5.122}$$

The parameter estimates $\hat{\theta}_1(x, t)$, $\hat{\theta}_2(x, t)$, \hat{r}_0 and \hat{r}_1 are generated from the update laws. We can obtain $\hat{K}_2(x, t)$ by solving online the Volterra equation in (5.88). The Lyapunov stability proof is shown in the next section, which is derived from modifications of the proof in [?]. The key idea in proving stability of $(\tilde{\alpha}, \tilde{\beta}, \hat{\alpha}, \eta, \phi_1, \phi_2)$ -system is to take advantage of the cascade structure of the system. Due to the invertibility between (\tilde{q}, \tilde{v}) -system and (\tilde{w}, \tilde{v}) -system, we arrive at our main theorem for adaptive control design.

Theorem 5.1 *Consider the plant (5.1)–(5.3) with the adaptive control law (5.117) and update laws (5.42)–(5.45). For any initial conditions $\hat{\theta}_1(\cdot, 0)$, $\hat{\theta}_2(\cdot, 0)$, $r_0(0)$, $r_1(0) \in C^1[0, L]$, \tilde{w}_0 , \tilde{v}_0 , ϕ_{10} , ϕ_{20} , $\hat{\psi}_0$ that verify boundary conditions, the solution $(\tilde{w}, \tilde{v}, \phi_1, \phi_2, \hat{\psi}, \hat{\theta}_1, \hat{\theta}_2, \hat{r}_0, \hat{r}_1)$ is bounded for $t \geq 0$ and for $\forall x \in [0, L]$ it verifies that, as $t \rightarrow \infty$,*

$$\|\tilde{w}(x, t)\| \rightarrow 0, \quad \|\tilde{v}(x, t)\| \rightarrow 0, \tag{5.123}$$

$$\|\tilde{q}(x, t)\| \rightarrow 0, \quad \|\tilde{v}(x, t)\| \rightarrow 0. \tag{5.124}$$

The proof of Theorem 5.1 is completed by the following sections on Lyapunov stability analysis.

5.9 Lyapunov Stability Analysis

L_2 boundedness

The boundedness of $\hat{\theta}_2$ is given by Lemma 2.7. Using (5.88) and Gronwall's inequality, we establish a bound on \hat{K}_2 ,

$$|\hat{K}_2(x)| \leq \Theta e^{\frac{\Theta}{\gamma p^* - v^*}} \triangleq K_2. \quad (5.125)$$

To prove the L_2 boundedness of system in (5.103)–(5.114), we construct the following Lyapunov functions:

$$V_1 = \frac{1}{2} \int_0^L e^{-x} \tilde{\alpha}^2(x) dx, \quad (5.126)$$

$$V_2 = \frac{1}{2} \int_0^L e^x \tilde{\beta}^2(x) dx, \quad (5.127)$$

$$V_3 = \frac{1}{2} \int_0^L e^{-x} \hat{\alpha}^2(x) dx, \quad (5.128)$$

$$V_4 = \frac{1}{2} \int_0^L e^x \eta^2(x) dx, \quad (5.129)$$

$$V_5 = \frac{1}{2} \int_0^L e^x \phi_1^2(x) dx, \quad (5.130)$$

$$V_6 = \frac{1}{2} \int_0^L e^x \phi_2^2(x) dx. \quad (5.131)$$

Then we get

$$\begin{aligned} \dot{V}_1 &\leq -\frac{v^*}{2e^L} \tilde{\alpha}^2(L) - \frac{1}{2} \left(\frac{v^*}{e^L} - \frac{c_1}{v^*} - c_2 \right) \|\tilde{\alpha}\|^2 + \left(v^* \tilde{r}_0^2 + \frac{1}{2c_2} \|\tilde{\theta}_1\|^2 \right) \hat{\eta}(0)^2 \\ &\quad + \left(\frac{1}{2v^* c_1} \|\partial_t \hat{\theta}_1\|^2 + \partial_t \hat{r}_0^2 \right) \|\phi_1\|^2 + \left(v^* \tilde{r}_0^2 + \frac{1}{2c_2} \|\tilde{\theta}_1\|^2 \right) \tilde{\beta}(0)^2 \\ &\leq -\frac{v^*}{2e^L} \tilde{\alpha}^2(L) - \frac{1}{2} \left(\frac{v^*}{e^L} - \frac{c_1}{v^*} - c_2 \right) \|\tilde{\alpha}\|^2 + \left(v^* \tilde{r}_0^2 + \|\tilde{\theta}_1\|^2 \right) \hat{\eta}(0)^2 + l_1 \|\phi_1\|^2 + l_2, \end{aligned} \quad (5.132)$$

and

$$\begin{aligned}
\dot{V}_2 &\leq e^L(\gamma p^\star - v^\star)\tilde{\alpha}^2(L) - \frac{1}{2}\left(\gamma p^\star - v^\star - \frac{e^L c_3}{2(\gamma p^\star - v^\star)} - e^L c_4\right)\|\tilde{\beta}\|^2 \\
&\quad + \frac{e}{4c_3(\gamma p^\star - v^\star)}\|\partial_t \hat{\theta}_2\|^2\|\phi_2\|^2 + \frac{e^L}{2c_4}\|\tilde{\theta}_2\|^2\hat{\eta}(0)^2 \\
&\quad + e^L(\gamma p^\star - v^\star)\hat{r}_1^2 U(t)^2 + \left(\frac{e^L}{2c_4}\|\tilde{\theta}_2\|^2 - \frac{\gamma p^\star - v^\star}{2}\right)\tilde{\beta}(0)^2 \\
&\leq e^L(\gamma p^\star - v^\star)\tilde{\alpha}^2(L) - \frac{1}{2}\left(\gamma p^\star - v^\star - \frac{e^L c_3}{2(\gamma p^\star - v^\star)} - e^L c_4\right)\|\tilde{\beta}\|^2 \\
&\quad + \frac{e^L}{2c_4}\|\tilde{\theta}_2\|^2\hat{\eta}(0)^2 + l_3\|\phi_2\|^2 + l_4 + l_5,
\end{aligned}$$

and

$$\begin{aligned}
\dot{V}_3 &\leq -\frac{v^\star}{2e^L}\hat{\alpha}^2(L) - \frac{1}{2}\left(\frac{v^\star}{e^L} - \frac{c_5}{v^\star} - c_6\right)\|\hat{\alpha}\|^2 + \left(\frac{1}{2v^\star c_5}\|\partial_t \hat{\theta}_1\|^2 + \hat{r}_0^2\right)\|\phi_1\|^2 \\
&\quad + \left(v^\star \hat{r}_0^2 + \frac{1}{2c_6}\|\hat{\theta}_1\|^2\right)\tilde{\beta}(0)^2 + \left(v^\star \hat{r}_0^2 + \frac{1}{2c_6}\|\hat{\theta}_1\|^2\right)\hat{\eta}(0)^2 \\
&\leq -\frac{v^\star}{2e^L}\hat{\alpha}^2(L) - \frac{1}{2}\left(\frac{v^\star}{e^L} - \frac{c_5}{v^\star} - c_6\right)\|\hat{\alpha}\|^2 \\
&\quad + \left(v^\star \hat{r}_0^2 + \frac{1}{2c_6}\|\hat{\theta}_1\|^2\right)\hat{\eta}(0)^2 + l_6\|\phi_1\|^2 + l_7,
\end{aligned} \tag{5.133}$$

and

$$\begin{aligned}
\dot{V}_4 &\leq -\frac{1}{2}\left(\gamma p^\star - v^\star - \frac{e^L c_7}{2(\gamma p^\star - v^\star)} - e^L c_8 - c_9\right)\|\eta\|^2 + \frac{e^L(1+K_2^2)}{4c_7(\gamma p^\star - v^\star)}\|\partial_t \hat{\theta}_2\|^2\|\phi_2\|^2 \\
&\quad + \frac{2(1+K_2^2)}{c_9}\|\partial_t \hat{\theta}_2\|^2\|\eta\|^2 - \left(\frac{\gamma p^\star - v^\star}{2} + \frac{e^L K_2^2}{2c_8}\right)\eta^2(0) + \frac{e^L K_2^2}{2c_8}\tilde{\beta}(0)^2 \\
&\leq -\frac{1}{2}\left(\gamma p^\star - v^\star - \frac{e^L c_7}{2(\gamma p^\star - v^\star)} - e^L c_8 - c_9\right)\|\eta\|^2 - \left(\frac{\gamma p^\star - v^\star}{2} + \frac{e^L K_2^2}{2c_8}\right)\eta^2(0) \\
&\quad + l_8\|\phi_2\|^2 + l_9\|\eta\|^2 + l_{10},
\end{aligned} \tag{5.134}$$

and

$$\begin{aligned}
\dot{V}_5 &\leq -\frac{\gamma p^\star - v^\star}{2}\|\phi_2\|^2 + e^L(\gamma p^\star - v^\star)\hat{\eta}(0)^2 + e^L(\gamma p^\star - v^\star)\tilde{\beta}(0)^2 \\
&\leq -\frac{\gamma p^\star - v^\star}{2}\|\phi_2\|^2 + e^L(\gamma p^\star - v^\star)\hat{\eta}(0)^2 + l_{11},
\end{aligned} \tag{5.135}$$

and

$$\begin{aligned}\dot{V}_6 &\leq -\frac{v^\star}{2e^L} \|\phi_1\|^2 + v^\star \hat{\eta}(0)^2 + v^\star \tilde{\beta}(0)^2 \\ &\leq -\frac{v^\star}{2e^L} \|\phi_1\|^2 + v^\star \hat{\eta}(0)^2 + l_{12},\end{aligned}\quad (5.136)$$

where the nonnegative functions of time $l_i(t)$, denoted as

$$l_1 = \partial_t \hat{r}_0^2 + \frac{1}{2v^\star c_1} \|\partial_t \hat{\theta}_1\|^2, \quad l_2 = \left(v^\star \hat{r}_0^2 + \frac{1}{2c_2} \|\tilde{\theta}_1\|^2 \right) \tilde{\beta}(0)^2, \quad (5.137)$$

$$l_3 = \frac{e^L \|\partial_t \hat{\theta}_2\|^2}{4c_2(\gamma p^\star - v^\star)}, \quad l_4 = \left(e^L \|\tilde{\theta}_2\|^2 - \frac{\gamma p^\star - v^\star}{2} \right) \tilde{\beta}(0)^2, \quad (5.138)$$

$$l_5 = e^L (\gamma p^\star - v^\star) \hat{r}_1^2 U(t)^2, \quad l_6 = \frac{1}{2v^\star c_5} \|\partial_t \hat{\theta}_1\|^2 + \hat{r}_0^2, \quad (5.139)$$

$$l_7 = \left(v^\star \hat{r}_0^2 + \frac{1}{2c_6} \|\hat{\theta}_1\|^2 \right) \tilde{\beta}(0)^2, \quad l_8 = \frac{e^L (1 + K_2^2) \|\partial_t \hat{\theta}_2\|^2}{4c_7(\gamma p^\star - v^\star)}, \quad (5.140)$$

$$l_9 = \frac{2(1 + K_2^2)}{c_9} \|\partial_t \hat{\theta}_2\|^2, \quad l_{10} = \frac{e^L K_2^2}{2c_8} \tilde{\beta}^2(0), \quad (5.141)$$

$$l_{11} = e^L (\gamma p^\star - v^\star) \tilde{\beta}(0)^2, \quad l_{12} = v^\star \tilde{\beta}(0)^2, \quad (5.142)$$

are integrable thanks to Lemma 5.1, and c_i are positive constants chosen as

$$c_1 = \frac{v^{\star 2}}{2e^L}, \quad c_2 = \frac{v^\star}{4e^L}, \quad c_3 = \frac{(\gamma p^\star)^2}{e^L}, \quad (5.143)$$

$$c_4 = \frac{(\gamma p^\star - v^\star)}{4e^L}, \quad c_5 = \frac{v^{\star 2}}{2e^L}, \quad c_6 = \frac{v^\star}{4e^L}, \quad (5.144)$$

$$c_7 = \frac{(\gamma p^\star)^2}{e^L}, \quad c_8 = \frac{(\gamma p^\star - v^\star)}{4e^L}, \quad c_9 = \frac{(\gamma p^\star - v^\star)}{8}. \quad (5.145)$$

Taking the overall Lyapunov function

$$V = g_1 V_1 + V_2 + V_3 + g_2 V_4 + V_5 + V_6, \quad (5.146)$$

with positive constants g_1 and g_2 defined as

$$g_1 = 2e^{2L} \frac{\gamma p^\star - v^\star}{v^\star}, \quad (5.147)$$

$$\begin{aligned}g_2 &= \frac{2(\gamma p^\star - v^\star)}{(\gamma p^\star - v^\star)^2 + 4e^{2L} K_2^2} \left(\frac{2e^{2L} (\gamma p^\star - v^\star)}{v^\star} \left(v^\star \hat{r}_0^2 + \|\tilde{\theta}_1\|^2 \right) \right. \\ &\quad \left. + \frac{2e^{2L}}{\gamma p^\star - v^\star} \|\tilde{\theta}_2\|^2 + \left(v^\star + \frac{2e^L}{v^\star} \right) \Theta^2 + e^L \gamma p^\star - e^L v^\star + v^\star \right),\end{aligned}\quad (5.148)$$

we get

$$\dot{V} \leq -g_0 V + lV + l, \quad (5.149)$$

where g_0 is a positive constant defined as

$$g_0 = \min \left(\frac{v^*}{4}, \frac{\gamma p^* - v^*}{8} \right), \quad (5.150)$$

and l is the linear combination of l_i and therefore is also integrable, nonnegative function of time. Since the following inequalities are satisfied

$$\frac{1}{2e^L} \|\tilde{\alpha}\|^2 \leq V_1 \leq \frac{1}{2} \|\tilde{\alpha}\|^2, \quad (5.151)$$

$$\frac{1}{2} \|\tilde{\beta}\|^2 \leq V_2 \leq \frac{e^L}{2} \|\tilde{\beta}\|^2, \quad (5.152)$$

$$\frac{1}{2e^L} \|\hat{\alpha}\|^2 \leq V_3 \leq \frac{1}{2} \|\hat{\alpha}\|^2, \quad (5.153)$$

$$\frac{1}{2} \|\eta\|^2 \leq V_4 \leq \frac{e^L}{2} \|\eta\|^2, \quad (5.154)$$

$$\frac{1}{2e^L} \|\phi_1\|^2 \leq V_5 \leq \frac{1}{2} \|\phi_1\|^2, \quad (5.155)$$

$$\frac{1}{2} \|\phi_2\|^2 \leq V_6 \leq \frac{e^L}{2} \|\phi_2\|^2 \quad (5.156)$$

the Lyapunov function V is bounded and integrable (Lemma D.3. in [?]), and the following holds:

$$\|\tilde{\alpha}\|, \|\tilde{\beta}\|, \|\hat{\alpha}\|, \|\eta\|, \|\phi_1\|, \|\phi_2\| \in \mathcal{L}_2 \cap \mathcal{L}_\infty. \quad (5.157)$$

Then with the inverse transformation (5.100)–(5.102) from the final target system $(\tilde{\alpha}, \tilde{\beta}, \hat{\alpha}, \hat{\eta}, \phi_1, \phi_2)$ to the $(\bar{w}, \bar{v}, \hat{\psi}, \phi_1, \phi_2)$ -system, we have

$$\|\bar{w}\|, \|\bar{v}\| \in \mathcal{L}_2 \cap \mathcal{L}_\infty. \quad (5.158)$$

Finally, from the inverse transformation (4.15)–(4.16) from the (\bar{w}, \bar{v}) -system to the (\tilde{q}, \tilde{v}) -system, we get

$$\|\tilde{q}\|, \|\tilde{v}\| \in \mathcal{L}_2 \cap \mathcal{L}_\infty. \quad (5.159)$$

Convergence

The above Lyapunov proof shows that \dot{V} is bounded from above and V is positive and integrable. According to Lemma D.2. in [?], we have

$$\|\bar{w}(x, t)\| \rightarrow 0, \quad \|\bar{v}(x, t)\| \rightarrow 0. \quad (5.160)$$

The inverse transformation (3.27)–(3.28) from (\bar{w}, \bar{v}) -system to (\tilde{q}, \tilde{v}) -system gives

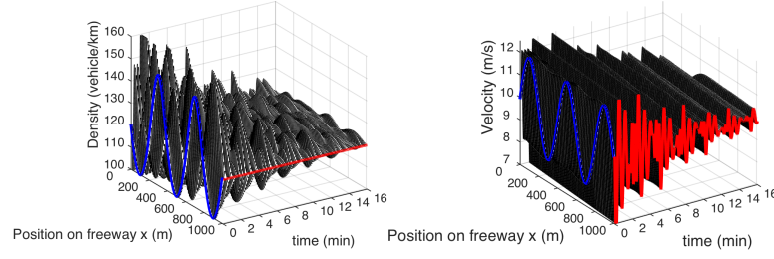


Fig. 5.1 Open-loop system response without adaptive UORM output feedback.

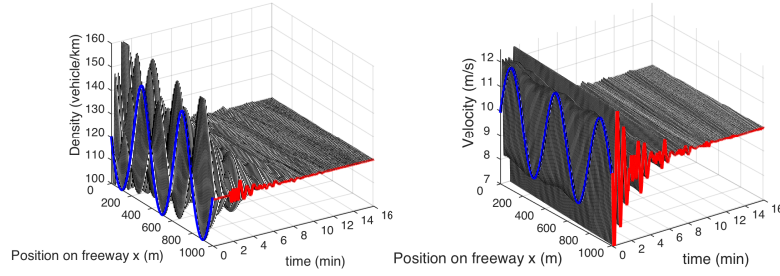


Fig. 5.2 Closed-loop system response with adaptive UORM output feedback.

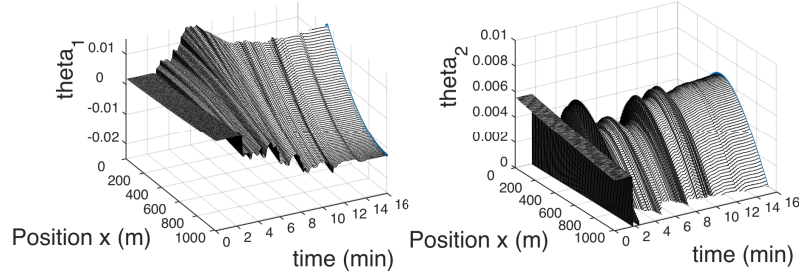


Fig. 5.3 Estimates of spatially-varying parameters.

$$\|\tilde{q}(x, t)\| \rightarrow 0, \quad \|\tilde{v}(x, t)\| \rightarrow 0. \quad (5.161)$$

□

5.10 Numerical Simulation

The length of the freeway section is chosen to be $L = 1$ km. The free speed is $v_m = 40$ m/s and the maximum density is $\rho_m = 150$ vehicles /km. The steady-states

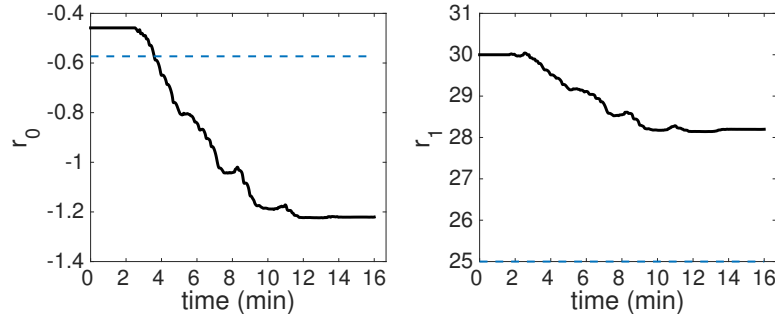


Fig. 5.4 Estimates of constant parameters.

(ρ^*, v^*) are chosen as (120 vehicles /km, 10 m/s) which is in the congested regime. We take $\gamma = 1$ and relaxation time $\tau = 60$ s. We assume a constant incoming flow and constant outgoing density for boundary conditions and use sinusoidal initial conditions.

In the adaptive simulation, we simulate the traffic on a freeway road of $L = 1$ km. We choose $\tau = 100$ s and other model parameters are chosen to be the same with the non-adaptive simulation. The open-loop system is more oscillatory than that of the non-adaptive case due to the longer relaxation time. It takes a longer time to stabilize the traffic with the adaptive output-feedback control law. In Fig. 5.1, we see that the open-loop system is lightly damped. The the adaptive output feedback result is shown in Fig. 5.2. The estimations of the spatially varying parameters of the system are given in Fig. 5.3 and the estimation of constant parameters is shown in Fig. 5.4. The blue lines in Fig. 5.4 represent the true values of the constant parameters. The parameter estimates do not necessarily converge to the true values, due to the local property of gradient methods.

5.11 Notes and References

In [?], an early and abbreviated publication on which the present chapter is based, in the absence of the knowledge of some of the traffic parameters, we solved the adaptive boundary control problem for the linearized ARZ model using the PDE backstepping method, gradient-based update laws, and a Kresselmeier filter-based approach to adaptive observer design. The main step is to transform the hetero-directional coupled hyperbolic system to the observer canonical form that is suitable for adaptive design. Parameters are estimated based on an input-output model representation of the ARZ PDE, while the filter-based observer design estimates the state values.

The adaptive output-feedback control design approach in this chapter is inspired by two previous results. First, by the design in Chapter 13 of the book [?]. While that chapter deals with parabolic PDEs, the main ideas originate there—the trans-

formation into a (parabolic) PDE equivalent of the observer canonical form, the employment of the Kreisselmeier filters, and the output-feedback adaptive design for the observer canonical form. The second source of inspiration is the design for a single first-order hyperbolic PDE in the paper [?], which in turn is inspired by Chapter 13 of [?] and where, again, the observer canonical form and the K-filters are employed.

In addition to the books [?] (for parabolic PDEs) and [?] (for coupled hyperbolic PDEs), the reader should be made aware of another comprehensive book on adaptive control in infinite dimension—the 2020 book on adaptive control for systems with unknown delays [?]. This book bears some relation with [?] in the sense that delays are, in fact, transport PDEs, namely, first-order hyperbolic PDEs.

This is the only adaptive PDE control chapter in this book. There are several other non-adaptive designs in this book, which are more complex than the designs in Chapter 3, and which can be made adaptive. Specifically, using the general adaptive control methodologies for hyperbolic PDEs in [?], the problems in our Chapters 8, 9, and 10 can be solved adaptively, for unknown values of various traffic and driver parameters.

In Chapter 7 we explore another adaptive, albeit not real-time adaptive control approach for suppressing stop-and-go in the ARZ model: reinforcement learning.

Chapter 6

Event-Triggered Control of ARZ Model

This chapter develops event-triggered boundary control strategies for VSL to stabilize the stop-and-go traffic on a freeway segment. We have already designed full-state feedback ramp metering controller for the linearized ARZ model in Chapter 3. However, the continuous-time control input signal cannot be directly implemented on a digital platform as required by a on-ramp traffic light or the electronic display of a VSL. With the proposed method in this chapter, the controlled velocity signal is only updated when an event triggering condition is satisfied. Compared with the continuous input signal, the signal of the event-based VSL controller is piecewise constant and thus it allows the adaptation time for drivers to follow the advisory speed.

The traffic dynamics of density and velocity are described with the linearized ARZ macroscopic traffic PDE model. The event-triggered boundary controllers rely on the emulation of the full-state backstepping boundary feedback, introduced in Section 3.5. Two different Lyapunov-based event-triggered strategies are developed to determine the time instances at which the control value must be sampled/updated. One event-triggered strategy makes use of a dynamic triggering condition under which it is possible to state the existence of a uniform minimal dwell-time (independent of initial conditions). The exponential stability under event-triggered control is achieved and validated with numerical simulations.

For networked control systems modeled by ODEs, discretization and sampling strategies have been extensively developed to implement continuous time controllers on digital platform, including sampled-data control that periodically or aperiodically modulates the frequency of signal changes [?, ?], and event-triggered control that updates control values only when needed [?, ?, ?, ?]. For the PDE system, the sampled data and event-triggered control strategies focus on studying how fast sampling the continuous in time controller could preserve stability and convergence of the closed-loop system [?, ?, ?, ?, ?]. In [?], event-triggered boundary control is proposed for the second-order coupled hyperbolic PDE system, relying on the backstepping method. A full-state feedback controller is sampled according to a dynamic triggering condition. As the event-triggered mechanism reduces the computational and communication cost, it has been incorporated with the model predictive control of freeway traffic

governed by a linearized second-order macroscopic traffic model which is discrete in time [?]. In this chapter, we adopt the event triggered boundary control strategies for a VSL full-state feedback controller in order to reduce the stop-and-go traffic congestion described with the linearized ARZ model.

6.1 VSL Full-state Feedback Control Design

We consider the ARZ model on $x \in [0, L]$, $t \in [0, \infty)$,

$$\partial_t \rho + \partial_x(\rho v) = 0, \quad (6.1)$$

$$\partial_t(v + p(\rho)) + v \partial_x(v + p(\rho)) = \frac{V(\rho) - v}{\tau}, \quad (6.2)$$

$$\rho(0, t) = \frac{q^*}{v(0, t)}, \quad (6.3)$$

$$v(L, t) = U(t) + v^*, \quad (6.4)$$

linearized around the steady-states (q^*, v^*) is given by

$$\tilde{q}_t + v^* \tilde{q}_x - \frac{q^*(\gamma p^* - v^*)}{v^*} \tilde{v}_x = -\frac{q^*}{\tau} \left(\frac{1}{v^*} - \frac{1}{\gamma p^*} \right) \tilde{v} - \frac{\gamma p^*}{\tau v^*} \tilde{q}, \quad (6.5)$$

$$\tilde{v}_t - (\gamma p^* - v^*) \tilde{v}_x = \frac{\gamma p^* - v^*}{\tau v^*} \tilde{v} - \frac{\gamma p^*}{\tau q^*} \tilde{q}, \quad (6.6)$$

$$\tilde{q}(0, t) = 0, \quad (6.7)$$

$$\tilde{v}(L, t) = \frac{1}{\rho^*} \tilde{q}(L, t), \quad (6.8)$$

with zero flow rate variations from the inlet and the VSL boundary control input from the outlet,

$$\tilde{q}(x, t) = 0, \quad (6.9)$$

$$\tilde{v}(x, t) = U(t). \quad (6.10)$$

Writing the linearized ARZ model in the Riemann coordinate and through a spatial transformation as introduced in the Chapter 3, we obtain a first-order 2×2 hyperbolic system in (\bar{w}, \bar{v}) with an in-domain spatially-varying coupling,

$$\partial_t \bar{w} + v^* \partial_x \bar{w} = 0, \quad (6.11)$$

$$\partial_t \bar{v} - (\gamma p^* - v^*) \partial_x \bar{v} = \bar{c}(x) \bar{w}, \quad (6.12)$$

$$\bar{w}(0, t) = -k_0 \bar{v}(0, t), \quad (6.13)$$

$$\bar{v}(L, t) = U(t), \quad (6.14)$$

where the spatially-varying coefficient and boundary coefficients are defined as

$$c(x) = -\frac{1}{\tau} \exp\left(-\frac{x}{\tau v^\star}\right), \quad (6.15)$$

$$k_0 = \frac{\gamma p^\star - v^\star}{v^\star}. \quad (6.16)$$

We aim to stabilize the closed-loop system (6.11)-(6.14) on events while sampling the continuous-time controller $U(t)$ in (6.14) at certain sequence of time instants $(t_k)_{k \in \mathbb{N}}$. The control value is held constant between two successive time instants and it is updated when some triggering condition is verified. To that end, we need to suitably modify the controlled boundary condition (6.14) such that

$$\bar{v}(t, L) = U_d(t), \quad (6.17)$$

where

$$U_d(t) = U(t) + d(t), \quad (6.18)$$

for all $t \in [t_k, t_{k+1})$, $k \geq 0$ and $d(t)$ will be seen as a deviation that will be rigorously defined later on. We apply the following Volterra backstepping transformation:

$$\begin{aligned} \alpha(t, x) &= \bar{w}(t, x), \\ \beta(t, x) &= \bar{v}(t, x) - \int_0^x K_1(x, \xi) \bar{w}(t, \xi) d\xi - \int_0^x K_2(x, \xi) \bar{v}(t, \xi) d\xi, \end{aligned} \quad (6.19)$$

where the Kernels $K_i(x, \xi)$, $i = 1, 2$ evolve in the triangular domain $\mathcal{T} = \{(x, \xi) : 0 \leq \xi \leq x \leq L\}$ and are solution of the well-posed linear hyperbolic PDE kernel equations discussed in Chapter 2. Therefore, with the transformation (6.19), one maps the system (6.11)-(6.13) with boundary input (6.17), into the following target system:

$$\alpha_t(t, x) + v^\star \alpha_x(t, x) = 0, \quad (6.20)$$

$$\beta_t(t, x) - (\gamma p^\star - v^\star) \beta_x(t, x) = 0, \quad (6.21)$$

$$\alpha(t, 0) = -k_0 \beta(t, 0), \quad (6.22)$$

$$\beta(t, L) = d(t), \quad (6.23)$$

where $\alpha, \beta : \mathbb{R}^+ \times [0, L] \rightarrow \mathbb{R}$. The inverse transformation of (6.19) is given as follows:

$$\bar{w}(t, x) = \alpha(t, x), \quad (6.24)$$

$$\bar{v}(t, x) = \beta(t, x) + \int_0^x L_1(x, \xi) \alpha(t, \xi) d\xi + \int_0^x L_2(x, \xi) \beta(t, \xi) d\xi, \quad (6.25)$$

where $L_i(x, \xi)$, $i, j = 1, 2$ are solution of linear hyperbolic PDE kernel equations given in Chapter 2. The continuous-time control $U(t)$ is

$$U(t) = \int_0^L L_1(L, \xi) \alpha(t, \xi) d\xi + \int_0^L L_2(L, \xi) \beta(t, \xi) d\xi, \quad (6.26)$$

and its emulated modification is given as:

$$U_d(t) = \int_0^L L_1(L, \xi) \alpha(t_k, \xi) d\xi + \int_0^L L_2(L, \xi) \beta(t_k, \xi) d\xi, \quad (6.27)$$

for all $t \in [t_k, t_{k+1})$, where $d(t)$ is given by

$$d(t) = \int_0^L L_1(L, \xi) (\alpha(t_k, \xi) - \alpha(t, \xi)) d\xi - \int_0^L L_2(L, \xi) (\beta(t_k, \xi) - \beta(t, \xi)) d\xi. \quad (6.28)$$

It represents an actuation deviation between the continuous and the event-triggered controllers. Therefore, one can realize the backstepping transformation with U_d given by (6.27). Since $U_d(t)$ is given in the form of the transformed states, we can represent the α, β with inverse Volterra operator on (\tilde{q}, \tilde{v}) . Then we propose two event-triggered boundary control strategies in the next section.

6.2 Event-triggered Strategies for boundary control

We introduce two event-triggered boundary control strategies which are based on the backstepping feedback controller (6.27) and update the controller with a suitable triggering condition.

The boundary feedback law is defined

$$U_d(t) = \int_0^L L_1(L, \xi) \alpha(t_k, \xi) d\xi + \int_0^L L_2(L, \xi) \beta(t_k, \xi) d\xi, \quad (6.29)$$

for all $t \in [t_k, t_{k+1})$, where the events $(t_k)_{k \in \mathbb{N}}$ can be determined with either the static or dynamic event-triggering mechanisms.

Static triggering condition

We consider a triggering condition which relies on the evolution of the square of the actuation deviation (6.28) and the evolution of the following Lyapunov function candidate of the target system (6.20)-(6.23),

$$V(\alpha, \beta) := \int_0^L \left(\frac{A}{v^*} \alpha^2(x) \exp\left(-\frac{\mu x}{v^*}\right) + \frac{B}{(\gamma p^* - v^*)} \beta^2(x) \exp\left(\frac{\mu x}{(\gamma p^* - v^*)}\right) \right) dx, \quad (6.30)$$

with positive constant coefficients A, B and μ .

Definition 6.1 (Static triggering condition)

Let $\sigma \in (0, 1)$, $T > 0$, $\mu > 0$, $B > 0$. Let $t \mapsto V(\alpha(t, \cdot), \beta(t, \cdot))$ be given by (6.30). The event-triggered boundary control is defined in a static event-trigger mechanism. The times of the events $t_k \geq 0$ with $t_0 = 0$ form a finite or countable set of times which is determined by the following rules for some $k \geq 0$:

- I) if $\{t > t_k + T \mid B \exp\left(\frac{\mu L}{\gamma p^* - v^*}\right) r_1^2 d^2(t) \geq \sigma \mu V(t)\} = \emptyset$ then the set of the times of the events is $\{t_0, \dots, t_k\}$.
- II) if $\{t > t_k + T \mid B \exp\left(\frac{\mu L}{\gamma p^* - v^*}\right) r_1^2 d^2(t) \geq \sigma \mu V(t)\} \neq \emptyset$, then the next event time is given by:

$$t_{k+1} = \inf\{t > t_k + T \mid B \exp\left(\frac{\mu L}{\gamma p^* - v^*}\right) r_1^2 d^2(t) \geq \sigma \mu V(t)\}. \quad (6.31)$$

In the definition of the next triggering time (6.31), $T > 0$ is satisfied, which can be viewed as a time threshold (or waiting time) to implement a time regularization. It enforces a positive minimal inter-event time of at least T units of time. Only after the waiting time, the triggering condition is checked.

Without such time regularization, there may not be guarantees for avoiding the so-called Zeno phenomenon, that is, infinite triggering times in a finite-time interval. It represents infeasible practical implementations into digital platforms because it would be required to sample/update the controller infinitely fast. On the other hand, if the existence of a minimal dwell-time can be proved, the next event time can be simply defined as (6.31) without introducing $T > 0$, as introduced later in the dynamic triggering condition.

It is also important to remark that T has to be suitably chosen. To that end, one option is to look at periodic implementations for the system (6.11)-(6.14) where the control is updated periodically in a sample-and-hold fashion while meeting stability guarantees. Therefore, we adopt the idea of using looped functionals [?] to take into account the time regularization and its impact into the stability analysis with Linear Matrix Inequality conditions.

Dynamic triggering condition

The second event-triggering condition is based on the evolution of the square of the actuation deviation (6.28) and the evolution of a dynamic variable which can be viewed as a filtered value of the static triggering condition.

Definition 6.2 (Dynamic triggering condition)

Let $\sigma \in (0, 1)$, $\theta > 0$, $\eta > 0$, $\mu > 0$, $\kappa_1 > 0$, $m^0 \in \mathbb{R}_0^-$, $B > 0$. Let $t \mapsto V(\alpha(t, \cdot), \beta(t, \cdot))$ be given by (6.30). The event-triggered boundary control with dynamic triggering condition is defined in the following. The times of the events $t_k \geq 0$ with $t_0 = 0$ form a finite or countable set of times which is determined by the following rules for some $k \geq 0$:

- I) if $\{t > t_k | \theta B \exp\left(\frac{\mu L}{(\gamma p^* - v^*)}\right) r_1^2 d^2(t) \geq -m(t)\} = \emptyset$ then the set of the times of the events is $\{t_0, \dots, t_k\}$.
- II) if $\{t > t_k | \theta B \exp\left(\frac{\mu L}{(\gamma p^* - v^*)}\right) r_1^2 d^2(t) \geq -m(t)\} \neq \emptyset$, then the next event time is given by:

$$t_{k+1} = \inf\{t > t_k | \theta B \exp\left(\frac{\mu L}{(\gamma p^* - v^*)}\right) r_1^2 d^2(t) \geq -m(t)\} \quad (6.32)$$

where m satisfies the ordinary differential equation,

$$\dot{m}(t) = -\eta m(t) + \left(B \exp\left(\frac{\mu L}{(\gamma p^* - v^*)}\right) r_1^2 d^2(t) - \sigma \mu V(t) - \kappa_1 \alpha^2(t, L)\right) \quad (6.33)$$

for a given $\eta \geq \mu(1 - \sigma)$ and $m(0) = m^0$.

Definition 6.2 does not impose any time regularization, compared with the static triggering condition. The reason is that, under (6.32), it is possible to show the existence of a minimal dwell-time between two event time instants. With this strategy, we aim at reducing execution times, i.e. triggering less frequent than with a static triggering mechanism.

In the following sections we present our main results: the absence of the zeno phenomenon and the exponential stability of the closed-loop system with the two event triggered controllers.

6.3 Absence of the Zeno Phenomenon

We use the following estimate to study the growth-in-time of the actuation deviation, in order to derive the existence of a waiting time T for the time regularization in the static triggering condition and to establish the existence of a minimal dwell-time for the dynamic triggering condition.

Lemma 6.1 *For $d(t)$ given by (6.28), it holds for all $t \in (t_k, t_{k+1})$,*

$$(\dot{d}(t))^2 \leq \varepsilon_0 V(t) + \varepsilon_1 \alpha^2(t, L) + \varepsilon_2 d^2(t), \quad (6.34)$$

with

$$\varepsilon_0 = \frac{4}{r_1^2} \min \left\{ \frac{1}{v^*} \exp\left(-\frac{\mu L}{v^*}\right), \frac{r_0^2 + 1}{(\gamma p^* - v^*)} \right\}^{-1} \times \max \{ (v^*)^2 \tilde{L}_1, (\gamma p^* - v^*)^2 \tilde{L}_2 \}, \quad (6.35)$$

$$\varepsilon_1 = \frac{1}{r_1^2} 4(v^*)^2 (L_1(L, L))^2, \quad (6.36)$$

$$\varepsilon_2 = 2(\gamma p^* - v^*)^2 (L_2(L, L))^2. \quad (6.37)$$

where

$$\tilde{L}_1 = \int_0^L (L_1(L, \xi))^2 d\xi, \quad (6.38)$$

$$\tilde{L}_2 = \int_0^L (L_2(L, \xi))^2 d\xi. \quad (6.39)$$

Static triggering condition

For the event-triggered boundary control (6.29),(6.31) we have imposed a time regularization so that $t_{k+1} - t_k \geq T$, for all $k \geq 0$. As we discussed before, due to this fact, the Zeno phenomenon is immediately excluded.

Dynamic triggering condition

The main result states that under the event triggered control (6.29),(6.32), there exists a minimal dwell-time and therefore the Zeno phenomenon is avoided.

Theorem 6.1 *Under the the event-triggered boundary control (6.29),(6.32) in Definition 6.2, with positive scalars, $\sigma \in (0, 1)$, θ , η , μ , B , κ_1 , and ε_0 , ε_1 , and ε_2 (from Lemma 6.1) satisfying the following conditions,*

$$\begin{aligned} \theta B \exp\left(\frac{\mu L}{\gamma p^* - v^*}\right) \varepsilon_0 &\leq (1 - \sigma) \sigma \mu, \\ \theta B \exp\left(\frac{\mu L}{\gamma p^* - v^*}\right) \varepsilon_1 &\leq (1 - \sigma) \kappa_1, \end{aligned} \quad (6.40)$$

there exists a minimal dwell-time $\tau^ > 0$ between two triggering times, i.e. there exists a constant $\tau^* > 0$ (independent of the initial conditions) such that $t_{k+1} - t_k \geq \tau^*$, for all $k \geq 0$. Moreover, the minimal dwell-time is given by:*

$$\tau^* = \int_0^1 \frac{1}{a_0 + a_1 s + a_2 s^2} ds, \quad (6.41)$$

where

$$a_0 = \left(1 + \varepsilon_2 + \frac{(1-\sigma)}{\theta} + \eta\right) \frac{(1-\sigma)}{\sigma}, \quad (6.42)$$

$$a_1 = 1 + \varepsilon_2 + \frac{2(1-\sigma)}{\theta} + \eta, \quad (6.43)$$

$$a_2 = \frac{\sigma}{\theta}. \quad (6.44)$$

Since there exists a minimal dwell-time which is uniform and does not depend on the initial conditions, no Zeno solution will appear.

6.4 Stability Results

We perform a Lyapunov-based analysis by taking into account the two event-triggered strategies proposed in the previous section. We refer the interested reader to [?] for detailed proof. We will only state the main stability results.

Static triggering condition

We state first the stability of the closed-loop system under the event-triggered boundary control (6.29),(6.31).

Theorem 6.2 *Let $\sigma \in (0, 1)$, $\mu > 0$, $T > 0$, $\bar{\gamma}_0, \bar{\gamma}_1 > 0$, $B := \bar{\gamma}_0(r_0^2 \exp\left(\frac{\mu L}{v^*}\right) + 1)$, $\varepsilon_0, \varepsilon_1$ and ε_2 given in Lemma 6.1. If the following conditions hold,*

$$B \exp\left(\frac{\mu L}{(\gamma p^* - v^*)}\right) - \bar{\gamma}_1 \leq 0, \quad (6.45)$$

$$-\sigma \mu + T \varepsilon_0 r_1^2 \bar{\gamma}_1 \leq 0, \quad (6.46)$$

$$-\bar{\gamma}_0 + T \varepsilon_1 r_1^2 \bar{\gamma}_1 \leq 0, \quad (6.47)$$

$$\Pi(T) \leq 0, \quad (6.48)$$

where:

$$\Pi(T) = B \exp\left(\frac{\mu L}{(\gamma p^* - v^*)}\right) r_1^2 - \bar{\gamma}_1 r_1^2 + T r_1^2 \bar{\gamma}_1 (1 + \mu(1 - \sigma) + \varepsilon_2)$$

then, the closed-loop system (6.11)-(6.13),(6.17) with event-triggered control (6.29),(6.31) is exponentially stable.

Dynamic triggering condition

We state then the stability of the closed-loop system with event-triggered boundary control (6.29),(6.32).

Theorem 6.3 *Let $\sigma \in (0, 1)$, $\mu > 0$, $\eta \geq \mu(1 - \sigma)$, $A = \bar{\gamma}_0 \exp\left(\frac{\mu L}{v^*}\right)$, $B = \bar{\gamma}_0(r_0^2 \exp\left(\frac{\mu L}{v^*}\right) + 1)$ and $\kappa_1 > 0$ (from Definition 6.1). If $\kappa_1 \leq \bar{\gamma}_0$ and $\theta > 0$ is such that conditions (6.40) hold, then the closed-loop system (6.11)-(6.13), (6.17) with event-triggered control (6.29),(6.32) is exponentially stable.*

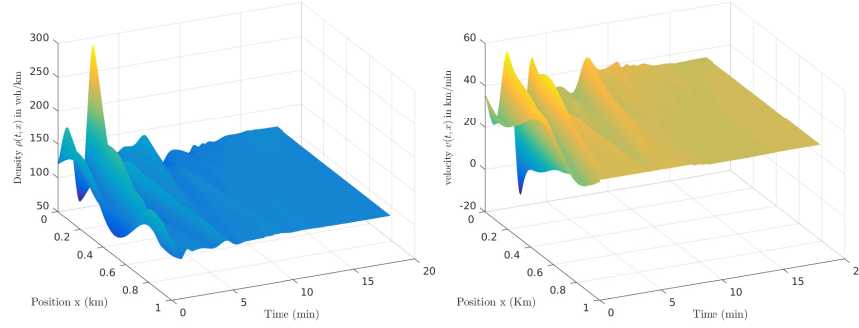


Fig. 6.1 Density $\rho(t, x)$ and velocity $v(t, x)$ of the closed-loop system (6.1)-(6.4) under the event-triggered boundary control (6.29),(6.32) with dynamic triggering condition.

6.5 Numerical simulations

We consider the original nonlinear ARZ model with initial conditions

$$\rho(x, 0) = \frac{\rho^*}{3} \sin\left(\frac{3\pi}{L}x\right) + \rho^*, \quad (6.49)$$

$$v(x, 0) = -\frac{v^*}{5} \sin\left(\frac{3\pi}{L}x\right) + v^* \quad (6.50)$$

where the steady-states in congested regime are chosen as $(\rho^*, v^*) = (120 \text{ veh/km}, 36 \text{ km/h})$. We take $\gamma = 1$. The length of the freeway segment is chosen to be $L = 1 \text{ km}$. The free speed is $v_f = 144 \text{ km/h}$ and the maximum density is $\rho_m = 160 \text{ vehicles/km}$. The relaxation time is $\tau = 1.5 \text{ min}$. We perform the simulation on a time horizon of 18 min.

We stabilize the system on events under the event-triggered boundary control (6.29),(6.31) with static triggering condition and time regularization. To set the parameters of the triggering condition, we first perform a line search on μ and on T while finding $\bar{\gamma}_0$ and $\bar{\gamma}_1$. This gives $T = 0.13 \text{ min}$, $\mu = 0.1$, $\bar{\gamma}_0 = 0.0204$ and $\bar{\gamma}_1 = 0.0487$ along with $\sigma = 0.9$ such that conditions of Theorem 6.2 hold.

Then, we stabilize on events with (6.29),(6.32) (with dynamic triggering condition). The parameters are chosen as $\kappa_1 = 0.0102$, $\theta = 0.5$, $\eta = 0.33$ such that Theorems 6.1 and 6.3 apply. Figure 6.1 shows the numerical solutions of the density and velocity ($\rho(t, x)$, $v(t, x)$, respectively) of the closed-loop system (6.1)-(6.4) under the event-triggered boundary control (6.29),(6.32) with dynamic triggering condition.

Moreover, we compute the minimal dwell-time between two triggering times according to (6.41), i.e. $\tau^* = 0.87 \text{ min}$ which is larger than T . In fact, τ^* can also be used as a suitable waiting time (much less conservative) for time regularization in periodic schemes where the control is sampled/updated in a sample-and-hold fashion.

Finally, Figure 6.2 shows time-evolution of the control functions. The red curve corresponds to the continuous-time control (6.26). The black curve corresponds to the

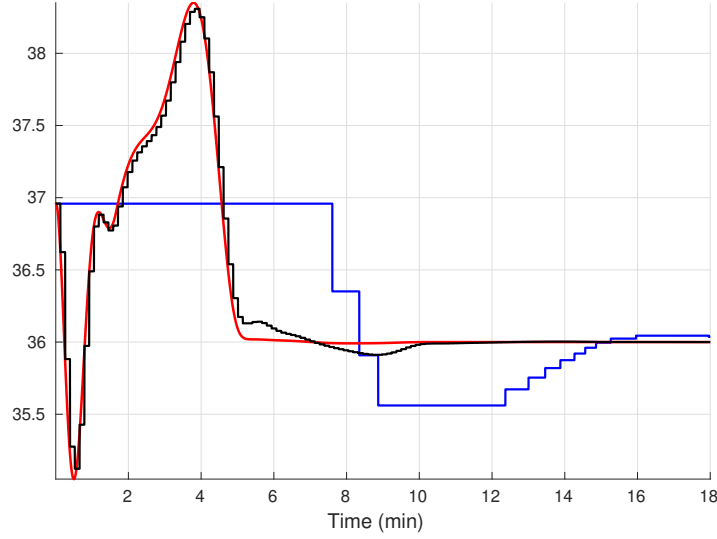


Fig. 6.2 Time-evolution of the velocity control input: the continuous-time control U (6.26) (depicted in red line), the event-triggered boundary control U_d (6.29),(6.31) (static triggering condition with time regularization $T = 0.13$) (depicted in black line) and the event-triggered boundary control U_d (6.29),(6.32) (dynamic triggering condition) (depicted in blue line).

event-triggered control (6.29) with static triggering condition in (6.31). Finally, The blue curve corresponds to the event-triggered control (6.29) with dynamic triggering condition in (6.32). With a dynamic triggering condition, we are able to stabilize on events while reducing more execution times than with the static triggering strategy and also meeting the theoretical guarantees. With this approach we can update the control value only when needed which translates into the way that the VSL sign, located at the outlet of a freeway segment, changes the advisory speed only when needed.

6.6 Notes and References

In [?] an early and abbreviated publication on which the present chapter is based, we proposed two event-triggered boundary control strategies for varying speed limit sign to reduce oscillations of the stop-and-go traffic congestion problem. Exponential stability and Zeno free behavior are achieved. The results can be adopted to implement in practice the ramp metering control strategy for the traffic congestion problem. We expect to address observer-based event-triggered boundary with validations on freeway data. In addition, self-triggered and periodic-event-triggered boundary control are of great interest. The latter suggests to monitor periodically the triggering condition while the actuation remains to be on events.

Chapter 7

Comparison of Backstepping with Reinforcement Learning

7.1 From (Model-Based) Adaptive Control to (Less Model-Based) Reinforcement Learning

Adaptive backstepping

In Chapter 5 we introduced a parameter-adaptive backstepping controller for the ARZ model. This controller allows for some uncertainty in the fundamental diagram $Q(\rho)$ and in the relaxation constant τ . However, the maximum speed v_m and the driver aggressiveness γ are assumed known. The reason for requiring v_m and γ to be known is that our adaptive design is of an output-feedback or observer-based kind, with a measurement of only the velocity at the inlet of the freeway segment, when the ramp metering is applied at the outlet of the freeway segment.

The complexity of the design in Chapter 5 may overwhelm a reader. Indeed, the multitude of techniques needed in order to design a model-based controller, a model-based observer, and a model-based parameter estimator for a PDE system requires a quite advanced degree of expertise in several subareas of PDE control and estimation. A few practitioners of traffic control may acquire such expertise. Many will either lack the motivation or the time to master all that it takes to understand the adaptive design in Chapter 5 and the guarantees of stability and convergence that the design provides.

It is, for this reason, tempting to explore the alternatives to the model-based adaptive control design. Reinforcement learning (RL) is a natural step in this exploration. To be specific, a traffic engineer interested in suppressing stop-and-go oscillations in congested traffic, and faced with the degree of expertise that the adaptive output-feedback control design in Chapter 5 demands of him, will likely ask the question whether control laws that achieve the stop-and-go suppression can be arrived at by training, namely, by an RL approach.

Relative merits of RL and adaptive backstepping

Of course, there is no free lunch in controlling unstable high-dimensional and highly uncertain systems. A saving in analytical effort is accompanied by a price paid in the form of extensive off-line training (on the ARZ model, not on the experiment) and in the loss of the ability to perform training (stably and safely) in real time. Our goal in this chapter is to illuminate this tradeoff, through a comparison between RL and adaptive PDE backstepping control.

We will discuss the details of RL control structure and its training in great length but let us briefly mention, at this early stage in the chapter, that RL employs a proximal policy optimization, a neural network as a parametric approximator of a function of the plant state, weight updating using a policy gradient algorithm, and off-line training on a numerical simulator of the ARZ PDE to maximize the reward function, which we chose as the L^2 spatial norm of states to achieve stabilization.

Since they are stabilization-inspired, we evaluate the RL state-feedback boundary controllers against the rigorously stabilizing backstepping controllers, first in a system with perfect knowledge of the traffic flow dynamics, i.e., on the same model for which the backstepping controller is designed, and then on a simulation model that differs in several ways from the model used for backstepping design. Our simulations show that RL controllers nearly recover the performance of the backstepping controller designed with perfect knowledge. Additionally, the RL controllers outperform the backstepping controller in some cases with partial modeling knowledge.

The price paid with the RL approach is that they are trained by conducting about one thousand episodes of iterative training on the ARZ PDE simulation model. This training cannot be performed in a collision-free fashion in real traffic. The convergence of the training process is not guaranteed. And, finally, stabilizing behavior for the ARZ PDE is achieved in simulations but is not theoretically guaranteed.

The areas in which RL potentially exhibits some advantages are (1) the significantly reduced reliance on modeling knowledge than the PDE backstepping (non-adaptive or adaptive design) and (2) the potential of the RL approach to be trained to the presence of nonlinearities in the ARZ PDE because the neural network structure in the RL feedback is agnostic regarding the linearity or nonlinearity of the PDE plant.

Let us examine these two advantages of RL in some detail, and from multiple angles, aiming at objectivity.

First, while PDE backstepping employs the ARZ PDE in an analytical design, RL is computationally trained on the same PDE. On the account of this, RL could be regarded to also be model based, or at least not model-free but “less model based” than backstepping. Additionally, the RL controller is a feedback law employing the states of the ARZ PDE (density and velocity), namely, it certainly presupposes the ARZ model structure. However, RL makes no assumption regarding the form of the right-hand side of the ARZ PDE. In that sense, it is indeed “less model based” than even the adaptive version of the PDE backstepping design, let alone than the non-adaptive backstepping.

Second, the RL approach is agnostic regarding the nonlinearity of the ARZ model. Its form, based on neural networks, is nonlinear regardless of whether ARZ is linear (or linearized) or not. This is a potential advantage over the backstepping design, which is based on the linearized ARZ PDE. However, one should not overlook the fact that the backstepping designs (non-adaptive and adaptive) guarantee stability, at least locally, of the closed-loop ARZ PDE. RL, in contrast, comes with no guarantees—only with a hope that a trainable neural network structure may work well for a nonlinear system.

Learning characteristics of RL and adaptive backstepping

This is an important place to discuss whether both RL and the adaptive backstepping controllers are “learning-based.” *Learning* is a part of the name of the Reinforcement Learning controller and nobody will dispute the learning nature of RL. How about adaptive backstepping? The adaptive backstepping controller employs estimation of the parameters of the ARZ model—it is continuously *learning* the parts of the ARZ model that are not a priori known. So, the adaptive backstepping controller is certainly also a learning controller. While facing less uncertainty than RL, and tasked with learning fewer aspects of the ARZ model, the adaptive backstepping controller is performing its learning online, and with a stability guarantee. So, if one wishes to be terminologically precise and fair, one would refer to RL as “offline heuristic learning” and to adaptive backstepping as “online learning with stability guarantee.”

Since both RL and backstepping are “learning-based” controllers, it is important to note that the RL controller has far more to learn—many more parameters to be trained in its neural network parametrization than the adaptive backstepping controller. In fact, if we had allowed ourselves in Chapter 5 to use full-state measurement, our adaptive controller would involve the estimation of only a few parameters. But even with our output-feedback design, much less learning is needed with adaptive backstepping than with RL. It is no surprise then that the learning with adaptive backstepping can be done online, whereas with RL it must be performed offline.

For a specialist in adaptive control it is worth noting another difference in learning between RL and adaptive backstepping. With adaptive backstepping it is the plant parameters that are being estimated and, using these estimates, the parameters of the controller (the gain kernel functions) are computed online through a solution of a simple integral equation. An adaptive controller that employs the estimation of the plant parameters is called an *indirect* adaptive controller, so adaptive backstepping is an indirect adaptive controller. In contrast, an adaptive feedback law whose gains or parameters are directly tuned is called a *direct* adaptive controller. RL is a direct adaptive controller. The tradeoff between direct and indirect adaptive controllers is that direct controllers require no gain computation online but usually involve an overparametrization—often by one or several orders of magnitude relative to the physically uncertain parameters. This tradeoff is in play between RL and adaptive backstepping. With a small saving in online computation (of the integral equation in adaptive backstepping), the RL control pays a high price in offline computation and

in the absence of the ability of online learning, adjustment, and re-learning as ARZ parameter values drift or change abruptly.

Reliance on full-state measurement

As we indicated earlier, the RL feedback employs the full measurement of the state of the ARZ PDE—the density and the velocity along the entire freeway. In Section 2.4, as well as in Chapter 4, we discussed in detail that measuring the distributed state bears a prohibitive cost on the infrastructure. The observer-based backstepping control designs in 3.5 and 5 require the measurement only at one location on the freeway segment (either at the entry or at the exit, i.e., at the location of ramp metering). Hence, PDE backstepping supplies a much more usable feedback law than RL. If RL were to match the capability of PDE backstepping, it would need to be equipped also with a state estimator, i.e., an observer. Given that observers, to work accurately, need to incorporate a copy of the system model, it is not clear how an RL-based observer as free of information regarding the form of the right-hand side of the ARZ PDE could be designed.

Even though backstepping is available in both its full-state feedback and output-feedback versions (as well as adaptive and non-adaptive versions), the comparisons between RL and backstepping which we conduct in this chapter is for the non-adaptive full-state feedback version. The reason for this is to give a chance to RL to be compared against the “most model-based” among the backstepping designs which, due to its availability of the full state and the parameter knowledge, is the best performing among the backstepping designs.

Is RL learning the backstepping feedback law?

As shall be seen, after sufficient training, RL nearly recovers the performance of the backstepping design, measured by the L^2 norm (in space and time, i.e., over the given spatial interval on the freeway and over a chosen time interval) of the error between the density and velocity states and their respective equilibrium values. The reader will naturally wonder whether, by recovering the performance of the backstepping controller, the RL approach has “learned” the backstepping controller. There is no reason to expect that the achievement of the same spatiotemporal norm means that two feedback laws are identical. For a given initial condition, “infinitely many” gain combinations can result in the same spatiotemporal norm of the stabilized closed-loop system. If the RL controller were trained on a reward function that matches the Lyapunov function employed in the backstepping design, there would be a chance for RL to learn the backstepping feedback. But the training of RL is done based on the simple spatial L^2 norm of the density and velocity errors, whereas the backstepping Lyapunov function involves a Volterra transformation of those states. Hence, there is no basis to expect that RL would learn backstepping. In conclusion, it is appropriate

to say that “RL attains the performance of the model-based backstepping design” but not that “RL learns the model-based backstepping feedback law.”

Comparison of RL with Proportional-Integral controllers

In our comparison of RL against controllers that provide stability guarantees, in addition to backstepping we also consider the simple collocated Proportional (P) and Proportional-Integral (PI) controllers. For limited values of ARZ parameters, they also provide stability guarantees. They can be regarded both as model-based and model-free. They are model-free because, traditionally, P and PI feedback laws are not model-based designs but heuristic choices. But P and PI can also be regarded as model based for ARZ because, under restricted parameter values, they can guarantee stability. Backstepping, in turn, requires no restriction on the values of the parameters of the ARZ model; it is applicable to arbitrarily unstable stop-and-go motions.

It should be clear that, in the three-way comparison—among backstepping, P/PI, and RL controllers—the comparison of primary relevance is between the backstepping and RL controllers, which both, in principle, are not restricted in their applicability to traffic regimes that are at most mildly unstable. The comparison of RL with P/PI is of secondary relevance, mostly providing ‘another point of reference’ for the assessment of the RL controller.

Since both the backstepping and the P/PI controllers are equipped with Lyapunov proofs (the former in unrestricted traffic regimes and the latter under restriction), we occasionally refer to both backstepping and P/PI as Lyapunov-based controllers. Their respective Lyapunov functions are very different—the Lyapunov function for P/PI is a spatially weighted L^2 norm of the state error, whereas the Lyapunov function for the backstepping controller is the spatial L^2 norm of the state error transformed with the Volterra transformation whose kernel is specially designed to allow any degree of coupling between the density and velocity PDEs and, hence, any degree of open-loop instability.

7.2 RL Control Approach

Learning-based methods have attracted attention by both the PDE modeling community and the transportation community. Algorithms for solving high-dimensional parabolic PDE systems were derived using deep learning in [?] by reformulating the PDEs as stochastic differential equations and approximating the gradient of unknown solutions with deep neural networks (DNN). More recent work in [?] proposed RL-learned numerical solutions for scalar conservation laws which autonomously generate accurate numerical schemes for various situations. For the PDE control problem, boundary control of time-varying 2D convection-diffusion PDEs with an application for heating, ventilating, air conditioning (HVAC) control design was developed in [?, ?].

In the domain of traffic management, researchers have been applying RL to various traffic problems. Different levels of traffic modeling are employed, depending on the problem. For example, the authors in [?] examined traffic light signal timing at one intersection using deep Q-learning with a traffic simulator, Paramics, which is based on microscopic traffic models. Studies on the traffic signal scheduling problem were further extended to multi-agent control for five centrally-connected traffic intersections [?], which was described with a traffic queuing model. The article [?] used a multi-agent RL algorithm to control the traffic light around a traffic junction. The authors proposed a framework where each agent was able to switch between independent and integrated modes in which the agent solved the multi-agent RL problem using modular Q-learning. The authors of [?] formulated a deep RL framework for mixed-autonomy traffic in some experimental scenarios using the traffic microsimulator SUMO. Under the same framework, [?] developed RL controllers for connected autonomous vehicles to de-congest traffic bottlenecks.

Surprising few RL designs for macroscopic traffic models exist in the literature, at present, in spite of the fact that the PDE model is particularly well-suited for modeling congested traffic flow patterns. The reason is that RL control of PDEs involves high-dimensional state spaces which makes the approximation of value functions challenging. The authors in [?] considered the cell transmission model which is obtained from discretization of the LWR first-order PDE model. An RL-based controller was designed using different policy gradient methods, such as REINFORCE, Trust Policy Optimization (TRPO), and the Truncated Natural Policy Gradient (TNPG) algorithm. Incoming traffic flow is actuated by the RL controller such that the traffic flow is optimized for some target outflow.

Our effort on RL control presented in this chapter differs from [?] on the traffic problem to be solved, the model being used, and the methodology being employed, which guides our study and analysis from a very different perspective. We focus on the stabilization problem, and examine a second-order PDE model to describe stop-and-go traffic oscillations. The resulting RL controllers are tested, and we examine under what circumstances RL could be a better choice relative to a Lyapunov-based PDE controller.

7.3 Boundary Control Problem Reformulation

ARZ PDE traffic model

We consider the ARZ PDE model to describe the traffic dynamics on a freeway segment. The state variables are traffic density $\rho(x, t)$ and traffic speed $v(x, t)$, defined on the domains $x \in [0, L]$, $t \in [0, T]$. The detailed discussion of ARZ PDE Traffic model is found in Section 1.2 in Chapter 1.

Our control objective is to regulate the state around an equilibrium reference state (ρ^*, v^*) , where

$$v^* = V(\rho^*), \quad (7.1)$$

satisfies the equilibrium density and velocity relation. We choose the density ρ^* such that the reference system (ρ^*, v^*) is in the congested regime for dense traffic, which can be characterized by the two characteristics of the linearized PDE model, as discussed in Chapter 1.23.

$$\lambda_1 = v^* > 0, \quad (7.2)$$

$$\lambda_2 = v^* + \rho^* V'(\rho^*) < 0. \quad (7.3)$$

As shown in Fig. 7.1, the control inputs U_{in} and U_{out} are transported from the actuated boundaries to in-domain states with the two characteristic speeds respectively.

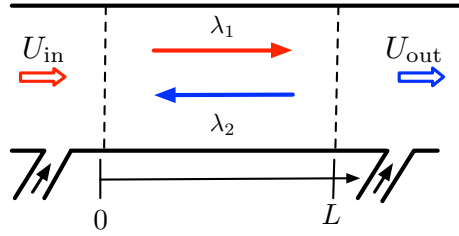


Fig. 7.1 Stabilization of stop-and-go traffic on freeway with ramp metering located at boundaries of the segment.

Boundary control design

Our control objective is the regulation, by ramp-metering on the boundary, of the L^2 norm of the density and velocity error states relative to their respective uniform steady state values. The oscillations can occur due to delayed driver response without ramp-metering control. In order to reduce oscillations in congested traffic, we actuate traffic flow from the upstream inlet and downstream outlet of the freeway segment, using on-ramp metering as shown in Fig. 7.1. Alternatively, one can actuate velocity by installing VSLs.

Boundary control algorithms are designed to stabilize the traffic around the reference steady state. For the ARZ PDE model, the control design guarantees that the state variables $(\rho(x, t), v(x, t))$ are regulated to the reference system (ρ^*, v^*) in the spatial L^2 norm, i.e.

$$\|\rho(x, t) - \rho^*\| \rightarrow 0, \quad (7.4)$$

$$\|v(x, t) - v^*\| \rightarrow 0, \quad (7.5)$$

Table 7.1 Lyapunov-based Boundary Control Design

Design method	U_{in}	U_{out}
Setpoint	q^*	q^*
Backstepping	q^*	$U_{\text{out, BKST}}$
Proportional	$U_{\text{in, L}}$	q^*
Proportional Integral	$U_{\text{in, PI}}$	$U_{\text{out, PI}}$

where $\|\cdot\|$ is the spatial L^2 norm, i.e., $\|f(x, t)\| = \left(\int_0^L f^2(x, t) dx\right)^{1/2}$.

For the segment of freeway traffic, boundary actuation is implemented with ramp metering controlling the traffic flow rate entering from the on-ramp to the mainline. Both inlet and outlet flow rates can be controlled through ramp metering

$$\rho(0, t)v(0, t) = U_{\text{in}}(t), \quad (7.6)$$

$$\rho(L, t)v(L, t) = U_{\text{out}}(t), \quad (7.7)$$

We denote the boundary control inputs of different strategies with $U_{\text{in}, \star}(t)$, $U_{\text{out}, \star}(t)$, where \star represents the name of the control design.

As summarized in Table 7.1, the Lyapunov-based boundary control algorithms consist of setpoint boundary inputs, backstepping PDE control in Section 3.5 of Chapter 3, Proportional in Section 3.4 of Chapter 3 and Proportional Integral control [?]. Despite different actuation locations and assumptions, three different state-feedback controllers achieve Lyapunov stabilization of the PDE system by collectively shifting the linearized PDE eigenvalues onto the open left half plane. The control gains used for the backstepping method are computed numerically in Chapter 3. The static proportional gain in inlet control is derived by solving the linearized PDE system analytically in Section 3.4 of Chapter 3. The static proportional and integral gains in PI control are obtained through trial and error. We then summarize the Lyapunov-based control algorithms in the boundary control framework, as illustrated in Fig. 7.1.

Setpoint control

We simply limit the outgoing flow rate to be the setpoint state value as the boundary control. The setpoint control is open-loop control which does not use feedback of the system. This simple method is considered as a baseline case to compare against more sophisticated control designs. The constant incoming and outgoing flow rate at the boundaries are implemented as,

$$U_{\text{in, O}}(t) = q^*, \quad (7.8)$$

$$U_{\text{out, O}}(t) = q^*. \quad (7.9)$$

where $q^* = \rho^* v^*$ is the reference steady state flow rate.

PDE backstepping control

The backstepping controller produces a full-state-feedback control law located at the outlet boundary. The control design in Section 3.5 of Chapter 3 is developed for the linearized ARZ PDE model, and then is applied to the original nonlinear ARZ model. For initial conditions near the reference, the system is locally exponentially stable under outlet actuation. The key idea of the backstepping method is to transform the original linearized ARZ model to a target system where the undesirable instabilities in the PDEs are transformed to the outlet boundary. The controller is designed such that the instability is cancelled out and an exponentially stable target system with zero boundary input is obtained for the closed-loop system.

The boundary condition at the inlet, and the full-state-feedback outlet backstepping controller are given by

$$U_{\text{in, BKST}}(t) = q^*, \quad (7.10)$$

$$U_{\text{out, BKST}}(t) = q^* + \rho^* \int_0^L c_v(\xi)(v(\xi, t) - v^*)d\xi + \int_0^L c_q(\xi)(q(\xi, t) - q^*)d\xi, \quad (7.11)$$

where the control gains are given by

$$c_v(\xi) = M(L - \xi) + \frac{\lambda_2}{\lambda_1} K(L, \xi) \exp\left(\frac{\xi}{\tau v^*}\right), \quad (7.12)$$

$$c_q(\xi) = \frac{\lambda_1 - \lambda_2}{\lambda_1} K(L, \xi) \exp\left(\frac{\xi}{\tau v^*}\right) \quad (7.13)$$

for $\xi \in [0, L]$. The control gain kernels $K(L, \xi)$, $M(L - \xi)$ are obtained by solving hyperbolic equations that govern the kernel variables $K(x, \xi)$ in a triangular spatial domain $\mathcal{T} = \{(x, \xi) : 0 \leq \xi \leq x \leq 1\}$. The numerical solution of the kernel equations is easily obtained, given the model parameters and steady states. The equilibrium (ρ^*, v^*) of the linearized system is exponentially stable in the L^2 sense and the equilibrium is reached in a finite time.

P control

The proportional controller is an output-feedback control law that actuates traffic flow rate at the inlet boundary, as discussed in Section 3.4 of Chapter 3. The control input only requires online measurements of velocity at the inlet boundary, collocated with the actuation location. The key intuition of the control design is to cancel the forward coupling in the system and then the closed-loop system can be directly solved. Local exponential stability and finite-time convergence is guaranteed. The boundary condition at the outlet is a constant flow rate and the inlet boundary is actuated by the collocated output-feedback controller,

$$U_{in,L}(t) = q^* + g_P(v(0,t) - v^*), \quad (7.14)$$

$$U_{out,L}(t) = q^*, \quad (7.15)$$

where $g_P = \rho^* + v^*/V'(\rho^*)$ is a constant control gain.

PI control

In the proportional-integral controller, feedback control is applied to both the inlet and outlet boundary values. The PI boundary feedback controllers are proposed in [?] for the linearized ARZ model, which guarantees local exponential stability of the closed-loop system. The exit velocity at the outlet is controlled such that $v(L,t) = U_{out,PI}(t)$. Ramp metering controls the incoming flow rates, given by

$$U_{in,PI}(t) = q^* + k_P^r(\rho(L,t) - \rho^*) + k_I^r \int_0^t (\rho(L,t) - \rho^*) ds, \quad (7.16)$$

$$U_{out,PI}(t) = v^* + k_P^v(v(0,t) - v^*) + k_I^v \int_0^t (v(0,t) - v^*) ds, \quad (7.17)$$

where $k_P^v, k_I^v, k_P^r, k_I^r$ are tuning gains. For this anti-collocated output-feedback structure, a set of linear matrix inequalities are given for allowable control gains that guarantee Lyapunov stability. Within these conditions, the specific values are obtained through trial and error, as detailed in [?]. The Theorem in [?] states that the equilibrium $\rho(x,t) \equiv \rho^*, v(x,t) \equiv v^*$ of the linearized system is exponentially stable in the L^2 sense.

[t!] Feedback boundary stabilization **initial conditions:** $s_0 = \rho(x, 0), v(x, 0)$;

Input: parameters $V(\rho), \tau$, steady state $s^* = (\rho^*, v^*)$

$t = 1 \text{ } N-1$ Compute Lyapunov-based boundary controllers $U_{in,out} = u(s_t, V(\rho), \tau, s^*)$,

where the functional of boundary control u depends on the choice of control design in Table.1

Update the state variables s_{t+1} with actuated boundary control inputs $U_{in,out}$ and s_t

Boundary Control Scheme

All of the aforementioned Lyapunov-based controllers are designed from the linearized ARZ model, and therefore the stabilization guarantees are local. In addition, model uncertainty has not been taken into consideration, such as random events that frequently appear in traffic. This motivates us to explore a RL approach.

7.4 Control of ARZ Model by Reinforcement Learning

In this section, we introduce a reinforcement learning approach for boundary control of the nonlinear ARZ traffic flow model. The explicit knowledge of the PDE model

is not required. RL assumes that the traffic dynamics are governed by a Markov Decision Process (MDP). In particular, we will use a policy gradient method since they are applicable to continuously valued control actions.

[t!] Initialize parameters for actor θ_0 and critic ϕ_0
 $k = 1$ E Initialize the states s_0 from random distribution
 $t = 1$ N Compute reward $r_t = \|s_t - s^*\|_2$;
 Draw an action a_t from stochastic policy, i.e., $a_t \sim \mathcal{N}(\mu(s_t), \sigma^2(s_t))$;
 a_n goes to boundary conditions of PDE system;
 Update state s_{t+1} using a_t and s_t ;
 Collect set of trajectories \mathcal{D} driven by policy π_{θ_k}
 Compute total discounted reward R_t .
 Compute advantage estimates, A_t from critic V_{ϕ_k} .
 Update the actor, θ_{k+1} by (7.37).
 Update the critic, ϕ_{k+1} by regression. RL Control Procedure

Boundary control of PDE as a MDP

In the MDP setting, we seek the policy that maximizes the total reward received from the environment, i.e. the plant. At each time step t the environment conditions are described by a state vector, $s_t \in \mathcal{S}$, where \mathcal{S} is the state space while the control policy picks an action $a_t \in \mathcal{A}$, with \mathcal{A} being the action space. The control policy is a full state feedback control law that selects an action a_t based on an observation of the state s_t . The action is applied to the environment, whose state evolves to $s_{t+1} \in \mathcal{S}$, according to the state-transition probability $\mathcal{P}(s_{t+1}|s_t, a_t)$, and the agent receives a scalar reward $r_{t+1} = r(s_t, a_t)$. The policy is represented by π which maps the state to the action and can be either deterministic or stochastic. The total discounted reward from time t onward can be expressed as:

$$R_t = \sum_{k=0}^{\infty} \gamma^k r(s_{t+k}, a_{t+k}) \quad (7.18)$$

where $\gamma \in [0, 1]$ is the discount factor. Note, we have abused notation by allowing t to represent both continuous and discrete-valued times. Nevertheless, the meaning will be clear from context.

The implementation of the RL controller is summarized in Algorithm 7.3. We represent the state at time t with $s_t = (\rho(\cdot, t), v(\cdot, t))$. When the nonlinear ARZ model is boundary actuated, then it naturally forms a sequential decision making problem, which is modeled as a MDP.

We consider a discretized approximation of the nonlinear ARZ PDE model using the Lax-Wendroff scheme with conservative state variables, as discussed in Section 1.8 in Chapter 1. The discretized ARZ PDE model is a difference equation which numerically approximates the infinite-dimensional PDE model with second-order accuracy in space and time. The solution $\rho(x, t)$ and $v(x, t)$ to the ARZ PDE model

is approximated by piecewise constant functions on discretized temporal and spatial domains. The solution domain is $[0, L] \times [0, T]$. The discretization resolution $\Delta t = T/(N - 1)$ and $\Delta x = L/(M - 1)$ are chosen such that the Courant-Friedrichs-Lewy (CFL) condition is met, i.e. $\Delta t \leq c\Delta x$, where M, N are the number of nodes for the spatial and temporal domains respectively and c is defined as the maximum characteristic speed of the nonlinear hyperbolic ARZ PDE model $\frac{\Delta x}{\Delta t} \geq \max |\lambda_{1,2}|$. We can compactly write the discretized nonlinear ARZ PDE system as the following difference equation

$$s_{t+1} = f(s_t, u_t), \quad (7.19)$$

where s_t describes the density and velocity state at time t , and u_t represents the boundary control inputs, depending on the choice of control design in Table 1. The function f represents the discretized deterministic dynamics for the temporal evolution of the PDE system. The PDE dynamics at the current time instant are fully described given the current state s_t and control inputs u_t .

Given the discretized ARZ PDE in (7.19), we may write the deterministic dynamics as

$$\mathcal{P}(s_{t+1}|s_t, a_t) = \delta(s_{t+1} - f(s_t, u_t)), \quad (7.20)$$

where $\delta(\cdot)$ is the Dirac delta function. In the MDP, $\mathcal{P}(s_{t+1}|s_t, a_t)$ represents the probability that action a in state s at time t will lead to the state at time $t + 1$. Therefore, if there is stochasticity in the dynamics, such as some random model parameters, as introduced later in the chapter, the deterministic temporal evolution of the PDE system can be generalized to stochastic dynamics by the MDP state transition probability.

$$s_{t+1} \sim \mathcal{P}(s_{t+1}|s_t, a_t). \quad (7.21)$$

The discretized states, s_t , and boundary control input, a_t are written as:

$$s_t = [\rho(0, t), \rho(\Delta x, t), \dots, \rho(L, t), \\ v(0, t), v(\Delta x, t), \dots, v(L, t)]^\top, \quad (7.22)$$

$$a_t = [q(0, t), q(L, t)]^\top. \quad (7.23)$$

where $\rho(\cdot, t)$ and $v(\cdot, t)$ are the traffic density and velocity that are discretized in the spatial and temporal domains.

The reward $r(s, a)$ is defined by the L_2 norm of the states, namely,

$$r_t(s_t, a_t) = - \left\| \frac{\sum_i \rho(i \cdot \Delta x, t) - \rho^*}{\rho^*} \right\|_2 - \left\| \frac{\sum_i v(i \cdot \Delta x, t) - v^*}{v^*} \right\|_2. \quad (7.24)$$

The reward is equivalent to the control objective that achieves regulation of the traffic states to a spatially uniform density and velocity.

Value function and Q-function

In the next few paragraphs, we briefly review some essential reinforcement learning concepts to aid the subsequent discussion. A thorough exposition can be found in [?] [?].

The *state value function*, $V^\pi(s_t)$ is the expected total discounted reward starting from state s_t . In the controls community, this is sometimes called the cost-to-go, or reward-to-go. Importantly, note that the value function depends on the control policy. If the agent uses a given policy π to select actions starting from the state s_t , then the corresponding value function is given by:

$$V^\pi(s_t) = \mathbb{E} \left[R_t \mid s_t \right] \quad (7.25)$$

Then, the optimal policy π^* is the policy that corresponds to the maximum value $V^*(s_t)$ of the value function

$$\pi^* = \arg \max_{\pi} V^\pi(s_t) \quad (7.26)$$

The solution of (7.26) is pursued by Dynamic Programming (DP) methods. DP, however, requires knowledge of the model / environment.

The next definition, known as the “Q-function”, is fundamental since it enables the concept of model-free reinforcement learning. Consider the *state-action value function*, $Q^\pi(s_t, a_t)$, which is a function of the state-action pair that returns a real value. In other words, it corresponds to the expected total discounted reward when the action a_t is taken in state s_t , and then the policy π is followed henceforth. Mathematically,

$$Q^\pi(s_t, a_t) = \mathbb{E} \left[R_t \mid s_t, a_t \right] \quad (7.27)$$

The optimal Q-function is given by

$$Q^*(s_t, a_t) = \arg \max_{\pi} Q^\pi(s_t, a_t) \quad (7.28)$$

and represents the expected total discounted reward received by an agent that starts in s_t , picks (possibly non-optimal) action a_t , and then behaves optimally afterwards. Since $V^*(s_t)$ is the maximum expected total discounted reward starting from state s_t , it will also be the maximum of $Q^*(s_t, a_t)$ over all possible actions $a_t \in \mathcal{A}$,

$$V^*(s_t) = \max_{a_t \in \mathcal{A}} Q^*(s_t, a_t) \quad (7.29)$$

If the optimal Q-function is known, then the optimal action a_t^* can be extracted by choosing the action a_t that maximizes $Q^*(s_t, a_t)$ for state s_t (i.e. the optimal policy π^* is retrieved),

$$a_t^* = \arg \max_{a_t \in \mathcal{A}} Q^*(s_t, a_t) \quad (7.30)$$

without requiring knowledge of the environment dynamics. This last point is precisely why the Q-function enables model-free RL.

Lastly, the advantage function is defined to measure how advantageous the action is compared to the action drawn from policy,

$$A^\pi(s_t, a_t) = Q^\pi(s_t, a_t) - V^\pi(s_t) \quad (7.31)$$

Actor-Critic

Actor-critic is an approximate dynamic programming (ADP) method which solves dynamic programming heuristically. Importantly, the actor-critic approach allows for continuous state/action spaces by using a function approximator, e.g., a neural network. In RL, as well as in dynamic programming, the action is taken by a *policy* to maximize the expected total discounted reward. By following a given policy and processing the rewards, one should estimate the expected return given states from the *value function*. In the actor-critic approach, the *actor* improves the policy based on the value function that is estimated by the *critic*. We specifically focus on the policy gradient-based actor-critic algorithm in this work, and, in particular, the Proximal Policy Optimization (PPO) [?] is considered. The critic is the parameterized value function V_ϕ and the actor is the parameterized policy π_θ .

Critic

The role of the critic is to evaluate the current policy prescribed by the actor. The action is drawn from a Gaussian distribution, namely,

$$a_t \sim \mathcal{N}(\mu, \sigma^2), \quad \text{where} \quad [\mu, \sigma] = f_{\text{DNN}}(s_t; \theta), \quad (7.32)$$

where a mean μ and standard deviation σ computed from a deep neural network (DNN), $f_{\text{DNN}}(s_t; \theta) : \mathcal{S} \rightarrow \mathbb{R}^2$, and the DNN is parameterized by weight vector θ . After applying the action, we observe the reward r_{t+1} and the next state s_{t+1} . For each time step t , the tuple $(s_t, a_t, r_{t+1}, s_{t+1})$ is stored in the buffer, \mathcal{D} . From a collected set of trajectories, the parameterized value function denoted by V_ϕ is updated to minimize the following loss function, \mathcal{L} :

$$\mathcal{L} = \frac{1}{N} \sum_{i \in \mathcal{D}} \sum_{t=0}^N (V_\phi(s_{i,t}) - R_{i,t})^2 \quad (7.33)$$

where $R_{i,t}$ is the total discounted reward at time t in the i -th trajectory stored in the buffer. The critic network parameters, ϕ , are updated numerically via gradient descent.

Actor

The actor is updated based on the value function estimates. The objective function for the actor is formulated in terms of the expected reward of policy π_θ and the advantage of $\pi_{\theta_{\text{old}}}$ [?, ?]:

$$\max_{\theta} \quad \hat{\mathbb{E}}_t \left[\frac{\pi_\theta(a_t|s_t)}{\pi_{\theta_{\text{old}}}(a_t|s_t)} \hat{A}_t \right] \quad (7.34)$$

where the hats on $\hat{\mathbb{E}}_t$ signify a sample mean, and \hat{A}_t indicates an estimated advantage function obtained from the critic. In [?], the authors prove the expected reward corresponding to π_θ increases relative to $\pi_{\theta_{\text{old}}}$, if a distance measure between π_θ and $\pi_{\theta_{\text{old}}}$ is sufficiently bounded. This motivates the following trust region policy optimization algorithm:

$$\max_{\theta} \quad \hat{\mathbb{E}}_t \left[\frac{\pi_\theta(a_t|s_t)}{\pi_{\theta_{\text{old}}}(a_t|s_t)} \hat{A}_t \right] \quad (7.35)$$

$$\text{subject to} \quad \hat{\mathbb{E}}_t \left[\text{KL}[\pi_{\theta_{\text{old}}}(\cdot|s_t), \pi_\theta(\cdot|s_t)] \right] \leq \delta, \quad (7.36)$$

where θ_{old} is the vector of policy parameters before the update. KL-divergence measures the difference between the old policy and current policy. The constraint ensures that the new policy does not deviate from the old policy by δ .

In this work, we adopt the PPO reinforcement learning algorithm [?], which is based on trust region policy optimization (TRPO) [?]. The PPO algorithm similarly limits the new policy from being excessively far from the previous one. However, it does so with a modified objective that penalizes changes to the policy that move $r_t(\theta) = \pi_\theta(a_t|s_t)/\pi_{\theta_{\text{old}}}(a_t|s_t)$ away from 1. The key idea is to use probability clipping, as follows:

$$\max_{\theta} \quad \hat{\mathbb{E}}_t \left[\min(r_t(\theta)\hat{A}_t, \text{clip}(r_t(\theta), 1 - \varepsilon, 1 + \varepsilon)\hat{A}_t) \right]. \quad (7.37)$$

The main idea of PPO is to modify the objective by clipping the probability ratio. This removes the incentive for moving r_t outside of the interval $[1 - \varepsilon, 1 + \varepsilon]$. With this clipping method, the lower bound of objective function is maximized. Readers are referred to [?] for more details.

Proximal Policy Optimization

We adopt a policy gradient-based approach to obtain a continuous-valued stochastic control policy. Mathematically, the goal is to find:

$$\theta^* = \arg \max_{\theta} \mathbb{E} [\mathcal{R}_t] \quad (7.38)$$

where the expectation is taken w.r.t. $\mathcal{P}(s_{t+1}|s_t, a_t)$ and $\pi_\theta(a_t|s_t)$, and θ parameterizes the control policy distribution. Policy gradient methods essentially solve (7.38) via gradient ascent. The key challenge is estimating the gradient since it is computationally intractable to compute it exactly.

One can re-formulate this optimization problem (7.38) in terms of the expected reward of policy π_θ and the advantage of $\pi_{\theta_{\text{old}}}$ [?, ?]:

$$\max_{\theta} \quad \hat{\mathbb{E}}_t \left[\frac{\pi_\theta(a_t|s_t)}{\pi_{\theta_{\text{old}}}(a_t|s_t)} \hat{A}_t \right] \quad (7.39)$$

where the hats on $\hat{\mathbb{E}}_t$ signify a sample mean, and \hat{A}_t indicates an estimated advantage function from simulations. In [?], the authors prove the expected reward corresponding to π_θ increases relative to $\pi_{\theta_{\text{old}}}$, if a distance measure between π_θ and $\pi_{\theta_{\text{old}}}$ is sufficiently bounded. This motivates the following trust region policy optimization algorithm:

$$\max_{\theta} \quad \hat{\mathbb{E}}_t \left[\frac{\pi_\theta(a_t|s_t)}{\pi_{\theta_{\text{old}}}(a_t|s_t)} \hat{A}_t \right] \quad (7.40)$$

$$\text{subject to} \quad \hat{\mathbb{E}}_t \left[\text{KL}[\pi_{\theta_{\text{old}}}(\cdot|s_t), \pi_\theta(\cdot|s_t)] \right] \leq \delta, \quad (7.41)$$

where θ_{old} is the vector of policy parameters before the update. KL-divergence measures the difference between the old policy and current policy. The constraint ensures that the new policy does not deviate from the old policy by δ .

Both the RL and Lyapunov-based approaches provide state-feedback controllers for the ARZ PDE model. Figure 7.2 compares the RL and Lyapunov-based approaches as signal flow diagrams. The Expert Design system developed by a Control Engineer is replaced with an iterative learning process by a RL algorithm. In addition, the prior assumption of the initial condition and model parameters are not required in the RL approach. In the next section, we will conduct several numerical simulations to compare these two methodologies.

7.5 Comparative Simulation Study

In this section, we numerically test the RL controller and compare its performance with that of the Lyapunov-based controllers. Two settings are considered: (i) full knowledge of the system dynamics, and (ii) partial knowledge of the system. In the full knowledge setting, both the Lyapunov-based and model-free RL controllers have perfect knowledge of the model with known model parameters and steady state conditions. For the partial knowledge setting, both controllers have partial knowledge of the model, i.e., the true steady state has deviated from the ones used in the model. For each setting, we test the model-free RL controller with the following cases: (i) outlet control, (ii) inlet control, and (iii) outlet & inlet control, as defined in

(7.6), (7.7). For each case, one Lyapunov-based controller is used to evaluate the performance of the RL controller.

Simulation configuration

We simulate traffic on a freeway segment with length $L = 500$ m for a time period $T = 240$ s = 4 min for system with full knowledge of dynamics and 8 min for system with partial knowledge. Steady states density $\rho^* = 120$ veh/km, $v^* = 36$ km/h are chosen given the maximum density $\rho_m = 160$ veh/km, and maximum velocity $v_m = 40$ m/s. The steady state traffic is lightly congested such that $\lambda_1 = 10$ m/s, $\lambda_2 = -20$ m/s, which satisfy the conditions in (7.2), (7.3). This configuration represents heterogeneous propagation of oscillatory waves of density and velocity in congested traffic. The 500 m long road segment is considered and the simulation is run for 4 min. The spatial grid size is chosen as $\Delta x = 10$ m and the temporal grid size is chosen as $\Delta t = 0.25$ s. The discretization in spatial-temporal domain guarantees the convergence of the numerical scheme. Besides, the computational time for training a RL controller increases with the number of grid size but the closed-loop performance is not affected significantly for the order of discretization we choose. The following simulations are performed on a Python running an Intel core i9-9900K CPU with a clock rate of 3.60 GHz, and GPU device, GeForce RTX 2080 Ti.

Comparative study with full knowledge of system dynamics

We assume sinusoidal initial conditions:

$$\rho(x, 0) = 0.1 \sin\left(\frac{3\pi x}{L}\right) \rho^* + \rho^*, \quad (7.42)$$

$$v(x, 0) = -0.1 \sin\left(\frac{3\pi x}{L}\right) v^* + v^*. \quad (7.43)$$

Learning process of RL controllers

The learning process for RL controllers is illustrated in Fig. 7.3 and Fig. 7.4. The learning curve for RL corresponding to each control scheme is presented in Fig. 7.3. The evolution of the cumulative reward R_t , defined in (7.18), reflects the overall learning performance. In addition, several episodes of the simulation in the learning process are compared more closely in Fig. 7.4. We plot the reward values r_t , defined in (7.24), over several hundreds of iterations of testing candidate RL outlet feedback laws on ARZ model simulations over a time window of 4 minutes for each simulation.

In Fig. 7.3, the shaded area represents min/max of different actor-critic parameterizations while the bold line measures the average of the performance during training. Notice that the training process converges over different numbers of episodes across the controllers. This motivates us to set a large enough number of episodes in order to make sure that RL converges. We obtain the actor-critic parameters by the end of training. It is also observed that there is a spike in cumulative reward for the inlet and outlet RL controller at the episode around 500 which indicates that the closed-loop system at the iteration becomes unstable and states diverge. For example, if density state is greater than the maximum density, there will be collision in the ARZ model. Therefore, this training process cannot perform in a collision free fashion in real traffic.

In Fig. 7.4, we choose the outlet control case to illustrate the RL learning process. We plot the reward evolution for the closed-loop system with RL outlet controllers that are obtained from training episodes 1, 100, 200, 400 and 800 respectively. In addition, the reward of the setpoint control is also plotted as a baseline comparison. It turns out that the initial reward is worse than the baseline performance. After 100 iterations of training, the outlet RL controller plotted with dotted blue line performs even worse with reward decreasing with time and the lowest cumulative reward $R = -615.5$. However, the RL performance improves after the iteration number increases from 200 to 400 and reaches its best at episode 800. As demonstrated in this figure, the learning process does not guarantee a monotonically improving performance. Certain episodes can be even worse than the baseline case due to some iterations of unsuccessful training.

State evolution, reward and control inputs

In Figs. 7.5–7.16, the initial condition is highlighted in blue. The actuated inlet and/or outlet boundaries are highlighted in red. In other words, the red curves visualize the control inputs for the setpoint control, backstepping control, P control, PI control and the RL controllers in each case. Specifically, the closed loop results are compared between the outlet backstepping controller and the outlet RL controller, as shown in Figures 7.7–7.10, between inlet P controller and inlet RL controller as shown in Figures 7.11–7.14, between inlet and outlet PI controller and inlet and outlet RL controller as shown in Figures 10.9–7.18.

Figure 7.5 plots the evolution of density and velocity under setpoint control. The setpoint control is open-loop that does not use feedback of the system. We observe the persisting oscillations, although they appear lightly damped. We regard the setpoint control as a baseline case against which the subsequent feedback control designs should outperform. In setpoint control, the outlet and inlet boundary flow rates are controlled to be constant (7.8), (7.9). As highlighted with red in 7.5, the product of density and velocity values is constant at inlet and outlet boundary whereas the boundary states of density and velocity oscillate over time.

Figures 7.7–7.10 present the closed-loop result of the outlet backstepping controller and outlet RL controller. In Figures 7.7 and 7.8, the states are stabilized to

Table 7.2 Closed-loop results comparison

	Lyapunov-based			RL		
Stability	outlet	inlet	outlet&inlet	outlet	inlet	outlet&inlet
S_T	79.5	84	140	121	204	139
S_E	7.9	10.5	12.6	5.5	9.4	9.5

spatially uniform steady state values by the outlet backstepping controller and outlet RL controller, respectively. An interesting finding from comparing between the two controllers is that RL learns a policy which produces a control input (red line in Fig. 7.8) that closely replicates the backstepping control input (red line in Fig. 7.7). The RL policy is developed without explicit knowledge of the differential equations and parameters. It is trained iteratively on the nonlinear simulation model. As a state-feedback controller, the RL policy produces an action for boundary input given the current state. In contrast, the PDE backstepping state-feedback control law is obtained by rigorous theoretical control design assuming perfect knowledge of the model.

As shown in Fig. 7.10, both methods yield similar control input trajectories. However, RL underperforms relative to backstepping in terms of the instantaneous reward over time. The convergence of the L^2 spatial norm represents the stabilization of the closed-loop system. Unlike the finite-time convergence for the backstepping controller shown with red line, the RL controller's reward in blue takes a longer time for convergence, about 3 min. The cumulative reward for the RL outlet controller is $R = -104.9$ while the cumulative reward of backstepping is $R = -81.7$.

In the same fashion, we compare closed-loop results for inlet P controller and inlet RL controller in Fig. 7.11–7.14. The incoming flow rate is actuated either with the P controller or RL controller. The control inputs at the inlet are highlighted with red in Fig. 7.11 and Fig. 7.12. As shown in the Fig. 7.14, the inlet RL controller needs more than 4 min to converge, longer than the P control. Although the inlet RL controller almost recovers the performance of the inlet P controller, we can see from Fig. 7.13 that the RL control input is quite different than the P control input, requiring longer convergence time and is oscillated.

Figure 7.15–7.18 describe the closed-loop results for PI controller and RL controller, actuating the incoming and outgoing flow rates. We observe that the RL controller achieves a better reward evolution in Fig. 7.17. The convergence of the closed-loop system with RL is faster than that of the PI controller, and with a slightly smaller cumulative reward. It could also be noted that control efforts are smaller for the RL controller in terms of magnitude, as shown in Fig. 7.17. These results will vary, however, with the PI controller gain selection.

The comparison of closed-loop results between the Lyapunov-based and RL approaches is summarized in the Table. 7.2. The stabilization result is mainly evaluated by convergence time S_T and control effort S_E . The convergence time is defined as the time instance such that the instant reward converges to zero $r_{t=S_T} = 0$. We mainly focus on the control efforts that varies around the nominal values q^* . Therefore, the control effort is defined as $S_E = \int_0^{S_T} |U_{\text{in,out}}(t) - q^*| dt$.

Table 7.3 Performance improvement

	Lyapunov-based/baseline			RL/baseline		
Percent	outlet	inlet	outlet&inlet	outlet	inlet	outlet&inlet
J_{TTT}	1.6%	1.5%	1.5%	1.4%	1.6%	1.4%
J_{fuel}	3.4%	2.5%	3.3%	3.9%	3.6%	4.0%
$J_{comfort}$	30.6%	37.3%	30.1%	48.3%	47.8%	47.9%

Figure 7.19 includes all the closed-loop results with the Lyapunov-based controllers and their corresponding RL controllers. All of the Lyapunov-based feedback controllers and RL controllers outperform the setpoint controllers. The RL agent achieves sub-optimal performance compared to Lyapunov-based approaches. In addition, backstepping outperforms the P and PI controllers for stabilization of the traffic flow. RL controllers almost recover the closed-loop results of the Lyapunov-based design in the outlet control or inlet control cases. RL outperforms the PI controllers when both the inlet and outlet boundaries are controlled. The aforementioned results are uncertain model parameters, which we will discuss in the next subsection. Note that the reward in (7.24) is defined as the L^2 spatial norm of the state values without considering control effort. The RL controllers were design for comparison with the stabilizing Lyapunov-based controllers, and thus control effort was not penalized. However, RL controllers can be trained to consider control effort by modifying (7.24) with a control effort penalty.

Other performance measures

Common traffic performance indices include total travel time (TTT), fuel consumption, and travel comfort. These indices are calculated for the closed-loop system with either the Lyapunov-based controllers or the RL controllers. The performance indices are given by

$$J_{TTT} = \int_0^T \int_0^L \rho(x, t) dx dt, \quad (7.44)$$

$$J_{fuel} = \int_0^T \int_0^L \max\{0, b_0 + b_1 v(x, t) + b_3 v(x, t) + b_4 v(x, t) a(x, t)\} \rho(x, t) dx dt, \quad (7.45)$$

$$J_{comfort} = \int_0^T \int_0^L (a(x, t)^2 + a_t(x, t)^2) \rho(x, t) dx dt \quad (7.46)$$

where $a(x, t)$ is defined as the local acceleration

As shown in Table. 7.3, the performance indices of each controller are compared with their improvement percentage over the baseline setpoint controller. Among the three performance indices, drivers' comfort is the most significantly improved for all Lyapunov-based and RL controls, since the stop-and-go oscillations are suppressed

in the closed-loop system. For fuel consumption of total traffic, RL actually performs better than its corresponding Lyapunov-based controller. This may be coincidental, or could be related to RL's control effort and the induced acceleration. In any case, RL provides the flexibility to define the reward as fuel consumption, which can be directly optimized. Backstepping does not provide this capability. We also see that total travel time is only marginally improved, since the traffic dynamics are stabilized to steady state and the average speed remains relatively similar.

Comparison study with partial knowledge of system

In the previous comparative study, we assume a perfect knowledge of the traffic system for the Lyapunov-based controllers. In practice, model parameters are obtained by calibrating the nonlinear ARZ PDE model with field data obtained from loop detectors measuring the traffic flow rate or by high-speed cameras recording vehicle trajectories. The model calibration process can be laborious. More importantly, it is hard to determine some model parameters such as the steady state density, fundamental diagram and relaxation time. These macroscopic models are just that – model idealizations of reality. In Chapter 5, see also [?], an adaptive output-feedback controller is designed to stabilize the linearized ARZ model with a gradient-based estimator for unknown relaxation time. The adaptive stabilization problem has not been studied when the steady state is uncertain. In traffic field data, it is observed that a certain steady state density in the congested regime possesses a significant spread of flow rates. Therefore, it is hard to accurately determine the steady state for a real world traffic system that is often periodically evolving, as exhibited in freeway traffic data [?]. On the other hand, the steady states in the reward function encode our belief in the current averaged and aggregated traffic condition which could deviate from reality. Moreover, there are measurement errors in raw data. The data needs to be pre-processed leading to more approximation and processing errors. In [?] and [?], the ARZ model was calibrated with the Next Generation Simulation (NGSIM) traffic data which records the trajectories of vehicles on a 500 m freeway segment over a 45 min rush-hour period. Data reconstruction is conducted to obtain the aggregated state values. All in all, the Lyapunov-based control approaches cannot overcome the limitation of model uncertainty when they are implemented in practice. In other words, their performance is limited by the best prediction the PDE model can make.

Therefore, it is of practical relevance to evaluate the closed-loop performance of the Lyapunov-based and RL controllers given partial or inaccurate models. Here we investigate the performance of the Lyapunov-based controllers that employ incorrect steady state density, and then compare with RL controllers obtained from a stochastic training process.

We choose two representative scenarios characterized by the steady state density. We define ρ_r as the real steady state density while $\rho^* = 120$ veh/km is assumed by the Lyapunov-based feedback controllers. We consider $\rho_r = 115$ veh/km for the outlet backstepping control case, representing that the actual traffic is lighter than

the parameters used by the PDE backstepping controller. In the second scenario, we consider $\rho_r = 125$ veh/km for the inlet control such that the actual traffic is denser than the value employed by the P controller. For both scenarios, RL controllers are trained in a stochastic environment where a steady state density value of the traffic system ρ^* is randomly chosen from a uniform distribution of the integer values $\{115, 120, 125\}$ in each episode. Then the RL controllers are validated for each specific scenario.

The RL learning curve is plotted in Fig. 7.20. Note that the steady state density used to calculate the cumulative reward is randomly chosen at each episode, which affects the initial condition and the associated steady state velocity in (7.1) during training. The shaded area represents min/max of different actor-critic parameterizations, while the bold line measures the average performance. Similar to Fig. 7.19, it should be noted that the performance of RL controllers do not monotonically improve in the learning process as the number of training episodes increases. Additionally, cumulative reward convergence for some initiations of the actor-critic parameters is not guaranteed.

We observe that the RL controllers are more adaptable to the stochastic environment. Figure 7.21 shows all the closed-loop controller results in Scenario 1 where the Lyapunov-based controllers assume a greater steady state density value than the actual traffic environment. It is interesting to find out that all of the RL controllers in blue outperform the setpoint control in green, with larger reward values. Among them, the inlet RL controller ultimately performs the best. In addition, all the Lyapunov-based feedback controllers in red have smaller rewards, indicating the traffic states do not converge to the actual steady state value after applying the controllers. Assuming an incorrect steady state density value deteriorates the closed-loop stabilization results. The backstepping outlet controller, which performs the best in a system with perfect knowledge from Section. 7.5, turns out to be the worst controller in terms of cumulative reward in Scenario 1, as depicted in Fig. 7.21. This observation demonstrates that Lyapunov-based control is sensitive to full knowledge of the system dynamics, and even perturbing the steady state values can result in worse performance than a baseline control method.

Scenario 1 of lighter in-domain traffic

As shown in Fig. 7.22, we apply the outlet backstepping controller to a nonlinear ARZ model with lighter steady-state traffic density, $\rho_r = 115$ veh/km than the controller assumes, i.e. $\rho_r < \rho^*$. The closed-loop simulation is run for 8 min, since the stabilization requires a longer time. When we apply the PDE backstepping controller in (7.11), which is constructed using $\rho^* = 120$ veh/km, the traffic is actually slowed down, leading to a reduction of velocity and an increase of density in Fig. 7.22. The closed-loop traffic is more congested, due to the controller's incorrect model assumptions. In contrast, since the RL controller is trained in an environment with stochastic conditions, where some episodes use a lighter traffic scenario, it successfully stabilizes the traffic state to a uniform value. We find out in Fig. 7.23

that the closed-loop system with the RL outlet controller converges close to the actual steady state. This leads to a larger cumulative reward $R = -534.3$ for RL than the backstepping controller $R = -3093.3$ in Fig. 7.24. Comparing the backstepping control input and RL outlet control input in Fig. 7.25, we find out that backstepping applies less control effort than RL. Backstepping's discharging flow rate is less than the actual steady state flow rate in the segment, thus unnecessarily holding vehicles back from leaving the segment and thus exacerbating traffic congestion. As shown in Fig. 7.22, traffic congestion forms and propagates backwards to the segment inlet, whereas there is no such congestion in Fig. 7.23.

Scenario 2 of denser in-domain traffic

In Fig. 7.26, we apply the inlet P controller to a nonlinear ARZ model with denser traffic $\rho_r = 125$ veh/km than the controller assumes, i.e. $\rho_r > \rho^*$. The inlet controller in (7.14) assumes $\rho^* = 120$ veh/km to design the control gain. As a result, the P controller applies a larger incoming traffic flow rate than it should, since it receives the feedback of slower velocity than the incorrect reference value. This creates congestion in the downstream traffic. As shown at the inlet of the Fig. 7.26, the traffic density increases while velocity reduces. In contrast, the RL controller trained from the stochastic environment alleviates this situation in Fig. 7.28, and also exhibits an improved cumulative reward. However, the RL controller cannot stabilize the system to the true steady state ρ_r , as shown by the blue reward initially increasing and then decreasing. Figure 7.29 describes the evolution of the P and RL inlet control inputs. The incoming flow rate is eventually regulated by the inlet controllers to the real steady state value, at the inlet. However, neither the RL controller nor the P controller successfully stabilizes the states to their true steady state values across the segment, as highlighted in red Fig. 7.26 and Fig. 7.28. This is also demonstrated by the reward evolution in Fig. 7.28. However, the RL controller does not diverge as quickly, and in this sense is more robust.

In both scenarios, the performance of the Lyapunov-based controllers deteriorates with small errors to the assumed steady state conditions. Comparing the state and reward evolution with outlet control and perfect system knowledge in Fig. 7.7, 7.9 and Fig. 7.22, 7.24 in Scenario 1, with the same comparison between Fig. 7.11, 7.13 and Fig. 7.26, 7.28 in Scenario 2, the Lyapunov-based control systems do not converge to the actual steady states and the corresponding rewards do not converge to 0. On the other hand, the RL controllers trained in a stochastic environment perform worse in the deterministic setting, but are more robust to steady state errors compared to the Lyapunov-based controllers, as shown in Fig. 7.24 for Scenario 1 and in Fig. 7.28. It should also be noted in Fig. 7.27 and Fig. 7.28 that RL controllers do not guarantee convergence of the closed-loop system, despite some improvements of the reward.

Simulation results show that RL controllers achieve comparable performance with the Lyapunov-based controllers in a traffic system with perfect knowledge of model parameters, with slightly longer convergence times. The analysis becomes more interesting when we consider the reality of model uncertainty and imperfect

knowledge. Specifically, the RL controllers outperform the Lyapunov-based controllers when the assumed steady-state conditions contain errors. Importantly, we find the Lyapunov-based controller loses its stabilizing properties, whereas the RL controllers obtained from a stochastic training process maintain stability or at least slow down divergence. Nevertheless, the RL controllers are obtained from thousands of iterative training episodes, and reward convergence is not guaranteed. For practical considerations, RL controllers should be developed in a simulation environment where trial and error are allowed.

7.6 Notes and References

In this chapter, we have address the freeway traffic control problem within a reinforcement learning paradigm. We are motivated by two challenges currently unaddressed in the literature: (i) Controllers natively designed for nonlinear macroscopic traffic dynamics do not exist, and existing stabilization results are local and derived with linearized systems; (ii) Model-based controllers depend on accurate models.

We have formulated a state regulation control problem for the ARZ PDE model via boundary control and then developed a RL control approach based on the PPO algorithm, which falls within the class of policy gradient methods. PPO ultimately yields a state-feedback boundary controller from iterative interactions with a simulation environment, as opposed to direct synthesis from a mathematical model. The performance of the RL controller is compared with a PDE backstepping controller, a P controller, and PI controllers.

Comparative assessment of RL and backstepping

RL controllers nearly recover the stabilization performance of the Lyapunov-based PDE control approaches for a system with perfect knowledge of the model. In a system with partial knowledge where the steady state traffic is lighter or denser than what we assumed in constructing Lyapunov-based controllers, the RL controller obtained from a stochastic training process outperforms the Lyapunov-based controllers.

However, any apparent advantage of the RL approach, except for the fact that it is expertise-free, is questionable:

- The RL controllers are obtained by conducting about one thousand training episodes on a simulation model. Collision-free training is not possible in real life traffic, nor is the iterative training guaranteed to converge. Although RL demonstrates learning (i.e. adaptation) potential under uncertain and changing conditions, it is neither simple nor a fully safe substitute for model-based control in real traffic systems. For real world implementation, it is an active research area to develop safe RL strategies with some safety constraints guaranteed. Readers are referred to a more exhaustive review on this topic [?], and constrained policy optimization approach [?].

- In the “partial knowledge” scenario, the RL control is given an unfair advantage of being trained. In a real traffic application, the ARZ model, calibrated on one data set, would have to be recalibrated to accommodate parameter shifts due to changes in weather, evolving commute patterns, discrete events, and other big uncertainties. This poses a major challenge for the RL method because the controller’s re-training would require first a recalibration of the ARZ model, with the new data. No such challenges are faced by the adaptive backstepping controllers in Chapter 5 which perform online estimation and controller adjustment.

RL versus Extremum Seeking

Extremum Seeking (ES), a real-time adaptive optimization technique, is an alternative to RL for tuning controller gains in a model-free fashion. The algorithms in [?] [?] [?] can be applied for offline learning of feedback laws based on simulation models, as with RL and the ARZ model in this chapter. There even exists an ES algorithm [?] which is designed for online tuning of feedback laws and is equipped with online convergence guarantees. In ES, a small excitation is used to perturb the feedback gains being tuned and to produce estimates of the gradient of a cost function. Convergence to a neighborhood of the optimal gain values is proved by means of averaging analysis and singular perturbation theory. While performing the same task of learning a reward-maximizing feedback law, RL techniques do not possess convergence guarantees. In contrast, guaranteed convergence is the hallmark of controller training by Extremum Seeking.

The traffic control community would be well advised to give the ES training techniques at least the same amount attention as is given to the heuristic techniques traditionally used in the training of RL controllers. ES has been used with experimental success, and even as a technological game changer, in a number of applications that mathematically resemble, and are even physically analogous to traffic: charged particle accelerators, lasers in chip manufacturing, elongated combustion chambers with thermoacoustic instabilities, and other applications.

In fact, the reader need not go far to get acquainted with the power and advantages of Extremum Seeking. In Chapter 14, maximization of a reward in the form of outflow through a bottleneck is accomplished using ES. Moreover, this is accomplished without offline training and with a guarantee of online convergence.

Possible advances with RL

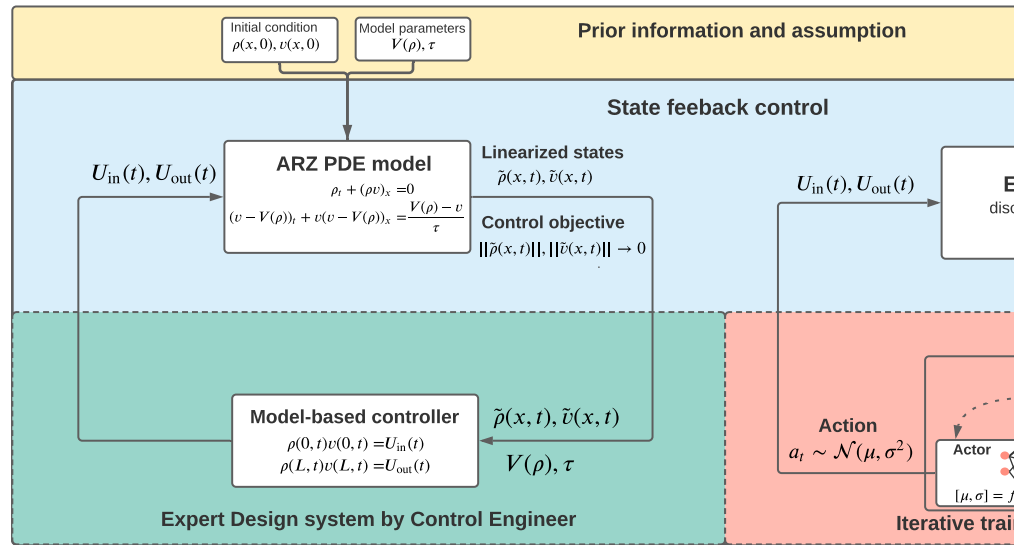
The traffic performance on ramp, such as total waiting time, can be incorporated into the reward function and the evaluation of the mainline traffic under RL control.

It is worth exploring the incorporation of elements of Lyapunov-based designs, which provide stability guarantees, in order to endow the RL controllers with faster learning rates and more robust performance.

Code availability

All the data and experiment codes are made available online. <https://github.com/sachong/RL-ARZ-PPO>.

Fig. 7.2 State-feedback control loop of ARZ PDE Lyapunov-based control scheme and model-free RL boundary control scheme



addcode=control=90,center

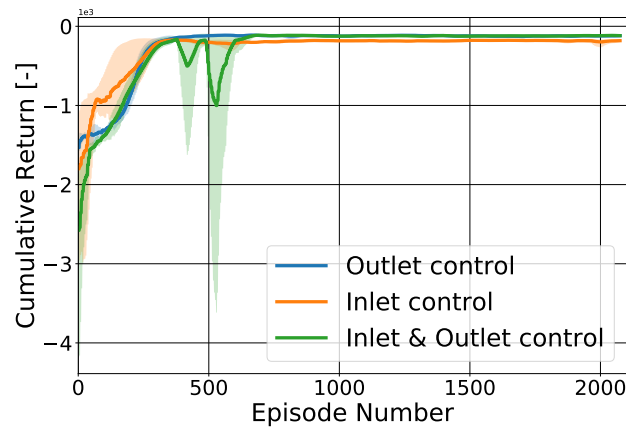


Fig. 7.3 The learning curve of RL controllers with different initializations of the actor-critic network.

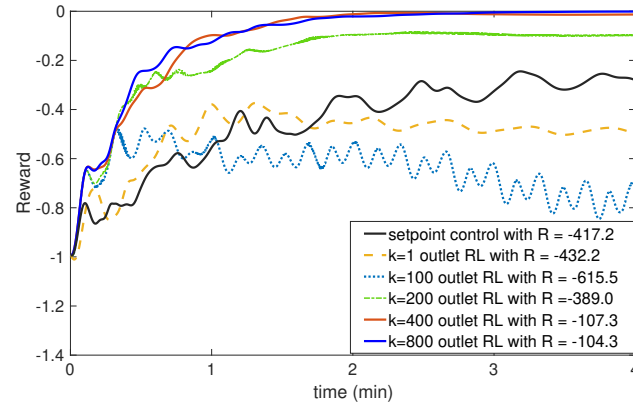


Fig. 7.4 The reward evolution for the closed-loop system with outlet RL controller that is obtained for different episode numbers k .

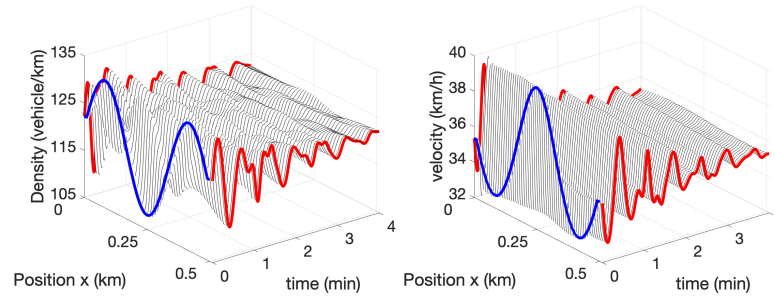


Fig. 7.5 Density and velocity evolution in space and time with setpoint inputs.

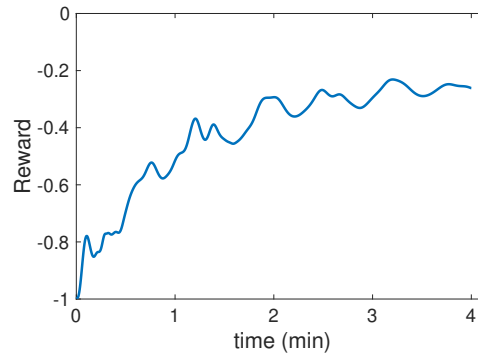


Fig. 7.6 Reward evolution for setpoint control

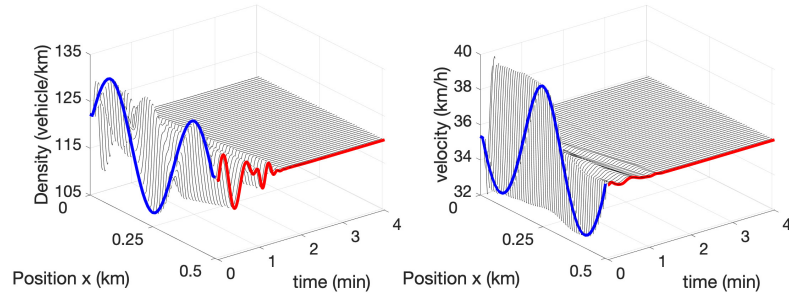


Fig. 7.7 Density and velocity evolution in space and time with **outlet backstepping controller**

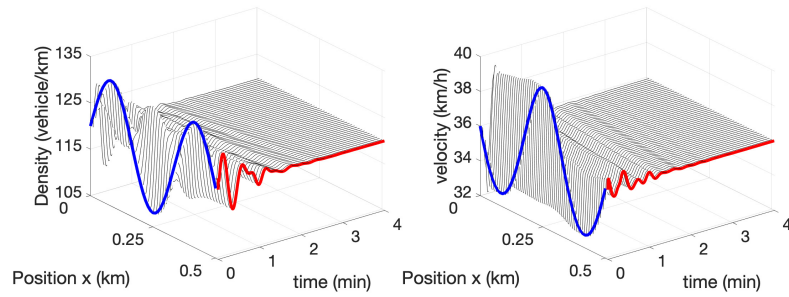


Fig. 7.8 Density and velocity evolution in space and time with **outlet RL controller**

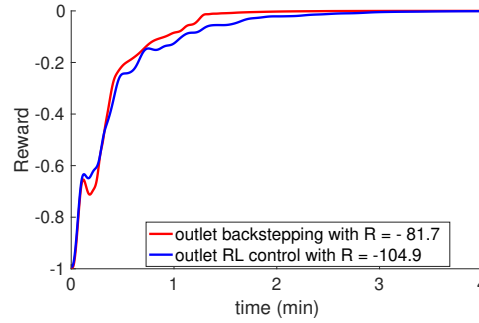


Fig. 7.9 Reward evolution for closed-loop with backstepping and RL controller at outlet

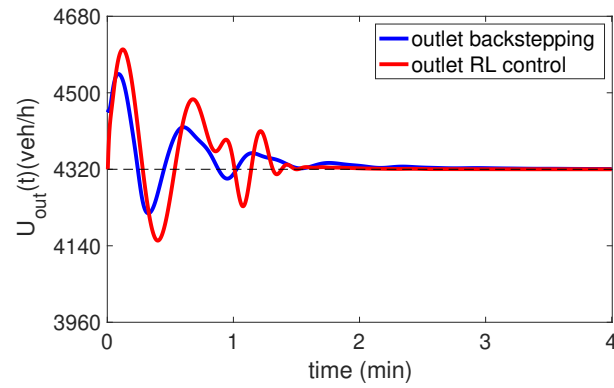


Fig. 7.10 Backstepping and RL control inputs at outlet

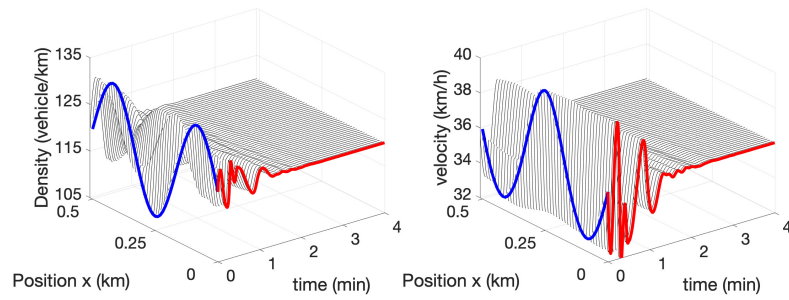


Fig. 7.11 Density and velocity evolution in space and time **inlet P controller**

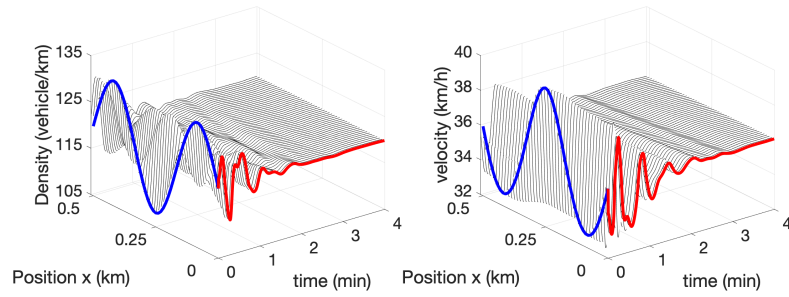


Fig. 7.12 Density and velocity evolution in space and time **inlet RL controller**

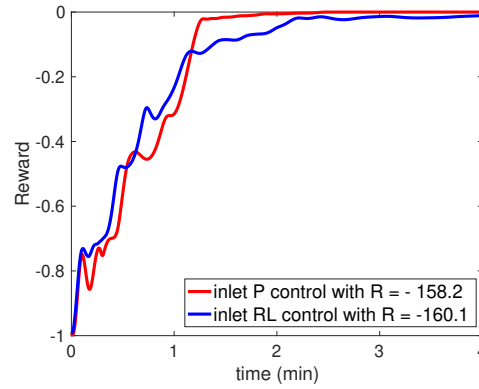


Fig. 7.13 Reward evolution for closed-loop with P and RL controller at inlet.

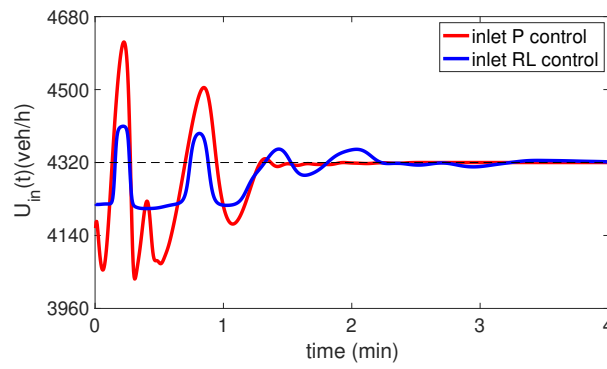


Fig. 7.14 P and RL control inputs at inlet.

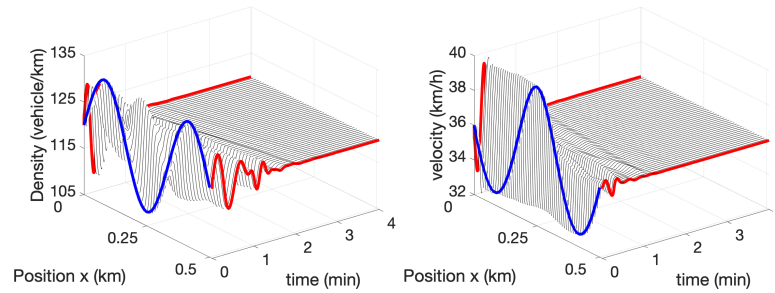


Fig. 7.15 Density and velocity evolution in space and time with **PI controllers** at inlet and outlet

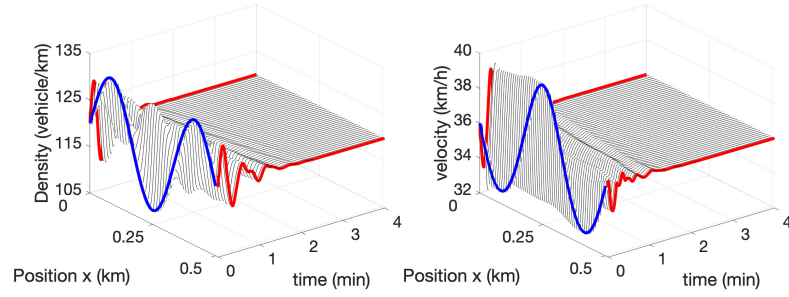


Fig. 7.16 Density and velocity evolution in space and time with **RL controllers** at inlet and outlet

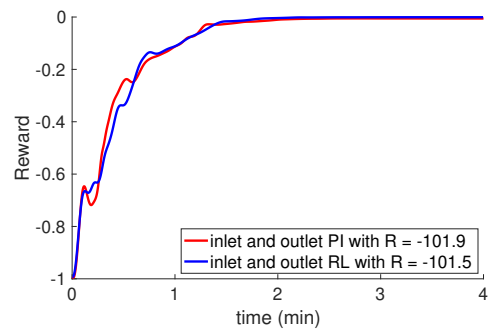


Fig. 7.17 Reward evolution for closed-loop with PI and RL controller at inlet and outlet

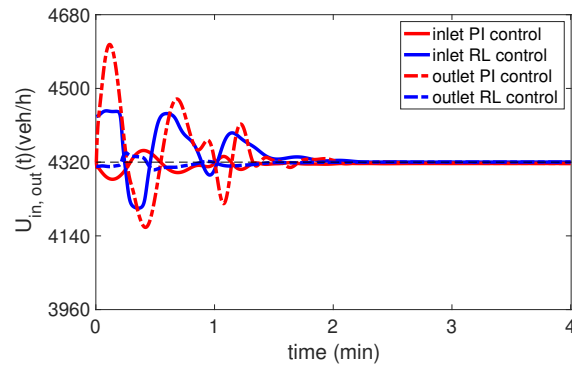


Fig. 7.18 Inlet and outlet PI and RL control inputs

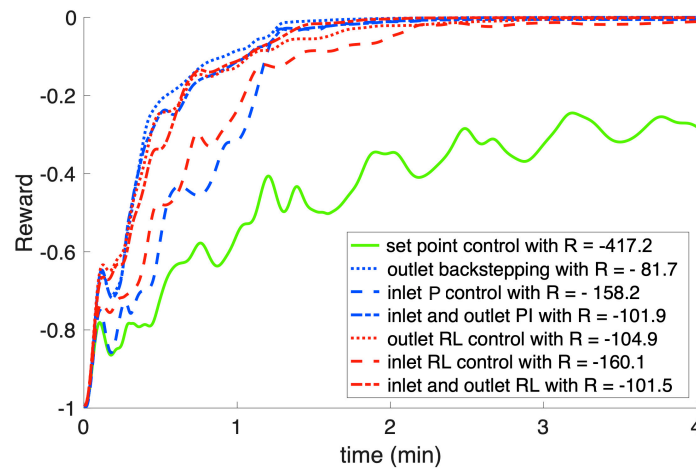


Fig. 7.19 The reward evolution of the Lyapunov-based approaches (blue), the corresponding RL controllers after 2000 episodes of iterative training (red).

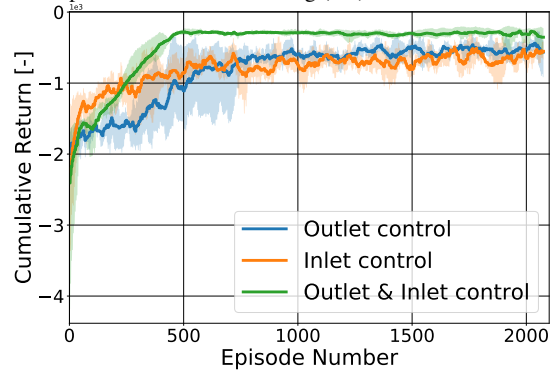


Fig. 7.20 RL learning curve with different initializations of actor-critic network, for randomly generated steady-state values.

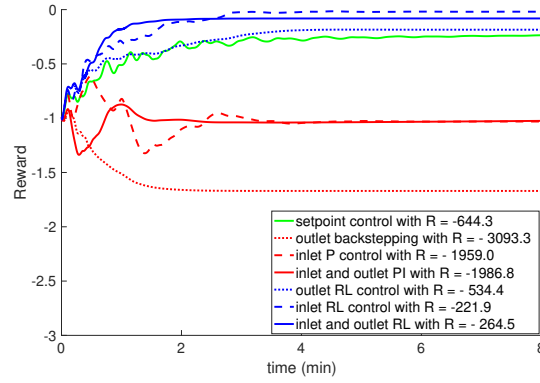


Fig. 7.21 In the system with partial knowledge, the reward evolution of the Lyapunov-based approaches (red), corresponding RL approaches (blue), and setpoint control (green).

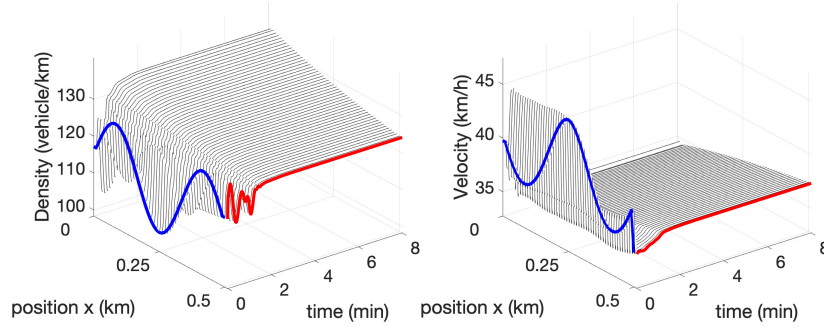


Fig. 7.22 Density and velocity evolution in space and time with outlet backstepping controller in a lighter traffic

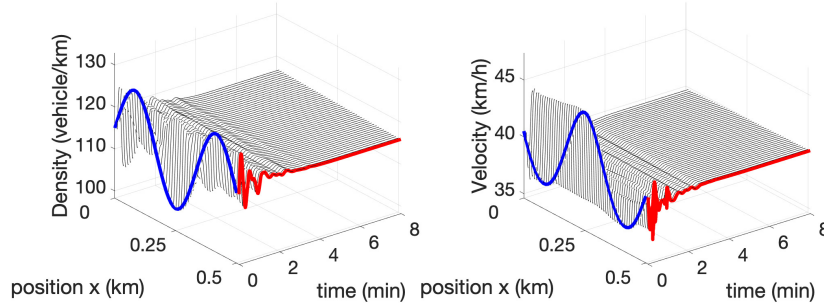


Fig. 7.23 Density and velocity evolution in space and time with outlet RL controller in a lighter traffic

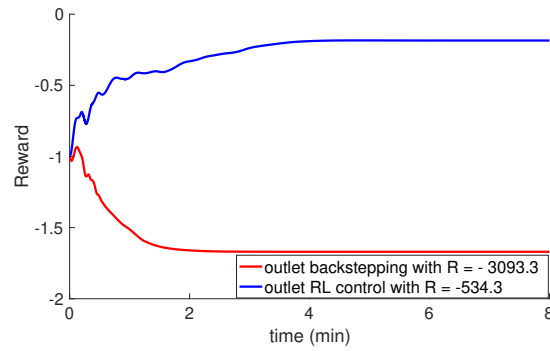


Fig. 7.24 Reward evolution for closed-loop with backstepping and RL controller at outlet in a lighter traffic

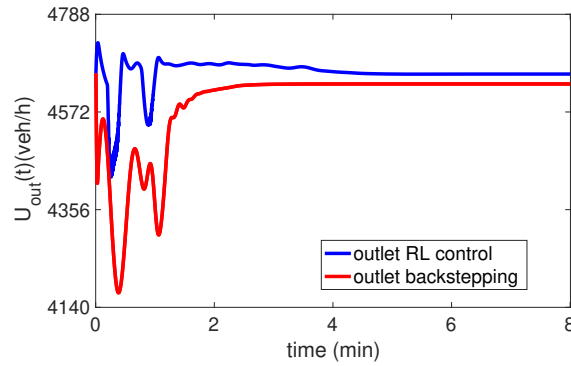


Fig. 7.25 Backstepping and RL control inputs at outlet in a lighter traffic

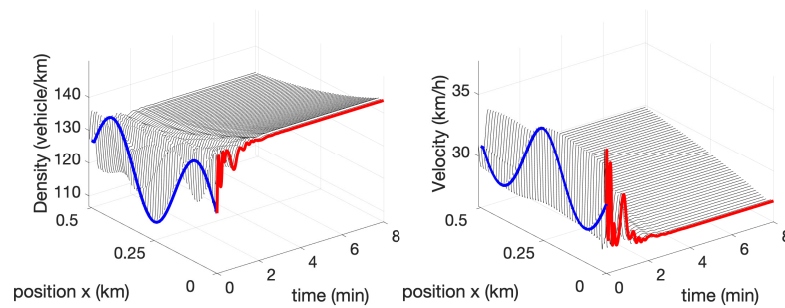


Fig. 7.26 Density and velocity evolution in space and time with inlet P controller in a denser traffic

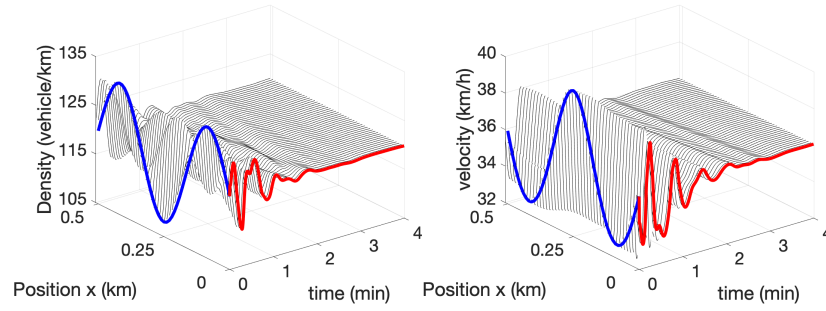


Fig. 7.27 Density and velocity evolution in space and time with inlet RL controller in a denser traffic

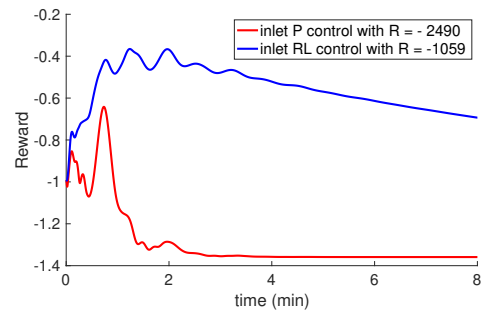


Fig. 7.28 Reward evolution for closed-loop with P and RL controller at inlet in a denser traffic

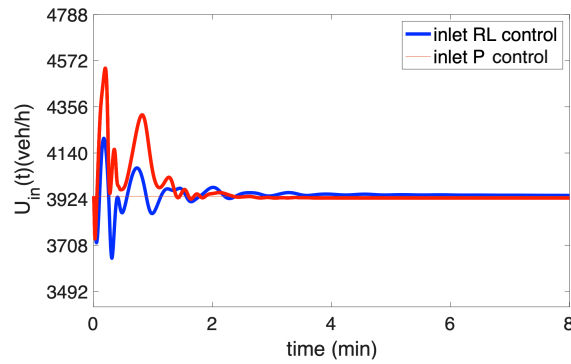


Fig. 7.29 P and RL control inputs at inlet in a denser traffic

Part III
Advanced Backstepping for Traffic Flows

Chapter 8

Two-Lane Traffic Control

8.1 Modeling and Controlling Two Lanes—by Four PDEs and Two VSL Inputs

The basic ARZ model, such as the one for which control design was proposed in Chapter 3, is applicable to freeways with one or more lanes. However, modeling traffic in which there are lane changes using a model that is a physical equivalent of gas flowing through a thin duct, is less precise than employing a model in which lane changes are specifically accounted for. In this chapter we pursue a control design in which traffic takes place in two lanes, each lane has its own density and velocity states, and there is density and flow “exchange” between the lanes when significant density and flow differentials exist between the lanes, as in real traffic.

The Chapter 3 treated multi-lane freeway traffic cumulatively as a single lane by assuming averaged velocity and density over cross section of all lanes. The individual dynamics of each lane and inter-lane interactions were neglected. In fact, the different velocity equilibria in the multi-lane problem give rise to lane-changing interactions and further lead to traffic congestion [?]. To address the phenomenon, a number of macroscopic multi-lane models [?, ?, ?, ?] have been developed from microscopic, then kinetic to macroscopic descriptions. In this chapter, we adopt the multi-lane ARZ traffic model by [?, ?] to describe a two-lane freeway traffic with lane-changing between the two lanes. Lane interactions appear as interchanging source terms in the system, leading to more involved couplings and a higher order of PDEs. The complexity of the PDE model for multi-lane problem is greatly increased compared to the one-lane problem.

The two-lane traffic is modeled by an appropriate extension of the basic ARZ model. With one density and one velocity state per lane, the two-lane traffic is modeled using four first-order hyperbolic nonlinear PDEs. Lane-changing interactions between the two lanes lead to exchanging source terms between the two pairs of PDEs. Based on the driver’s preference for the slow and fast lanes, a reference system of lane-specific uniform steady-states in congested traffic arises.

To stabilize traffic densities and velocities of both lanes to their steady-states, two distinct VSL inputs are applied at the outlet boundary, controlling the traffic velocity of each lane. It is not possible to stabilize traffic to distinct and lane-specific steady states using a single ramp-metering input.

In terms of the structure for control design, the ARZ system of four physical PDEs can be regarded, in the Riemann variables, as what we refer to as a $(2 + 2) \times (2 + 2)$ heterodirectional hyperbolic system. Two inputs (VSL) are applied at the downstream boundaries of two PDEs that convect in the upstream direction. The task of a stabilizing control law is to sever the coupling of the two additional downstream-convecting PDEs with the upstream-convecting ones.

In comparison with the basic $(1 + 1) \times (1 + 1)$ ARZ model of Chapter 3, the additional challenge is to also deal with the mutual coupling of the two upstream-convecting PDEs, as well as the mutual coupling of the two downstream-convecting PDEs.

Using a backstepping transformation, we map the coupled heterodirectional hyperbolic PDE system into a cascade target system, in which the traffic oscillations are damped out through actuation of the velocities at the downstream boundary. Two full-state feedback boundary control laws are developed. We also design a collocated boundary observer for state estimation with sensing of the densities at the outlet. Output feedback boundary controllers are obtained by combining the collocated observer and full-state feedback controllers. The finite-time convergence to equilibrium is achieved and a performance improvement in fuel consumption, drivers' comfort and total travel time is demonstrated with the proposed output-feedback controllers for some parameter choice, compared with the open-loop system. The proposed output-feedback design is also validated for different congested traffic scenarios and compared with one-lane backstepping and PI control designs.

We limit ourselves to a two-lane freeway purely for notational convenience and for the sake of clarity. The clutter of sums and integer subscripts for enumerated lanes would impede comprehension of how multi-lane traffic is dealt with by VSL boundary control. It is straightforward to extend the results of this chapter to a freeway with N lanes, using N VSL inputs, one for each lane.

8.2 Two-lane Traffic ARZ Model

The two-lane traffic on unidirectional roads is described with the following two-lane traffic ARZ model by [?, ?]. We use two VSL at the outlet to regulate the exiting velocities of the fast lane and slow lane traffic. The two-lane traffic ARZ model is given by

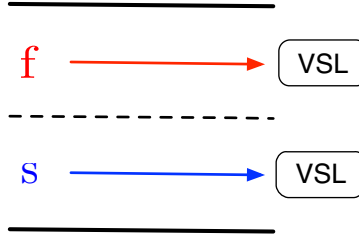


Fig. 8.1 A unidirectional freeway segment of the fast and slow lanes, with a VSL for each lane regulating the exiting velocities.

$$\partial_t \rho_f + \partial_x (\rho_f v_f) = \frac{1}{T_s} \rho_s - \frac{1}{T_f} \rho_f, \quad (8.1)$$

$$\partial_t (\rho_f v_f) + \partial_x (\rho_f v_f^2) - (\gamma p_f) \partial_x v_f = \frac{1}{T_s} \rho_s v_s - \frac{1}{T_f} \rho_f v_f + \frac{\rho_f (V(\rho_f) - v_f)}{T_f^e}, \quad (8.2)$$

$$\partial_t \rho_s + \partial_x (\rho_s v_s) = \frac{1}{T_f} \rho_f - \frac{1}{T_s} \rho_s, \quad (8.3)$$

$$\partial_t (\rho_s v_s) + \partial_x (\rho_s v_s^2) - (\gamma p_s) \partial_x v_s = \frac{1}{T_f} \rho_f v_f - \frac{1}{T_s} \rho_s v_s + \frac{\rho_s (V(\rho_s) - v_s)}{T_s^e}. \quad (8.4)$$

The traffic density $\rho_i(x, t)$ and velocity $v_i(x, t)$ ($i = f, s$) are defined in $x \in [0, L]$ for position, $t \in [0, \infty)$ for time, where L is the length of the freeway segment.

The above nonlinear hyperbolic PDEs consist of two subsystems of second-order nonlinear hyperbolic PDEs, each describing one-lane traffic dynamics. Lane-changing interactions and drivers' behavior adapting to the traffic appear as source terms on the right hand side of PDEs. The variable $p_i(\rho_i)$ is defined as the traffic density pressure

$$p_i(\rho_i) = v_m \left(\frac{\rho_i}{\rho_m} \right)^\gamma, \quad (8.5)$$

which is an increasing function of density ρ_i . v_m is the maximum traffic velocity, ρ_m is the maximum traffic density and the constant coefficient $\gamma \in \mathbb{R}_+$ reflects the aggressiveness of drivers on the road. The parameter T_i^e is defined as relaxation time that reflects driver's behavior adapting to the traffic equilibrium velocity in the lane i . The parameter $T_i \in \mathbb{R}_+$ describes the driver's preference for remaining in lane i , which relates to both lanes' density and velocity. The equilibrium velocity-density relationship $V(\rho_i)$ is given in the form of the Greenshield's model,

$$V(\rho_i) = v_m \left(1 - \left(\frac{\rho_i}{\rho_m} \right)^\gamma \right). \quad (8.6)$$

The equilibrium flow-density relation $Q(\rho_i)$ is then given by

$$Q(\rho_i) = \rho_i v_m \left(1 - \left(\frac{\rho_i}{\rho_m} \right)^\gamma \right). \quad (8.7)$$

The Greenshield's model is proposed for equilibrium velocity-density relation of cumulative one-lane traffic. However, distinct velocity equilibrium does exist in each of the two lanes [?, ?]. The two-lane control model is sketched in Fig. 8.1. The lane-specific steady traffic velocities will be discussed in the following section.

Driver's preference over two lanes

Our first step towards developing a control design for a two-lane model is to linearize the nonlinear hyperbolic system (ρ_i, v_i) around uniform steady-states (ρ_i^*, v_i^*) . We obtain the following equations that need to be satisfied by the steady-states

$$\frac{1}{T_s} \rho_s^* - \frac{1}{T_f} \rho_f^* = 0, \quad (8.8)$$

$$\frac{1}{T_s} \rho_s^* v_s^* - \frac{1}{T_f} \rho_f^* v_f^* + \frac{\rho_f^* (V(\rho_f^*) - v_f^*)}{T_f^e} = 0, \quad (8.9)$$

$$\frac{1}{T_f} \rho_f^* v_f^* - \frac{1}{T_s} \rho_s^* v_s^* + \frac{\rho_s^* (V(\rho_s^*) - v_s^*)}{T_s^e} = 0. \quad (8.10)$$

The steady-state density-velocity relations are defined based on the Greenshield's model. Thus the steady-states $(\rho_f^*, v_f^*, \rho_s^*, v_s^*)$ need to satisfy

$$\rho_f^* = \sigma \rho_s^*, \quad (8.11)$$

$$v_f^* = v_m \left(1 - r_f \left(\frac{\rho_f^*}{\rho_m} \right)^\gamma \right), \quad (8.12)$$

where v_f^* and v_s^* differ from single-lane $V(\rho_i)$. The ratio coefficients r_f and r_s are defined as

$$r_f = \frac{1 + \left(\frac{1}{\sigma} \right)^\gamma \frac{T_f^e}{T_f} + \frac{T_s^e}{T_s}}{1 + \frac{T_f^e}{T_f} + \frac{T_s^e}{T_s}}, \quad (8.13)$$

$$r_s = \frac{1 + \frac{T_f^e}{T_f} + \frac{T_s^e}{T_s} (\sigma)^\gamma}{1 + \frac{T_f^e}{T_f} + \frac{T_s^e}{T_s}}. \quad (8.14)$$

The parameter $\sigma = T_f/T_s$ defines the drivers' preference for the fast lane over the slow lane according to (8.11).

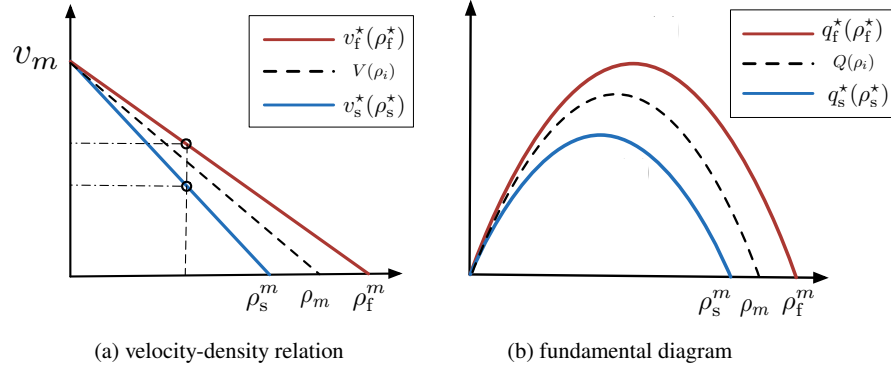


Fig. 8.2 Steady states of one-lane traffic, and two-lane traffic including a fast and slow lane

Compared with the single-lane Greenshield's model, the relations of steady-state traffic velocities v_i^* and densities ρ_i^* depend on the drivers' lane-changing preference parameter σ . Assuming that the drivers, overall, prefer the fast lane over the slow lane, we use Fig. 8.2 ($\sigma > 1, \gamma = 1$) to show the equilibrium velocity-density relation and the fundamental diagrams of the single-lane, the fast and slow lane. ρ_m represents the equivalent maximum density of the single-lane. The actual maximum density in the fast lane ρ_f^m and the slow lane ρ_s^m are related to ρ_m by

$$\rho_f^m = \sqrt[3]{r_f} \rho_s, \quad (8.15)$$

$$\rho_s^m = \sqrt[3]{r_s} \rho_s. \quad (8.16)$$

If the drivers prefer the fast lane, the decrease of velocity gets steeper in the slow lane and less steep in the fast lane, and then we have

$$\sigma > 1 \implies r_f < 1 < r_s. \quad (8.17)$$

At the same density, the fast lane traffic is "more tolerant to risk" of high density than in the single-lane case, and the slow lane traffic is "less tolerant to risk" than in the single-lane case. As a result, the traffic flow in the fast lane is higher than in the slow lane at the same density in the fundamental diagram shown in Fig. 1. If the drivers prefer the slow lane, it holds that

$$\sigma < 1 \implies r_f > 1 > r_s. \quad (8.18)$$

In general, the activities of lane changing segregate the drivers into the more "risk-tolerant" ones in the fast lane and the more "risk-averse" ones in the slow lane. The risk-tolerant drivers prefer to drive with a faster speed at the same density, compared with the risk-averse drivers.

VSL control of linearized two-lane ARZ Model

We assume that a constant traffic flow is entering from the inlet boundary $x = 0$ of the two lanes. Two VSL implemented at the outlet $U_f(t)$ and $U_s(t)$ actuate the traffic velocity variations for the fast and slow lanes respectively. So, the boundary conditions are given as

$$\rho_f(0, t) = \frac{\rho_f^* v_f^*}{v_f(0, t)}, \quad (8.19)$$

$$\rho_s(0, t) = \frac{\rho_s^* v_s^*}{v_s(0, t)}, \quad (8.20)$$

$$v_f(L, t) = U_f(t) + v_f^*, \quad (8.21)$$

$$v_s(L, t) = U_s(t) + v_s^*. \quad (8.22)$$

The control objective is to stabilize and to homogenize the traffic upstream with the VSL. Observers for state estimation are also designed by measurements of boundary values around the steady-states,

$$y_s(t) = \tilde{\rho}_s(L, t), \quad (8.23)$$

$$y_f(t) = \tilde{\rho}_f(L, t). \quad (8.24)$$

Each lane's exiting traffic density is measured, which in practice could be obtained by video cameras.

Next, we linearize the above nonlinear hyperbolic system $(\rho_f, v_f, \rho_s, v_s)$ around the steady-state $(\rho_f^*, v_f^*, \rho_s^*, v_s^*)$, satisfies (8.11)–(8.12). The deviations from the steady-states are defined as $\tilde{\rho}_i = \rho_i - \rho_i^*$, $\tilde{v}_i = v_i - v_i^*$, $i = f, s$.

$$\tilde{\rho}_f = \rho_f - \rho_f^*, \quad \tilde{v}_f = v_f - v_f^*, \quad (8.25)$$

$$\tilde{\rho}_s = \rho_s - \rho_s^*, \quad \tilde{v}_s = v_s - v_s^*. \quad (8.26)$$

The linearized hyperbolic system is

$$\partial_t \tilde{\rho}_s + v_s^* \partial_x \tilde{\rho}_s + \rho_s^* \partial_x \tilde{v}_s = -\frac{1}{T_s} \tilde{\rho}_s + \frac{1}{T_f} \tilde{\rho}_f, \quad (8.27)$$

$$\partial_t \tilde{\rho}_f + v_f^* \partial_x \tilde{\rho}_f + \rho_f^* \partial_x \tilde{v}_f = \frac{1}{T_s} \tilde{\rho}_s - \frac{1}{T_f} \tilde{\rho}_f, \quad (8.28)$$

$$\begin{aligned} \partial_t \tilde{v}_s + (v_s^* - \gamma p_s^*) \partial_x \tilde{v}_s = & -\frac{1}{T_s} \frac{v_f^* - v_s^*}{\rho_s^*} \tilde{\rho}_s + \frac{1}{T_f} \frac{v_f^* - v_s^*}{\rho_s^*} \tilde{\rho}_f \\ & + \frac{1}{T_s} (\tilde{v}_f - \tilde{v}_s) + \frac{\tilde{\rho}_s V'(\rho_s^*) - \tilde{v}_s}{T_s^e}, \end{aligned} \quad (8.29)$$

$$\begin{aligned} \partial_t \tilde{v}_f + (v_f^* - \gamma p_f^*) \partial_x \tilde{v}_f = & \frac{1}{T_s} \frac{v_s^* - v_f^*}{\rho_f^*} \tilde{\rho}_s - \frac{1}{T_f} \frac{v_s^* - v_f^*}{\rho_f^*} \tilde{\rho}_f \\ & + \frac{1}{T_f} (\tilde{v}_s - \tilde{v}_f) + \frac{\tilde{\rho}_f V'(\rho_f^*) - \tilde{v}_f}{T_f^e}, \end{aligned} \quad (8.30)$$

with the linearized boundary conditions

$$\tilde{\rho}_s(0, t) = -\frac{\rho_s^*}{v_s^*} \tilde{v}_s(0, t), \quad (8.31)$$

$$\tilde{\rho}_f(0, t) = -\frac{\rho_f^*}{v_f^*} \tilde{v}_f(0, t), \quad (8.32)$$

$$\tilde{v}_s(L, t) = U_s(t), \quad (8.33)$$

$$\tilde{v}_f(L, t) = U_f(t). \quad (8.34)$$

In order to diagonalize the spatial derivatives on the left hand side of the PDEs, we convert the above linearized hyperbolic system into the Riemann variables

$$\tilde{w}_i = \frac{\gamma p_i^*}{\rho_i^*} \tilde{\rho}_i + \tilde{v}_i, \quad (8.35)$$

$$\tilde{v}_i = \tilde{v}_i. \quad (8.36)$$

Furthermore, in order to design a backstepping boundary controller, we scale the state variables \tilde{v}_s and \tilde{v}_f with functions that depend exponentially on the spatial variable x , in order to cancel the diagonal terms in the source terms of the equations. The Riemann variables \tilde{w}_s and \tilde{w}_f remain the same, whereas the Riemann variables \tilde{v}_s and \tilde{v}_f are scaled as

$$\bar{v}_s = \exp\left(\frac{a_{11}^{vv}}{\mu_1} x\right) \tilde{v}_s, \quad (8.37)$$

$$\bar{v}_f = \exp\left(\frac{a_{22}^{vv}}{\mu_2} x\right) \tilde{v}_f \quad (8.38)$$

With the Riemann and scaling transformations, we arrive at a scaled coupled 4×4 first-order hetero-directional hyperbolic system in $(\tilde{w}_s, \tilde{w}_f, \bar{v}_s, \bar{v}_f)$,

$$\partial_t \tilde{w}_s + v_s^* \partial_x \tilde{w}_s = \bar{a}_{11}^{ww} \tilde{w}_s + \bar{a}_{12}^{ww} \tilde{w}_f + \bar{a}_{11}^{wv} \tilde{v}_s + \bar{a}_{12}^{wv} \tilde{v}_f, \quad (8.39)$$

$$\partial_t \tilde{w}_f + v_f^* \partial_x \tilde{w}_f = \bar{a}_{21}^{ww} \tilde{w}_s + \bar{a}_{22}^{ww} \tilde{w}_f + \bar{a}_{21}^{wv} \tilde{v}_s + \bar{a}_{22}^{wv} \tilde{v}_f, \quad (8.40)$$

$$\partial_t \tilde{v}_s - (\gamma p_s^* - v_s^*) \partial_x \tilde{v}_s = \bar{a}_{11}^{vw} \tilde{w}_s + \bar{a}_{12}^{vw} \tilde{w}_f + \bar{a}_{12}^{vv} \tilde{v}_f, \quad (8.41)$$

$$\partial_t \tilde{v}_f - (\gamma p_f^* - v_f^*) \partial_x \tilde{v}_f = \bar{a}_{21}^{vw} \tilde{w}_s + \bar{a}_{22}^{vw} \tilde{w}_f + \bar{a}_{21}^{vv} \tilde{v}_s, \quad (8.42)$$

$$\tilde{w}_s(0, t) = k_s \tilde{v}_s(0, t), \quad (8.43)$$

$$\tilde{w}_f(0, t) = k_f \tilde{v}_f(0, t), \quad (8.44)$$

$$\tilde{v}_s(L, t) = l_s U_s(t), \quad (8.45)$$

$$\tilde{v}_f(L, t) = l_f U_f(t), \quad (8.46)$$

where the constant boundary coefficients k_i are defined as

$$k_i = -\frac{\gamma p_i^* - v_i^*}{v_i^*}. \quad (8.47)$$

The constant coefficients l_f and l_s are defined as

$$l_s = \exp\left(\frac{a_{11}^{vv}}{\mu_1} L\right), \quad l_f = \exp\left(\frac{a_{22}^{vv}}{\mu_2} L\right). \quad (8.48)$$

The in-domain coefficient matrix $\bar{A}(x)$ of the PDE system (8.39)–(8.42) is obtained by applying the spatial transformation (8.37)–(8.38), given by the matrix

$$T(x) = \begin{bmatrix} I_{2 \times 2} & 0 \\ 0 & T^{vv}(x) \end{bmatrix}, \quad (8.49)$$

where

$$T^{vv} = \begin{bmatrix} \exp\left(\frac{a_{11}^{vv}}{\mu_1} x\right) & 0 \\ 0 & \exp\left(\frac{a_{22}^{vv}}{\mu_2} x\right) \end{bmatrix}, \quad (8.50)$$

to the constant matrix A obtained after applying the conversion to the Riemann variables to the PDE system (8.27)–(8.30), which is given in the block form

$$A = \begin{bmatrix} A^{ww} & A^{wv} \\ A^{vw} & A^{vv} \end{bmatrix}, \quad (8.51)$$

and whose blocks are defined as

$$\begin{aligned}
A^{ww} &= \begin{bmatrix} -\frac{1}{T_s^e} - \frac{1}{T_s} \frac{v_f^* - v_s^* + \gamma p_s^*}{\gamma p_s^*} & \frac{1}{T_s} \frac{v_f^* - v_s^* + \gamma p_s^*}{\gamma p_f^*} \\ \frac{1}{T_f} \frac{v_s^* - v_f^* + \gamma p_f^*}{\gamma p_s^*} & -\frac{1}{T_f^e} - \frac{1}{T_f} \frac{v_s^* - v_f^* + \gamma p_f^*}{\gamma p_f^*} \end{bmatrix}, \\
A^{wv} &= \begin{bmatrix} \frac{1}{T_s} \frac{v_f^* - v_s^*}{\gamma p_s^*} & -\frac{1}{T_s} \frac{(\gamma p_s^* - v_s^*) - (\gamma p_f^* - v_f^*)}{\gamma p_f^*} \\ -\frac{1}{T_f} \frac{(\gamma p_f^* - v_f^*) - (\gamma p_s^* - v_s^*)}{\gamma p_s^*} & \frac{1}{T_f} \frac{v_s^* - v_f^*}{\gamma p_f^*} \end{bmatrix}, \\
A^{vw} &= \begin{bmatrix} -\frac{1}{T_s^e} - \frac{1}{T_s} \frac{v_f^* - v_s^*}{\gamma p_s^*} & \frac{1}{T_s} \frac{v_f^* - v_s^*}{\gamma p_f^*} \\ \frac{1}{T_f} \frac{v_s^* - v_f^*}{\gamma p_s^*} & -\frac{1}{T_f^e} - \frac{1}{T_f} \frac{v_s^* - v_f^*}{\gamma p_f^*} \end{bmatrix}, \\
A^{vv} &= \begin{bmatrix} \frac{1}{T_s} \frac{v_f^* - v_s^* - \gamma p_s^*}{\gamma p_s^*} & -\frac{1}{T_s} \frac{v_f^* - v_s^* - \gamma p_f^*}{\gamma p_f^*} \\ -\frac{1}{T_f} \frac{v_s^* - v_f^* - \gamma p_s^*}{\gamma p_s^*} & \frac{1}{T_f} \frac{v_s^* - v_f^* - \gamma p_f^*}{\gamma p_f^*} \end{bmatrix}.
\end{aligned}$$

In the derivation, the following property is used:

$$A = TAT^{-1}. \quad (8.52)$$

Among the blocks of the transformed matrix $\bar{A}(x)$, the block \bar{A}^{ww} is constant and the blocks $\bar{A}^{wv}(x)$, $\bar{A}^{vw}(x)$ and $\bar{A}^{vv}(x)$ are spatially varying.

We consider the congested regime in [?] where steady-state traffic density disturbances convect downstream and the velocity disturbances travel upstream. Therefore the conditions

$$v_s^* - \gamma p_s^* < 0, \quad (8.53)$$

$$v_f^* - \gamma p_f^* < 0, \quad (8.54)$$

hold for the characteristic speeds of \tilde{v}_i . States \tilde{w}_i convect downstream while states \tilde{v}_i propagate upstream. We denote the transports speeds as

$$\epsilon_1 = v_s^*, \quad (8.55)$$

$$\epsilon_2 = v_f^*, \quad (8.56)$$

$$\mu_1 = (\gamma p_s^* - v_s^*), \quad (8.57)$$

$$\mu_2 = (\gamma p_f^* - v_f^*). \quad (8.58)$$

The steady velocity of the fast lane is larger than that of the slow lane, the constant transport speeds satisfy the following inequalities,

$$-\mu_1 < -\mu_2 < 0 < \epsilon_1 < \epsilon_2. \quad (8.59)$$

The flow diagram of $(\tilde{w}_i, \tilde{v}_i)$ -system is shown in Fig. 8.3 . The above 4×4 first-order hyperbolic system is composed of two coupled second-order heterodirectional hyperbolic systems. We use two VSL to damp out the oscillations to zero from the outlet.

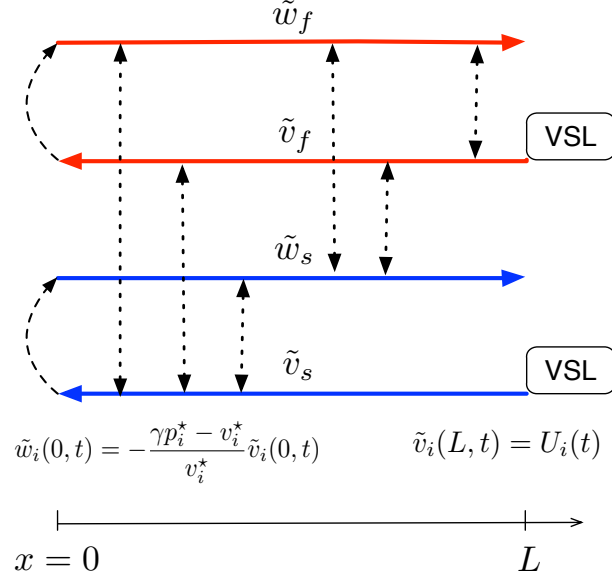


Fig. 8.3 Flow diagram of linearized two-lane ARZ model

8.3 Full-state Feedback Control Design

Following the full-state feedback design introduced in Chapter 2.3, we introduce the backstepping transformation to the scaled $(\tilde{w}_i, \tilde{v}_i)$ -system in (8.39)–(8.46),

$$\begin{bmatrix} \alpha_s(x, t) \\ \alpha_f(x, t) \end{bmatrix} = \begin{bmatrix} \tilde{w}_s(x, t) \\ \tilde{w}_f(x, t) \end{bmatrix}, \quad (8.60)$$

$$\begin{bmatrix} \beta_s(x, t) \\ \beta_f(x, t) \end{bmatrix} = \begin{bmatrix} \tilde{v}_s(x, t) \\ \tilde{v}_f(x, t) \end{bmatrix} - \int_0^x \begin{bmatrix} K_{11} & K_{12} \\ K_{21} & K_{22} \end{bmatrix} \begin{bmatrix} \tilde{w}_s(x, t) \\ \tilde{w}_f(x, t) \end{bmatrix} d\xi \\ - \int_0^x \begin{bmatrix} L_{11} & L_{12} \\ L_{21} & L_{22} \end{bmatrix} \begin{bmatrix} \tilde{v}_s(x, t) \\ \tilde{v}_f(x, t) \end{bmatrix} d\xi. \quad (8.61)$$

The kernel variables $\{K(x, \xi)\}$ and $\{L(x, \xi)\}$ evolve in a triangular domain $\mathcal{T} = \{(x, \xi) : 0 \leq \xi \leq x \leq 1\}$. Taking derivatives with respect to time and space on both sides of (8.60)–(8.61) along the solution of a target system, we obtain the kernel equations that govern the kernels $\{K(x, \xi)\}$ and $\{L(x, \xi)\}$.

$$\mu_1 \partial_x K_{11} - \epsilon_1 \partial_\xi K_{11} = \bar{a}_{11}^{ww} K_{11} + \bar{a}_{21}^{ww} K_{12} + \bar{a}_{11}^{vw} L_{11} + \bar{a}_{21}^{vw} L_{12}, \quad (8.62)$$

$$\mu_1 \partial_x K_{12} - \epsilon_2 \partial_\xi K_{12} = \bar{a}_{12}^{ww} K_{11} + \bar{a}_{22}^{ww} K_{12} + \bar{a}_{12}^{vw} L_{11} + \bar{a}_{22}^{vw} L_{12}, \quad (8.63)$$

$$\mu_2 \partial_x K_{21} - \epsilon_1 \partial_\xi K_{21} = \bar{a}_{11}^{ww} K_{21} + \bar{a}_{21}^{ww} K_{22} + \bar{a}_{11}^{vw} L_{21} + \bar{a}_{21}^{vw} L_{22}, \quad (8.64)$$

$$\mu_2 \partial_x K_{22} - \epsilon_2 \partial_\xi K_{22} = \bar{a}_{12}^{ww} K_{21} + \bar{a}_{22}^{ww} K_{22} + \bar{a}_{12}^{vw} L_{21} + \bar{a}_{22}^{vw} L_{22}, \quad (8.65)$$

$$\mu_1 \partial_x L_{11} + \mu_1 \partial_\xi L_{11} = \bar{a}_{21}^{vv} L_{12} + \bar{a}_{11}^{vw} K_{11} + \bar{a}_{21}^{vw} K_{12}, \quad (8.66)$$

$$\mu_1 \partial_x L_{12} + \mu_2 \partial_\xi L_{12} = \bar{a}_{12}^{vv} L_{11} + \bar{a}_{12}^{vw} K_{11} + \bar{a}_{22}^{vw} K_{12}, \quad (8.67)$$

$$\mu_2 \partial_x L_{21} + \mu_1 \partial_\xi L_{21} = \bar{a}_{21}^{vv} L_{22} + \bar{a}_{11}^{vw} K_{21} + \bar{a}_{21}^{vw} K_{22}, \quad (8.68)$$

$$\mu_2 \partial_x L_{22} + \mu_2 \partial_\xi L_{22} = \bar{a}_{12}^{vv} L_{21} + \bar{a}_{12}^{vw} K_{21} + \bar{a}_{22}^{vw} K_{22}, \quad (8.69)$$

$$K_{11}(x, x) = -\frac{\bar{a}_{11}^{vw}(x)}{\epsilon_1 + \mu_1}, \quad K_{12}(x, x) = -\frac{\bar{a}_{12}^{vw}(x)}{\epsilon_2 + \mu_1}, \quad (8.70)$$

$$K_{21}(x, x) = -\frac{\bar{a}_{21}^{vw}(x)}{\epsilon_1 + \mu_2}, \quad K_{22}(x, x) = -\frac{\bar{a}_{22}^{vw}(x)}{\epsilon_2 + \mu_2}, \quad (8.71)$$

$$L_{11}(x, 0) = \frac{\epsilon_1 k_s}{\mu_1} K_{11}(x, 0), \quad L_{12}(x, x) = -\frac{\bar{a}_{12}^{vv}(x)}{\mu_1 - \mu_2}, \quad (8.72)$$

$$L_{12}(x, 0) = \frac{\epsilon_2 k_f}{\mu_2} K_{12}(x, 0), \quad L_{21}(x, x) = -\frac{\bar{a}_{21}^{vv}(x)}{\mu_2 - \mu_1}, \quad (8.73)$$

$$L_{21}(L, \xi) = 0, \quad L_{22}(x, 0) = \frac{\epsilon_2 k_f}{\mu_2} K_{22}(x, 0). \quad (8.74)$$

The well-posedness of the kernel equations is proved using the method of characteristics and the successive approximations, following the result for a general class of kernel system in [?]. There exists a unique solution $K, L \in L^\infty(\mathcal{T})$. Therefore, we establish the invertibility of the backstepping transformation (8.60), (8.61) and can study the stability of the target system due to its equivalence to the $(\tilde{w}_i, \tilde{v}_i)$ -system. More details on the target system and the kernel equations are included in [?]. It should be noted that we impose an artificial boundary condition $L_{21}(L, \xi)$ in (8.74) for the well-posedness of the kernel equations. This leads to one degree of freedom in backstepping transformation of the hyperbolic system as well as the associated control design. The stabilization of the target system is achieved with two controllers and the one degree of freedom enables the coordination between the two VSL.

With the backstepping transformation and the kernel equations, we map the $(\tilde{w}_i, \tilde{v}_i)$ -system in (8.39)–(8.46) to a cascade target system

$$\begin{aligned}
\partial_t \alpha_s = & -v_s^* \partial_x \alpha_s \bar{a}_{11}^{ww} \alpha_s + \bar{a}_{12}^{ww} \alpha_f + \bar{a}_{11}^{wv}(x) \beta_s + \bar{a}_{12}^{wv}(x) \beta_f \\
& + \int_0^x b_{11}(x, \xi) \alpha_s(\xi) d\xi + \int_0^x b_{12}(x, \xi) \alpha_f(\xi) d\xi \\
& + \int_0^x c_{11}(x, \xi) \beta_s(\xi) d\xi + \int_0^x c_{12}(x, \xi) \beta_f(\xi) d\xi, \quad (8.75)
\end{aligned}$$

$$\begin{aligned}
\partial_t \alpha_f = & -v_f^* \partial_x \alpha_f \bar{a}_{21}^{ww} \alpha_s + \bar{a}_{22}^{ww} \alpha_f + \bar{a}_{21}^{wv}(x) \beta_s + \bar{a}_{22}^{wv}(x) \beta_f \\
& + \int_0^x b_{21}(x, \xi) \alpha_s(\xi) d\xi + \int_0^x b_{22}(x, \xi) \alpha_f(\xi) d\xi \\
& + \int_0^x c_{21}(x, \xi) \beta_s(\xi) d\xi + \int_0^x c_{22}(x, \xi) \beta_f(\xi) d\xi, \quad (8.76)
\end{aligned}$$

$$\partial_t \beta_s = (\gamma p_s^* - v_s^*) \partial_x \beta_s, \quad (8.77)$$

$$\partial_t \beta_f = (\gamma p_f^* - v_f^*) \partial_x \beta_f + \theta(x) \beta_s(0, t), \quad (8.78)$$

$$\alpha_f(0, t) = k_f \beta_f(0, t), \quad (8.79)$$

$$\alpha_s(0, t) = k_s \beta_s(0, t), \quad (8.80)$$

$$\beta_s(L, t) = 0, \quad (8.81)$$

$$\beta_f(L, t) = 0, \quad (8.82)$$

where the spatially varying parameter matrices $B(x, \xi)$ and $C(x, \xi)$ are given by

$$B(x, \xi) = \bar{A}^{wv}(x) K(x, \xi) + \int_\xi^x B(x, s) K(s, \xi) d\xi, \quad (8.83)$$

$$C(x, \xi) = \bar{A}^{wv}(x) L(x, \xi) + \int_\xi^x C(x, s) L(s, \xi) d\xi, \quad (8.84)$$

and $\theta(x)$ is obtained from the kernel variables $K_{21}(x, \xi)$ and $L_{21}(x, \xi)$, $\theta(x) = -\epsilon_1 k_s K_{21}(x, 0) + \mu_1 L_{21}(x, 0)$.

The boundary conditions (8.45), (8.46), along with the boundary conditions (8.81), (8.82), as well as the backstepping transformation (8.61), yield the full-state feedback control laws, to be stated in Theorem 8.1.

The following stability result holds for the target system.

Lemma 8.1 *Consider the target system (8.75)–(8.78) and the actuated boundary conditions (8.79)–(8.82). The equilibrium $\alpha_s = \alpha_f = \beta_s = \beta_f = 0$ is stable and reached in finite time*

$$t_f = \frac{L}{v_s^*} + \frac{L}{\gamma p_f^* - v_f^*} + \frac{L}{\gamma p_s^* - v_s^*}. \quad (8.85)$$

Proof By solving (8.78) and (8.82) directly, we obtain that after $t > \frac{L}{\gamma p_f^* - v_f^*}$,

$$\beta_f(x, t) \equiv 0. \quad (8.86)$$

Using the cascade structure of the β_f -system, we have

$$\beta_s(s, t) \equiv 0 \quad (8.87)$$

after $t > \frac{L}{\gamma p_f^* - v_f^*} + \frac{L}{\gamma p_s^* - v_s^*}$. Then, after $t > \frac{L}{\gamma p_f^* - v_f^*} + \frac{L}{\gamma p_s^* - v_s^*} + \frac{L}{v_s^*}$, we obtain that

$$\alpha_f(x, t) \equiv 0, \quad (8.88)$$

$$\alpha_s(x, t) \equiv 0 \quad (8.89)$$

which concludes the proof. \square

By employing the properties of the backstepping transformation and its inverse, we arrive at the main stabilization result.

Theorem 8.1 *Consider the linearized two-lane traffic ARZ model with the boundary conditions in (8.39)–(8.46), the initial conditions $\tilde{w}_i(x, 0), \tilde{v}_i(x, 0) \in L^\infty([0, L])$ and the following control laws*

$$\begin{aligned} U_s(t) = & \exp\left(-\frac{a_{11}^{vv}}{\mu_1} L\right) \int_0^L \frac{\gamma p_s^*}{\rho_s^*} K_{11}(L, \xi) (\rho_s(\xi, t) - \rho_s^*) + \frac{\gamma p_f^*}{\rho_f^*} K_{12}(L, \xi) (\rho_f(\xi, t) - \rho_f^*) \\ & + \left[K_{11}(L, \xi) + L_{11}(L, \xi) \exp\left(\frac{a_{11}^{vv}}{\mu_1} \xi\right) \right] (v_s(\xi, t) - v_s^*) \\ & + \left[K_{12}(L, \xi) + L_{12}(L, \xi) \exp\left(\frac{a_{22}^{vv}}{\mu_2} \xi\right) \right] (v_f(\xi, t) - v_f^*) d\xi, \end{aligned} \quad (8.90)$$

$$\begin{aligned} U_f(t) = & \exp\left(-\frac{a_{22}^{vv}}{\mu_2} L\right) \int_0^L \frac{\gamma p_s^*}{\rho_s^*} K_{21}(L, \xi) (\rho_s(\xi, t) - \rho_s^*) + \frac{\gamma p_f^*}{\rho_f^*} K_{22}(L, \xi) (\rho_f(\xi, t) - \rho_f^*) \\ & + \left[K_{21}(L, \xi) + L_{21}(L, \xi) \exp\left(\frac{a_{11}^{vv}}{\mu_1} \xi\right) \right] (v_s(\xi, t) - v_s^*) \\ & + \left[K_{22}(L, \xi) + L_{22}(L, \xi) \exp\left(\frac{a_{22}^{vv}}{\mu_2} \xi\right) \right] (v_f(\xi, t) - v_f^*) d\xi, \end{aligned} \quad (8.91)$$

where the kernels $\{K\}$ and $\{L\}$ are obtained by solving the kernel equations (8.62)–(8.74). The steady-states $(\rho_f^*, v_f^*, \rho_s^*, v_s^*)$ are stable and reached in finite time t_f given in (8.85).

8.4 Collocated Observer and output-feedback control

In this section, we develop a collocated observer by taking measurement of density states at the outlet of the segment defined in (8.24). Using the state estimates obtained from the observer design and the full-state feedback control laws, we construct output-feedback controllers.

An anti-collocated observer can be also designed by taking measurement of velocity states $\tilde{v}_s(0, t)$ and $\tilde{v}_f(0, t)$ at the inlet. The anti-collocated observer design is trivial as it involves little more than a copy of the $(\tilde{w}_f, \tilde{w}_s, \tilde{v}_s, \tilde{v}_f)$ -system. More

importantly, we limit ourselves to the collocated observer design because of its practical benefit in the implementation along with the full-state feedback control design where the sensor is placed near the actuator.

Collocated observer design

For state estimation of the scaled system in (8.39)–(8.46), we generate the measurements of $\tilde{w}_s(L, t)$ and $\tilde{w}_f(L, t)$ from (8.35), namely, in the following fashion:

$$Y_s(t) = \tilde{w}_s(L, t) = \frac{\gamma p_s^*}{\rho_s^*} \tilde{\rho}_s(L, t) + \tilde{v}_s(L, t), \quad (8.92)$$

$$Y_f(t) = \tilde{w}_f(L, t) = \frac{\gamma p_f^*}{\rho_f^*} \tilde{\rho}_f(L, t) + \tilde{v}_f(L, t). \quad (8.93)$$

Thus, the values of $Y_s(t)$ and $Y_f(t)$ are obtained from $y_s(t) = \tilde{\rho}_s(L, t)$, $y_f(t) = \tilde{\rho}_f(L, t)$ and control inputs $U_s(t)$, $U_f(t)$,

$$Y_s(t) = \frac{\gamma p_s^*}{\rho_s^*} y_s(t) + U_s(t), \quad (8.94)$$

$$Y_f(t) = \frac{\gamma p_f^*}{\rho_f^*} y_f(t) + U_f(t). \quad (8.95)$$

The observer equations (\hat{w}_f , \hat{w}_s , \hat{u}_s , \hat{u}_f) that estimate (\tilde{w}_f , \tilde{w}_s , \tilde{v}_s , \tilde{v}_f) read as follows:

$$\begin{aligned} \partial_t \hat{w}_s = & -v_s^* \partial_x \hat{w}_s \bar{a}_{11}^{ww} \hat{w}_s + \bar{a}_{12}^{ww} \hat{w}_f + \bar{a}_{11}^{wv}(x) \hat{u}_s + \bar{a}_{12}^{wv}(x) \hat{u}_f \\ & + p_{11}(x) \tilde{w}_s(L, t) + p_{12}(x) \tilde{w}_f(L, t), \end{aligned} \quad (8.96)$$

$$\begin{aligned} \partial_t \hat{w}_f = & -v_f^* \partial_x \hat{w}_f \bar{a}_{21}^{ww} \hat{w}_s + \bar{a}_{22}^{ww} \hat{w}_f + \bar{a}_{21}^{wv}(x) \hat{u}_s + \bar{a}_{22}^{wv}(x) \hat{u}_f \\ & + p_{21}(x) \tilde{w}_s(L, t) + p_{22}(x) \tilde{w}_f(L, t), \end{aligned} \quad (8.97)$$

$$\begin{aligned} \partial_t \hat{u}_s = & (\gamma p_s^* - v_s^*) \partial_x \hat{u}_s + \bar{a}_{11}^{vw}(x) \hat{w}_s + \bar{a}_{12}^{vw}(x) \hat{w}_f + \bar{a}_{12}^{vv}(x) \hat{u}_f \\ & + q_{11}(x) \tilde{w}_s(L, t) + q_{12}(x) \tilde{w}_f(L, t), \end{aligned} \quad (8.98)$$

$$\begin{aligned} \partial_t \hat{u}_f = & (\gamma p_f^* - v_f^*) \partial_x \hat{u}_f + \bar{a}_{21}^{vw}(x) \hat{w}_s + \bar{a}_{22}^{vw}(x) \hat{w}_f + \bar{a}_{21}^{vv}(x) \hat{u}_s \\ & + q_{21}(x) \tilde{w}_s(L, t) + q_{22}(x) \tilde{w}_f(L, t), \end{aligned} \quad (8.99)$$

$$\hat{w}_s(0, t) = k_s \hat{u}_s(0, t), \quad \hat{w}_f(0, t) = k_f \hat{u}_f(0, t), \quad (8.100)$$

$$\hat{u}_s(L, t) = l_s U_s(t), \quad \hat{u}_f(L, t) = l_f U_f(t). \quad (8.101)$$

The output injections in (8.96)–(8.99) are defined as

$$\tilde{w}_s(L, t) = Y_s(t) - \hat{w}_s(L, t), \quad (8.102)$$

$$\tilde{w}_f(L, t) = Y_f(t) - \hat{w}_f(L, t). \quad (8.103)$$

The observer output injection gains matrices $P(x)$ and $Q(x)$ are to be designed so that the estimation error system is driven to converge to zero in finite-time. The error system $(\check{w}_s, \check{w}_f, \check{v}_s, \check{v}_f)$ is straightforward to derive by subtracting the observer (8.96)–(8.101) from the original linearized system (8.39)–(8.46),

$$\begin{aligned} \partial_t \check{w}_s = & -v_s^* \partial_x \check{w}_s + \bar{a}_{11}^{ww} \check{w}_s + \bar{a}_{12}^{ww} \check{w}_f + \bar{a}_{11}^{wv}(x) \check{v}_s + \bar{a}_{12}^{wv}(x) \check{v}_f \\ & - p_{11}(x) \check{w}_s(L, t) - p_{12}(x) \check{w}_f(L, t), \end{aligned} \quad (8.104)$$

$$\begin{aligned} \partial_t \check{w}_f = & -v_f^* \partial_x \check{w}_f + \bar{a}_{21}^{ww} \check{w}_s + \bar{a}_{22}^{ww} \check{w}_f + \bar{a}_{21}^{wv}(x) \check{v}_s + \bar{a}_{22}^{wv}(x) \check{v}_f, \\ & - p_{21}(x) \check{w}_s(L, t) - p_{22}(x) \check{w}_f(L, t), \end{aligned} \quad (8.105)$$

$$\begin{aligned} \partial_t \check{v}_s = & (\gamma p_s^* - v_s^*) \partial_x \check{v}_s + \bar{a}_{11}^{vw}(x) \check{w}_s + \bar{a}_{12}^{vw}(x) \check{w}_f + \bar{a}_{12}^{vv}(x) \check{v}_f \\ & - q_{11}(x) \check{w}_s(L, t) - q_{12}(x) \check{w}_f(L, t), \end{aligned} \quad (8.106)$$

$$\begin{aligned} \partial_t \check{v}_f = & (\gamma p_f^* - v_f^*) \partial_x \check{v}_f + \bar{a}_{21}^{vw}(x) \check{w}_s + \bar{a}_{22}^{vw}(x) \check{w}_f + \bar{a}_{21}^{vv}(x) \check{v}_s, \\ & - q_{21}(x) \check{w}_s(L, t) - q_{22}(x) \check{w}_f(L, t), \end{aligned} \quad (8.107)$$

$$\check{w}_s(0, t) = k_s \check{v}_s(0, t), \quad (8.108)$$

$$\check{w}_f(0, t) = k_f \check{v}_f(0, t), \quad (8.109)$$

$$\check{v}_s(L, t) = 0, \quad (8.110)$$

$$\check{v}_f(L, t) = 0, \quad (8.111)$$

where the estimation errors are defined

$$\check{w}_i = \tilde{w}_i - \hat{w}_i, \quad (8.112)$$

$$\check{v}_i = \tilde{v}_i - \hat{u}_i. \quad (8.113)$$

We then apply the backstepping transformation to the error system given by

$$\begin{bmatrix} \check{w}_s(x, t) \\ \check{w}_f(x, t) \end{bmatrix} = \begin{bmatrix} \check{\alpha}_s(x, t) \\ \check{\alpha}_f(x, t) \end{bmatrix} + \int_x^L \begin{bmatrix} M_{11} & M_{12} \\ M_{21} & M_{22} \end{bmatrix} \begin{bmatrix} \check{\alpha}_s(\xi, t) \\ \check{\alpha}_f(\xi, t) \end{bmatrix} d\xi, \quad (8.114)$$

$$\begin{bmatrix} \check{v}_s(x, t) \\ \check{v}_f(x, t) \end{bmatrix} = \begin{bmatrix} \check{\beta}_s(x, t) \\ \check{\beta}_f(x, t) \end{bmatrix} + \int_x^L \begin{bmatrix} N_{11} & N_{12} \\ N_{21} & N_{22} \end{bmatrix} \begin{bmatrix} \check{\alpha}_s(\xi, t) \\ \check{\alpha}_f(\xi, t) \end{bmatrix} d\xi, \quad (8.115)$$

where the kernels $\{M(x, \xi)\}, \{N(x, \xi)\}$ evolve in the triangular domain $\mathcal{T} = \{(x, \xi) : 0 \leq x \leq \xi \leq L\}$ and are defined later. Then we obtain the following cascade target system

$$\begin{aligned}\partial_t \check{\alpha}_s = & -v_s^* \partial_x \check{\alpha}_s + \bar{a}_{11}^{ww} \check{\alpha}_s + \bar{a}_{11}^{wv}(x) \check{\beta}_s + \bar{a}_{12}^{wv}(x) \check{\beta}_f \\ & + \int_x^L d_{11}(x, \xi) \check{\beta}_s(\xi) d\xi + \int_x^L d_{12}(x, \xi) \check{\beta}_f(\xi) d\xi,\end{aligned}\quad (8.116)$$

$$\begin{aligned}\partial_t \check{\alpha}_f = & -v_f^* \partial_x \check{\alpha}_f + \bar{a}_{21}^{wv}(x) \check{\beta}_s + \bar{a}_{22}^{wv}(x) \check{\beta}_f \\ & + \int_x^L d_{21}(x, \xi) \check{\beta}_s(\xi) d\xi + \int_x^L d_{22}(x, \xi) \check{\beta}_f(\xi) d\xi,\end{aligned}\quad (8.117)$$

$$\begin{aligned}\partial_t \check{\beta}_s = & (\gamma p_s^* - v_s^*) \partial_x \check{\beta}_s + \bar{a}_{12}^{vv}(x) \check{\beta}_f \\ & + \int_x^L f_{11}(x, \xi) \check{\beta}_s(\xi) d\xi + \int_x^L f_{12}(x, \xi) \check{\beta}_f(\xi) d\xi,\end{aligned}\quad (8.118)$$

$$\begin{aligned}\partial_t \check{\beta}_f = & (\gamma p_f^* - v_f^*) \partial_x \check{\beta}_f + \bar{a}_{21}^{vv}(x) \check{\beta}_s \\ & + \int_x^L f_{21}(x, \xi) \check{\beta}_s(\xi) d\xi + \int_x^L f_{22}(x, \xi) \check{\beta}_f(\xi) d\xi,\end{aligned}\quad (8.119)$$

$$\check{\alpha}_s(0, t) = k_s \check{\beta}_s(0, t), \quad \check{\alpha}_f(0, t) = k_f \check{\beta}_f(0, t) - \int_0^L \lambda(x) \check{\alpha}_s(x, t) d\xi, \quad (8.120)$$

$$\check{\beta}_s(L, t) = 0, \quad \check{\beta}_f(L, t) = 0, \quad (8.121)$$

where the coefficient matrices $\{D(x, \xi)\}$ and $\{F(x, \xi)\}$ are given by

$$D(x, \xi) = -M(x, \xi) \bar{A}^{wv} + \int_\xi^x M(x, s) D(s, \xi) d\xi, \quad (8.122)$$

$$F(x, \xi) = -N(x, \xi) \bar{A}^{ww} + \int_\xi^x N(x, s) F(s, \xi) d\xi. \quad (8.123)$$

The spatially-varying coefficient $\lambda(x)$ is obtained from the kernel variables

$$\lambda(x) = M_{21}(0, x) - k_f N_{21}(0, x). \quad (8.124)$$

Lemma 8.2 *Consider the target system (8.116)–(8.119) with the boundary conditions (8.120)–(8.121). The equilibrium $\check{\alpha}_s = \check{\alpha}_f = \check{\beta}_s = \check{\beta}_f = 0$ is stable and reached in finite time*

$$t_o = \frac{L}{v_s^*} + \frac{L}{v_f^*} + \frac{L}{\gamma p_f^* - v_f^*}. \quad (8.125)$$

Proof Noting that the cascade structure of $\check{\alpha}_s, \check{\alpha}_f$ and $\check{\beta}_s, \check{\beta}_f$ system, $\check{\beta}$ variables appear as the right hand source terms in $\check{\alpha}$ equations and through the inlet boundaries. The integral of variable $\check{\alpha}_s$ enters the boundary condition of $\check{\alpha}_f$. Therefore we solve the target system explicitly, in several steps. The $\check{\beta}$ -system is independent of the $\check{\alpha}$ system. Given the homogeneous boundary conditions at $x = L$ in (8.121), and given that the integrals in the $\check{\beta}_s, \check{\beta}_f$ systems are forward (from x to L , not from 0 to x), after $t > \frac{1}{\gamma p_f^* - v_f^*}$, we have that $\check{\beta}_s(x, t) \equiv 0, \quad \check{\beta}_f(x, t) \equiv 0$. When $t > \frac{1}{\gamma p_f^* - v_f^*}$, the $\check{\alpha}$ -system becomes

$$\partial_t \check{\alpha}_s = -v_s^* \partial_x \check{\alpha}_s + \bar{a}_{11}^{ww} \check{\alpha}_s, \quad (8.126)$$

$$\partial_t \check{\alpha}_f = -v_f^* \partial_x \check{\alpha}_f + \bar{a}_{22}^{ww} \check{\alpha}_f, \quad (8.127)$$

$$\check{\alpha}_s(0, t) = 0, \quad (8.128)$$

$$\check{\alpha}_f(0, t) = - \int_0^L \lambda(x) \check{\alpha}_s(x, t) d\xi. \quad (8.129)$$

After $t > \frac{1}{v_s^*} + \frac{1}{\gamma p_f^* - v_f^*}$, we have that $\check{\alpha}_s(x, t) \equiv 0$. Then $\check{\alpha}_f(x, t) \equiv 0$ follows after another time period $\frac{1}{v_f^*}$. Therefore, $\check{\alpha}$ -system eventually identically vanishes after t_o which concludes the proof. \square

Taking spatial and temporal derivatives of the backstepping transformation (8.114), (8.115) along the target system (8.116)–(8.121), then plugging the result into the error system, we obtain the kernel equations that govern the kernels $M(x, \xi)$ and $N(x, \xi)$, for $j, k = 1, 2$, as

$$\epsilon_j \partial_x M_{jk} + \epsilon_k \partial_\xi M_{jk} = - \sum_{n=1}^2 \bar{a}_{jn}^{ww} M_{nk} - \sum_{n=1}^2 \bar{a}_{jn}^{wv} N_{nk}, \quad (8.130)$$

$$\mu_j \partial_x N_{jk} - \epsilon_k \partial_\xi N_{jk} = \bar{a}_{kk}^{ww} N_{jk} + \sum_{n=1}^2 \bar{a}_{jn}^{vv} N_{nj} + \sum_{n=1}^2 \bar{a}_{jn}^{vw} M_{nj}, \quad (8.131)$$

$$N_{jk}(x, x) = \frac{\bar{a}_{jk}^{vw}(x)}{\mu_j + \epsilon_k}, \quad M_{21}(x, L) = - \frac{\bar{a}_{21}^{ww}}{\epsilon_2 - \epsilon_1} \quad (8.132)$$

$$M_{1k}(0, \xi) = k_s N_{1k}(0, \xi), \quad M_{22}(0, \xi) = k_f N_{22}(0, \xi), \quad (8.133)$$

$$M_{12}(x, x) = - \frac{\bar{a}_{12}^{ww}}{\epsilon_1 - \epsilon_2}, \quad M_{21}(x, x) = - \frac{\bar{a}_{21}^{ww}}{\epsilon_2 - \epsilon_1}, \quad (8.134)$$

Introducing the new spatial variables $\bar{x} = L - x$, $\bar{\xi} = L - \xi$,

$$\bar{M}(\bar{x}, \bar{\xi}) = M(L - \bar{x}, L - \bar{\xi}) = M(x, \xi), \quad (8.135)$$

$$\bar{N}(\bar{x}, \bar{\xi}) = N(L - \bar{x}, L - \bar{\xi}) = N(x, \xi), \quad (8.136)$$

on the triangular domain $\mathcal{D} = \{(\bar{x}, \bar{\xi}) : 0 \leq \bar{\xi} \leq \bar{x} \leq L\}$, we find that the kernel equations obtained for $\bar{M}(\bar{x}, \bar{\xi})$ and $\bar{N}(\bar{x}, \bar{\xi})$, and given by

$$\epsilon_1 \partial_{\bar{x}} \bar{M}_{11} + \epsilon_1 \partial_{\bar{\xi}} \bar{M}_{11} = \bar{a}_{12}^{ww} \bar{M}_{21} + \bar{a}_{11}^{wv} \bar{N}_{11} + \bar{a}_{12}^{vv} \bar{N}_{21}, \quad (8.137)$$

$$\epsilon_1 \partial_{\bar{x}} \bar{M}_{12} + \epsilon_2 \partial_{\bar{\xi}} \bar{M}_{12} = \bar{a}_{11}^{ww} \bar{M}_{12} + \bar{a}_{12}^{ww} \bar{M}_{22} + \bar{a}_{11}^{wv} \bar{N}_{12} + \bar{a}_{12}^{vv} \bar{N}_{22}, \quad (8.138)$$

$$\epsilon_2 \partial_{\bar{x}} \bar{M}_{21} + \epsilon_1 \partial_{\bar{\xi}} \bar{M}_{21} = \bar{a}_{21}^{ww} \bar{M}_{11} + \bar{a}_{22}^{ww} \bar{M}_{21} + \bar{a}_{21}^{wv} \bar{N}_{11} + \bar{a}_{22}^{vv} \bar{N}_{21}, \quad (8.139)$$

$$\epsilon_2 \partial_{\bar{x}} \bar{M}_{22} + \epsilon_2 \partial_{\bar{\xi}} \bar{M}_{22} = \bar{a}_{21}^{ww} \bar{M}_{12} + \bar{a}_{21}^{wv} \bar{N}_{12} + \bar{a}_{22}^{vv} \bar{N}_{22}, \quad (8.140)$$

$$\mu_1 \partial_{\bar{x}} \bar{N}_{11} - \epsilon_1 \partial_{\bar{\xi}} \bar{N}_{11} = -\bar{a}_{11}^{ww} \bar{N}_{11} - \bar{a}_{12}^{vv} \bar{N}_{21} - \bar{a}_{11}^{vw} \bar{M}_{11} - \bar{a}_{12}^{vw} \bar{M}_{21}, \quad (8.141)$$

$$\mu_1 \partial_{\bar{x}} \bar{N}_{12} - \epsilon_2 \partial_{\bar{\xi}} \bar{N}_{12} = -\bar{a}_{22}^{ww} \bar{N}_{12} - \bar{a}_{12}^{vv} \bar{N}_{22} - \bar{a}_{11}^{vw} \bar{M}_{12} - \bar{a}_{12}^{vw} \bar{M}_{22}, \quad (8.142)$$

$$\mu_2 \partial_{\bar{x}} \bar{N}_{21} - \epsilon_1 \partial_{\bar{\xi}} \bar{N}_{21} = -\bar{a}_{11}^{ww} \bar{N}_{21} - \bar{a}_{21}^{vv} \bar{N}_{11} - \bar{a}_{21}^{vw} \bar{M}_{11} - \bar{a}_{22}^{vw} \bar{M}_{21}, \quad (8.143)$$

$$\mu_2 \partial_{\bar{x}} \bar{N}_{22} - \epsilon_2 \partial_{\bar{\xi}} \bar{N}_{22} = -\bar{a}_{22}^{ww} \bar{N}_{22} - \bar{a}_{21}^{vv} \bar{N}_{12} - \bar{a}_{21}^{vw} \bar{M}_{12} - \bar{a}_{22}^{vw} \bar{M}_{22}, \quad (8.144)$$

$$\bar{N}_{11}(\bar{x}, \bar{x}) = \frac{\bar{a}_{11}^{vw}(L - \bar{x})}{\epsilon_1 + \mu_1}, \quad \bar{N}_{12}(\bar{x}, \bar{x}) = \frac{\bar{a}_{12}^{vw}(L - \bar{x})}{\epsilon_2 + \mu_1}, \quad (8.145)$$

$$\bar{N}_{21}(\bar{x}, \bar{x}) = \frac{\bar{a}_{21}^{vw}(L - \bar{x})}{\epsilon_1 + \mu_2}, \quad \bar{N}_{22}(\bar{x}, \bar{x}) = \frac{\bar{a}_{22}^{vw}(L - \bar{x})}{\epsilon_2 + \mu_2}, \quad (8.146)$$

$$\bar{M}_{11}(L, \bar{\xi}) = k_s \bar{N}_{11}(L, \bar{\xi}), \quad \bar{M}_{22}(L, \bar{\xi}) = k_f \bar{N}_{22}(L, \bar{\xi}), \quad (8.147)$$

$$\bar{M}_{12}(L, \bar{\xi}) = k_s \bar{N}_{12}(L, \bar{\xi}), \quad \bar{M}_{21}(\bar{x}, \bar{x}) = -\frac{\bar{a}_{21}^{ww}}{\epsilon_2 - \epsilon_1}, \quad (8.148)$$

$$\bar{M}_{21}(\bar{x}, 0) = 0, \quad \bar{M}_{12}(\bar{x}, \bar{x}) = -\frac{\bar{a}_{12}^{ww}}{\epsilon_1 - \epsilon_2}, \quad (8.149)$$

have the same structure with the controller kernel system. The well-posedness is therefore obtained following the same steps as in the proof in [?]. Therefore, there exists a unique solution $M, N \in L^\infty(\mathcal{T})$. The stability of target system (8.116)–(8.121) is equivalent to the error system. The observer gains matrices P and Q are obtained from the kernel matrices

$$P(x) = M(x, L) \begin{bmatrix} v_s^* & 0 \\ 0 & v_f^* \end{bmatrix}, \quad (8.150)$$

$$Q(x) = N(x, L) \begin{bmatrix} v_s^* & 0 \\ 0 & v_f^* \end{bmatrix}. \quad (8.151)$$

Note that the states estimation of the original traffic flow variables $(\hat{\rho}_f, \hat{v}_f, \hat{\rho}_s, \hat{v}_s)$ are obtained by the inverse transformation of (8.36).

The following conclusion is reached for the observer design.

Theorem 8.2 *Consider the linearized two-lane traffic ARZ model with the boundary conditions in (8.39)–(8.46), the initial conditions $\tilde{w}_i(x, 0), \tilde{v}_i(x, 0) \in L^\infty([0, L])$, the state estimates obtained from the collocated observer design (8.96)–(8.101) for $(\hat{w}_s, \hat{w}_f, \hat{v}_s, \hat{v}_f)$, and the output injection gains P and Q obtained in (8.151) by solving the kernels M and N from (8.130)–(8.134). The equilibrium $\check{w}_s = \check{w}_f = \check{v}_s = \check{v}_f = 0$ of the observer error system is stable and reached in finite time t_o given by (8.125).*

Proof Lemma 8.2, along with the backstepping transformation for the observer in (8.114), (8.115), yields stability and the convergence of the estimation errors $(\check{w}_s, \check{w}_f, \check{v}_s, \check{v}_f)$ to zero for $t > t_o$, given in (8.125). \square

Output-feedback controller

The output-feedback control laws for the slow and fast VSL are constructed by employing the states estimates generated by the collocated observer (8.96)–(8.101) in their respective full-state feedback laws (8.90), (8.91), which yields finite-time stability of the closed-loop system at the zero equilibrium.

Theorem 8.3 *Consider the linearized two-lane traffic ARZ model with the boundary conditions in (8.39)–(8.46), the initial conditions $\tilde{w}_i(x, 0), \tilde{v}_i(x, 0) \in L^\infty([0, L])$, and the output-feedback laws combining the full state feedback (8.90), (8.91) and the collocated observer (8.96)–(8.101), where the output injection gains are obtained by solving for the kernels M and N from the system (8.130)–(8.131). The equilibrium $(\rho_f, \rho_s, v_s, v_f) = (\hat{\rho}_f, \hat{\rho}_s, \hat{v}_s, \hat{v}_f) = (\rho_f^*, \rho_s^*, v_s^*, v_f^*)$ is finite-time stable and reached in t_{out} defined as*

$$t_{out} = t_o + t_f, \quad (8.152)$$

where t_o is given in (8.125) and t_f in (8.85).

Proof Theorem 8.2 guarantees that state estimates $(\hat{\rho}_f, \hat{\rho}_s, \hat{v}_s, \hat{v}_f)$ reach and remain at $(\rho_f, \rho_s, v_s, v_f)$ after $t = t_o$. Applying Theorem 8.1, one has that $(\rho_f, \rho_s, v_s, v_f)$ reach and remain at $(\rho_f^*, \rho_s^*, v_s^*, v_f^*)$ after $t = t_f$. Therefore, after $t = t_o + t_f$, we have the convergence of the state variables to the steady-states. Stability of the equilibrium can be established either from the explicit solutions of the target systems or using the Lyapunov stability of the target systems (for the observer error system and for the observer or the plant), along with the direct and inverse backstepping transformations. \square

8.5 Numerical Simulation

The control design presented in the previous sections are validated by numerical simulation. The simulation is performed for the linearized two-lane ARZ PDE model and the two-step Lax Wendroff method is used to approximate the solution. Both the fast-lane and slow-lane are considered in the congested regime. Steady-state density $\rho_s^* = 180$ veh/km, $v_s^* = 28.5$ km/h and $\rho_f^* = 90$ veh/km, $v_f^* = 33$ km/h are chosen given the maximum density $\rho_s^m = 220$ veh/km, $\rho_f^m = 142$ veh/km, $\gamma = 0.8$ and maximum velocity $v_m = 140$ km/h so that the traffic of both lanes are lightly congested. We consider the situation that overall drivers prefer remaining in the slow

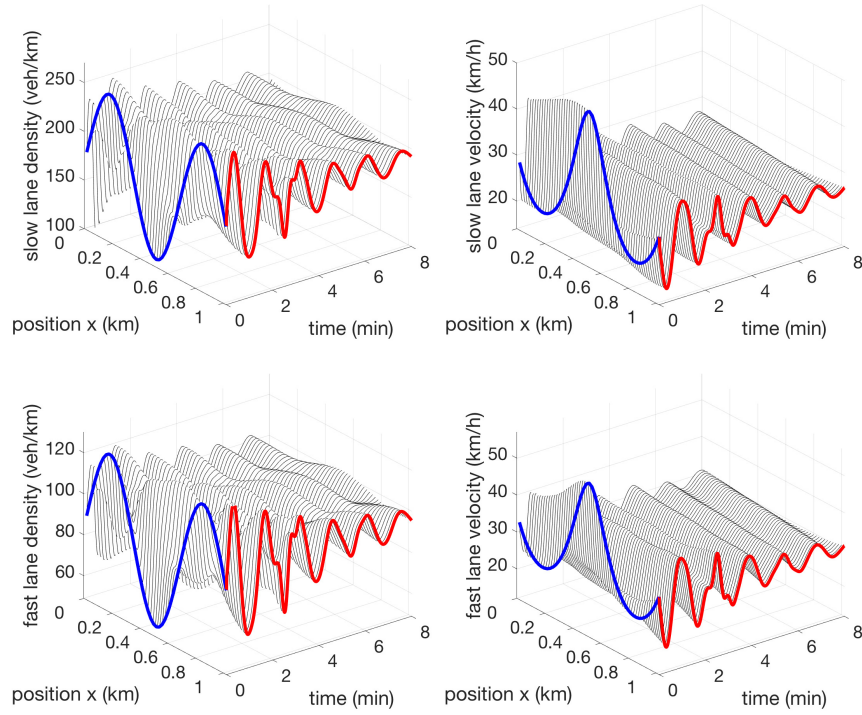


Fig. 8.4 Density and velocity of slow and fast lane traffic of open-loop system with sinusoid initial conditions.

lane rather than changing to the fast lane so that $T_f = 15$ s is chosen to be smaller than $T_s = 30$ s. Therefore, higher density traffic appears in the slow lane and it can contain a higher rate of traffic flow. The relaxation time is chosen as $T_f^e = 100$ s and $T_s^e = 200$ s.

output-feedback stabilization and performance

Since we are interested in stop-and-go traffic and its suppression, we assume that the initial traffic states are oscillatory around the equilibrium states. Hence, we implement sinusoidal initial conditions, which are highlighted in blue. The constant incoming flow and outgoing flow are considered for the open-loop simulation as shown in Fig. 8.4. Considering the steady-state velocity as the averaged traffic velocity, it takes around 2 minutes for both the fast-lane and slow-lane vehicles to leave the considered freeway segment. But the oscillations sustain for more than 12 minutes. The full state feedback stabilization results are shown in Fig. 8.5. The finite-time

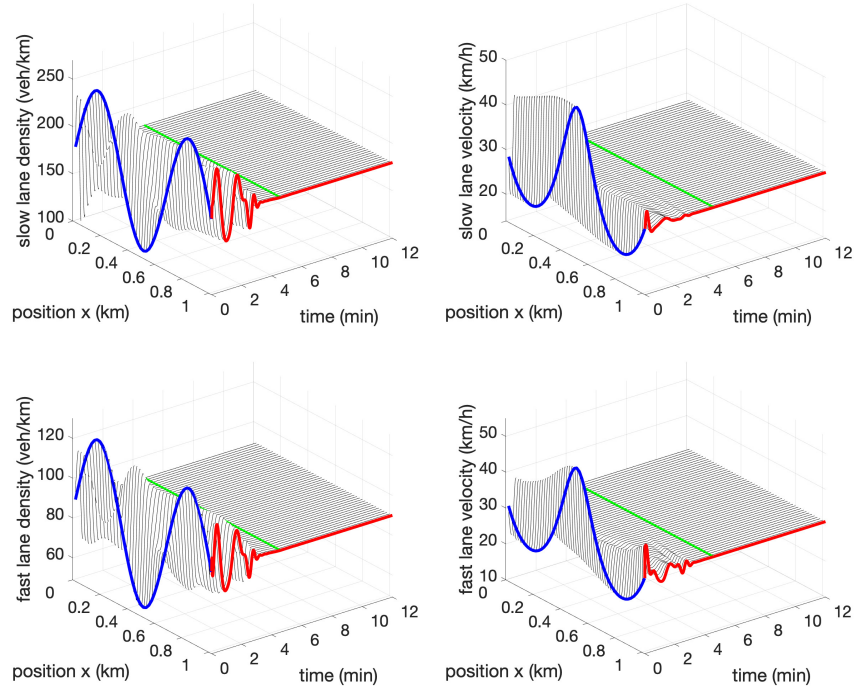


Fig. 8.5 Density and velocity of slow and fast lane traffic of closed-loop system with full-state feedback controllers.

convergence of the density and velocity to the spatially constant steady-states is achieved in $t_f = 5$ min, which is highlighted in green.

Combining the observer design and the full-state feedback controllers, we derive the output-feedback controllers and then simulate the closed-loop system in Fig. 8.6. The finite convergence time of the closed-loop with output-feedback controllers is $t = t_o + t_f = 10$ min, as illustrated in the figures with green highlighted lines. We can see that the states converge to the steady-state values before the green highlighted lines. The velocity control inputs that are displayed on the VSL for fast and slow lanes are plotted in Fig. 8.7. Compared with the slow lane velocity control input, the variation of the fast lane control input around the steady-state velocity is larger. For example, the output feedback driving speed advisory for vehicles in the fast lane to leave the segment varies in a range of 25 km/h to 44 km/h while that of the slow lane varies in a range of 26 km/h to 34 km/h.

For practical consideration, it is not feasible to directly implement the continuous time-varying velocity control inputs as shown in Fig. 8.7, since drivers need reaction time to follow the driving speed displayed by VSL. The digital post processing of the continuous in time control signals is thus required in the implementation of VSL and we briefly discuss it in the next section. It should also be noted that if VSL cannot

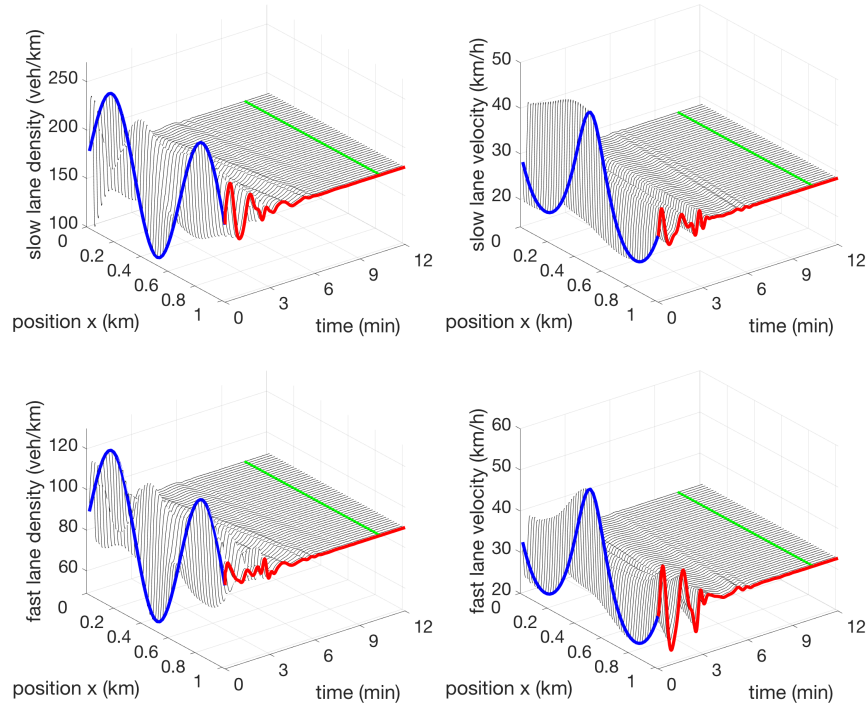


Fig. 8.6 Density and velocity of slow and fast lane closed-loop system with output-feedback controllers.

be changed discretely on the time scale of the stop-and-go oscillations, then such oscillations are not stabilizable by any VSL-implemented algorithm. For example, in Fig. 8.7, if VSL can only be changed every 2 minutes on the time scale exhibited by the stop-and-go oscillations in Fig. 8.4, no VSL control can stabilize such congested traffic.

The performance of the output-feedback controllers is evaluated for three performance indices which are total travel time (TTT), drivers' comfort and fuel consumption. The considered performance indices are defined as

$$J_{\text{fuel}} = \int_0^{t_{\text{sim}}} \int_0^L \max\{0, b_0 + b_1 v(x, t) + b_2 v(x, t) a(x, t) + b_3 a^2(x, t)\} \rho(x, t) dx dt \quad (8.153)$$

$$J_{\text{comfort}} = \int_0^{t_{\text{sim}}} \int_0^L (a(x, t)^2 + a_t(x, t)^2) \rho(x, t) dx dt \quad (8.154)$$

$$J_{\text{TTT}} = \int_0^{t_{\text{sim}}} \int_0^L \rho(x, t) dx dt \quad (8.155)$$

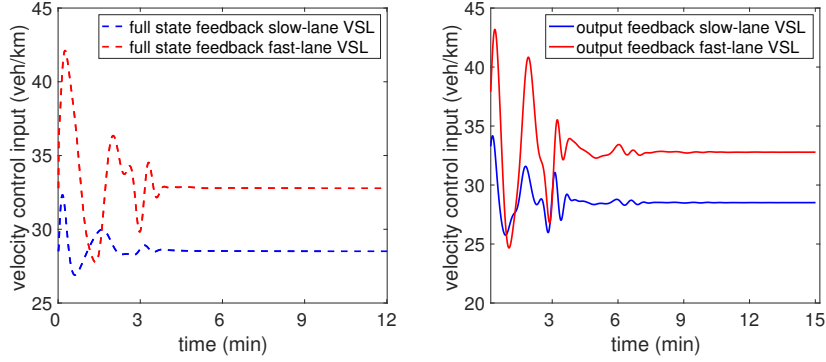


Fig. 8.7 Velocity control inputs of full-state feedback and output-feedback controllers for the slow and fast lanes.

according to [?] where $a(x, t)$ is defined as the local acceleration $a(x, t) = v_t(x, t) + v(x, t)v_x(x, t)$ and the parameters for fuel consumption are taken from [?] as $b_0 = 25 \cdot 10^{-3}$ l/s, $b_1 = 24.5 \cdot 10^{-6}$ l/m, $b_3 = 32.5 \cdot 10^{-9}$ l/s³/m², $b_4 = 125 \cdot 10^{-6}$ l/s²/m² for a $L = 1$ km, $t_{sim} = 12$ min. We denote $J_{X,open}$ as the performance indices with respect to the open-loop results, whereas $J_{X,output}$ as the indices with respect to the closed-loop results, where $X = \{\text{fuel, comfort, TTT}\}$. The improved performance indices are

$$\frac{J_{\text{fuel,output}}}{J_{\text{fuel,open}}} = 92.74\%, \quad (8.156)$$

$$\frac{J_{\text{comfort,output}}}{J_{\text{comfort,open}}} = 82.63\%, \quad (8.157)$$

$$\frac{J_{\text{TTT,output}}}{J_{\text{TTT,open}}} = 92.79\%. \quad (8.158)$$

The fuel consumption of total traffic reduces 7.26% with driver's comfort improved 17.37% and the total travel time reduced 7.21% for the closed-loop system with the output feedback VSL controllers in 12 min. The numerical simulation demonstrates that the proposed output-feedback control design not only stabilizes the two-lane traffic flow system in the finite time but also improves all the performance indices.

Different traffic scenarios, one-lane backstepping and PI controllers

To demonstrate the effect and relevance of the proposed VSL controllers, we compare the stabilization result for different traffic scenarios and simulate one-lane backstepping and PI controllers.

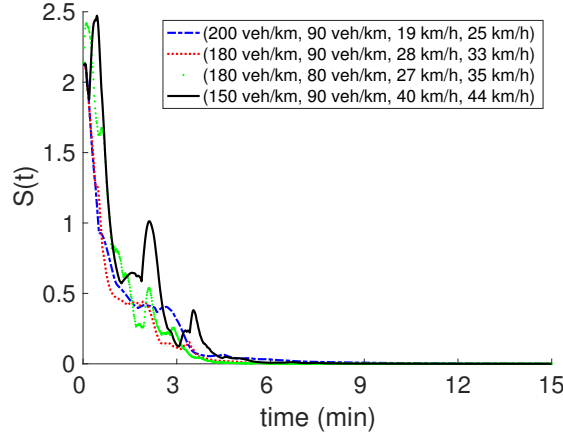


Fig. 8.8 Output stabilization for different traffic steady-states.

For different traffic scenarios, we evaluate the overall closed-loop stabilization result with the state variables in the L^∞ -norm, defined as $S(t) = S_s(t) + S_f(t)$, where

$$S_i(t) = \left\| \frac{\rho_i(x, t) - \rho_i^*}{\rho_i^*} \right\|_\infty + \left\| \frac{v_i(x, t) - v_i^*}{v_i^*} \right\|_\infty. \quad (8.159)$$

The stabilization result is demonstrated with the temporal evolution of the stabilization result $S(t)$, whose convergence to zero is guaranteed by Theorem 8.3. Four different traffic scenarios that are represented by different steady-states $(\rho_s^*, \rho_f^*, v_s^*, v_f^*)$ are plotted in Fig. 8.8. The same sinusoidal initial conditions around the steady-states are considered. The red dashed line represents the output-feedback stabilization result. We can see that the traffic becomes less dense from the blue dashed line to the black line. As the traffic density becomes smaller and velocity becomes bigger, the closed-loop system goes through a larger transient before being stabilized. This is because the faster velocity in the congested traffic requires a larger VSL control effort and induces a more oscillatory system behavior. On the other hand, comparing the red dashed line and green dotted line, it is found that the green dotted line shows a bigger transient than the red dashed line since it has larger density and velocity discrepancies between the fast and slow lane than that of the red dashed line. More lane-changing activities exist when the speed difference is larger between lanes.

For comparison, we consider the two-lane traffic as a general one-lane and impose the same displayed VSL values for the two lanes at the outlet. Then the lane-changing activities are ignored. Two existing control strategies for one-lane ARZ model are employed including the PDE backstepping VSL in [?] and PI control by VSL and ramp in [?]. The general one-lane density is defined as the lateral spatial summation and the averaged velocity is

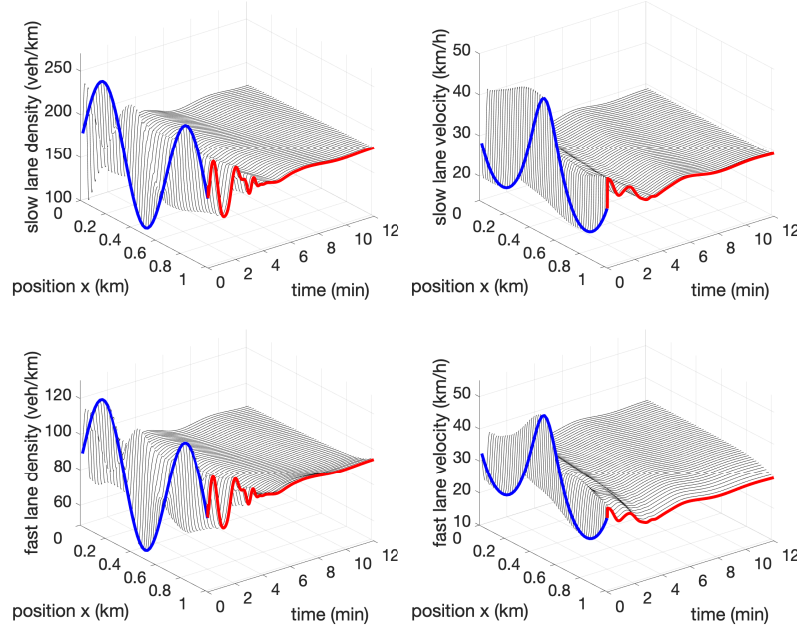


Fig. 8.9 Density and velocity of slow and fast lane closed-loop system with one-lane backstepping controller.

$$\rho_a(x, t) = \rho_s(x, t) + \rho_f(x, t), \quad (8.160)$$

$$v_a(x, t) = \frac{\rho_s(x, t)v_s(x, t) + \rho_f(x, t)v_f(x, t)}{\rho_a(x, t)}. \quad (8.161)$$

The control objective is to regulate the one-lane traffic to averaged steady-states $\rho_a^* = 270$ veh/m, $v_a^* = 29.8$ km/h. We use the previous model parameters and conduct the simulation under the same initial conditions. The two-lane traffic evolution is shown in Fig. 8.9. There are still oscillations when the same backstepping controller is applied to both lanes. Meanwhile, the steady-state velocity of the fast lane and slow lane slowly adapt to the general one-lane velocity v_a^* .

PI boundary feedback controllers are developed in [?] for the linearized ARZ model. Boundary values of velocity at the inlet is measured to construct one PI VSL implemented at the outlet, actuating the exit velocity of the two lanes. The PI controller is given by

$$v_a(L, t) = v_a^* + k_P^v \tilde{v}_a(0, t) + k_I^v \int_0^t (v_a(0, s) - v_a^*) ds, \quad (8.162)$$

where $k_P^v = -0.1$, $k_I^v = -0.02$ are the PI gains. The density and velocity in the fast and slow lane still oscillate, as shown in Fig. 8.10. The slow lane traffic increases in velocity and the fast lane traffic decreases in velocity, as a result of using a

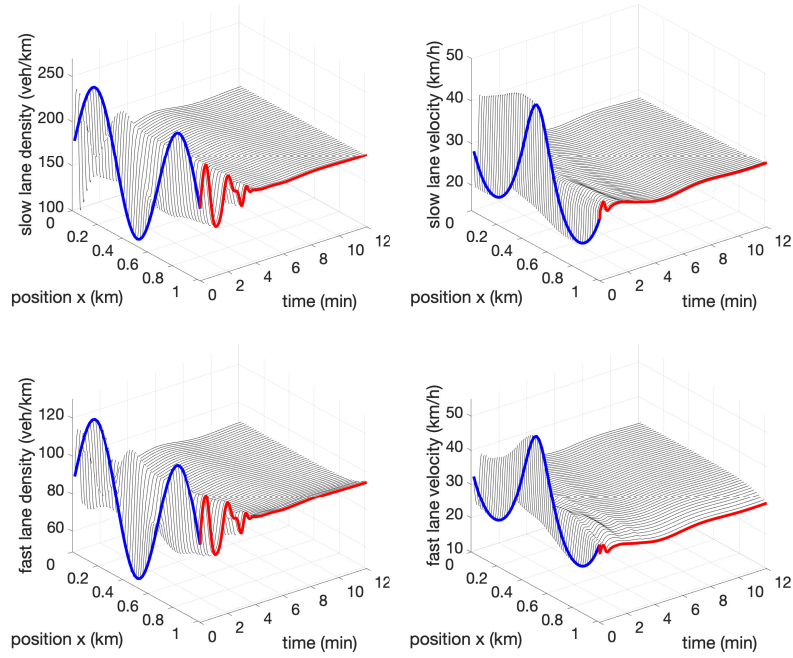


Fig. 8.10 Density and velocity of slow and fast lane closed-loop system with one-lane PI controller.

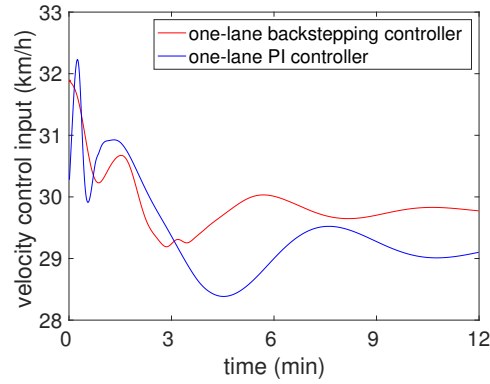


Fig. 8.11 Velocity control inputs of one-lane backstepping and PI.

single VSL. The backstepping and PI velocity control inputs are plotted in Fig. 8.11. The PI control signal has some offset relative to the steady-state v_a^* , in addition to oscillations. Both of the one-lane VSL control algorithms fail to obtain satisfactory stabilization results when applied to the two-lane traffic. This is because the inter-lane

activities and distinct fast and slow lane steady-states are neglected in the one-lane control designs.

8.6 Notes and References

This chapter has presented a solution to the output-feedback stabilization of stop-and-go oscillations in a congested two-lane traffic with lane changing. The finite-time convergence of the linearized two-lane ARZ model is achieved with two VSL actuating velocities at the outlet of a freeway segment. By taking the collocated boundary measurement of density variations, observers are designed for state estimation. The control designs are simulated for different traffic scenarios, evaluated with several performance indices and compared with two one-lane control approaches. This result paves the way for applying PDE backstepping techniques for multi-lane traffic with inter-lane activities. With suitable advances in coupled 2D hyperbolic PDEs, this work on two lanes is a stepping stone towards stabilization of oscillations in 2D traffic flows and lane-free traffic, including first-order models [?] and second-order models [?].

Chapter 9

Two-Class Traffic Control

9.1 Diverse Driver and Vehicle Classes: Additional PDEs Controlled by a Single Input

In this chapter, we develop an output-feedback control law to damp out oscillations in the condition of traffic that is congested and involves two classes of vehicles. A vehicle class is defined to be a group of driver-vehicle entities that share the same properties, see [?]. For instance a vehicle class may be characterized by the vehicle size and, therefore, inertia (small/large, light/heavy), driver's style in operating the vehicle (deferential/aggressive, cautious/rash, attentive/inattentive), propensity to delayed reaction (old/young, tired/fresh, under-the-influence/sober), and other factors.

With so many possible categories, and so many classes within each category, one can envision many combinations, resulting in dozens of classes of vehicles (young and tired driver of a large pickup truck, old and attentive driver of a small sporty car, and so on). In fact, one can envision finer classifications, on a continuum, rather than through coarse categories (tired vs. fresh). With many possible classes, and even a possible continuum of classes, one could be formulating problems much more general and complex than the problem with two vehicle classes which we tackle in this chapter. What our chapter offers should be regarded as a first step in a possible much more general direction of designing controller for the suppression of stop-and-go oscillations on a freeway with a very diverse population of vehicles and drivers. For problems with a finite number of classes the control design methodology would not differ substantively. Therefore, our deliberate restriction to two classes is relevant beyond what it offers on the face value. We restrict our attention to two classes for reasons of notational simplicity and conceptual clarity.

The interactions between different classes of vehicles and drivers lead to many phenomena such as the existence of more than one equilibrium state, frequent lane changing movements in congested traffic, fast vehicles overtaking slow vehicles, and platoons dispersion [?, ?, ?].

Multi-class traffic models are an important extension of single-class models, decomposing the homogeneous single class traffic flow into class-based macroscopic

component flows. For each component flow, PDEs of the single-class models are employed to describe traffic states including density and velocity. The first-order macroscopic multi-class traffic models are developed based on the LWR model [?, ?, ?]. The second-order extensions of the ARZ model can be found in [?, ?, ?, ?].

In this chapter, we adopt the macroscopic multi-class ARZ model [?]. In this model, the dynamics of each vehicle class is described with the density and velocity for each class, i.e., with two PDEs per class. The model of our two-class ARZ traffic, therefore, consists of four hyperbolic PDEs—two density PDEs and two velocity PDEs.

The stabilization problem of the two-class traffic is more challenging than stabilization of single-class traffic since instabilities arise not only from congestion within each class but also from interactions between the two classes of vehicles. In the macroscopic models, these interactions take place at each location on the freeway, in other words, as in every macroscopic model, multiple vehicle could be present at any location and, by extension, in multi-class traffic, vehicles of different classes can coexist at any location. The real-world interaction of vehicles of different classes, such as sports cars passing trucks, aggressive drivers passing defensive drivers, etc., is aggregated into the PDE models density and velocity states for the classes, rather than being microscopically captured.

In a multi-class model, the concept of “area occupancy” is introduced to describe how each class of vehicles affects the overall traffic dynamics. In particular, area occupancy is used in the traffic pressure and equilibrium velocity relationship, yielding a coupling between the two classes of vehicles.

We develop boundary feedback control laws in order to damp out traffic oscillations in the congested regime. As in the rest of the book, we employ the backstepping design to design a boundary controller. The design objective for backstepping is to stabilize the 4×4 heterodirectional hyperbolic PDE system, which arises from the two-class ARZ model. The control input actuates the traffic flow using a single ramp metering input at the outlet of the freeway segment.

The solvability of the problem with a single (ramp metering) input is a crucial difference between the two-class problem and the two-lane problem, the latter of which we studied in Chapter 8. While both the two-class and the two-lane problems involve one pair of density PDEs and one pair of velocity PDEs, totaling four PDEs in both cases, for suppressing the two-class stop-and-go oscillations a single ramp input suffices, whereas for suppressing the two-lane stop-and-go oscillations two VSL inputs are needed. The reason for this difference is not revealed by the ARZ models, namely, by the density and velocity PDEs. The reason for the controllability of the four-PDE model of two-class traffic with a single input is revealed by examining the differences between the two four-PDE models in the Riemann variables. In the Riemann variables, it is revealed that, while in the two-lane traffic there are two downstream waves and two upstream waves, in the two-class traffic there are three downstream waves and only one upstream wave. Therefore, it suffices to use a single input, to sever the destabilizing feedback from the three downstream waves into the single upstream wave.

We first design a full-state feedback law to achieve finite-time convergence of the density and velocity variations to the zero equilibrium. The state feedback controller is then combined with an anti-collocated observer, which we design in order to estimate the density and velocity states of the two classes of traffic. Hence, an output feedback control law is constructed. The performance of the proposed output-feedback controller is validated by simulation of the open-loop and closed-loop models, and also quantified by performance indices including fuel consumption, comfort and total travel time.

9.2 Two-class ARZ Traffic Model

The extended ARZ model for multi-class heterogeneous traffic in [?] is considered in its special two-class case. The two-class ARZ traffic model is given by

$$\partial_t \rho_1 + \partial_x (\rho_1 v_1) = 0, \quad (9.1)$$

$$\partial_t (v_1 + p_1(AO)) + v_1 \partial_x (v_1 + p_1(AO)) = \frac{V_{e,1}(AO) - v_1}{\tau_1}, \quad (9.2)$$

$$\partial_t \rho_2 + \partial_x (\rho_2 v_2) = 0, \quad (9.3)$$

$$\partial_t (v_2 + p_2(AO)) + v_2 \partial_x (v_2 + p_2(AO)) = \frac{V_{e,2}(AO) - v_2}{\tau_2}, \quad (9.4)$$

where each vehicle class is represented by the traffic density $\rho_i(x, t)$ and velocity $v_i(x, t)$, where $(x, t) \in [0, L] \times [0, \infty)$, $i = 1, 2$. The parameter L is the length of the freeway segment.

The traffic density $\rho_1(x, t)$ and velocity $v_1(x, t)$ refer to the first vehicle class and the traffic density $\rho_2(x, t)$ and velocity $v_2(x, t)$ refer to the second vehicle class. The traffic density $\rho_i(x, t)$ is defined as the number of vehicles in a given class per unit length, at location x at time t . The higher the traffic density ρ_i , the more crowding of vehicles of class i is present at a specific spatial point x . In addition, the higher the velocity $v_i(x, t)$, the faster the vehicles of class i at a specified spatial point in the freeway segment. This velocity of a class at a particular place and time is unrelated with the propensity of vehicles in a given class to go fast or slow, or accelerate fast or slow. For instance, if the two vehicle classes are heavy (potentially fast) and light (potentially slow) vehicles, it is entirely possible that, at a particular time and location, the vehicles from the “slow class” go faster than the vehicles of the “fast class.” The two-class ARZ model matches the reality in this regard—it is not uncommon to see trucks pass slow-moving high-performance cars on the freeway.

The non-zero terms on the right hand side of the four-PDE model above represent the adaption of velocity of the vehicles of each class to the desired velocity for that class, where τ_i is the adaptation time of class i .

The variable $AO(\rho_1, \rho_2)$ describes the area occupancy, defined as

$$AO(\rho_1, \rho_2) = \frac{a_1 L \rho_1 + a_2 L \rho_2}{WL}, \quad (9.5)$$

where a_i is the occupied surface per vehicle class i and W the width of the investigated freeway segment. The traffic densities of class 1 and class 2 are $\rho_1(x, t)$ and $\rho_2(x, t)$ on the considered freeway segment, the area occupancy $AO(\rho_1, \rho_2)$ is the percentage of occupied road space by both classes of vehicles. It holds that $0 \leq AO \leq 1$. The area occupancy depends on both densities since the occupied road surface is influenced by the vehicles of both classes.

The traffic pressure function $p_i(AO)$ is formulated as

$$p_i(AO) = V_i \left(\frac{AO(\rho_1, \rho_2)}{\overline{AO}_i} \right)^{\gamma_i}, \quad (9.6)$$

where V_i corresponds to the free-flow velocity, $\gamma_i > 1$ to the traffic pressure exponent and $0 < \overline{AO}_i \leq 1$ to the maximum area occupancy. The traffic pressure $p_i(AO)$ is the traffic pressure of class i vehicles and depends on the area occupancy. The higher the area occupancy, the higher the experienced traffic pressure. For instance, if a vehicle suddenly decelerates, then the following vehicle experiences a high traffic pressure forcing the follower vehicle to decelerate. Therefore, the free-flow velocity V_i represents the desired velocity of a driver, if no other vehicles of any class are present. The pressure exponent γ_i is a parameter that models the experience of the traffic pressure. The maximum area occupancy \overline{AO}_i describes the percentage of occupied road surface for which the corresponding vehicle class is jammed. To obtain physically meaningful results, $0 < \overline{AO} \leq 1$ holds. For instance, $\overline{AO}_2 = 0.8$ means that if 80% of the highway is covered by vehicles of *any* class, then the class 2 vehicles are jammed and therefore their desired velocity is zero.

Finally, the equilibrium speed- AO relationship is based on the Greenshield's model and given by

$$V_{e,i}(AO) = V_i \left(1 - \left(\frac{AO(\rho_1, \rho_2)}{\overline{AO}_i} \right)^{\gamma_i} \right), \quad (9.7)$$

which represents the desired velocity of the class i vehicles. If the area occupancy is at the maximum \overline{AO}_i , then the corresponding equilibrium speed- AO relationship value is $V_{e,i}(\overline{AO}_i) = 0$. In order to show the qualitative behavior of the traffic pressure function (9.6) and the equilibrium speed- AO relationship (9.7), both functions are plotted in Fig. 9.1. The plots on this figure indicate that, the more crowded the highway, corresponding to a higher area occupancy, the higher the traffic pressure and the lower the equilibrium speed.

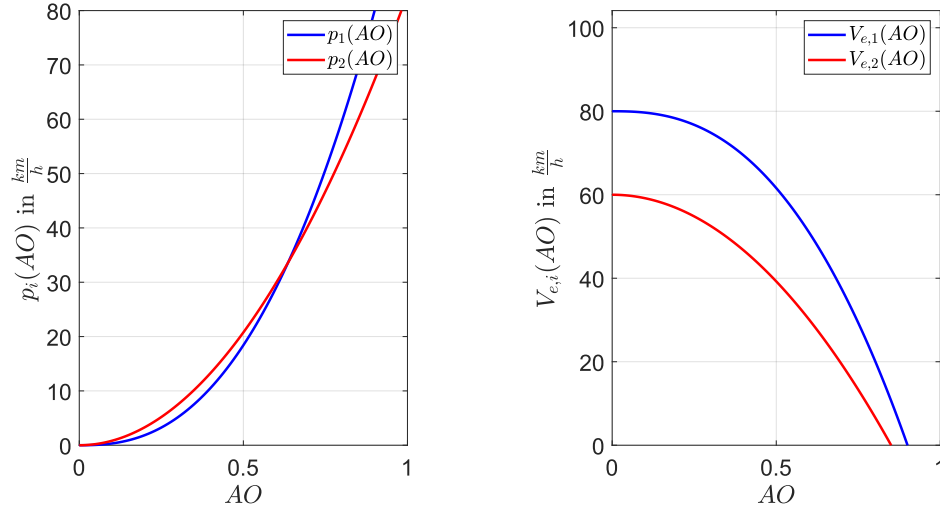


Fig. 9.1 Traffic pressure functions $p_1(AO)$ and $p_2(AO)$ (left) and equilibrium speed-AO relationships $V_{e,1}(AO)$ and $V_{e,2}(AO)$ (right) for the example parameter set $\gamma_1 = 2.5$, $V_1 = [80]km/h$, $\overline{AO} = 0.9$ for class 1 and $\gamma_2 = 2$, $V_2 = [60]km/h$, $\overline{AO}_2 = 0.85$ for class 2.

Linearized two-class PDE model

The two-class ARZ traffic model (9.1)–(9.4) is linearized around a constant equilibrium state $(\rho_1^*, v_1^*, \rho_2^*, v_2^*)$. Inserting this constant state in (9.1)–(9.4) yields the conditions

$$v_1^*(\rho_1^*, \rho_2^*) = V_{e,1}(AO(\rho_1^*, \rho_2^*)), \quad (9.8)$$

$$v_2^*(\rho_1^*, \rho_2^*) = V_{e,2}(AO(\rho_1^*, \rho_2^*)). \quad (9.9)$$

The equilibrium velocities are determined by the equilibrium densities ρ_1^* and ρ_2^* . The variations of the state variables $\rho_i(x, t)$ and $v_i(x, t)$ are defined as

$$\tilde{\rho}_i(x, t) = \rho_i(x, t) - \rho_i^*, \quad (9.10)$$

$$\tilde{v}_i(x, t) = v_i(x, t) - v_i^*, \quad (9.11)$$

for each class i and the linearized model equations are given by

$$J_t \begin{bmatrix} \tilde{\rho}_{1t} \\ \tilde{v}_{1t} \\ \tilde{\rho}_{2t} \\ \tilde{v}_{2t} \end{bmatrix} + J_x \begin{bmatrix} \tilde{\rho}_{1x} \\ \tilde{v}_{1x} \\ \tilde{\rho}_{2x} \\ \tilde{v}_{2x} \end{bmatrix} + J \begin{bmatrix} \tilde{\rho}_1 \\ \tilde{v}_1 \\ \tilde{\rho}_2 \\ \tilde{v}_2 \end{bmatrix} = \begin{bmatrix} 0 \\ 0 \\ 0 \\ 0 \end{bmatrix}, \quad (9.12)$$

where the introduced Jacobian matrices are

$$J_t = \begin{bmatrix} 1 & 0 & 0 & 0 \\ \beta_{11} & 1 & \beta_{12} & 0 \\ 0 & 0 & 1 & 0 \\ \beta_{21} & 0 & \beta_{22} & 1 \end{bmatrix}, \quad (9.13)$$

$$J_x = \begin{bmatrix} v_1^* & \rho_1^* & 0 & 0 \\ v_1^* \beta_{11} & v_1^* & v_1^* \beta_{12} & 0 \\ 0 & 0 & v_2^* & \rho_2^* \\ v_2^* \beta_{21} & 0 & v_2^* \beta_{22} & v_2^* \end{bmatrix}, \quad (9.14)$$

$$J = \begin{bmatrix} 0 & 0 & 0 & 0 \\ \frac{1}{\tau_1} \beta_{11} & \frac{1}{\tau_1} & \frac{1}{\tau_1} \beta_{12} & 0 \\ 0 & 0 & 0 & 0 \\ \frac{1}{\tau_2} \beta_{21} & 0 & \frac{1}{\tau_2} \beta_{22} & \frac{1}{\tau_2} \end{bmatrix}, \quad (9.15)$$

where

$$\beta_{ij}(\rho_1^*, \rho_2^*) = \left. \frac{\partial p_i(AO(\rho_1, \rho_2))}{\partial \rho_j} \right|_{\rho_1=\rho_1^*, \rho_2=\rho_2^*} \quad (9.16)$$

are introduced with $i, j = 1, 2$. The abbreviations $\beta_{ij}(\rho_1^*, \rho_2^*)$ represent the derivative of the class i traffic pressure function with respect to class j traffic density. The boundary conditions are assumed to be

$$\rho_1(0, t) = \rho_1^*, \quad (9.17)$$

$$\rho_2(0, t) = \rho_2^*, \quad (9.18)$$

$$q_1(0, t) + q_2(0, t) = q_1^* + q_2^*, \quad (9.19)$$

$$q_1(L, t) + q_2(L, t) = q_1^* + q_2^*, \quad (9.20)$$

where (9.19) and (9.20) assume that the constant total traffic flow enters and leaves the considered freeway segment, which is given by the sum of the class 1 and class 2 equilibrium flows q_1^* and q_2^* . The traffic flow of class i is defined as

$$q_i(x, t) = \rho_i(x, t) v_i(x, t). \quad (9.21)$$

Boundary conditions (9.17) and (9.18) indicate that the traffic densities of the incoming traffic flow are equivalent to the equilibrium densities. The linearization of the introduced boundary conditions (9.17)–(9.20) is

$$0 = \tilde{\rho}_1(0, t), \quad (9.22)$$

$$0 = \tilde{\rho}_2(0, t), \quad (9.23)$$

$$0 = v_1^* \tilde{\rho}_1(0, t) + \rho_1^* \tilde{v}_1(0, t) + v_2^* \tilde{\rho}_2(0, t) + \rho_2^* \tilde{v}_2(0, t), \quad (9.24)$$

$$0 = v_1^* \tilde{\rho}_1(L, t) + \rho_1^* \tilde{v}_1(L, t) + v_2^* \tilde{\rho}_2(L, t) + \rho_2^* \tilde{v}_2(L, t). \quad (9.25)$$

Free/congested regime analysis of two-class traffic

In the previous chapters the reader has encountered numerous times the two distinct regimes for one-class traffic: the free-flow regime and the congested regime. The free-flow regime is characterized by the fact that all traffic states travel in the downstream direction. In the free-flow regime, the two-class traffic model is a fourth-order homodirectional hyperbolic PDE system, whereas in the congested regime, there are traffic waves propagating upstream such that the traffic model becomes a heterodirectional hyperbolic PDE system.

The heterodirectional propagation phenomenon induces feedback coupling, with delays, among the counter-convecting PDEs, and causes the formation of stop-and-go traffic. Therefore, we investigate which choices of equilibrium densities and parameters lead to homodirectional/heterodirectional propagation of waves, namely free and congested traffic. The characteristic speeds are studied next.

The linearized PDEs (9.12) have a matrix J_t , which multiplies the time derivatives. This matrix is invertible. By inverting this matrix, one obtains a PDE system that is solved for the temporal velocities and given by

$$\begin{bmatrix} \tilde{\rho}_{1t} \\ \tilde{v}_{1t} \\ \tilde{\rho}_{2t} \\ \tilde{v}_{2t} \end{bmatrix} + \tilde{J}_x \begin{bmatrix} \tilde{\rho}_{1x} \\ \tilde{v}_{1x} \\ \tilde{\rho}_{2x} \\ \tilde{v}_{2x} \end{bmatrix} = \tilde{J} \begin{bmatrix} \tilde{\rho}_1 \\ \tilde{v}_1 \\ \tilde{\rho}_2 \\ \tilde{v}_2 \end{bmatrix} \quad (9.26)$$

with the new Jacobian matrices

$$\tilde{J}_x = \begin{bmatrix} v_1^* & \rho_1^* & 0 & 0 \\ 0 & v_1^* - \beta_{11}\rho_1^* & \beta_{12}(v_1^* - v_2^*) & -\beta_{12}\rho_2^* \\ 0 & 0 & v_2^* & \rho_2^* \\ \beta_{21}(v_2^* - v_1^*) & -\beta_{21}\rho_1^* & 0 & v_2^* - \beta_{22}\rho_2^* \end{bmatrix}$$

and

$$\tilde{J} = \begin{bmatrix} 0 & 0 & 0 & 0 \\ -\frac{1}{\tau_1}\beta_{11} & -\frac{1}{\tau_1} & -\frac{1}{\tau_1}\beta_{12} & 0 \\ 0 & 0 & 0 & 0 \\ -\frac{1}{\tau_2}\beta_{21} & 0 & -\frac{1}{\tau_2}\beta_{22} & -\frac{1}{\tau_2} \end{bmatrix}. \quad (9.27)$$

System (9.26) is still not in a conventional form for coupled hyperbolic PDEs from which the characteristic speeds could be noted by inspection. To find the characteristic speeds we compute the eigenvalues of \tilde{J}_x and obtain

$$\lambda_1 = v_1^*(\rho_1^*, \rho_2^*), \quad (9.28)$$

$$\lambda_2 = v_2^*(\rho_1^*, \rho_2^*), \quad (9.29)$$

$$\lambda_3 = \frac{v_1^*(\rho_1^*, \rho_2^*) + v_2^*(\rho_1^*, \rho_2^*) - \alpha_1(\rho_1^*, \rho_2^*) - \alpha_2(\rho_1^*, \rho_2^*)}{2} + \frac{\Delta(\rho_1^*, \rho_2^*)}{2}, \quad (9.30)$$

$$\lambda_4 = \frac{v_1^*(\rho_1^*, \rho_2^*) + v_2^*(\rho_1^*, \rho_2^*) - \alpha_1(\rho_1^*, \rho_2^*) - \alpha_2(\rho_1^*, \rho_2^*)}{2} - \frac{\Delta(\rho_1^*, \rho_2^*)}{2}, \quad (9.31)$$

where

$$\Delta(\rho_1^*, \rho_2^*) = \sqrt{(\alpha_2 \rho_2^* - \alpha_1 \rho_1^* + v_1^* - v_2^*)^2 + 4\alpha_1 \alpha_2 \rho_1^* \rho_2^*} \quad (9.32)$$

and

$$\alpha_i(\rho_1^*, \rho_2^*) = \beta_{ii}(\rho_1^*, \rho_2^*) = \left. \frac{\partial p_i(AO(\rho_1, \rho_2))}{\partial \rho_i} \right|_{\rho_1=\rho_1^*, \rho_2=\rho_2^*}. \quad (9.33)$$

For physical validity of the model as a model of traffic of human-operated vehicles, where no driver would operate his vehicle on the freeway in reverse, the equilibrium velocities of both vehicle classes are chosen to be positive, i.e. $v_1^* > 0$ and $v_2^* > 0$. Thus, the first two characteristic speeds (9.28) and (9.29) are positive. It is straightforward to find that the following inequality holds

$$\lambda_4 \leq \min\{\lambda_1, \lambda_2\} \leq \lambda_3 \leq \max\{\lambda_1, \lambda_2\}. \quad (9.34)$$

Since $\lambda_1 > 0$ and $\lambda_2 > 0$, (9.34) implies that λ_3 is also positive.

Hence, the only characteristic speed that may have a negative sign is λ_4 .

- Free-flow regime : $\lambda_1, \lambda_2, \lambda_3, \lambda_4 > 0$.

In the free regime, we have all the four traffic waves propagating in the downstream direction of traffic flow. All the characteristics speeds are positive. The density variations of class 1 transport downstream with characteristic speed of λ_1 and the density variations of class 2 transport downstream with characteristic speed of λ_2 . The velocity differences between the classes 1 and 2 are also carried downstream with the speed λ_3 . Finally the average velocity variations of the two classes transport downstream with the speed λ_4 .

- Congested regime : $\lambda_1, \lambda_2, \lambda_3 > 0, \lambda_4 < 0$.

In the congested regime, the first three waves transport with the vehicles in the downstream direction, while the fourth wave, governing the average of the variations in the class velocities, propagates in the upstream direction. Since the traffic is dense, the braking or accelerating action of the leading vehicles results in the following vehicles acting in the same fashion.

When the two classes of vehicles are the same, namely, when there is actually only one vehicle class on the freeway, we have $v_1^* = v_2^*$ and then $\lambda_1 = \lambda_2 = \lambda_3$. The fourth-order hyperbolic PDE system (9.26) reduces to the second-order one-class ARZ traffic model.

The critical value of the fourth characteristic speed, which distinguishes the two regimes, is $\lambda_4 = 0$. In case of the two-class traffic model, this boundary is a curve

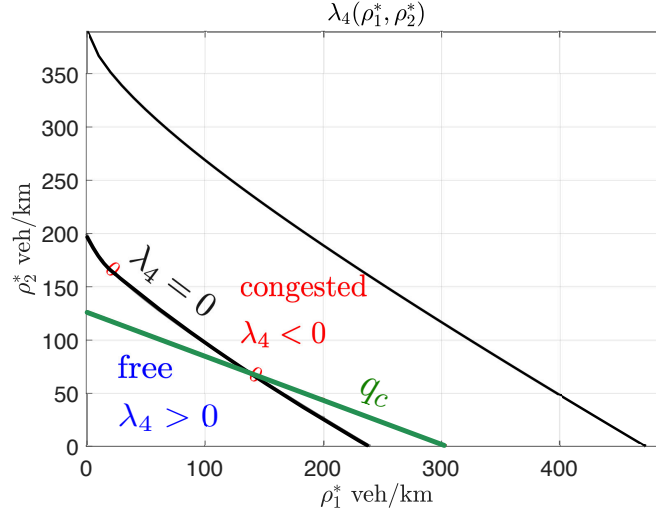


Fig. 9.2 The contour plots of the fourth characteristic speed $\lambda_4 = 0$ and the maximum flow rate q_c against ρ_1^* and ρ_2^* .

which can be drawn in the ρ_1^* - ρ_2^* -plane. In the one-class traffic, the boundary is equivalent to a single density which is the critical density segregating the free-flow and congested regime. The numerically computed boundary between the two regimes is plotted as a contour plot for an example parameter set in Fig. 9.2. The figure indicates that small values for equilibrium densities ρ_1^* and ρ_2^* correspond to $\lambda_4 > 0$, in which case homo-directional transport results, namely, the traffic is in free flow. When the density of either of the phases is large, we get that $\lambda_4 < 0$, namely, hetero-directional transport, congested traffic, and stop-and-go behavior.

Another interesting difference between the single-class and two-class traffic lie in the densities that maximize the traffic flow. In the general one-class traffic, the maximum traffic flow is achieved at the critical density of the fundamental diagram, as introduced in Chapter 1. In addition, the critical density is the same density that segregates the free-flow and congested density. However, in the two-class traffic Model, the densities that maximize the traffic flow and the ones that satisfy $\lambda_4 = 0$ are not the same set.

The equilibrium flow and density relation are given by,

$$Q_i(AO) = \rho_i V_i(AO). \quad (9.35)$$

For the two-class traffic, the total equilibrium total flow rate is defined as

$$Q_c(AO) = Q_1(AO(\rho_1, \rho_2)) + Q_2(AO(\rho_1, \rho_2)), \quad (9.36)$$

and the maximum equilibrium flow rate q_c is defined as

$$q_c(\rho_1, \rho_2) = Q_c(AO(\rho_1, \rho_2))|_{Q'_c(AO)=0}, \quad (9.37)$$

as plotted with the green line in Fig. 9.2.

9.3 Boundary control design model

In this section, we introduce the backstepping control design that stabilizes the linearized two-class ARZ traffic model using a boundary input. The preparation for backstepping control design is done using two transformations, including the transformation to the Riemann coordinates and a second spatial transformation to further simplify the equations.

We use ramp metering located at the outlet of the freeway segment to regulate the traffic outflow so that upstream traffic is stabilized in the freeway segment.

$$\tilde{q}_1(0, t) + \tilde{q}_2(0, t) = U(t). \quad (9.38)$$

The boundary condition (9.25) becomes

$$v_1^* \tilde{\rho}_1(L, t) + \rho_1^* \tilde{v}_1(L, t) + v_2^* \tilde{\rho}_2(L, t) + \rho_2^* \tilde{v}_2(L, t) = U(t). \quad (9.39)$$

Similar to the application of multi-phase flow in oil pipelines [?], a ramp metering works as a valve at the end of the pipe to regulate the total outgoing flow by controlling on-ramp flow.

The system is transformed to the Riemann coordinates to decouple the spatial derivatives. The Riemann variables $(\tilde{w}_1, \tilde{w}_2, \tilde{w}_3, \tilde{w}_4)$ are defined in the new coordinates. The linear state transformation is given by

$$\begin{bmatrix} \tilde{w}_1 \\ \tilde{w}_2 \\ \tilde{w}_3 \\ \tilde{w}_4 \end{bmatrix} = V^{-1} \begin{bmatrix} \tilde{\rho}_1 \\ \tilde{v}_1 \\ \tilde{\rho}_2 \\ \tilde{v}_2 \end{bmatrix} \quad (9.40)$$

where the matrix V is a standard similarity transformation that diagonalizes the Jacobian J_t and satisfies

$$\begin{bmatrix} \lambda_1 & 0 & 0 & 0 \\ 0 & \lambda_2 & 0 & 0 \\ 0 & 0 & \lambda_3 & 0 \\ 0 & 0 & 0 & \lambda_4 \end{bmatrix} = V^{-1} \tilde{J}_x V. \quad (9.41)$$

The entries of V are denoted as

$$V = \{v_{ij}\}_{1 \leq i \leq 4, 1 \leq j \leq 4} \quad (9.42)$$

and can be obtained from the eigenvectors of J_t . Since the eigenvalues λ_i of J_t are known explicitly, the eigenvectors of J_t can also be obtained explicitly and, therefore, V can be found explicitly, making the transformation (9.40) into the Riemann variables also available explicitly. We omit this explicit computation as it amounts to freshman linear algebra and it does not make a difference in the control design for the PDE system.

Substituting the transformation (9.40) into (9.12) yields the model equations in Riemann coordinates

$$\begin{bmatrix} \bar{w}_{1t} \\ \bar{w}_{2t} \\ \bar{w}_{3t} \\ \bar{w}_{4t} \end{bmatrix} + \begin{bmatrix} \lambda_1 & 0 & 0 & 0 \\ 0 & \lambda_2 & 0 & 0 \\ 0 & 0 & \lambda_3 & 0 \\ 0 & 0 & 0 & \lambda_4 \end{bmatrix} \begin{bmatrix} \bar{w}_{1x} \\ \bar{w}_{2x} \\ \bar{w}_{3x} \\ \bar{w}_{4x} \end{bmatrix} = \hat{J} \begin{bmatrix} \bar{w}_1 \\ \bar{w}_2 \\ \bar{w}_3 \\ \bar{w}_4 \end{bmatrix}, \quad (9.43)$$

where

$$\hat{J} = V^{-1} \tilde{J} V, \quad (9.44)$$

and the entries of the Jacobian \hat{J} are denoted by

$$\hat{J} = \{\hat{J}_{ij}\}_{1 \leq i \leq 4, 1 \leq j \leq 4}. \quad (9.45)$$

Since the coefficient matrix of the spatial derivatives is now diagonal, decoupling in spatial derivatives is achieved. The characteristic speeds (9.28)–(9.31) form a diagonal matrix because they are the eigenvalues of \tilde{J}_x . In addition, the same transformation is applied to the boundary conditions (9.22), (9.23), (9.24) and (9.39), yielding

$$\begin{bmatrix} \bar{w}_1(0, t) \\ \bar{w}_2(0, t) \\ \bar{w}_3(0, t) \end{bmatrix} = \hat{Q}_0 \bar{w}_4(0, t), \quad (9.46)$$

$$\bar{w}_4(L, t) = \hat{R}_1 \begin{bmatrix} \bar{w}_1(L, t) \\ \bar{w}_2(L, t) \\ \bar{w}_3(L, t) \end{bmatrix} + \hat{U}(t). \quad (9.47)$$

The matrices are given by

$$\hat{Q}_0 = - \begin{bmatrix} v_{11} & v_{12} & v_{13} \\ v_{31} & v_{32} & v_{33} \\ \kappa_1 & \kappa_2 & \kappa_3 \end{bmatrix}^{-1} \begin{bmatrix} v_{14} \\ v_{34} \\ \kappa_4 \end{bmatrix}, \quad (9.48)$$

$$\hat{R}_1 = - \frac{1}{\kappa_4} \begin{bmatrix} \kappa_1 & \kappa_2 & \kappa_3 \end{bmatrix}. \quad (9.49)$$

where

$$\kappa_i = v_1^* v_{1i} + \rho_1^* v_{2i} + v_2^* v_{3i} + \rho_2^* v_{4i}, \quad i = 1, 2, 3, 4, \quad (9.50)$$

The control input in (9.47) is obtained by transforming (9.38)

$$\hat{U}(t) = \frac{1}{\kappa_4} U(t). \quad (9.51)$$

The next transformation sets to zero the diagonal elements of \hat{J} in (9.43) and sorts the positive characteristic speeds (9.28)–(9.30) in the ascending order in the resulting diagonal matrix of coefficients that multiply the vector of spatial derivatives. We define an ascending order $\lambda_1 > \lambda_2$ without loss of generality. It is assumed that class 1 vehicles represent small-size and fast vehicles whereas class 2 describes big trucks which are large and slow. Thus, for the equilibrium velocities $v_1^* > v_2^*$ holds and therefore the ascending order of positive characteristic speeds is $\lambda_2 < \lambda_3 < \lambda_1$. We take the transformation

$$w_1 = e^{-\frac{j_{22}}{v_2^*} x} \bar{w}_2, \quad (9.52)$$

$$w_2 = e^{-\frac{j_{33}}{\lambda_3} x} \bar{w}_3, \quad (9.53)$$

$$w_3 = e^{-\frac{j_{11}}{v_1^*} x} \bar{w}_1, \quad (9.54)$$

$$w_4 = e^{-\frac{j_{44}}{\lambda_4} x} \bar{w}_4, \quad (9.55)$$

apply it to (9.43), and obtain the following PDEs:

$$\begin{bmatrix} w_{1t} \\ w_{2t} \\ w_{3t} \end{bmatrix} + \Lambda^+ \begin{bmatrix} w_{1x} \\ w_{2x} \\ w_{3x} \end{bmatrix} = \Sigma^{++}(x) \begin{bmatrix} w_1 \\ w_2 \\ w_3 \end{bmatrix} + \Sigma^{+-}(x) w_4, \quad (9.56)$$

$$w_{4t} - \Lambda^- w_{4x} = \Sigma^{-+}(x) \begin{bmatrix} w_1 \\ w_2 \\ w_3 \end{bmatrix}, \quad (9.57)$$

where

$$\Lambda^+ = \begin{bmatrix} v_2^* & 0 & 0 \\ 0 & \lambda_3 & 0 \\ 0 & 0 & v_1^* \end{bmatrix}, \quad (9.58)$$

$$\Lambda^- = -\lambda_4, \quad (9.59)$$

$$\Sigma^{++}(x) = \begin{bmatrix} 0 & \bar{J}_{12}(x) & \bar{J}_{13}(x) \\ \bar{J}_{21}(x) & 0 & \bar{J}_{23}(x) \\ \bar{J}_{31}(x) & \bar{J}_{32}(x) & 0 \end{bmatrix}, \quad (9.60)$$

$$\Sigma^{+-}(x) = [\bar{J}_{14}(x) \bar{J}_{24}(x) \bar{J}_{34}(x)]^T, \quad (9.61)$$

$$\Sigma^{-+}(x) = [\bar{J}_{41}(x) \bar{J}_{42}(x) \bar{J}_{43}(x)]. \quad (9.62)$$

The coefficients of the source term, $\bar{J}_{ij}(x)$, $i, j = 1, 2, 3, 4$, are:

$$\begin{aligned}
\bar{J}_{12}(x) &= \hat{J}_{23} e^{\left(\frac{J_{33}}{\lambda_3} - \frac{J_{22}}{v_2^*}\right)x}, & \bar{J}_{13}(x) &= \hat{J}_{21} e^{\left(\frac{J_{11}}{v_1^*} - \frac{J_{22}}{v_2^*}\right)x}, & \bar{J}_{14}(x) &= \hat{J}_{24} e^{\left(\frac{J_{44}}{\lambda_4} - \frac{J_{22}}{v_2^*}\right)x}, \\
\bar{J}_{21}(x) &= \hat{J}_{32} e^{\left(\frac{J_{22}}{v_2^*} - \frac{J_{33}}{\lambda_3}\right)x}, & \bar{J}_{23}(x) &= \hat{J}_{31} e^{\left(\frac{J_{11}}{v_1^*} - \frac{J_{33}}{\lambda_3}\right)x}, & \bar{J}_{24}(x) &= \hat{J}_{34} e^{\left(\frac{J_{44}}{\lambda_4} - \frac{J_{33}}{\lambda_3}\right)x}, \\
\bar{J}_{31}(x) &= \hat{J}_{12} e^{\left(\frac{J_{22}}{v_2^*} - \frac{J_{11}}{v_1^*}\right)x}, & \bar{J}_{32}(x) &= \hat{J}_{13} e^{\left(\frac{J_{33}}{\lambda_3} - \frac{J_{11}}{v_1^*}\right)x}, & \bar{J}_{34}(x) &= \hat{J}_{14} e^{\left(\frac{J_{44}}{\lambda_4} - \frac{J_{11}}{v_1^*}\right)x}, \\
\bar{J}_{41}(x) &= \hat{J}_{42} e^{\left(\frac{J_{22}}{v_2^*} - \frac{J_{44}}{\lambda_4}\right)x}, & \bar{J}_{42}(x) &= \hat{J}_{43} e^{\left(\frac{J_{33}}{\lambda_3} - \frac{J_{44}}{\lambda_4}\right)x}, & \bar{J}_{43}(x) &= \hat{J}_{41} e^{\left(\frac{J_{11}}{v_1^*} - \frac{J_{44}}{\lambda_4}\right)x}.
\end{aligned}$$

The diagonal elements of Λ^+ are sorted in an ascending order. The in-domain coupling terms $\Sigma^{++}(x)$, $\Sigma^{+-}(x)$ and $\Sigma^{-+}(x)$ are spatially varying functions. Their entries $\bar{J}_{ij}(x)$ are bounded and either positive or negative on the whole domain, depending on the sign of the corresponding \hat{J}_{ij} in (9.45). Applying the transformation (9.52)–(9.55) on the boundary conditions (9.46) and (9.47) yields

$$\begin{bmatrix} w_1(0, t) \\ w_2(0, t) \\ w_3(0, t) \end{bmatrix} = \bar{Q}_0 w_4(0, t), \quad (9.63)$$

$$w_4(L, t) = \bar{R}_1 \begin{bmatrix} w_1(L, t) \\ w_2(L, t) \\ w_3(L, t) \end{bmatrix} + \bar{U}(t) \quad (9.64)$$

with

$$\begin{aligned}
\bar{Q}_0 &= \begin{bmatrix} 0 & 0 & 1 \\ 1 & 0 & 0 \\ 0 & 1 & 0 \end{bmatrix}^{-1} \hat{Q}_0, \\
\bar{R}_1 &= \hat{R}_1 \begin{bmatrix} 0 & 0 & e^{\left(\frac{J_{11}}{v_1^*} - \frac{J_{44}}{\lambda_4}\right)L} \\ e^{\left(\frac{J_{22}}{v_2^*} - \frac{J_{44}}{\lambda_4}\right)L} & 0 & 0 \\ 0 & e^{\left(\frac{J_{33}}{\lambda_3} - \frac{J_{44}}{\lambda_4}\right)L} & 0 \end{bmatrix}. \quad (9.65)
\end{aligned}$$

In addition, the control input given in (9.64) is defined as

$$\bar{U}(t) = e^{-\frac{J_{44}}{\lambda_4}L} \hat{U}(t). \quad (9.66)$$

In summary, the control design model is given by (9.56), (9.57), (9.63) and (9.64). The system diagram is illustrated by Fig. 9.3. According to the sign of the characteristic speeds, the propagation direction for each state $w_i(x, t)$ is drawn in Figure 9.3. It shows that the control input $\bar{U}(t)$ actuates the outlet of the traffic system. In the congested traffic PDE system, there are three states transporting downstream and one state transporting in the upstream direction.

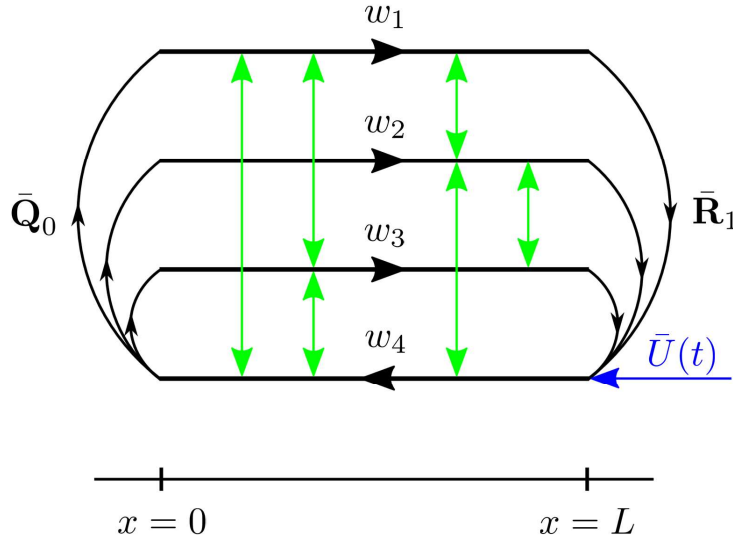


Fig. 9.3 Schematic diagram of the heterodirectional PDE model used for control design. The blue arrow indicates the location where the control input is applied, namely, the point of actuation. The green arrows represent the in-domain couplings between all four states.

The composition of the two transformations is summarized as

$$\begin{bmatrix} w_1 \\ w_2 \\ w_3 \\ w_4 \end{bmatrix} = T^{-1}(x) \begin{bmatrix} \tilde{\rho}_1 \\ \tilde{v}_1 \\ \tilde{\rho}_2 \\ \tilde{v}_2 \end{bmatrix} \Leftrightarrow \begin{bmatrix} \tilde{\rho}_1 \\ \tilde{v}_1 \\ \tilde{\rho}_2 \\ \tilde{v}_2 \end{bmatrix} = T(x) \begin{bmatrix} w_1 \\ w_2 \\ w_3 \\ w_4 \end{bmatrix}, \quad (9.67)$$

where

$$T^{-1}(x) = \begin{bmatrix} 0 & e^{-\frac{j_{22}}{v_2}x} & 0 & 0 \\ 0 & 0 & e^{-\frac{j_{33}}{\lambda_3}x} & 0 \\ e^{-\frac{j_{11}}{v_1}x} & 0 & 0 & 0 \\ 0 & 0 & 0 & e^{-\frac{j_{44}}{\lambda_4}x} \end{bmatrix} V^{-1}, \quad (9.68)$$

$$T(x) = V \begin{bmatrix} 0 & 0 & e^{\frac{j_{11}}{v_1}x} & 0 \\ e^{\frac{j_{22}}{v_2}x} & 0 & 0 & 0 \\ 0 & e^{\frac{j_{33}}{\lambda_3}x} & 0 & 0 \\ 0 & 0 & 0 & e^{\frac{j_{44}}{\lambda_4}x} \end{bmatrix}. \quad (9.69)$$

The above transformation $T(x)$ is a transformation that involves only spatial scaling. In addition to being linear, it is also local (it involves no integrals in x) and bounded (no derivatives in x). In addition, we have

$$\bar{U}(t) = e^{-\frac{j_{44}}{\lambda_4}L} \frac{1}{\kappa_4} U(t) \quad (9.70)$$

and the inverse is given by

$$U(t) = \kappa_4 e^{\frac{j_{44}}{\lambda_4}L} \bar{U}(t). \quad (9.71)$$

Since all the transformations are invertible, the stability properties of the linearized model (9.12) with boundary conditions (9.22)–(9.24), (9.39), and the control design model (9.56), (9.57), (9.63) and (9.64) are equivalent.

9.4 Full-state Feedback Control

In the section, a full-state feedback control design is proposed for the system of four coupled hyperbolic PDEs given by (9.56) and (9.57) with boundary conditions (9.63) and (9.64). The control objective is to achieve the stabilization of the states to zero equilibrium in finite time. The full-state feedback controller is designed using the backstepping method for general hetero-directional coupled hyperbolic PDEs, as stated in Chapter 2. The essential idea is to transform the coupled hyperbolic PDEs to a cascade target system. The control law is chosen such that the instabilities of the system are eliminated through the application of a boundary control input.

The states of the target system are denoted as $(\alpha_1, \alpha_2, \alpha_3, \beta)$. The kernels of the backstepping transformation are denoted by $K(x, \xi)$ and $L_{11}(x, \xi)$. The backstepping transformation is defined as

$$\alpha_1(x, t) = w_1(x, t), \quad (9.72)$$

$$\alpha_2(x, t) = w_2(x, t), \quad (9.73)$$

$$\alpha_3(x, t) = w_3(x, t), \quad (9.74)$$

$$\beta(x, t) = w_4(x, t) - \int_0^x \left(K(x, \xi) \begin{bmatrix} w_1(\xi, t) \\ w_2(\xi, t) \\ w_3(\xi, t) \end{bmatrix} + L_{11}(x, \xi) w_4(\xi, t) \right) d\xi, \quad (9.75)$$

where

$$K(x, \xi) = \begin{bmatrix} k_{11}(x, \xi) & k_{12}(x, \xi) & k_{13}(x, \xi) \end{bmatrix} \quad (9.76)$$

and $L_{11}(x, \xi)$ are defined on a triangular domain $\mathcal{T} = \{0 \leq \xi \leq x \leq 1\}$. The kernels $K(x, \xi)$ and $L_{11}(x, \xi)$ will be determined later on.

The target system is postulated as

$$\begin{aligned} \begin{bmatrix} \alpha_{1t} \\ \alpha_{2t} \\ \alpha_{3t} \end{bmatrix} &= -\Lambda^+ \begin{bmatrix} \alpha_{1x} \\ \alpha_{2x} \\ \alpha_{3x} \end{bmatrix} + \Sigma^{++}(x) \begin{bmatrix} \alpha_1 \\ \alpha_2 \\ \alpha_3 \end{bmatrix} \\ &\quad + \Sigma^{+-}(x)\beta + \int_0^x C^+(x, \xi) \begin{bmatrix} \alpha_1(\xi, t) \\ \alpha_2(\xi, t) \\ \alpha_3(\xi, t) \end{bmatrix} d\xi \\ &\quad + \int_0^x C^-(x, \xi)\beta(\xi, t) d\xi, \end{aligned} \quad (9.77)$$

$$\beta_t = \Lambda^- \beta_x. \quad (9.78)$$

The coefficients $C^+(x, \xi) \in \mathbb{R}^{3 \times 3}$ and $C^-(x, \xi) \in \mathbb{R}^{3 \times 1}$ are defined on the same triangular domain \mathcal{T} and will be given later. The boundary conditions of the target system are formulated as

$$\begin{bmatrix} \alpha_1(0, t) \\ \alpha_2(0, t) \\ \alpha_3(0, t) \end{bmatrix} = \bar{Q}_0 \beta(0, t), \quad (9.79)$$

$$\beta(L, t) = 0. \quad (9.80)$$

For $t \geq 0, x \in [0, L]$, the target system (9.77)–(9.80) converges to its equilibrium at zero

$$\alpha_{e,i}(x) \equiv \beta_e(x) \equiv 0, \quad i = 1, 2, 3, \quad (9.81)$$

in the finite time

$$t_F = \frac{L}{\lambda_2} + \frac{L}{-\lambda_4}. \quad (9.82)$$

The proof of stability of this target system is a special case of Lemma 2.1 and thus omitted in this section.

Taking the derivatives of (9.75) with respect to space and time, substituting the resulting derivatives and (9.63) into (9.78) yields the kernel equations that determine $K(x, \xi)$ and $L_{11}(x, \xi)$. The kernel equations are given by the following coupled first order hyperbolic PDEs as well as four boundary conditions

$$-\Lambda^- K_x(x, \xi) + K_\xi(x, \xi) \Lambda^+ = -K(x, \xi) \Sigma^{++}(\xi) - L_{11}(x, \xi) \Sigma^{-+}(\xi), \quad (9.83)$$

$$-\Lambda^- L_{11x}(x, \xi) - L_{11\xi}(x, \xi) \Lambda^- = -K(x, \xi) \Sigma^{+-}(\xi), \quad (9.84)$$

$$K(x, 0) \Lambda^+ \bar{Q}_0 - L_{11}(x, 0) \Lambda^- = 0, \quad (9.85)$$

$$K(x, x) \Lambda^+ + \Lambda^- K(x, x) = -\Sigma^{-+}(x). \quad (9.86)$$

Substituting Λ^- , $K(x, \xi)$, Λ^+ , $\Sigma^{++}(\xi)$, $\Sigma^{-+}(\xi)$, $\Sigma^{+-}(\xi)$ and denoting the entries of $\bar{Q}_0 = \{\bar{Q}_{0i1}\}_{1 \leq i \leq 3}$, the kernel equations in matrix form become

$$\lambda_4 \begin{bmatrix} k_{11x} \\ k_{12x} \\ k_{13x} \\ L_{11x} \end{bmatrix} + \begin{bmatrix} v_2^* & 0 & 0 & 0 \\ 0 & \lambda_3 & 0 & 0 \\ 0 & 0 & v_1^* & 0 \\ 0 & 0 & 0 & \lambda_4 \end{bmatrix} \begin{bmatrix} k_{11\xi} \\ k_{12\xi} \\ k_{13\xi} \\ L_{11\xi} \end{bmatrix} = \begin{bmatrix} 0 & -\bar{J}_{21}(\xi) & -\bar{J}_{31}(\xi) & -\bar{J}_{41}(\xi) \\ -\bar{J}_{12}(\xi) & 0 & -\bar{J}_{32}(\xi) & -\bar{J}_{42}(\xi) \\ -\bar{J}_{13}(\xi) & -\bar{J}_{23}(\xi) & 0 & -\bar{J}_{43}(\xi) \\ -\bar{J}_{14}(\xi) & -\bar{J}_{24}(\xi) & -\bar{J}_{34}(\xi) & 0 \end{bmatrix} \begin{bmatrix} k_{11} \\ k_{12} \\ k_{13} \\ L_{11} \end{bmatrix} \quad (9.87)$$

with boundary condition at $\xi = 0$,

$$\begin{bmatrix} \bar{Q}_{011}v_2^* & \bar{Q}_{021}\lambda_3 & \bar{Q}_{031}v_1^* & \lambda_4 \end{bmatrix} \begin{bmatrix} k_{11}(x, 0) \\ k_{12}(x, 0) \\ k_{13}(x, 0) \\ L_{11}(x, 0) \end{bmatrix} = 0, \quad (9.88)$$

and boundary conditions at $\xi = x$,

$$k_{11}(x, x) = \frac{\bar{J}_{41}(x)}{\lambda_4 - v_2^*}, \quad (9.89)$$

$$k_{12}(x, x) = \frac{\bar{J}_{42}(x)}{\lambda_4 - \lambda_3}, \quad (9.90)$$

$$k_{13}(x, x) = \frac{\bar{J}_{43}(x)}{\lambda_4 - v_1^*}. \quad (9.91)$$

Following [?], it is straightforward to show that the kernel equations (9.83)–(9.86) are well-posed and thus there exist unique solutions $K(x, \xi)$ and $L_{11}(x, \xi)$ in $L^\infty(\mathcal{T})$. Moreover, solving the equations (9.84) and (9.85) with the method of characteristics yields

$$L_{11}(x, \xi) = -\frac{1}{\lambda_4} K(x - \xi, 0) \Lambda^+ \bar{Q}_0 + \int_0^{-\frac{\xi}{\lambda_4}} K(\lambda_4 v + x, \lambda_4 v + \xi) \Sigma^{+-}(\lambda_4 v + \xi) dv. \quad (9.92)$$

Substituting (9.92) into the remaining PDEs (9.83) reduces the kernel equations to three coupled first-order hyperbolic PDEs with three boundary conditions

$$\begin{aligned}
0 = & \lambda_4 K_x(x, \xi) + \Lambda^+ K_\xi(x, \xi) + K(x, \xi) \Sigma^{++}(\xi) - \frac{1}{\lambda_4} K(x - \xi, 0) \Lambda^+ \bar{Q}_0 \Sigma^{-+}(\xi) \\
& + \int_0^{-\frac{\xi}{\lambda_4}} K(\lambda_4 v + x, \lambda_4 v + \xi) \Sigma^{+-}(\lambda_4 v + \xi) dv \Sigma^{-+}(\xi)
\end{aligned} \tag{9.93}$$

$$0 = K(x, x) \Lambda^+ + \Lambda^- K(x, x) + \Sigma^{-+}(x) \tag{9.94}$$

Furthermore, taking the derivatives of (9.72)–(9.74) with respect to space and time and substituting (9.75) and (9.56) into (9.77) yields

$$C^-(x, \xi) = \Sigma^{+-}(x) L(x, \xi) + \int_\xi^x C^-(x, s) L(s, \xi) ds, \tag{9.95}$$

$$C^+(x, \xi) = \Sigma^{+-}(x) K(x, \xi) + \int_\xi^x C^-(x, s) K(s, \xi) ds. \tag{9.96}$$

Finally, evaluating (9.75) at $x = L$ and then substituting (9.64) and (9.80) into it, we obtain the full-state feedback control law

$$\bar{U}(t) = -\bar{R}_1 \begin{bmatrix} w_1(L, t) \\ w_2(L, t) \\ w_3(L, t) \end{bmatrix} \int_0^L \left(K(L, \xi) \begin{bmatrix} w_1(\xi, t) \\ w_2(\xi, t) \\ w_3(\xi, t) \end{bmatrix} + L_{11}(L, \xi) w_4(\xi, t) \right) d\xi. \tag{9.97}$$

In order to formulate the control law with the original physical variables, i.e. the densities and velocities of two classes, we apply the inverse transformation to the states. The transformation matrix $T^{-1}(x)$ in (9.68), is represented as

$$T^{-1}(x) = \begin{bmatrix} T_u^{-1}(x) \\ T_l^{-1}(x) \end{bmatrix}, \tag{9.98}$$

where $T_u^{-1}(x) \in \mathbb{R}^{3 \times 4}$ and $T_l^{-1}(x) \in \mathbb{R}^{1 \times 4}$. Hence, the states of the control design model can be formulated as

$$\begin{bmatrix} w_1(\xi, t) \\ w_2(\xi, t) \\ w_3(\xi, t) \end{bmatrix} = T_u^{-1}(\xi) \begin{bmatrix} \tilde{\rho}_1(\xi, t) \\ \tilde{v}_1(\xi, t) \\ \tilde{\rho}_2(\xi, t) \\ \tilde{v}_2(\xi, t) \end{bmatrix}, \tag{9.99}$$

$$w_4(L, t) = T_l^{-1}(\xi) \begin{bmatrix} \tilde{\rho}_1(\xi, t) \\ \tilde{v}_1(\xi, t) \\ \tilde{\rho}_2(\xi, t) \\ \tilde{v}_2(\xi, t) \end{bmatrix} \tag{9.100}$$

and the control law after applying the inverse input transformation (9.71) becomes

$$\begin{aligned}
U(t) = & -\kappa_4 e^{\frac{j_{44}}{\lambda_4} L} \bar{R}_1 T_u^{-1}(L) \begin{bmatrix} \rho_1(L, t) - \rho_1^* \\ v_1(L, t) - v_1^* \\ \rho_2(L, t) - \rho_2^* \\ v_2(L, t) - v_2^* \end{bmatrix} \\
& - \kappa_4 e^{\frac{j_{44}}{\lambda_4} L} \int_0^L K(L, \xi) T_u^{-1}(\xi) \begin{bmatrix} \rho_1(\xi, t) - \rho_1^* \\ v_1(\xi, t) - v_1^* \\ \rho_2(\xi, t) - \rho_2^* \\ v_2(\xi, t) - v_2^* \end{bmatrix} d\xi \\
& - \kappa_4 e^{\frac{j_{44}}{\lambda_4} L} \int_0^L L_{11}(L, \xi) T_l^{-1}(\xi) \begin{bmatrix} \rho_1(\xi, t) - \rho_1^* \\ v_1(\xi, t) - v_1^* \\ \rho_2(\xi, t) - \rho_2^* \\ v_2(\xi, t) - v_2^* \end{bmatrix} d\xi. \quad (9.101)
\end{aligned}$$

The result is now summarized in the following theorem.

Theorem 9.1 *Consider the linearized two-class ARZ traffic model (9.12) by $(\tilde{\rho}_1, \tilde{\rho}_2, \tilde{v}_1, \tilde{v}_2)$, with the boundary conditions (9.22)–(9.24) and (9.39), the initial conditions $(\tilde{\rho}_1(x, 0), \tilde{v}_1(x, 0), \tilde{\rho}_2(x, 0), \tilde{v}_2(x, 0)) \in \mathcal{L}^\infty([0, L])$, and a full-state feedback control law (9.101), where the kernels $K(x, \xi)$ and $L_{11}(x, \xi)$ are obtained by solving the kernel equations (9.93) and (9.94). The equilibrium $(\rho_1^*, \rho_2^*, v_1^*, v_2^*)$ is stable and reached in finite time t_F , given by (9.82).*

The full-state feedback law in (9.101) requires measurements of the densities and velocities of both classes at every spatial point. In practice, it is usually not feasible to measure the densities and velocities at every spatial point. Therefore, it is important to develop an observer for traffic state estimation with only boundary sensing of the traffic states.

9.5 Anti-allocated Boundary Observer Design

In this section, an observer design for the estimation of the full traffic state from its boundary measurements is proposed. In particular, an anti-allocated boundary observer is designed, i.e., the sensing of boundary states is performed at the opposite boundary from the one where the control input acts.

It is assumed that

$$\bar{y}(t) = w_4(0, t), \quad (9.102)$$

is measured. This signal is obtained by measuring the densities $\rho_i(0, t)$ as well as velocities $v_i(0, t)$ and applying the transformation (9.67) afterwards.

The observer states $\hat{w}_c = (\hat{w}_1, \hat{w}_2, \hat{w}_3, \hat{w}_4)^T$ are estimates of the control design model states $w_c = (w_1, w_2, w_3, w_4)^T$. The observer is given

$$\begin{bmatrix} \hat{w}_{1t} \\ \hat{w}_{2t} \\ \hat{w}_{3t} \end{bmatrix} = -\Lambda^+ \begin{bmatrix} \hat{w}_{1x} \\ \hat{w}_{2x} \\ \hat{w}_{3x} \end{bmatrix} + \Sigma^{++}(x) \begin{bmatrix} \hat{w}_1 \\ \hat{w}_2 \\ \hat{w}_3 \end{bmatrix} + \Sigma^{+-}(x) \hat{w}_4 \\ - P^+(x)(\hat{w}_4(0, t) - w_4(0, t)), \quad (9.103)$$

$$\hat{w}_{4t} = \Lambda^- \hat{w}_{4x} + \Sigma^{-+}(x) \begin{bmatrix} \hat{w}_1 \\ \hat{w}_2 \\ \hat{w}_3 \end{bmatrix} \\ - P_{11}^-(x)(\hat{w}_4(0, t) - w_4(0, t)), \quad (9.104)$$

with the boundary conditions

$$\begin{bmatrix} \hat{w}_1(0, t) \\ \hat{w}_2(0, t) \\ \hat{w}_3(0, t) \end{bmatrix} = \bar{Q}_0 w_4(0, t), \quad (9.105)$$

$$\hat{w}_4(L, t) = \bar{R}_1 \begin{bmatrix} \hat{w}_1(L, t) \\ \hat{w}_2(L, t) \\ \hat{w}_3(L, t) \end{bmatrix} + \bar{U}(t), \quad (9.106)$$

where the output injection gains $P^+(x)$ and $P_{11}^-(x)$ need to be designed such that estimation errors converge to zero.

The estimation errors are defined as

$$\tilde{w}_i(x, t) = \hat{w}_i(x, t) - w_i(x, t), \quad i = 1, 2, 3, 4. \quad (9.107)$$

Subtracting the linearized PDEs model (9.56), (9.57), (9.63) and (9.64) from the observer equations (9.103)–(9.106) yields the following error system

$$\begin{bmatrix} \tilde{w}_{1t} \\ \tilde{w}_{2t} \\ \tilde{w}_{3t} \end{bmatrix} = -\Lambda^+ \begin{bmatrix} \tilde{w}_{1x} \\ \tilde{w}_{2x} \\ \tilde{w}_{3x} \end{bmatrix} + \Sigma^{++}(x) \begin{bmatrix} \tilde{w}_1 \\ \tilde{w}_2 \\ \tilde{w}_3 \end{bmatrix} \\ + \Sigma^{+-}(x) \tilde{w}_4 - P^+(x) \tilde{w}_4(0, t), \quad (9.108)$$

$$\tilde{w}_{4t} = \Lambda^- \tilde{w}_{4x} + \Sigma^{-+}(x) \begin{bmatrix} \tilde{w}_1 \\ \tilde{w}_2 \\ \tilde{w}_3 \end{bmatrix} \\ - P_{11}^-(x) \tilde{w}_4(0, t) \quad (9.109)$$

with the boundary conditions

$$\begin{bmatrix} \tilde{w}_1(0, t) \\ \tilde{w}_2(0, t) \\ \tilde{w}_3(0, t) \end{bmatrix} = 0, \quad (9.110)$$

$$\tilde{w}_4(L, t) = \bar{R}_1 \begin{bmatrix} \tilde{w}_1(L, t) \\ \tilde{w}_2(L, t) \\ \tilde{w}_3(L, t) \end{bmatrix}. \quad (9.111)$$

Using the backstepping method, the output injection gains are designed such that the error system converges to the equilibrium at zero in finite time. Similar to the control design, a target system and a backstepping transformation are defined in the observer design. The output injections gains $P^+(x)$ and $P_{11}^-(x)$ are chosen such that the equilibrium at zero of the target system is reached in finite time. The state of the target system is denoted as $(\tilde{\alpha}_1, \tilde{\alpha}_2, \tilde{\alpha}_3, \tilde{\beta})$ and the kernels introduced in the backstepping transformation are $M(x, \xi)$ and $N_{11}(x, \xi)$.

The backstepping transformation is postulated as

$$\begin{bmatrix} \tilde{w}_1(x, t) \\ \tilde{w}_2(x, t) \\ \tilde{w}_3(x, t) \end{bmatrix} = \begin{bmatrix} \tilde{\alpha}_1(x, t) \\ \tilde{\alpha}_2(x, t) \\ \tilde{\alpha}_3(x, t) \end{bmatrix} + \int_0^x M(x, \xi) \tilde{\beta}(\xi, t) d\xi, \quad (9.112)$$

$$\tilde{w}_4(x, t) = \tilde{\beta}(x, t) + \int_0^x N_{11}(x, \xi) \tilde{\beta}(\xi, t) d\xi, \quad (9.113)$$

where

$$M(x, \xi) = [m_{11}(x, \xi) \ m_{21}(x, \xi) \ m_{31}(x, \xi)]^T. \quad (9.114)$$

The kernels $M(x, \xi)$ and $N_{11}(x, \xi)$ are defined in the triangular domain $\mathcal{T} = \{0 \leq \xi \leq x \leq 1\}$. The target system is chosen as

$$\begin{bmatrix} \tilde{\alpha}_{1t} \\ \tilde{\alpha}_{2t} \\ \tilde{\alpha}_{3t} \end{bmatrix} = -\Lambda^+ \begin{bmatrix} \tilde{\alpha}_{1x} \\ \tilde{\alpha}_{2x} \\ \tilde{\alpha}_{3x} \end{bmatrix} + \Sigma^{++}(x) \begin{bmatrix} \tilde{\alpha}_1 \\ \tilde{\alpha}_2 \\ \tilde{\alpha}_3 \end{bmatrix} + \int_0^x D^+(x, \xi) \begin{bmatrix} \tilde{\alpha}_1(\xi, t) \\ \tilde{\alpha}_2(\xi, t) \\ \tilde{\alpha}_3(\xi, t) \end{bmatrix} d\xi, \quad (9.115)$$

$$\tilde{\beta}_t = \Lambda^- \tilde{\beta}_x + \Sigma^{--}(x) \begin{bmatrix} \tilde{\alpha}_1 \\ \tilde{\alpha}_2 \\ \tilde{\alpha}_3 \end{bmatrix} + \int_0^x D^-(x, \xi) \begin{bmatrix} \tilde{\alpha}_1(\xi, t) \\ \tilde{\alpha}_2(\xi, t) \\ \tilde{\alpha}_3(\xi, t) \end{bmatrix} d\xi \quad (9.116)$$

with the boundary conditions

$$\begin{bmatrix} \tilde{\alpha}_1(0, t) \\ \tilde{\alpha}_2(0, t) \\ \tilde{\alpha}_3(0, t) \end{bmatrix} = 0, \quad (9.117)$$

$$\tilde{\beta}(L, t) = \bar{R}_1 \begin{bmatrix} \tilde{\alpha}_1(L, t) \\ \tilde{\alpha}_2(L, t) \\ \tilde{\alpha}_3(L, t) \end{bmatrix}. \quad (9.118)$$

As discussed in Chapter 2, the target system converges to zero in finite time t_F , given by (9.82). Besides, the coefficients $D^+(x, \xi) \in \mathbb{R}^{3 \times 3}$ and $D^-(x, \xi) \in \mathbb{R}^{1 \times 3}$ need to be determined.

The kernel equations for $M(x, \xi)$ and $N_{11}(x, \xi)$ are

$$M_\xi(x, \xi)\Lambda^- - \Lambda^+ M_x(x, \xi) = -\Sigma^{++}(x)M(x, \xi) - \Sigma^{+-}(x)N_{11}(x, \xi), \quad (9.119)$$

$$N_{11\xi}(x, \xi)\Lambda^- + \Lambda^- N_{11x}(x, \xi) = -\Sigma^{-+}(x)M(x, \xi), \quad (9.120)$$

$$M(\xi, \xi)\Lambda^- + \Lambda^+ M(\xi, \xi) = \Sigma^{+-}(\xi), \quad (9.121)$$

$$N_{11}(L, \xi) - \bar{R}_1 M(L, \xi) = 0, \quad (9.122)$$

where (9.119), (9.120) and (9.121) are obtained by applying the transformation (9.112) and (9.113) to the error system (9.108) and (9.109), followed by partial integration and noticing that $\tilde{\beta}(0, t) = \tilde{w}(0, t)$. In addition, (9.122) is deduced by evaluating (9.113) at $x = L$, Plugging in Λ^+ , $M(x, \xi)$, Λ^- , $\Sigma^{++}(x)$, $\Sigma^{+-}(x)$ and $\Sigma^{-+}(x)$, yields the kernel equations in the matrix form:

$$\begin{aligned} & \lambda_4 \begin{bmatrix} m_{11\xi}(x, \xi) \\ m_{21\xi}(x, \xi) \\ m_{31\xi}(x, \xi) \\ N_{11\xi}(x, \xi) \end{bmatrix} + \begin{bmatrix} v_2^* & 0 & 0 & 0 \\ 0 & \lambda_3 & 0 & 0 \\ 0 & 0 & v_1^* & 0 \\ 0 & 0 & 0 & \lambda_4 \end{bmatrix} \begin{bmatrix} m_{11x}(x, \xi) \\ m_{21x}(x, \xi) \\ m_{31x}(x, \xi) \\ N_{11x}(x, \xi) \end{bmatrix} \\ &= \begin{bmatrix} 0 & \bar{J}_{12}(x) & \bar{J}_{13}(x) & \bar{J}_{14}(x) \\ \bar{J}_{21}(x) & 0 & \bar{J}_{23}(x) & \bar{J}_{24}(x) \\ \bar{J}_{31}(x) & \bar{J}_{32}(x) & 0 & \bar{J}_{34}(x) \\ \bar{J}_{41}(x) & \bar{J}_{42}(x) & \bar{J}_{43}(x) & 0 \end{bmatrix} \begin{bmatrix} m_{11}(x, \xi) \\ m_{21}(x, \xi) \\ m_{31}(x, \xi) \\ N_{11}(x, \xi) \end{bmatrix} \end{aligned} \quad (9.123)$$

with boundary conditions at $x = \xi$ and $x = L$,

$$m_{11}(\xi, \xi) = \frac{\bar{J}_{14}(\xi)}{v_2^* - \lambda_4}, \quad (9.124)$$

$$m_{21}(\xi, \xi) = \frac{\bar{J}_{24}(\xi)}{\lambda_3 - \lambda_4}, \quad (9.125)$$

$$m_{31}(\xi, \xi) = \frac{\bar{J}_{34}(\xi)}{v_1^* - \lambda_4}, \quad (9.126)$$

$$N_{11}(L, \xi) = \bar{R}_1 \begin{bmatrix} m_{11}(L, \xi) \\ m_{21}(L, \xi) \\ m_{31}(L, \xi) \end{bmatrix}. \quad (9.127)$$

Following [?], it is straightforward to show that the well-posedness of the kernel equations (9.119)–(9.122) is equivalent to the kernel equations (9.83)–(9.86) since they share the same mathematical structure. Similar to the full-state feedback design, solving the PDE (9.120) and boundary condition (9.122) with the method of characteristics yields the relation

$$\begin{aligned} N_{11}(x, \xi) &= \bar{R}_1 M(L, L - (x - \xi)) \\ &+ \int_0^{\frac{x-L}{\lambda_4}} \Sigma^{-+}(-\lambda_4 v + x) M(-\lambda_4 v + x, -\lambda_4 v + \xi) dv. \end{aligned} \quad (9.128)$$

Substituting the above relation into (9.119), the kernel equations reduces to the following three PDEs with three boundary conditions

$$\begin{aligned}
0 = & -\Lambda^- M_\xi(x, \xi) + \Lambda^+ M_x(x, \xi) - \Sigma^{++}(x)M(x, \xi) - \Sigma^{+-}(x)\bar{R}_1 M(L, L - (x - \xi)) \\
& - \Sigma^{+-}(x) \int_0^{\frac{x-L}{\lambda_4}} \Sigma^{-+}(x - \lambda_4 \nu) M(x - \lambda_4 \nu, \xi - \lambda_4 \nu) d\nu, \quad (9.129)
\end{aligned}$$

$$0 = M(\xi, \xi)\Lambda^- + \Lambda^+ M(\xi, \xi) - \Sigma^{+-}(\xi). \quad (9.130)$$

Besides, we obtain that for $M(x, \xi)$ and $N_{11}(x, \xi)$,

$$D^+(x, \xi) = -M(x, \xi)\Sigma^{-+}(\xi) + \int_\xi^x M(x, s)D^-(s, \xi)ds, \quad (9.131)$$

$$D^-(x, \xi) = -N_{11}(x, \xi)\Sigma^{-+}(\xi) + \int_\xi^x N_{11}(x, s)D^-(s, \xi)ds, \quad (9.132)$$

and the output injection gains are given by

$$P^+(x) = -\lambda_4 M(x, 0), \quad (9.133)$$

$$P_{11}^-(x) = -\lambda_4 N_{11}(x, 0). \quad (9.134)$$

Since the kernels $M(x, \xi)$ and $N_{11}(x, \xi)$ are well-posed, (9.131)–(9.134) imply that the output injection gains as well as the target system coefficients are well-posed. Thus, the observer design is summarized in the following theorem.

Theorem 9.2 *Consider the estimation error system $(\tilde{w}_1, \tilde{w}_2, \tilde{w}_3, \tilde{w}_4)$ in (9.108)–(9.111), obtained from the observer (9.103)–(9.106) and control design model (9.56)–(9.64), with initial conditions $\tilde{w}_i(x, 0) \in \mathcal{L}^\infty([0, L])$, $i = 1, 2, 3, 4$. The output injection gains $P^+(x)$ and $P_{11}^-(x)$ are chosen as (9.133) and (9.134), where the kernel $M(x, \xi)$ is obtained by solving equations (9.129), (9.130) and $N_{11}(x, \xi)$ by (9.128). The observer error systems equilibrium*

$$\tilde{w}_{e,i}(x) \equiv 0, \quad i = 1, 2, 3, 4, \quad (9.135)$$

is stable and reached in finite time t_F given by (9.82).

The estimates $(\hat{w}_1, \hat{w}_2, \hat{w}_3, \hat{w}_4)$ can be transformed to the estimates of the density and velocity variations $(\check{\rho}_1, \check{v}_1, \check{\rho}_2, \check{v}_2)$ of two-class vehicles according to

$$\begin{bmatrix} \check{\rho}_1 \\ \check{v}_1 \\ \check{\rho}_2 \\ \check{v}_2 \end{bmatrix} = T(x) \begin{bmatrix} \hat{w}_1 \\ \hat{w}_2 \\ \hat{w}_3 \\ \hat{w}_4 \end{bmatrix}. \quad (9.136)$$

Furthermore, the estimates of the original state variables are obtained by

$$\hat{\rho}_i(x, t) = \check{\rho}_i(x, t) + \rho_i^*, \quad (9.137)$$

$$\hat{v}_i(x, t) = \check{v}_i(x, t) + v_i^* \quad (9.138)$$

with respect to the estimates of the densities and velocities $(\hat{\rho}_1, \hat{v}_1, \hat{\rho}_2, \hat{v}_2)$.

9.6 Output feedback control design

The output-feedback control law for the two-class traffic ARZ PDE model is constructed by employing the state estimates generated by the anti-collocated observer (9.103)–(9.106) and substituting the state estimates into the full-state feedback law (9.101), which yields finite-time stability of the closed-loop system at the zero equilibrium.

The output-feedback control law is given by

$$\begin{aligned}
 U(t) = & -\kappa_4 e^{\frac{j_{44}}{\lambda_4} L} \bar{R}_1 T_u^{-1}(L) \begin{bmatrix} \hat{\rho}_1(L, t) - \rho_1^* \\ \hat{v}_1(L, t) - v_1^* \\ \hat{\rho}_2(L, t) - \rho_2^* \\ \hat{v}_2(L, t) - v_2^* \end{bmatrix} \\
 & - \kappa_4 e^{\frac{j_{44}}{\lambda_4} L} \int_0^L K(L, \xi) T_u^{-1}(\xi) \begin{bmatrix} \hat{\rho}_1(\xi, t) - \rho_1^* \\ \hat{v}_1(\xi, t) - v_1^* \\ \hat{\rho}_2(\xi, t) - \rho_2^* \\ \hat{v}_2(\xi, t) - v_2^* \end{bmatrix} d\xi \\
 & - \kappa_4 e^{\frac{j_{44}}{\lambda_4} L} \int_0^L L_{11}(L, \xi) T_l^{-1}(\xi) \begin{bmatrix} \hat{\rho}_1(\xi, t) - \rho_1^* \\ \hat{v}_1(\xi, t) - v_1^* \\ \hat{\rho}_2(\xi, t) - \rho_2^* \\ \hat{v}_2(\xi, t) - v_2^* \end{bmatrix} d\xi, \quad (9.139)
 \end{aligned}$$

where the estimates $(\hat{\rho}_1, \hat{v}_1, \hat{\rho}_2, \hat{v}_2)$ are obtained by transforming the states of the anti-collocated observer (9.103)–(9.106) according to (9.136)–(9.138), the transformation matrices $T_u^{-1}(\cdot)$ and $T_l^{-1}(\cdot)$ are given by (9.98), the kernel $K(x, \xi)$ is obtained by the solutions of (9.93) and (9.94), $L_{11}(x, \xi)$ is given by (9.92), and the coefficient κ_4 is introduced in (9.50). We reach the result formulated through the following theorem for output-feedback stabilization.

Theorem 9.3 *Consider the linearized two-class ARZ model given by (9.12) with the boundary conditions (9.22)–(9.24) and (9.39), the initial conditions $\tilde{\rho}_1(x, 0), \tilde{v}_1(x, 0), \tilde{\rho}_2(x, 0), \tilde{v}_2(x, 0) \in \mathcal{L}^\infty([0, L])$, and the output-feedback control law (9.139), where the estimates are generated by the anti-collocated observer (9.103)–(9.106). Let the kernels $K(x, \xi)$ and $L_{11}(x, \xi)$ be obtained by solving the kernel equations (9.93), (9.94) and let the observer output injection gains be given by (9.133) and (9.134), where the kernel $M(x, \xi)$ is obtained by solving (9.129), (9.130) and $N_{11}(x, \xi)$ is given by (9.128). The equilibrium $(\rho_1^*, \rho_2^*, v_1^*, v_2^*)$ is stable and reached in finite time $2t_F$, where t_F is given by (9.82).*

The finite convergence time of the output feedback stabilization is twice as long as the convergence time of full-state feedback stabilization or observer estimation, because it requires t_F to obtain accurate state estimates and then the control needs another t_F to achieve convergence of the state variable to the equilibrium state.

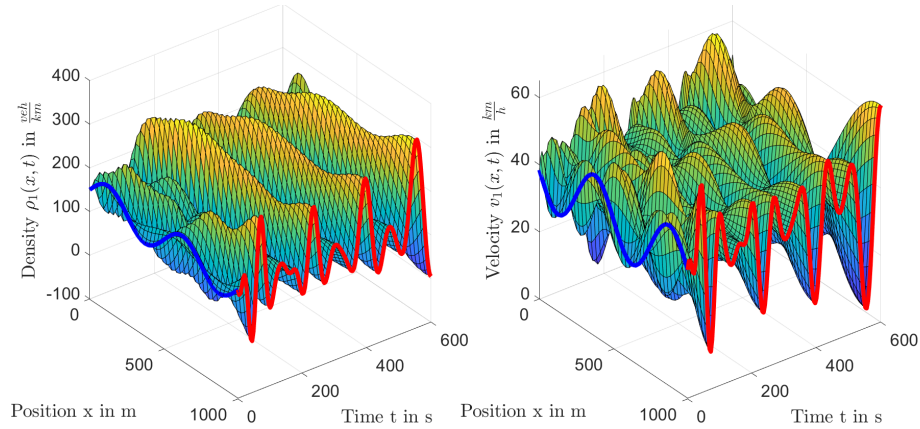


Fig. 9.4 Traffic density and velocity of class 1 without control.

9.7 Numerical Simulation

In this section, the performance of the output-feedback controller is investigated by a simulation of the closed loop involving the original nonlinear model (9.1)–(9.4). First, we discuss the simulation results for the open-loop system and for the closed-loop system. Then performance indices are introduced to evaluate whether the output-feedback controller achieves fuel savings, more comfort, and reduced total travel time.

For the implementation, the traffic state variables ρ_1, ρ_2, v_1, v_2 are transformed to the conservative variables $\rho_1, \rho_2, y_1 = \rho_1(v_1 - V_{e,1}(\rho_1, \rho_2))$ and $y_2 = \rho_2(v_2 - V_{e,2}(\rho_1, \rho_2))$. The update for each time step is computed in a two-stage Lax-Wendroff scheme. More details on applying the scheme to ARZ-type traffic models can be found in Section 1.8. The equilibrium densities are chosen as $\rho_1^* = [150] \text{ veh/km}$ and $\rho_2^* = [75] \text{ veh/km}$ such that the investigated traffic is in the congested regime. The equilibrium velocities are determined by the choice of the equilibrium densities and result in $v_1^* = [38] \text{ km/h}$ and $v_2^* = [20] \text{ km/h}$. The initial condition

$$\rho_i(x, 0) = \rho_i^* + \frac{\rho_i^*}{4} \sin\left(\frac{4\pi}{L}x\right), \quad i = 1, 2, \quad (9.140)$$

$$v_i(x, 0) = v_i^* - \frac{v_i^*}{4} \sin\left(\frac{4\pi}{L}x\right), \quad i = 1, 2 \quad (9.141)$$

represents stop-and-go oscillations described by density and velocity of sinusoidal shape.

The simulation results for the open-loop system are displayed in Figure 9.4 for the vehicle class 1 and in Figure 9.5 for the vehicle class 2. In each figure, the left plot shows the density of the corresponding vehicle class, whereas the plot on the

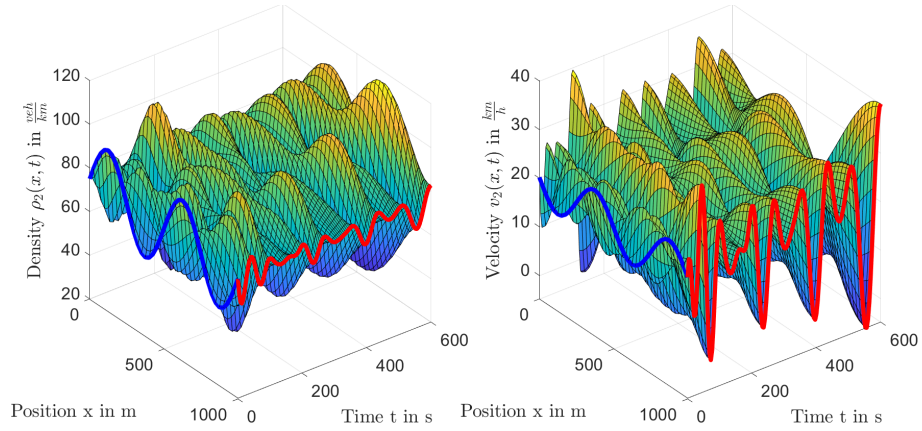


Fig. 9.5 Traffic density and velocity of class 2 without control.

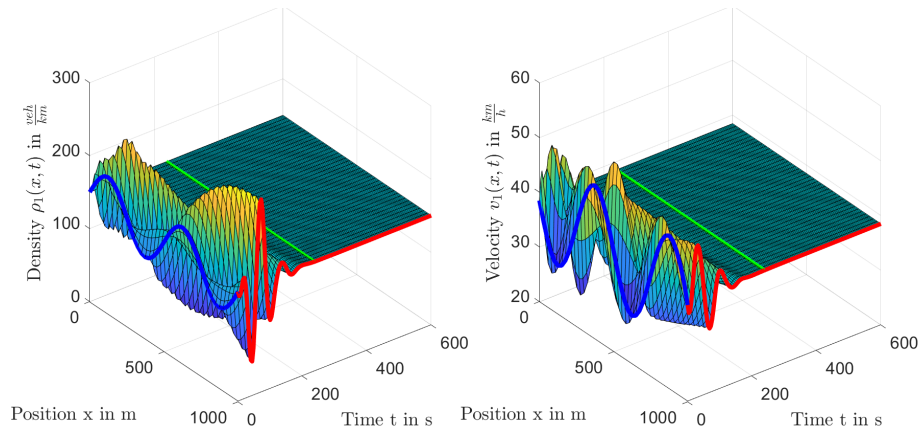


Fig. 9.6 Traffic density and velocity of class 1 with full-state feedback control. The green line indicates t_F .

right hand side shows the velocity. The values of the states at the outlet of the track section are marked with a red line, whereas the blue line emphasizes the initial profiles (9.140). The four plots indicate that the stop-and-go oscillations do not vanish without the influence of control.

Next, Figures 9.6 and 9.7 illustrate the simulation results for the same initial condition but with activated full-state feedback control. The green line marks the finite convergence time $t_F \approx [237]s$. Thus, it is easy to see that the convergence to the constant equilibrium profile in t_F is achieved.

Finally, Figure 9.8 and Figure 9.9 show the simulation results for the initial profiles using the designed output feedback control. Since the observer requires t_F

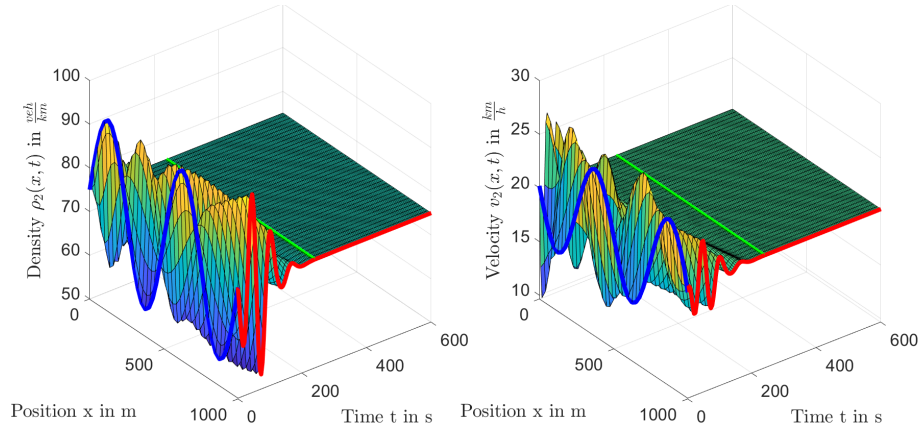


Fig. 9.7 Traffic density and velocity of class 2 with full-state feedback control. The green line indicates t_F .

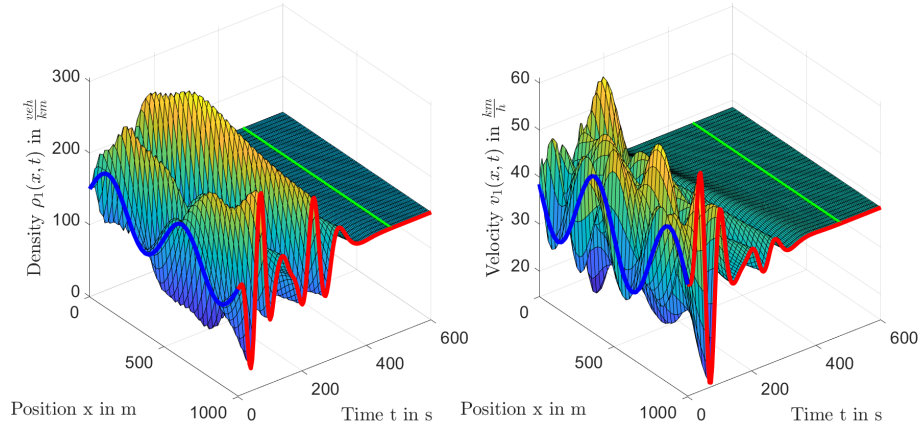


Fig. 9.8 Traffic density and velocity of class 1 with output feedback control. The green line indicates $2t_F$.

to estimate the states without error and afterwards the controller needs t_F to achieve finite time convergence, the total finite convergence time is now $2t_F \approx [474]s$ and therefore green line is adjusted accordingly.

Let us also examine the control input in Figure 9.10. This plot shows that $U(t)$ is continuous and nontrivial (non-monotonic) for this test case. Additionally, the control input is negative and bounded satisfying $|U(t)| < [0.25]veh/s$. While taking (9.20) into account, the constant total boundary flow rate is $q^* = \rho_1^* v_1^* + \rho_2^* v_2^* = [2.0242]veh/s$. Furthermore, the open-loop ramp inflow that we take, $q_{in}^* = [0.4]veh/s$, is around 20% of the mainline flow, which implies that

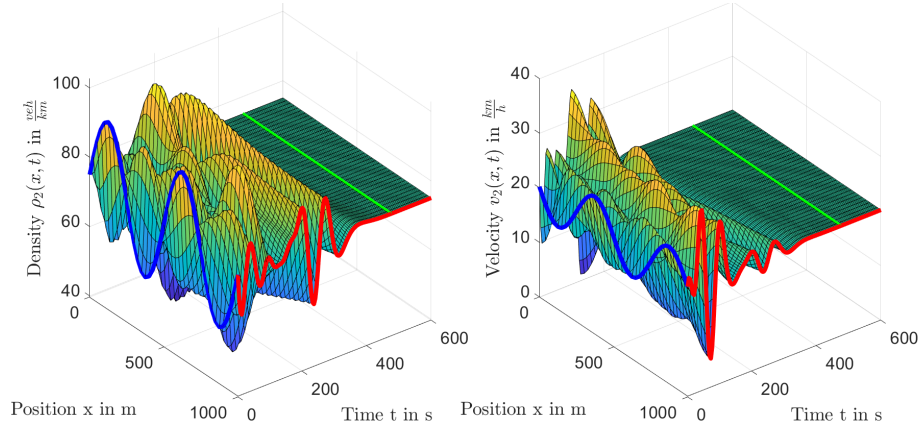


Fig. 9.9 Traffic density and velocity of class 2 with output feedback control. The green line indicates $2t_F$.

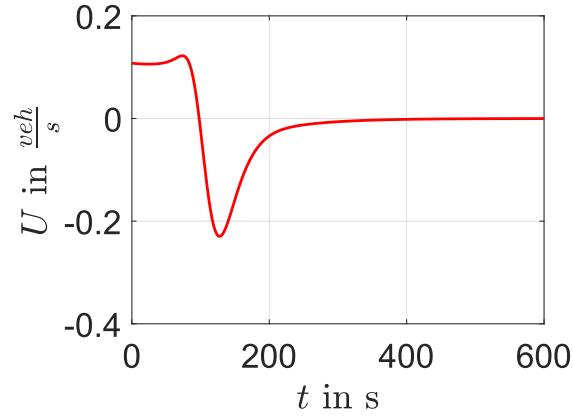


Fig. 9.10 Traffic flow perturbation $U(t)$ controlled by the ramp metering.

$$q_{in}^* + U(t) > 0, \forall t \in [0, t_{sim}] \quad (9.142)$$

and, therefore, the traffic flow leaving the track section is positive.

Performance indices

The considered performance indices

$$J_{\text{fuel}} = \int_0^{t_{\text{sim}}} \int_0^L \max\{0, b_0 + b_1 v(x, t) + b_2 v(x, t) a(x, t) + b_3 a^2(x, t)\} \rho(x, t) dx dt \quad (9.143)$$

$$J_{\text{comfort}} = \int_0^{t_{\text{sim}}} \int_0^L (a(x, t)^2 + a_t(x, t)^2) \rho(x, t) dx dt \quad (9.144)$$

$$J_{\text{TTT}} = \int_0^{t_{\text{sim}}} \int_0^L \rho(x, t) dx dt \quad (9.145)$$

are introduced in Chapter 21 of [?]. The traffic flow control objectives are the minimization of the fuel consumption and of the total travel time, as well as the maximization of the driving comfort.

The performance of closed-loop system is considered for a freeway segment of length $L = [1] \text{ km}$ and the simulation is run for $t_{\text{sim}} = [600] \text{ s}$. The parameters are chosen as $b_0 = [25 \cdot 10^{-3}] \frac{\text{L}}{\text{s}}$, $b_1 = [24.5 \cdot 10^{-6}] \frac{\text{L}}{\text{m}}$, $b_2 = [125 \cdot 10^{-6}] \frac{\text{L s}^2}{\text{m}^2}$ and it is assumed that $b_3 = [95 \cdot 10^{-4}] \frac{\text{L s}^3}{\text{m}^2}$. Notice that $a(x, t)$ is defined as the local acceleration $a(x, t) = v_t(x, t) + v(x, t) v_x(x, t)$. The performance of the controller is evaluated by computing (9.7) for the open loop simulation and comparing it to the values obtained by the closed loop simulation.

In the expressions given next, terms of the form $J_{X, \text{OL}}$ denote the performance indices obtained for the open-loop results, whereas terms of the form $J_{X, \text{CL}}$ denote the indices obtained for the closed-loop results, where $X \in \{\text{fuel}, \text{comfort}, \text{TTT}\}$. The relative values

$$\frac{J_{\text{fuel, CL}}}{J_{\text{fuel, OL}}} = 0.9407, \quad \frac{J_{\text{comfort, CL}}}{J_{\text{comfort, OL}}} = 0.7933, \quad \frac{J_{\text{TTT, CL}}}{J_{\text{TTT, OL}}} \approx 1.0 \quad (9.146)$$

indicate that the vehicles that are controlled by the PDE backstepping feedback law implemented by ramp metering consume 5.93% less fuel, enjoy 20.67% more driving comfort, and require the same total travel time, when the controller is applied within $t_{\text{sim}} = [600] \text{ s}$. Over a longer testing interval, the improvements would only be higher, though possibly only by a marginal amount relative to the reported 5.93% and 20.67% improvements.

9.8 Notes and References

This chapter develops an output-feedback controller for the linearized two-class ARZ traffic PDE model. We develop the boundary control design model in its characteristic form and investigate the obtained characteristic speeds for the free and congested traffic regimes. Backstepping control design is employed to stabilize the 4×4 heterodirectional hyperbolic PDEs for the congested two-class traffic and an anti-collocated observer is designed for traffic state estimation with boundary

sensing. This result can be extended to multi-class traffic models, for which $n + m$ heterodirectional backstepping control design can be applied.

Chapter 10

Control of Two Cascaded Freeway Segments

10.1 Taking the ARZ Control Design Beyond a Single Freeway Segment

Thus far our attention in this book has been restricted to traffic on a single freeway segment. The segment could have various real-world attributes. First, it can be curved, on an incline or decline, affected by weather or visibility changes—which would all manifest itself through the fundamental diagram. Second, the traffic on the freeway can be in multiple lanes, with lane changes, or multiple classes of vehicles or drivers may be participating in traffic, which is captured by ARZ models that incorporate more than two PDEs.

The reader will have observed that not a word has been said thus far in this book about freeway networks. Even though our focus is on traffic stability and the suppression of stop-and-go oscillations, which readily emerge in single freeway stretch configurations, there surely must be an effect on traffic flow stability from freeway branches merging or diverging, from branches looping back or forming a “beltway,” and from more general freeway network configurations.

While, for a single freeway stretch (with possibly multiple lanes and multiple vehicle or driver classes) the controllability of the density and velocity states from a ramp, via metering, is a question that is easily answerable, and is answered in the negative only in the case of a free traffic regime upstream of a ramp (in which case stop-and-go doesn’t arise anyway), the controllability of general networks of ARZ models, with inputs at various locations along the interconnected freeway branches, is a very complex question in its own right.

Indeed, before designing controllers to suppress stop-and-go in a freeway network one needs to determine first what are the input locations and actuation types that would make the density and velocity at all locations in the network controllable. This controllability would be expected to hold only in the sense commonly seen for wave PDEs and coupled hyperbolic PDEs, namely, after sufficient time determined by the propagation speed through the hyperbolic PDEs. Posing the question in this fashion—namely, what input locations and types yield controllability—is a design

mindset, applicable at the time of designing infrastructure. More realistically, given the freeway network and the ramps that have already been built, the controllability question may have either negative or positive answers, and the answers may depend on the flow regime (free or congested).

Questions of controllability, or stabilizability, of networks of 1D flow channels, have been tackled to various degrees of completion in the literature. The answers to these questions, for such physical models, do not necessarily translate to ARZ dynamics and traffic so we shall not review in detail such literature. However, we shall highlight that efforts on controllability and stabilizability of networks of pipes with gas (compressible, as is traffic) and of water channels (where the states like water height and velocity are somewhat analogous to the traffic density and velocity) are of definite relevance to the study of control of traffic networks, though the traffic models are more complex.

In fact, it is instructive to even recall results on networks of ODE models of fluid flow, such as control of mine ventilation networks [?]. Such results, while different in terms of actuation (mine ventilation networks are actuated by doors that open or close to react to the presence of the dangerous methane—a gas that is both noxious and explosive—namely, through actuation that is nothing like ramp metering) do inform us that a fluid network can be satisfactorily controlled without having to place an actuator in each branch of the network. Instead, actuators in a co-tree of the graph of the network suffice for successful control. This is intuitively obvious, thanks to the Kirchhoff current law which acts as an algebraic constraint on the flows through the branches, which are governed by ODEs. Simply put, a door in a branch of a mine ventilation network may be able to control the flow through that branch and another branch as well, or control, additionally, a combination of flows through other branches, at least in the ODE model of the network. Such a capability may not carry over to a spatially distributed (PDE) flow model.

This is all to indicate that, while it is certainly practically relevant to consider control of dynamical behaviors like stop-and-go in traffic networks, it may be premature to engage in stabilizing feedback design for ARZ networks before their controllability is thoroughly studied. And, judging from the experience with mine ventilation networks, whose models in [?] involve a single ODE per branch for the flow state, enormous complexity is expected to arise for a general network topology, shifting the problem from PDE dynamics and control to graph theory problems.

In fact, one has to imagine the potential complexity of answering the controllability question for a general traffic network in which not only may the flow be congested in one branch and free in another branch, but a transition from free to congested may be occurring within the same branch.

For this reason, we believe that stabilization of general ARZ networks is beyond the scope of this book. And perhaps even beyond the scope of future interest for researchers focused on feedback design under challenges arising from PDEs (rather than from graph theory), such as ourselves.

Therefore, in this book we make only a couple of modest steps beyond control of a single stretch of freeway. In this chapter, we consider the simplest configuration beyond a single freeway branch: a cascade of two freeway segments, with ramp

metering applied either where they connect or at the exit from the downstream branch.

At first that may seem as a rather trivial configuration—a “glorified single freeway segment,” misrepresented as two. But there are non-trivial challenges there. First, if applying control at the junction of the two segments, one has to simultaneously control both downstream and upstream traffic. The propagation speeds in the downstream and upstream directions are different even if the two segments of freeway have identical fundamental diagrams and are operated at the same density and speed. But, structurally, the system exhibits challenges that cast it outside of the methodologies reviewed in Chapter 2. The system is of the $(2 + 2) \times (2 + 2)$ form, but with only one input, i.e., it is an *underactuated* set of coupled hyperbolic PDEs. Such a system requires an assumption on the model parameters to permit stabilizability.

Second, even if the control is applied at the exit of the downstream segment, in which case the cascade of segments may appear as a single longer segment, things are not quite trivial. Suppose the freeway loses a lane or two at the point of transitioning from the upstream to the downstream segment. This creates a discontinuity in many things—the fundamental diagram, the density and velocity (while the flow is continuous), and the feedback gains. The single-segment design does not apply and backstepping needs to be carefully recrafted for this configuration.

Taking into account also the need to design an observer in order to eliminate the need for the unrealistic full-state feedback, the set of actuator and sensor placement options go up from two to four and the design challenges multiply.

From the configuration of a cascade of two freeway segments in this chapter, we go one step further in Chapter 10 where we consider the “diverge” configuration, i.e., one stretch of freeway branching out into two. We do not consider in this book the comparably canonical “merge” configuration.

In closing this lengthy discussion on controlling ARZ networks, when this inquiry attains the topological generality of [?], the field of control of macroscopic flows in traffic networks can be considered to have matured. To get to that point may take a few decades. Is this prediction overly pessimistic? Are we inflating the magnitude of the challenge because we are unable to meet it at present, in this book? Are we setting the expectation low so that any partial success is impressive? No. Expecting that it will take decades until control of macroscopic models of traffic flows is fairly exhaustively understood is informed by the awareness that it has taken nearly seven decades since the formulation of the LWR PDE model, for a single freeway segment, until the achievement of the current results on stabilization of ARZ PDE models for a single segment. Of course, heuristic leapfrogging is possible using practically-minded tools, such as RL, but methods that supply stability guarantees will take decades to develop for general traffic network topologies.

What we actually do in this chapter is described next.

We develop boundary output feedback control laws for the simplest nontrivial example of a traffic flow network system: two cascaded freeway segments connected by a junction. The macroscopic traffic dynamics are governed by the ARZ network model in which two subsystems of second-order nonlinear PDEs describe the evolution of traffic density and velocity on each segment. Due to the change of road access

at the junction, different equilibria are considered for the two connected segments. To suppress stop-and-go traffic oscillations on the cascaded roads, we consider a ramp metering that regulates the traffic flow rate entering from the on-ramp to the mainline freeway. Different control designs are proposed such that the output feedback stabilization is realized with either the ramp metering located at the middle junction or the outlet with only boundary measurements of flow rate and velocity. The control objective is to simultaneously stabilize the upstream and downstream traffic to a given spatially-uniform constant steady-state. The distinct actuation locations motivate our design of two different delay-robust full state feedback control laws. The proposed designs are based on the PDE backstepping methodology and guarantee the exponential stability of the under-actuated network of two systems of two hyperbolic PDEs. Two types of collocated boundary observers are proposed to construct output feedback controllers where the sensor location is the same as the actuator location. Numerical simulations are performed to validate the control designs. The two collocated output feedback controllers are compared for their stabilization performance. Robustness to delays is also investigated. The proposed controllers are also compared with some PI boundary feedback controllers.

10.2 Possible Control Configurations for a Cascade of Freeway Segments

Macroscopic modeling of a cascade of freeway segments

Macroscopic modeling is well-established in the previous chapters to describe freeway traffic dynamics since the aggregated state values used by the models are easy to sense and actuate, leading to a particular interest in freeway traffic management. The macroscopic models predict the evolution of continuous traffic states in the temporal and spatial domain by employing hyperbolic PDEs to govern the dynamics of traffic density and velocity. Macroscopic modeling of traffic flow on a network has been considered using different approaches, taking into consideration the complexity of the road network structure [?].

The traffic network model based on the LWR model is developed in [?, ?, ?]. A two-dimensional conservation law for a dense urban area is studied in [?]. An urban-scale macroscopic fundamental diagrams exist for space-mean flow, density and speed [?]. More recently, the macroscopic road networks based on the ARZ family of models have been developed in [?, ?]. Considering the problem of suppressing the stop-and-go congested traffic on cascaded freeway segments, it is, therefore, essential to study the state-of-art second-order macroscopic traffic network models.

In this chapter, we adopt the second-order macroscopic traffic network model in [?] for the two cascaded freeway segments. The model is chosen such that the junction connecting the two roads conserves the mass and drivers' properties, as detailed later in the chapter. This property is not smooth across the junction in [?].

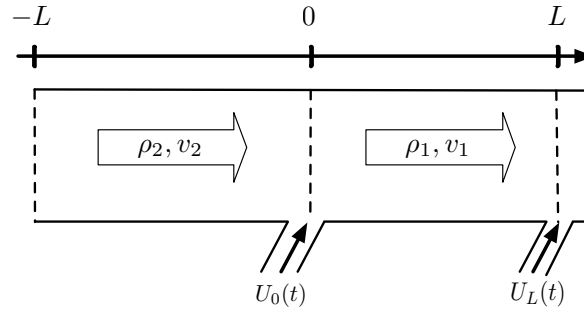


Fig. 10.1 Traffic flow on upstream and downstream roads of a junction, actuation is implemented at the junction or at the outlet of the downstream road segment.

The solution in [?] is a weak solution (in the sense of the conservative variables of the ARZ model) that guarantees the well-posedness of a closed-loop system for our control design. The considered system of two cascaded freeway segments can then be rewritten as a network of two interconnected PDE systems coupled through their boundaries. Each subsystem corresponds to a 2×2 coupled hyperbolic system.

Boundary control of a cascade of freeway segments

Traffic control strategies have been developed and successfully implemented for the traffic management infrastructures for a single freeway segment, as introduced in previous chapters. These control laws are restricted to control problem of traffic on one freeway segment which necessitates certain road homogeneity. As shown in Fig. 10.1, the traffic flow rate is actuated through on-ramp traffic lights so that either the upstream or the downstream traffic is stabilized. Such control design can not stabilize the two segments simultaneously, and distinct traffic scenarios appearing on the cascaded segments are not addressed by the model. Ramp metering control of the upstream traffic may cause congestion for downstream traffic and vice versa.

In this chapter, we solve the boundary control problem of two cascaded traffic freeway. The control design proposed in this chapter mainly advances previous designs in the following aspects:

- **Stabilization by single ramp metering control:** the downstream and upstream traffic be stabilized simultaneously, using only one actuator. We introduce output-feedback control designs that simultaneously stabilize the traffic on two cascaded segments modeled as an underactuated a fourth-order PDE system. The actuation and measurement are only taken from either the middle junction or the outlet. The underactuated formulation presents significant challenges, which backstepping design overcomes by exploiting the cascaded structure of the traffic system.

Table 10.1 Output feedback law

actuator/sensor location	sensor $x = 0$	sensor $x = L$
actuator at $x = 0$	collocated	anti-collocated
actuator at $x = L$	anti-collocated	collocated

- **Collocated controller and observer:** in the same fashion, backstepping provides boundary observers with sensing information from only one location. Moreover, the sensor can be at the same the location as the actuator, unlike for PI control. For instance, for two cascaded freeway segments in Fig. 10.1, PI [?] requires ramp metering controllers located at $x = -L$ and $x = 0$, and VSLs located at $x = 0$ and $x = L$, i.e., a total of four actuators. Ramp metering takes density sensing at $x = 0$ and $x = L$ and VSL control takes velocity sensing at $x = -L$ and $x = 0$. Backstepping requires only one ramp metering with two options: 1) Control U_0 at the middle junction $x = 0$ and measurements of flow rate and velocity at the same location; 2) Control U_L at the outlet $x = L$ and measurements of flow rate and velocity at the same location.
- **Output feedback control with flexible actuation and sensing location combinations:** we design four output-feedback controllers shown in Table. 10.1: two collocated and two anti-collocated. Such design is of practical relevance when collocated implementation fails temporarily or anti-collocated implementation is unavailable.
- **Robustness to input delays:** Perturbations that are common in traffic flow include boundary disturbances, uncertain model parameters, and actuation and measurement delays. The adaptive backstepping control design for uncertain model parameters is provided in Chapter 5 for the ARZ model on one segment. However, the backstepping design is finite-time stabilizing but not robust to actuation delays. This chapter provides output feedback robust to input delays.
- **Comparison between PI control and Backstepping:** This chapter provides a conclusive comparison between PI control and Backstepping method, and trade-offs are discussed.

10.3 ARZ PDE Model of a Cascade of Freeway Segments

We consider a road network that consists of two connected road segments with unidirectional traffic flow and different road conditions, as shown in Fig. 10.1. The two segments are assumed to have the same length L for simplicity of notation. The spatial scaling can be easily made for equations that are used to describe traffic states on segments with different lengths. The downstream traffic is defined on $[0, L]$ while the upstream traffic is defined on $[-L, 0]$. These two segments are connected at the junction through the boundary $x = 0$. The traffic dynamics are described with the ARZ PDE model and the junction between the two segments is represented with the boundary conditions of the PDE model. The adopted ARZ PDE-based traffic

network model by [?] allows the existence of weak solutions, which we will define later for the open-loop and closed-loop system.

The evolution of traffic density $\rho_1(x, t)$ and velocity $v_1(x, t)$ (with $(x, t) \in [0, L] \times [0, \infty)$) on the downstream road segment and traffic density $\rho_2(x, t)$ and velocity $v_2(x, t)$ ($(x, t) \in [-L, 0] \times [0, \infty)$) on the upstream road segment are modeled by the following ARZ model.

$$\partial_t \rho_i + \partial_x (\rho_i v_i) = 0, \quad (10.1)$$

$$\partial_t (\rho_i (v_i + p_i)) + \partial_x (\rho_i v_i (v_i + p_i)) = - \frac{\rho_i (v_i - V(\rho_i))}{\tau_i}, \quad (10.2)$$

where $i \in \{1, 2\}$ represents downstream and upstream road respectively. The labeling of freeway segments is chosen as the reverse direction of traffic flow but same as the propagation direction of the control signal, which will be explained later. The traffic pressure $p_i(\rho_i)$ is defined as an increasing function of the density

$$p_i(\rho_i) = c_i \rho_i^{\gamma_i}, \quad (10.3)$$

where $\gamma_i, c_i \in \mathbb{R}^+$ is defined as $c_i = v_m / \rho_{m,i}^{\gamma_i}$. The coefficient γ_i represents the overall drivers' property, reflecting their change of driving behavior to the increase of density. The positive constant v_m represents the maximum velocity and the positive constant $\rho_{m,i}$ is the maximum density defined as the number of vehicles per unit length. The equilibrium density-velocity relation $V_i(\rho_i)$ is given by $V(\rho_i) = v_m - p_i(\rho_i)$ for both segments, which assumes the same maximum velocity for the two segments when there are no vehicles on the road $\rho_i = 0$. We define the following variable

$$w_i = v_i + p_i(\rho_i), \quad (10.4)$$

which is interpreted as traffic "friction" or drivers' property [?]. This property transports in the traffic flow with vehicle velocity, representing the heterogeneity of individual driver with respect to the equilibrium density-velocity relation $V_i(\rho_i)$. The maximum velocity v_m is assumed to be the same for the two road segments while the maximum density $\rho_{m,i}$ and coefficient γ_i are allowed to vary. The positive constant τ_i is the relaxation time that represents the time scale for traffic velocity v_i adapting to the equilibrium density-velocity relation $V_i(\rho_i)$.

We denote the traffic flow rate on each road as

$$q_i = \rho_i v_i. \quad (10.5)$$

The equilibrium flow and density relation, also known as the fundamental diagram, is then given by

$$Q_i(\rho_i) = \rho_i V(\rho_i) = \rho_i v_m (1 - (\rho_i / \rho_{m,i})^{\gamma_i}). \quad (10.6)$$

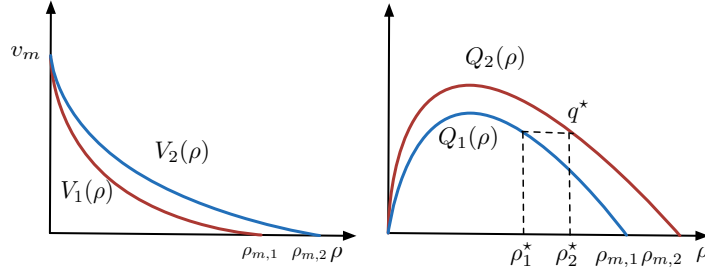


Fig. 10.2 The equilibrium density and velocity relation $V_i(\rho)$ on the left, the equilibrium density and flux relation $Q_i(\rho)$ on the right

We assume that the equilibrium traffic relation is different for the two segments due to the change of road situations and access to road junction. The illustration is given in Fig 10.2. The critical density ρ_c segregates the free and congested regimes of traffic states. The critical density is given by $\rho_{c,i} = \rho_{m,i}/(1 + \gamma_i)^{1/\gamma_i}$ such that $Q'_i(\rho)|_{\rho=\rho_c} = 0$. The traffic is free when the density satisfies $\rho < \rho_{c,i}$. The traffic is defined as the congested one when the density satisfies $\rho > \rho_{c,i}$. For the free traffic, oscillations around the steady states will be damped out fast. For the congested traffic, there are two directional waves on road with one being the velocity oscillation propagating upstream and the other one being the density oscillation propagating downstream with the traffic.

We consider the situation that the upstream road segment 2 for $x \in [-L, 0]$ has more lanes than the downstream road segment for $x \in [0, L]$, in which congested traffic is usually formed up from downstream to upstream. Therefore, the maximum density $\rho_{m,2} > \rho_{m,1}$. The maximum driving speed v_m is assumed to be the same for the two segments. The maximum flow rate of the upstream road $Q_2(\rho_c)$ is reduced in the downstream to $Q_1(\rho_c)$, due to the change of road conditions from segment 2 to segment 1.

Actuated boundary at two different locations

Regarding the boundary conditions connecting the two PDE systems, the Rankine-Hugoniot condition is satisfied at the junction such that the weak solution exists for the network (10.1)-(10.2). This condition implies piecewise smooth solutions and corresponds to the conservation of the mass and of the drivers' properties defined in (10.4) at the junction. Thus the flux and drivers' property are assumed to be continuous across the boundary conditions at $x = 0$, that is

$$\rho_1(0, t)v_1(0, t) = \rho_2(0, t)v_2(0, t), \quad (10.7)$$

$$w_2(0, t) = w_1(0, t). \quad (10.8)$$

For open-loop system, we assume a constant inflow q^* entering the inlet boundary $x = -L$ and a constant outflow q^* at the outlet boundary for $x = L$:

$$q_2(-L, t) = q^*, \quad (10.9)$$

$$q_1(L, t) = q^*, \quad (10.10)$$

The control problem we solve consists in stabilizing the traffic flow in both the upstream and downstream road segments with a single actuator. Three possible locations for implementing a ramp metering control input are either at the inlet $x = -L$, at the junction $x = 0$ or at the outlet $x = L$. We only present the control and estimation results for control input either from the middle junction or from the outlet, as shown in Fig.1. Actuation at the inlet is a less challenging control problem that can be solved following [?] by reducing the traffic inflow. Except for the controlled boundaries, the boundary conditions remain to be the same with the open-loop system in (8.20)-(10.10).

Ramp metering control $U_0(t)$ from the junction $x = 0$: The traffic flow entering from the junction to the mainline road is controlled by $U_0(t)$. Given the flux continuity condition, the boundary condition at the junction is

$$q_1(0, t) = q_2(0, t) + U_0(t), \quad (10.11)$$

where the downstream segment flow consists of the inflow from the mainline upstream segment and the actuated traffic flow from the on-ramp.

Ramp metering control $U_L(t)$ from the outlet $x = L$: The downstream outflow at $x = L$ is actuated by $U_L(t)$,

$$q_1(L, t) = q^* + U_L(t), \quad (10.12)$$

where the outflow rate equals to the summation of the on-ramp metering flow and the constant mainline flow. In what follows, when we implement one choice of control input, the other control input equals to zero. It should be noted that the designed controllers U_0 in (35) and U_L in (49) are the flow rate perturbations around a nominal flow rate. We assume that the steady state flow rate consists of a nominal on-ramp flow rate $q_r > 0$ which is a component of the steady state flow rate q^* . Then the actual ramp flow input at a on-ramp is given by

$$q_{\text{ramp}}(t) = q_r + U_{0,L}(t) \geq 0 \quad (10.13)$$

In practice, we only need to guarantee that $q_{\text{ramp}}(t)$ is non-negative so that $U_{0,L}(t) \geq -q_r$. The value of q_r depends on the road configuration and real-time traffic conditions. We assume that there exists $q_r > 0$ such that (10.13) always holds.

Congested steady states $(\rho_1^*, v_1^*, \rho_2^*, v_2^*)$

We are concerned with the congested traffic and assume that the equilibrium of both segments (ρ_1^*, v_1^*) , (ρ_2^*, v_2^*) are in the congested regime, which is the only one of theoretical control interest among all four traffic scenarios including free and free, free and congested, congested and free, congested and congested. As shown in Fig. 10.11, if the traffic of both segments is free, there is no need for ramp metering control. If the upstream segment 2 is in the free regime and the downstream segment 1 is congested, then we only need to control the congested downstream traffic with either $U_0(t)$ or $U_L(t)$, as introduced in Chapter 3. The oscillations propagated from the congested segment to the free regime segment will be damped out soon. The same applies to the scenario of free traffic in downstream segment 1 and congested traffic in upstream segment 2. The control objective is to stabilize the traffic flow in the two segments around the steady states. In practice, the steady states represent the equilibrium state values of the traffic flow when oscillations are successfully suppressed by our control design.

The steady states (ρ_1^*, v_1^*) , (ρ_2^*, v_2^*) are considered to be in the congested regime and the boundary conditions (10.7) and (10.8) are satisfied, i.e.,

$$\rho_1^* v_1^* = \rho_2^* v_2^* = q^*, \quad (10.14)$$

$$w_1^* = w_2^* = v_m, \quad (10.15)$$

where the steady state velocities satisfy the equilibrium density-velocity relation $v_i^* = V_i(\rho_i^*)$. According to (10.4), the constant driver's property in (10.15) implies that we have the same maximum velocity v_m for the two segments (which corresponds to our initial assumption):

$$v_1^* + p_1^* = v_2^* + p_2^* = v_m, \quad (10.16)$$

where $p_i^* = p_i(\rho_i^*)$. The steady states can be solved from the above nonlinear equations (10.14), (10.16), however there are no explicit solutions. Therefore we show the derivation process for obtaining the steady state values when ρ_1^* and the model parameters v_m , $\rho_{m,i}$ and γ_i are given. The functions $V_i(\rho)$, $Q_i(\rho)$ and $p(\rho)$ are also known. The steady state flow rate in (10.14) is obtained as $q^* = Q_1(\rho_1^*)$, and the constant flux (10.14) $Q_1(\rho_1^*) = Q_2(\rho_2^*)$, yields a relation for the steady state densities of the two segments $\frac{\rho_1^* \rho_{m,1}^{\gamma_1} - (\rho_1^*)^{\gamma_1+1}}{\rho_2^* \rho_{m,2}^{\gamma_2} - (\rho_2^*)^{\gamma_2+1}} = \frac{\rho_{m,1}^{\gamma_1}}{\rho_{m,2}^{\gamma_2}}$. Knowing ρ_1^* , ρ_2^* and q^* , the steady states velocities are obtained as $v_i^* = q^* / \rho_i^*$.

Linearized model in the Riemann coordinates

We linearize the ARZ based traffic network model (ρ_i, v_i) in (10.1), (10.2) with the boundary conditions (10.7), (10.8), (10.9), (10.10) around the steady states (ρ_i^*, v_i^*)

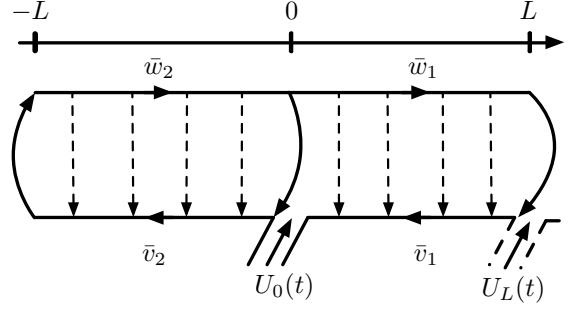


Fig. 10.3 Control diagram for the closed-loop system with either the actuation from the middle junction $x = 0$ or from the outlet $x = L$.

defined in the previous section. In order to obtain simplify the model for control design, the linearized model is then rewritten into the Riemann variables and then a invertible spatial transformation is applied

$$\tilde{w}_i = \exp\left(\frac{x}{\tau_i v_i^*}\right) \left(\frac{\gamma_i p_i^*}{q^*} (\rho_i v_i - \rho_i^* v_i^*) + \frac{1}{r_i} (v_i - v_i^*) \right), \quad (10.17)$$

$$\tilde{v}_i = v_i - v_i^*, \quad (10.18)$$

where the constant coefficients r_i are defined as

$$r_i = -\frac{v_i^*}{\gamma_i p_i^* - v_i^*}. \quad (10.19)$$

For the congested regime we have $\rho_i^* > \frac{\rho_{m,i}}{(1+\gamma_i)^{1/\gamma_i}}$ so that the characteristic speed $\gamma_i p_i^* - v_i^* > 0$. The velocity variations $\tilde{v}_i(x, t)$ transport upstream. More precisely, we have $p_i^* = v_m - V(\rho_i^*) = v_m (\frac{\rho_i^*}{\rho_{m,i}})^{\gamma_i} > v_m$, since $\rho_i^* > \frac{\rho_{m,i}}{(1+\gamma_i)^{1/\gamma_i}}$. Thus, $(\gamma_i + 2)p_i^* > 2v_m$, which implies $\gamma_i p_i^* > 2v_m - 2p_i^* = 2v_i^*$. Thus the inequalities

$$-1 < r_i < 0, \quad (10.20)$$

are satisfied for r_i . The more congested of the traffic, the smaller the absolute value of the ratio constant.

With such a change of variable, the linearized system with the controlled boundary conditions (10.11) and (10.12) rewrites as

$$\partial_t \tilde{w}_i + v_i^* \partial_x \tilde{w}_i = 0, \quad (10.21)$$

$$\partial_t \tilde{v}_i - (\gamma_i p_i^* - v_i^*) \partial_x \tilde{v}_i = c_i(x) \tilde{w}_i, \quad (10.22)$$

$$\tilde{w}_1(0, t) = \tilde{w}_2(0, t), \quad (10.23)$$

$$\tilde{v}_1(L, t) = r_1 \exp\left(\frac{-L}{\tau_1 v_1^*}\right) \tilde{w}_1(L, t) + \frac{1-r_1}{\rho_1^*} U_L(t), \quad (10.24)$$

$$\tilde{w}_2(-L, t) = \exp\left(\frac{-L}{\tau_2 v_2^*}\right) \frac{1}{r_2} \tilde{v}_2(-L, t), \quad (10.25)$$

$$\tilde{v}_2(0, t) = \delta \frac{r_2}{r_1} \tilde{v}_1(0, t) + r_2(1 - \delta) \tilde{w}_2(0, t) + \frac{1-r_2}{\rho_2^*} U_0(t), \quad (10.26)$$

where the spatially varying coefficients $c_i(x)$ are defined as

$$c_i(x) = -\frac{1}{\tau_i} \exp\left(-\frac{x}{\tau_i v_i^*}\right). \quad (10.27)$$

and the constant coefficient δ is

$$\delta = \frac{\gamma_2 p_2^*}{\gamma_1 p_1^*} > 0. \quad (10.28)$$

The constant δ represents the ratio related to the traffic pressure of the segments. Derivation of the linearization and the spatial transformation is straightforward to obtain by following [?] and thus are omitted here. The control diagram is shown in Fig. 10.3 for the transformed system (10.21)-(10.26).

The well-posedness and the existence of the weak solutions for both the open-loop and closed-loop system in (10.21)-(10.26) are defined and then discussed. The initial conditions are denoted $(\tilde{v}_0)_i = \tilde{v}_i(\cdot, 0)$, $(\tilde{w}_0)_i = \tilde{w}_i(\cdot, 0)$ and belong to L^2 such that $(\tilde{v}_0)_1, (\tilde{w}_0)_1 \in (L^2([0, L]))^2$ and $(\tilde{v}_0)_2, (\tilde{w}_0)_2 \in (L^2([-L, 0]))^2$. We consider weak solutions of the system (10.21)-(10.26) with the initial conditions $(\tilde{v}_0)_i, (\tilde{w}_0)_i$. More precisely, as suggested in [?], multiplying formally (10.21)-(10.22) by smooth test functions (ϕ_i, ψ_i) and integrating by parts, the following definition of a weak solution is given.

Definition 10.1 Let us consider $T > 0$. A L^2 -solution (weak solution) of the problem (10.21)-(10.26) with the initial conditions $(\tilde{v}_0)_1, (\tilde{w}_0)_1 \in (L^2([0, L]))^2$ and $(\tilde{v}_0)_2, (\tilde{w}_0)_2 \in (L^2([-L, 0]))^2$ and the control laws $U_L \in L^2([0, T])$ and $U_0 \in L^2([0, T])$, is a map $(\tilde{v}_1, \tilde{w}_1) \in (C^0([0, T]; L^2([0, L])))^2$ and $(\tilde{v}_2, \tilde{w}_2) \in (C^0([0, T]; L^2([-L, 0])))^2$ such that for every $(\phi_1, \psi_1) \in C^1([0, L] \times [0, T])^2$ and $(\phi_2, \psi_2) \in C^1([-L, 0] \times [0, T])^2$ such that

$$\begin{aligned}
\psi_2(-L, t) &= \frac{v_2^*}{r_2(\gamma_2 p_2^* - v_2^*)} \exp\left(\frac{-L}{\tau_2 v_2^*}\right) \phi_2(-L, t), \\
\psi_1(0, t) &= \frac{r_2(\gamma_2 p_2^* - v_2^*)}{r_1(\gamma_1 p_1^* - v_1^*)} \delta \psi_2(0, t), \\
\phi_1(L, t) &= \frac{\gamma_1 p_1^* - v_1^*}{v_1^*} r_1 \exp\left(-\frac{L}{\tau_1 v_1^*}\right) \psi_1(L, t), \\
\phi_2(-L, t) &= \frac{\gamma_2 p_2^* - v_2^*}{v_2^*} r_2 (1 - \delta) \psi_2(t, 0) + \frac{v_1^*}{v_2^*} \phi_1(0, t),
\end{aligned}$$

we have

$$\begin{aligned}
0 = & - \int_0^T \int_0^L (\partial_t \phi_1(x, t) + v_1^* \partial_x \phi_1(x, t) + c_1 \psi_1(x, t)) \tilde{w}_1(x, t) dx dt \\
& - \int_0^T \int_0^L (\partial_t \psi_1(x, t) - (\gamma_1 p_1^* - v_1^*) \partial_x \psi_1(x, t)) \tilde{v}_1(x, t) \\
& - \int_0^T \int_{-L}^0 (\partial_t \phi_2(x, t) + v_2^* \partial_x \phi_2(x, t) + c_2 \psi_2(x, t)) \tilde{w}_2(x, t) dx dt \\
& - \int_0^T \int_{-L}^0 (\partial_t \psi_2(x, t) - (\gamma_2 p_2^* - v_2^*) \partial_x \psi_2(x, t)) \tilde{v}_2(x, t) \\
& + \int_0^L [\phi_1(x, t) \tilde{w}_1(x, t) + \psi_1(x, t) \tilde{v}_1(x, t)]_0^T dx \\
& + \int_{-L}^0 [\phi_2(x, t) \tilde{w}_2(x, t) + \psi_2(x, t) \tilde{v}_2(x, t)]_0^T dx \\
& - \int_0^T (\gamma_1 p_1^* - v_1^*) \frac{1 - r_1}{\rho_1^*} \psi_1(L, t) U_L(t) dx \\
& - \int_0^T (\gamma_2 p_2^* - v_2^*) \frac{1 - r_2}{\rho_2^*} \psi_2(0, t) U_0(t) dx
\end{aligned} \tag{10.29}$$

The open-loop system (10.21)-(10.26) (for which $U_L \equiv U_0 \equiv 0$) is well-posed by [?, Theorem A.4], that is, for any initial conditions $(\tilde{v}_0)_1, (\tilde{w}_0)_1 \in (L^2([0, L]))^2$ and $(\tilde{v}_0)_2, (\tilde{w}_0)_2 \in (L^2([-L, 0]))^2$, there is only one L^2 -solution. It is shown in [?] that only marginal linear stability holds for the open-loop system of one segment. Our objective is to design the control law $U_0(t)$ or $U_L(t)$ to stabilize the system (10.21)-(10.26) in the sense of the L^2 -norm. More precisely, we want to design the control laws such that the closed-loop system is exponentially stable in the sense of the following definition.

Definition 10.2 The linearized traffic PDE network system (10.21)-(10.26) is exponentially stable for the L^2 -norm if there exists $\mu_i, v_i > 0$ and $c_i, d_i > 0$ such that, for every L^2 initial condition $(\tilde{w}_i(\cdot, 0), \tilde{v}_i(\cdot, 0))$, the L^2 solution of the closed-loop system with designed controllers (10.21)-(10.26) satisfies

$$\|\tilde{w}_i(\cdot, t)\| \leq c_i e^{-\mu_i t} \|\tilde{w}_i(\cdot, 0)\|, \quad (10.30)$$

$$\|\tilde{v}_i(\cdot, t)\| \leq d_i e^{-\nu_i t} \|\tilde{v}_i(\cdot, 0)\|. \quad (10.31)$$

The control operator is admissible. Consequently, for any $U_L \in L^2([0, T])$ and $U_0 \in L^2([0, T])$, and for any initial conditions $(\tilde{v}_0)_1, (\tilde{w}_0)_1 \in (L^2([0, L]))^2$ and $(\tilde{v}_0)_2, (\tilde{w}_0)_2 \in (L^2([-L, 0]))^2$, there is only one L^2 -solution to (10.21)-(10.26).

We make the following non-restrictive assumption so that the proposed feedback laws have some (delay)-robustness margins.

The boundary couplings of the system (10.21)-(10.26) are such that

$$\delta < \frac{1 + \exp(\frac{L}{\tau_2 v_2^*})}{1 + \exp(\frac{-L}{\tau_1 v_1^*})}. \quad (10.32)$$

If this assumption is not satisfied, then it is not possible to robustly stabilize the system (10.21)-(10.26) when there are input delays (as the open-loop transfer function would have an infinite chain of poles in the complex right half-plane). An detailed discussion on robustness will be given in Section 10.7 after we introduce control and estimation designs.

10.4 State feedback Control Designs

In this section, we design full-state feedback laws that guarantee the stabilization of the system (10.21)-(10.26) for the different actuation locations. In each case, the backstepping method is employed. Using a Volterra transformation (eventually combined with an affine transformation in the case of the actuation located at the outlet), we map the original under-actuated system to a target system for which the in-domain coupling terms c_1 and c_2 have been moved at the actuated boundary in the form of integral couplings. We can then use the actuation to eliminate these terms. The resulting system is exponentially stable due to Assumption 10.3. As such a control law does not modify the boundary couplings, it is strictly proper, and consequently, the robustness margins are preserved.

Feedback law $U_0(t)$ with flow rate control from $x = 0$

We consider the following backstepping transformations

$$\alpha_i(x, t) = \tilde{w}_i(x, t), \quad (10.33)$$

$$\begin{aligned} \beta_1(x, t) = & \tilde{v}_1(x, t) - \int_x^L K_1^{vw}(x, \xi) \tilde{w}_1(\xi, t) d\xi \\ & - \int_x^L K_1^{vv}(x, \xi) \tilde{v}_1(\xi, t) d\xi, \end{aligned} \quad (10.34)$$

$$\begin{aligned} \beta_2(x, t) = & \tilde{v}_2(x, t) - \int_{-L}^x K_2^{vw}(x, \xi) \tilde{w}_2(\xi, t) d\xi \\ & - \int_{-L}^x K_2^{vv}(x, \xi) \tilde{v}_2(\xi, t) d\xi, \end{aligned} \quad (10.35)$$

where the kernels K_1^{vw} and K_1^{vv} are defined on the set $\mathcal{T}_1 = \{(x, \xi) \in [0, L]^2, \xi \geq x\}$, while the kernels K_2^{vw} and K_2^{vv} are continuous functions defined on the set $\mathcal{T}_2 = \{(x, \xi) \in [-L, 0]^2, \xi \leq x\}$. On their corresponding domains of definition, they satisfy the following set of PDEs:

$$(\gamma_i p_i^* - v_i^*) \partial_x K_i^{vw} - v_i^* \partial_\xi K_i^{vw} = c_i(\xi) K_i^{vv}, \quad (10.36)$$

$$\partial_x K_i^{vv}(x, \xi) + \partial_\xi K_i^{vv}(x, \xi) = 0, \quad (10.37)$$

along with the following boundary conditions

$$K_1^{vw}(x, x) = \frac{c_1(x)}{\gamma_1 p_1^*}, \quad (10.38)$$

$$K_2^{vw}(x, x) = -\frac{c_2(x)}{\gamma_2 p_2^*}, \quad (10.39)$$

$$K_1^{vv}(x, L) = \frac{v_1^*}{r_1(\gamma_1 p_1^* - v_1^*)} \exp\left(\frac{L}{\tau_1 v_1^*}\right) K_1^{vw}(x, L), \quad (10.40)$$

$$K_2^{vv}(x, -L) = \frac{v_2^*}{r_2(\gamma_2 p_2^* - v_2^*)} \exp\left(\frac{-L}{\tau_2 v_2^*}\right) K_2^{vw}(x, -L). \quad (10.41)$$

The well-posedness of this kernel PDE-system is guaranteed by the following lemma.

Lemma 10.1 [?] *Consider system (10.36)-(10.41). There exists a unique solution K_1^{vw} , K_1^{vv} in $C(\mathcal{T}_1)$ and K_2^{vw} , K_2^{vv} in $C(\mathcal{T}_2)$.*

The transformation (10.34)-(10.35) maps the original system (10.21)-(10.26) to the decoupled target system

$$\partial_t \alpha_i + v_i^* \partial_x \alpha_i = 0, \quad (10.42)$$

$$\partial_t \beta_i - (\gamma_i p_i^* - v_i^*) \partial_x \beta_i = 0, \quad (10.43)$$

$$\alpha_1(0, t) = \alpha_2(0, t), \quad (10.44)$$

$$\beta_1(L, t) = r_1 \exp\left(-\frac{L}{\tau_1 v_1^*}\right) \alpha_1(L, t), \quad (10.45)$$

$$\alpha_2(-L, t) = \exp\left(\frac{-L}{\tau_2 v_2^*}\right) \frac{1}{r_2} \beta_2(-L, t), \quad (10.46)$$

$$\beta_2(0, t) = \delta \frac{r_2}{r_1} \beta_1(0, t) + r_2(1 - \delta) \alpha_2(0, t). \quad (10.47)$$

The controlled boundary (10.47) is obtained by defining the control input $U_0(t)$ as

$$U_0(t) = \frac{\rho_2^*}{1 - r_2} \left(\int_{-L}^0 K_2^{vw}(0, \xi) \tilde{w}_2(\xi, t) + K_2^{vv}(0, \xi) \tilde{v}_2(\xi, t) d\xi \right. \\ \left. - \delta \frac{r_2}{r_1} \int_0^L K_1^{vw}(0, \xi) \tilde{w}_1(\xi, t) + K_1^{vv}(0, \xi) \tilde{v}_1(\xi, t) d\xi \right). \quad (10.48)$$

This control law is a L^2 function. According to Definition 1, for any initial conditions $(\tilde{v}_0)_1, (\tilde{w}_0)_1 \in (L^2([-L, 0]))^2$ and $(\tilde{v}_0)_2, (\tilde{w}_0)_2 \in (L^2([-L, 0]))^2 (L^2([0, L]))$, there is only one L^2 -solution to the closed-loop system for (10.21)-(10.26) with (10.48). Moreover, since the kernels are bounded functions, our control operator is a linear bounded operator. Consequently, it is a continuous operator. Thus the control law $U_0 : [0, T] \rightarrow \mathbb{R}$ is continuous. For practical implementation of the ramp metering control input, we need to modulate the changing frequency of the on-ramp traffic light. The event-triggered control in [?] provides a way to implement the continuous-time controllers into digital forms by updating the input values only when needed. It is strictly proper as it is only composed of integral terms. Following the ideas of [?], we prove that it is robust with respect to delays in the actuation and uncertainties on the parameters. We have the following theorem.

Theorem 10.1 *Consider the PDE system (10.21)-(10.26) with the feedback law U_0 defined in (10.48). Then for any L^2 initial condition $(\tilde{w}_i(\cdot, 0), \tilde{v}_i(\cdot, 0))$, the closed-loop system is exponentially stable at the origin.*

Proof The proof is a simple consequence of Assumption 10.3. The system (10.42)-(10.47) has the same structure as the one of system (10.21)-(10.26) in the absence of in-domain couplings and actuation. As Assumption 10.3 implies the exponential stability of this second system, the system (10.42)-(10.47) is exponentially stable. Due to the invertibility of the Volterra transformations (10.34)-(10.35), the systems (10.21)-(10.26) and (10.42)-(10.47) have equivalent stability properties. This implies the exponential stability of (10.21)-(10.26). \square

Feedback law $U_L(t)$ with flow rate control from $x = L$

We now consider that the available actuation is located at the outlet $x = L$.

$$\bar{\alpha}_1(x, t) = \tilde{w}_1(x, t), \quad (10.49)$$

$$\begin{aligned} \bar{\beta}_1(x, t) = & \tilde{v}_1(x, t) - \int_0^x \bar{K}_1^{vw}(x, \xi) \tilde{w}_1(\xi, t) d\xi - \int_0^x \bar{K}_1^{vv}(x, \xi) \tilde{v}_1(\xi, t) d\xi \\ & - \int_{-L}^0 M^w(x, \xi) \tilde{w}_2(\xi, t) d\xi - \int_{-L}^0 M^v(x, \xi) \tilde{v}_2(\xi, t) d\xi, \end{aligned} \quad (10.50)$$

$$\bar{\alpha}_2(x, t) = \tilde{w}_2(x, t), \quad (10.51)$$

$$\bar{\beta}_2(x, t) = \tilde{v}_2(x, t) - \int_{-L}^x \bar{K}_2^{vw}(x, \xi) \tilde{w}_2(\xi, t) d\xi - \int_{-L}^x \bar{K}_2^{vv}(x, \xi) \tilde{v}_2(\xi, t) d\xi, \quad (10.52)$$

where the kernels \bar{K}_1^{vw} and \bar{K}_1^{vv} are defined on the set $\bar{\mathcal{T}}_1 = \{(x, \xi) \in [0, L]^2, \xi \leq x\}$, the kernels \bar{K}_2^{vw} and \bar{K}_2^{vv} are defined on the set $\bar{\mathcal{T}}_2$. Finally the kernels M^w and M^v are bounded functions defined on $\mathcal{T} = \{(x, \xi) \in [0, L] \times [-L, 0]\}$. The Volterra transformation (10.51)-(10.52) is invertible. Thus, the first transformation (10.49)-(10.50) is invertible as it is a combination of a Volterra transformation with an affine transformation. The different kernels satisfy the following set of PDEs on their corresponding domains of definition

$$(\gamma_i p_i^* - v_i^*) \partial_x \bar{K}_i^{vw} - v_i^* \partial_\xi \bar{K}_i^{vw} = c_i(\xi) \bar{K}_i^{vv}, \quad (10.53)$$

$$\partial_x \bar{K}_i^{vv} + \partial_\xi \bar{K}_i^{vv} = 0, \quad (10.54)$$

$$(\gamma_1 p_1^* - v_1^*) \partial_x M^v + (\gamma_2 p_2^* - v_2^*) \partial_\xi M^v = 0, \quad (10.55)$$

$$(\gamma_1 p_1^* - v_1^*) \partial_x M^w - v_2^* \partial_\xi M^w = c_2(\xi) M^v, \quad (10.56)$$

along with the boundary conditions

$$\bar{K}_i^{vw}(x, x) = -\frac{c_i(x)}{\gamma_i p_i^*}, \quad (10.57)$$

$$\bar{K}_1^{vv}(x, 0) = \frac{v_2^*}{v_1^*} \delta M^v(x, 0), \quad (10.58)$$

$$\bar{K}_2^{vv}(x, -L) = -\exp\left(\frac{-L}{\tau_2 v_2^*}\right) \bar{K}_2^{vw}(x, -L), \quad (10.59)$$

$$M^w(0, \xi) = \frac{r_1}{\delta r_2} \bar{K}_2^{vw}(0, \xi), \quad (10.60)$$

$$M^v(0, \xi) = \frac{r_1}{\delta r_2} \bar{K}_2^{vv}(0, \xi), \quad (10.61)$$

$$M^w(x, 0) = (1 - \delta)M^v(x, 0) + \frac{v_1^*}{v_2^*} \bar{K}_1^{vw}(x, 0), \quad (10.62)$$

$$M^v(x, -L) = -\exp\left(\frac{-L}{\tau_2 v_2^*}\right) M^w(x, -L). \quad (10.63)$$

We have the following lemma.

Lemma 10.2 *For system (10.53)-(10.63), there exists a unique solution \bar{K}_1^{vw} , \bar{K}_1^{vv} in $\mathcal{B}(\bar{\mathcal{T}}_1)$, \bar{K}_2^{vw} , \bar{K}_2^{vv} in $\mathcal{B}(\mathcal{T}_2)$ and M^v , M^w in $\mathcal{B}(\mathcal{T})$.*

Proof We start by assessing the existence of \bar{K}_2^{vw} and \bar{K}_2^{vv} using [?]. The rest of the proof is based on an induction argument and is adjusted from the one given in [?]. Let us define $\chi = \frac{\gamma_2 p_2^* - v_2^*}{v_2^*}$ and let us define the sequence x_k by

$$x_k = \min(\chi \times k, 1).$$

Let us now define the following triangular domains defined for $k \geq 1$.

$$\begin{aligned} \mathcal{R}_k &= \{(x, \xi) \in [0, 1] \times [-1, 0], \xi \leq -\frac{1}{\chi}(x - x_{k-1})\}, \\ \bar{\mathcal{R}}_k &= \{(x, \xi) \in [0, 1] \times [-1, 0], \xi \geq -\frac{1}{\chi}(x - x_{k-1})\}, \\ \mathcal{S}_k &= \{(x, \xi) \in [0, x_k]^2, x \geq \xi\} \end{aligned}$$

Applying [?, Theorem 3.2] on equation (10.55)-(10.56) with the boundary conditions (10.61) and (10.63), we prove the existence of the kernels M^v and M^w on the triangular domain \mathcal{R}_1 . Consequently, these kernels are defined on the line $x = -\chi\xi$. Let us now perform the change of variables $\bar{\xi} = -\frac{1}{\chi}\xi$ to map the domain \mathcal{S}_1 to $\bar{\mathcal{R}}_1$. Consequently, we can express the kernels $\bar{K}_1^{\cdot\cdot}$ on the domain $\bar{\mathcal{R}}_1$ (when $x \leq \chi$). We denote by \hat{K}_1 the corresponding kernels after this change of variables. Again, we can apply [?, Theorem 3.2] to prove the existence of the kernels M^w , M^v and $\hat{K}_1^{\cdot\cdot}$ on $\bar{\mathcal{R}}_1$. This imply the existence of $\bar{K}_1^{\cdot\cdot}$ on \mathcal{S}_1 . We then iterate the procedure on the intervals $[x_{k-1}, x_k]$ to conclude the proof. \square

The kernels here are bounded functions (instead of continuous functions) since we decided to apply the results from [?, Theorem 3.2]. This theorem has been stated in a more general framework where the kernels may present some discontinuities. However, these discontinuities occur along the characteristic lines and do not have any consequence on the backstepping transformation. The transformation (10.50)-(10.52) maps the original system (10.21)-(10.26) to the decoupled target system, same with (10.42)-(10.47). The control input $U_L(t)$ is obtained as

$$U_L(t) = \frac{\rho_1^*}{1-r_1} \left(\int_0^L \bar{K}_1^{vw}(L, \xi) w_1(\xi, t) d\xi + \bar{K}_1^{vv}(L, \xi) v_1(\xi, t) d\xi + \int_{-L}^0 M^w(L, \xi) w_2(\xi, t) d\xi + M^v(L, \xi) v_2(\xi, t) d\xi \right). \quad (10.64)$$

We have the following theorem.

Theorem 10.2 *Consider the PDE system (10.21)-(10.26) with the feedback law U_L defined in (10.64). Then for any L^2 initial condition $(\tilde{w}_i(\cdot, 0), \tilde{v}_i(\cdot, 0))$, the closed-loop system is exponentially stable at the origin.*

10.5 Boundary Observer Designs

The control laws designed in the previous section require the value of the state all over the spatial domain. This is not realistic when considering a real implementation for freeway traffic. This is why in this section, we design boundary observers which either rely on the measurement of traffic states from the junction or from the outlet of the system.

Observer with measurement $Y_0(t)$ at $x = 0$

This section discusses the case of an observer that relies on the measurement of \tilde{q}_i and \tilde{v}_i at the left side of the junction. Since it holds that $\tilde{w}_2(0, t) = \frac{\gamma_2 \rho_2^*}{q^*} \tilde{q}_2(0, t) - \frac{1}{r_2} \tilde{v}_2(0, t)$, we consider that the following measurement is available

$$Y_0(t) = \tilde{w}_2(0, t). \quad (10.65)$$

We choose the measurement at the left side of the junction $\tilde{w}_2(0, t)$. In order to preserve the robustness properties of the closed-loop system, we will not use the measurement $Y_0(t)$ in the boundary conditions of the observer system.

The observer equations are a copy of the original dynamics with output injection gains. They read as follows

$$\partial_t \hat{w}_i + v_i^* \partial_x \hat{w}_i = -\phi_i(x)(\tilde{w}_2(0, t) - \hat{w}_i(0, t)), \quad (10.66)$$

$$\partial_t \hat{v}_i - (\gamma_i p_i^* - v_i^*) \partial_x \hat{v}_i = c_i(x) \hat{w}_i - \chi_i(x)(\tilde{w}_2(0, t) - \hat{w}_i(0, t)), \quad (10.67)$$

$$\hat{w}_1(0, t) = \hat{w}_2(0, t), \quad (10.68)$$

$$\hat{v}_1(L, t) = r_1 \exp\left(\frac{-L}{\tau_1 v_1^*}\right) \hat{w}_1(L, t) + \frac{1-r_1}{\rho_1^*} U_L(t), \quad (10.69)$$

$$\hat{w}_2(-L, t) = \exp\left(\frac{-L}{\tau_2 v_2^*}\right) \frac{1}{r_2} \hat{v}_2(-L, t), \quad (10.70)$$

$$\hat{v}_2(0, t) = \delta \frac{r_2}{r_1} \hat{v}_1(0, t) + (1 - \delta) r_2 \hat{w}_2(0, t) + \frac{1-r_2}{\rho_2^*} U_0(t), \quad (10.71)$$

where $\hat{w}_i(x, t)$, $\hat{v}_i(x, t)$ are the estimates of the state variables $\tilde{w}_i(x, t)$ and $\tilde{v}_i(x, t)$. The terms ϕ_i and χ_i are output injection gains that have to be designed. They are *continuous* functions respectively defined on $([0, L])$ and $([-L, 0])$. The corresponding initial conditions are L^2 functions. This system can be seen as the adjoint system of the closed-loop system presented in the previous section. This can be seen using an operator framework analogous to the one used in [?]. Consequently, it is well-posed. Its well-posedness could be stated in a similar way to what is done in Definition 10.1. Defining the error estimates $\check{w}_i = \tilde{w}_i - \hat{w}_i$ and $\check{v}_i = \tilde{v}_i - \hat{v}_i$ and using the fact that $\hat{w}_1(0, t) = \hat{w}_2(0, t)$, the error system is obtained by subtracting the observer equations in (10.66)-(10.71) from (10.21)-(10.26),

$$\partial_t \check{w}_i + v_i^* \partial_x \check{w}_i = \phi_i(x) \check{w}_i(0, t), \quad (10.72)$$

$$\partial_t \check{v}_i - (\gamma_i p_i^* - v_i^*) \partial_x \check{v}_i = c_i(x) \check{w}_i + \chi_i(x) \check{w}_i(0, t), \quad (10.73)$$

$$\check{w}_1(0, t) = \check{w}_2(0, t), \quad (10.74)$$

$$\check{v}_1(L, t) = r_1 \exp\left(-\frac{L}{\tau_1 v_1^*}\right) \check{w}_1(L, t), \quad (10.75)$$

$$\check{w}_2(-L, t) = \exp\left(\frac{-L}{\tau_2 v_2^*}\right) \frac{1}{r_2} \check{v}_2(-L, t), \quad (10.76)$$

$$\check{v}_2(0, t) = \delta \frac{r_2}{r_1} \check{v}_1(0, t) + (1 - \delta) r_2 \check{w}_2(0, t). \quad (10.77)$$

Let us consider the following backstepping transformations

$$\check{w}_1(x, t) = \check{\alpha}_1(x, t) - \int_0^x N_1^{ww}(x, \xi) \check{\alpha}_1(\xi, t) d\xi, \quad (10.78)$$

$$\check{v}_1(x, t) = \check{\beta}_1(x, t) - \int_0^x N_1^{vw}(x, \xi) \check{\alpha}_1(\xi, t) d\xi, \quad (10.79)$$

$$\check{w}_2(x, t) = \check{\alpha}_2(x, t) - \int_x^0 N_2^{ww}(x, \xi) \check{\alpha}_2(\xi, t) d\xi, \quad (10.80)$$

$$\check{v}_2(x, t) = \check{\beta}_2(x, t) - \int_x^0 N_2^{vw}(x, \xi) \check{\alpha}_2(\xi, t) d\xi, \quad (10.81)$$

where the kernels N_1^{ww} and N_1^{vw} are continuous functions defined on the set $\bar{\mathcal{T}}_1$, while the kernels N_2^{ww} and N_2^{vw} are continuous functions defined on the set $\bar{\mathcal{T}}_2 = \{(x, \xi) \in [-L, 0], \xi \geq x\}$. On their corresponding domains of definition, they satisfy the following set of PDEs:

$$\partial_x N_i^{ww} + \partial_\xi N_i^{ww} = 0, \quad (10.82)$$

$$(\gamma_i p_i^* - v_i^*) \partial_x N_i^{vw} - v_i^* \partial_\xi N_i^{vw} = -c_i(x) N_i^{ww}, \quad (10.83)$$

$$N_1^{ww}(L, x) = \frac{1}{r_1} \exp\left(\frac{L}{\tau_1 v_1^*}\right) N_1^{vw}(L, x), \quad (10.84)$$

$$N_2^{ww}(-L, x) = \frac{1}{r_2} \exp\left(\frac{-L}{\tau_2 v_2^*}\right) N_2^{vw}(-L, x), \quad (10.85)$$

$$N_1^{vw}(x, x) = \frac{c_1(x)}{\gamma_1 p_1^*}, \quad (10.86)$$

$$N_2^{vw}(x, x) = \frac{-c_2(x)}{\gamma_2 p_2^*}. \quad (10.87)$$

The well-posedness of this kernel PDE-system is guaranteed by the following lemma.

Lemma 10.3 [?] *Consider system (10.82)-(10.87). There exists a unique solution N_1^{vw} , N_1^{vv} in $C(\mathcal{T}_1)$ and N_2^{vw} , N_2^{vv} in $C(\mathcal{T}_2)$.*

Let us now define the output injection gains ϕ_i and χ_i as

$$\phi_1(x) = -v_1^* N_1^{ww}(x, 0), \quad \chi_1(x) = -v_1^* N_1^{vw}(x, 0), \quad (10.88)$$

$$\phi_2(x) = v_2^* N_2^{ww}(x, 0), \quad \chi_2(x) = v_2^* N_2^{vw}(x, 0). \quad (10.89)$$

With this choice of injection gains, differentiating the transformations (10.78)-(10.79) and (10.80)-(10.81) with respect to time and space, it can be proved that the error system (10.72)-(10.77) is mapped to the following system

$$\partial_t \check{\alpha}_i + v_i^* \partial_x \check{\alpha}_i = 0, \quad (10.90)$$

$$\partial_t \check{\beta}_i - (\gamma_i p_i^* - v_i^*) \partial_x \check{\beta}_i = 0, \quad (10.91)$$

$$\check{\beta}_1(L, t) = r_1 \exp\left(-\frac{L}{\tau_1 v_1^*}\right) \check{\alpha}_1(L, t), \quad (10.92)$$

$$\check{\alpha}_1(0, t) = \check{\alpha}_2(0, t), \quad (10.93)$$

$$\check{\alpha}_2(-L, t) = \exp\left(\frac{-L}{\tau_2 v_2^*}\right) \frac{1}{r_2} \check{\beta}_2(-L, t), \quad (10.94)$$

$$\check{\beta}_2(0, t) = \delta \frac{r_2}{r_1} \check{\beta}_1(0, t) + (1 - \delta) r_2 \check{\alpha}_2(0, t). \quad (10.95)$$

This system is exponentially stable due to Assumption 10.3. Due to the invertibility of the Volterra transformations (10.78)-(10.79) and (10.80)-(10.81), we have the following theorem

Theorem 10.3 *Consider the PDE system (10.66)-(10.71) with the output injections gains defined in (10.88)-(10.89). Then for any L^2 initial condition $(\hat{w}_i(\cdot, 0), \hat{v}_i(\cdot, 0))$, the states (\hat{w}_i, \hat{v}_i) exponentially converge to the states $(\tilde{w}_i, \tilde{v}_i)$.*

10.5.1 Observer with measurement at outlet

In this section, we now assume that the measurement available corresponds to the values of \tilde{q}_i and \tilde{v}_i at the left side of the outlet $x = L$. Since we have

$$\tilde{w}_1(L, t) = \exp\left(\frac{L}{\tau_1 v_1^*}\right) \left(\frac{\gamma_1 p_1^*}{q^*} \tilde{q}_1(L, t) - \frac{1}{r_1} \tilde{v}_1(L, t) \right), \quad (10.96)$$

we can consider that the boundary measurement is

$$Y_L(t) = \tilde{w}_1(L, t). \quad (10.97)$$

The observer system is given by

$$\partial_t \hat{w}_i + v_i^* \partial_x \hat{w}_i = -\mu_i(x)(\tilde{w}_1(L, t) - \hat{w}_1(L, t)), \quad (10.98)$$

$$\partial_t \hat{v}_i - (\gamma_i p_i^* - v_i^*) \partial_x \hat{v}_i = c_i(x) \hat{w}_i - v_i(x)(\tilde{w}_1(L, t) - \hat{w}_1(L, t)), \quad (10.99)$$

$$\hat{w}_1(0, t) = \hat{w}_2(0, t), \quad (10.100)$$

$$\hat{v}_1(L, t) = r_1 \exp\left(-\frac{L}{\tau_1 v_1^*}\right) \hat{w}_1(L, t) + \frac{1-r_1}{\rho_1^*} U_L(t), \quad (10.101)$$

$$\hat{w}_2(-L, t) = \exp\left(\frac{-L}{\tau_2 v_2^*}\right) \frac{1}{r_2} \hat{v}_2(-L, t), \quad (10.102)$$

$$\hat{v}_2(0, t) = \delta \frac{r_2}{r_1} \hat{v}_1(0, t) + (1-\delta) r_2 \hat{w}_2(0, t) + \frac{1-r_2}{\rho_2^*} U_0(t), \quad (10.103)$$

where $\hat{w}_i(x, t)$, $\hat{v}_i(x, t)$ are the estimates of the state variables $\tilde{w}_i(x, t)$ and $\tilde{v}_i(x, t)$. The terms μ_i and v_i are output injection gains that still have to be designed. They are bounded functions respectively defined on $([0, L])^2$ and $([-L, 0])^2$. The corresponding initial conditions of the observer are L^2 functions. Defining the error estimates $\check{w}_i = \tilde{w}_i - \hat{w}_i$ and $\check{v}_i = \tilde{v}_i - \hat{v}_i$, the error system is obtained by subtracting the observer equations in (10.99)-(10.103) from (10.21)-(10.26).

Then us consider the following backstepping transformations

$$\check{\alpha}_1(x, t) = \check{w}_1(x, t) - \int_x^L \bar{N}_1^{ww}(x, \xi) \check{w}_1(\xi, t), \quad (10.104)$$

$$\check{\beta}_1(x, t) = \check{v}_1(x, t) - \int_x^L \bar{N}_1^{vw}(x, \xi) \check{w}_1(\xi, t) d\xi, \quad (10.105)$$

$$\check{\alpha}_2(x, t) = \check{w}_2(x, t) - \int_x^0 \bar{N}_2^{ww}(x, \xi) \check{w}_2(\xi, t) d\xi - \int_0^L F^w(x, \xi) \check{w}_1(\xi, t) d\xi, \quad (10.106)$$

$$\check{\beta}_2(x, t) = \check{v}_2(x, t) - \int_x^0 \bar{N}_2^{vw}(x, \xi) \check{w}_2(\xi, t) d\xi - \int_0^L F^v(x, \xi) \check{w}_1(\xi, t) d\xi, \quad (10.107)$$

where the kernels \bar{N}_1^{ww} and \bar{N}_1^{vw} are bounded functions defined on the set \mathcal{T}_1 , while the kernels \bar{N}_2^{ww} and \bar{N}_2^{vw} are bounded functions defined on the set $\bar{\mathcal{T}}_2$. The kernels F^w and F^v are bounded functions defined on the set $\bar{\mathcal{T}} = \{(x, \xi) \in [-L, 0] \times [0, L]\}$. Note that the transformation (10.104)-(10.105) is invertible. The transformation (10.106)-(10.107) is a combination of a Volterra transformation with an affine transformation and is consequently invertible. The kernels satisfy the following set of PDEs:

$$(\gamma_i p_i^* - v_i^*) \partial_x \bar{N}_i^{vw}(x, \xi) - v_i^* \partial_\xi \bar{N}_i^{vw}(x, \xi) = 0, \quad (10.108)$$

$$\partial_x \bar{N}_i^{ww}(x, \xi) + \partial_\xi \bar{N}_i^{ww}(x, \xi) = 0, \quad (10.109)$$

$$v_2^* \partial_x F^w(x, \xi) + v_1^* \partial_\xi F^w(x, \xi) = 0, \quad (10.110)$$

$$(\gamma_2 p_2^* - v_2^*) \partial_x F^v(x, \xi) - v_1^* \partial_\xi F^v(x, \xi) = 0, \quad (10.111)$$

with the boundary conditions

$$\bar{N}_2^{vw}(x, x) = \frac{c_2(x)}{\gamma_2 p_2^*}, \quad (10.112)$$

$$\bar{N}_1^{vw}(x, x) = \frac{c_1(x)}{\gamma_1 p_1^*}, \quad (10.113)$$

$$\bar{N}_2^{ww}(-L, \xi) = \exp\left(-\frac{L}{\tau_2 v_2^*}\right) \frac{1}{r_2} \bar{N}_2^{vw}(-L, \xi) \quad (10.114)$$

$$F^v(x, 0) = \frac{v_2^*}{v_1^*} \bar{N}_2^{vw}(x, 0), \quad (10.115)$$

$$F^w(x, 0) = \frac{v_2^*}{v_1^*} \bar{N}_2^{ww}(x, 0), \quad (10.116)$$

$$F^w(-L, \xi) = \exp\left(\frac{-L}{\tau_2 v_2^*}\right) \frac{1}{r_2} F^v(-L, \xi), \quad (10.117)$$

$$F^v(0, \xi) = \delta \frac{r_2}{r_1} \bar{N}_1^{vw}(0, \xi) + (1 - \delta) r_2 F^w(0, \xi), \quad (10.118)$$

$$\bar{N}_1^{ww}(0, \xi) = F^w(0, \xi), \quad (10.119)$$

The well-posedness of this kernel PDE-system is guaranteed by the following lemma.

Lemma 10.4 *Consider system (10.108)-(10.119). There exists a unique solution \bar{N}_1^{ww} , \bar{N}_1^{vw} in $\mathcal{B}(\mathcal{T}_1)$, \bar{N}_2^{ww} , \bar{N}_2^{vw} in $L^\infty(\bar{\mathcal{T}}_2)$ and F^w , F^v in $L^\infty(\bar{\mathcal{T}})$.*

Proof The well-posedness of the kernels \bar{N}_2^{ww} and \bar{N}_2^{vw} is proved following [?]. Then we prove the well-posedness of the kernels F^w , F^v , \bar{N}_1^{ww} and \bar{N}_1^{vw} adjusting [?]. \square

Let us now define the output injection gains μ_i and ν_i as

$$\mu_1(x) = -v_1^* \bar{N}_1^{ww}(x, L) + \int_x^L \mu_1(\xi) \bar{N}_1^{ww}(x, \xi) d\xi, \quad (10.120)$$

$$\nu_1(x) = -v_1^* \bar{N}_1^{vw}(x, L) + \int_x^L \mu_1(\xi) \bar{N}_1^{vw}(x, \xi) d\xi, \quad (10.121)$$

$$\mu_2(x) = -v_1^* F^w(x, L) + \int_x^0 \mu_2(\xi) \bar{N}_2^{ww}(x, \xi) d\xi + \int_0^L \mu_1(\xi) \bar{F}^w(x, \xi) d\xi, \quad (10.122)$$

$$\nu_2(x) = -v_1^* F^v(x, L) + \int_x^0 \mu_2(\xi) \bar{N}_2^{vw}(x, \xi) d\xi + \int_0^L \mu_1(\xi) \bar{F}^v(x, \xi) d\xi. \quad (10.123)$$

These output injection gains are perfectly defined: since (10.120) is a Volterra equation of second kind, it is invertible and we can obtain μ_1 . Once μ_1 is obtained, then equation (10.122) becomes a Volterra equation and we can compute μ_2 . Once μ_1 and μ_2 are obtained, the expressions of ν_1 and ν_2 are explicit. With this choice of injection gains, differentiating the transformations (10.104)-(10.105) and (10.106)-(10.107) with respect to time and space, it is straightforward to obtain that the convergence of the observer in the following theorem.

Theorem 10.4 *Consider the PDE system (10.99)-(10.103) with the output injections gains defined in (10.120)-(10.121). Then for any L^2 initial condition $(\hat{w}_i(\cdot, 0), \hat{v}_i(\cdot, 0))$, the states (\hat{w}_i, \hat{v}_i) exponentially converge to the states $(\tilde{w}_i, \tilde{v}_i)$.*

10.6 Output Feedback Laws

The two state feedback laws and the two observers that we have previously designed are employed to construct four possible output feedback laws, which consist of two collocated and two anti-collocated ones, as shown in Table. 1. We are now able to give the main theorem of this chapter.

Theorem 10.5 *Consider the system (10.21)-(10.26) with the control law at $x = 0$*

$$U_0(t) = \frac{\rho_2^*}{1-r_2} \left(\int_{-L}^0 K_2^{vw}(0, \xi) \hat{w}_2(\xi, t) + K_2^{vv}(0, \xi) \hat{v}_2(\xi, t) d\xi \right. \\ \left. - \frac{r_2}{r_1} \int_0^L K_1^{vw}(0, \xi) \hat{w}_1(\xi, t) + K_1^{vv}(0, \xi) \hat{v}_1(\xi, t) d\xi \right), \quad (10.124)$$

or at $x = L$

$$U_L(t) = \frac{\rho_1^*}{1-r_1} \left(\int_0^L \bar{K}_1^{vw}(L, \xi) \hat{w}_1(\xi, t) d\xi + \bar{K}_1^{vv}(L, \xi) \hat{v}_1(\xi, t) d\xi \right. \\ \left. + \int_{-L}^0 M^w(L, \xi) \hat{w}_2(\xi, t) d\xi + M^v(L, \xi) \hat{v}_2(\xi, t) d\xi \right). \quad (10.125)$$

where the estimated states are either given by equations (10.66)-(10.71) or (10.99)-(10.103), depending on the available measurements. Then for any L^2 initial condition, the closed-loop system with the controller (10.124) or (10.125) is exponentially stable at the origin in the sense of Definition 10.2. This implies the local convergence of the initial states of ρ_i and v_i to the steady states ρ_i^* and v_i^* .

Proof We will do the proof only considering the case of an actuation located at $x = L$. First it should be noted that the control law is a L^2 function and that consequently the closed-loop system is well-posed in the sense of Definition 10.1. The other case (actuation at $x = 0$) is treated in a similar way. We consider that an observer is available (either given by (10.66)-(10.71) or by (10.99)-(10.103). The proof uses the same ideas as the ones given in [?, Theorem 5]. As we have $\tilde{v} = -\check{v}_i + \hat{v}_i$ and $\tilde{w} = -\check{w}_i + \hat{w}_i$, the control law (10.125) can be rewritten as

$$U_L(t) = \frac{\rho_1^*}{1-r_1} \left(\int_0^L \bar{K}_1^{vw}(L, \xi) \tilde{w}_1(\xi, t) d\xi \right. \\ \left. + \int_0^L \bar{K}_1^{vv}(L, \xi) \tilde{v}_1(\xi, t) d\xi + \int_{-L}^0 M^w(L, \xi) \tilde{w}_2(\xi, t) d\xi \right. \\ \left. + \int_{-L}^0 M^v(L, \xi) \tilde{v}_2(\xi, t) d\xi \right) + \mathcal{D}(t), \quad (10.126)$$

where \mathcal{D} is function that corresponds to U_L (as given in 10.125) in which the terms \hat{v}_i and \hat{w}_i have been replaced by \check{v}_i and \check{w}_i respectively. Since \check{v}_i and \check{w}_i converge to zero due to Theorem 10.3 or Theorem 10.4, the term \mathcal{D} can be seen as a bounded disturbance that converges to zero. The rest of the proof is a consequence of the Input-to-State Stability of our control law (as shown in [?]). Using the transformation (10.49)-(10.52), we can map the original system (10.21)-(10.26) to the target system the only difference being that a term $\frac{1-r_1}{\rho_1^*} \mathcal{D}(t)$ remains in the actuated boundary. Using the method of the characteristics, we can express $\bar{\alpha}_2(0, t)$ as the solution of a difference equation. This yields

$$\begin{aligned}
\bar{\alpha}_2(0, t) = & (1 - \delta) \exp\left(\frac{-L}{\tau_2 v_2^*}\right) \bar{\alpha}_2\left(0, t - \frac{1}{v_2^*} - \frac{1}{\gamma_2 p_2^* - v_2^*}\right) \\
& + \delta \exp\left(\frac{-L}{\tau_1 v_1^*} - \frac{L}{\tau_2 v_2^*}\right) \bar{\alpha}_2\left(0, t - \frac{1}{v_2^*} - \frac{1}{\gamma_2 p_2^* - v_2^*} - \frac{1}{v_1^*} - \frac{1}{\gamma_1 p_1^* - v_1^*}\right) \\
& + \frac{1 - r_1}{r_1 \rho_1^*} \exp\left(-\frac{L}{\tau_2 v_2^*}\right) \delta \mathcal{D}\left(t - \frac{1}{v_2^*} - \frac{1}{\gamma_2 p_2^* - v_2^*} - \frac{1}{\gamma_1 p_1^* - v_1^*}\right). \quad (10.127)
\end{aligned}$$

In the absence of the disturbance term \mathcal{D} , equation (10.127) is exponentially stable, due to Assumption 10.3. Thus, the corresponding operator generates a contraction semigroup. Using the variations of constants formula (see [?, Section 9.5]) and the fact that \mathcal{D} converges to zero, we can conclude to the convergence to zero of the state $\bar{\alpha}_2(0, t)$. Using the transport structure of the target system, we can conclude to the convergence of the state $(\bar{\alpha}_i, \bar{\beta}_i)$ to zero. The invertibility of the transformation (10.49)-(10.52), implies the stabilization of (10.21)-(10.26) and consequently the local convergence of the initial states of ρ_i and v_i to the steady states ρ_i^* and v_i^* . \square

10.7 Robustness to Input Delays

Considering the uncertainty of traffic flow system, it is practically meaningful to investigate the robustness of our control design. In this section, we mainly discuss the robustness of the proposed controllers to input delays $U_0(t - D_0)$ and $U_L(t - D_L)$, where D_0 and D_L are the constant input delays, as shown in Fig. 10.4. Boundary disturbances are also depicted in Fig. 10.4, including time-varying upstream demand disturbance $d_{-L}(t)$, off-ramp traffic flow disturbances $d_0(t)$ at the middle junction and the outlet boundary flow rate disturbance $d_L(t)$. The proposed controllers can be adapted to reject the boundary disturbances and therefore the assumptions on boundary conditions (8.20), (10.9), (10.10) are relaxed accordingly.

The control and estimation problem for one segment of traffic flow is discussed in [?], of which the finite-time convergence result is not robust to delays in the actuation. However, the proposed output feedback design in this chapter with Assumption 1 guarantees the existence of robustness (delay-) margins for the closed-loop system. More precisely, we have the following theorem

Theorem 10.6 *Consider the system (10.21)-(10.26) with the control law (10.124) at $x = 0$ or the control law (10.125) at $x = L$, where the estimated states are either given by equations (10.66)-(10.71) or (10.99)-(10.103), depending on the available measurements. Then, there exists δ^* such that, for all $(\delta_m, \delta_U) \in [0, \delta^*]^2$, the control law $U_0(t - \delta_U)$ (or $U_L(t - \delta_U)$) computed using the measurement $y(t - \delta_m)$ exponentially stabilizes the system (10.21)-(10.26), that is for any L^2 initial condition, the states \tilde{w} and \tilde{v} exponentially converge to zero in the sense of Definition 10.2. This*

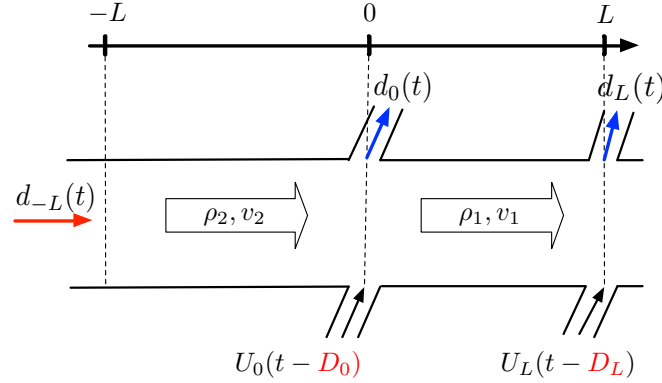


Fig. 10.4 Robustness of the control design to boundary disturbances from time-varying upstream demand $d_{-L}(t)$, to boundary disturbances from off-ramp traffic flow $d_0(t)$ at the junction and the outlet boundary $d_L(t)$, to input delays $U_0(t - D_0)$ and $U_L(t - D_L)$.

implies the local convergence of the initial states of ρ_i and v_i to the steady states ρ_i^* and v_i^* .

Proof The robustness properties of the state-feedback control law and the output-feedback law is obtained adjusting the approach developed in [?]. It is a consequence of the fact that the control law is strictly proper. It has been proved in [?] that a necessary condition to guarantee the existence of robustness (delay-) margins for the closed-loop system is that the open-loop transfer function must have a finite number of poles on the closed right half-plane. For the considered interconnected linear hyperbolic system, such a condition is equivalent to requiring that the open-loop system (10.21)-(10.26) with zero in-domain couplings (i.e. $c_1 \equiv c_2 \equiv 0$) must be exponentially stable in open-loop. Necessary and sufficient stability conditions to guarantee such an open-loop stability can be obtained by writing the corresponding characteristic equations. For the system (10.21)-(10.26), in the absence of in-domain couplings and actuation, we obtain the following equation using the method of characteristics

$$\begin{aligned} \tilde{w}_2(0, t) = & (1 - \delta) \exp\left(\frac{-L}{\tau_2 v_2^*}\right) \tilde{w}_2\left(0, t - \frac{1}{v_2^*} - \frac{1}{\gamma_2 p_2^* - v_2^*}\right) \\ & + \delta \exp\left(\frac{-L}{\tau_1 v_1^*}\right) \exp\left(\frac{-L}{\tau_2 v_2^*}\right) \tilde{w}_2\left(0, t - \frac{1}{v_2^*} - \frac{1}{\gamma_2 p_2^* - v_2^*} - \frac{1}{v_1^*} - \frac{1}{\gamma_1 p_1^* - v_1^*}\right) \end{aligned} \quad (10.128)$$

Using the transport structure of the system (10.21)-(10.26) when $c_i \equiv 0$, if $\tilde{w}_2(t, 0)$ exponentially converges to zero, then the whole state $(\tilde{v}_i, \tilde{w}_i)$ exponentially converges to zero. A simple necessary and sufficient condition to guarantee the exponential stability of (10.128) can be found in [?]:

$$|1 - \delta| \exp\left(\frac{-L}{\tau_2 v_2^*}\right) + \delta \exp\left(\frac{-L}{\tau_1 v_1^*}\right) \exp\left(\frac{-L}{\tau_2 v_2^*}\right) < 1.$$

It is observed that this condition is always satisfied when $\delta < 1$. Then, Assumption 10.3 guarantees that the proposed feedback laws have some delay-robustness margins. \square

Here we briefly discuss the boundary disturbances for practical interests. Assume that there is traffic leaving the freeway from off-ramp located at $x = 0$ with a flow rate of $d_0(t) > 0$, then the boundary condition at the junction becomes

$$q_1(0, t) = q_2(0, t) + U_0(t) - d_0(t). \quad (10.129)$$

We assume that the off-ramp flow rate $d_0(t) > 0$ is measured in real-time, then the $U_0(t)$ can be directly adjusted to reject the off-ramp boundary disturbances. For the outlet boundary, the controller $U_L(t)$ can be designed in the same fashion

$$q_1(L, t) = q^* + U_L(t) - d_L(t). \quad (10.130)$$

The time-varying upstream traffic demand results into inlet boundary disturbance $d_{-L}(t)$,

$$q_2(-L, t) = q^* + d_{-L}(t). \quad (10.131)$$

In the linearized model, the disturbed boundary condition (10.25) becomes $\tilde{w}_2(-L, t) = \exp\left(\frac{-L}{\tau_2 v_2^*}\right) \frac{1}{\tau_2} \tilde{v}_2(-L, t) + d_{-L}(t)$. Adjusting the techniques and methods presented in [?, ?], we can show that as long as the proposed control law remains strictly proper, the closed-loop system is Input-to-State Stable (ISS) concerning boundary disturbances $d_{-L}(t)$. The analysis can be done by expressing the system in its neutral form. The complete robustness proof is however outside the scope of this chapter. If off-ramp flow rate $d_0(t)$, $d_L(t)$ and varying upstream traffic demand $d_{-L}(t)$ are unknown, adaptive disturbance rejection control problem needs to be solved. The existing adaptive design in [?] can be applied to the fully actuated system with both controllers being employed. We do not pursue this further here. Some delay robustness results will be demonstrated with numerical simulation in the next section.

10.8 Simulation results

In this section, we first validate the control design with numerical simulations and two collocated output feedback closed-loop results are compared. Then we demonstrate the robustness of the proposed controllers to delays in the actuation path. In the end, our control design is compared with PI boundary controllers which fully actuate the interconnected system. As stated in Table.1, there are four proposed output feedback controllers but only the simulation results of the two collocated ones are conducted.

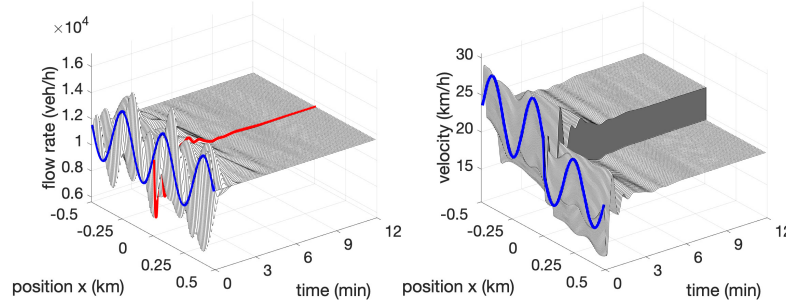


Fig. 10.5 The closed-loop simulation of traffic flow rate and velocity, with the ramp metering control input $U_0(t)$ and measurement $Y_0(t)$ from the middle junction $x = 0$, converges to steady states. The controlled flow rate evolution at $x = 0$ is highlighted in red.

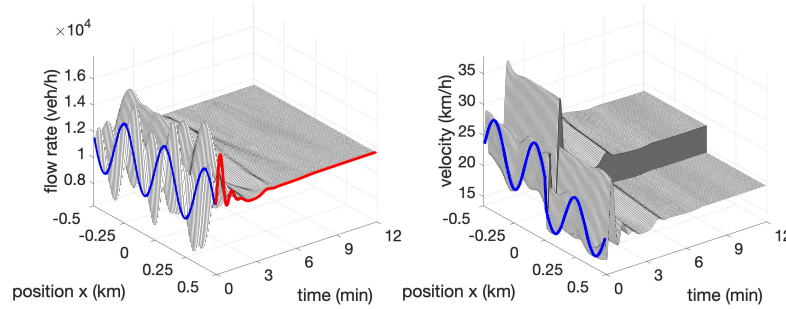


Fig. 10.6 The closed-loop simulation of traffic flow rate and velocity, with the ramp metering control input $U_L(t)$ and measurement $Y_L(t)$ from the outlet boundary $x = L$, converges to steady states. The controlled flow rate evolution at $x = L$ is highlighted in red.

The collocated controllers are the most relevant in practice since the anti-collocated sensor and actuator in the distance will have delays and errors caused by long-distance communication.

The length of each freeway segment is chosen to be $L = 0.5$ km so the total length of the two connected segments are 1 km. The simulation time is $T = 12$ min. The maximum speed limit is $v_m = 40$ m/s = 144 km/h. We consider 6 lanes for the downstream freeway segment 1. Assuming the average vehicle length is 5 m plus the minimum safety distance of 50% vehicle length, the maximum density of the road is obtained as $\rho_{m,1} = 6/7.5$ vehicles/m = 800 vehicles/km. The upstream segment has less functional lanes thus its maximum density is $\rho_{m,2} = 700$ vehicles/km. We take $\gamma_i = 0.5$. The steady states (ρ_1^*, v_1^*) and (ρ_2^*, v_2^*) are chosen respectively as (600 vehicles/km, 19.4 km/h) and (488.6 vehicles/km, 23.8 km/h), both of which are in the congested regime and satisfy (10.14) and (10.15). The constant flow rate is $q^* = \rho_1^* v_1^* = \rho_2^* v_2^* = 11640$ vehicles/h, same for the two segments. If we consider the segment 1 with 6 lanes, then the averaged flow rate of each lane

is 1940 vehicles /h/lane. The equilibrium steady state of the downstream road has higher density and lower velocity, thus is more congested than the upstream road. The relaxation time is $\tau_1 = 90$ s and $\tau_2 = 60$ s. We use sinusoid initial conditions for flow rate and velocity field which represent the stop-and-go oscillations on the connected freeway and are highlighted in the figures with blue. The two-step Lax-wendroff numerical scheme discussed in Chapter 1 is applied to the original plant.

Output feedback stabilization

We consider the traffic scenario that the downstream traffic in segment 1 is denser with slower velocity, compared with the upstream traffic in segment 2, as illustrated by the steady states. The closed-loop simulation with the collocated output feedback control input from the middle junction shows that the exponential convergence to the steady states is achieved simultaneously for the upstream and downstream segments in Fig. 10.5, where the actuated junction flow rate by the on-ramp metering is highlighted in red. Note that the steady state velocities are different for two freeway segments and the flow rates are constant across the two segments. The output feedback stabilization with the control input and measurement of velocity and flow rate from the outlet boundary is shown in Fig. 10.6. The controlled flow rate at the outlet boundary is highlighted in red. Comparing the two output feedback closed-loop simulations in Fig. 10.5 and Fig. 10.6, we find out that the outlet controller takes around the same convergence time but has larger transient to stabilize the system. The controlled flow rate at the middle junction with ramp metering input $U_0(t)$, highlighted in red in Fig. 10.5, firstly decreases such that less traffic is allowed into the downstream where traffic is denser. The controlled flow rate at the outlet with $U_L(t)$, highlighted in red in Fig. 10.6, increases initially such that more traffic is discharged from the segment.

To further compare the two collocated output feedback stabilization results, the closed-loop performance is demonstrated with the temporal evolution of the state variables in the spatial averaged L^2 -norm, defined as

$$S_{q_i}(t) = \left| \frac{1}{L} \int_X \left(\frac{q_i(x,t) - q^*}{q^*} \right)^2 dx \right|^{1/2}, \quad (10.132)$$

$$S_{v_i}(t) = \left| \frac{1}{L} \int_X \left(\frac{v_i(x,t) - v_i^*}{v_i^*} \right)^2 dx \right|^{1/2}, \quad (10.133)$$

where $X = [-L, 0] \cup [0, L]$ represents the spatial domain of the two segments. As shown in the Fig. 10.7, the closed-loop convergence time of both output controllers are around the same at $t = 9$ min, whereas the output feedback controller at the outlet has a larger transient for all the state variables than the output feedback at the middle junction. At around $t = 2$ min, the blue highlighted line has a bigger overshoot than the red one. In addition, the appearance of transient peak appears later in the blue

line than the red one. we explain these observations by the different mechanism of the proposed two controllers.

The ramp metering control input located at the downstream outlet is carried upstream by the propagation of velocity variations to mitigate traffic oscillations in both segments. In contrast, the ramp metering control input located at the middle junction works in a way that the actuated velocity variation at the junction travels upstream and the actuated flow rate variations travel downstream with the traffic. Therefore, it takes a longer time for the control input to take effect on the upstream segment 2 when the output feedback is applied at the downstream outlet, whereas the output feedback at the middle junction instantly starts stabilizing both the upstream segment 2 and downstream segment 1. In addition, before the oscillations states are suppressed, the overshoot develops into a larger value and appears a bit later, as demonstrated in the Fig. 10.7.

Robustness to delays

In Section 10.7, we discuss the robustness of our control design to external boundary disturbances and delays in actuation path. We conduct a simulation for the closed-loop system with actuation constant delays D_0 and D_L that are respectively 0 s, 30 s, 60 s, 120 s, where 0 s represents no delay and 120 s is the time length for the control input signal to traverse the two segments. Based on the definition in (10.132)-(10.133), we define an overall closed-loop performance index

$$S(t) = S_{q_i}(t) + S_{v_i}(t), \quad (10.134)$$

where $i = 1, 2$. Then the temporal evolution of $S(t)$ is plotted for the closed-loop system with the delayed collocated output feedback in Fig. 10.8.

For the collocated controller located at the middle junction U_0 , as shown in the left figure of Fig. 10.8, we found out that the stabilization result still holds for $D_0 = 0$ min, 0.5 min, 1 min, and 2 min but deteriorates for the case of $D_0 = 2$ min, plotted with dotted line. We validate that some robustness margins are conserved with Assumption 1 being satisfied. The transient gets larger as the delay time is increased from $D_0 = 0$ min till $D_0 = 2$ min. A similar behavior can be observed for the closed-loop with the collocated controller at the outlet. Therefore, both control designs have some robustness margins to delays. Besides, the delay effect is exhibited by the right figure of Fig. 10.8. The transient peak appears later as the actuation delay is increased from $D_0 = 0$ min till $D_0 = 2$ min. It is also noted that the same behavior is not observed in the case with middle actuation. This is due to the difference between the way that two controllers work in the interconnected segments. The middle junction controller U_0 stabilizes the upstream traffic by affecting velocity variation which propagates upstream and at the same time actuating the downstream traffic flow rate which travels in the same direction of traffic. In contrast, the outlet controller U_L stabilizes the traffic through upstream propagation of velocity variation which only

involves a single direction. Therefore the delayed actuation is easily manifest in the right figure of Fig. 10.8. The last observation is that more control effort is needed for the delayed outlet controller than that of the middle one, which agrees with the output stabilization comparison.

Comparison with PI controllers

PI control has been applied for a wide range of engineering problems including traffic control by ramp metering and VSL [?, ?]. The PI boundary control was developed in [?] to stabilize the first-order density-flow hyperbolic system. For macroscopic second-order PDE model, [?, ?] developed PI boundary feedback controllers for the linearized ARZ model. For one-segment freeway traffic in [?], boundary values of velocity at the inlet and density at the outlet are measured to construct a PI feedback ramp metering controlling the inflow rate and a varying speed limit at the outlet controlling the velocity of outgoing traffic. Besides, [?] applied the same method for a cascaded freeway with each segment being controlled in the same fashion. In comparison, if two cascaded freeway segments are considered, four boundary controllers are employed by [?] including one ramp metering at inlet $x = -L$, one ramp metering and one VSL at middle junction $x = 0$, and one VSL at outlet $x = L$, as illustrated in Fig. 10.9. The controlled system is fully actuated since there are four boundary conditions and all of them are being actuated, whereas, in our design, only one boundary is actuated by ramp metering, either at the middle junction or at the outlet.

We applied the PI boundary feedback laws in [?] to the control model (10.1)-(10.2) where both segments are congested and traffic oscillations need to be suppressed. The four PI boundary controllers R_{-L}, R_0, V_0, V_L are defined respectively for the controlled flow rate at inlet $x = -L$, the controlled flow rate at middle junction $x = 0$, the controlled velocity at middle junction $x = 0$ and the controlled velocity at outlet $x = L$. The fully actuated boundaries are defined as

$$q_2(-L, t) = R_{-L}(t), \quad v_2(0, t) = V_0(t), \quad (10.135)$$

$$q_1(0, t) = R_0(t), \quad v_1(L, t) = V_L(t), \quad (10.136)$$

where the boundary feedback controllers are given by

$$R_{-L}(t) = q^* + k_P^r \tilde{\rho}_2(0, t) + k_I^r \int_0^t \tilde{\rho}_2(0, t) ds, \quad (10.137)$$

$$V_0(t) = v_2^* + k_P^v \tilde{v}_2(-L, t) + k_I^v \int_0^t \tilde{v}_2(-L, t) ds, \quad (10.138)$$

$$R_0(t) = q^* + l_P^r \tilde{\rho}_1(L, t) + l_I^r \int_0^t \tilde{\rho}_1(L, t) ds, \quad (10.139)$$

$$V_L(t) = v_1^* + l_P^v \tilde{v}_1(0, t) + l_I^v \int_0^t \tilde{v}_1(0, t) ds. \quad (10.140)$$

where $k_P^r, k_I^r, k_P^v, k_I^v$ are tuning gains for the upstream segment 2, $l_P^r, l_I^r, l_P^v, l_I^v$ are tuning gains for the downstream segment 1 and q^*, v_i^* are the steady states. We use the previous model parameters and conduct the simulation under the same initial conditions such that the PI controllers can be directly compared with the control design in this chapter. The tuning gains are chosen to be $k_P^r = -55, k_I^r = -0.035, k_P^v = -0.6, k_I^v = -0.025$ and $l_P^r = -10, l_I^r = -0.035, l_P^v = -0.5, l_I^v = -0.005$.

Then the output feedback stabilization result is shown in Fig. 10.10 where the temporal evolution of the four PI control inputs are highlighted including two ramp metering in red and two VSLs with green. We then compare the closed-loop performance of the PDE backstepping controller and the PI controllers with the evolution of state variables in the spatial averaged L^2 -norm, defined with $S(t)$ in (10.134). In Fig. 10.11, the closed-loop performance with the ramp metering backstepping controller at middle junction $U_0(t)$ is plotted with the blue line, the one with the ramp metering backstepping controller at outlet $U_L(t)$ is plotted in red dotted line and the one with the four PI controllers is plotted with the yellow dashed line. We can see that the convergence time and the transient is about the same for $U_0(t)$ and four PI controllers. The outlet backstepping controller $U_L(t)$ takes a relatively longer time and larger transient to stabilize the system.

The main differences between the PI control design and PDE backstepping design lie in the following aspects: first, PDE backstepping control design in this chapter utilizes the cascaded system structure and then achieves the stabilization with one ramp metering output feedback controller, whereas the fully actuated system needs four PI controllers implemented with both ramp metering and VSLs. Secondly, PI controllers only employ constant control gains and therefore easy to construct. PDE backstepping controller has spatially varying control gains that are directly solved from the kernel equations given by the model parameters. Tuning of eight control gains of the PI controllers could be time-consuming and is thus avoided with the PDE backstepping control design. Besides, the collocated sensor and actuator proposed in this chapter is easier for implementation in practice, without concerns about the long-distance signal communication on the freeway. Finally, it should be noted that the PI controllers can still work for partial road segment if one of the actuators fails. PDE backstepping controllers do not have such resilience since they rely on the freeway cascaded structure.

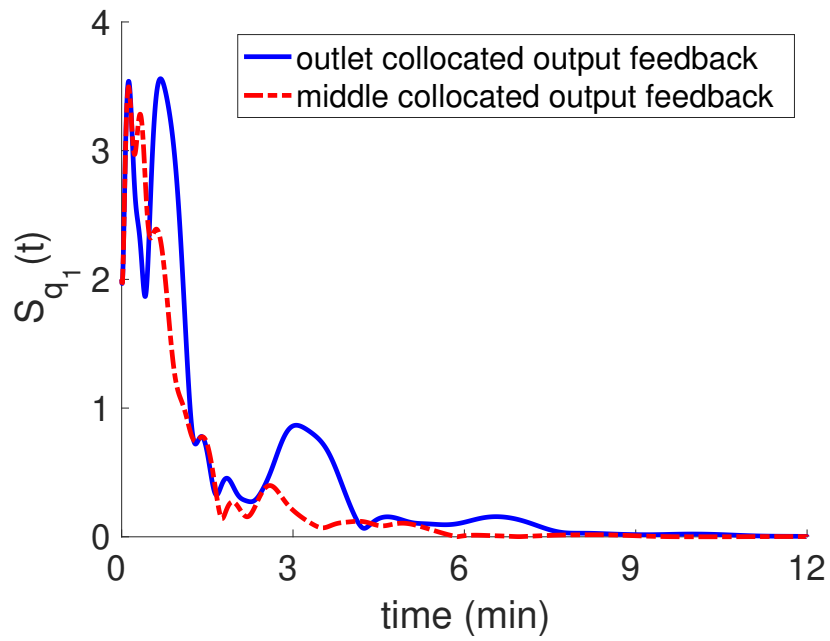
10.9 Notes and References

We design stabilizing output feedback control laws that guarantee the simultaneous stabilization of the traffic flow on two cascaded roads around given steady states. The flow actuation is realized with the ramp metering at the junction or the downstream outlet. The observers are designed collocated by sensing traffic velocity and flow rate at the two locations. The proposed controllers are robust to actuation delays. A more comprehensive robust control design to model parameters, external boundary, and in-domain disturbances will be of future research interest. Comparing the two collocated output feedback controllers, the middle junction one has faster convergence and smaller transient than the outlet one. The trade-offs between the proposed PDE backstepping controller with the PI static output feedback controllers are also discussed. This work will serve as a step forward towards the stabilization of congested traffic on multiple cascaded freeway road networks.

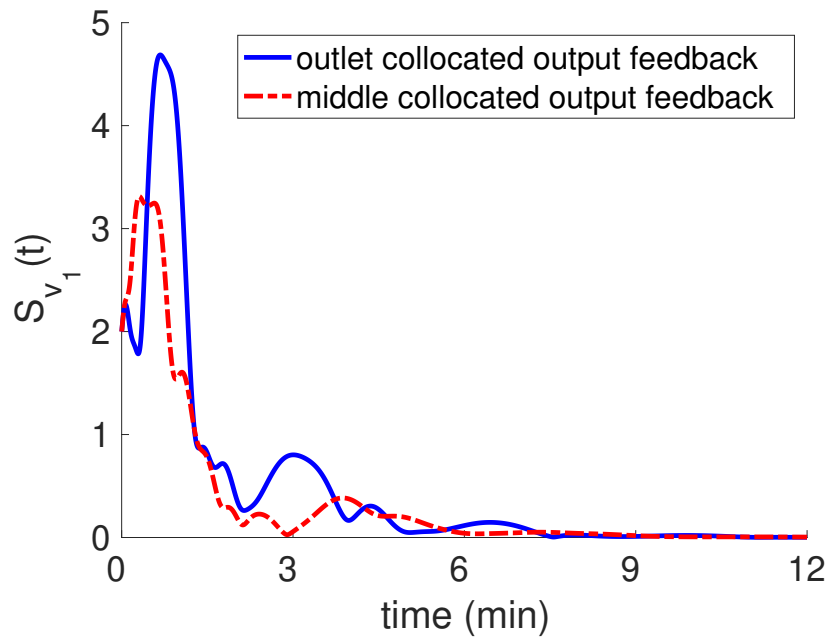
Boundary control strategies for macroscopic traffic network have been studied using other approaches [?, ?, ?, ?, ?], focused on controlling the spatially discretized approximation of LWR model, namely cell transmission model and its derivation, but the discretized systems sometimes exhibit discrepancies from the original continuous traffic PDE model. Article [?] develops an optimal control framework based on Hamilton-Jacobi formulation of the LWR model. Papers [?, ?] consider adjoint-based optimization formulation for the control problem of a LWR-based traffic network by regulating nodes of the network. Besides controlling from fixed-locations by ramp metering and VSLs, the emerging Lagrangian sensing and actuation with connected autonomous vehicles have been intensively studied in recent years for traffic freeway management [?, ?, ?, ?, ?, ?, ?, ?, ?].

Boundary control of the network of hyperbolic PDEs has been intensively studied over the past years. Despite many theoretical results in the literature, boundary control of PDE networks remains a challenging research topic. This is because these systems are underactuated. For practical consideration, only the PDEs located at some nodes of the network can be actuated. To tackle this problem, multiple approaches have been proposed: PI boundary controllers for fully actuated networks [?, ?], flatness based design of feedforward control laws for tree-like transmission networks [?, ?]. While the backstepping approach has been successfully applied to design boundary controls for a large class of hyperbolic PDE system as introduced in Chapter 2, the considered system always have (at least) one boundary which is fully actuated. Recently [?] developed backstepping-based state feedback control laws for the underactuated network of hyperbolic PDEs. This class of system is also used to model the dynamics of many industrial applications, including water networks in open-channels [?], communication networks [?], and gas networks in pipelines [?, ?].

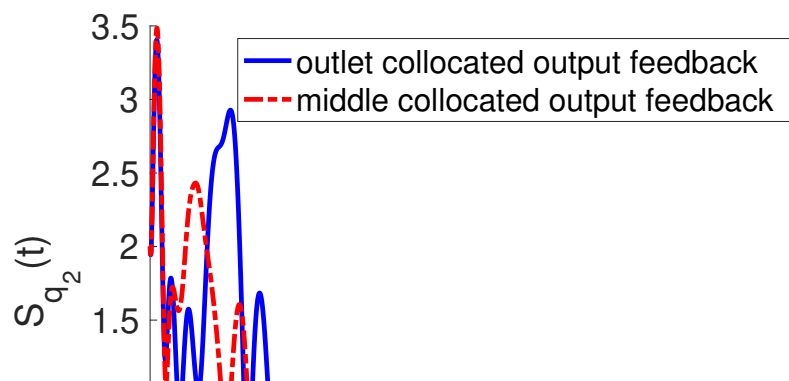
[b]0.49



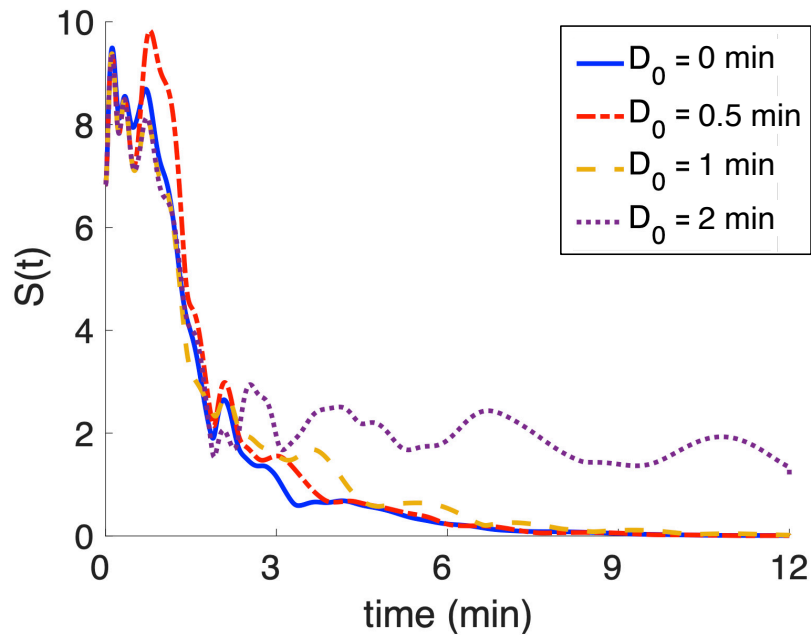
[b]0.49



[b]0.49



[b]0.49



[b]0.49

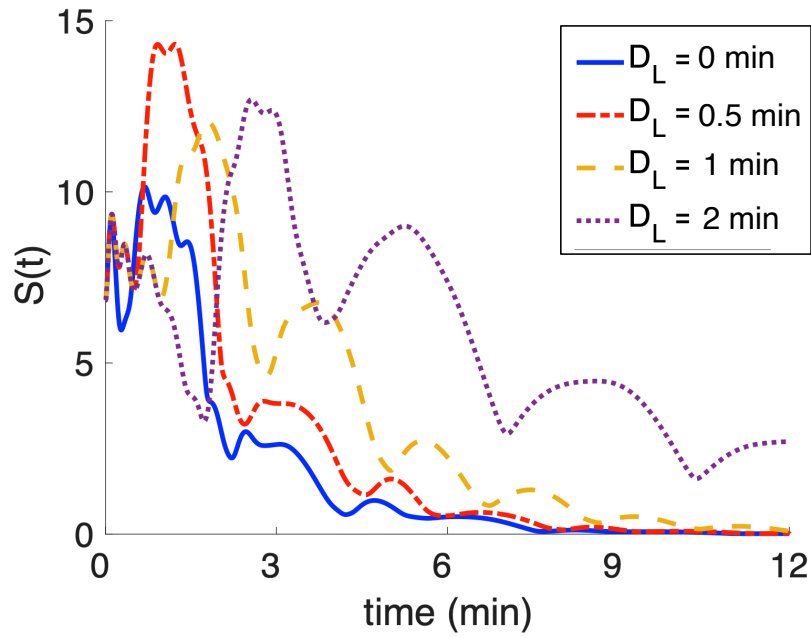


Fig. 10.8 The temporal evolution of $S(t)$ of the closed-loop with delayed control inputs with delay time to be 0 min, 0.5 min, 1 min and 2 min.

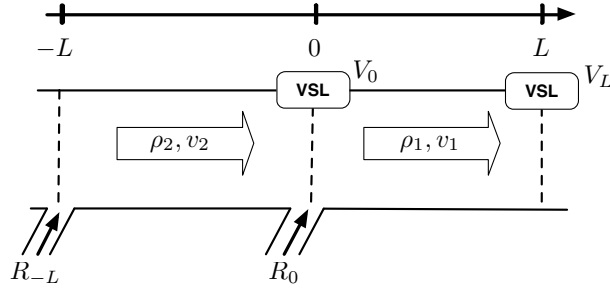


Fig. 10.9 The fully-actuated traffic system with two ramp metering R_{-L} , R_0 and two VSL PI controllers V_0 and V_L .

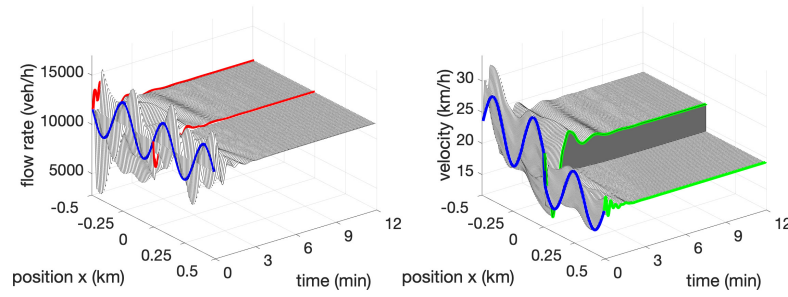


Fig. 10.10 The closed-loop simulation with two PI boundary feedback ramp metering controllers $R_{-L}(t)$, $R_0(t)$, highlighted in red, and two VSL PI controllers $V_0(t)$ and $V_L(t)$, highlighted with green.

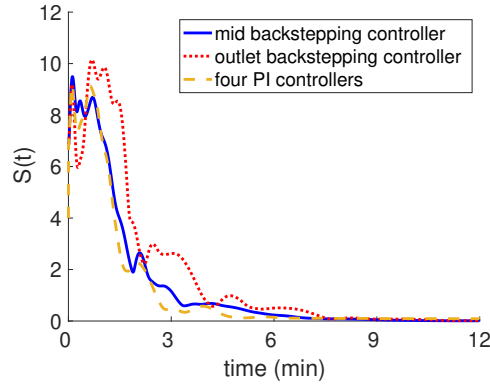


Fig. 10.11 The closed-loop performance with ramp metering backstepping controller $U_0(t)$, ramp metering backstepping controller $U_L(t)$ and with four PI controllers including two ramp metering $R_{-L}(t)$, $R_0(t)$, and two VSLs $V_0(t)$ and $V_L(t)$.

Chapter 11

Estimation of Freeway Diverge Flows

In Section 10.1 we discussed at length the issues of extending the results on control of traffic flows from a single freeway segment to more general traffic flow topologies—to networks of segments. In the rest of Chapter 10 we developed designs for the simplest traffic network, a cascade of two segment.

The next step in increasing the complexity of traffic networks is to go to a tree structure with three segments. There exist two possible three-segment tree topologies: a *merge* and a *diverge*. We assume that the reader knows what these two terms mean, either from experience or from common sense. But we explain. A merge is where two parallel traffic segments converge and form a single segment with traffic flowing in the same direction. A diverge is where a single traffic segment “forks out” (bifurcates) into two distinct segments flowing in the same direction.

Many problems can be formulated for merge and diverge configurations. For instance, a control problem can be formulated for the merge configuration, with ramp metering available at the inlets of the two in-flowing segments, as well as with a third ramp metering at the outlet of the out-flowing segment. Other actuation possibilities exist for the merge configuration and, likewise, for the diverge configuration.

Analogously to control of merge with ramp metering at the two inlets and the one outlet, state estimation can be formulated for the *diverge* configuration, with sensors at the one inlet and the two outlets.

Since, in Chapter 10, we explored the problems for a cascade of two traffic segments as a problem of control, it is interesting to explore the three-segment merge and diverge configurations with a focus on state estimation, instead of control.

So, in this chapter, we focus on the diverge configuration, which we shall also refer to as a “Y” junction, and explore the estimation of the flows using measurements at the one inlet and the two outlets.

Traffic state estimation refers to acquisition of traffic state information from partially observed traffic data. The macroscopic traffic dynamics on each road segment of the Y-junction we study in this chapter are governed by the ARZ model, consisting of second-order nonlinear PDEs of traffic density and velocity. Using PDE backstepping method, we first construct a boundary observer from a copy of the plant and output injections from boundary measurement errors. The exponential stability of

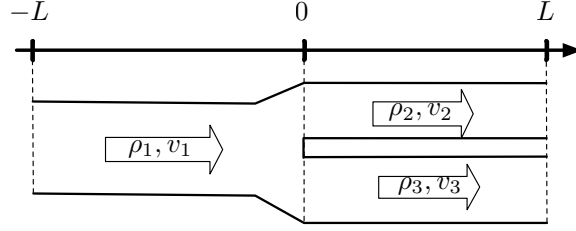


Fig. 11.1 Traffic flow on one incoming road and two outgoing road connected with a junction.

the estimation error system to zero in the L^2 norm is achieved. For robustness of the observer design, we prove the Input-to-State Stability (ISS) of the estimation error system with respect to in-domain spatially distributed disturbances and measurement noise.

The Input-to-State Stability (ISS) which discusses the robustness of system with respect to initial states and external disturbances has been studied for linear and nonlinear PDEs in [?, ?, ?, ?, ?, ?, ?]. Among the two different methodologies for deriving the ISS estimates pointed out in [?], we use ISS-Lyapunov functionals to obtain the ISS estimates in the L^2 norm. The ISS estimate in the sup-norm can be derived through transformation to integral delay equations and integration on the characteristic line as in [?, ?].

11.1 PDE model of one incoming and two outgoing roads

We describe the traffic network as shown in Fig. 11.1 based on the ARZ PDE model, given in [?]. The evolution of traffic density $\rho_1(x, t)$ and velocity $v_1(x, t)$ on the incoming road for $(x, t) \in [-L, 0] \times [0, \infty)$ and traffic densities $\rho_2(x, t)$, $\rho_3(x, t)$ and velocity $v_2(x, t)$, $v_3(x, t)$ for $(x, t) \in [0, L] \times [0, \infty)$ is modeled by the following ARZ model,

$$\partial_t \rho_i + \partial_x (\rho_i v_i) = 0, \quad (11.1)$$

$$\partial_t (\rho_i w_i) + \partial_x (\rho_i v_i w_i) = - \frac{\rho_i (v_i - V_i(\rho_i))}{\tau_i}, \quad (11.2)$$

$$\rho_1(-L, t) v_1(-L, t) = y_1(t), \quad (11.3)$$

$$\rho_1(0, t) v_1(0, t) = \rho_2(0, t) v_2(0, t) + \rho_3(0, t) v_3(0, t), \quad (11.4)$$

$$w_2(0, t) = w_1(0, t), \quad (11.5)$$

$$w_3(0, t) = w_1(0, t), \quad (11.6)$$

$$q_2(L, t) = y_2(t), \quad (11.7)$$

$$q_3(L, t) = y_3(t), \quad (11.8)$$

where $i = 1, 2, 3$. The time-varying $y_i(t)$ represent the measured boundary inputs of traffic flow rate, among which $y_1(t)$ represents the upstream traffic demand, and $y_2(t)$, $y_3(t)$ represent the boundary flow rate from link 2 and link 3 respectively.

The variable w_i is interpreted as traffic "friction" or drivers' aggressiveness which transports with vehicles in the traffic flow. The traffic flow velocity v_i is related to w_i by

$$v_i = w_i - p_i(\rho_i), \quad (11.9)$$

where the traffic pressure is defined as an increasing function of the density,

$$p_i(\rho_i) = (v_m / \rho_{m,i}^{\gamma_i}) \rho_i^{\gamma_i}. \quad (11.10)$$

The traffic pressure $p_i(\rho_i)$ is interpreted as the effect that forces drivers to slow down when there is a dense local traffic density ahead. The maximum velocity v_m is assumed to be the same for the three road segments while the maximum density $\rho_{m,i}$ and coefficient $\gamma_i \in \mathbb{R}^+$ representing drivers' property are allowed to vary in the different segments, due to different compositions of drivers and road attributes. The equilibrium density-velocity relation on each road is given in the form of Greenshield's model

$$V_i(\rho_i) = v_m \left(1 - (\rho_i / \rho_{m,i})^{\gamma_i}\right). \quad (11.11)$$

We denote the traffic flow rate on each road as

$$q_i = \rho_i v_i. \quad (11.12)$$

The equilibrium flow rate and density relation, also known as the fundamental diagram, is then given by

$$Q_i(\rho_i) = \rho_i V_i(\rho_i) = \rho_i v_m \left(1 - \left(\frac{\rho_i}{\rho_{m,i}}\right)^{\gamma_i}\right). \quad (11.13)$$

The relaxation time $\tau_i \in \mathbb{R}^+$ is assumed to be constant. If we consider an empty road so that $\rho_i = 0$, then $V_i(\rho_i) = v_m$ and $w_i = v_i$. Therefore, the state variable w_i represents the heterogeneity of traffic flow, namely, the property of each vehicle, with respect to aggregated equilibrium density-velocity relation $V(\rho)$. The critical density $\rho_{c,i}$ is given by

$$\rho_{c,i} = \frac{\rho_{m,i}}{(1 + \gamma_i)^{1/\gamma_i}} \quad (11.14)$$

such that $Q_i'(\rho_i)|_{\rho_i=\rho_{c,i}} = 0$. The critical density segregates the free regime and congested regime of equilibrium traffic states. The traffic flow is said to be in the free regime when the density satisfies $\rho_i < \rho_{c,i}$. The traffic flow is said to be congested when the density satisfies $\rho_i > \rho_{c,i}$. We are interested in a situation that the traffic is congested for all three of the segments.

Regarding the boundary conditions at the junction, the Rankine-Hugoniot condition is satisfied. This implies the conservation of the mass and drivers' property. We assume that the continuity of the flux and drivers' property across the boundary conditions as defined in (11.4),(11.5),(11.6). The measurement of the traffic flow rate $y_i(t)$ defined in (11.3),(11.7),(11.8) are taken at the inlet $x = -L$ and the outlet $x = L$. The objective of the observer design is to estimate the PDE states of the traffic flow in all of the road segments as shown in Fig. 11.1 with only boundary sensing.

11.2 Linearized model in the Riemann coordinates

The linearized model is given in the following Riemann variables defined as

$$\tilde{w}_i = w_i - w_i^*, \quad (11.15)$$

$$\tilde{v}_i = v_i - v_i^*. \quad (11.16)$$

where w_i^* and v_i^* are the steady state values that are derived from the steady states of (ρ_i^*, v_i^*) . They are chosen such that the boundary conditions (11.3) and (11.8) are satisfied, i.e.

$$\rho_1^* v_1^* = \rho_2^* v_2^* + \rho_3^* v_3^*, \quad (11.17)$$

$$w_2^* = w_3^* = w_1^* = v_m, \quad (11.18)$$

where the steady state velocities satisfy the equilibrium density-velocity relation $v_i^* = V_i(\rho_i^*)$. The constant flux q_i^* in (11.17) satisfies $q_i^* = Q_i(\rho_i^*)$ according to the density-flow relation. Since we have $q_1^* = q_2^* + q_3^*$ in (11.17), we assume that

$$q_2^* = \delta q_1^*, \quad (11.19)$$

$$q_3^* = (1 - \delta) q_1^*, \quad (11.20)$$

where δ represents the splitting ratio of the traffic flux at the junction from the incoming road to the two outgoing roads and satisfies $0 \leq \delta \leq 1$. The constant driver's property in (11.18) implies that we have the same maximum velocity v_m for the three segments. Then a spatial transformation

$$\bar{w}_i(x, t) = \exp\left(\frac{x}{\tau_i v_i^*}\right) \tilde{w}_i(x, t), \quad (11.21)$$

is applied to simplify the linearized model $(\tilde{w}_i, \tilde{v}_i)$. The linearized system rewrites as

$$\partial_t \bar{w}_i + v_i^* \partial_x \bar{w}_i = 0, \quad (11.22)$$

$$\partial_t \tilde{v}_i - (\gamma_i p_i^* - v_i^*) \partial_x \tilde{v}_i = c_i(x) \bar{w}_i, \quad (11.23)$$

$$\bar{w}_1(-L, t) = \exp(-L/(\tau_1 v_1^*)) \left(\frac{1}{r_1} \bar{v}_1(-L, t) + \tilde{y}_1(t) \right), \quad (11.24)$$

$$\bar{w}_j(0, t) = \bar{w}_1(0, t), \quad (11.25)$$

$$\begin{aligned} \tilde{v}_1(0, t) = & r_1 \left[(1 - \delta \sigma_{12} - (1 - \delta) \sigma_{13}) \bar{w}_1(0, t) \right. \\ & \left. + \frac{\delta \sigma_{12}}{r_2} \tilde{v}_2(0, t) + \frac{(1 - \delta) \sigma_{13}}{r_3} \tilde{v}_3(0, t) \right], \end{aligned} \quad (11.26)$$

$$\tilde{v}_j(L, t) = r_j \exp(-L/(\tau_j v_j^*)) \bar{w}_1(L, t) - \tilde{y}_j(t), \quad (11.27)$$

where $j = 2, 3$ are for traffic states and parameters on the two outgoing roads, the spatially varying coefficients $c_i(x)$ are defined as

$$c_i(x) = -\frac{1}{\tau_i} \exp\left(-\frac{x}{\tau_i v_i^*}\right). \quad (11.28)$$

The varying demand and supply of the traffic flow at the inlet and outlet of the segments is reflected by the errors between the steady traffic flow rates and the actual measurements

$$\tilde{y}_i(t) = y_i(t) - q_i^*, \quad (11.29)$$

as shown in (4.7), (11.27). The constant coefficients σ_{12} and σ_{13} are defined by

$$\sigma_{12} = \frac{\gamma_2 p_2^*}{\gamma_1 p_1^*} > 0, \quad (11.30)$$

$$\sigma_{13} = \frac{\gamma_3 p_3^*}{\gamma_1 p_1^*} > 0. \quad (11.31)$$

They represent the ratios between the drivers' aggressiveness and the traffic pressure of either of the outgoing segments and the incoming segment. The constant coefficients r_i represent the ratio of characteristic speeds

$$r_i = -\frac{v_i^*}{\gamma_i p_i^* - v_i^*}, \quad (11.32)$$

and

$$p_i^* = p_i(\rho_i^*). \quad (11.33)$$

For the congested regime we have $\rho_i^* > \frac{\rho_{m,i}}{(1+\gamma_i)^{1/\gamma_i}}$ so that the characteristic speed $\gamma_i p_i^* - v_i^* > 0$. Thus the following inequalities are satisfied,

$$-1 < r_i < 0. \quad (11.34)$$

The smaller the absolute value of the ratio constant r_i indicates a more congested traffic.

11.3 Boundary observer design

In this section we design a boundary observer that relies on the measurement of \tilde{q}_1 and \tilde{v}_1 at the left side of the junction $x = 0$. We take the measurement of

$$Y(t) = \bar{w}_1(0, t). \quad (11.35)$$

where

$$\bar{w}_1(0, t) = \frac{\gamma_1 p_1^*}{q_1^*} \tilde{q}_1(0, t) - \frac{1}{r_1} \tilde{v}_1(0, t), \quad (11.36)$$

is obtained from the measurement of flow rate and velocity variations.

The observer equations read as follows, consisting of a copy of the linearized system (11.22)-(11.27) and injection terms of output measurement errors

$$\partial_t \hat{w}_i + v_i^* \partial_x \hat{w}_i = \mu_i(x)(Y(t) - \hat{w}_i(0, t)), \quad (11.37)$$

$$\partial_t \hat{v}_i - (\gamma_i p_i^* - v_i^*) \partial_x \hat{v}_i = c_i(x) \hat{w}_i + v_i(x)(Y(t) - \hat{w}_i(0, t)) \quad (11.38)$$

$$\hat{w}_1(-L, t) = \exp(-L/(\tau_1 v_1^*)) \left(\frac{1}{r_1} \hat{v}_1(-L, t) + \tilde{y}_1(t) \right), \quad (11.39)$$

$$\hat{w}_j(0, t) = \hat{w}_1(0, t), \quad (11.40)$$

$$\begin{aligned} \hat{v}_1(0, t) = & r_1 \left[(1 - \delta \sigma_{12} - (1 - \delta) \sigma_{13}) \hat{w}_1(0, t) \right. \\ & \left. + \frac{\delta \sigma_{12}}{r_2} \hat{v}_2(0, t) + \frac{(1 - \delta) \sigma_{13}}{r_3} \hat{v}_3(0, t) \right], \end{aligned} \quad (11.41)$$

$$\hat{v}_j(L, t) = r_j \exp(-L/(\tau_j v_j^*)) \hat{w}_1(L, t) - \tilde{y}_j(t), \quad (11.42)$$

where $\hat{w}_i(x, t)$, $\hat{v}_i(x, t)$ are the estimates of the state variables $\bar{w}_i(x, t)$ and $\bar{v}_i(x, t)$. The varying demand and supply \tilde{y}_i are known due to the measurement at the boundaries. The steady states are also known due to prior knowledge of the averaged traffic conditions. The terms μ_i and v_i are output injection gains that are designed to drive the estimation error system to zero equilibrium using backstepping method.

Define the error estimates

$$\check{w}_i = \hat{w}_i - \bar{w}_i, \quad (11.43)$$

$$\check{v}_i = \hat{v}_i - \bar{v}_i. \quad (11.44)$$

Given the relation

$$\hat{w}_1(0, t) = \hat{w}_2(0, t) = \hat{w}_3(0, t), \quad (11.45)$$

the error system is obtained by subtracting the observer equations in (11.37)-(11.42) from (11.22)-(11.27),

$$\partial_t \check{w}_i + v_i^* \partial_x \check{w}_i = -\mu_i(x) \check{w}_i(0, t), \quad (11.46)$$

$$\partial_t \check{v}_i - (\gamma_i p_i^* - v_i^*) \partial_x \check{v}_i = c_i(x) \check{w}_i - v_i(x) \check{w}_i(0, t) \quad (11.47)$$

$$\check{w}_1(-L, t) = \frac{\exp(-L/(\tau_1 v_1^*))}{r_1} \hat{v}_1(-L, t), \quad (11.48)$$

$$\check{w}_j(0, t) = \check{w}_1(0, t), \quad (11.49)$$

$$\begin{aligned} \check{v}_1(0, t) = & r_1 \left[(1 - \sigma_{12}\delta - \sigma_{13}(1 - \delta)) \check{w}_1(0, t) \right. \\ & \left. + \frac{\delta\sigma_{12}}{r_2} \check{v}_2(0, t) + \frac{\sigma_{13}(1 - \delta)}{r_3} \check{v}_3(0, t) \right], \end{aligned} \quad (11.50)$$

$$\check{v}_j(L, t) = r_j \exp(-L/(\tau_j v_j^*)) \check{w}_j(L, t), \quad (11.51)$$

We consider the following backstepping transformations

$$\check{w}_1(x, t) = \check{\alpha}_1(x, t) - \int_x^0 N_1^{ww}(x, \xi) \check{\alpha}_1(\xi, t) d\xi, \quad (11.52)$$

$$\check{v}_1(x, t) = \check{\beta}_1(x, t) - \int_x^0 N_1^{vw}(x, \xi) \check{\alpha}_1(\xi, t) d\xi, \quad (11.53)$$

$$\check{w}_j(x, t) = \check{\alpha}_j(x, t) - \int_0^x N_j^{ww}(x, \xi) \check{\alpha}_j(\xi, t) d\xi, \quad (11.54)$$

$$\check{v}_j(x, t) = \check{\beta}_j(x, t) - \int_0^x N_j^{vw}(x, \xi) \check{\alpha}_j(\xi, t) d\xi, \quad (11.55)$$

where the kernels N_1^{ww} and N_1^{vw} are L^∞ functions defined on a triangular domain $\bar{\mathcal{T}}_1 = \{(x, \xi) \in [-L, 0]^2, \xi \leq x\}$, while the kernels N_2^{ww} , N_2^{vw} and N_3^{ww} and N_3^{vw} are L^∞ functions defined on a triangular domain $\bar{\mathcal{T}}_2 = \{(x, \xi) \in [0, L]^2, \xi \leq x\}$. They are governed by the following set of kernel PDEs:

$$\partial_x N_i^{ww} + \partial_\xi N_i^{ww} = 0, \quad (11.56)$$

$$(\gamma_i p_i^* - v_i^*) \partial_x N_i^{vw} - v_i^* \partial_\xi N_i^{vw} = -c_i(x) N_i^{ww}, \quad (11.57)$$

along with the following six boundary conditions where $i = 1, 2, 3$ and $j = 2, 3$,

$$N_1^{ww}(-L, x) = \frac{\exp(-L/(\tau_1 v_1^*))}{r_1} N_1^{vw}(-L, x), \quad (11.58)$$

$$N_1^{vw}(x, x) = -\frac{c_1(x)}{\gamma_1 p_1^*}, \quad (11.59)$$

$$N_j^{vw}(x, x) = \frac{c_j(x)}{\gamma_j p_j^*}, \quad (11.60)$$

$$N_j^{vw}(L, x) = r_j \exp(-L/(\tau_j v_j^*)) N_j^{ww}(L, x). \quad (11.61)$$

The well-posedness of this kernel PDE-system is straightforward to prove using method of characteristics and successive approximation. There exists a unique solution N_1^{vw} , N_1^{vv} in $L^\infty(\mathcal{T}_3)$ and N_2^{vw} , N_2^{vv} in $L^\infty(\mathcal{T}_4)$. The output injection gains μ_i and ν_i are then defined as

$$\nu_1(x) = v_1^* N_1^{vw}(x, 0), \quad (11.62)$$

$$\mu_1(x) = v_1^* N_1^{ww}(x, 0), \quad (11.63)$$

$$\nu_j(x) = -v_j^* N_j^{vw}(x, 0), \quad (11.64)$$

$$\mu_j(x) = -v_j^* N_j^{ww}(x, 0). \quad (11.65)$$

With the above output injection gains, taking the spatial and temporal differentiation of the backstepping transformations (11.52)-(11.55) along the error system (11.46)-(11.51), we obtain the following target system

$$\partial_t \check{\alpha}_i + v_i^* \partial_x \check{\alpha}_i = 0 \quad (11.66)$$

$$\partial_t \check{\beta}_i - (\gamma_i p_i^* - v_i^*) \partial_x \check{\beta}_i = 0, \quad (11.67)$$

$$\check{\alpha}_1(-L, t) = \frac{\exp(-L/(\tau_1 v_1^*))}{r_1} \check{\beta}_1(-L, t), \quad (11.68)$$

$$\check{\alpha}_j(0, t) = \check{\alpha}_1(0, t), \quad (11.69)$$

$$\begin{aligned} \check{\beta}_1(0, t) = & r_1 \left[(1 - \delta \sigma_{12} - (1 - \delta) \sigma_{13}) \check{\alpha}_1(0, t) \right. \\ & \left. + \frac{\delta \sigma_{12}}{r_2} \check{\beta}_2(0, t) + \frac{(1 - \delta) \sigma_{13}}{r_3} \check{\beta}_3(0, t) \right], \end{aligned} \quad (11.70)$$

$$\check{\beta}_j(L, t) = r_j \exp(-L/(\tau_j v_j^*)) \check{\alpha}_j(L, t). \quad (11.71)$$

This target system is exponentially stable in L^2 norm if the following Assumption 11.3 is satisfied.

The spectral radius of boundary couplings of the system (11.66)-(11.71) are such that

$$R = \max \{R_1, R_2, R_3, b_0, b_1\} < 1, \quad (11.72)$$

where

$$R_1 = -\exp(-L/(\tau_1 v_1^*)) / r_1, \quad (11.73)$$

$$R_j = -r_j \exp(-L/(\tau_j v_j^*)), \quad j = 2, 3 \quad (11.74)$$

and recalling $-1 < r_i < 0$,

$$b_0 = -r_1 \left[(1 - \delta\sigma_{12} - (1 - \delta)\sigma_{13})^2 + \frac{\delta^2\sigma_{12}^2}{r_2^2} + \frac{(1 - \delta)^2}{r_3^2} \right]^{1/2}, \quad (11.75)$$

$$b_1 = -r_1/b_0 \left[2(1 - (1 - \delta\sigma_{12} - (1 - \delta)\sigma_{13})^2) \right]^{1/2} \quad (11.76)$$

The above assumption is usually satisfied for the type of traffic networks considered in this chapter. In a straightforward case, if we consider the steady states of the traffic flow in the two splitting segments to be the same, in which case $\delta = 1/2$, $\sigma_{12} = \sigma_{13} = 1$, $\gamma_1 = \gamma_2 = \gamma_3$, $r_1 = r_2 = r_3$, then (11.72) becomes

$$R = \max \left\{ R_1, R_2, R_3, \frac{\sqrt{2}}{2}, -r_1 \right\} < 1, \quad (11.77)$$

which holds when $\exp(-L/(\tau_1 v_1^*)) < -r_1$, recalling $-1 < r_i < 0$ in (11.34).

Theorem 11.1 *Consider the estimation error system (11.46)-(11.51) under Assumption 11.3. The equilibrium $\check{w}_i \equiv \check{v}_i \equiv 0$ of the estimation error system is exponentially stable in the L^2 norm.*

Proof Consider the target system (11.66)-(11.101). Theorem 3.2 in [?] proves that the system is exponentially stable in the L^2 norm if Assumption 11.3 is satisfied. Due to the invertibility of the backstepping transformation (11.52)-(11.55) and the boundedness of the kernel variables, we obtain the exponential stability of the original estimation error system. \square

11.4 Robustness to disturbance and noise

In practice, measurements are noisy. For this reason, we design a robust observer that relies on the measurements with an unknown noise $d_0(t)$.

$$Y_0(t) = \bar{w}_1(0, t) + d_0(t) \quad (11.78)$$

In addition, there are spatially distributed disturbances d_i^w, d_i^v acting on the right hand side of the equations (11.22)-(11.27) and the corresponding locations of these distributed disturbances are $m_i^w(x)$ and $m_i^v(x)$. We assume that the spatially distributed disturbances $d_i^w(t), d_i^v(t) \in W^{2,\infty}((0, \infty); \mathbb{R})$ with disturbance input locations $m_i^w(x), m_i^v(x) \in C([0, L]; \mathbb{R}^+)$ and the noise $d_0(t) \in L^\infty((0, \infty); \mathbb{R})$. The following disturbed system with the initial condition $\bar{w}_i^0, \bar{v}_i^0 \in L^2((0, L); \mathbb{R})$ has a unique solution.

The system with disturbances to be estimated is given by

$$\partial_t \bar{w}_i + v_i^* \partial_x \bar{w}_i = m_i^w(x) d_i^w(t), \quad (11.79)$$

$$\partial_t \bar{v}_i - (\gamma_i p_i^* - v_i^*) \partial_x \bar{v}_i = c_i(x) \bar{w}_i + m_i^v(x) d_i^v(t), \quad (11.80)$$

$$\bar{w}_1(-L, t) = \exp(-L/(\tau_1 v_1^*)) \left(\frac{1}{r_1} \bar{v}_1(-L, t) + \bar{y}_1(t) \right), \quad (11.81)$$

$$\bar{w}_j(0, t) = \bar{w}_1(0, t), \quad (11.82)$$

$$\begin{aligned} \bar{v}_1(0, t) = & r_1 \left[(1 - \sigma_{12}\delta - \sigma_{13}(1 - \delta)) \bar{w}_1(0, t) \right. \\ & \left. + \frac{\delta\sigma_{12}}{r_2} \bar{v}_2(0, t) + \frac{\sigma_{13}(1 - \delta)}{r_3} \bar{v}_3(0, t) \right], \end{aligned} \quad (11.83)$$

$$\bar{v}_j(L, t) = r_j \exp(-L/(\tau_j v_j^*)) \bar{w}_j(L, t) - \bar{y}_j(t). \quad (11.84)$$

Now we move to discuss the robustness of the observer (11.37)-(11.42) by replacing $Y(t)$ with $Y_0(t)$ in the observer equations and modifying the boundary conditions (11.40) as follows

$$\hat{w}_j(0, t) = (1 - \epsilon) \hat{w}_1(0, t) + \epsilon Y_0(t), \quad (11.85)$$

where the coefficient $\epsilon \in (0, 1]$ represents a measure of trust in the measurement $Y_0(t)$. When the trust coefficient $\epsilon = 1$, it indicates that we fully trust our measurement in the observer. On the contrary, $\epsilon = 0$ means sensing is completely unreliable and therefore cannot be used for constructing the observer.

Subtracting the robust observer from the disturbed system (11.79)-(11.84) yields the error system

$$\partial_t \check{w}_1 + v_1^* \partial_x \check{w}_1 = \mu_1(x) (\check{w}_1(0, t) + d_0(t)) + m_1^w(x) d_1^w(t), \quad (11.86)$$

$$\partial_t \check{w}_j + v_j^* \partial_x \check{w}_j = \epsilon \mu_j(x) (\check{w}_j(0, t) + d_0(t)) + m_j^w(x) d_j^w(t), \quad (11.87)$$

$$\begin{aligned} \partial_t \check{v}_1 - (\gamma_1 p_1^* - v_1^*) \partial_x \check{v}_1 = & c_1(x) \check{w}_1 + v_1(x) (\check{w}_1(0, t) + d_0(t)) \\ & + m_1^v(x) d_1^v(t), \end{aligned} \quad (11.88)$$

$$\begin{aligned} \partial_t \check{v}_j - (\gamma_j p_j^* - v_j^*) \partial_x \check{v}_j = & c_j(x) \check{w}_j + \epsilon v_j(x) (\check{w}_j(0, t) + d_0(t)) \\ & - v_j(x) d_j^v(t) + m_j^v(x) d_j^v(t), \end{aligned} \quad (11.89)$$

$$\check{w}_1(-L, t) = \frac{\exp(-L/(\tau_1 v_1^*))}{r_1} \hat{v}_1(-L, t), \quad (11.90)$$

$$\check{w}_j(0, t) = (1 - \epsilon) \check{w}_1(0, t) - \epsilon d_0(t), \quad (11.91)$$

$$\begin{aligned} \check{v}_1(0, t) = & r_1 \left[(1 - \sigma_{12}\delta - \sigma_{13}(1 - \delta)) \check{w}_1(0, t) \right. \\ & \left. + \frac{\delta\sigma_{12}}{r_2} \check{v}_2(0, t) + \frac{\sigma_{13}(1 - \delta)}{r_3} \check{v}_3(0, t) \right], \end{aligned} \quad (11.92)$$

$$\check{v}_j(L, t) = r_j \exp(-L/(\tau_j v_j^*)) \check{w}_j(L, t). \quad (11.93)$$

Applying the same backstepping transformation (11.52),(11.55), the above error system is mapped to the following target system

$$\partial_t \alpha_1 + v_1^* \partial_x \alpha_1 = f_1^w(x) d_1^w(t) + h_1^w(x) d_0(t), \quad (11.94)$$

$$\partial_t \alpha_j + v_j^* \partial_x \alpha_j = f_j^w(x) d_j^w(t) + h_j^w(x) d_0(t), \quad (11.95)$$

$$\partial_t \beta_1 - (\gamma_1 p_1^* - v_1^*) \partial_x \beta_1 = f_1^v(x) d_1^w(t) + m_1^v(x) d_1^v(t) + h_1^v(x) d_0(t), \quad (11.96)$$

$$\partial_t \beta_j - (\gamma_j p_j^* - v_j^*) \partial_x \beta_j = f_j^v(x) d_j^w(t) + m_j^v(x) d_j^v(t) + h_j^v(x) d_0(t), \quad (11.97)$$

$$\alpha_1(-L, t) = \frac{\exp(-L/(\tau_1 v_1^*))}{r_1} \beta_1(-L, t), \quad (11.98)$$

$$\alpha_j(0, t) = (1 - \epsilon) \alpha_1(0, t) - \epsilon d_0(t), \quad (11.99)$$

$$\begin{aligned} \beta_1(0, t) = & r_1 \left[(1 - \sigma_{12} \delta - \sigma_{13} (1 - \delta)) \alpha_1(0, t) \right. \\ & \left. + \frac{\delta \sigma_{12}}{r_2} \beta_2(0, t) + \frac{\sigma_{13} (1 - \delta)}{r_3} \beta_3(0, t) \right], \end{aligned} \quad (11.100)$$

$$\beta_j(L, t) = r_j \exp(-L/(\tau_j v_j^*)) \alpha_j(L, t), \quad (11.101)$$

where the spatially varying functions $f_1^w(x)$, $f_1^v(x)$, $h_1^w(x)$, $h_1^v(x)$, $x \in [-L, 0]$ and $f_j^w(x)$, $f_j^v(x)$, $h_j^w(x)$, $h_j^v(x)$, $\forall x \in [0, L]$ are defined as the solutions of following integral equations

$$f_1^w(x) = m_1^w(x) + \int_x^0 N_1^{ww}(x, \xi) f_1^w(\xi) d\xi, \quad (11.102)$$

$$h_1^w(x) = \mu_1(x) + \int_x^0 N_1^{ww}(x, \xi) h_1^w(\xi) d\xi, \quad (11.103)$$

$$f_1^v(x) = \int_x^0 N_1^{wv}(x, \xi) f_1^w(\xi) d\xi, \quad (11.104)$$

$$h_1^v(x) = v_1(x) + \int_x^0 N_1^{wv}(x, \xi) h_1^w(\xi) d\xi, \quad (11.105)$$

$$f_j^w(x) = m_j^w(x) + \int_0^x N_j^{ww}(x, \xi) f_j^w(\xi) d\xi, \quad (11.106)$$

$$h_j^w(x) = \epsilon \mu_j(x) + \int_0^x N_j^{ww}(x, \xi) h_j^w(\xi) d\xi, \quad (11.107)$$

$$f_j^v(x) = \int_0^x N_j^{wv}(x, \xi) f_j^w(\xi) d\xi, \quad (11.108)$$

$$h_j^v(x) = \epsilon v_j(x) + \int_0^x N_j^{wv}(x, \xi) h_j^w(\xi) d\xi. \quad (11.109)$$

We now state the main result of the chapter.

Theorem 11.2 Consider the estimation error system (11.86)-(11.93) under Assumption 11.3. The system is ISS with respect to d_0 , d_i^w and d_i^v . There exists a \mathcal{KL} function h_1 and a \mathcal{K} function h_2 such that for any initial condition

$(\check{w}_1^0, \check{v}_1^0, \check{w}_2^0, \check{v}_2^0, \check{w}_3^0, \check{v}_3^0)^T \in L^2((0, L); \mathbb{R}^6)$, the following estimate holds for all $t \geq 0$,

$$\begin{aligned} \|(\check{w}_1, \check{v}_1, \check{w}_2, \check{v}_2, \check{w}_3, \check{v}_3)^T\| &\leq h_1(\|(\check{w}_1^0, \check{v}_1^0, \check{w}_2^0, \check{v}_2^0, \check{w}_3^0, \check{v}_3^0)^T\|, t) \\ &\quad + h_2\left(\|(d_0, d_1^w, d_1^v, d_2^w, d_2^v, d_3^w, d_3^v)^T\|_{L^\infty((0, t); \mathbb{R}^7)}\right) \end{aligned} \quad (11.110)$$

Proof We denote the right-side terms of the equations (11.94)-(11.97) as $D_i^\alpha(x, t)$ and $D_i^\beta(x, t)$ in (11.98)-(11.101),

$$D_i^\alpha(x, t) = f_i^w(x) d_i^w(t) + h_i^w(x) d_0(t), \quad (11.111)$$

$$D_i^\beta(x, t) = f_i^v(x) d_i^w(t) + m_i^v(x) d_i^v(t) + h_i^v(x) d_0(t). \quad (11.112)$$

We construct the Lyapunov function

$$V(t) = \sum_{i=1}^3 (\lambda_i^\alpha V_i^\alpha(t) + \lambda_i^\beta V_i^\beta(t)). \quad (11.113)$$

The component Lyapunov functions are defined as follows,

$$V_1^\alpha(t) = \frac{1}{2v_1^\star} \int_{-L}^0 \exp(-\theta_1 x) \alpha_1^2(x, t) dx, \quad (11.114)$$

$$V_1^\beta(t) = \frac{1}{2(\gamma_1 p_1^\star - v_1^\star)} \int_{-L}^0 \exp(\theta_1 x) \beta_1^2(x, t) dx, \quad (11.115)$$

$$V_j^\alpha(t) = \frac{1}{2v_j^\star} \int_0^L \exp(-\theta_j x) \alpha_j^2(x, t) dx, \quad (11.116)$$

$$V_j^\beta(t) = \frac{1}{2(\gamma_j p_j^\star - v_j^\star)} \int_0^L \exp(\theta_j x) \beta_j^2(x, t) dx, \quad (11.117)$$

where the constant coefficients $\theta_i, \lambda_i^\alpha, \lambda_i^\beta > 0$ defined later. By taking differentiation of the Lyapunov functions in time and using Cauchy-Schwarz Inequality and Young's Inequality, we obtain that

$$\begin{aligned}\dot{V}_1^\alpha &\leq \frac{1}{2} \left(\exp(\theta_1 L) \alpha_1^2(-L, t) - \alpha_1^2(0, t) \right) - \frac{\theta_1}{4} \|\alpha_1(x, t)\|^2 \\ &\quad + \frac{1}{\theta_1 (v_1^*)^2} \|D_1^\alpha(x, t)\|^2, \end{aligned} \quad (11.118)$$

$$\begin{aligned}\dot{V}_1^\beta &\leq \frac{1}{2} \left(\beta_1^2(0, t) - \exp(-\theta_1 L) \beta_1^2(-L, t) \right) \\ &\quad - \frac{\theta_1 \exp(-\theta_1 L)}{4} \|\beta_1(x, t)\|^2 + \frac{\exp(\theta_1 L)}{\theta_1 (\gamma_1 p_1^* - v_1^*)^2} \|D_1^\beta(x, t)\|^2, \end{aligned} \quad (11.119)$$

$$\begin{aligned}\dot{V}_j^\alpha &\leq \frac{1}{2} \left(\alpha_j^2(0, t) - \exp(-\theta_j L) \alpha_j^2(L, t) \right) \\ &\quad - \frac{\theta_j \exp(-\theta_j L)}{4} \|\alpha_j(x, t)\|^2 + \frac{\exp(\theta_j L)}{\theta_j (v_j^*)^2} \|D_j^\alpha(x, t)\|^2, \end{aligned} \quad (11.120)$$

$$\begin{aligned}\dot{V}_j^\beta &\leq \frac{1}{2} \left(\exp(\theta_j L) \beta_j^2(L, t) - \beta_j^2(0, t) \right) - \frac{\theta_j}{4} \|\beta_j(x, t)\|^2 \\ &\quad + \frac{1}{\theta_j (\gamma_j p_j^* - v_j^*)^2} \|D_j^\beta(x, t)\|^2. \end{aligned} \quad (11.121)$$

Applying Cauchy-Schwarz Inequality to the boundary conditions (11.99),(11.100) yields the following inequalities,

$$\begin{aligned}\alpha_j^2(0, t) &\leq \left((1 - \epsilon)^2 + \epsilon^2 \right) (\alpha_1^2(0, t) + |d_0(s)|^2) \\ &\leq \alpha_1^2(0, t) + |d_0(t)|^2 \end{aligned} \quad (11.122)$$

$$\beta_1^2(0, t) \leq b_0^2 (\alpha_0^2(0, t) + \beta_2^2(0, t) + \beta_3^2(0, t)) \quad (11.123)$$

Combining the above inequalities and substituting the following $\lambda_i^\alpha, \lambda_i^\beta$ into $\dot{V}(t)$,

$$\lambda_1^\alpha = 1, \quad (11.124)$$

$$\lambda_1^\beta = \exp(2\theta_1 L) \varrho_1^2, \quad (11.125)$$

$$\lambda_j^\alpha = \exp(2\theta_j L) \lambda_1^\beta b_0^2 \varrho_j^2, \quad (11.126)$$

$$\lambda_2^\beta = \lambda_3^\beta = \lambda_1^\beta b_0^2, \quad (11.127)$$

we obtain that for all $t > 0$,

$$\begin{aligned}
\dot{V}(t) \leq & -\frac{\theta_1}{4} \|\alpha_1(x, t)\|^2 - \frac{\lambda_1^\beta \theta_1 \exp(-\theta_1 L)}{4} \|\beta_1(x, t)\|^2 \\
& - \sum_{j=2}^3 \left(\frac{\lambda_j^\alpha \theta_j \exp(-\theta_j L)}{4} \|\alpha_j(x, t)\|^2 - \frac{\lambda_j^\beta \theta_j}{4} \|\beta_j(x, t)\|^2 \right) \\
& + \frac{1}{\theta_1 (v_1^*)^2} \|D_1^\alpha(x, t)\|^2 + \frac{\lambda_1^\beta \exp(\theta_1 L)}{\theta_1 (\gamma_1 p_1^* - v_1^*)^2} \|D_1^\beta(x, t)\|^2 \\
& + \sum_{j=2}^3 \left(\frac{\lambda_j^\alpha \exp(\theta_j L)}{\theta_j (v_j^*)^2} \|D_j^\alpha(x, t)\|^2 + \frac{\lambda_j^\alpha}{2} |d_0(t)|^2 \right) \\
& + \sum_{j=2}^3 \frac{\lambda_j^\beta}{\theta_j (\gamma_j p_j^* - v_j^*)^2} \|D_j^\beta(x, t)\|^2 \\
& - \frac{1}{2} \left(1 - \lambda_1^\beta b_0^2 - \lambda_2^\alpha - \lambda_3^\alpha \right) \alpha_1^2(0, t).
\end{aligned} \tag{11.128}$$

We choose θ_i such that the followings inequalities are satisfied

$$0 < \theta_2 = \theta_3 < \frac{1}{2L} \ln \left(\frac{1 - \rho_1^2 b_0^2}{\rho_1^2 b_0^2 (\rho_2^2 + \rho_3^2)} \right), \tag{11.129}$$

$$0 < \theta_1 < -\frac{1}{2L} \ln(1 + \exp(2L\theta_2)\rho_2^2 + \exp(2L\theta_3)\rho_3^2). \tag{11.130}$$

Given $0 < \rho_i, b_0 < 1$ in Assumption 11.3, it follows that

$$1 - \lambda_1^\beta b_0^2 - \lambda_2^\alpha - \lambda_3^\alpha > 0. \tag{11.131}$$

Therefore, we obtain for all $t > 0$,

$$\dot{V}(t) \leq -\frac{\theta_0 \exp(-\theta_0 L)}{4} V(t) + \phi \sum_{i=1}^3 \left(\|D_i^\alpha(x, t)\|^2 + \|D_i^\beta(x, t)\|^2 \right) + \chi |d_0(t)|^2,$$

where the positive constant coefficients $\phi, \theta_0, \chi > 0$ are defined as

$$\phi = \max \left\{ \frac{1}{\theta_1 (v_1^*)^2}, \frac{\lambda_1^\beta \exp(\theta_1 L)}{\theta_1 (\gamma_1 p_1^* - v_1^*)^2}, \frac{\lambda_j^\alpha \exp(\theta_j L)}{\theta_j (v_j^*)^2}, \frac{\lambda_j^\beta}{\theta_j (\gamma_j p_j^* - v_j^*)^2} \right\}, \tag{11.132}$$

$$\theta_0 = \max\{\theta_1, \theta_2, \theta_3\}, \tag{11.133}$$

$$\chi = \frac{\lambda_2^\alpha + \lambda_3^\alpha}{2}. \tag{11.134}$$

Integrating the linear differential inequality (11.132), we get for all $t > 0$,

$$\begin{aligned}
V(t) \leq & \exp\left(\frac{-\theta_0 \exp(-\theta_0 L)}{4} t\right) V(0) + \frac{4\chi \max_{0 \leq s \leq t} (|d_0(t)|^2)}{\theta_0 \exp(-\theta_0 L)} \\
& + \frac{4\chi \exp(\theta_0 L)}{\theta_0} \sum_{i=1}^3 \left(\max_{0 \leq s \leq t} (||D_i^\alpha(x, t)||^2) + \max_{0 \leq s \leq t} (||D_i^\beta(x, t)||^2) \right).
\end{aligned} \tag{11.135}$$

The definition of the Lyapunov function $V(t)$ implies that

$$\underline{\psi} ||z||^2 \leq V(t) \leq \bar{\psi} ||z||^2, \tag{11.136}$$

where

$$z = (\alpha_1, \beta_1, \alpha_2, \beta_2, \alpha_3, \beta_3)^T \tag{11.137}$$

and the positive constants $\underline{\psi}, \bar{\psi}$ are given by

$$\underline{\psi} = \min\{\lambda_1^\alpha / (2v_1^*), \exp(-\theta_1 L) \lambda_1^\beta / (2(\gamma_1 p_1^* - v_1^*)), \exp(-\theta_j L) \lambda_j^\alpha / (2v_j^*), \lambda_j^\beta / (2(\gamma_j p_j^* - v_j^*))\}, \tag{11.138}$$

and

$$\bar{\psi} = \max\{\exp(\theta_1 L) \lambda_1^\alpha / (2v_1^*), \lambda_1^\beta / (2(\gamma_1 p_1^* - v_1^*)), \lambda_j^\alpha / (2v_j^*), \exp(\theta_j L) \lambda_j^\beta / (2(\gamma_j p_j^* - v_j^*))\}. \tag{11.139}$$

Therefore, we obtain that the following estimate is satisfied for the target system (11.94)-(11.101) with the initial condition $z_0 = (\alpha_1^0, \beta_1^0, \alpha_2^0, \beta_2^0, \alpha_3^0, \beta_3^0)^T \in L^2((0, L); \mathbb{R}^6)$,

$$\begin{aligned}
||z|| \leq & \left(\bar{\psi} / \underline{\psi}\right)^{1/2} \exp\left(-\frac{\theta_0 \exp(-\theta_0 L)}{4} t\right) ||z_0|| + 2 \left(\frac{\exp(\theta_0 L) \chi}{\theta_0 \underline{\psi}}\right)^{1/2} \max_{0 \leq s \leq t} (|d_0(t)|) \\
& + 2 \left(\frac{\bar{\psi} \exp(\theta_0 L) \chi}{\theta_0 \underline{\psi}}\right)^{1/2} \sum_{i=1}^3 \left(\max_{0 \leq s \leq t} (||D_i^\alpha(x, t)||^2) + \max_{0 \leq s \leq t} (||D_i^\beta(x, t)||^2) \right).
\end{aligned} \tag{11.140}$$

The above inequality gives ISS estimate in L^2 -norm of the target system. Due to the invertibility of the backstepping transformation and the boundedness of the kernel equations, we obtain the ISS estimate in L^2 -norm of the estimation error system (11.86)-(11.93) to measurement noise and in-domain disturbances, which completes our proof. \square

11.5 Notes and References

In this chapter, we develop a boundary observer for a traffic network PDE system of one incoming and two outgoing roads. The measurements of flow rates are taken at the inlet, the middle junction and the outlet boundary and the measurement of velocity is taken at the middle junction. Using backstepping transformation and Lyapunov analysis, the estimate of the L^2 -norm in the sense of ISS with respect to the spatially distributed disturbances and the measurement noise is derived for the estimation error system. Developing robust output feedback stabilization problem of such a traffic network structure is of future research interest.

Chapter 12

Control under Routing-induced Instability

As drivers, we have come to rely heavily on routing apps like Google Maps, Apple maps, and Waze. We use their recommendations both to navigate to locations to which we are going for the first time, as well as to pick one among several possible routes known to us when traffic is heavy and getting to our destination on time is critical.

By following the recommendations from the routing apps, we let them become joint operators, along with us, of our vehicles. As the apps assume that role, the model of traffic flow fundamentally changes. While the classical ARZ model incorporates the behavioral characteristics of the drivers in response to their local environment, i.e., the density and speed very near to them, the routing apps introduce the information from much ahead of the driver's position and, in fact, from a much broader traffic network, regionally and even beyond.

We focus on a single freeway segment and on the fact that routing apps use a preview of the whole freeway segment to direct traffic into that segment. This has a major consequence on the ARZ model—from having a local boundary condition at the inlet to the segment, the ARZ model has a *non-local* (spatial integral) boundary condition at the inlet.

Such a non-local boundary condition introduces a “recirculation” of the density and velocity state back to the inlet into the domain. Such a recirculation can be destabilizing. In heuristic terms, sparse traffic may result in routing apps directing a large amount of additional traffic into that segment, causing congestion and, hence, stop-and-go motion. While it is conceivable that routing apps could anticipate this outcome and direct only a moderate amount of traffic to that segment, it is up to the driver whether they use the recommendations, or even consult the apps, so the destabilizing effect of the apps is possible, in principle.

In this chapter we postulate a “recirculatory” boundary condition at the freeway's inlet, resulting from the routing apps, and design a controller that prevents the possible destabilizing effect of the apps.

We first study small-time H^1 solutions of the linearized model with the addition of the app-routing for sufficiently small initial data. We introduce an extended, multi-tiered boundary control design based on the backstepping method introduced in the

previous chapters. Using an intermediate decoupling transformation, we account for the non-local boundary condition arising from routing app feedback. It is shown that for sufficiently small H^1 data, the equilibrium congestion solution is exponentially stable and guarantees the existence of closed-loop solutions on the infinite time interval.

Routing apps generally route in a ‘greedy’ manner. Their impact on traffic has been studied in [?]. The dynamic traffic routing problem is usually formulated as a feedback control problem to reach user-equilibrium system-wide under different control objectives in [?]. It is indicated in [?] that the interaction between traffic routing and the control of traffic by traffic signals, including by ramp metering, needs to be taken into consideration in developing traffic control strategies. This is what we do in this chapter, by developing a boundary feedback control for preventing a possible instability resulting from non-local feedback introduced by routing apps. A control design for hyperbolic balance laws with non-local behavior has been studied in the underactuated case in [?] and with non-local integral terms in [?].

12.1 ARZ Model with Routing Feedback

In this section we introduce a linearized ARZ model in which the routing feedback enters the inlet boundary condition, whereas the outlet boundary condition is set by ramp metering control.

Around the steady-state (q^*, v^*) , the linearized ARZ model is given by the following (\tilde{q}, \tilde{v}) -system for $x \in [0, L]$, $t \in [0, \infty)$,

$$\partial_t \tilde{q}(x, t) + v^* \partial_x \tilde{q}(x, t) - \frac{q^*(\gamma p^* - v^*)}{v^*} \partial_x \tilde{v}(x, t) = -\frac{q^*}{\tau} \left(\frac{1}{v^*} - \frac{1}{\gamma p^*} \right) \tilde{v}(x, t) - \frac{\gamma p^*}{\tau v^*} \tilde{q}(x, t), \quad (12.1)$$

$$\partial_t \tilde{v}(x, t) - (\gamma p^* - v^*) \partial_x \tilde{v}(x, t) = \frac{\gamma p^* - v^*}{\tau v^*} \tilde{v}(x, t) - \frac{\gamma p^*}{\tau q^*} \tilde{q}(x, t), \quad (12.2)$$

with the actuated boundary conditions

$$\tilde{q}(0, t) = U_{\text{rout}}(t), \quad (12.3)$$

$$\tilde{q}(L, t) = U_{\text{ramp}}(t), \quad (12.4)$$

where the inputs U_{rout} and U_{ramp} are the routing and ramp metering inputs, respectively. The inputs $U_{\text{rout}}, U_{\text{ramp}}$ arise as perturbations to the equilibrium traffic flow rate q^* and play the following roles:

- $U_{\text{rout}}(t)$ represents the influence that the routing app has on the influx of cars at the inlet boundary. It is reasonable to expect that if the road is more congested, $U_{\text{rout}}(t)$ should decrease, and conversely, the opposite should be true if the road exhibits more free-flow characteristics.

- $U_{\text{ramp}}(t)$ represents on-ramp metering control of flow rate at the outlet boundary.

Following the spatial transformation in Section 3.3, the linearized ARZ model is rewritten as the (v, w) -system:

$$\partial_t w(x, t) = -v^* \partial_x w(x, t), \quad (12.5)$$

$$\partial_t v(x, t) = (\gamma p^* - v^*) \partial_x v(x, t) + c(x) w(x, t), \quad (12.6)$$

with the boundary conditions

$$w(0, t) = k_1 v(0, t) + U_{\text{rout}}(t), \quad (12.7)$$

$$v(L, t) = k_2 w(L, t) + U_{\text{ramp}}(t). \quad (12.8)$$

The spatial coefficient is given by

$$c(x) = -\frac{\exp\left(-\frac{x}{\tau v^*}\right)}{\tau}, \quad (12.9)$$

and the boundary coefficients are

$$k_1 = \frac{\gamma p^* - v^*}{v^*}, \quad k_2 = \exp\left(-\frac{L}{\tau v^*}\right), \quad (12.10)$$

We consider the congested regime, in which $v^* > 0$ and $\gamma p^* - v^* > 0$.

We postulate that the app-routing feedback has a strict-feedback form in the Riemann variables. In general, the routing feedback may include feedforward as well as feedback components in the Riemann variable, even if it is only of the strict-feedback nature in the original density variable. However, as traffic congestion propagates in the direction opposite to the direction of the flow of traffic, we focus on the feedback routing information that affects the incoming traffic according to downstream traffic condition. We assume (heuristically) the following destabilizing app-routing feedback that preserves the strict-feedback character of the overall two-PDE model with non-local interconnections:

$$U_{\text{rout}}(t) = \int_0^L a(y) w(y, t) dy. \quad (12.11)$$

One can interpret the routing app to be an *adversarial* feedback controller that potentially destabilizes the system. The kernel $a \in L^2(0, L)$ represents a spatial weighting of traffic feedback information for the routing app over the road.

12.2 Feedback design for the linearized system

In this section, we develop a backstepping transformation-based control design to establish an H^1 equivalence relation between (12.5)-(12.8) to the following target

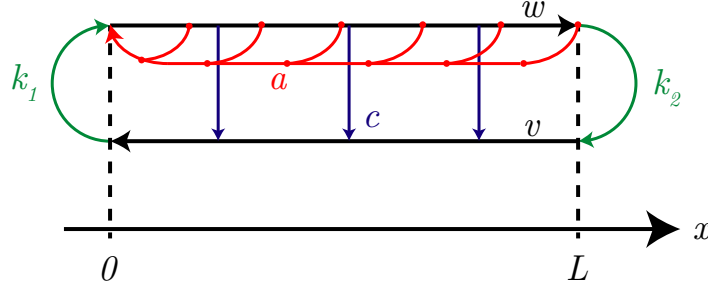


Fig. 12.1 Schematic representation of the linearized ARZ model. Potentially destabilizing coupling appears in two ways: via the internal coupling c , and/or via the routing feedback a .

system:

$$\partial_t w(x, t) = -v^* \partial_x w(x, t), \quad (12.12)$$

$$\xi_t(x, t) = (\gamma p^* - v^*) \xi_x(x, t), \quad (12.13)$$

$$w(0, t) = \xi(0, t), \quad (12.14)$$

$$\xi(L, t) = 0. \quad (12.15)$$

We will use a tiered-backstepping design with a decoupling transformation imposed in the middle. In general, one can compose these transformations into a single transformation, but doing so obfuscates the purpose of each individual transformation – thus, we use consecutive transformations to make clear the method of transformation.

We first utilize the following backstepping transformation to shift the interior term $c(x)w(x, t)$ in (12.5)–(12.8) to the $x = L$ boundary, where it can be neutralized with the boundary controller

$$\begin{aligned} z(x, t) = & v(x, t) - \int_0^x k(x, y)v(y, t)dy \\ & - \int_0^x l(x, y)w(y, t)dy - \int_x^L m(x, y)w(y, t)dy. \end{aligned} \quad (12.16)$$

The kernels of transformation $k, l \in C^1(\mathcal{T}_l), m \in C^1(\mathcal{T}_u)$ are to be determined, where $\mathcal{T}_l = \{(x, y) \in \mathbb{R}^2 | 0 \leq y \leq x \leq L\}$ and $\mathcal{T}_u = \{(x, y) \in \mathbb{R}^2 | 0 \leq x \leq y \leq L\}$. This transformation is an extension to the backstepping technique introduced and applied in the previous chapters. The Volterra integral operator characterized by the kernel m contains so called *forwarding* transformation. The transformation (12.16) leads to the following intermediate target system,

$$\partial_t w(x, t) = -v^* \partial_x w(x, t) \quad (12.17)$$

$$\partial_t z(x, t) = (\gamma p^* - v^*) \partial_x z(x, t) \quad (12.18)$$

$$w(0, t) = k_1 z(0, t) + \int_0^L a(x) w(x, t) dx \quad (12.19)$$

$$z(L, t) = V_{\text{ramp}}(t), \quad (12.20)$$

where $V_{\text{ramp}}(t)$ is defined to be

$$\begin{aligned} V_{\text{ramp}}(t) := & U_{\text{ramp}}(t) + k_2 w(L, t) - \int_0^L k(L, y) v(y, t) dy \\ & - \int_0^L l(L, y) w(y, t) dy. \end{aligned} \quad (12.21)$$

The kernels of transformation k, l, m satisfy the following hyperbolic PDE system:

$$\partial_x k + \partial_y k = 0 \quad (12.22)$$

$$(\gamma p^* - v^*) \partial_x l - v^* \partial_y l = c(y) k + v^* l(x, 0) a(y) \quad (12.23)$$

$$(\gamma p^* - v^*) \partial_x m - v^* \partial_y \partial_y m = v^* l(x, 0) a(y) \quad (12.24)$$

$$k(x, 0) = \frac{k_1 v^*}{\gamma p^* - v^*} l(x, 0), \quad (12.25)$$

$$l(x, x) = m(x, x) - \frac{c(x)}{\gamma p^*} \quad (12.26)$$

$$m(x, L) = 0, \quad (12.27)$$

$$m(0, y) = 0 \quad (12.28)$$

The wellposedness of this PDE system will be studied in a later section.

The target system (12.17)-(12.20) still contains feedback. However, due to the first transformation (12.16), the recirculatory non-local feedback now appears *only* at the inlet boundary. We apply a series of two more invertible transformations to eliminate this recirculation in the target system. We define the following parameter

$$\mu^* = \frac{v^*}{\gamma p^* - v^*}, \quad (12.29)$$

which is the ratio of characteristic speeds between states v, w in (12.5),(12.6).

The app routing feedback, a nonstandard recirculation behavior, motivates the use of a new, “two-piece” (or ‘piecewise’) transformation that converts the non-local boundary coupling to a trace term coupling appearing in PDE in the interior of the freeway segment. We define the following piecewise transformation,

$$(12.31)$$

$$\eta(x, t) = k_1 z(x, t) + \int_{\mu^* x}^L a(y) w(y - \mu^* x, t) dy \in \left[0, \frac{L}{\mu^*}\right] k_1 z(x, t)$$

The piecewise transformation (12.2), as well as the bounded spatial domain $x \in [0, L]$ prescribes only the first case if $\mu^* \leq 1$. That is, $x \in \left[0, \frac{L}{\mu^*}\right] \cap [0, L]$ will necessarily restrict the cases when appropriate.

The transformation (12.2) is continuous. Taking the temporal and spatial derivatives of (12.2) and substituting into (12.18), the following equation is obtained for $\eta(x, t)$,

$$\partial_t \eta(x, t) - (\gamma p^* - v^*) \partial_x \eta(x, t) = \check{a}(x) w(0, t), \quad (12.32)$$

where the parameter $\check{a}(x)$ is defined as the piecewise function:

$$(12.34)$$

$$\check{a}(x) := (\gamma p^* - v^*) a(\mu^* x) x, \in [0, L/\mu^*] 0$$

The (w, η) system is then expressed as

$$\partial_t w(x, t) = -v^* \partial_x w(x, t), \quad (12.35)$$

$$\eta_t(x, t) = (\gamma p^* - v^*) \eta_x(x, t) + \check{a}(x) \eta(0, t), \quad (12.36)$$

$$w(0, t) = \eta(0, t), \quad (12.37)$$

$$\eta(L, t) = W_{\text{ramp}}(t). \quad (12.38)$$

where $W_{\text{ramp}}(t)$ is obtained from evaluating the transform (12.2) at $x = L$, compactly formulated as:

$$W_{\text{ramp}}(t) := k_1 V_{\text{ramp}}(t) + \int_{\min\{\mu^* L, L\}}^L a(y) w(y - \mu^* x, t) dy \quad (12.39)$$

The final step involves a single backstepping transformation from $\eta(x, t)$ to $\xi(x, t)$. The target system is obtained as

$$\xi_t(x, t) = (\gamma p^* - v^*) \eta_x(x, t) \xi_x(x, t), \quad (12.40)$$

$$\xi(L, t) = 0, \quad (12.41)$$

which is achieved by the backstepping transformation

$$\xi(x, t) = \eta(x, t) - \int_0^x n(x - y) \eta(y, t) dy. \quad (12.42)$$

This leads us to our final target system (w, ξ) , which is trivially finite-time stable. The kernel of transformation (12.42) must satisfy the following Volterra integral equation of the second kind:

$$n(x) = (v^* - \gamma p^*)^{-1} \left[\check{\alpha}(x) + \int_0^x \check{\alpha}(y) n(x-y) dy \right] \quad (12.43)$$

The controller $W_{\text{ramp}}(t)$ can be found by evaluating transform (12.42) at $x = L$:

$$W_{\text{ramp}}(t) = \int_0^L n(L-y) \eta(y, t) dy. \quad (12.44)$$

By combining (12.21), (12.39), (12.44), the feedback controller $U_{\text{ramp}}(t)$ is obtained:

$$\begin{aligned} U_{\text{ramp}}(t) = & \alpha(t) - k_2 w(L, t) + \int_0^L F_v(y) v(y, t) dy \\ & + \int_0^L F_w(y) w(y, t) dy - \int_{\min\{\mu^* L, L\}}^L k_1^{-1} a(y) w(y - \mu^* x, t) dy, \end{aligned} \quad (12.45)$$

where the control gains $F_v(y)$, $F_w(y)$ are given by the following relations:

$$F_v(y) = k(L, y) + n(L-y) - \int_y^1 n(L-\xi) k(\xi, y) d\xi, \quad (12.46)$$

$$\begin{aligned} F_w(y) = & l(L, y) + \int_0^{\frac{L-y}{\mu^*}} k_1^{-1} n(L-\xi) a(y + \mu^* \xi) d\xi \\ & - \int_y^1 n(L-\xi) l(\xi, y) d\xi - \int_0^y n(L-\xi) m(\xi, y) d\xi, \end{aligned} \quad (12.47)$$

and $\alpha(t)$ is defined as

$$\dot{\alpha}(t) = -k_3 \alpha(t), \quad (12.48)$$

where $k_3 > 0$, and the initial condition $\alpha(0)$ is chosen to fulfill compatibility conditions between the initial control value $U(0)$ and the initial condition v_0 . It is important to note that the dynamically extended state is trivially exponentially stable, and therefore does not compromise the (exponential) stability of the system. We then state the main theorem of the chapter.

Theorem 12.1 *The boundary controller (12.45) guarantees exponential stability, in the sense of the spatial H^1 norm, of the zero solution of the linearized ARZ model (12.5), (12.6). That is, there exist $M, \gamma \in \mathbb{R}_+$ such that*

$$\|v, w\|_{H^1} \leq M \exp(-\gamma t) \|v_0, w_0\|_{H^1} \quad \forall t \geq 0. \quad (12.49)$$

Moreover, (12.45) ensures the global (in time) existence of solutions for sufficiently small initial conditions $\|v_0, w_0\|_{H^1} < M^{-1}\varepsilon$, where (12.49) generates a priori H^1 energy estimates for the solution (v, w) .

The proof is obtained using an H^1 stability estimate of the target system (12.12)-(12.15) coupled with invertible and regularity-preserving backstepping transformations (12.16),(12.2),(12.42) to derive H^1 stability for (v, w) . These properties are studied briefly in Section 12.3.

12.3 Closed-loop stability

We use the the Lyapunov stability analysis to prove that the closed-loop system with the feedback controller (12.45) is exponentially stabilized at the equilibrium (v^*, q^*) . It is not only necessary to prove convergence, but also to prove pointwise boundedness in our stability estimate. To ensure existence of solutions to the closed-loop system, the states can neither exceed the limits arising due to the linear model approximation failing beyond the domain of attraction nor exceed physical flow rate/velocity constraints (positivity, maximum capacity, speed limits).

We give a series of lemmas that establish H^1 stability in the target system and establish equivalence in H^1 norm between all transformed states. The combination of the following lemmas establishes the result of Theorem 12.1.

Lemma 12.1 *The zero solution of the target system (12.12)-(12.15) is exponentially stable in the sense of H^1 , that is, there exist $M_1, \gamma \in R_+$ such that*

$$\|\eta, w\|_{H^1} \leq M_1 \exp(-\gamma t) \|\eta_0, w_0\|_{H^1} \quad (12.50)$$

for all $t \in [0, \infty)$.

Lemma 12.1 is straightforward to prove using the standard Lyapunov function for w and v in the H^1 sense. One can utilize the following Lyapunov function

$$\begin{aligned} V(t) = \int_0^L & \left[e^{-\delta_1 x} w(x, t)^2 + d_1 e^{\delta_2 x} v(x, t)^2 \right. \\ & \left. + e^{-\delta_3 x} \partial_x w(x, t)^2 + d_2 e^{\delta_4 x} \partial_x v(x, t)^2 \right] dx, \end{aligned} \quad (12.51)$$

where the coefficients are chosen $\delta_i > 0, i \in \{1, \dots, 4\}$, and $d_1 > \mu^*, d_2 > 1/\mu^*$. The coefficients M_1, γ are then given by

$$M_1 = \frac{\max\{e^{\delta_2 L}, e^{\delta_4 L}\}}{\min\{e^{-\delta_1 L}, e^{-\delta_3 L}\}} \quad (12.52)$$

$$\gamma = \frac{1}{4} \min\{\delta_1 v^*, \delta_3 v^*, d_1 \delta_2 (\gamma p^* - v^*), d_2 \delta_4 (\gamma p^* - v^*)\}. \quad (12.53)$$

Lemma 12.2 *The transformation (12.42) and its associated inverse transform establishes H^1 equivalence in norm between (ξ, w) and (η, w) , i.e. there exist $C_1, C_2 > 0$ such that*

$$C_1 \|\xi, w\|_{H^1} \leq \|\eta, w\|_{H^1} \leq C_2 \|\xi, w\|_{H^1} \quad (12.54)$$

with $C_1 = (1 + 3\|n\|_{L^2})^{-1}$, $C_2 = (1 + 3\|\hat{n}\|_{L^2})^{-1}$, where \hat{n} is the inverse kernel related to n .

The reason why the H^1 equivalence between system norms is nontrivial is because of the regularity of the kernel n . In general, n is only L^2 , which makes establishing H^1 more difficult. However, due to the convolution structure of the kernel, H^1 equivalence can be derived by exploiting integration by parts and the Sobolev embedding theorem.

Lemma 12.3 *The transformation (12.2) and its associated inverse transform establishes H^1 equivalence in norm between (η, w) and (z, w) , i.e., there exist $C_3, C_4 > 0$ such that*

$$C_3 \|\eta, w\|_{H^1} \leq \|z, w\|_{H^1} \leq C_4 \|\eta, w\|_{H^1} \quad (12.55)$$

For (12.2), the equivalence is straightforward to obtain as (12.2) is just a piecewise affine transformation.

Lemma 12.4 *The transformation (12.16) and its associated inverse transform establishes H^1 equivalence in norm between (z, w) and (v, w) , i.e., there exist $C_5, C_6 > 0$ such that*

$$C_5 \|z, w\|_{H^1} \leq \|v, w\|_{H^1} \leq C_6 \|z, w\|_{H^1} \quad (12.56)$$

The norm equivalence property is standard as (12.16) is an extensively studied backstepping transformation.

12.4 Existence of solutions to kernel equations

For the backstepping transformations (12.16) and (12.42) to exist, both the companion boundary value problem given by (12.22)-(12.24) with boundary conditions (12.25)-(12.28) and the integral equation (12.43) must have solutions. We will begin by studying the existence of solutions to (12.22)-(12.24).

Lemma 12.5 *Consider the boundary value problem given by the system of hyperbolic equations (12.22)-(12.24) with boundary conditions (12.25)-(12.28). Assume that $a, c \in C([0, L])$. Then there exist unique solutions $k, l \in C(\mathcal{T}_l)$ and $m \in C(\mathcal{T}_u)$.*

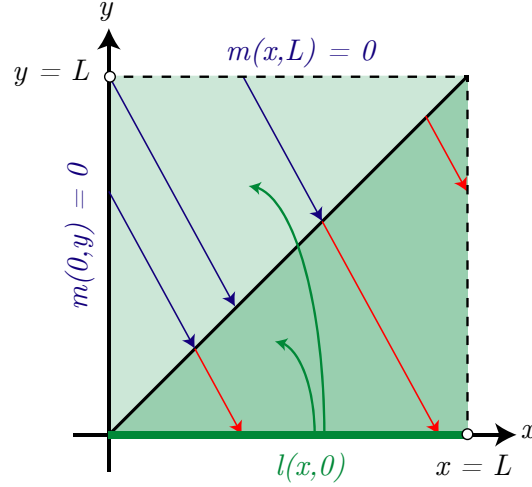


Fig. 12.2 Characteristic lines for (l, m) companion kernel PDE. A transmission condition between the two kernels appears at $y = x$. The boundary value $l(x, 0)$ introduces feedback via trace terms in the evolution equation for both l, m .

Proof The proof follows from finding a solution via the method of characteristics. Since there is non-local behavior arising in the plant, the companion kernel PDEs will exhibit non-local coupling as well, which must be treated using the method of characteristics.

We begin by inspecting the k -PDE. By directly applying the characteristics method, it is not hard to see that k has the following representation for a solution in \mathcal{T}_I :

$$k(x, y) = k(x - y, 0) = k_1 \mu^* l(x - y, 0). \quad (12.57)$$

By using (12.57) as a representation for k in (12.23), one can find the self-contained system (l, m) . The (l, m) characteristics are sketched in Figure 12.2. In particular, note how boundary conditions between l, m are coupled at $y = x$ and $y = 0$.

By a direct application of the method of characteristics to (12.23), one can recover an integral equation for l

$$\begin{aligned} l(x, y) = & m(\sigma_1(x, y), \sigma_1(x, y)) - \frac{1}{\gamma p^*} c(\sigma_1(x, y)) \\ & + \int_0^{\frac{x-y}{\gamma p^*}} \left[k_1 \mu^* c(-v^* s + \sigma_1(x, y)) l(\gamma p^* s, 0) + v^* a(-v^* s + \sigma_1(x, y)) \times l((\gamma p^* - v^*)s + \sigma_1(x, y), 0) \right] ds \end{aligned} \quad (12.58)$$

where

$$\sigma_1(x, y) = \frac{v^*x + (\gamma p^* - v^*)y}{\gamma p^*}. \quad (12.59)$$

Similarly, a direct application of the method of characteristics to (12.24) will yield the following piecewise defined integral relation for m :

$$m(x, y) = \begin{cases} m_1(x, y) & y \leq -\mu^*x + L \\ m_2(x, y) & y > -\mu^*x + L \end{cases} \quad (12.60)$$

$$m_1(x, y) = \int_0^{\frac{x}{\gamma p^* - v^*}} v^* a(-v^*s + \sigma_2(x, y)) \times l((\gamma p^* - v^*)s, 0) ds$$

$$m_2(x, y) = \int_0^{\frac{L-y}{v^*}} v^* a(-v^*s + L) \times l((\gamma p^* - v^*)s + \sigma_3(x, y), 0) ds$$

where σ_2, σ_3 are

$$\sigma_2(x, y) = \mu^*x + y. \quad (12.61)$$

$$\sigma_3(x, y) = x - \frac{1}{\mu^*}(L - y). \quad (12.62)$$

By substituting (12.60) into (12.58) and evaluating it at $y = 0$, one generates the following integral equation that is defined piecewise:

$$l(x, 0) = \begin{cases} l_d(x) & x \leq \frac{L}{\mu^*} \\ l_u(x) & x > \frac{L}{\mu^*} \end{cases} \quad (12.63)$$

$$l_d(x) = -\frac{1}{\gamma p^*} c \left(\frac{v^*}{\gamma p^*} x \right) + I(x) + \int_0^{\frac{\mu^*x}{\gamma p^*}} v^* a(-v^*s + \mu^*x) l((\gamma p^* - v^*)s, 0) ds \quad (12.64)$$

$$l_u(x) = -\frac{1}{\gamma p^*} c \left(\frac{v^*}{\gamma p^*} x \right) + I(x) + \int_0^{\frac{L}{v^*} - \frac{1}{\gamma p^*} x} v^* a(-v^*s + L) l \left((\gamma p^* - v^*)s + x - \frac{L}{\mu^*}, 0 \right) ds \quad (12.65)$$

where

$$I(x) = \int_0^{\frac{x}{\gamma p^*}} k_1 \mu^* c \left(-v^*s + \frac{v^*}{\gamma p^*} x \right) l(\gamma p^*s, 0) + v^* a \left(-v^*s + \frac{v^*}{\gamma p^*} x \right) \times l \left((\gamma p^* - v^*)s + \frac{v^*}{\gamma p^*} x, 0 \right) ds. \quad (12.66)$$

The separate cases of $\mu^* > 1$, and $\mu^* \leq 1$ are self contained in the definition (12.63): for $\mu^* \leq 1$, only the condition corresponding to $l_d(x)$ is activated since $x \in (0, L)$, while for $\mu^* > 1$, both cases must be considered.

Using the method of successive approximations, we establish an iteration $\{l_n\}_{n=0}^\infty \rightarrow l(x, 0)$, which can be shown to converge uniformly since the integral

equations admitted are affine. This establishes the existence of a solution which can be shown to be unique due to the linearity. The regularity is recovered by noting that the pieces of the solution $l(x, 0)$ are $C([0, L])$ compatible. Then the $C(\mathcal{T}_l)$ solutions k, l and $C(\mathcal{T}_u)$ solution m can be directly generated by evaluating (12.57), (12.58), (12.60), respectively. \square

Lemma 12.6 *Consider the integral equation given by (12.43), and the definition of \check{a} in (12.2). If $\check{a} \in L^2(0, L)$, then there exists a unique $L^2(0, L)$ solution n .*

Proof The proof is relatively straightforward, and one may employ standard linear integral equation techniques to recover n . Since \check{a} is assumed piecewise continuous, then one such potential method is utilizing the Laplace transform on (12.43): $\hat{n}(s) = (\gamma p^* - v^*)^{-1} [\hat{\check{a}}(s) + \hat{n}(s)\hat{\check{a}}(s)]$. The solution $n \in L^2$ is found applying the inverse Laplace transform: $n(x) = \mathcal{L}^{-1} \left\{ (\gamma p^* - v^*)^{-1} [\hat{\check{a}}(s) + \hat{n}(s)\hat{\check{a}}(s)] \right\}$. \square

12.5 Notes and References

The present chapter is based on an early and abbreviated publication [?]. In this chapter, we present a ramp metering control design for damping app-routing instabilities in a linearized ARZ traffic model. The full state feedback design is an extension to the classical backstepping control, allowing for the additional component in the control law to account for the non-local boundary condition arising from the routing feedback. One limitation to be addressed in future is the assumption that the app routing flow is known a priori.

Chapter 13

Bilateral Regulation of Moving Shock Position

13.1 Delay-Compensating Predictors for PDE-ODE Models of Traffic Shock Movement

Stop-and-go oscillations are not the only annoyance to the drivers on a freeway. Even in the absence of oscillations, congestion alone, with its increased density and reduced velocity, frustrates drivers and results in wasted fuel.

Congestion is often experienced by driving on the freeway in relatively sparse traffic and all of a sudden reaching a point where the traffic is denser and slower—a congestion. This point on the freeway, which is not in a fixed place but moves, is a point of sharp change in traffic density. As such, it is referred to as a “shock.” Since the shock moves, often in the upstream direction of traffic, the shock’s motion is often referred to as a “shock wave.” At the beginning of a rush hour, traffic typically transitions from free on the entire freeway to congested by the shock wave traveling in the upstream direction.

Completely preventing congestion on the freeway entails a high price—keeping vehicles in queues to enter the freeway and congesting the streets. If freeway congestion is, therefore, accepted as an inevitable consequence of traffic demand, the next best objective is to keep the congestion from consuming it entirely, namely, keeping the shock from progressing all the way upstream.

Managing the progression of a shock between the sparse and dense traffic is the objective of this chapter. We wish to design controllers that exert control over the motion of the shock—for example, controllers that regulate the position of the shock to a desired location on the freeway. Of course, one can also formulate a goal of regulating the shock to follow a certain trajectory (to move up and down the freeway in accordance with a desired waveform). This is a pretty routine extension of the setpoint regulation problem, so we restrict our attention to setpoint regulation for a moving shock.

Once we shift our attention from suppressing oscillations to regulating the movement of a shock, there is no longer a reason to employ a model of stop-and-go oscillations, the ARZ model. The shock motion being of interest, we can restrict

our study to the LWR model whose key function is the modeling of spatiotemporal evolution of density.

If the goal is to regulate the shock's position to a setpoint, what kind of input, or inputs, can we employ towards that goal? In order to answer this question, let us recall that the variations of density in the LWR model travel in the downstream direction in free traffic and in the upstream direction in the congested traffic. So, on a freeway segment with ramps at both of the segment's boundaries, and with a shock somewhere in the domain, with free traffic upstream of the shock and congested traffic downstream of the shock, both ramps can be employed to propagate a control action towards the shock. From the upstream ramp in the downstream direction towards the shock, and from the downstream ramp in the upstream direction towards the shock.

So this is the problem we pursue in this chapter: consider a freeway segment modeled by the LWR model, with ramp metering inputs at both of the segment's boundaries, and design controllers for the two inputs to regulate the shock's position to the setpoint, somewhere in between the two ramps.

Because of the availability of two boundary inputs, at the opposite ends of the freeway segment, we refer to this problem as "bilateral regulation."

The model that we use to study this problem is not a simple LWR model but a pair of LWR models, on domains that vary with time, as the shock moves, and connected using a scalar ODE that models the position of the shock (the Rankine-Hugoniot condition). So, the position of the shock is both an ODE state of the PDE-ODE-PDE system and a position of the boundary for both of the LWR PDEs.

The two LWR models, modeling traffic upstream and downstream of the shock, are nonlinear. However, the control objective of regulating the position of the shock, translates into the objective of regulating the density upstream of the shock to a lower value (corresponding to free traffic) and of regulating the density downstream of the shock to a higher value (corresponding to congested traffic). So, the objective of the two ramp metering inputs is to regulate the density on their respective sides of the shock to the respective free/congested density setpoints.

Since the regulation of the LWR models to their equilibria is the control objective, it makes sense to pursue this objective by performing a control design on the linearized version of the LWR model, around the respective equilibrium. When the LWR model is linearized, its linearization is the linear transport PDE, namely, the pure delay. This is a crucial observation—ramp metering inputs are faced with the task of controlling the shock position through input delays.

When input delays are present in control systems, if not accounted for in the design, and if either the delay values are large or the control gains are large, instability not only may arise but it will certainly arise for long enough delays. Accounting for the input delay in the design means applying "predictor feedback" [?], which compensates for the presence of the delay and prevents the control input from getting too large, out of impatience of its effect not being instantly reflected at the system's output, and destabilizing the system due to aggressive action. So, predictor feedback imposes restraint on the control input and ensures stability. Predictor feedback is just a form of PDE backstepping, specialized to cascades of a transport PDE into an ODE.

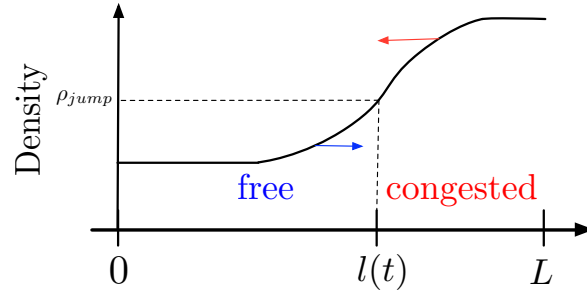


Fig. 13.1 Traffic moving shockwave front on freeway, the arrows represent propagation directions of density variations. In LWR model, the propagation directions are given by the characteristic speeds of density $Q'(\rho)$.

The availability of predictor feedback, for the purpose of compensating the delay in propagating the ramp metering inputs to the current shock location, is good news. However, conventional predictor feedback is for constant delays, whereas, when the shock is moving, the delay from the ramp metering input varies with time. In fact, the delay does not vary in time in a fashion that is a priori set but depends on the current shock location, which will change in the future. To send a good control signal from the ramp metering input one has to be able to predict where the shock will be once this input reaches the shock, i.e., how long it will take the input signal to reach the location of the shock, which is not known at the time of selecting the input. If this task of compensating the delays that depend on the current and future shock positions appears as a nightmare it is. But it is possible to get through it using the technique developed in [?]. Compensation techniques for delays that depend on the state—both the current state and a value of the state in the past (which is a problem that arises in internet traffic)—are available in that 2013 book.

So, in this chapter we employ the techniques for compensating state-dependent (shock-dependent) delays for regulating the shock position through the (linearized) LWR PDE dynamics over varying domain lengths.

Using Lyapunov stability analysis, we show local stability of the closed-loop system, with the fully nonlinear LWR model, in the H_1 norm with an arbitrarily fast convergence rate. The shock regulation and overall PDE-ODE-PDE stabilization result is demonstrated by a numerical simulation on the fully nonlinear LWR model.

Let us close this section by noting that traffic discontinuities can be caused by various inhomogeneities of freeway or vehicles. Some studies consider a shock front as a moving traffic flow constraint [?, ?] due to a reduction of road capacity. Slow moving vehicles, also known as moving bottlenecks, are represented in [?, ?, ?] with ODEs governing the velocity of slow vehicles. These are out of the scope of this chapter and relevant to the controllability problem with boundary actuation.

13.2 Moving Shockwave Model

The moving shockwave front is the head of a shockwave, segregating traffic on a segment of freeway into two different traffic conditions. The upstream traffic of the shockwave front is free and the downstream traffic is congested, as shown in Fig. 13.1. The traffic densities are described with the LWR model.

Recall the first-order LWR PDE that governs traffic density $\rho(x, t)$,

$$\partial_t \rho + Q'(\rho) \partial_x \rho = 0, \quad (13.1)$$

where $x \in [0, L]$, $t \in [0, \infty)$, $Q(\rho)$ is a fundamental diagram which shows the equilibrium relation of density and traffic flow. The fundamental diagram $Q(\rho)$ is defined as

$$Q(\rho) = \rho V(\rho). \quad (13.2)$$

The equilibrium velocity $V(\rho)$ is an affine decreasing function of density which we choose the following Greenshield's model,

$$V(\rho) = v_m \left(1 - \frac{\rho}{\rho_m} \right), \quad (13.3)$$

where v_m is the maximum speed, ρ_m is the maximum density. The Greenshield's model $V(\rho)$ yields a strictly concave fundamental diagram $Q(\rho)$, shown in Fig. 13.2. The jump density ρ_{jump} segregates densities into two sections, free regime on the left and congested regime on the right.

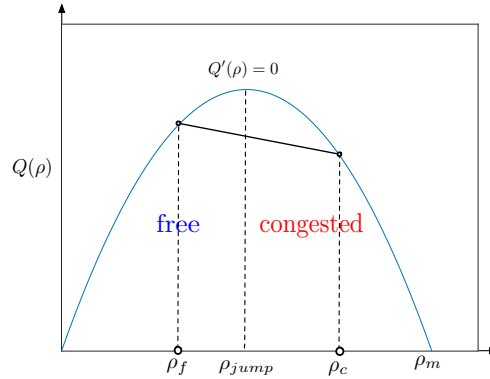


Fig. 13.2 Fundamental diagram of traffic density and traffic flow relation.

In the LWR PDE (13.1), density variations propagate with the characteristic speed $Q'(\rho)$. The free regime with light traffic, equivalently, $\rho_f < \rho_{\text{jump}}$, has its density variations transported downstream with

$$Q'(\rho)|_{\rho=\rho_f} = V(\rho_f) + \rho_f V'(\rho_f) > 0, \quad (13.4)$$

while the congested regime with denser traffic, namely, $\rho_c > \rho_{\text{jump}}$ has its density variations transported upstream with

$$Q'(\rho)|_{\rho=\rho_c} = V(\rho_c) + \rho_c V'(\rho_c) < 0. \quad (13.5)$$

As shown in Fig. 13.1, the moving shockwave considered here is the shock of a traffic wave, physically representing the discontinuity of density. The congested traffic density propagates upstream while the light traffic density propagates downstream. Therefore, the upstream front of the shockwave becomes steeper in propagation and eventually, the gradient $\partial_x \rho$ tends to be infinity [?]. In this scenario, drivers located in the upstream front of the shock will experience transition from the free to congested traffic. The position of the shockwave front is later defined by an ODE according to Rankine-Hugoniot condition. The dynamics of the upstream free traffic, the downstream congested traffic and the position of the moving interface are presented below.

Define the traffic density of the free regime as $\rho_f(x, t)$ for $x \in [0, l(t)]$, $t \in [0, +\infty)$, and the congested regime as $\rho_c(x, t)$, for $x \in [l(t), L]$, $t \in [0, +\infty)$, the LWR model that describes the traffic is given by

$$\partial_t \rho_f + \partial_x (\rho_f v_f) = 0, \quad x \in [0, l(t)], \quad (13.6)$$

$$\partial_t \rho_c + \partial_x (\rho_c v_c) = 0, \quad x \in [l(t), L], \quad (13.7)$$

where $l(t) \in [0, L]$ is the location of the moving interface. The density and velocity relation is given by the Greenshield's model (13.3), ($i = f, c$),

$$v_i(x, t) = V_i(\rho_i(x, t)) = v_m \left(1 - \frac{\rho_i(x, t)}{\rho_m} \right). \quad (13.8)$$

Due to the flow discontinuity at the moving boundary, a traveling vehicle leaves the free regime to enter the congested regime. Dynamics of moving interface $l(t)$ is derived under the Rankine-Hugoniot condition which guarantees that the mass of traffic flow is conserved at the moving interface. The upstream propagation of the shockwave front is driven by the flow discontinuity,

$$\dot{l}(t) = \frac{\rho_c(l(t), t) v_c(l(t), t) - \rho_f(l(t), t) v_f(l(t), t)}{\rho_c(l(t), t) - \rho_f(l(t), t)}, \quad (13.9)$$

where the initial position of the shockwave front $0 < l(0) < L$. The following inequalities for initial conditions of PDEs (13.6), (13.7) are assumed:

$$\rho_c(l(0), 0)v_c(l(0), 0) < \rho_f(l(0), 0)v_f(l(0), 0), \quad (13.10)$$

$$\rho_c(l(0), 0) > \rho_f(l(0), 0). \quad (13.11)$$

Initially, the traffic downstream the interface is denser but with a smaller flow which lets less vehicles to pass through while the traffic upstream is light and let more vehicles to come in the segment. With the above assumptions to hold, we obtain from (13.9) that $\dot{l}(0) < 0$. The moving interface travels upstream, driven by a flow difference induced by the density discontinuity.

Substituting density-velocity relation (13.8) into (13.6), (13.7), and (13.9), we have two nonlinear PDEs and an ODE coupled system that governs the dynamics of $\rho_f(x, t)$, $\rho_c(x, t)$ and $l(t)$, given by

$$\partial_t \rho_f(x, t) = -v_m \partial_x \left(\rho_f(x, t) - \frac{\rho_f^2(x, t)}{\rho_m} \right), \quad (13.12)$$

$$\partial_t \rho_c(x, t) = -v_m \partial_x \left(\rho_c(x, t) - \frac{\rho_c^2(x, t)}{\rho_m} \right), \quad (13.13)$$

$$\dot{l}(t) = v_m - \frac{v_m}{\rho_m} (\rho_c(l(t), t) + \rho_f(l(t), t)). \quad (13.14)$$

We consider the following controlled boundary condition for the nonlinear coupled PDE-ODE system consisting of (13.12), (13.13), and (13.14)

$$\rho_f(0, t) = U_{\text{in}}(t) + \rho_f^*, \quad (13.15)$$

$$\rho_c(L, t) = U_{\text{out}}(t) + \rho_c^*, \quad (13.16)$$

where we control the incoming and outgoing density variations of the freeway segment $U_{\text{in}}(t)$ and $U_{\text{out}}(t)$. The well-posedness of the coupled PDE-ODE system can be proved following [?] by defining a shock free solution to the quasilinear hyperbolic system (7)-(9) with compatibility condition verified by the initial conditions, which establish an equivalence relation with the shockwave solutions of the scalar Burgers equation. Our control objective is to stabilize both free and congested regime traffic $\rho_i(x, t)$ to uniform steady-states ρ_i^* and at the same time, the moving interface $l(t)$ to a desirable static setpoint l^* . Therefore, the shockwave becomes standstill within the freeway segment instead of moving upstream.

The incoming traffic flow is assumed to be in the free regime and the downstream of the outlet is assumed to be congested. The bilateral control of density can be realized with ramp metering actuating the flow at both boundaries: we have at inlet $q_{\text{in}}(t) = Q(\rho_f(0, t))$, and at outlet $q_{\text{out}}(t) = Q(\rho_c(L, t))$. In practical implementation of the bilateral controllers, the flow variations of

$$q_{\text{ramp, in}} = q_{\text{in}}(t) - Q(\rho_f^*), \quad (13.17)$$

$$q_{\text{ramp, out}} = q_{\text{out}}(t) - Q(\rho_c^*), \quad (13.18)$$

are regulated with traffic lights on ramp.

13.3 State-dependent PDE-ODE Model

We linearize the original coupled PDE-ODE model $(\rho_f(x, t), \rho_c(x, t), l(t))$ -system defined in (13.12), (13.13), (13.14) around steady-states $(\rho_f^*, \rho_c^*, l^*)$. The constant equilibrium setpoint values are chosen so that the following conditions that ensure the model validity hold

$$0 < \rho_f^* < \rho_{\text{jump}} < \rho_c^* < \rho_m, \quad (13.19)$$

$$0 < l^* < L. \quad (13.20)$$

At steady-state, the flow equilibrium needs to be achieved for both sides of the moving interface,

$$\rho_f^* V(\rho_f^*) = \rho_c^* V(\rho_c^*). \quad (13.21)$$

Using condition (13.21), the quadratic fundamental diagram yields that

$$\rho_f^* + \rho_c^* = \rho_m. \quad (13.22)$$

Define the state deviations from the system reference as

$$\tilde{\rho}_i(x, t) = \rho_i(x, t) - \rho_i^*, \quad (13.23)$$

$$X(t) = l(t) - l^*, \quad (13.24)$$

where $\dot{X}(t) = \dot{l}(t)$ is satisfied. Thus, the linearized PDE-ODE model (13.12)–(13.14) with the boundary conditions (13.15) and (13.16) around the system reference $(\rho_f^*, \rho_c^*, l^*)$ is defined as the following $(\tilde{\rho}_f(x, t), \tilde{\rho}_c(x, t), X(t))$ -system

$$\partial_t \tilde{\rho}_f(x, t) = -u \partial_x \tilde{\rho}_f(x, t), \quad x \in [0, l(t)], \quad (13.25)$$

$$\partial_t \tilde{\rho}_c(x, t) = u \partial_x \tilde{\rho}_c(x, t), \quad x \in [l(t), L], \quad (13.26)$$

$$\tilde{\rho}_f(0, t) = U_{\text{in}}(t), \quad (13.27)$$

$$\tilde{\rho}_c(L, t) = U_{\text{out}}(t), \quad (13.28)$$

$$\dot{X}(t) = -b (\tilde{\rho}_f(l(t), t) + \tilde{\rho}_c(l(t), t)), \quad (13.29)$$

where the transport speed is defined as

$$u = v_m \left(1 - \frac{2\rho_f^*}{\rho_m} \right), \quad (13.30)$$

and satisfy $0 < u < v_m$. The constant coefficient b in ODE is defined as $b = \frac{v_m}{\rho_m} > 0$. The model after linearization in (13.25)–(13.29) is a state-dependent coupled PDE-ODE system with bilateral boundary control inputs from inlet and outlet. Notice that the PDE states are linearized around the steady-states, but the ODE is dependent on PDE states and PDE states evolve in ODE-dependent space domain. Therefore the PDE-ODE coupled system (13.25)–(13.30) is a quasilinear system. The nonlinearity

is geometrical and induced by the phase change between the free and congested regimes.

Remark 13.1 For model validity, we assume that there exists a constant $L > 0$ such that the ODE state $l(t)$ satisfies

$$0 < l(t) < L, \quad (13.31)$$

so that (13.12), (13.13), and (13.14) are well-defined for $x \in [0, L]$, $t \in [0, +\infty)$. We emphasize that the proposed control law needs to guarantee the above condition.

13.4 Predictor-based Control Design

In this section, we first introduce the equivalent delay system representation to the system (13.25)–(13.29). Then, a backstepping transformation is applied to obtain predictor-based state feedback controls to compensate the PDE state-dependent delays to the ODE.

From coupled PDE-ODE to delay system representation

The system (13.25)–(13.29) can be represented by an unstable ODE with two distinct state-dependent input delays. Introduce the following state-dependent delays for the two transport PDEs

$$D_f(t) = \frac{l(t)}{u}, \quad D_c(t) = \frac{L - l(t)}{u}, \quad (13.32)$$

where

$$l(t) = X(t) + l^*. \quad (13.33)$$

The PDE states at $x = l(t)$ are represented by

$$\tilde{\rho}_f(l(t), t) = U_{\text{in}}(t - D_f(t)), \quad (13.34)$$

$$\tilde{\rho}_c(l(t), t) = U_{\text{out}}(t - D_c(t)), \quad (13.35)$$

where $U_{\text{in}}(t)$ and $U_{\text{out}}(t)$ are the boundary control inputs defined in (13.27) and (13.28) and the representations are valid when Remark 13.1 and Remark 13.2 hold and initial conditions are bounded as introduced in Theorem 13.1 later. The assumptions guarantee that the corresponding solution is defined for all $t \geq 0$, which implies that the moving interface $l(t)$ stays in the spatial domain before the control inputs reach it.

Substituting (13.34) and (13.35) into the ODE (13.29), the following state-dependent input delay system representation is derived

$$\dot{X}(t) = -b(U_{\text{in}}(t - D_f(X(t))) + U_{\text{out}}(t - D_c(X(t))). \quad (13.36)$$

If the position of the moving shock front is close to the inlet half segment such that $l(t) \in [0, \frac{L}{2}]$, it holds that $\forall t \in [0, \infty)$,

$$D_f(t) \leq D_c(t). \quad (13.37)$$

As a result, delayed inlet control input $U_{\text{in}}(t - D_f(t))$ reaches the moving shock front faster than delayed outlet control input $U_{\text{out}}(t - D_c(t))$. If $l(t) \in [\frac{L}{2}, L]$, $\forall t \in [0, \infty)$, it holds that

$$D_f(t) \geq D_c(t), \quad (13.38)$$

Then $U_{\text{out}}(t - D_c(t))$ reaches the moving shock front faster than $U_{\text{in}}(t - D_f(t))$.

We introduce a new coordinate z defined as

$$(13.41)$$

$$z = \frac{l(t) - x}{u}, \quad x \in [0, l(t)], \frac{x - l(t)}{u},$$

and new variables $\tilde{\rho}_f(z, t)$ and $\tilde{\rho}_c(z, t)$ defined in z -coordinate. The transformations between $\tilde{\rho}_f(x, t)$, $\tilde{\rho}_c(x, t)$ and $\tilde{\rho}_f(z, t)$, $\tilde{\rho}_c(z, t)$ are given by

$$\tilde{\rho}_f(z, t) = \tilde{\rho}_f(l(t) - uz, t), \quad z \in [0, D_f(t)], \quad (13.42)$$

$$\tilde{\rho}_c(z, t) = \tilde{\rho}_c(l(t) + uz, t), \quad z \in [0, D_c(t)], \quad (13.43)$$

and the associated inverse transformations of (13.42) and (13.43) are given by

$$\tilde{\rho}_f(x, t) = \tilde{\rho}_f\left(\frac{l(t) - x}{u}, t\right), \quad x \in [0, l(t)], \quad (13.44)$$

$$\tilde{\rho}_c(x, t) = \tilde{\rho}_c\left(\frac{x - l(t)}{u}, t\right), \quad x \in [l(t), L]. \quad (13.45)$$

Using (13.42) and (13.43), the original system (13.25)–(13.29) is rewritten in the new z -coordinate as

$$\partial_t \tilde{\varrho}_f(z, t) = \left(1 - \frac{\dot{l}(t)}{u}\right) \partial_z \tilde{\varrho}_f(z, t), \quad z \in [0, D_f(t)], \quad (13.46)$$

$$\partial_t \tilde{\varrho}_c(z, t) = \left(1 + \frac{\dot{l}(t)}{u}\right) \partial_z \tilde{\varrho}_c(z, t), \quad z \in [0, D_c(t)], \quad (13.47)$$

$$\tilde{\varrho}_f(D_f(t), t) = U_{\text{in}}(t), \quad (13.48)$$

$$\tilde{\varrho}_c(D_c(t), t) = U_{\text{out}}(t), \quad (13.49)$$

with the ODE state $l(t) = X(t) + l^*$ given by

$$\dot{X}(t) = -b (\tilde{\varrho}_f(0, t) + \tilde{\varrho}_c(0, t)). \quad (13.50)$$

Remark 13.2 The proposed control laws U_{in} and U_{out} need to be designed such that the following condition for the ODE state $l(t)$ is guaranteed

$$-u < \dot{l}(t) < u, \quad (13.51)$$

so that well-posedness of the system (13.46)–(13.50) for $x \in [0, L]$, $t \in [0, +\infty)$ is guaranteed.

Based on the above system in a delay representation, we construct the following predictor-based backstepping transformation so that the delays are compensated with the control design.

Predictor-based backstepping transformation

We consider the following backstepping transformation, motivated by the predictor-based transformation for delay representation $\varrho_f(z, t)$ and $\varrho_c(z, t)$ defined in (13.46)–(13.49),

$$\begin{aligned} \omega_f(z, t) = & \tilde{\varrho}_f(z, t) - K_f \left(X(t) - b \int_0^z \tilde{\varrho}_f(\xi, t) d\xi \right. \\ & \left. - b \int_0^{\min\{D_c(t), z\}} \tilde{\varrho}_c(\xi, t) d\xi \right), \quad z \in [0, D_f(t)], \end{aligned} \quad (13.52)$$

$$\begin{aligned} \omega_c(z, t) = & \tilde{\varrho}_c(z, t) - K_c \left(X(t) - b \int_0^z \tilde{\varrho}_c(\xi, t) d\xi \right. \\ & \left. - b \int_0^{\min\{D_f(t), z\}} \tilde{\varrho}_f(\xi, t) d\xi \right), \quad z \in [0, D_c(t)], \end{aligned} \quad (13.53)$$

where $K_f, K_c > 0$ are positive constant gain kernels. The above transformation in the original PDE state variables $\rho_f(x, t)$ for $x \in [0, l(t)]$ and $\rho_c(x, t)$ for $x \in [l(t), L]$, is given by

$$w_f(x, t) = \tilde{\rho}_f(x, t) - K_f \left(X(t) - \frac{b}{u} \int_x^{l(t)} \tilde{\rho}_f(\xi, t) d\xi - \frac{b}{u} \int_{l(t)}^{\min\{L, 2l(t)-x\}} \tilde{\rho}_c(\xi, t) d\xi \right), \quad x \in [0, l(t)], \quad (13.54)$$

$$w_c(x, t) = \tilde{\rho}_c(x, t) - K_c \left(X(t) - \frac{b}{u} \int_{l(t)}^x \tilde{\rho}_c(\xi, t) d\xi - \frac{b}{u} \int_{\max\{0, 2l(t)-x\}}^{l(t)} \tilde{\rho}_f(\xi, t) d\xi \right), \quad x \in [l(t), L]. \quad (13.55)$$

- For the case $D_f(t) \leq D_c(t)$, it follows that $l(t) \in [0, \frac{L}{2}]$ and the following holds

$$x \in [0, l(t)] \implies \min\{L, 2l(t) - x\} = 2l(t) - x. \quad (13.56)$$

- For the case $D_f(t) \geq D_c(t)$, it follows that $l(t) \in [\frac{L}{2}, L]$ and the following holds

$$x \in [l(t), L] \implies \max\{0, 2l(t) - x\} = 2l(t) - x. \quad (13.57)$$

Later on, two pairs of state feedback controllers are obtained respectively for $l(t) \in [0, \frac{L}{2}]$ and $l(t) \in [\frac{L}{2}, L]$. The inverse transformation of (13.54), (13.55) is given by

$$\tilde{\rho}_f(x, t) = w_f(x, t) + K_f \left(X(t) - \frac{b}{u} \int_x^{l(t)} w_f(\xi, t) d\xi - \frac{b}{u} \int_{l(t)}^{\min\{L, 2l(t)-x\}} w_c(\xi, t) d\xi \right), \quad x \in [0, l(t)], \quad (13.58)$$

$$\tilde{\rho}_c(x, t) = w_c(x, t) + K_c \left(X(t) - \frac{b}{u} \int_{l(t)}^x w_c(\xi, t) d\xi - \frac{b}{u} \int_{\max\{0, 2l(t)-x\}}^{l(t)} w_f(\xi, t) d\xi \right), \quad x \in [l(t), L]. \quad (13.59)$$

The derivation of the inverse transformation is straightforward following [?] and [?] and thus omitted here. Let us denote the above transformations as

$$\tilde{\rho}_f = \mathcal{T}_f[w_f, w_c], \quad (13.60)$$

$$\tilde{\rho}_c = \mathcal{T}_c[w_f, w_c]. \quad (13.61)$$

At the moving interface, we have

$$w_f(l(t), t) = \tilde{\rho}_f(l(t), t) - K_f X(t), \quad (13.62)$$

$$w_c(l(t), t) = \tilde{\rho}_c(l(t), t) - K_c X(t). \quad (13.63)$$

We take temporal and spatial derivative on both sides of (13.54), (13.55) and substitute into the PDE-ODE original system (13.25)–(13.29). With the designed bilateral boundary controllers U_{in} and U_{out} introduced later, we obtain the target system satisfied by $w_f(x, t)$ and $w_c(x, t)$,

$$\partial_t w_f + u \partial_x w_f = \frac{K_f b}{u} \dot{l}(t)(g(t) + 2\epsilon_c(x, t)), \quad x \in [0, l(t)], \quad (13.64)$$

$$\partial_t w_c - u \partial_x w_c = \frac{K_c b}{u} \dot{l}(t)(g(t) - 2\epsilon_f(x, t)), \quad x \in [l(t), L], \quad (13.65)$$

$$w_f(0, t) = 0, \quad (13.66)$$

$$w_c(L, t) = 0, \quad (13.67)$$

$$\dot{X}(t) = -aX(t) - b(w_c(l(t), t) + w_f(l(t), t)), \quad (13.68)$$

where (13.66), (13.67) are the controlled boundaries and the constant coefficient

$$a = b(K_f + K_c) > 0, \quad (13.69)$$

is obtained by substituting (13.62), (13.63) into (13.29), given $b, K_f, K_c > 0$. The time-varying term $g(t)$ is defined as

$$g(t) = (K_f - K_c)X(t) + w_f(l(t), t) - w_c(l(t), t), \quad (13.70)$$

and the space and time-varying terms $\epsilon_c(x, t)$ and $\epsilon_f(x, t)$ are given by

$$\epsilon_c(x, t) = \tilde{\rho}_c(2l(t) - x, t) = \mathcal{T}_c[w_f, w_c](2l(t) - x, t), \quad (13.71)$$

$$\epsilon_f(x, t) = \tilde{\rho}_f(2l(t) - x, t) = \mathcal{T}_f[w_f, w_c](2l(t) - x, t). \quad (13.72)$$

We assume that densities outside freeway segment $[0, L]$ are at steady-states, therefore $\tilde{\rho}_c(2l(t) - x, t) = 0$ when $2l(t) - x > L$, and $\tilde{\rho}_f(2l(t) - x, t) = 0$ when $2l(t) - x < 0$. Hence, the followings hold for $\epsilon_f(x, t)$ and $\epsilon_c(x, t)$,

$$(13.74)$$

$$\epsilon_f(x, t) = 0, \quad l(t) \in (0, L/2) \text{ and } x \in [2l(t), L], \quad \epsilon_c(x, t) = 0, \quad l(t) \in (L/2,$$

Otherwise, $\epsilon_f(x, t)$ and $\epsilon_c(x, t)$ are given by expressions in (13.71) and (13.72). The bilateral state feedback boundary actuations for inlet and outlet of the segment are derived from (13.54), (13.55) and (13.66), (13.67) as

$$U_{\text{in}}(t) = K_f \left(X(t) - \frac{b}{u} \int_0^{l(t)} \tilde{\rho}_f(\xi, t) d\xi - \frac{b}{u} \int_{l(t)}^{\min\{L, 2l(t)\}} \tilde{\rho}_c(\xi, t) d\xi \right), \quad (13.75)$$

$$U_{\text{out}}(t) = K_c \left(X(t) - \frac{b}{u} \int_{l(t)}^L \tilde{\rho}_c(\xi, t) d\xi - \frac{b}{u} \int_{\max\{0, 2l(t)-L\}}^{l(t)} \tilde{\rho}_f(\xi, t) d\xi \right). \quad (13.76)$$

We obtain two pairs of controller designs for $l(t) \in [0, \frac{L}{2}]$ and $l(t) \in [\frac{L}{2}, L]$, respectively. When $l(t) \in [0, \frac{L}{2}]$, it holds that

$$\min\{L, 2l(t)\} = 2l(t), \max\{0, 2l(t) - L\} = 0, \quad (13.77)$$

and when $l(t) \in [\frac{L}{2}, L]$ one gets

$$\min\{L, 2l(t)\} = L, \max\{0, 2l(t) - L\} = 2l(t) - L. \quad (13.78)$$

In addition, when $l(t) = \frac{L}{2}$, controller integral forms become identical for $l(t) \in [0, \frac{L}{2}]$ and $l(t) \in [\frac{L}{2}, L]$:

$$U_{\text{in}}(t) = K_f \left(X(t) - \frac{b}{u} \int_0^{\frac{L}{2}} \tilde{\rho}_f(\xi, t) d\xi - \frac{b}{u} \int_{\frac{L}{2}}^L \tilde{\rho}_c(\xi, t) d\xi \right) \quad (13.79)$$

$$U_{\text{out}}(t) = K_c \left(X(t) - \frac{b}{u} \int_0^{\frac{L}{2}} \tilde{\rho}_f(\xi, t) d\xi - \frac{b}{u} \int_{\frac{L}{2}}^L \tilde{\rho}_c(\xi, t) d\xi \right). \quad (13.80)$$

The bilateral control input continuously switches between the above control laws when the moving interface position passes through the middle of the freeway segment.

Due to the invertibility of the transformation in (13.54), (13.55), stability of the target system $(w_c(x, t), w_f(x, t), X(t))$ and stability the plant $(\tilde{\rho}_f(x, t), \tilde{\rho}_c(x, t), X(t))$ are equivalent. In the next section, we apply Lyapunov analysis to prove the stability of the target system. Define the H^1 -norm $\|f(\cdot, t)\|_{H^1_{(a,b)}}$ as

$$\|f(\cdot, t)\|_{H^1_{(a,b)}} = \sqrt{\int_a^b f^2(x, t) + f_x^2(x, t) dx}. \quad (13.81)$$

We now state the main result of the chapter.

Theorem 13.1 *Consider a closed-loop system consisting of the PDE-ODE system (13.25)–(13.29) and the bilateral full-state feedback control laws for the inlet and the outlet (13.75), (13.76). For any system reference $(\rho_f^*, \rho_c^*, l^*) \in H^1((0, l^*); \mathbb{R}) \times H^1((l^*, L); \mathbb{R}) \times (0, L)$ which satisfies conditions (13.19), (13.20) and (13.22), and for any given $L > 0$, there exist $c > 0$, $\gamma > 0$, $\zeta > 0$ such that if the initial conditions of the system $(\rho_f(x, 0), \rho_c(x, 0), l(0))$ satisfy $Z(0) < \zeta$, local exponential stability with an arbitrary fast convergence rate of the closed-loop system with bilateral control laws holds $\forall t \in [0, \infty)$, namely,*

$$Z(t) \leq c e^{-\gamma t} Z(0), \quad (13.82)$$

where $Z(t)$ is defined as

$$Z(t) = \|\rho_f(x, t) - \rho_f^*\|_{H^1_{[0, l(t)]}} + \|\rho_c(x, t) - \rho_c^*\|_{H^1_{[l(t), L]}} + |l(t) - l^*|^2, \quad (13.83)$$

and conditions (13.31), (13.51) are satisfied for model validity.

13.5 Lyapunov Analysis

In the proof, local stability of the closed-loop system in the H^1 sense is shown with Lyapunov analysis and the conditions (13.31), (13.51) are guaranteed by our control design. The proof of Theorem 13.1 is established through following steps: we first prove the local stability of the target system (13.64)–(13.68) given time interval $\forall t \in [0, t^*)$ under the assumption that conditions (13.31), (13.51) are satisfied. Then we prove that with the initial conditions of states variables bounded, the local exponential stability of the above target system holds for $\forall t \in [0, +\infty)$ with the assumption removed. This is achieved by comparison principle and contradiction proof in a lemma. In the end, the stability analysis of the target system yields the stability of original PDE-ODE system in (13.12)–(13.14).

Let us define the Lyapunov functional

$$V(t) = V_1(t) + V_2(t) + V_3(t) + V_4(t) + c_5 V_5(t), \quad (13.84)$$

where $\lambda > 0$ with the component Lyapunov functions

$$V_1(t) = \int_0^{l(t)} e^{-c_1 x} w_f^2(x, t) dx, \quad (13.85)$$

$$V_2(t) = \int_{l(t)}^L e^{c_2(x-L)} w_c^2(x, t) dx, \quad (13.86)$$

$$V_3(t) = \int_0^{l(t)} e^{-c_3 x} \partial_x w_f^2(x, t) dx, \quad (13.87)$$

$$V_4(t) = \int_{l(t)}^L e^{c_4(x-L)} \partial_x w_c^2(x, t) dx, \quad (13.88)$$

$$V_5(t) = X(t)^2. \quad (13.89)$$

Lemma 13.1 Assume $\exists t^* > 0$ such that for all $t \in [0, t^*]$ the conditions (13.31), (13.51) are satisfied, then there exists $\sigma > 0$ such that the following holds $\forall t \in [0, t^*]$,

$$\dot{V}(t) \leq -\sigma V + \tau V^{3/2} + \theta V^2. \quad (13.90)$$

Proof Taking time derivative of the Lyapunov function (13.84) along the solution of the target system (13.64)–(13.68) and using the inequality (13.51), we have

$$\begin{aligned}
\dot{V}_1(t) = & -c_1 u \int_0^{l(t)} e^{-c_1 x} w_f^2(x, t) dx \\
& + \frac{2K_f b}{u} \dot{l}(t) g(t) \int_0^{l(t)} e^{-c_1 x} w_f(x, t) dx \\
& + \frac{4K_f b}{u} \dot{l}(t) \int_0^{l(t)} e^{-c_1 x} \epsilon_c(x, t) w_f(x, t) dx,
\end{aligned} \tag{13.91}$$

$$\begin{aligned}
\dot{V}_2(t) = & -c_2 u \int_{l(t)}^L e^{c_2(x-L)} w_c^2(x, t) dx \\
& + \frac{2K_c b}{u} \dot{l}(t) g(t) \int_{l(t)}^L e^{c_2(x-L)} w_c(x, t) dx \\
& - \frac{4K_c b}{u} \dot{l}(t) \int_{l(t)}^L e^{c_2(x-L)} \epsilon_f(x, t) w_c(x, t) dx,
\end{aligned} \tag{13.92}$$

$$\begin{aligned}
\dot{V}_3(t) = & -c_3 u \int_0^{l(t)} e^{-c_3 x} \partial_x w_f^2(x, t) dx + u \partial_x w_f^2(0, t) \\
& + \frac{4K_f b}{u} \dot{l}(t) \int_0^{l(t)} e^{-c_3 x} \partial_x \epsilon_c(x, t) \partial_x w_f(x, t) dx,
\end{aligned} \tag{13.93}$$

$$\begin{aligned}
\dot{V}_4(t) = & -c_4 u \int_{l(t)}^L e^{c_4(x-L)} \partial_x w_c^2(x, t) dx + u \partial_x w_c^2(L, t) \\
& - \frac{4K_c b}{u} \dot{l}(t) \int_{l(t)}^L e^{c_4(x-L)} \partial_x \epsilon_c(x, t) \partial_x w_c(x, t) dx,
\end{aligned} \tag{13.94}$$

$$\dot{V}_5(t) = -2aX(t)^2 - 2b(w_c(l(t), t) + w_f(l(t), t))X(t). \tag{13.95}$$

Using the boundary conditions (13.66)(13.67), Agmon's inequality, Young's inequality and Poincaré inequality, we obtain the following

$$w_f^2(l(t), t) \leq \|w_f\|_\infty^2 \leq 4\|\partial_x w_f\|_2^2 \leq 4e^{c_3 L} V_3, \tag{13.96}$$

$$w_c^2(l(t), t) \leq \|w_c\|_\infty^2 \leq 4\|\partial_x w_c\|_2^2 \leq 4e^{c_4 L} V_4. \tag{13.97}$$

Plugging the above inequalities into the ODE (13.68) yields that there exists $\delta > 0$ such that

$$\begin{aligned}
|\dot{l}(t)| & \leq a\sqrt{V_5} + 2b(\sqrt{e^{c_3 L} V_3} + \sqrt{e^{c_4 L} V_4}) \\
& \leq \delta\sqrt{V}.
\end{aligned} \tag{13.98}$$

Using Young's inequality, Cauchy-Schwarz inequality for (13.70) and (13.96), (13.97), there exists $\mu > 0$,

$$\begin{aligned}
g(t)^2 & \leq 2((K_f - K_c)^2 V_5 + 4e^{c_3 L} V_3 + 4e^{c_4 L} V_4) \\
& \leq \mu V,
\end{aligned} \tag{13.99}$$

By definition of $\epsilon_c(x, t)$ in (13.71), there exist $\eta > 0$, such that

$$\int_0^{l(t)} \epsilon_c^2(x, t) dx \leq \eta V. \quad (13.100)$$

It follows that

$$\begin{aligned} \dot{V}_1(t) \leq & -c_1 u V_1 + \frac{2K_f b}{u} |\dot{l}(t)| \left(g^2(t) + \int_0^{l(t)} w_f^2(x, t) dx \right) \\ & + \frac{4K_f b}{u} |\dot{l}(t)| \left(\int_0^{l(t)} \epsilon_c^2(x, t) dx + \int_0^{l(t)} w_f^2(x, t) dx \right). \end{aligned} \quad (13.101)$$

Plugging (13.99) and (13.100) into the above inequality, there exists $\kappa_1 > 0$ such that

$$\dot{V}_1(t) \leq -c_1 u V_1 + \kappa_1 V^{3/2}. \quad (13.102)$$

Taking total time derivative of boundary condition (13.66) yields,

$$\partial_x w_f(0, t) = \frac{K_f b}{u^2} \dot{l}(t) (g(t) + 2\epsilon_c(0, t)), \quad (13.103)$$

where it holds that $\epsilon_c(0, t) = 0$, according to the definition (13.4). Given the definition of $\epsilon_c(x, t)$ in (13.71), there exists $\nu > 0$ such that

$$\int_0^{l(t)} \partial_x \epsilon_c^2(x, t) dx \leq \nu V. \quad (13.104)$$

Using Young's inequality and plugging (13.98), (13.99) into (13.103), we obtain that there exists $\theta_1 > 0$ such that

$$\begin{aligned} \partial_x w_f^2(0, t) & \leq \frac{K_c^2 b^2}{u^4} |\dot{l}(t)|^2 g^2(t) \\ & \leq \theta_1 V^2, \end{aligned} \quad (13.105)$$

Plugging (13.96), (13.98), (13.104) and (13.105) into (13.93), we obtain that there exists $\kappa_3 > 0$ such that

$$\dot{V}_3(t) \leq -u V_3 + \kappa_3 V^{3/2} + \theta_1 V^2. \quad (13.106)$$

In the same fashion, we could obtain that there exist $\kappa_2, \kappa_4 > 0$ and $\theta_2 > 0$ such that

$$\dot{V}_2(t) \leq -u V_2 + \kappa_2 V^{3/2}, \quad (13.107)$$

$$\dot{V}_4(t) \leq -u V_4 + \kappa_4 V^{3/2} + \theta_2 V^2. \quad (13.108)$$

For the last Lyapunov component, the following holds

$$\dot{V}_5(t) \leq -\left(2a - \frac{a}{2} - \frac{a}{2}\right) V_5 + \frac{8e^{c_3 L} b^2}{a} V_3 + \frac{8e^{c_4 L} b^2}{a} V_4. \quad (13.109)$$

Substituting inequalities (13.102) and (13.106)–(13.109) into (13.84), it follows that

$$\begin{aligned}\dot{V}(t) \leq & -c_1 u V_1 - c_2 u V_2 - \left(c_3 u - c_5 \frac{8e^{c_3 L} b^2}{a} \right) V_3 \\ & - \left(c_4 u - c_5 \frac{8e^{c_4 L} b^2}{a} \right) V_4 - c_5 a V_5 + \tau V^{3/2} + \theta V^2.\end{aligned}\quad (13.110)$$

where $\tau = \kappa_1 + \kappa_2 + \kappa_3 + \kappa_4 > 0$ and $\theta = \theta_1 + \theta_2$. We choose

$$c_5 = \min \left\{ \frac{c_3 a u}{16b^2} e^{-c_3 L}, \frac{c_4 a u}{16b^2} e^{-c_4 L} \right\}, \quad (13.111)$$

such that

$$\dot{V}(t) \leq -\sigma V + \tau V^{3/2} + \theta V^2. \quad (13.112)$$

holds for

$$\sigma = \min \left\{ c_1 u, c_2 u, \frac{c_3 u}{2}, \frac{c_4 u}{2}, a \right\}. \quad (13.113)$$

Lemma 13.2 *For any function V that satisfies (13.90) and $V(0) < \delta_0$, where $\delta_0 = \frac{-\tau + \sqrt{\tau^2 + 2\sigma\theta}}{2\theta}$, it holds that*

$$\dot{V}(t) \leq -\frac{\sigma}{2} V. \quad (13.114)$$

By comparison principle, the following estimate holds for all $t \in [0, t^*)$:

$$V(t) \leq V(0) e^{-\frac{\sigma}{2} t} < \delta_0. \quad (13.115)$$

Recalling that $a = b(K_f + K_c)$, the control gains K_f and K_c and the coefficients $c_i, i = 1, 2, 3, 4$ can be chosen arbitrarily large such that an arbitrarily fast convergence rate $\frac{\sigma}{2}$ could be achieved, namely, rapid stabilization is achieved for the closed-loop system.

Lemma 13.3 *If the initial conditions of the target system ($w_f(x, 0), w_c(x, 0), X(0)$) satisfy*

$$V(0) < \min\{\delta_0, \delta_1, \delta_2\}, \quad (13.116)$$

where the positive constant δ_1 and δ_2 are defined as

$$\delta_1 = \min \left\{ (L - l^*)^2, (l^*)^2 \right\}, \quad \delta_2 = \frac{u^2}{\delta^2}, \quad (13.117)$$

the Lyapunov inequality (13.114) and conditions (13.31), (13.51) hold for all $t \in [0, \infty)$.

Proof We assume that there exists $t^* > 0$ such that condition (13.31) is satisfied for $t \in [0, t^*)$ but is violated at $t = t^*$. Given (13.116) and by comparison principle, the following inequality holds

$$V(t^\star) \leq V(0) < \delta_1. \quad (13.118)$$

According to the definition of $V(t)$ in (13.84), we obtain that $X^2(t^\star) \leq V(t^\star)$. Combining (13.117) and (13.118), we have

$$X^2(t^\star) < \delta_1 = \min \{(L - l^\star)^2, (l^\star)^2\}. \quad (13.119)$$

Since $l(t^\star) = X(t^\star) + l^\star$ and $0 < l^\star < L$, we obtain from (13.119) that

$$0 < l(t^\star) < L. \quad (13.120)$$

We conclude that (13.120) contradicts the assumption that (13.31) is violated at $t = t^\star$. Therefore, the condition (13.31) is guaranteed for $t \in [0, \infty)$ when the initial condition $V(0)$ satisfies (13.116). By inequality (13.98), we have

$$|\dot{l}(t^\star)|^2 \leq \delta^2 V(t^\star). \quad (13.121)$$

Given (13.116), it holds that

$$V(t^\star) \leq V(0) < \frac{u^2}{\delta^2}. \quad (13.122)$$

Thus we have

$$|\dot{l}(t^\star)|^2 < u^2, \quad (13.123)$$

and it follows that

$$-u < \dot{l}(t) < u. \quad (13.124)$$

This completes the proof Lemma 13.3. \square

Due to invertibility of the transformation in (13.54), (13.55), we conclude that the system (13.25)–(13.29) with control laws (13.75), (13.76) is locally exponentially stable in the H^1 norm, which completes the proof of Theorem 13.1.

13.6 Numerical Simulation

We simulate the proposed control design considering a moving traffic shockwave in a 500-meter freeway segment. The maximum velocity is $v_m = 144$ km/hr and maximum density is $\rho_m = 160$ vehs/km. The initial traffic profile and the desirable target traffic profile $\rho_f^\star = 32$ vehs/km, $\rho_c^\star = 128$ vehs/km, $l^\star = 0.2$ km, $\rho_{\text{jump}} = 80$ vehs/km are shown in Fig. 13.4, where the position of the shockwave front is initially located at 330-meter and the final setpoint location is at 200-meter, as shown in Fig. 13.3. The initial position of the shockwave front is in the right-half plane of the segment while its final position is located at the left-half plane. The control objective

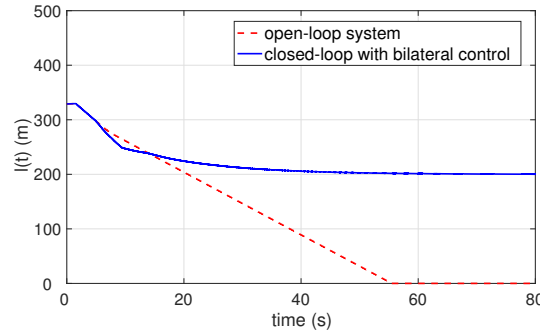


Fig. 13.3 Evolution of the moving interface position $l(t)$ for open-loop system and for closed-loop system with bilateral boundary control.

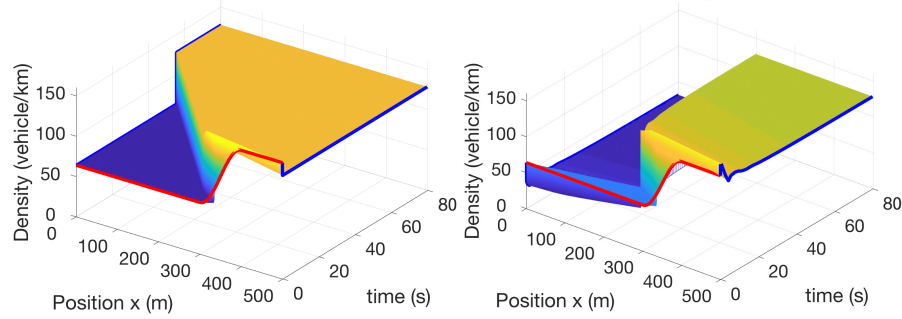


Fig. 13.4 Evolution of traffic density PDE states for the open-loop system on left and for the closed-loop system on right. Traffic density profile for initial condition with a soft shockwave is highlighted with color red and the target profile is that there is a shock steady-state located at $x = 200$ m where its upstream is free and its downstream congested, shown on the right after 50s.

is to regulate PDE states and ODE state from the initial profile to the reference profile, as shown in Fig. 13.4. After around 50s, the moving interface position stops at the setpoint location $l = 200$ m with bilateral control while in open-loop system it propagates upstream and travels out of the freeway segment before 1 min in Fig. 13.3. In Fig. 13.4, PDE density states of the whole segment becomes congested in the open-loop system while the upstream traffic remains to be free in the closed-loop system. In Fig. 13.5, one can observe that the bilateral control signals also converge to zeros after around 50s. In addition, total travel time (TTT) is defined in [?] as

$$\text{TTT} = \int_0^{t_{\text{sim}}} \int_0^L \rho(x, t) dx dt, \quad (13.125)$$

where $t_{\text{sim}} = 80$ s. The closed-loop system reduces the total travel time by 12%, compared with the open-loop.

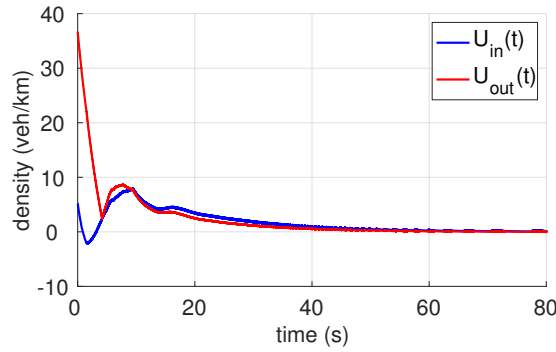


Fig. 13.5 Evolution of bilateral control inputs over time.

13.7 Notes and References

This chapter addresses boundary feedback control problem of moving shockwave in congested traffic described by a PDE-ODE-PDE system. To stabilize the coupled system to a desired setpoint, we use the predictor-based backstepping method to transform the state-dependent PDE-ODE-PDE coupled system to a target system, where the PDE state-dependent input delays to ODE are compensated by the bilateral boundary control inputs to PDEs. Actuation of traffic densities at both boundaries is considered. The local exponential stability in H^1 norm with an arbitrarily fast convergence rate is achieved.

Boundary control of PDE with state-dependent boundary locations governed by ODE systems has been intensively studied over the past few years. Backstepping control design method is used in solving these problems. In parabolic PDE system, the problem is known as the Stefan problem with application to control of screw extruders for 3D printing, laser sintering, and arctic sea ice temperature estimation [?]. For hyperbolic PDE systems, theoretical results and general designs are available in [?, ?, ?, ?]. On the side of applications, [?] develops a boundary control law for the piston position in inviscid gas, vibration suppression of mining cable elevators [?], control of Saint-Venant equation with hydraulic jumps [?].

Using Lyapunov analysis, [?] achieves exponential stability in the H^2 norm of a shock steady-state for the inviscid Burgers equation by choosing appropriate feedback boundary conditions. However, the proposed method in [?] cannot be directly applied to the traffic shockwave problem due to the constraint on boundary feedback coefficients.

Chapter 14

Extremum Seeking of Downstream Bottleneck

14.1 Bottleneck: Unknown Fundamental Diagram and Maximizing the Flow

Up to this point, this book has been entirely dedicated to PDE backstepping-based control and estimation of traffic flows. Even Chapter 7, which deals with the use of reinforcement learning for control of traffic, was focused essentially on learning the PDE backstepping algorithm through hundreds of simulation training tests on the ARZ PDE model.

This chapter is different. It differs from the rest of the book both in terms of the objective and in terms of the method. This chapter's goal is not stabilization, i.e., suppression of stop-and-go oscillations. The goal of the chapter is optimization—the maximization of the traffic flow through a bottleneck.

More importantly, the chapter differs from the rest of the book methodologically. Rather than being an application of PDE backstepping, this is the book's sole chapter that employs the method of *extremum seeking* (ES). More about ES in Section 14.6.

In terms of modeling, the chapter differs from most of the book's other chapters, which employ the ARZ second-order model and is comparable with the previous chapter, Chapter 13, where the traffic is modeled using the LWR first-order model.

This chapter deals with traffic through a *bottleneck*. We discuss the bottleneck phenomenon in more precise terms shortly but it is worth recalling, even if one has no background in traffic dynamics or modeling, of some examples of bottlenecks: segments of the freeway that are constricted either due to road work, a traffic accident, or for other reasons.

When a bottleneck forms, obviously the flow passing through the bottleneck gets reduced and congestion may form upstream of the bottleneck. The stop-and-go dynamics that may ensue due to congestion are not our focus. Our focus is on the fact that the traffic through a bottleneck operates in accordance with its own fundamental diagram, distinct from the unconstricted road.

It is clear that drivers are more risk averse through a segment of the road that has narrowed and that their speed-versus-density relationship will be different (the speed

will be lower, for a given density, though a bottleneck than on the unconstricted road). To see this clearly it is worth recalling that a bottleneck forms as a result of capacity drop which, in turn, can be caused by lane-drop, hills, tunnel, bridge or curvature on the road—resulting in a wide variety of speed-versus-density dependencies.

The fundamental diagram of the bottleneck has its own peak flow, distinct from the rest of the road, and this peak flow is the desirable, optimal flow on the entire road upstream of the bottleneck.

The peak flow through the bottleneck is achieved for a particular maximizing value of traffic density through the bottleneck. Higher or lower density than the maximizing density will result in suboptimal flow through the bottleneck. If the incoming density into the bottleneck is not reduced, inundating the bottleneck with vehicles will result in the flow being lower than if some of the vehicles are held back from arriving at the bottleneck.

While a model of traffic on a given road can be obtained and calibrated after enough observation, a bottleneck cannot be modeled a priori. Neither its width nor length are known, much less its location. Hence, control of traffic through a bottleneck has to be performed for a highly uncertain, or completely unknown, fundamental diagram.

This makes the control of traffic through a bottleneck an optimization problem that needs to be performed online, in a model-free fashion. And it is for this reason that we employ extremum seeking for this problem.

But how can flow through a bottleneck be actuated? To answer this question, let us first imagine that a bottleneck has formed immediately downstream of a ramp, i.e., that the bottleneck is collocated with a ramp actuated with ramp metering. The probability of this happening is zero. But let us first entertain the possibility that the traffic engineer is lucky enough that the bottleneck takes place immediately after the ramp. The problem of maximizing the flow would through the bottleneck is then just a static problem. One simply needs to search in real time, by modulation of the incoming flow using ramp metering, for the optimal density at the entry to the bottleneck.

In most situations, however, the bottleneck is some distance downstream from ramp metering. It is such a ramp metering input that we employ for maximizing the flow through a bottleneck that is located downstream of the actuated ramp.

Once the ramp metering input and the bottleneck are separated by a stretch of freeway, especially a stretch of freeway of significant length (on the order of hundreds of meters or more), the problem of flow maximization through the bottleneck turns from a static optimization problem to a problem of optimization for a dynamical system (the traffic flow) with an unknown output map (the bottleneck fundamental diagram).

As we recall, particularly from Chapter 13, the dynamics of traffic density on the freeway segment can be described with the LWR macroscopic PDE model. This is the model of the traffic dynamics that we adopt for the freeway stretch between the actuated ramp and the bottleneck.

Our goal is both to maximize the flow through the bottleneck and to keep the flow upstream of the bottleneck from getting congested. Assuming we are successful

with the latter goal, the wave of the LWR model will be flowing in the downstream direction. Hence, the fluctuations that we apply at the ramp metering input will be reaching the bottleneck after some time.

As we have already learned in Chapter 13, the linearized LWR model acts as the linear transport PDE, i.e., as a pure delay. So, for small variations around the traffic flow equilibrium, the problem at hand is the problem of seeking the extremum (maximum) of the fundamental diagram in the presence of an input delay (the linearized LWR dynamics in the free regime).

This is a realization of great significance since, while performing ES in the presence of a large delay at the unknown map is difficult, this problem is actually tractable using an approach that the second author and his collaborators developed in [?].

We apply ES control, a non-model based real-time adaptive control technique, in order to find the unknown optimal density at the bottleneck. The delay effect of the upstream traffic needs to be compensated in designing ES control. The input delay is normally compensated using the predictor approach [?]. The predictor approach is a model-based approach in which the future state of the system is represented, using the past inputs, as a solution map with the current state as the initial condition. Then this predicted future state can be employed in a control design for the delay-free case since the predicted state, applied through the delay-free control law, will reach the plant as the current state, at the time the input reaches the plant, and the delay will be compensated. For linear systems, the representation of the future state using the current state can be done explicitly, using the variation of constants formula. The predictor-based approach is based on PDE backstepping, with which the first proof of stability of predictor feedback was provided.

Due to its model-based nature of the predictor feedback, this approach is not immediately compatible with extremum seeking, in which a part of the model—the fundamental diagram in the case of traffic—is unknown. Special modifications of the ES algorithm are invented in [?] to perform a perturbation-based estimation of the gradient and the Hessian of the unknown map so that predictor feedback can be employed. It is those tools that we employ here, to estimate the gradient of the fundamental diagram and to drive to zero, thereby achieving maximum flow.

Before we begin our presentation, it is important to develop an appreciation for the effect that the difference between the fundamental diagrams between the bottleneck and the freeway have on the problem of delay-compensated online optimization by ES. The fundamental diagram through the bottleneck has a lower peak flow and the peak flow occurs for a lower density through the bottleneck than the density that maximizes the flow through the freeway. This relationship between the two maximizing densities—for the bottleneck flow and for the freeway flows—are crucial. Since, at the maximizing density for the bottleneck flow, the freeway density is below its critical value, the flow through the freeway is in the downstream direction, at positive speed. If the maximizing/critical densities of the bottleneck and freeway were the same, if we were to want to maximize the flow through the bottleneck, we would need to have the freeway operate at the critical density. At the critical density, where the fundamental diagram is at its peak, and the slope of the diagram

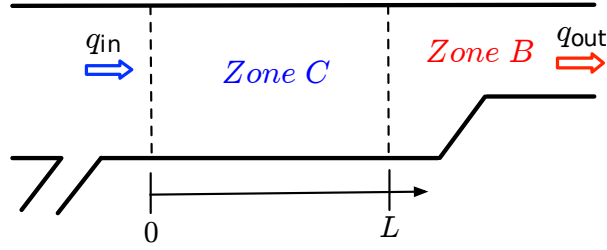


Fig. 14.1 Traffic on a freeway segment with lane-drop

is zero, the wave speed of the linearized LWR model would be zero. As a result, the delay from the ramp to the bottleneck would be infinite and we would not be able to compensate the delay or even to perturb the density at the bottleneck for the sake of ES-based optimization. Hence, it is fortunate that, at the maximal flow through the bottleneck, the density dynamics leading to the bottleneck are controllable and, thus, the maximal flow through the bottleneck is attainable by feedback.

14.2 Lane-Drop Bottleneck Control Problem

We consider a traffic congestion problem on a freeway-segment with lane drop bottleneck downstream of the segment. The freeway segment upstream of the bottleneck and the lane-drop area are shown in Fig. 14.1 which illustrates the clear “Zone C” and the bottleneck “Zone B”, respectively. The flow is conserved through the clear Zone C to the bottleneck Zone B. The local road capacity is changed due to the lane-drop in Zone B which could be caused by road work, accidents, or lane closure. Due to the reduction of lanes in Zone B, the fundamental diagram for the flow and density relation usually changes, which leads to a capacity drop in Zone B. To prevent the traffic in Zone B from overflowing its capacity and then causing congestion in the freeway segment, we aim to find the optimal density ahead of Zone C which maximizes the outgoing flow of Zone B given unknown density-flow relation.

The traffic dynamics in Zone C upstream of Zone B is described with the first-order, hyperbolic LWR model. Traffic density $\rho(x, t)$ in Zone C is governed by the following nonlinear hyperbolic PDE, where $x \in [0, L]$, $t \in [0, \infty)$,

$$\partial_t \rho + \partial_x (Q_C(\rho)) = 0. \quad (14.1)$$

The fundamental diagram of traffic flow and density function $Q_C(\rho)$ is given by

$$Q_C(\rho) = \rho V(\rho), \quad (14.2)$$

where traffic velocity follows an equilibrium velocity-density relation $V(\rho)$ of the Greenshield’s model, given by

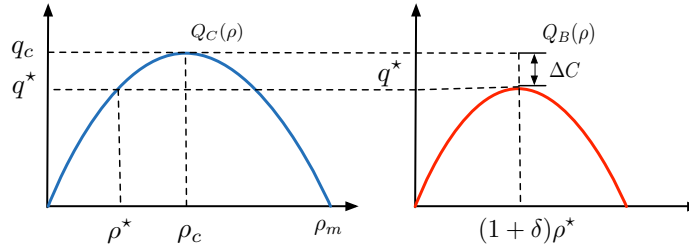


Fig. 14.2 Quadratic fundamental diagram for the clear Zone C and the bottleneck Zone B

$$V(\rho) = v_m \left(1 - \frac{\rho}{\rho_m}\right), \quad (14.3)$$

where $v_m \in \mathbb{R}^+$ is defined as maximum velocity and $\rho_m \in \mathbb{R}^+$ is maximum density for Zone C. Then the fundamental diagram of flow and density function $Q_C(\rho)$ is in a quadratic form of density,

$$Q_C(\rho) = -\frac{v_m}{\rho_m} \rho^2 + v_m \rho. \quad (14.4)$$

A critical value of density segregates the traffic into the free flow regime whose density is smaller than the critical value and the congested regime whose density is greater than the critical value. The critical density is

$$\rho_c = \rho_m/2. \quad (14.5)$$

for the fundamental diagram in (14.4).

In practice, the quadratic fundamental diagram sometimes does not fit well with traffic density-flow field data. The critical density usually appears at 20% of the maximum value of the density [?]. The following assumption is made for the nonlinear fundamental diagram. According to Taylor expansion, second-order differentiable nonlinear function can be approximated as a quadratic function in the neighborhood of its extremum. The stability results derived in this chapter holds locally for the general form of fundamental diagram $Q(\rho)$ that satisfies the following assumption. Here we can adopt other density-flow relations for the fundamental diagram $Q(\rho)$ but require Assumption 14.2 to be satisfied.

The fundamental diagram $Q(\rho)$ is a smooth function, and it holds that $Q'(\rho_c) = 0$, $Q''(\rho_c) < 0$.

Under Assumption 14.2, the fundamental diagram can be approximated around the critical density ρ_c as follows:

$$Q(\rho(t)) = q_c + \frac{Q''(\rho_c)}{2} (\rho(t) - \rho_c)^2, \quad (14.6)$$

where $q_c = Q(\rho_c)$ is defined as the road capacity or maximum flow, with $Q''(\rho_c) < 0$.

Lane-drop bottleneck model

Due to the reduction of the number of the lanes from Zone C to Zone B, we consider the equilibrium density-flow relation of Zone B as shown in Fig. 14.2, as pointed out in [?]. There is a capacity drop ΔC of Q_B in Zone B compared to Q_C in Zone C after the congestion has formed upstream of the lane-drop area. The capacity drop caused by a sudden lane-drop is hard to measure in real-time and the traffic dynamics of Zone B are affected by the lane-changing and merging activities. Therefore we assume that the fundamental diagram $Q_B(\rho)$ of Zone B is unknown. In Fig. 14.2, the capacity is

$$\Delta C = Q_C(\rho_c) - Q_B((1 + \delta)\rho^*), \quad (14.7)$$

$$q^* = Q_C(\rho^*) = Q_B((1 + \delta)\rho^*), \quad (14.8)$$

where ΔC is unknown. The quantity $\rho^* \in \mathbb{R}^+$ represents the optimal density that keeps Zone C in the free regime while $(1 + \delta)\rho^*$ reaches the critical density of Zone B so that the discharging flow rate reaches its maximum value $q^* \in \mathbb{R}^+$. The ratio δ accounts for the density discontinuity before the outlet in Zone C and after the outlet in Zone B. We assume that ΔC and δ are unknown and therefore the optimal density and flow rate (ρ^*, q^*) are unknown.

When a lane-drop bottleneck occurs downstream, the density at the outlet of Zone C is $\rho(L, t)$ governed by the PDE in (14.1) for $x \in [0, L]$, $t \in [0, \infty)$. The inlet boundary flow is,

$$q_{\text{in}}(t) = Q_C(\rho(0, t)). \quad (14.9)$$

The output measurement of traffic flow in Zone B, $q_{\text{out}}(t)$ is given by $Q(\rho)$ with outlet density $\rho(L, t)$,

$$q_{\text{out}}(t) = Q(\rho(L, t)). \quad (14.10)$$

where the function $Q(\rho)$ of outlet boundary $x = L$ connecting Zone C and Zone B is defined as follows

$$Q(\rho(L, t)) = \begin{cases} Q_C(\rho(L, t)), & \rho(L, t) < \rho^*, \\ Q_C(\rho^*) = q^* = Q_B((1 + \delta)\rho^*), & \rho(L, t) = \rho^*, \\ Q_B((1 + \delta)\rho(L, t)), & \rho(L, t) > \rho^*, \end{cases} \quad (14.11)$$

so that the flow is conserved through the boundary, entering from Zone C to Zone B. When the optimal density ρ^* is reached, the flow rate at the outlet of Zone C and the input of Zone B reaches the equilibrium and its maximum value q^* .

The control objective is to design the traffic flow input $q_{\text{in}}(t)$ so that the outgoing flow in lane-drop area Zone B $q_{\text{out}}(t)$ is maximized. We aim to find the optimal outlet density $\rho(L, t) = \rho^*$ that maximizes $q_{\text{out}}(t)$ of Zone B and then, using the PDE that describes the dynamics of traffic in the Zone C, to obtain the desirable flow

input $q_{\text{in}}(t)$ from the inlet of Zone C. Here we assume that we approximate $q_{\text{out}}(t)$ with a function that satisfies Assumption 1 and $q_{\text{out}}(t)$ can be written as

$$q_{\text{out}}(t) = q^* + \frac{H}{2}(\rho(L, t) - \rho^*)^2, \quad (14.12)$$

where $H < 0$ is the unknown Hessian of the approximated static map $q_{\text{out}}(t)$.

We use a static fundamental diagram to model the traffic in the bottleneck Zone B. Therefore, the upstream propagating traffic waves from Zone B to Zone C cannot be captured by our model if Zone B is very congested. This result is focused on maximizing the discharging flow rate at the bottleneck area and the ES control seeks the optimal traffic density value in its neighborhood. In bottleneck Zone B, the closer the outlet traffic density $\rho(L, t)$ to the optimal value ρ^* where $Q'(\rho^*) = 0$ is satisfied, the lower the propagating characteristic speed of the traffic waves $Q'(\rho)$. Therefore, the spill-back traffic from Zone B to Zone C is negligible in our model.

In order to find the unknown optimal density at the bottleneck area, we design ES control for the unknown static map $Q(\rho)$ with actuation dynamics governed by a nonlinear hyperbolic PDE in (14.1). In the following section, we linearize the nonlinear PDE and the traffic dynamics are represented by the delay effect for the control input signal.

Linearized Reference Error System

We linearize the nonlinear LWR model around a constant reference density $\rho_r \in \mathbb{R}^+$, which is assumed to be close to the optimal density ρ^* . The reference density ρ_r is in the free regime of $Q(\rho)$ of Zone C thus is smaller than the critical density ρ_c and therefore the following is satisfied $\rho_r < \rho_c$. Define the reference error density as

$$\tilde{\rho}(x, t) = \rho(x, t) - \rho_r, \quad (14.13)$$

and reference flow q_r is $q_r = Q(\rho_r) > 0$. By the governing equation (14.1) together with (14.4), the linearized reference error model is derived as

$$\partial_t \tilde{\rho}(x, t) + u \partial_x \tilde{\rho}(x, t) = 0, \quad (14.14)$$

$$\tilde{\rho}(0, t) = \rho(0, t) - \rho_r, \quad (14.15)$$

where the constant transport speed u is given by

$$u = Q'(\rho)|_{\rho=\rho_r} = V(\rho_r) + \rho_r V'(\rho)|_{\rho=\rho_r}. \quad (14.16)$$

The equilibrium velocity-density relation $V(\rho)$ is a strictly decreasing function. The reference density ρ_r is in the left-half plane of the fundamental diagram $Q_c(\rho)$ which yields the following inequality for the propagation speed u , $u > 0$. We define the input density as

$$\varrho(t) = \rho(0, t), \quad (14.17)$$

and the input variation at the inlet is

$$\tilde{\varrho}(t) = \varrho(t) - \rho_r. \quad (14.18)$$

The linearized error dynamics in (14.14), (14.15) is a transport PDE with an explicit solution for $t > \frac{x}{u}$ and thus is represented with input density

$$\tilde{\rho}(x, t) = \tilde{\varrho}\left(t - \frac{x}{u}\right). \quad (14.19)$$

The density variation at outlet is

$$\tilde{\rho}(L, t) = \tilde{\varrho}(t - D). \quad (14.20)$$

where the time delay

$$D = \frac{L}{u} \quad (14.21)$$

depends both on the transport speed u and on the distance L of the bottleneck from the ramp. Therefore, the density at the outlet is given by the delayed input density variation and the reference, namely, by

$$\rho(L, t) = \rho_r + \tilde{\rho}(L, t). \quad (14.22)$$

Finally, substituting (14.20), (14.22) into the static map (14.12), we arrive at the following

$$\begin{aligned} q_{\text{out}}(t) &= q^* + \frac{H}{2} (\tilde{\varrho}(t - D) + \rho_r - \rho^*)^2 \\ &= q^* + \frac{H}{2} (\varrho(t - D) - \rho^*)^2. \end{aligned} \quad (14.23)$$

The control objective is to regulate the input $q_{\text{in}}(t)$ so that $\varrho(t - D)$ reaches the unknown optimal ρ^* . In this fashion, the maximum of the uncertain quadratic flow-density map $q_{\text{out}}(t)$ is achieved. We can, therefore, apply the method of extremum seeking for static maps with delays, which was developed in [?], to find the maximum of the unknown fundamental diagram.

In practice, control of density at the inlet can be realized with a coordinated operation of ramp metering and a VSL at inlet [?]. The controlled density at inlet is implemented as

$$\varrho(t) = \frac{q_{\text{in}}(t)}{v_c}, \quad (14.24)$$

where v_c is the speed limit implemented by VSL and $q_{\text{in}}(t)$ is actuated by on-ramp metering upstream of the inlet. The linearized model is valid at the optimal density ρ^* since the reference density is assumed to be chosen near the optimal value.

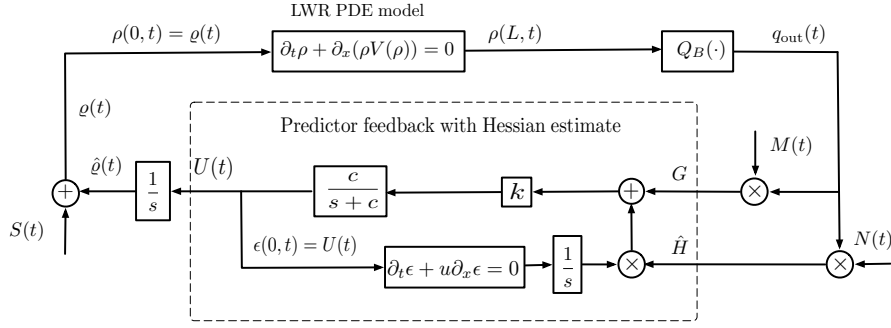


Fig. 14.3 Block diagram for implementation of ES control design for nonlinear LWR PDE model

14.3 Online Optimization by Extremum Seeking Control

In this section, we present the design of extremum seeking control with delay by following the procedure in [?]. The block diagram of the delay-compensated ES algorithm applied to LWR PDE model is depicted in Fig. 14.3. Let $\hat{\rho}(t)$ be the estimate of ρ^* , and $e(t)$ be the estimation error defined as

$$e(t) = \hat{\rho}(t) - \rho^*. \quad (14.25)$$

where $\hat{\rho}(t)$ is an integrator of the predictor-based feedback signal $U(t)$ as $\dot{\hat{\rho}}(t) = U(t)$. From Fig. 14.3, the error dynamics can be written as

$$\dot{e}(t - D) = U(t - D), \quad (14.26)$$

given the delayed estimation error dynamics modeled by $\epsilon(x, t) = U(t - \frac{x}{u})$. We introduce the dither signals $(M(t), N(t))$ given by

$$M(t) = \frac{2}{a} \sin(\omega t), \quad (14.27)$$

$$N(t) = -\frac{8}{a^2} \cos(2\omega t), \quad (14.28)$$

where a and ω are amplitude and frequency of a slow periodic perturbation signal $a \sin(\omega t)$ introduced later. Using the dither signals, we calculate the estimates of the gradient and Hessian of the cost function, denoted as $(G(t), \hat{H}(t))$, using the “demodulation” given by

$$G(t) = M(t)q_{out}(t), \quad (14.29)$$

$$\hat{H}(t) = N(t)q_{out}(t), \quad (14.30)$$

where $\hat{H}(t)$ is to estimate the unknown Hessian H . The averaging of $G(t)$ and $\hat{H}(t)$ yields

$$G_{\text{av}}(t) = H e_{\text{av}}(t - D), \quad \hat{H}_{\text{av}} = (Nq_{\text{out}})_{\text{av}} = H. \quad (14.31)$$

Taking the average of (14.26), we have

$$\dot{e}_{\text{av}}(t - D) = U_{\text{av}}(t - D), \quad (14.32)$$

where $U_{\text{av}}(t)$ is the averaged value for $U(t)$ designed later. Substituting the above equation into (14.31) gives

$$\dot{G}_{\text{av}}(t) = H U_{\text{av}}(t - D). \quad (14.33)$$

The motivation for predictor feedback design is to compensate for the delay by feeding back future states in the equivalent averaged system $G_{\text{extrmav}}(t + D)$. Given an arbitrary control gain $k > 0$, we aim to design

$$U_{\text{av}}(t) = k G_{\text{av}}(t + D), \quad \forall t \geq 0. \quad (14.34)$$

which requires knowledge of future states. Therefore we have the following by plugging (14.34) into (14.32),

$$\dot{e}_{\text{av}}(t) = U_{\text{av}}(t) = k H e_{\text{av}}(t), \quad \forall t \geq D. \quad (14.35)$$

Recalling that $k > 0, H < 0$, the equilibrium of the average system $e_{\text{av}}(t) = 0$ is exponentially stable. Applying the variation of constants formula

$$G_{\text{av}}(t + D) = G_{\text{av}}(t) + \hat{H}_{\text{av}}(t) \int_{t-D}^t U_{\text{av}}(\tau) d\tau \quad (14.36)$$

and, from (14.34), one has:

$$U_{\text{av}}(t) = k \left(G_{\text{av}}(t) + \hat{H}_{\text{av}}(t) \int_{t-D}^t U_{\text{av}}(\tau) d\tau \right), \quad (14.37)$$

which involves $G_{\text{av}}(t + D)$, the future version of the state governed by the system (14.33) in terms of the average control signal $U_{\text{av}}(\tau)$ for $\tau \in [t - D, t]$. The control input is infinite-dimensional due to its use of history over the past D time units.

For the stability analysis in which the averaging theorem for infinite-dimensional systems is used, we employ a low-pass filter for the above basic predictor feedback controller and then derive an infinite-dimensional and averaging-based predictor feedback given by

$$U(t) = \mathcal{T} \left\{ k \left(G(t) + \hat{H}(t) \int_{t-D}^t U(\tau) d\tau \right) \right\}, \quad (14.38)$$

where $k > 0$ is an arbitrary control gain and the Hessian estimate $\hat{H}(t)$ is updated according to (14.30), satisfying average property in (14.31). The operator $\mathcal{T}\{\cdot\}$ is a low-pass filter defined by

$$\mathcal{T} \{\varphi(t)\} = \mathcal{L}^{-1} \left\{ \frac{c}{s+c} \right\} * \varphi(t), \quad (14.39)$$

where $-c < 0$ is the filter's pole, \mathcal{L}^{-1} is the inverse Laplace transformation, and $*$ is the convolution in time.

Theorem 14.1 *Consider the closed-loop system in Fig. 14.3. There exists $c_0 > 0$ such that $\forall c \geq c_0$, there exists $\omega_0(c_0) > 0$ such that $\forall \omega > \omega_0$, the closed-loop system has a unique exponentially stable periodic solution of period $T = \frac{2\pi}{\omega}$, denoted by $e^T(t-D), U^T(\tau), \forall \tau \in [t-D, t]$, satisfying $\forall t > 0$*

$$\left(|e^T(t-D)|^2 + |U^T(t)|^2 + \int_0^D |U^T(\tau)|^2 d\tau \right)^{\frac{1}{2}} \leq O(1/\omega). \quad (14.40)$$

Furthermore,

$$\lim_{t \rightarrow +\infty} \sup |\varrho(t) - \rho^*| = O(a + 1/\omega), \quad (14.41)$$

$$\lim_{t \rightarrow +\infty} \sup |q_{out}(t) - q^*| = O(a^2 + 1/\omega^2). \quad (14.42)$$

The detailed proof of Theorem 14.1 is carried out in the next section.

14.4 Stability Analysis (Averaging, Backstepping, and Lyapunov)

First, we show the exponential stability of the average error-dynamics system using a backstepping transformation. Then the averaging theorem for infinite-dimensional systems [?] is invoked to show the exponential stability of the original error-dynamics system (14.48)–(14.50). Using Lyapunov analysis, we show the convergence of $(\varrho(t), q_{out}(t))$ to a neighborhood of the extremum (ρ^*, q^*) . The proof of Theorem 14.1 is carried out through the following steps.

Closed-Loop System

The estimate $\hat{\varrho}(t)$ of the unknown optimal outgoing ρ^* is an integrator of the predictor-based feedback signal $U(t)$, as represented by

$$\dot{\hat{\varrho}}(t) = U(t). \quad (14.43)$$

It then follows that

$$\dot{e}(t-D) = U(t-D). \quad (14.44)$$

The input $\varrho(t)$ to LWR PDE model is given by

$$\varrho(t) = \hat{\varrho}(t) + S(t), \quad (14.45)$$

where the dither signal $S(t)$ is the “predicted” (or time-advanced) version of the perturbation signal $a \sin(\omega t)$, which the input delay retards by D , and is therefore given by

$$S(t) = a \sin(\omega(t + D)). \quad (14.46)$$

Substituting $S(t)$ into (14.45), we have

$$\varrho(t) = \hat{\varrho}(t) + a \sin(\omega(t + D)). \quad (14.47)$$

The delayed estimation error dynamics can be written as transport PDE system, $x \in [0, L]$

$$\dot{\epsilon}(t - D) = \epsilon(L, t), \quad (14.48)$$

$$\partial_t \epsilon(x, t) = -u \partial_x \epsilon(x, t), \quad (14.49)$$

$$\epsilon(0, t) = U(t). \quad (14.50)$$

where it is straightforward to obtain that

$$\epsilon(x, t) = U\left(t - \frac{x}{u}\right). \quad (14.51)$$

Combining (14.23), (14.25), the relation among the estimation error $e(t)$, the input density $\varrho(t)$, and optimal outlet density ρ^* is given by

$$e(t) + a \sin(\omega t) = \varrho(t) - \rho^*, \quad (14.52)$$

Substituting the above relation into the output map in (14.23), we obtain the following equation

$$q_{\text{out}}(t) = \rho^* + \frac{H}{2} (e(t - D) + a \sin(\omega t))^2. \quad (14.53)$$

Plugging $M(t)$ and $G(t)$ into (14.30) and representing the delayed input with PDE state $\epsilon(x, t)$, we have

$$U(t) = \mathcal{T} \left\{ k \left(G(t) + \hat{H}(t) \int_0^L \epsilon(\tau, t) d\tau \right) \right\}, \quad (14.54)$$

$$G(t) = \frac{2}{a} \sin(\omega t) q_{\text{out}}(t), \quad (14.55)$$

$$\hat{H}(t) = -\frac{8}{a^2} \cos(2\omega t) q_{\text{out}}(t). \quad (14.56)$$

This is then written out explicitly as

$$U(t) = \mathcal{T} \left\{ k q_{\text{out}}(t) \left(\frac{2}{a} \sin(\omega t) - \frac{8}{a^2} \cos(2\omega t) \int_0^L \epsilon(\tau, t) d\tau \right) \right\}, \quad (14.57)$$

and, by substituting q_{out} with (14.53) and combining with transport PDE in (14.48)–(14.50), we write the closed-loop system as

$$\dot{e}(t - D) = \epsilon(L, t), \quad (14.58)$$

$$\partial_t \epsilon(x, t) = -u \partial_x \epsilon(x, t), \quad (14.59)$$

$$\begin{aligned} \epsilon(0, t) = \mathcal{T} \left\{ k \left(q^* + \frac{H}{2} (e(t - D) + a \sin(\omega t))^2 \right) \right. \\ \left. \times \left(\frac{2}{a} \sin(\omega t) - \frac{8}{a^2} \cos(2\omega t) \int_0^L \epsilon(\tau, t) d\tau \right) \right\}. \end{aligned} \quad (14.60)$$

Average System

Expanding (14.60) and taking average of the closed-loop system, we obtain the average model by recalling that the average of sine and cosine functions of $n\omega$, ($n = 1, 2, 3, 4$) is zero. The averaged controller satisfies

$$\dot{U}_{\text{av}}(t) + c U_{\text{av}}(t) = ck \left(G_{\text{av}}(t) + H \int_0^L \epsilon_{\text{av}}(\tau, t) d\tau \right), \quad (14.61)$$

where $c > 0$ is the corner frequency of the low pass filter and $k > 0$ is the control gain. Denoting

$$\theta(t) = e(t - D), \quad (14.62)$$

the average system of (14.58)–(14.60) is rewritten by

$$\dot{\theta}_{\text{av}}(t) = \epsilon_{\text{av}}(L, t), \quad (14.63)$$

$$\partial_t \epsilon_{\text{av}}(x, t) = -u \partial_x \epsilon_{\text{av}}(x, t), \quad (14.64)$$

$$\partial_t \epsilon_{\text{av}}(0, t) = -c \epsilon_{\text{av}}(0, t) + ckH \left(\theta_{\text{av}}(t) + \int_0^L \epsilon_{\text{av}}(\tau, t) d\tau \right). \quad (14.65)$$

Backstepping Transformation

We apply backstepping transformation for the averaged delay state

$$w(x, t) = \epsilon_{\text{av}}(x, t) - kH \left[\theta_{\text{av}}(t) + \int_x^L \epsilon_{\text{av}}(\tau, t) d\tau \right]. \quad (14.66)$$

where $k > 0$ and $H < 0$. The average system is mapped into the target system:

$$\dot{\theta}_{\text{av}}(t) = kH\theta_{\text{av}}(t) + w(L, t), \quad (14.67)$$

$$\partial_t w(x, t) = -u\partial_x w(x, t), \quad (14.68)$$

$$\begin{aligned} \partial_t w(0, t) = & -(c + kH)w(0, t) \\ & - (kH)^2 \left[e^{\frac{kHL}{u}} \theta_{\text{av}}(t) + \int_0^L e^{\frac{kH(L-\tau)}{u}} w(\tau, t) d\tau \right]. \end{aligned} \quad (14.69)$$

Combining (14.65) and (14.66), we have

$$w(0, t) = -\frac{1}{c} \partial_t \epsilon_{\text{av}}(0, t). \quad (14.70)$$

Taking time derivative on (14.66) for $w(0, t)$, we obtain

$$\partial_t w(0, t) = \partial_t \epsilon_{\text{av}}(0, t) - kH\epsilon_{\text{av}}(0, t). \quad (14.71)$$

The inverse transformation of (14.66) is given by

$$\epsilon_{\text{av}}(x, t) = w(x, t) + kH \left[e^{\frac{kH(L-x)}{u}} \theta_{\text{av}}(t) + \int_x^L e^{\frac{kH(L-x+\tau)}{u}} \epsilon_{\text{av}}(\tau, t) d\tau \right]. \quad (14.72)$$

Plugging (14.72) and (14.65) into (14.71), we obtain (14.69) in the target system.

Lyapunov Functional

Now consider the following Lyapunov functional for the target system,

$$V(t) = \frac{a\theta_{\text{av}}^2(t)}{2} + \int_0^L e^{-x} w^2(x, t) dx + \frac{1}{2} w^2(0, t), \quad (14.73)$$

where the parameter $a > 0$ is chosen later. Taking a time derivative of the Lyapunov function, we have

$$\begin{aligned} \dot{V}(t) \leq & akH\theta_{\text{av}}^2 + \frac{a}{2b} \theta_{\text{av}}^2 + \left(\frac{ab - ue^{-L}}{2} \right) w^2(L, t) \\ & - \frac{u}{2} \int_0^L e^{-x} w^2(x, t) dx + w(0, t) \left(w_t(0, t) + \frac{u}{2} w(0, t) \right), \end{aligned} \quad (14.74)$$

where the positive constant b is defined as

$$b = \frac{ue^{-L}}{a}, \quad (14.75)$$

so that

$$ab - ue^{-L} = 0. \quad (14.76)$$

The positive constant a is chosen as

$$a = -ukHe^{-L}. \quad (14.77)$$

Substituting $w_t(0, t)$ by (14.69) and using Young's, Cauchy-Schwarz inequalities, the last term in (14.74) is bounded by

$$\begin{aligned} & w(0, t) \left(w_t(0, t) + \frac{u}{2} w(0, t) \right) \\ & \leq - \left(c - \frac{u}{2} + kH \right) w^2(0, t) + \frac{e^L a^2}{4u} \theta_{\text{av}}^2(t) + \frac{ue^{-L}}{a^2} \left| (kH)^2 e^{\frac{kHL}{u}} \right|^2 w(0, t)^2 \\ & \quad + \frac{ue^{-L}}{4} \|w(t)\|^2 + \frac{e^L}{u} \left\| (kH)^2 e^{\frac{kH(L-\tau)}{u}} \right\|^2 w(0, t)^2. \end{aligned} \quad (14.78)$$

Plugging (14.78) into (14.74), one arrives at

$$\begin{aligned} \dot{V}(t) & \leq - \frac{e^L a^2}{4u} \theta_{\text{av}}^2(t) - \frac{ue^{-L}}{4} \int_0^L w^2(x, t) dx \\ & \quad - (c - c_0) w^2(0, t), \end{aligned} \quad (14.79)$$

where c_0 is defined as

$$c_0 = \frac{u}{2} - kH + \frac{ue^{-L}}{a^2} \left| (kH)^2 e^{\frac{kHL}{u}} \right|^2 + \frac{e^L}{u} \left\| (kH)^2 e^{\frac{kH(L-\tau)}{u}} \right\|^2, \quad (14.80)$$

where $\tau \in [0, L]$. An upper bound for c_0 can be obtained from lower and upper bounds of the unknown Hessian H . Therefore, by choosing c such that $c > c_0$, we obtain

$$\dot{V}(t) \leq -\mu V(t), \quad (14.81)$$

for some $\mu > 0$. Thus, the closed-loop system is exponentially stable in the sense of the L^2 norm.

By the invertibility of the transformation, there exist constants α_1 and α_2 such that the following inequality is obtained

$$\alpha_1 \Psi(t) \leq V(t) \leq \alpha_2 \Psi(t), \quad (14.82)$$

where

$$\Psi(t) \triangleq |\theta_{\text{av}}(t)|^2 + \int_0^L \epsilon_{\text{av}}^2(x, t) dx + \epsilon_{\text{av}}^2(L, t), \quad (14.83)$$

or equivalently,

$$\Psi(t) \triangleq |\theta_{\text{av}}(t - D)|^2 + \int_{t-D}^t U_{\text{av}}^2(\tau) d\tau + U_{\text{av}}^2(t). \quad (14.84)$$

Hence, with (14.81), we get

$$\Psi(t) \leq \frac{\alpha_2}{\alpha_1} e^{-\mu t} \Psi(0), \quad (14.85)$$

which completes the proof of exponential stability of the averaged system.

Averaging Theorem

The closed-loop system is written as

$$\dot{e}(t - D) = U(t - D), \quad (14.86)$$

$$\dot{U}(t) = -cU(t) + c \left\{ k \left(G(t) + \hat{H}(t) \int_{t-D}^t U(\tau) d\tau \right) \right\}. \quad (14.87)$$

Defining the state vector $z(t)$ as

$$z(t) = [e(t - D), U(t)]^T. \quad (14.88)$$

Substituting

$$\int_{t-D}^t U(\tau) d\tau = \int_{-D}^0 U(t + \tau) d\tau, \quad (14.89)$$

into (14.87), we can write the dynamics of z as a functional differential equation described by

$$\dot{z}(t) = f(\omega t, z_t), \quad (14.90)$$

where $z_t(\tau) = z(t + \tau)$ for $-D \leq \tau \leq 0$. According to (14.85), the origin of the average closed-loop system with transport PDE is exponentially stable. Applying the averaging theorem for infinite dimensional systems developed in [?], for ω sufficiently large, (14.58)–(14.60) has a unique exponentially stable periodic solution around its equilibrium satisfying (14.40).

Asymptotic Convergence to a Neighborhood of the Extremum (ρ^*, q^*)

By using the change of variables (14.62) and then integrating both sides of (14.58) within the interval $[t, \sigma + D]$, we have:

$$\theta(\sigma + D) = \theta(t) + \int_t^{\sigma+D} \epsilon(L, s) ds. \quad (14.91)$$

From (14.51), we can rewrite (14.91) in terms of U , namely

$$\theta(\sigma + D) = \theta(t) + \int_{t-D}^{\sigma} U(\tau) d\tau. \quad (14.92)$$

Define

$$\vartheta(\sigma) = \theta(\sigma + D), \quad \forall \sigma \in [t - D, t]. \quad (14.93)$$

Applying (14.92) to the above equation, we get

$$\vartheta(\sigma) = \vartheta(t - D) + \int_{t-D}^{\sigma} U(\tau) d\tau, \quad \forall \sigma \in [t - D, t]. \quad (14.94)$$

By applying the supremum norm on both sides of (14.94) and using Cauchy-Schwarz inequality, we have

$$\begin{aligned} \sup_{t-D \leq \sigma \leq t} |\vartheta(\sigma)| &= \sup_{t-D \leq \sigma \leq t} |\vartheta(t - D)| + \sup_{t-D \leq \sigma \leq t} \left| \int_{t-D}^{\sigma} U(\tau) d\tau \right| \\ &\leq |\vartheta(t - D)| + \sqrt{D} \left(\int_{t-D}^t U^2(\tau) d\tau \right)^{1/2} \\ &\leq (1 + \sqrt{D}) \left(|\vartheta(t - D)|^2 + \int_{t-D}^t U^2(\tau) d\tau \right)^{1/2}. \end{aligned} \quad (14.95)$$

From (14.95), it is straightforward to conclude that

$$\sup_{t-D \leq \sigma \leq t} |\vartheta(\sigma)| \leq (1 + \sqrt{D}) \left(|\vartheta(t - D)|^2 + \int_{t-D}^t U^2(\tau) d\tau \right)^{1/2}, \quad (14.96)$$

and thus

$$|\vartheta(t)| \leq (1 + \sqrt{D}) \left(|\tilde{\theta}(t - D)|^2 + \int_{t-D}^t U^2(\tau) d\tau \right)^{1/2}. \quad (14.97)$$

The above inequality (14.97) can be given in terms of the periodic solution $\vartheta^T(t - D)$, $U^T(\sigma)$, $\forall \sigma \in [t - D, t]$ as follows

$$\begin{aligned} |\vartheta(t)| &\leq (1 + \sqrt{D}) \left(|\vartheta(t - D) - \vartheta^T(t - D) + \vartheta^T(t - D)|^2 \right. \\ &\quad \left. + \int_{t-D}^t [U(\tau) - U^T(\tau) + U^T(\tau)]^2 d\tau \right)^{1/2}. \end{aligned} \quad (14.98)$$

Applying Young's inequality, the right-hand side of (14.98) and $|\vartheta(t)|$ becomes

$$|\vartheta(t)| \leq \sqrt{2} (1 + \sqrt{D}) \left(|\vartheta(t-D) - \vartheta^T(t-D)|^2 + |\vartheta^T(t-D)|^2 + \int_{t-D}^t [U(\tau) - U^T(\tau)]^2 d\tau + \int_{t-D}^t [U^T(\tau)]^2 d\tau \right)^{1/2}. \quad (14.99)$$

From the averaging theorem, we have the exponential convergence

$$\vartheta(t-D) - \vartheta^T(t-D) \rightarrow 0, \quad (14.100)$$

$$\int_{t-D}^t [U(\tau) - U^T(\tau)]^2 d\tau \rightarrow 0. \quad (14.101)$$

Hence we obtain

$$\limsup_{t \rightarrow +\infty} |\vartheta(t)| = \sqrt{2} (1 + \sqrt{D}) \left(|\vartheta^T(t-D)|^2 + \int_{t-D}^t [U^T(\tau)]^2 d\tau \right)^{1/2}. \quad (14.102)$$

From (14.40) and (14.102), we can write

$$\limsup_{t \rightarrow +\infty} |\vartheta(t)| = O(1/\omega). \quad (14.103)$$

From (14.25) and recalling that $\varrho(t) = \hat{\rho}(t) + a \sin(\omega(t+D))$ and $\theta(t) = e(t-D)$, one has that

$$\varrho(t) - \rho^* = \vartheta(t) + a \sin(\omega(t+D)). \quad (14.104)$$

Since the first term on the right-hand side of (14.104) is ultimately of order $O(1/\omega)$ and the second term is of order $O(a)$, then

$$\limsup_{t \rightarrow +\infty} |\varrho(t) - \rho^*| = O(a + 1/\omega). \quad (14.105)$$

Finally, from (14.23), we get (14.42) and the proof is complete. \square

14.5 Numerical Simulation

For our simulation, we choose the model parameters based on the data fitted for the LWR model in [?]. The maximum density is chosen to be $\rho_m = 6 \text{ lanes}/7.5 \text{ m} = 0.8 \text{ veh/m} = 800 \text{ veh/km}$, where 7.5 m is the sum of the average vehicle length of 5 m and a 50% safety distance. The maximum velocity is $v_m = 16.7 \text{ m/s} = 60 \text{ km/h}$. The fundamental diagram $Q(\rho)$ which results from these choices is used in the nonlinear LWR PDE model simulation which describes the traffic dynamics upstream of the bottleneck area. The maximum output flow, also known as road capacity of Zone C, is

$$q_c = \max_{0 \leq \rho \leq \rho_m} Q(\rho) = 3.2 \text{ veh/s} = 1920 \text{ veh/h/lane}. \quad (14.106)$$

The length of the freeway segment is $L = 100 \text{ m}$. If we consider a linearized LWR for Zone C, the characteristic speed is

$$u = Q'_c(\rho)|_{\rho=\rho_r=0.2 \text{ veh/m}} = 8.4 \text{ m/s}. \quad (14.107)$$

The time delay for the input to reach the bottleneck area is

$$D = \frac{L}{u} = 12 \text{ s}. \quad (14.108)$$

The fundamental diagram in the bottleneck area $Q_B(\rho)$, the optimal/critical density ρ^* , and the maximum output flow q^* are assumed to be unknown when there is a sudden lane-closure due to an accident or a lane closure. The following function and parameters are chosen for simulation purpose. For the bottleneck section Zone B, we consider the situation that only 4 out of 6 lanes still function. As a result, the road capacity reduces and we define the capacity reduction rate as $C_d = 40\%$ compared with Zone C. The outgoing flow $q_{\text{out}}(t) = Q(\rho(L, t))$ of the bottleneck area is approximated with

$$q_{\text{out}}(t) = q^* + \frac{H}{2} (\varrho(t - D) - \rho^*)^2, \quad (14.109)$$

where $\varrho_m = 0.48 \text{ veh/m}$ is the maximum density for reduced lanes in the bottleneck area and the same maximum velocity v_m is considered. The optimal/critical density ρ^* and maximum output flow q^* are

$$\rho^* = \frac{1}{2} \varrho_m = 0.24 \text{ veh/m}, \quad (14.110)$$

$$q^* = (1 - \Delta C) q_c = 1.92 \text{ veh/s}. \quad (14.111)$$

Compared with the capacity of Zone C q_c , there is a capacity drop ΔC for optimal flow rate q^* of the bottleneck area. The Hessian is obtained by taking second derivative of $q_{\text{out}}(t)$

$$H = -\frac{2v_f}{\varrho_m} = -69.5. \quad (14.112)$$

The Godunov scheme is employed for simulation of nonlinear LWR PDE model, as introduced in Chapter 1. The road segment is divided into spatial cell Δx and the solution is advanced in time step Δt , which satisfy the following CFL condition $u_{\text{max}} \frac{\Delta t}{\Delta x} < 1$, where u_{max} is the maximum characteristic speed. We choose the spatial cell $\Delta x = 0.05 \text{ m}$ sufficiently small so that numerical errors are negligibly small relative to the errors of the model.

The simulation result of the closed-loop system with ES control is shown in Fig. 14.4-14.7. The parameters of the sinusoidal input and the designed controller

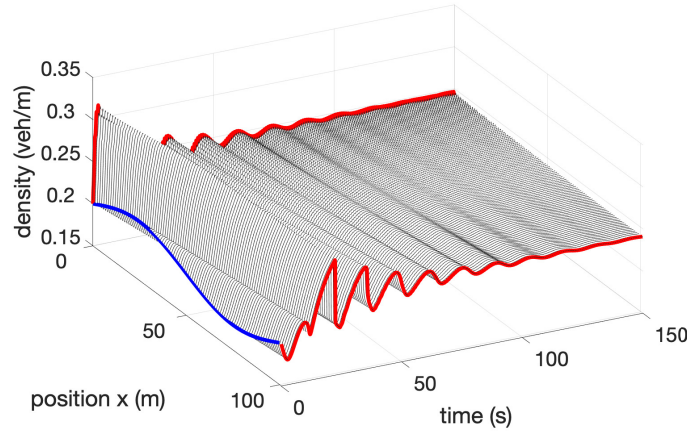


Fig. 14.4 Traffic density state evolution $\rho(x, t)$ of nonlinear LWR model in Zone C

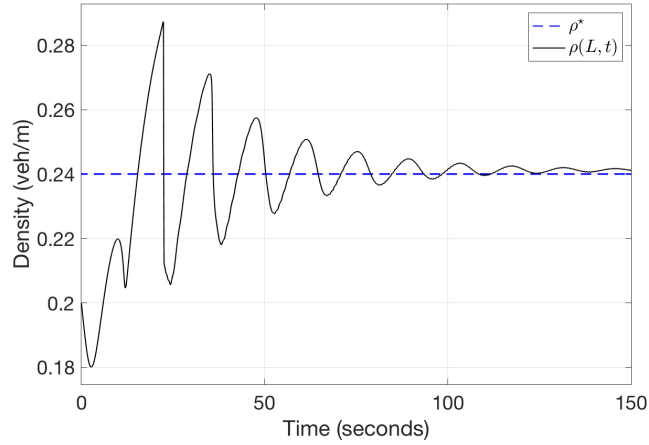


Fig. 14.5 Traffic density $\rho(L, t)$ at the outlet of Zone C by nonlinear LWR model which is the input density for bottleneck area

are chosen to be $\omega = 2.75\pi$, $a = 0.05$, $c = 50$, $K = 0.005$. The adaptation gain is k , while a and ω are used in the computation of the frequencies and amplitudes for the perturbation signals $M(t)$, $N(t)$ in (14.28) and $S(t)$ in (14.46). The speed of convergence and the ultimate residual sets of the ES algorithm are influenced by the values of k , a and ω .

The evolution of the density PDE state $\rho(x, t)$ modeled by the LWR model (14.1) is shown in Fig. 14.4. The inlet density boundary input and outlet boundary value are highlighted with color red and the initial condition is highlighted with color blue. One can observe that density value $\rho(L, t)$ in Fig. 14.5 converges to a neighborhood

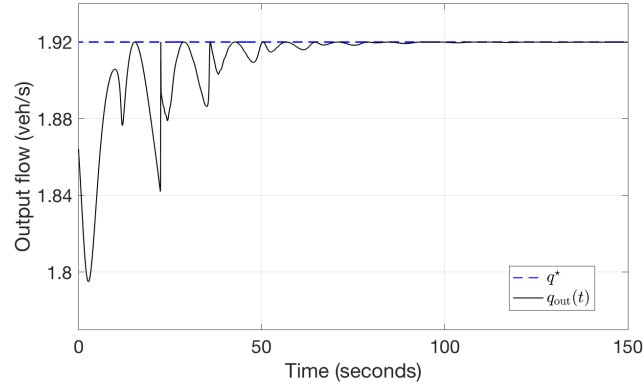


Fig. 14.6 Outgoing traffic flow of the bottleneck area $q_{\text{out}}(t)$ which is also the output flow for bottleneck area and the optimal value of outgoing flow q^*

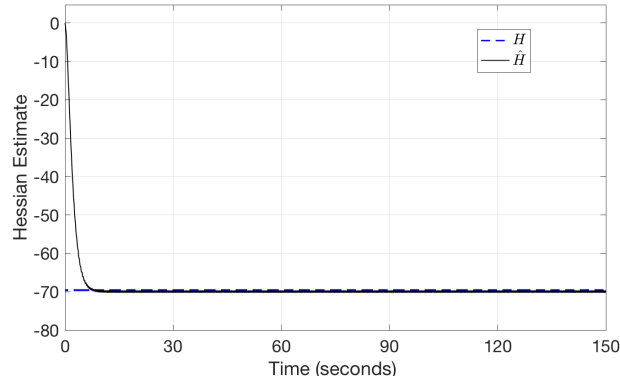


Fig. 14.7 Hessian estimate $\hat{H}(t)$ of the ES control and prescribed Hessian value H

of the optimal value $\rho^* = 0.24$ veh/m and the output flow of the bottleneck in Fig. 14.6 converges to a neighborhood of the extremum point $q^* = 1.92$ veh/s. The Hessian estimate converges to the prescribed value -69.5 in Fig. 14.7. The convergence to optimal values is achieved in 40 s. In contrast, if we do not employ ES control for input density and the incoming flow depends only on upstream traffic. The open-loop system is shown in Fig. 14.8. The evolution of outgoing flow at the bottleneck area is run for 150 s. The outgoing flow of the bottleneck area keeps decreasing and, therefore, congestion at the bottleneck area is getting worse, until a bumper-to-bumper jam results.

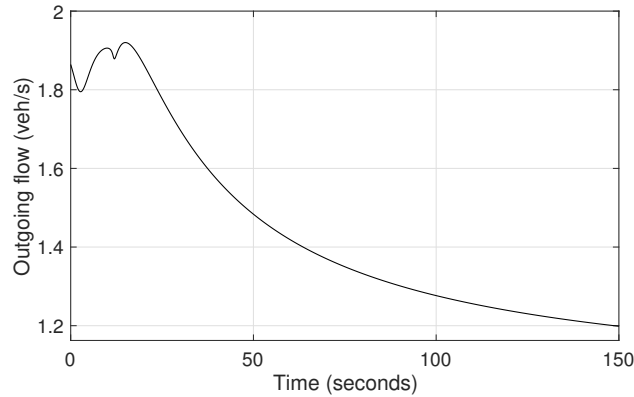


Fig. 14.8 Output traffic flow of the bottleneck area without ES Control

14.6 Notes and References

When there are uphill, curvatures, or lane-drops further downstream on freeway, a bottleneck with capacity drop appears, leading to a reduction of the total discharging flow rate from the bottleneck area and delay of travel time for the upstream traffic. Traffic congestion then forms upstream of the bottleneck as the upstream demand increases during the peak hour [?, ?, ?, ?]. Various models have been proposed to describe the capacity drop phenomenon of the bottleneck including the first-order traffic flow models [?], discontinuous fundamental diagram in [?] and kinematic wave model in [?], which usually assume some prior knowledge of the traffic condition at the bottleneck area. The fundamental diagram of the bottleneck area is incorporated with the upstream traffic dynamics which has been modeled with the LWR model, a first-order macroscopic PDE in [?], the cell transmission model (CTM) in [?] and the link queue model [?]. The traffic flow is conserved through the bottleneck. We adopt the LWR-based model proposed in [?] due to its simplicity and conciseness in capturing the capacity drop mechanism.

The traffic bottleneck congestion problem has been tackled by various traffic control approaches in recent years. Many studies focus on developing control strategies for ramp metering and VSL to avoid the capacity drop and to maximize the discharging flow rate at the bottleneck. For distant downstream bottleneck problem, Proportional-Integral (PI) local ramp metering strategy was developed by [?] to improve performance of downstream mainline traffic flow. A Proportional-Integral-Derivative (PID) controller was proposed in [?] for VSL control of lane-drop bottleneck. In [?], the VSL control design was proposed to maximize the traffic flow at an active bottleneck using model predictive control approach. The density dynamics is described with the CTM. The PDE boundary control of traffic with lane-drop problem was investigated by [?]. The traffic dynamics on a stretch of freeway upstream of the bottleneck area is governed by the LWR model. The predictor feedback control

law is designed for the ramp metering at the inlet of the freeway so that the density at bottleneck area is regulated to a desired equilibrium.

ES control has been a major segment of the field of control engineering over the past two decades, since the proof of the algorithm's stability in [?], where the convergence of the cost function to a neighborhood of the optimal value was established by means of averaging analysis and singular perturbation. About ten thousand papers on this topic have been published since, among which we can mention but a few on methodological advances [?, ?, ?, ?, ?, ?, ?, ?]. ES approach relies on a small periodic excitation, usually sinusoidal, to perturb the parameters being tuned and deduce an estimate of the gradient of the nonlinear map using this perturbation.

The result of this chapter is the first where ES is applied to a macroscopic traffic model. Besides traffic applications, the ES control algorithms has been successfully applied to many other applications including electromechanical valve actuators [?], in fuel-cell power maximization [?] and in trajectory optimization of high-degree-of-freedom robot [?].

The problem of ES control in the presence of delays is solved in [?]. Employing this methodology, we develop an ES controller with predictor-based feedback for delay compensation, which is applied to the bottleneck problem in this chapter to find an optimal density input for freeway traffic when there is a downstream bottleneck.

To prevent traffic flow in bottleneck area overflowing the road capacity and furthermore causing congestion upstream in the freeway segment, the incoming traffic density at inlet of the freeway segment is regulated. The control design is achieved with delay compensation for ES control considering the upstream traffic is governed by the linearized LWR model. The optimal density and flow are achieved in the bottleneck area. The theoretical result is validated in simulation with the control design being applied to the nonlinear LWR PDE model along with an unknown fundamental diagram.

There is one subtle issue regarding the delay-compensated ES for flow maximization through a bottleneck. The maximizing flow through the bottleneck ρ^* is unknown. This density determines the actual delay $D(\rho^*)$ through the freeway, which is determined by linearizing the LWR nonlinear PDE around the density ρ^* , computing the wave speed in the downstream direction of the resulting free flow regime, and computing the resulting delay for the given length L of the distance between the ramp and the bottleneck. However, the reader will have noticed that in our LWR linearization, as well as in the implementation of our delay-compensated ES scheme, we had used a density ρ_r for the freeway. This density ρ_r may be either larger or smaller than ρ^* . It is virtually impossible for ρ_r , employed in the ES scheme, to be accidentally equal to the unknown ρ^* . To put it another way, there is a mismatch between the actual delay $D(\rho^*)$ of the freeway and the delay $D(\rho_r)$ used in the ES scheme. What is the consequence of this delay mismatch for the operation of the predictor part of the ES scheme? This is a classical question of robustness to delay mismatch for predictor feedback. This question was positively resolved in [?], establishing robustness to delay mismatch. More specifically, whether the assumed delay

exceeds the actual delay a bit or is a bit smaller than the actual delay, the predictor is stabilizing. This robustness result holds in both spatial/temporal L^2 norm and the H^1 norm. In the context of our ES scheme for the bottleneck, whether ρ_r exceeds ρ^* a bit or is a bit smaller than ρ^* , the ES scheme is guaranteed to regulate the flow through the bottleneck to its maximum value. This robustness analysis would be performed on the averaged version of the system, using backstepping and a Lyapunov functional. The fact that the mismatch between ρ_r and ρ^* does not destroy the predictor-based ES algorithm is evident from Figures 14.4 and 14.5. In our simulation, $\rho^* = 0.24$ and $\rho_r = 0.2$, quite a significant difference. In spite of the resulting delay mismatch, where the actual delay $D(\rho^*)$ is underestimated by using the shorter delay $D(\rho_r)$ in the ES scheme, we can see that the density has been regulated to the optimal value for the bottleneck, $\rho^* = 0.24$, through both the bottleneck, as shown in Figures 14.5, and through the main freeway, as shown in Figures 14.4.

The result in this chapter can be extended to multi-lane bottleneck problem with multiple distinct delays. It is also of research interest to develop ES control with bounded update rates [?] under input delays exhibited through the LWR model and to develop a stochastic version of the algorithm presented in the chapter by applying the results from [?] and [?]. To further demonstrate the impact of this work for traffic application and understand how the proposed extremum seeking controller works in practice, it is of research interest to validate this result with traffic field data and test it with microscopic simulator.

Glossary

Use the template *glossary.tex* together with the Springer document class SVMono (monograph-type books) or SVMult (edited books) to style your glossary in the Springer layout.

glossary term Write here the description of the glossary term. Write here the description of the glossary term. Write here the description of the glossary term.

glossary term Write here the description of the glossary term. Write here the description of the glossary term. Write here the description of the glossary term.

glossary term Write here the description of the glossary term. Write here the description of the glossary term. Write here the description of the glossary term.

glossary term Write here the description of the glossary term. Write here the description of the glossary term. Write here the description of the glossary term.

glossary term Write here the description of the glossary term. Write here the description of the glossary term. Write here the description of the glossary term.

Solutions

Problems of Chapter ??

?? The solution is revealed here.

?? Problem Heading

- (a) The solution of first part is revealed here.
- (b) The solution of second part is revealed here.